Advances in Science, Technology & Innovation
IEREK Interdisciplinary Series for Sustainable Development

Attila Çiner · Santanu Banerjee · Federico Lucci · Ahmed E. Radwan · Afroz Ahmad Shah · Domenico M. Doronzo · Zakaria Hamimi · Wilfried Bauer *Editors*

Recent Research on Sedimentology, Stratigraphy, Paleontology, Tectonics, Geochemistry, Volcanology and Petroleum Geology

Proceedings of the 1st MedGU, Istanbul 2021 (Volume 2)

IEREK RESEARCH & KNOWLEDGE ENRICHMENT

Springer

Advances in Science, Technology & Innovation

IEREK Interdisciplinary Series for Sustainable Development

Advances in Science, Technology & Innovation (ASTI) is a series of peer-reviewed books based on important emerging research that redefines the current disciplinary boundaries in science, technology and innovation (STI) in order to develop integrated concepts for sustainable development. It not only discusses the progress made towards securing more resources, allocating smarter solutions, and rebalancing the relationship between nature and people, but also provides in-depth insights from comprehensive research that addresses the **17 sustainable development goals (SDGs)** as set out by the UN for 2030.

The series draws on the best research papers from various IEREK and other international conferences to promote the creation and development of viable solutions for a **sustainable future and a positive societal** transformation with the help of integrated and innovative science-based approaches. Including interdisciplinary contributions, it presents innovative approaches and highlights how they can best support both economic and sustainable development, through better use of data, more effective institutions, and global, local and individual action, for the welfare of all societies.

The series particularly features conceptual and empirical contributions from various interrelated fields of science, technology and innovation, with an emphasis on digital transformation, that focus on providing practical solutions to **ensure food, water and energy security to achieve the SDGs.** It also presents new case studies offering concrete examples of how to resolve sustainable urbanization and environmental issues in different regions of the world.

The series is intended for professionals in research and teaching, consultancies and industry, and government and international organizations. Published in collaboration with IEREK, the Springer ASTI series will acquaint readers with essential new studies in STI for sustainable development.

ASTI series has now been accepted for Scopus (September 2020). All content published in this series will start appearing on the Scopus site in early 2021.

Attila Çiner • Santanu Banerjee •
Federico Lucci • Ahmed E. Radwan •
Afroz Ahmad Shah •
Domenico M. Doronzo •
Zakaria Hamimi • Wilfried Bauer
Editors

Recent Research on Sedimentology, Stratigraphy, Paleontology, Tectonics, Geochemistry, Volcanology and Petroleum Geology

Proceedings of the 1st MedGU, Istanbul 2021 (Volume 2)

Springer

ISSN 2522-8714 ISSN 2522-8722 (electronic)
Advances in Science, Technology & Innovation
IEREK Interdisciplinary Series for Sustainable Development
ISBN 978-3-031-43221-7 ISBN 978-3-031-43222-4 (eBook)
https://doi.org/10.1007/978-3-031-43222-4

This Springer imprint is published by the registered company Springer Nature Switzerland AG
The registered company address is: Gewerbestrasse 11, 6330 Cham, Switzerland

Paper in this product is recyclable.

About the Conference

About MedGU

Steps toward the creation of a Mediterranean Geosciences Union (MedGU)

Mediterranean Geosciences Union (MedGU) aims to create a unique federation that brings together and represents the Mediterranean geoscience community specializing in the areas of Earth, planetary and space sciences.

MedGU will be structured along the lines of American Geophysical Union (AGU) and European Geosciences Union (EGU).

The plan is to establish a large organization for the Mediterranean region that is more influential than any one local geoscience society with the objective of fostering fundamental geoscience research, as well as applied research that addresses key societal and environmental challenges.

MedGU's overarching vision is to contribute to the realization of a sustainable future for humanity and for the planet.

The creation of this union will give the Earth sciences more influence in policy-making and in the implementation of solutions to preserve the natural environment and to create more sustainable societies for the people living in the Mediterranean region. It is hoped that the union will also provide opportunities to Mediterranean geoscientists to undertake interdisciplinary collaborative research. MedGU plans to recognize the work of the most active geoscientists with a number of awards and medals.

Although MedGU has not yet been officially inaugurated, its first annual meeting is planned for November 2021 in Istanbul. This will provide a forum to achieve a consensus for the formation of this non-profit international union of geoscientists. Membership will be open to individuals who have a professional engagement with the Earth, planetary and space sciences, and related studies, including students and retired seniors.

Nabil Khelifi and Attila Çiner have taken an ambitious approach to the launch of the first MedGU Annual Meeting 2021 and hope to develop it in the near future into the largest international geoscience event in the Mediterranean and the broader MENA region. Its mission is to support geoscientists based in this region by establishing a Global Geoscience Congress.

It is expected that hundreds of participants from all over the world will attend this first MedGU Annual Meeting 2021, making it one of the largest and most prominent geosciences

events in the region. So far, over 1300 abstracts have been submitted from 95 countries. The meeting's sessions will cover a wide range of topics with more details available on the conference tracks.

This first 2021 Annual Meeting will have a "hybrid" format, with both in-person and virtual participation. Springer, its official partner, will publish the proceedings in a book series (indexed in Scopus) as well as a number of special issues in diverse scientific journals (for more details, see Publications). The official journal of MedGU is Mediterranean Geoscience Reviews (Springer).

Conference Tracks

The scientific committee of the MedGU invites research papers on all cross-cutting themes of Earth sciences, with a main focus on the following 16 conference tracks:

- Track 1. Atmospheric Sciences, Meteorology, Climatology, Oceanography
- Track 2. Biogeochemistry, Geobiology, Geoecology, Geoagronomy
- Track 3. Earthquake Seismology and Geodesy
- Track 4. Environmental Earth Sciences
- Track 5. Applied and Theoretical Geophysics
- Track 6. Geo-Informatics and Remote Sensing
- Track 7. Geochemistry, Mineralogy, Petrology, Volcanology
- Track 8. Geological Engineering, Geotechnical Engineering
- Track 9. Geomorphology, Geography, Soil Science, Glaciology, Geoarchaeology, Geoheritage
- Track 10. Hydrology, Hydrogeology, Hydrochemistry
- Track 11. Marine Geosciences, Historical Geology, Paleoceanography, Paleoclimatology
- Track 12. Numerical and Analytical Methods in Mining Sciences and Geomechanics
- Track 13. Petroleum and Energy Engineering, Petroleum Geochemistry
- Track 14. Sedimentology, Stratigraphy, Paleontology, Geochronology
- Track 15. Structural Geology, Tectonics and Geodynamics, Petroleum Geology
- Track 16. Caves and Karst, a special session on the occasion of International Year of Caves and Karst

About the Conference Steering Committee

Executive Committee

Honorary Chair

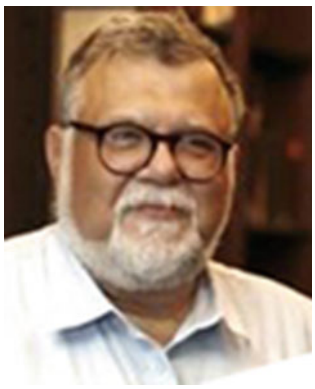

A. M. Celâl Sengör
Associate Editor, Mediterranean Geosciences Reviews (Springer)
Eurasia Institute of Earth Sciences,
Istanbul Technical University, Istanbul, Turkey

Organizing Chair

Attila Çiner
MedGU (Interim) President,
Founding Editor-in-Chief, *Mediterranean Geosciences Reviews* (Springer),
Chief Editor—Tracks 11 and 14, *Arabian Journal of Geosciences* (Springer),
Eurasia Institute of Earth Sciences,
Istanbul Technical University, Turkey

Conference Manager

Mohamed Sahbi Moalla
Performer—The Leading Conference Organizer, Tunisia,
Journal Coordinator, *Euro-Mediterranean Journal for Environmental Integration* (Springer),
ISET, University of Sfax, Tunisia

Conference Support

Mourad Amer
Founder and CEO of IEREK,
Editor of ASTI Series (Springer/IEREK),
IEREK, Alexandria, Egypt

Conference Supervisor

Nabil Khelifi
Senior Publishing Editor, MENA Program,
MedGU-21 Supervisor,
Springer, a part of Springer Nature, Germany

Local Organizing Team

Attila Çiner, Eurasia Institute of Earth Sciences, Istanbul Technical University, Turkey
Cengiz Yildirim, Eurasia Institute of Earth Sciences, Istanbul Technical University, Turkey
M. Akif Sarikaya, Eurasia Institute of Earth Sciences, Istanbul Technical University, Turkey
Tolga Gorum, Eurasia Institute of Earth Sciences, Istanbul Technical University, Turkey
Ömer Yetemen, Eurasia Institute of Earth Sciences, Istanbul Technical University, Turkey
Mustafa Üstüner, Artvin Çoruh University, Artvin, Turkey

Online Organizing Team

M. Sahbi Moalla, Performer—The Leading Conference Organizer, Tunisia
Melek Rebai, Performer—The Leading Conference Organizer, Tunisia
M. Bassem Abdelhedi, Performer—The Leading Conference Organizer, Tunisia
Oumayma Abidi, Performer—The Leading Conference Organizer, Tunisia
Toka M. Amer, IEREK—International Experts for Research Enrichment and Knowledge Exchange, Egypt

Advisory Committee

Hans Thybo
President of International Lithosphere Program (ILP),
Editor-in-Chief of *Earth and Planetary Science Letters* (EPSL),
Professor at:

- Eurasia Institute of Earth Sciences, Istanbul Technical University Turkey
- Center for Earth Evolution and Dynamics, University of Oslo, Norway

A. M. Celâl Sengör
Associate Editor, *Mediterranean Geosciences Reviews* (Springer),
Eurasia Institute of Earth Sciences, Istanbul Technical University, Istanbul, Turkey

François Roure
Chief Editor—Track 15,
Arabian Journal of Geosciences (Springer),
IFP—Energies Nouvelles, France

Giovanni Bertotti
Associate Editor, *Mediterranean Geosciences Reviews* (Springer),
Geoscience and Engineering, Delft University of Technology, The Netherlands

Abdullah Al-Amri
Founder and Editor-in-Chief,
Arabian Journal of Geosciences (Springer),
King Saud University, Saudi Arabia

Akiça Bahri
Director for Africa at the International Water Management Institute (IWMI), Ghana (2005–2010),
Coordinator of the African Water Facility (AWF) at the African Development Bank (2010–2015),
Director of Research at the National Research Institute for Agricultural Engineering, Water, and Forestry (INRGREF), Tunisia (since 2016),
Professor at the National Agricultural Institute of Tunisia (INAT), Tunisia (since 2017),
Awardee of the International Water Association (IWA) Women in Water Prize (2018),
Associate Editor, *Euro-Mediterranean Journal for Environmental Integration* (Springer) (since 2019),
Minister of Agriculture, Water Resources and Fisheries in Tunisia (2019–2020)

Program Committee

Mustapha Meghraoui
Editorial Board Member, *Mediterranean Geosciences Reviews* (Springer),
Editor of *Arabian Journal of Geosciences* (Springer),
IPG Strasbourg, France

Sami Khomsi
University Tunis El-Manar, Tunis, Tunisia, and King Abdulaziz University, Jeddah, Saudi Arabia

Scientific Committee

François Roure
Chief Editor—Track 15,
Arabian Journal of Geosciences (Springer),
IFP—Energies Nouvelles, France

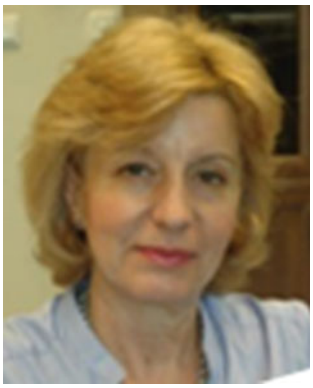

Anastasia Kiratzi
Professor of Seismology,
Faculty of Sciences, Aristotle University of Thessaloniki, Greece

Broder Merkel
Chief Editor—Track 10,
Arabian Journal of Geosciences (Springer),
Associate Editor of *Environmental Earth Science* (Springer),
Publisher of *Freiberg Online Geoscience* (FOG),
Institute of Geology, Technische Universität Bergakademie, Freiberg, Germany

Elena Xoplaki
Chief Editor, *Euro-Mediterranean Journal for Environmental Integration* (Springer),
Justus-Liebig-University Giessen, Germany

Publications Committee

Chair

Attila Çiner
MedGU (Interim) President,
Founding Editor-in-Chief, *Mediterranean Geosciences Reviews* (Springer),
Chief Editor—Tracks 11 and 14, *Arabian Journal of Geosciences* (Springer),
Eurasia Institute of Earth Sciences, Istanbul Technical University, Turkey

Zeynal Abiddin Erguler
Chief Editor—Track 8,
Arabian Journal of Geosciences (Springer),
Dumlupinar University, Kutahya, Turkey

Alina Polonia
The National Research Council (CNR),
Institute of Marine Sciences (ISMAR),
Bologna, Italy

Amjad Kallel
Chief Editor—Track 4,
Arabian Journal of Geosciences (Springer),
Managing and Development Editor, *Euro-Mediterranean Journal for Environmental Integration* (Springer),
ENIS, University of Sfax, Tunisia

Mourad Bezzeghoud
School of Sciences and Technology (ECT),
Insititute of Earth Sciences (IIFA),
University of Évora, Portugal

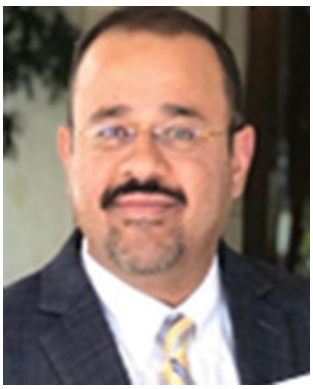

Hesham El-Askary
Professor of Remote Sensing and Earth Systems Science,
Editor of *Arabian Journal of Geosciences* (Springer),
Director Computational and Data Sciences Graduate Programs,
Center of Excellence in Earth Systems Modeling and Observations,
Schmid College of Science and Technology, Chapman University, USA

Zakaria Hamimi
President of ArabGU,
IAGETH VP for Africa and IAGETH National Chapter for Egypt,
Editor of *Arabian Journal of Geosciences* (Springer),
Professor, Benha University, Benha, Egypt

Outreach Committee

Hasnaa Chennaoui Aoudjehane
Member of the Nomenclature Committee of the Meteoritical Society,
Laureate, "Prix Paul Doistau–Émile Blutet" from the French Academy of Sciences,
Editor of *Arabian Journal of Geosciences* (Springer),
Professor, Hassan II University of Casablanca, Morocco

Catherine Kuzucuoglu
Associate Editor, *Mediterranean Geosciences Reviews* (Springer),
Research Director Emeritus,
CNRS, Laboratoire de Géographie Physique,
UMR 8591, Meudon, France

Preface

This proceedings volume consists of 57 papers accepted and presented during the 1st Mediterranean Geosciences Union (MedGU-21) Conference organized in Istanbul, Turkey, in 2021 under the auspices of Springer Nature. Here, we assembled a set of contributions investigating, through multidisciplinary and advanced methodologies, the most recent advances in the comprehension of geodynamic scenarios, geological processes and linkage with the anthropic environment.

The first part is related to Sedimentology, Stratigraphy and Paleontology. It contains 15 studies dealing with depositional environments, chronostratigraphy, chemostratigraphy, fossil records, paleoecology and paleoenvironment reconstruction.

Under the Geochemistry, Mineralogy, Petrology and Volcanology part, 19 papers address petrogenetic studies, geochronological investigations, ore geology works, mineralogical characterizations, hydrothermal and geothermal contributions and volcanological findings. Additionally, this section also contains contributions investigating volcanological hazards and environmental recovery.

The third part includes five articles focused on Structural Geology, Tectonics and Geodynamics, exploring the Meso-Cenozoic scenario from the western Mediterranean to the Iranian Makran, passing through the Balkans and Turkey.

Finally, the fourth part, with 18 contributions, is fully dedicated to the advancements in Petroleum and Energy Engineering and Petroleum Geology.

Although more than half of the inputs come from the Mediterranean region, many other countries around the globe also actively participated in contributing to this volume. This collection of studies is related to disciplines spanning from sedimentology and paleontology to structural geology and geodynamics, from petrology and mineralogy to volcanology, from geochemistry to ore geology and petroleum geology. Therefore, it could represent a privileged point of view for a better understanding of the Earth System.

The book is of interest to all researchers, practitioners and students in the abovementioned fields, presenting an updated complementary view on field studies, laboratory analyses and modeling aimed at better quantifying process-product binomials in geosciences.

Istanbul, Türkiye — Attila Çiner
Mumbai, India — Santanu Banerjee
Bari, Italy — Federico Lucci
Kraków, Poland — Ahmed E. Radwan
Gadong, Brunei — Afroz Ahmad Shah
Rome, Italy — Domenico M. Doronzo
Benha, Egypt — Zakaria Hamimi
Halban, Oman — Wilfried Bauer

July 2022

Contents

About the Editors

Attila Çiner is a sedimentology and Quaternary geology professor at the Eurasia Institute of Earth Sciences at Istanbul Technical University, Turkey. After graduating from the Middle East Technical University in Ankara (1985), he obtained his M.Sc. degree at the University of Toledo, USA (1988), and his Ph.D. at the University of Strasbourg, France (1992). He works on the tectono-sedimentary evolution of basins and Quaternary depositional systems such as moraines, fluvial terraces, alluvial fans, and deltas. He uses cosmogenic nuclides to date these deposits. He primarily focuses on the glacial deposits and landscapes and tries to understand paleoclimatic and paleoenvironmental changes since the Last Glacial Maximum. Lastly, he was part of the Turkish Antarctic Expedition. He spent two months working on the site recognition and decision of the future Turkish scientific research station to be implemented on the continent. He is the editor-in-chief of *Mediterranean Geoscience Reviews* and the chief editor of *Arabian Journal of Geosciences*, both published by Springer. He has published more than 100 peer-reviewed articles and chapters.

Santanu Banerjee currently works as a professor at the Department of Earth Sciences, Indian Institute of Technology Bombay. He does research in sedimentology and petroleum geology. His research areas include authigenic iron silicates, microbially induced sedimentary structures, basin analysis, provenance interpretations and alternate potash fertilizer. He is on the editorial board of *Journal of Palaeogeography*, *Minerals*, *Arabian Journal of Geosciences* and *Journal of Earth Systems Science*. He has published more than 150 papers in SCI-indexed journals, which have received more than 5000 citations.

Federico Lucci holds a B.Sc. in Earth Sciences (2004), an M.Sc. in Earth Sciences (2006) and a Ph.D. degree in Earth Sciences (2010) from Università degli Studi Roma Tre (Italy). Since February 2022, He is a researcher (RTDb) of petrography and petrology at the University of Bari, where he is dealing with the teaching course petrography of metamorphic rocks. His research is focused on modeling and timing of magmatic complexes as key constraint for understanding regional tectonics and geodynamic scenarios, through a multidisciplinary approach that integrates field survey, rock fabric characterization, mineral chemistry, geochemistry, geochronology, inverse and forward thermobarometry and FC-AFC-mixing modeling.

Dr. Ahmed E. Radwan is an adjunct professor at the Institute of Geological Sciences of the Jagiellonian University (Poland). He has academic and industrial experience, since he obtained his Ph.D. in geophysics at Sohag University, Egypt, besides his proficient work in the oil and gas industry as the department head at the exploration department of the Gulf of Suez petroleum company (Gupco), Egypt. As a postdoctoral research scientist, he attended Innsbruck University in Austria in 2019. In 2020, he joined the Jagiellonian University in Poland. Despite his youth, he has received numerous awards from international organizations such as the International Union of Geological Sciences (IUGS), the Geochemical Society (GS), the Clay Minerals Society (CMS), the Austrian Forschungsgemeinschaft (FG), the Narodowa Agencja Wymiany Akademickiej (NAWA), the Austrian Federal Ministry of Education, Science, and Research (BMBWF) and petroleum companies. He has authored more than 90 papers in highly indexed international peer-reviewed journals, published four chapters and presented at numerous international conferences. He is an associate editor in *Asian Earth Sciences*, *Marine and Petroleum Geology*, *Geoenergy Sciences and Engineering*, *Petroleum Exploration* and *Production Technology*, the *Geological Journal*, *Energy Geosciences and Petroleum Research*, in addition to being an editorial board member of *Unconventional Resources*. He is a book reviewer and a research article reviewer for several publishers and journals, and he organizes many special issues in different journals with the leading publishers. His research interests focused on multidisciplinary research integrating geosciences (geophysics, geochemistry and geology), petroleum engineering and reservoir engineering, as follows: (1) Geology areas include petroleum geology, reservoir characterization, sedimentology, facies analysis, depositional environment, diagenesis, paleoenvironment interpretations, subsurface analysis, basin analysis, reservoir quality, fluid flow, fractures, formation evaluation and unconventional and conventional resources; (2) petroleum engineering (petroleum geomechanics, drilling, fluids and casing design); (3) reservoir engineering (reservoir geology and geophysics, reservoir damage, production optimization, water

flooding, stimulations, fluid flow and enhanced recovery); (4) the geophysics fields of study (ex. formation evaluation, petrophysics, borehole geophysics and rock typing); (5) geochemistry fields of study include geochemical characterization, basin modeling, petroleum systems and isotope analysis; (6) petroleum geomechanics (pore pressure, wellbore stability, in situ stress orientation and magnitudes); (7) machine learning applications in the energy industry; (8) energy storage.

Afroz Ahmad Shah is an assistant professor of Structural Geology at the Department of Geosciences, Universiti of Brunei Darussalam (UBD). He completed Ph.D. at James Cook University, Australia, in 2010, a postdoctorate at Earth Observatory of Singapore in 2013 and joined his first academic job as a senior lecturer of Structural Geology at Curtin Sarawak, Miri, Malaysia, before joining UBD. His research mainly involves the brittle deformation of lithospheric plates, focusing on earthquake-causing faults in South and Southeast Asia. It also includes floods, landslides and land subsidence hazards. He works on earthquake science education and outreach and frequently writes in newspapers, magazines and blogs.

Dr. Domenico M. Doronzo holds a B.Sc., a M.Sc. and a Ph.D. degrees in Earth Sciences from Università degli Studi di Bari Aldo Moro, Italy. Investigation specialties related to those degrees are physical volcanology, experimental and computational fluid dynamics, petrology and natural hazards. Then, he has worked in volcanology and sedimentology, fluid dynamics and combustion, environmental sciences and rock physics in the USA, Mexico, Spain and Italy. Currently, he is a contract researcher at Istituto Nazionale di Geofisica e Vulcanologia, Italy. Particularly, he has received the Rittmann Medal from Associazione Italiana di Vulcanologia and Istituto Nazionale di Geofisica e Vulcanologia, which is assigned to the best young Italian volcanologist. His research interests focus on integrating theory, field measurements, numerical modeling, laboratory and outdoor experiments to study geological processes and products in volcanic areas (Vesuvio, Campi Flegrei, Etna, Vulcano, Colli Albani, Tenerife, Altiplano Puna, Colima) from fluid dynamic and natural hazard perspectives. He studies specifically pyroclastic energy currents, pre-eruption conditions, ground deformations, eruption forecasting, lahars and debris flows, flow-building interactions, sand and dust storms, turbidity currents, man-made environmental phenomena and geo-resources. Recently, he has published the first comprehensive review on the famous 79 CE "Pompeii" Plinian eruption of Vesuvius by means of a multidisciplinary approach in volcanology. He is a chief editor of the *Arabian Journal of Geosciences* responsible for evaluating submissions in the fields of Geochemistry, Mineralogy, Petrology and Volcanology.

Zakaria Hamimi is a tectonics and structural geologist, currently at Benha University in Egypt, and has worked previously at Sana'a University, Yemen (1995–1998) and King Abdulaziz University, Saudi Arabia (2003–2013). He obtained a B.Sc. (distinction with Honors) in 1984 at Assiut University, an M.Sc. in 1988 at Zagazig University and a Ph.D. in 1992 in Structural Geology and Tectonics at Cairo University. His research focuses on the tectonic evolution of the Arabian-Nubian Shield via structural/microstructural, paleostress and strain studies, aligned with geological mapping, geomorphology and remote sensing methodologies. His research output exceeds 80 research publications in national and international journals. He is the president and a founding member of the Arabian Geosciences Union, since 2012. He has been awarded the medal of the Egyptian Geological Society of Egypt in 2015 and the medal of the Arab Mining and Petroleum Association in 2016. His services to the profession include his roles as an associate editor of the *Egyptian Journal of Geology* (1998–2002) and the *Arabian Journal of Geosciences* (2016–now); a member of the Egyptian Universities Promotion Committee, Supreme Council for Universities, Egypt (2016–2019); the secretary of the National Committee for Geological Sciences, Academy of Scientific Research and Technology (2016–2019), and later nominated for the president of this Academic Committee in 2020; and the IUGS-representative for Egypt in Cape Town 2016 and Thailand 2017. He co-edited several special issues and five Springer's books: (1) *The Geology of Arab World—An Overview* (2019) https://www.springer.com/gp/book/9783319967936, (2) *The Geology of Egypt* (2020) https://www.springer.com/gp/book/9783030152642, (3) *The Geology of Egyptian Nubian Shield* (2021) https://www.springer.com/gp/book/9783030497705, (4) *The Geology of the Arabian-Nubian Shield* (2021) https://www.springer.com/gp/book/9783030729943, (5) *The Phanerozoic Geology and Natural Resources of Egypt* (in press-2023) Part of the book series: Advances in Science, Technology & Innovation (ASTI) https://link.springer.com/book/9783030956363.

Wilfried Bauer (b. 1963) obtained his diploma (1991) and Ph.D. (1995) in Geology from RWTH Aachen University. He continued his work in Aachen from 1995 to 2002 as a postdoc and later as a research assistant with a scientific focus on the structural geology, metamorphic petrology, mineral chemistry and geochronology of Precambrian metamorphic rocks in high-grade gneiss terranes of the East Antarctic Craton. As a member of an interdisciplinary team, he worked in 1997 and 1998 on balanced cross sections of the West-Uralian fold-and-thrust belt (EUROPROBE—URSEIS section) with special emphasis on the deformation of the Proterozoic crystalline basement within the southern Ural Mountains. In 2004, he worked for the commercial branch of the Norwegian Geological Survey in a mapping project that covered four

sheets of the geological map 1:250,000 of Mozambique. From 2005 to 2007, he held a position as a senior survey geologist at the British Geological Survey and was the deputy leader of a team that mapped and compiled 40 sheets of the geological map of Madagascar 1:100,000 in a World Bank-funded project. Between 2007 and 2014, he was the head of the Research and Development section of an Australian exploration company, focused on the exploration of gold, bauxite and graphite in Madagascar. In February 2015, he joined the German University of Technology in Oman. His research interests comprise structural geology, textures of ductile shear zones and mineral exploration.

Sedimentology and Depositional Facies Architecture of the Cenomanian Ain Tobi Formation, Nafusah Escarpment, NW Libya

Mohamed Hamruni and Ibrahim Mriheel

Abstract

This study deals with the facies architecture of the Cenomanian Ain Tobi Formation along Nafusah Escarpment (NE), Northwest Libya. The Ain Tobi succession was deposited broadly on a shallow carbonate ramp setting. Five detailed sections were measured from the northeastern to the southwestern parts of the NE and logged using the standard logging technique. Sixty thin sections were examined and interpreted better to understand the vertical and lateral facies variations through time. Six leading facies associations (FA-I to FA-VI) were identified. Peritidal facies association (FA-I) is characterized by red/yellow colored sandstone, microbial laminated bindstone with locally desiccation cracks, skeletal wacke-packstone with mechanical lamination, and sandy skeletal float-packstone with locally erosive base and oriented bioclasts. Rudist biostorm of ramp interior (FA-II) comprises sandy rudistic float-rudstone deposited within the lagoon. Shallow lagoonal subtidal (FA-III) consists of bioturbated mudstone/wackestone, packstone, and floatsone with locally wavy ripples. Deep lagoonal subtidal (FA-IV) mainly comprises marlstone and marly claystone. Shoal (FA-V) comprises cross-bedded oolitic, peloidal, and skeletal packstone/grainstone. Rudist bank and forebank (FA-VI) is characterized by scattered communities of rudist build-up, and these rudist shells redeposited basinward in the forebank as massive rudistic skeletal wackestone/floatstone. These facies are highly dolomitized. The Ain Tobi Formation represents a major third-order transgressive–regressive succession developed on the northern African passive margin during greenhouse conditions. The Formation has been subdivided into four fourth-order cycles in the northeastern parts of the NE and only three cycles in the southwestern part. These Cenomanian depositional sequences probably coincide with global glacio-eustatic cycles that are driven by the long eccentricity variation. Both eustatic sea-level change and paleotopography were the primary controls on spatial facies distributions and thickness variations.

Keywords

Facies architecture • Cenomanian • Ain Tobi formation • Nafusah Escarpment • NW Libya

1 Introduction

The Ain Tobi succession was deposited broadly on a shallow carbonate ramp setting (Christie, 1954). This study is focused on the lateral facies development of the Cenomanian depositional platform along NE in the NW Libya (Fig. 1). Although the excellent exposure of Ain Tobi Formation, published works used stratigraphic sequence approach remains limited along the scarp. This work will refine our understanding of the Formation's depositional environment and stratigraphic sequence framework. This contribution aims to construct the depositional model of the Formation and to build the depositional facies architecture of the Ain Tobi succession in the light of sequence stratigraphy. The methodology and results of this study are summarized in the following sections and supported by evidence (Fig. 1).

2 Methods

Logging of five sections from the central to the western part of NE was constructed using standard logging technique, and several field stops were checked (Fig. 1). Hand samples were collected for every bed and whenever there were

M. Hamruni (✉)
Geology Department, University of Tripoli, Tripoli, Libya
e-mail: geo.hamruni@gmail.com

I. Mriheel
National Oil Corporation, P. O. Box 2655 Tripoli, Libya

A. Çiner et al. (eds.), *Recent Research on Sedimentology, Stratigraphy, Paleontology, Tectonics, Geochemistry, Volcanology and Petroleum Geology*, Advances in Science, Technology & Innovation,
https://doi.org/10.1007/978-3-031-43222-4_1

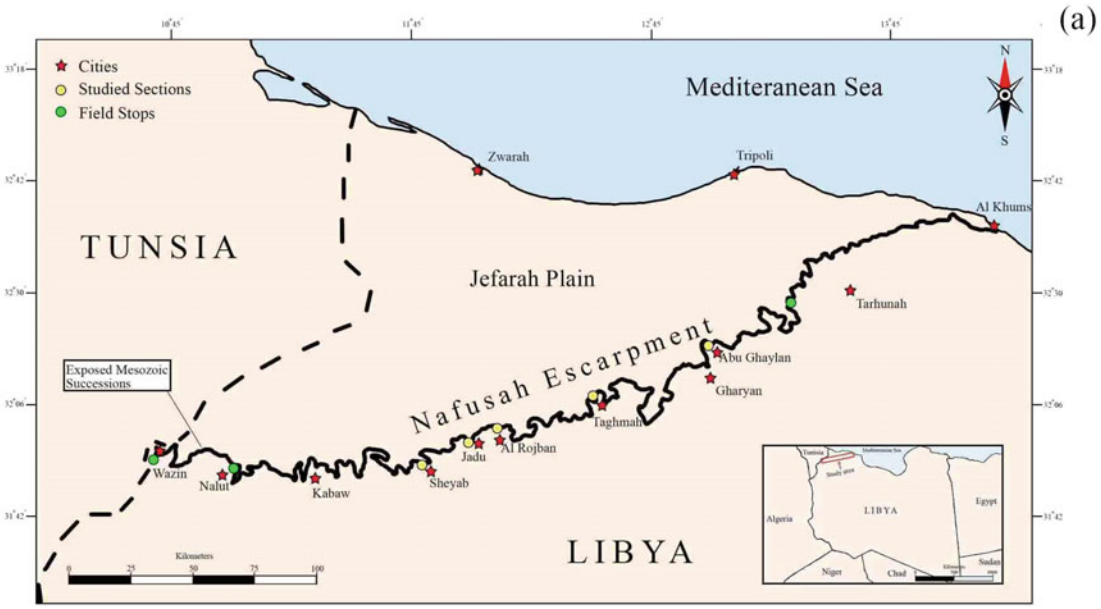

Facies Associations	Evidences for Depositional Setting	Environments
FA-I	Red to yellow colors, algal mats, oriented gastropoda, locally erosive base, mechnical lamination (upper flow regime), locally paleokarst	Peritidal
FA-II	Whole rudists accumulation occur within inner ramp	Rudist Biostorm Ramp Interior
FA-III	Mud supported, horizontal bioturbation, locally wavy ripple, relatively high abundant biclasts, mechanical lamination (low flow regime)	Shallow Lagoonal Subtidal
FA-V	Clay and lime mud mixture (marl), locally burrows and mechanical lamination (low flow regime), soft	Deep Lagoonal Subtidal
FA-IV	Grain-supported, small-large cross bedding, relatively high diversity funa	Shoal
FA-VI	Rudsit commintys (rudists build-up)	Rudist Bank
	Dismantling broken and unbroken rudist, massive, mud-supported	Fore-Bank or Fore-Shoal

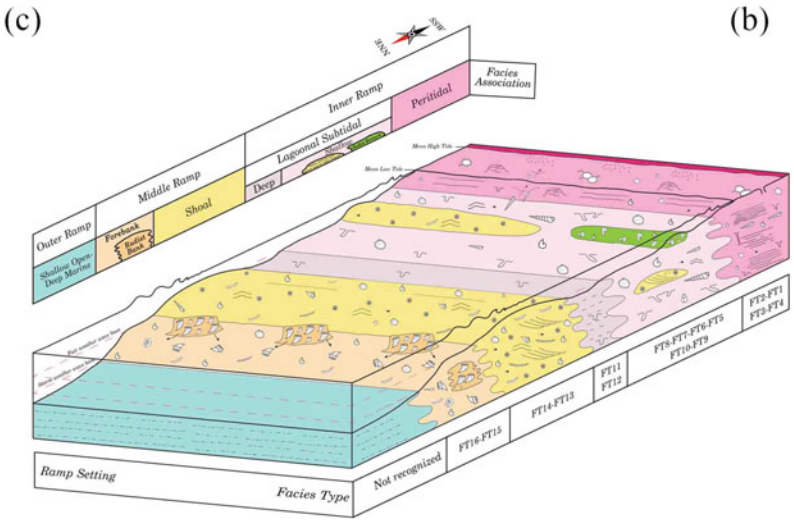

Fig. 1 Showing location map of the study area (**a**), facies belt within Ain Tobi carbonate ramp system (**b**) with their description (**c**)

changes in facies. In addition, representative samples were collected for both macro-structure and micro-texture examinations of Ain Tobi samples were conducted during outcrop and laboratory microscopic studies.

3 Results

The Ain Tobi facies association belt comprises peritidal, rudist biostorm, shallow lagoon, deep lagoon, shoal, and rudist bank and forebank (Hamruni, 2022). The Ain Tobi Formation is conformably overlain by Yifren Marl and overlying the marginal marine siliciclastic Jennawen Formation.

A model for classifying the depositional facies relating to the ramp depositional system along the NE is proposed (Fig. 1) (Hamruni, 2022). The main component facies association includes: **FA-I** Peritidal is characterized by red/yellow colored sandstone, algal dolobindstone with desiccation cracks, sandy skeletal float-packstone with locally erosive base and oriented bioclasts, and skeletal wacke-packstone with mechanical lamination of upper flow regime. **FA-II** Rudist biostorm ramp interior consists of a high accumulation of unbroken rudist shells and sandy rudistic floatstone-rudstone. **FA-III** Shallow lagoonal subtidal is mainly comprised of bioturbated mudstone/wackestone, packstone, and floatstone with locally wavy ripples and mechanical lamination of lower flow regime.

FA-IV Deep lagoonal subtidal consists of marlstone with local burrowing and mechanical lamination and marly claystone. **FA-V** Shoal is characterized by cross-bedded oolitic, pelodial and skeletal packstone-grainstone. **FA-VI** Rudist bank and forebank comprise scattered communities of in situ rudist build-up in front of shoal, rudistic boundstone. These rudist shells redeposited in the forebank, forming rudistic skeletal wackestone-floatstone. These facies associations are strongly dolomitized.

A stratigraphic sequence framework is conducted and reveals four fourth-order transgressive–regressive cycles in the northeastern flank and only three in the southwestern flank (Fig. 2) (Hamruni, 2022). They include: **S1** and **S2** Sequences one and two consist of tidal-influenced inner-ramp T/R depositional sequences. **S3** Sequence three is characterized by rudist bank and forebank facies, changing laterally to cross-bedded oolitic/skeletal shoal. **S4** Sequence four comprises retrograding and prograding stacking patterns of peritidal, inner-ramp shoal, and shallow and deep lagoonal facies.

4 Discussion

The overall Ain Tobi depositional sequences represent the lower part of the third-order sequence (Hamruni, 2022) that developed over the paleo north–south Ghadames-Tripoli passive margin. The depositional sequences one and two mark the first transgressive interval of Ain Tobi carbonate sediments. They comprise transgressive/regressive cycles, separated by the maximum regressive surface where the thickest peritidal facies occur. The maximum flooding surface (MFS) for both sequences in the northeastern part of the NE is placed on the thickest shallow lagoonal subtidal facies. However, in the southwestern part, the MFS of sequence two is picked on the rudist biostorm ramp interior. A major transgression of sequence three followed these sequences. It consists of rudist bank and fore-bank facies in the northeastern flank of escarp, which changes laterally into the oolitic shoal. The time of maximum flooding is placed on the thickest bed of the rudist forebank and its time equivalent shoal. The top of this sequence in the southwestern region

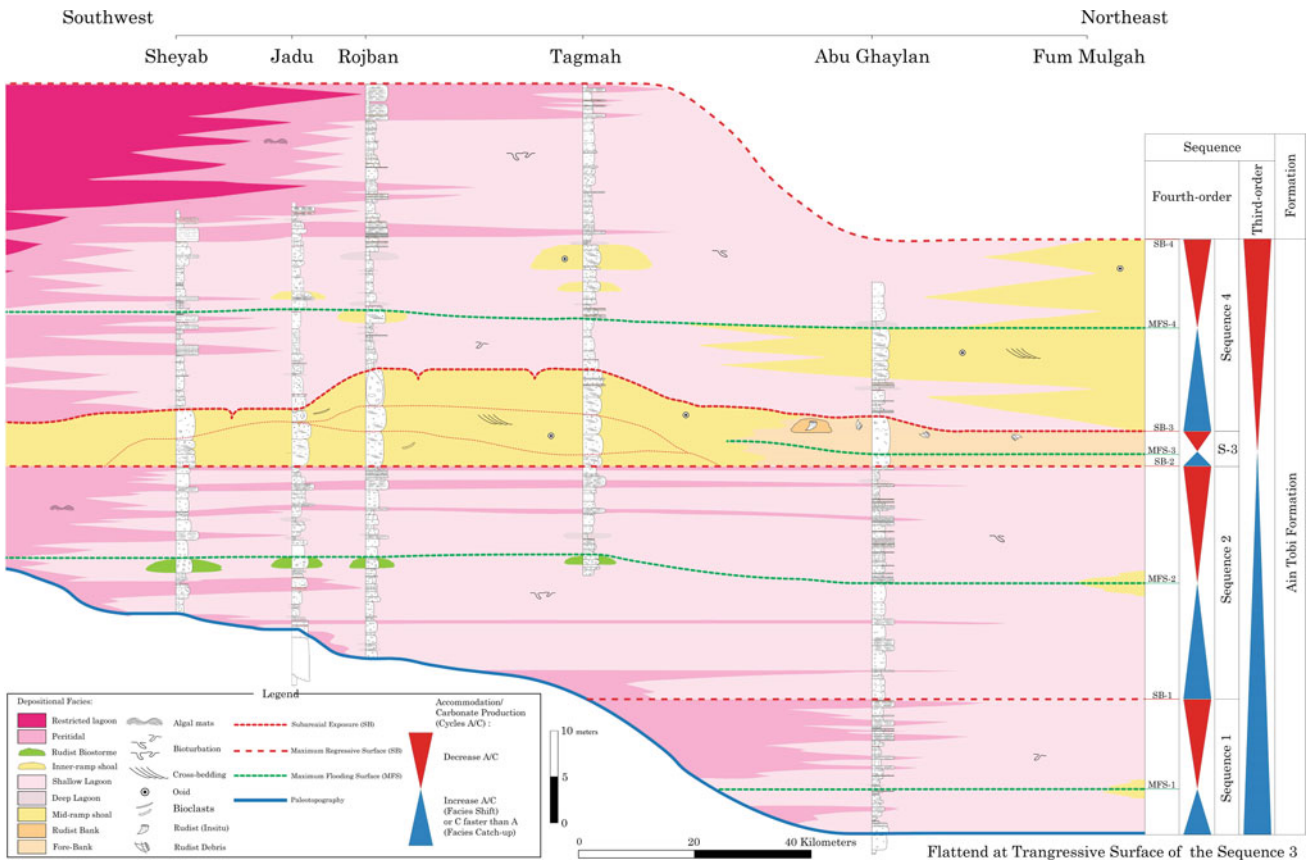

Fig. 2 Showing sequence-stratigraphic framework along Nafusah Escaprment

was affected by shallow karstification. The depositional sequence four is characterized by retrograding and prograding packages, in which the MFS occurs over the mid-ramp and inner-ramp shoal and deep lagoonal subtidal facies. The sequence boundary of the last prograding succession, sequence four, is placed on the red-colored oxidized peritidal facies. These depositional sequences are probably related to global Cenomanian sea-level fluctuations driven by the long eccentricity cycle (0.405 Myr) in the Milankovitch band, as noted by many authors (Gale et al., 2002).

5 Conclusions

The Cenomanian sedimentary succession of the Ain Tobi Carbonate ramp system comprises six main facies association. They are peritidal, rudist biostorm, shallow lagoon, deep lagoon, shoal, and rudist bank and forebank. Facies and environmental analyses, together with the reconstructed stratigraphic architecture of this succession, allowed sequence-stratigraphic interpretation of these depositional facies, containing four fourth-order sequences in the northeastern of the NE but only three in the southwestern flank.

References

Christie, A. M. (1954). *Geology of the Garian area, Tripolitania—United Nations Mission in Libya: Assistance Program Rept. TAA/LIB/2* (p. 60).

Gale, A. S., Hardenbol, J., Hathway, B., Kennedy, W. J., Young, J. R., & Phansalkar, V. (2002). Global correlation of Cenomanian (Upper Cretaceous) sequences: Evidence for Milankovitch control on sea level. *Geology*, 30, 291–294.

Hamruni, M. J. (2022). *Sedimentology and depositional facies architecture of the Cenomanian Ain Tobi formation, Nafusah Escarpment, NW Libya*. M.Sc. Thesis (Geology Department, University of Tripoli, Tripoli, Libya, p. 106).

Distribution of Surface Sediments at the Bottom of Lake Ladoga

Vladimir Anokhin, Dina Dudakova, Aleksey Aksenov, Mikhail Dudakov, and Anna Revunova

Abstract

Lake Ladoga is the largest source of fresh water in Europe, on which the health and lives of millions of people depend. Bottom sediments affect the water quality in the lake. Therefore, it is necessary to study them. Researchers from the Institute of Limnology of RAS are looking at the distribution of surface sediments at the bottom of Lake Ladoga using new methods. Based on the research results, a new map of the distribution of bottom sediments has been compiled, which can serve as a qualitative basis for monitoring the ecological situation in the lake.

Keywords

Lake • Sediments • Bottom relief • Distribution • Bottom sampling

1 Introduction

Lake Ladoga is the largest lake in Europe in terms of area and a source of fresh water for the metropolis of St. Petersburg and the adjacent regions. Therefore, studying the distribution of the lake's bottom sediments is an important and urgent task. During the study of the lithology of the base of Lake Ladoga, a significant amount of knowledge has been accumulated, and several works have been published, for example (Naumenko, 2020; Rumyantsev et al., 2015; Semenovich, 1966; State Geological Map of the Russian Federation Scale, 2015).

In 2019–21, employees of the Institute of limnology RAS (ILRAS) carried out a study of the bottom sediments of Lake Ladoga. The results of these works form the basis of the proposed publication.

2 Methods

The research methodology includes bottom sampling, echo sounding, an underwater photo-video survey of the tail, particle size analysis, and mapping bottom sediments based on digital bottom topography models.

Bottom sampling is the primary source of information in this study. It was carried out using a Lauri-Niemiste ground pipe on fine-grained sediments and an Ekman-Burge bottom grab on sandy sediments. Of the entire core of the tube, the top 10 cm of sediment was taken into account for mapping. Sampling was carried out over a subregular network of stations, more or less evenly distributed throughout the entire water area (191 stations).

The underwater survey was carried out using the "Limnoscout" underwater vehicle, designed and assembled at ILRAS (Anokhin & Dudakova, 2020), at a significant part of sampling stations. In addition, the bottom was a photo-video profiled in several local coastal areas.

Echo-sounding was applied at each station pointwise and in combination with photo-video profiling in coastal areas.

For cartographic constructions, a digital model of the relief of the bottom of Lake Ladoga was used, compiled by Mikhail Naumenko at ILRAS (Naumenko, 2020).

V. Anokhin (✉) · D. Dudakova · M. Dudakov · A. Revunova
Institute of Limnology RAS, St. Petersburg, 196105, Russia
e-mail: vladanokhin@yandex.ru

V. Anokhin
Herzen State University, St. Petersburg, 191186, Russia

St. Petersburg Research Centre RAS, St. Petersburg, 199034, Russia

A. Aksenov
St. Petersburg State University, St. Petersburg, 199034, Russia

Arctic and Antarctic Research Institute, St. Petersburg, 199397, Russia

A. Çiner et al. (eds.), *Recent Research on Sedimentology, Stratigraphy, Paleontology, Tectonics, Geochemistry, Volcanology and Petroleum Geology*, Advances in Science, Technology & Innovation,
https://doi.org/10.1007/978-3-031-43222-4_2

3 Results

Based on the results obtained, the authors created a map of the distribution of bottom sediments in Lake Ladoga (Fig. 1). The map shows that according to the distribution of deposits, the bottom of the lake, in the first approximation, can be divided into two zones—northern and southern.

The northern zone is dominated by olitic silts, which are replaced by other sediments at the bottom elevations. In the southern site, mainly sandy sediments are widespread, decreasing their size from the coast to the center of the water area from coarse-grained sands to aleuro-sands and sandy silts.

There is general preservation in the northern part of the usual zoning of bottom sediments in large reservoirs with bedrock banks with increasing depth (bedrocks—coarse-clastic—medium-clastic—fine-clastic—fine-clastic). There are also many deviations from this sequence. In particular, the filling of shallow-water zones in the fields of the northern coast of the lake with pelites is noticeable, where these sediments come almost to the very beach, composed of bedrocks, to a depth of several meters.

On the basins' sides are locally manifested olitic sediments, band-like, and band clays. According to many features, we refer to one group of sediments, well-known as deposits of the Baltic Glacial Lake. This ancient glacial reservoir occupied a vast area at the beginning of the Holocene, which included, in addition to the present-day Lake Ladoga, a large part of the Baltic Sea. Moraine (glacial) deposits most likely underlie band clays.

Glacial boulder-rubble deposits are distributed along the entire bottom in local glacial forms and in strips along the coast. Found that large glacial ridges have a bedrock base.

In the southern part of the lake, fragments of clay were found in bottom sediments, similar to the "blue" clay of the

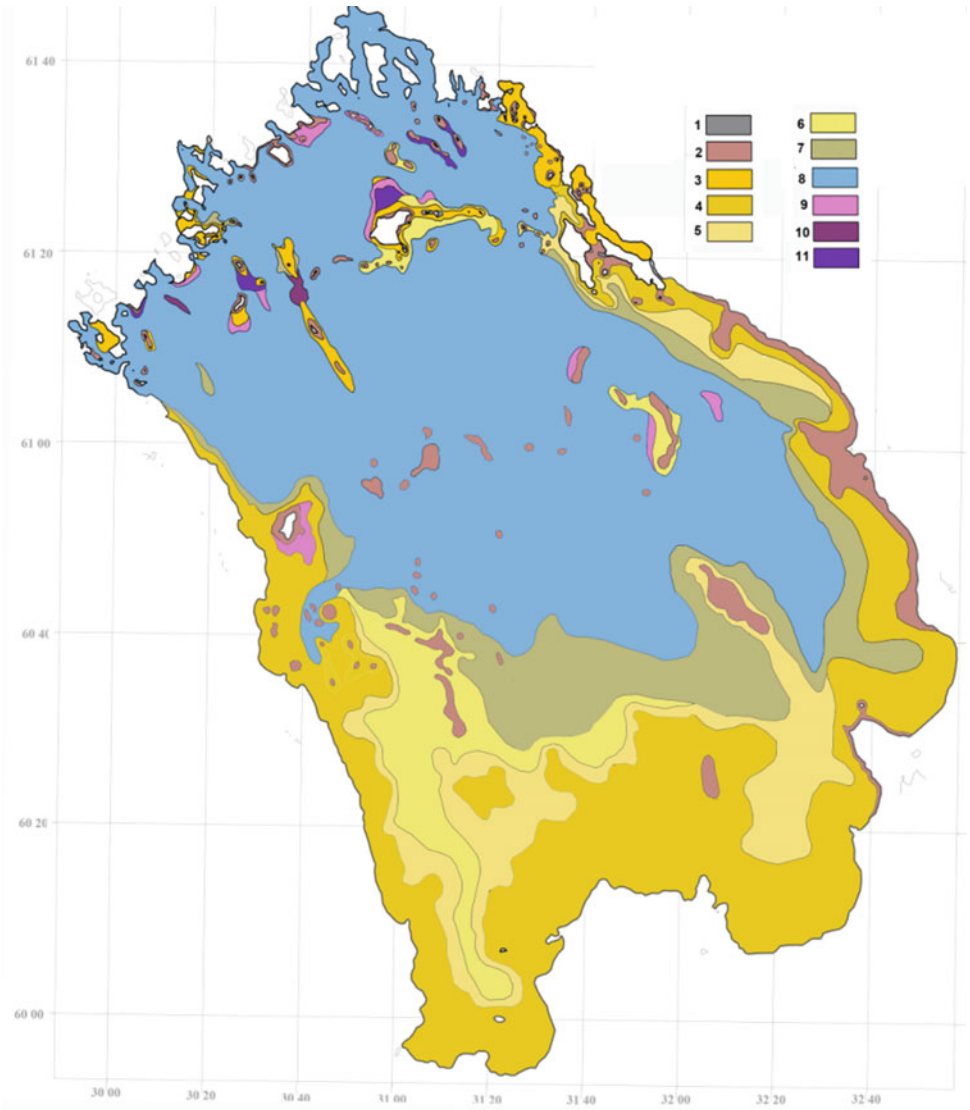

Fig. 1 Map of the distribution of surface sediments of the bottom of Lake Ladoga: 1—bedrocks and their large fragments, 2—boulder-block, pebble-gravelly deposits, 3—undivided sands, 4—coarse-grained sands, 5—medium-fine-grained sands, 6—silt-sands, 7—sandy silts, 8—pelitic silts, 9—silty pelites, 10—clays, 11—band-like, band clays

Cambrian age, which partially composes the southern shores of Lake Ladoga. Perhaps, this will make it possible to clarify the distribution of Cambrian clays at the bottom.

4 Discussion

Currently, two main cartographic products contain information on the distribution of bottom sediments at the bottom of Lake Ladoga. This is the scheme of the distribution of bottom sediments of Lake Ladoga, Semenovich (1966) and the scheme of bottom sediments from the set of the State Geological Map of the Russian Federation (2015).

Semenovich's scheme is the most detailed and substantiated factual material, and it has faithfully served researchers studying Lake Ladoga for over 50 years. However, the methods of the twentieth century's late 50 s were used when constructing it. In particular, the geographic referencing of the stations had an accuracy of 1–2 km. But much more serious is that there was no high-quality detailed bathymetric base at that time. And the bottom topography is a decisive factor in the distribution of bottom sediments. Thus, Semenovich's constructions are essentially outdated by now.

A much newer lithological scheme from the set of the State Geological Map has a rather small scale of 1:1,000,000. Therefore, it is impossible to see the geomorphological and lithological details of the bottom structure on it.

Our research was carried out using a GPS satellite binding, giving deviations in a matter of meters. When constructing our map, we used the most detailed digital elevation model available for Lake Ladoga. Of course, the authors made full use of all the constructions of their predecessors, paying particular attention to the two mentioned sources.

The authors are aware that all the above conclusions and constructions are debatable. Nevertheless, there is confidence that ongoing research will bring us closer to an accurate picture of the distribution of bottom sediments of Lake Ladoga.

5 Conclusions

The following features characterize the distribution of surface sediments at the bottom of Lake Ladoga. (1) In the northern part of the lake, pelitic silts dominate at the bottom, filling all depressions, the sides of which are composed, apparently, sediments of the Baltic glacial lake. (2) Band clays are probably underlain by glacial deposits, which, in turn, are capped by bedrocks. (3) In the southern part of the lake, mainly sandy sediments are widespread, the distribution of which obeys the usual zoning of decreasing the size of the constituent particles from the coast to the center of the water area, from coarse-grained sands to silty sands and sandy silts. (4) The discovery of fragments of (maybe) Cambrian clay in sediments of the southern part of Ladoga may make it possible to clarify the boundary of the distribution of bedrock clays.

The publication was compiled with State Project IL RAS No. 0154-2019-0001 No. of state registration AAAA-A19-119031890106-5. And State Project of St. Petersburg Scientific Center of the Russian Academy of Sciences 82.1 FNI.

References

Anokhin, V., Dudakova, D., & Dudakov, M. (2020). Studying the bottom landscapes of Lake Ladoga using underwater vehicles. In: *EGU General Assembly 2020 EGU2020–1743*.

Naumenko, M. A. (2020). Lake Ladoga digital bathymetric models: Development approaches and insight for limnological investigations. *Limnological Review, 20*(2), 65–80.

Rumyantsev, V. A., Sorokin, A. I., & Nesterov, N. A. (2015). *Ladoga Lake and the attractions of its coast*. Atlas: Nestor-History, St. Petersburg.

Semenovich, N. I. (1966). *Bottom sediments of Lake Ladoga*. Nauka.

State Geological Map of the Russian Federation Scale. (2015). *State Geological Map of the Russian Federation Scale 1:1,000,000 sheets R-35.36. Lithological map of the water area bottom surface. Third generation*. Baltic series. Ministry of Natural Resources of the Russian Federation VSEGEI.

Upper Pleistocene-Holocene Coastal Depositional Sediments of the Farwah Spit, NW Libya

Ibrahim Mriheel and Mohamed Hamruni

Abstract

This study examines sedimentary facies development of coastal deposits adjacent to the modern-day Farwah Spit in NW Libya. The modern-day coastal depositional system comprises salt marsh, tidal flat, lagoon, flood delta, and spits. Sedimentological analysis of outcrops, integrated with satellite image interpretation and comparison with equivalent deposits from neighbouring provinces, allows an understanding of the genesis and timing of the Holocene Farwah Spit Formation. The Holocene sediments unconformably overlie sediments of the Late Pleistocene age. This sequence boundary is represented by an exposed and weathered surface with Late Pleistocene marginal marine bioclastic and bioturbated sandy coastal sediments. The Holocene Farwah Spit Formation comprises bioclastic sands interpreted to record transgressive marginal shallow marine facies. These change laterally to grey muds, rich in organic matter (TOC up to 3.05%), deposited within a lagoon, and protected from the sea by Holocene sand spits. Locally, close to the eastern inlet, the lagoonal facies pass into rippled sands, interpreted to record flood delta deposits. Landward, the cycle is represented by supratidal sand and mudstones deposited in a salt marsh with characteristic halophile plants. Locally, a thin salt crust cover has occasional microbially induced sedimentary structures and/or yellow sands of aeolian origin. Mapping lateral facies changes allows identification of prograding succession, resembling sixth-order sedimentary cycles that extend for 13 km E-W along strike and vary from 100 m to a few km in width. The distribution of coastal depositional facies, particularly the spatial distribution of the Holocene prograding spits and the associated lagoonal-tidal flat sediments, records the progressive infilling of the lagoon. Progradation of the spit is interpreted to have developed within a highstand systems tract, following sea-level rise after the last glacial maximum. The main factors controlling facies development are local topography, sea-floor morphology, sedimentation rate, relative sea-level fluctuation, and climate change following the last glacial maximum. The response to sea-level rise offers insight into long-term changes in coastal morphology that are relevant to impact studies of future sea-level rise associated with climate change.

Keywords

Upper Pleistocene-Holocene • Coastal deposition • Farwah • NW Libya

1 Introduction

This study records the sedimentary facies development of Holocene coastal deposits adjacent to Farwah Spit in NW Libya (Fig. 1). No previous work has interpreted the sedimentological features of the Holocene Farwah coastal system on the southern margin of the Mediterranean Sea. This contribution examines macroscopic and microscopic features within these tidal flat sediments. Supratidal-subtidal lithofacies and associated sedimentary structures are described. These are interpreted to record coastal depositional systems (salt marshes, tidal flats, lagoon, flood delta, and spit), and a model is presented.

2 Methods

The different lithofacies were described and mapped locally using field observations. The areal extent was interpreted by utilizing Google Earth images (Fig. 1). To examine the tidal

I. Mriheel (✉)
National Oil Corporation, P. O. Box 2655 Tripoli, Libya
e-mail: imriheel@noc.ly

M. Hamruni
Earth Science Department, Tripoli University, Tripoli, Libya

A. Çiner et al. (eds.), *Recent Research on Sedimentology, Stratigraphy, Paleontology, Tectonics, Geochemistry, Volcanology and Petroleum Geology*, Advances in Science, Technology & Innovation,
https://doi.org/10.1007/978-3-031-43222-4_3

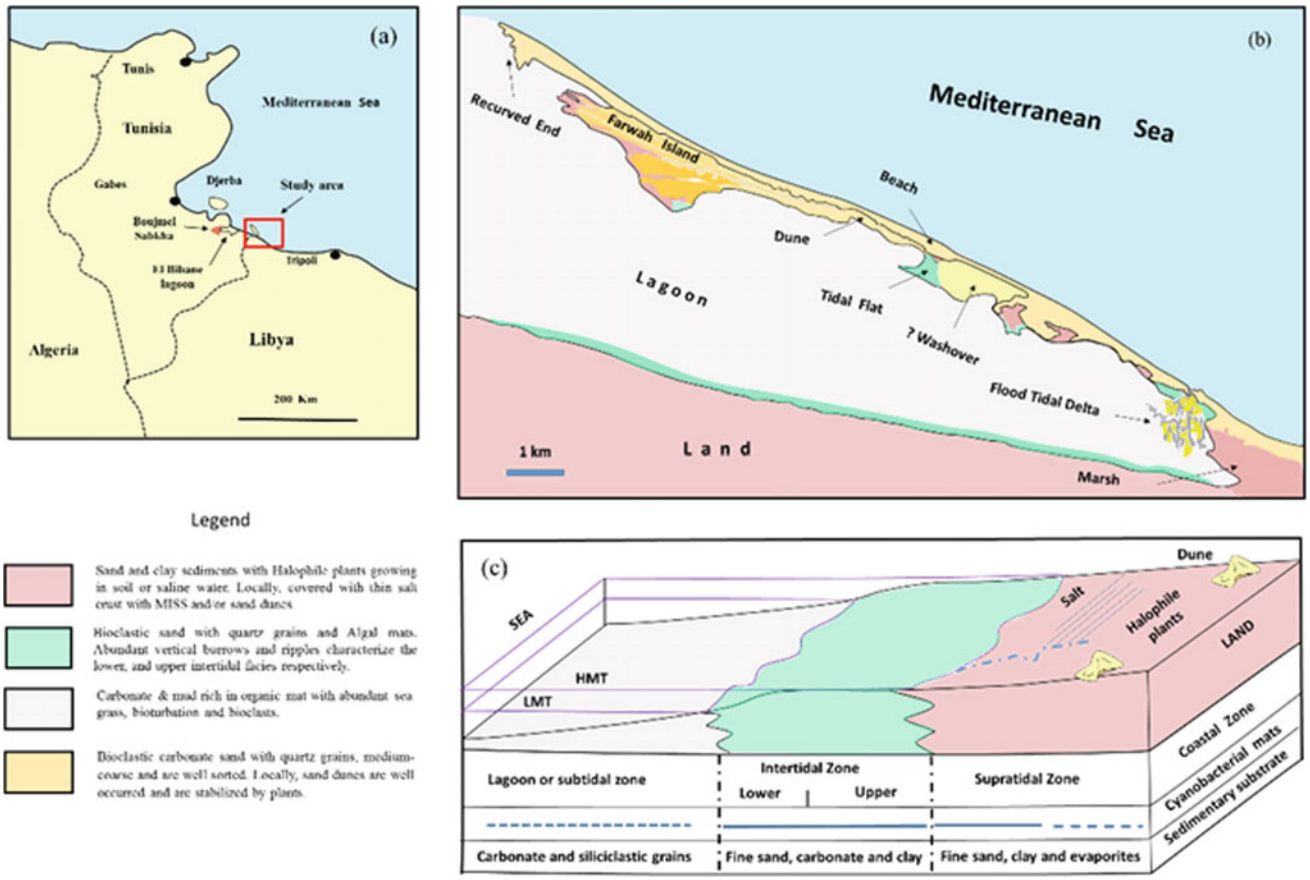

Fig. 1 **a** Location map of the study area, **b** interpretation of the depositional environment of the Farwah coastal system, and **c** a model of the peritidal-shallow lagoonal depositional facies, similar to the hypothetical profile proposed after Lakhdar et al. (2020) for the southeastern coast of Tunisia

changes through time, several visits were made during spring and neap tides. Facies belts were mapped based on satellite images covering the study area. Representative samples were collected from both surface and subaqueous depositional sites. Both macro-structure and micro-texture examinations of samples were conducted during field and laboratory microscopic studies. Several 30–50 cm excavations were dug using a shovel to observe near-surface sedimentary structures within the tidal flat sediments. The TOC of mud deposited within the Farwah lagoon was determined using Rock–Eval pyrolysis.

3 Results

The Holocene sediments comprise bioclastic sands, organic-rich muds, rippled bioclastic sand, and massive to cross-bedded sand, unconformably overlying marginal marine bioclastic and bioturbated sandy deposit of Late Pleistocene age. The lithofacies record the transgression of marginal shallow marine tidal facies. Seaward, the facies change laterally to lagoonal grey muds, rich in organic matter and locally bioturbated. Landward, the facies is covered with thin salt crust with many microbially induced sedimentary structures and/or yellowish sands of aeolian origin. These are interpreted to have been deposited within a lagoon, protected from the sea by a sand spit. Landward, the sand, clay, and evaporite sediments record a supratidal flat with salt marshes. A model for the coastal depositional system is proposed (Fig. 1).

Satellite imagery has been interpreted to extend the field observations, and the recent coastal systems can be observed that also reveal the present-day provenance of the barrier sediments along the Northern Africa continent (i.e., erosion of the Libyan Farwah and Ras Ejdeir headlands that form an essential source for the El Bibane barrier in Tunisia).

4 Discussion

The Holocene Farwah coastal sequence was formed during the last glacio-eustatic cycle, and the exposed prograding surfaces mark the last highstand systems tract (HST) development over the southern Mediterranean Sea that post-dated

the last glacial maximum. The marine flooding surface, which separates the transgressive systems tract (TST) from the overlying HST, occurs within submerged strata and has no exposure in the region.

Correlation with the adjacent Tunisian Boujmel Sabkha and Al Bibane lagoon (up to 6.8 ka BP) (Lakhdar et al., 2006, 2020), influenced by similar climatic events, sea-level changes (Hansen et al., 2013) and Mediterranean Sea influence (i.e., Adriatic Sea, SE Italy), reveals that the Farwah facies are prograding spit. The spit and its associated tidal flat and lagoonal facies belts developed within the HST followed postglacial sea-level rise after 22.1 ± 4.3 ka (Shakun & Carlson, 2010). The prograding spit consists almost entirely of a regressive succession emplaced during postglacial sea-level transgression between the latest Pleistocene (14 ka BP) and early Holocene (8 ka BP). Lateral facies changes within the spit allow for identification and lateral tracing of six stacked, prograding successions, which may resemble stacked sixth-order cycles.

5 Conclusions

The Holocene sedimentary succession of the Farwah coastal system records the short duration (approximately 10 ± 2 ka) progradation of spits and associated lagoonal and tidal flat sequences. Facies and environmental analyses, together with the reconstructed stratigraphic architecture of this succession, allow a sequence-stratigraphic interpretation, with the identification of a sequence boundary on the underlying Pleistocene and places most of the Farwah Formation into the HST. The maximum flooding surface, which separates the underlying TST from the overlying HST, occurs within submerged strata and has no apparent exposure in the region.

Correlation with the adjacent Tunisian Boujmel Sabkha and Al Bibane lagoon suggests coeval deposition influenced by the same climatic event and global sea-level change following the last glacial maximum (∼14 to 8 ka).

Our study documents the stratigraphic organization of the Farwah coastal facies. It records the interaction between global eustatic variations and sediment supply, both processes under the control of climatic change. Changes in sediment input, climatic variations, and, more recently, human activities close to the eastern opening (inlet) have played an essential role in the development of the flooded delta during the last century.

References

Lakhdar, R., Soussi, M., Ben Ismail, M. H., & M'Rabet, A. (2006). A Mediterranean Holocene restricted coastal lagoon under arid climate: Case of the sedimentary record of Sabkha Boujmel (SE Tunisia). *Palaeogeography, Palaeoclimatology, Palaeoecology, 241*, 177–191.

Lakhdar, R., Soussi, M., & Rachida, T. (2020). Modern and Holocene microbial mats and associated microbially induced sedimentary structures (MISS) on the southeastern coast of Tunisia (Mediterranean Sea). *Quaternary Research, 100*, 1–21.

Hansen, J., Sato, M., Russell, G., & Kharecha, P. (2013). Climate sensitivity, sea level and atmospheric carbon dioxide. *Philosophical Transactions of the Royal Society Series A,* 371, 20120294, https://doi.org/10.1098/rsta.2012.0294

Shakun, J. D., & Carlson, A. E. (2010). A global perspective on last glacial maximum to Holocene climate change. *Quaternary Science Reviews, 29*, 1801–1816.

Study of the Oligocene Sediments in the SW Boundary of Les Avellanes Diapir (NE Spain)

Gabriel Cofrade, Irene Cantarero, Òscar Gratacós, Anna Travé, Eduard Roca, and Oriol Ferrer

Abstract

The interpretation of the detritic Eocene–Oligocene sediments located at the SW margin of Les Avellanes Diapir (South-Central Pyrenees) allows for recognizing the advance and emplacement of a salt glacier during their sedimentation. Six (6) lithostratigraphic units have been identified as superimposed in the stratigraphic sequence recording the salt extrusion and advance. Units 1 to 4 record a southwards prograding alluvial fan system transporting detrital components from the diapir that must be exposed during this stage. Over a paleo-relief formed atop the alluvial fan system, the unconformable overlying unit 5 is a rubble zone made by a breccia of diapir rocks, which indicates the extrusive advance of the glacier. Finally, unit 6 belongs to the salt glacier, which flows toward SE and overlies all the upper Eocene–Oligocene succession.

Keywords

Diapirism • Pyrenees • Keuper • Salt glacier • Halokinetic sequences

1 Introduction

Sedimentary sequences in diapir margins serve as a proxy for understanding diapiric history (Hudec & Jackson, 2007). These studies can be especially useful in diapiric provinces inside orogenic belts where compression could reactivate previous salt structures, usually producing salt extrusion and controlling the contractional structures' location, type, and geometry (Rowan et al., 2012).

The South-Central Pyrenean fold and thrust belt is a thin-skinned imbricated thrust sheet sequence decoupled over the Upper Triassic evaporites during the Late Cretaceous to Oligocene. Here, pre-contractional salt diapirs of Triassic rocks are relatively common, affecting the syn-contractional deposits (Saura et al., 2016). Among them, the Les Avellanes Diapir (Serres Marginals, NE Spain) crops out in the central part of the Serres Marginals thrust sheet, which is formed of a syn-orogenic Upper Cretaceous to Oligocene unconformably overlaying the pre-orogenic Triassic to Jurassic succession. Les Avellanes Diapir is composed of evaporites (gypsum at the surface, halite, and anhydrite at depth), siltstones and carbonates of the Keuper facies, dolostones of the facies Muschelkalk, and dolerites.

Along its SW margin, north of *Os de Balaguer* village (Fig. 1), these diapir rocks overlie the syn-contractional detrital Eocene–Oligocene sediments with a contact that has been historically interpreted as a thrust (Pocoví, 1978). This contribution aims to: (1) decipher the precise nature of this contact and (2) better understand the evolution of the Les Avellanes Diapir during the sedimentation of the syn-contractional Eocene–Oligocene sediments. Furthermore, this exceptional outcrop presents an excellent opportunity to study Les Avellanes Diapir and other deformed diapirs in contractional settings (e.g., Zagros, Alps).

2 Methods

To characterize and interpret this outcrop, a field campaign was carried out in an outcrop located North of *Os de Balaguer* town. Sedimentary and structural data have been mapped in detail, and a stratigraphic section has been done. From these data, six lithostratigraphic units have been

G. Cofrade (✉) · I. Cantarero · A. Travé
Institut de Recerca Geomodels, Departament de Mineralogia, Petrologia i Geologia Aplicada, Facultat de Ciències de la Terra, Universitat de Barcelona (UB), Barcelona, Spain
e-mail: gcofrade@ub.edu

Ò. Gratacós · E. Roca · O. Ferrer
Institut de Recerca Geomodels, Departament de Dinàmica de la Terra i de L'Oceà, Facultat de Ciències de la Terra, Universitat de Barcelona (UB), Barcelona, Spain

A. Çiner et al. (eds.), *Recent Research on Sedimentology, Stratigraphy, Paleontology, Tectonics, Geochemistry, Volcanology and Petroleum Geology*, Advances in Science, Technology & Innovation,
https://doi.org/10.1007/978-3-031-43222-4_4

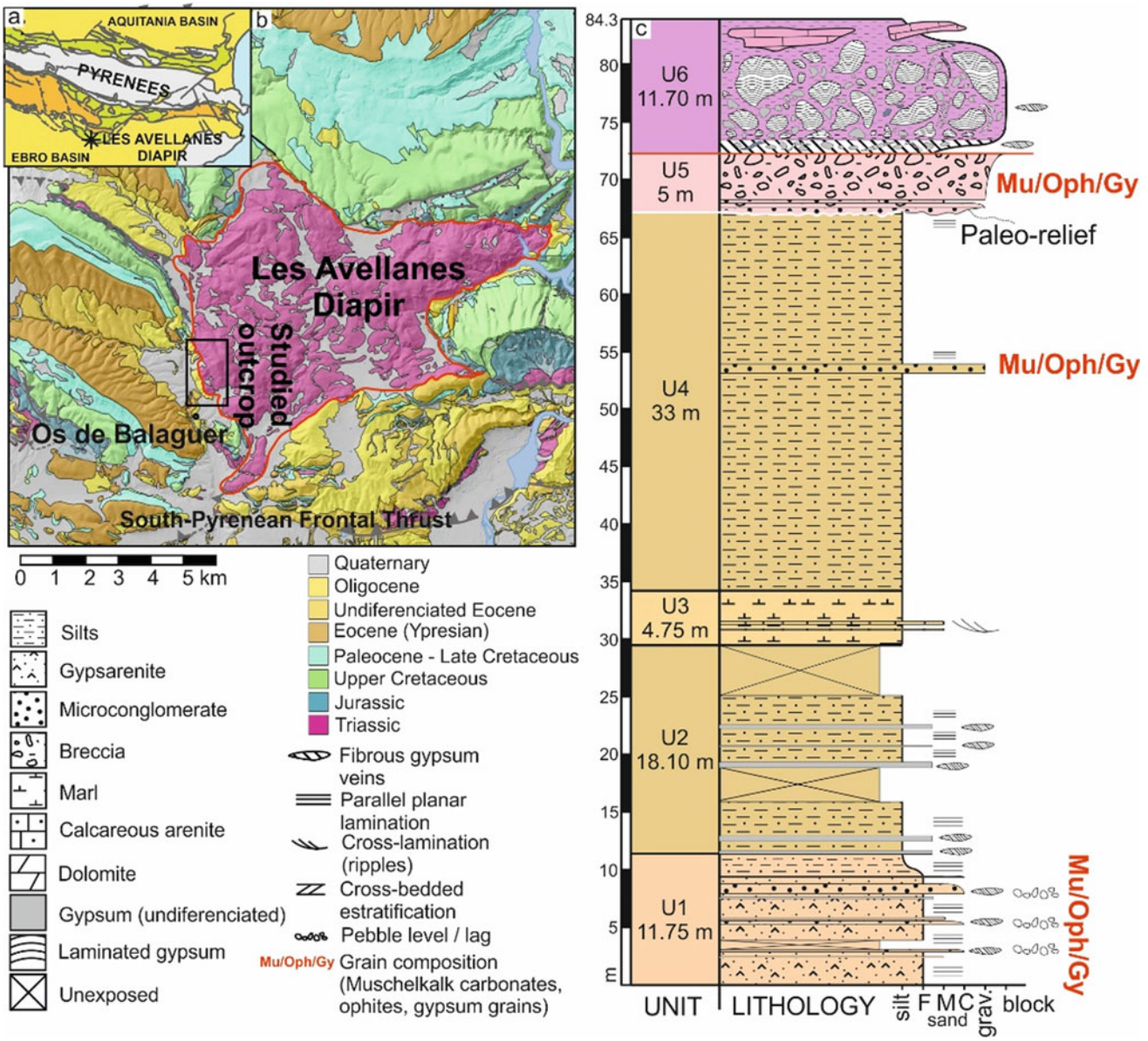

Fig. 1 **a** Eastern Pyrenees map with the approximated location of Les Avellanes Diapir. **b** Regional map of Les Avellanes Diapir. **c** General and in-detail stratigraphic sequence of the studied Eocene–Oligocene sediments

distinguished and correlated laterally and vertically. Each unit has been analyzed from a sedimentological and structural point of view, assigned to a diapiric or depositional environment, and interpreted to unravel the iaper evolution.

3 Stratigraphic Sequence

The studied syn-kinematic sediments onlap the underlying *Alveoline Limestones* (Ilerdian, Ypresian) toward the W-SW. The first lithostratigraphic unit (Fig. 1), U1, is composed of an alternation of fine parallel laminated gypsarenites and lithic arenites, intercalated with dm tabular microconglomerate layers in a thickening upwards sequence. U2 corresponds to silts intercalated with dm tabular alabastrine gypsum layers. U3 is a marly succession with cross-laminated calcareous arenites. U4 is mainly composed of reddish laminated silts intercalated with dm tabular beds of lithic arenites. These four units change laterally and vertically to the NW, first into an alternation of coarse sand with conglomerates, which further evolves into large-scale cross-bedded conglomerates and finally into massive conglomerates. Clasts consist of Muschelkalk carbonates, dolerites, gypsum, minor Illerdian limestones, and other carbonates. U5 unconformably overlies a paleo-relief located above U4. This upper unit is represented by a mud-supported, poorly sorted, inverse-graded breccia

composed only of pebble to boulder components of Muschelkalk carbonates, dolerites, and gypsum clasts. Forest planes made of oriented pebble levels are recognized at the base of the breccia. A net contact can be observed between U5 and the uppermost megabreccia of U6. This megabreccia comprises dm to m gypsum boulders, gypsum vein fragments, and dm blocks of Muschelkalk carbonates, usually located atop the deposit, floating in a fine matrix.

4 Units Interpretations and Halokinetic Implications

The presented lithostratigraphic units can be interpreted to recognize stages related to diapirism. U1 to U3 were deposited in a sabkha to salt pan environment that progressively evolved into a carbonated lacustrine/palustrine margin. U4 is interpreted as mudflats located at the distal part of an alluvial fan system that prograde toward the S-SW. The grain composition, facies distribution, and geometries of units 1 to 4 point that one of the source areas is Les Avellanes Diapir which had to be exposed a few kilometers to the NE. Later, an erosion stage occurred, as indicated by the paleo-relief filled by the breccia of U5. Breccia components are exclusively derived from the diapiric rocks and deposited in a very proximal position. The inverse grading indicates increasing energy which a gradually closer source area could explain. The uppermost gypsum megabreccia (U6) can be interpreted as the remains of an extruded salt mass in which highly soluble minerals (e.g., halite) have been dissolved, leaving gypsum and carbonate blocks floating in a fine-grained matrix (allochthonous diapiric breccias, (Hearon et al., 2015)). This salt extrusion most likely occurred at the iaper boundary and advanced toward S-SW as a salt glacier.

The erosion of this salt glacier produced the syn-halokinetic sedimentation of U5 at its frontal areas, which was later unconformably overlaid by the advancing salt glacier. Breccias under allochthonous salt bodies have also been recognized in the Gulf of Mexico, referred to as *rubble zones* (Rowan, 2017). The precise nature of these breccias is still being discussed, and thus, the importance of this work.

5 Conclusions

The studied syn-kinematic sediments, located at the SW margin of Les Avellanes Diapir, record the S-SW advance of a salt glacier over a breccia generated from its erosion, transport, and sedimentation. The salt-sediment boundary constitutes the net base of this glacier and is not a fault. The subsalt breccia filled a previous paleo-relief, developed over an alluvial fan's detrital sediments. This depositional system transported diapiric materials, demonstrating that the diapir was already exposed.

Acknowledgements This work was supported by the framework of Spanish Projects *SABREM* (PID2020-117598GB-C21), *SALTCONBELT* (CGL2017- 85532-P), and DGICYT (PID2021-122467NB-C22) funded by Ministerio de Ciencia, Innovación y Universidades/Agencia Estatal de Investigación/Fondo Europeo de Desarrollo Regional, Unión Europea, the Grups de Recerca reconeguts per la Generalitat de Catalunya, 2021SGR349 "*Geologia Sedimentària*" and 2021SGR76 "*Geodinàmica i Anàlisi de Conques*", and the UB scholarship PREDOC-UB19/20 5660400. We also acknowledge Aspentech (Paradigm Geophysical Corp.) and Petroleum Experts (Petex) for providing the academic licenses of GoCad and Move software, respectively.

References

Hearon, E., IV., Rowan, G., Giles, A., Kernen, A., Gannaway, E., Lawton, F., & Fiduk, C. (2015). Allochthonous salt initiation and advance in the northern Flinders and eastern Willouran ranges, South Australia: Using outcrops to test subsurface-based models from the Northern Gulf of Mexico. *Bulletin AAPG, 99*, 293–331.

Hudec, M., & Jackson, M. (2007). Terra infirma: Understanding salt tectonics. *Earth Science Reviews, 82*, 1–28.

Pocoví, A. J. (1978). Estudio geológico de las Sierras Marginales Catalanas (Prepirineo de Lérida). *XIII ACTA GEOLÓGICA HISPÁNICA, 3*, 73–79.

Rowan M. G. (2012). An overview of allochthonous salt tectonics. In Soto, J. I., Flinch J. F., & Gabor T. (eds.), *Tectonics and hydrocarbon potential, permo-triassic Salt Provinces of Europe, North Africa and the Atlantic Margins,* (pp. 97–144). Elsevier.

Rowan, M. G., Giles, K. A., Roca, E., & Arbues, P. O. F. (2012). Analysis of growth strata adjacent to an exposed deepwater salt diapir, Northern Spain. In *AAPG Annual Convention Program*.

Saura, E., Ardèvol i Oró, L., Teixell, A., & Vergés J. (2016). Rising and falling diapirs, shifting depocenters, and flap overturning in the Cretaceous Sopeira and Sant Gervàs subbasins (Ribagorça Basin, southern Pyrenees). *Tectonics,* 35, 1–25.

Facies, Sedimentology, and Characterization of the Depositional Environments of the Lower Liassic (Lower Jurassic) Deposits from the Mohammedia–Benslimane–ElGara–Berrechid Basin (Moroccan Meseta)

Ahmed Belqadi, Rachid Essamoud, Abdelkrim Afenzar, and Touria Hssaida

Abstract

The present study addresses the Mohammedia–Benslimane–ElGara–Berrechid Liassic basin (MBEB) belonging to the Mesetian domain. This basin is usually considered a vast, shallow depression originating from an N-S to NE-SW half-graben structure. According to up-to-date analyses, the deposits in the MBEB basin can be subdivided into two major series: lower argillaceous-salt series attributed to the Triassic and Upper argillaceous-salt series attributed to the Liassic. Both series are separated by a basaltic complex of the Late Triassic–Early Liassic age (200 Ma). The study aims to present a detailed sedimentological analysis of the ill-known upper supra-basaltic part to reconstruct the respective palaeoenvironment and provide a sequence-stratigraphic analysis as a base for stratigraphic correlation. During the Lower Liassic, the paleoslope in the MBEB basin after basaltic effusion was low with distal environments. Facies analysis of four sections evidenced the presence of four major lithofacies corresponding to sandstone, silt, clay, and evaporite facies in the field. We recognize two formations corresponding to two mega-sequences: the rock-salt bearing lower and the clayey upper mega-sequences. The sedimentation of the first mega-sequence was in a system of depression with free brine, followed by saline mudflats under continental influences. The upper clayey mega-sequence display facies documenting sea-level fluctuations of the final transgression from the Tethys or Proto-Atlantic Sea.

Keywords

Facies analysis • Architectural elements • Liassic • Meseta • Morocco

1 Introduction

The opening of the central Atlantic, which began in the Triassic and Lower Jurassic (Lower Liassic), was announced by the creation of coastal basins in North-West Africa, particularly Morocco. Detrital, evaporitic, and volcanic deposits characterize several basins. The MBEB is one of these basins formed mainly by salt deposits, which is a good cover for hydrocarbon deposits. Thus, it is essential to know the type of deposits and their evolution over time. The Triassic series has been well studied recently (Afenzar & Essamoud, 2020), but the Liassic series has never been approached, which justifies our interest in this Liassic series. The purposes of this study are (1) to identify the different lithofacies and (2) to characterize the facies associations to reconstruct the paleoenvironment in the basin.

2 Geological Setting

MBEB, located in the coastal Meseta in the North-West of Morocco (Fig. 1), is a Triassic–Liassic basin filled by detrital and evaporitic deposits, which produced the salt deposit exploited by the company of Mohammedia salt. The MBEB is a vast shallow depression that originated as a consequence of an N-S to NE-SW oriented semi-graben (Lyazidi, 2004).

A. Belqadi · R. Essamoud (✉) · A. Afenzar · T. Hssaida
Faculty of Sciences Ben M'sik, Hassan II University of Casablanca, BP 7955 Sidi Othmane Casablanca, Morocco
e-mail: rachid.essamoud@univh2c.ma

A. Afenzar
Faculty of Sciences, Sidi Mohamed Ben Abdellah University of Fes, Dhar ElMehraz, Morocco

A. Çiner et al. (eds.), *Recent Research on Sedimentology, Stratigraphy, Paleontology, Tectonics, Geochemistry, Volcanology and Petroleum Geology*, Advances in Science, Technology & Innovation,
https://doi.org/10.1007/978-3-031-43222-4_5

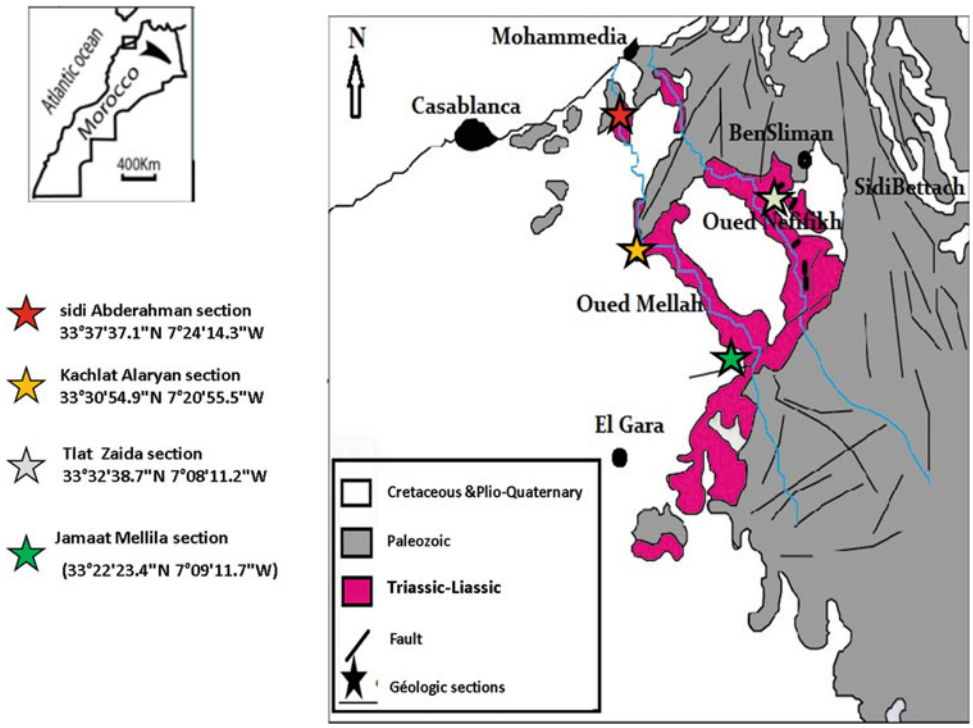

Fig. 1 Geographical and geological situation of the MBEB basin with different studied outcrops

3 Lithostratigraphic Framework

The latest works (Afenzar & Essamoud, 2020; Hssaida et al., 2012; Lyazidi, 2004) show that the sedimentary series in the basin are subdivided into two major series: Lower argillaceous-salt series attributed to Triassic and Upper argillaceous-salt series attributed to Liassic separated by a basaltic complex (Fig. 2).

This basalt was dated Upper Triassic-Lower Jurassic (Lower Liassic 200 Ma), belonging to the CAMP (Central Atlantic Magmatic Province), based on radiometric dating data (Peretsman, 1985). Subsequently, the supra-basaltic series can be attributed to the Lower Liassic (Hssaida et al., 2012).

4 Methodology

At first, our study will focus on four characteristics: lithology, grain size, texture, and sedimentary structures observed in outcrop. The facies nomenclature in this study corresponds to those determined by Miall (1977, 1978, 1996). The vertical and horizontal layouts of these facies give the characterized architectural elements according to several criteria specified by Allen (1983) and Miall (1985, 2006), which correspond to the nature of the upper and lower bounding surfaces, the external geometry, the scale, and the internal structures. The last step is the determination of the paleoenvironment based on nature and types of lithofacies already characterized and types of architectural elements formed by said lithofacies.

5 Facies Analysis and Architectural Elements

5.1 Lithofacies

We encountered four types of repeated lithofacies in the basin's Liassic (Lower Jurassic) outcrops. To make the sedimentological characterization of these facies, we corresponded with Miall facies (1977, 1978).

Table 1 summarizes the different facies, the lithology of each facies, and the sedimentary structures and interpretations.

Sandstone Facies LF1: The LF1 facies is reddish to purple massive coarse sandstone without sedimentary structures, 50 to 80 cm thick. It was observed only on the Kachlat Al Arian section at the Oued El Maleh dam level.

Silty Facies LF2: These facies are represented by massive reddish siltstone, with greenish to grayish levels of marmorization due to the transformation and then leaching of iron oxides, the origin of the red color of the sediments. These facies are found in almost all studied outcrops.

Clay Facies LF3: These facies is the most abundant. It is massive red claystone, sometimes marmorated without stratification and lamination. These claystones are considered lacustrine or overbank deposits (Miall, 1996).

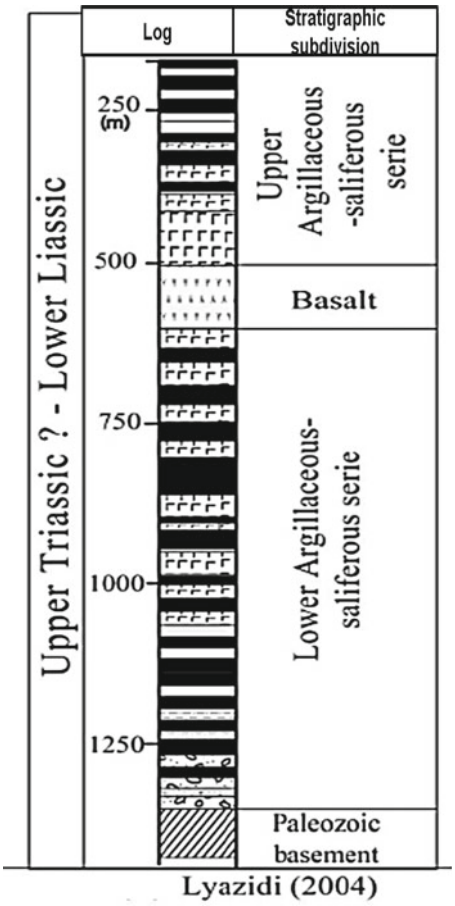

Fig. 2 Lithostratigraphic subdivision of the detrital, evaporite, and basaltic series of the MBEB basin (Lyazidi, 2004)

Evaporite facies EFa: The stratified gypsum facies EFa is identified at the top part of the Oued Elmaleh section and Sidi Abderrahmane hill. These facies may originate and be preserved under relatively humid environments with no flora (Afenzar & Essamoud, 2020).

Evaporite Facies EFb: The fibrous gypsum in veins facies EFb is identified in the basin at Sidi Abderrahmane hill. This satin spar (fibrous gypsum) may originate from a diagenetic process and/or dissolved elements.

5.2 Architectural Elements

To reconstitute the deposits' palaeoenvironments, we determine the relationship between the facies and the architectural elements by using the basic references (e.g., Allen, 1983 and Miall, 1985, 2006). According to Miall (1985, 2006), the description and interpretation of these architectural elements are based on four main criteria: (1) The nature of the lower and upper bounding surfaces; (2) External geometry; (3) The scale; (4) Internal geometry.

Generally, three architectural elements are encountered in our study (Fig. 3):

AE1: The association of sandstone facies (Sm), silty facies (Fl), and claystone facies (Fm) are interpreted as an association of playa facies. It presents a cyclicity of sandstone and silty-clay facies, which shows that their deposit was made in an unsalted playa lake. The presence of sandstone deposits also indicates that they were shallow (Afenzar & Essamoud, 2017, 2020; Liu & Wang, 2001).

AE2: This architectural element is formed by the association of Fl and Fm facies. These siltstones and claystone facies show a massive appearance indicating a calm deposition environment. The AE2 corresponds to the architectural element OF (overbank fine) of Miall (1985, 1996), which has a geometrical sheet form, reflecting its origin by vertical aggradation (Fig. 4).

AE3: Finally, the association of evaporitic facies is composed of claystone facies (Fm) and gypsum facies. These evaporitic facies often have a primary and/or a diagenetic origin. The evaporation of saline water forms them in mud flats and lagoons in a hot and humid climate (Afenzar & Essamoud, 2017, 2020).

6 Interpretation

The outcrops studied from the Lower Jurassic (infra-Liassic) in the MBEB are characterized by fine to very fine massive sediments, especially Sm, Fl, and Fm facies of Miall (1978, 2006): deposits of AE1, AE2, architectural elements, which

Table 1 Facies identified in the studied area, correspondence with Miall facies (1978, 2006)

Lithofacies	Code	Miall facies	Characteristic	Interpretation
Sandstone facies	LF1	Sm	Massive fine to coarse	Rapid deposition, gravity flow of sediments
Silty facies	LF2	Fl	Laminated to massive	Overbank or vanning flood deposits
Clay facies	LF3	Fm	Laminated to massive	Overbank, drape deposits, or abandoned channels
Evaporitic facies (a)	FEa	–	Stratified gypsum	Lake or lagoon deposits
Evaporitic facies (b)	FFb	–	Fibrous gypsum veins	Diagenetic origin

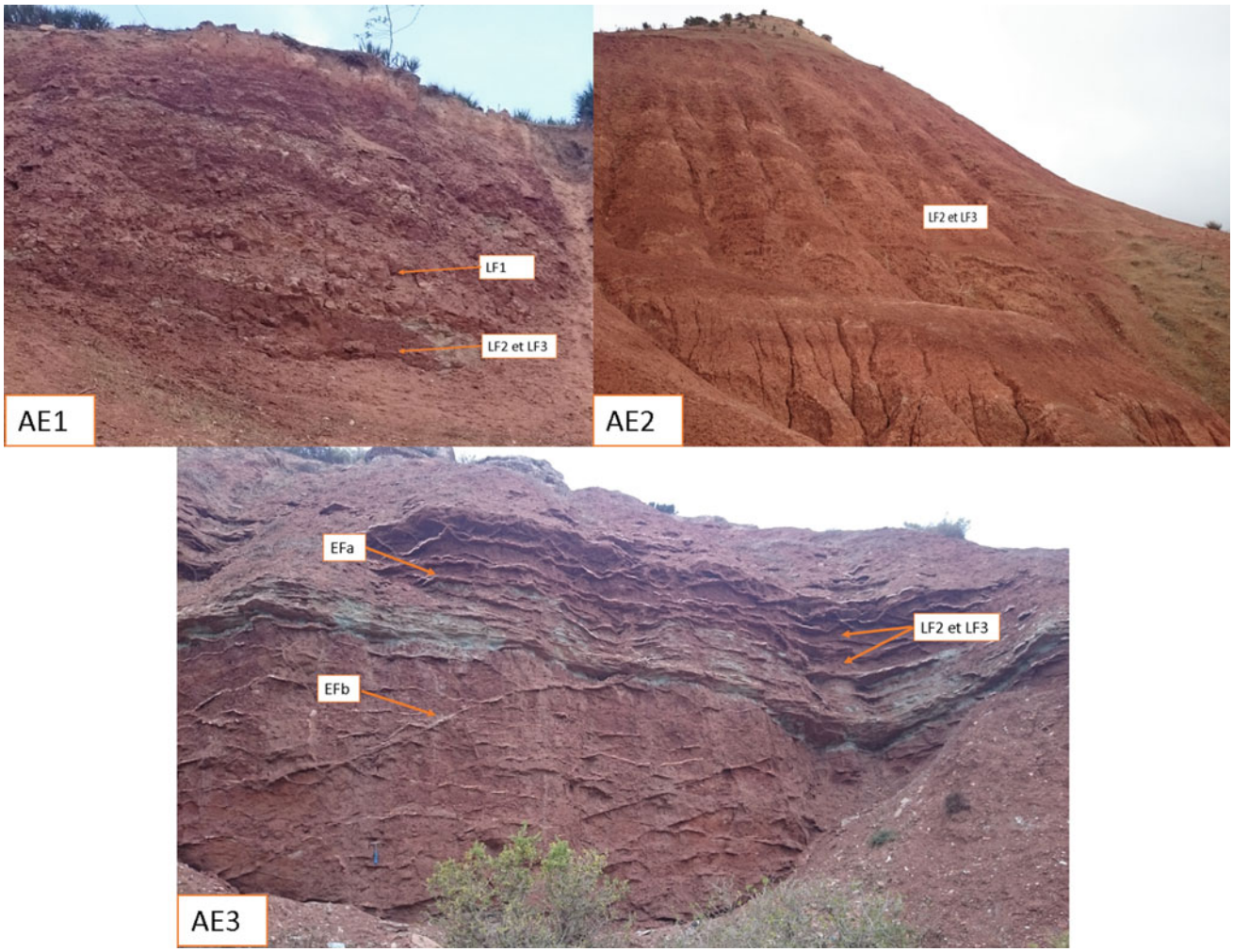

Fig. 3 Illustration of the different facies and architectural elements identified in the basin

we find at the Jmaat Melila and Tlet Ziaida sections, the dominating dynamics are overflows deposited in the floodplain (OF of Miall, 1985, 2006). The presence of an evaporate term with fine to very fine deposits in Sidi Abderrahmane hill; kachlat Al Aryan sections is probably due to the retrogradation of the clastic system and connection to a playa (Afenzar & Essamoud, 2020).

We can recognize two lower Liassic formations corresponding to two mega-sequences:

- The lower mega-sequence, rock-salt bearing, consists of two sequences with metric, marly, reddish brown argillites at the base and a whitish rock salt unit at the top of the first sequence, and an alternation of increasingly clayey rock salt and reddish-brown argillites.
- The second upper clayey mega-sequence contains reddish brown argillites and a mottled red, slightly sandstone.

The sedimentation of the first mega-sequence was in a depression system with free brine, followed by saline mudflats under continental influences (Et-Touhami, 1994). The upper argillaceous mega-sequence display facies documenting sea-level fluctuations of the final transgression from the Tethys or Proto-Atlantic Sea.

7 Conclusions

After establishing the underwater to subaerial basaltic flows, the sedimentation of the lower Liassic was mainly saliferous in a free-brine depression, subsequently subjected to continental influences (Salvan, 1984; Et-Touhami, 1994). The evaporite deposited in the middle and top of succession can be preserved in relatively humid environments.

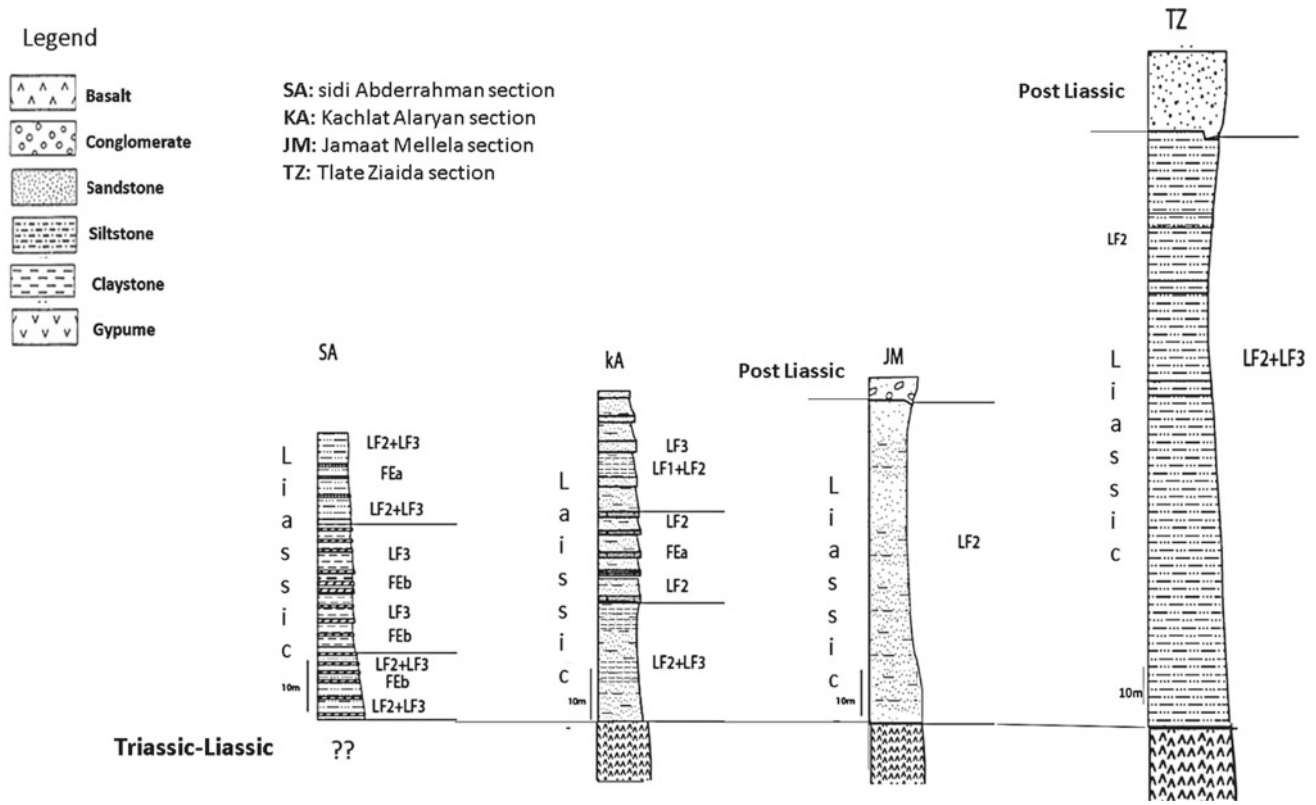

Fig. 4 Different sections studied in the basin with different facies

References

Afenzar, A., & Essamoud, R. (2017). Early Mesozoic detrital and evaporitic syn-rift series of Mohammedia-Benslimane-ElGara-Berrechid basin (Meseta, Morocco): Sedimentary and palaeoenvironmental evolution and comparison with neighboring basins. *International Journal of Advanced Earth Science and Engineering*.

Afenzar, A., & Essamoud, R. (2020). Sedimentological and sequence stratigraphy analyses of the syn-rift Triassic series of the Mohammedia-Benslimane-ElGara–Berrechid basin (Moroccan Meseta). *Comptes Rendus Géoscience-Sciences De La Planète, 352*(6–7), 417–441.

Allen, J. R. L. (1983). Studies in fluviatile sedimentation: bars, bar-complexes and sandstone sheets (low-sinuosity braided streams) in the Brownstones (L. Devonian), Welsh Borders. *Sedimententary Geology,* 33.

Et-Touhami, M. (1994). *Le Trias évaporitique du bassin de Khemisset (Maroc Central). Géométrie des dépôts, évolution sédimentaire et géochimie*. In : Notes et Mémoire du Service Géologique, Maroc, 373.

Hssaida, T., Zahour, G., Oumalch, F., Youssfi, Z., Chahidi, S., & Habid, A. (2012). Nouvelles datations des argilites post basaltiques du bassin de l'Oued Mellah (Meseta occidentale, Maroc). *Not. Mém. Service Géologique Du Maroc, 575*, 131–137.

Liu, Z., & Wang, C. (2001). Facies analysis and depositional systems of Cenozoic sediments in the Hoh Xil basin, northern Tibet. *Sedimentary Geology, 140*, 251–270.

Lyazidi, A. (2004). *Evolution géodynamique du bassin triasique de Berrechid-ElGara-Benslimane (Meseta Occidentale, Maroc)*. Université Mohammed V-Agdal Rabat, Maroc.

Miall, A. D. (1977). A review of the braided river depositional environment. *Earth Science Reviews, 13*, 1–62.

Miall, A. D. (1978). Lithofacies types and vertical profile models in braided river deposits: a summary. In Fluvial sedimentology, (Vol. 5, pp. 597–604). Canadian Society of Petroleum Geology.

Miall, A. D. (1985). Architectural-element analysis: A new method of facies analysis applied to fluvial deposits. *Earth-Science Reviews, 22*(1985), 261–308.

Miall, A. D. (1996). *The geology of fluvial deposits, sedimentary facies, basin analysis and petroleum geology* (4th ed.). Springer-Verlag.

Miall, A. D. (2006). *The geology of fluvial deposits, sedimentary facies, basin analysis, and petroleum geology* (4th corrected printing). Springer.

Peretsman, C. G. (1985). *A geochemical and petrographic analysis of early Mesozoic evaporites from Morocco: Implications for the history of the North Atlantic*. Ms. Thesis, University of Oregon, p. 87.

Salvan, H. M. (1984). Les formations évaporitiques du Trias marocain. Problèmes stratigraphiques, paléogéographiques et paléoclimatiques. Quelques réflexions. *Review of Geography Physics and Geology Dynamics,* 25, 187–203.

Paleoecology, Paleoenvironment, and Petroleum Potential of middle-upper Cretaceous Calabar Flank Sediments, Southeastern Nigeria

Moshood Olayiwola, Ernest Durugbo, Olugbenga Fajemila, Olaonipekun Oyebanjo, Adedotun Aderogba, Olufemi Olaleye-Otunla, and Adebayo Aderanti

Abstract

Three Upper Cretaceous sections belonging to Mfamosing, Ekenkpon and New Netim Formations from the Calabar Flank, southeastern Nigeria, have been investigated to evaluate ammonite, palynology and palynofacies, and to interpret their paleoecology, paleoenvironments and hydrocarbon potentials. Mfamosing Formation is composed predominantly of limestone with shale intercalations. Ekenkpon Formation is made up mainly of shale with mudstone and sandy-mud intercalations. The New Netim consists mainly of marl with shale and sandstone intercalations. The presence of shell fragments and ferruginous materials suggests a shallow marine environment for the deposition of the Mfamosing Formation. The palynomorphs recovered in this study are moderately to poorly preserved. The Mfamosing and Ekenkpon Formations were dated to early Albian and early to late Cenomanian, respectively. Four types of palyno-debris were recognized in this study. They comprise phytoclasts (degraded and structured), opaque, amorphous organic matter (AOM) and palynomorphs. These palynofacies suggested highly proximal shelf or basin and marginal dysoxic-anoxic basin paleoenvironments of deposition. In addition, Kerogen type III was revealed, which has moderate potential for hydrocarbon generation. Morphometric analysis revealed that the conch shape of ammonite taxa was thin to thick, discoidal and involute. The degree of whorl overlap was strongly embracing and the whorl cross-section shape was weakly compressed. The Westermann Morphospace analysis revealed that the studied ammonite shell shapes correspond to oxycone (i.e., low umbilical exposure, low inflation and high whorl expansion) with assumed nektonic life modes. This study contributes to understanding the sediment deposition and petroleum resources of the Calabar Flank regions.

Keywords

Ammonite • Morphometric analysis • Morphospace analysis • Palynology • Palynofacies

1 Introduction

Paleoecology and paleoenvironment are mainly concerned with reconstructing past biota, populations, communities, landscapes and ecosystems from available geological and paleontological data preserved in the rock record (e.g., Bishop, 2018; Terry, 2009). Equally, petroleum potential is the thermal maturity and ability of source rocks' organic matter (kerogen) constituents to produce hydrocarbon (e.g., Atta-Petters et al., 2015). The present work aimed at integrating invertebrate paleontology (using ammonite species), palynology and palynofacies analyses to reconstruct the paleoecology and paleoenvironment, and to infer petroleum potentials of the Mfamosing, Ekenkpon and New Netim Formations of Calabar Flank, southeastern Nigeria (Fig. 1).

M. Olayiwola (✉) · O. Oyebanjo · O. Olaleye-Otunla · A. Aderanti
A. G. Leventis Museum of Natural History, Obafemi Awolowo University, Ile-Ife, Osun State, Nigeria
e-mail: moshood.adegboyega@gmail.com; mayiwola@oauife.edu.ng

E. Durugbo
Department of Biological Sciences, Redeemer's University, P.M.B. 230 Ede, Osun State, Nigeria

O. Fajemila
Department of Geological Sciences, Osun State University, Osogbo, Osun State, Nigeria

A. Aderogba
Department of Geology, Niger Delta University, Wilberforce Island, Bayelsa State, Nigeria

A. Çiner et al. (eds.), *Recent Research on Sedimentology, Stratigraphy, Paleontology, Tectonics, Geochemistry, Volcanology and Petroleum Geology*, Advances in Science, Technology & Innovation,
https://doi.org/10.1007/978-3-031-43222-4_6

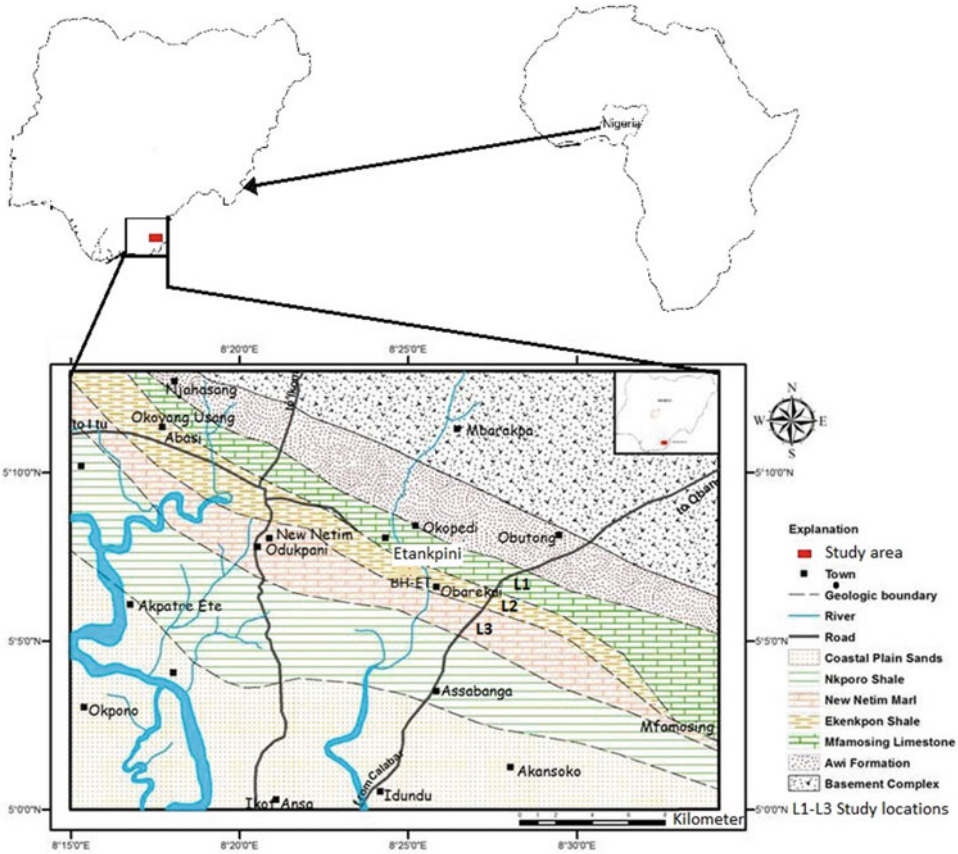

Fig. 1 Location map of the study area in the southeastern offshore Niger Delta (modified after Ukpong et al., 2018)

2 Materials and Methods

Fifteen (15) rock samples and twelve (12) ammonite mold samples were collected at different outcrop locations L1, L2 and L3, respectively (Fig. 1). Rock samples were subjected to standard lithostratigraphic description techniques for roundness, textures, color, sphericity, sizes and sorting of the sand particles. The presence and absence of accessory minerals such as ferruginous materials, glauconite, carbonaceous detritus, pyrites, calcites and shell fragments were also noted for each sample. Rock samples were further subjected to the standard palynological procedures based on the work of Faegri and Iversen (1989) to recover palynomorphs and organic matter particles (palynofacies). Ammonite mold samples were carefully cleaned with water and a paintbrush, and those embedded in rock were exposed with a chisel. The measurement of three cardinal conch parameters, conch diameter (Cd), whorl width (Ww) and whorl height (Wh), was carried out based on the works of Raup (1967). These parameters were used to generate Morphospace (i.e., the conch proportion and the expansion rate), which comprises conch width index (CWI), whorl width index (WWI), umbilical width index (UWI), whorl expansion rate (WER) and imprint zone rate (IZR).

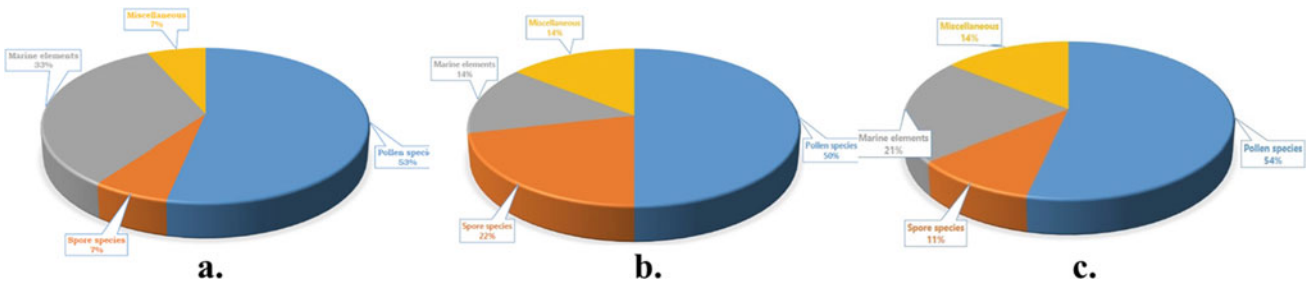

Fig. 2 Chart showing the distribution of palynomorphs species of the studied section of Calabar Flank. **a** Mfamosing formation at location L1, **b** Ekenkpon formation at location L2, and **c** New Netim Formation at location L3

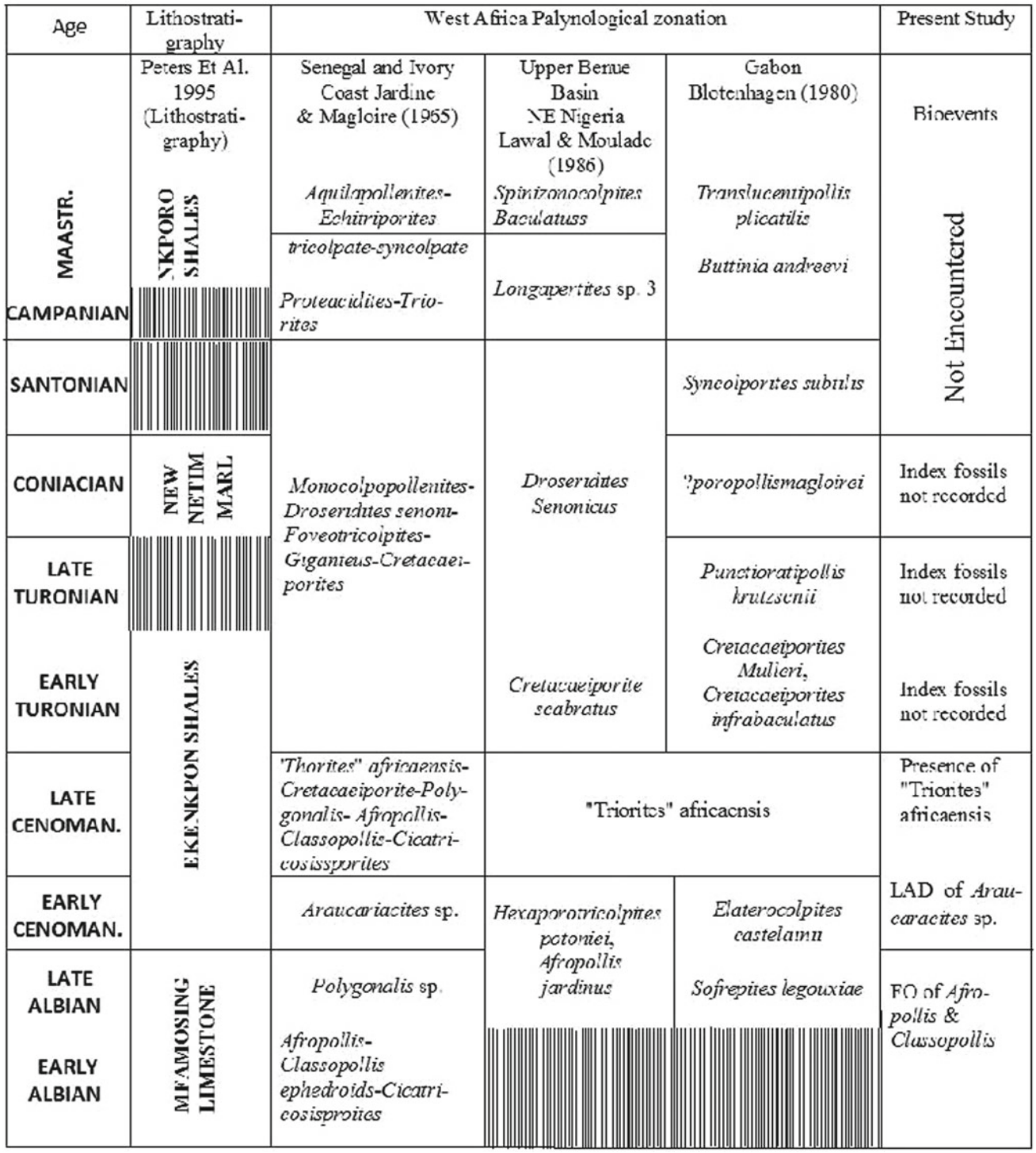

Fig. 3 Correlation charts of Cretaceous palynological biozonation in West Africa and the palynological zonation proposed in the present study. FO = First occurrence and LAD = Last appearance datum (Modified after Schrank 1992)

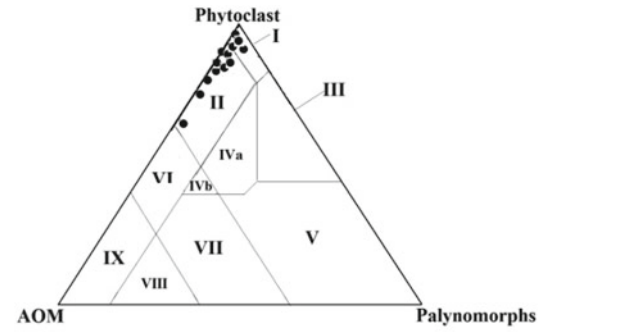

Palynofacies field	Environment of deposition
I.	Highly proximal shelf or basin
II.	Marginal dysoxic-anoxic basin
III.	Heterolithic oxic shelf (proximal shelf)
IV.	Shelf to basin transition
V.	Mud-dominated oxic shelf (distal shelf)
VI.	Proximal suboxic-anoxic shelf
VII.	Distal dysoxic-anoxic shelf
VIII.	Distal dysoxic-oxic shelf
IX.	Proximal suboxic-anoxic basin

Fig. 4 Ternary kerogen plots of the outcrop samples (Modified after Tyson, 1993)

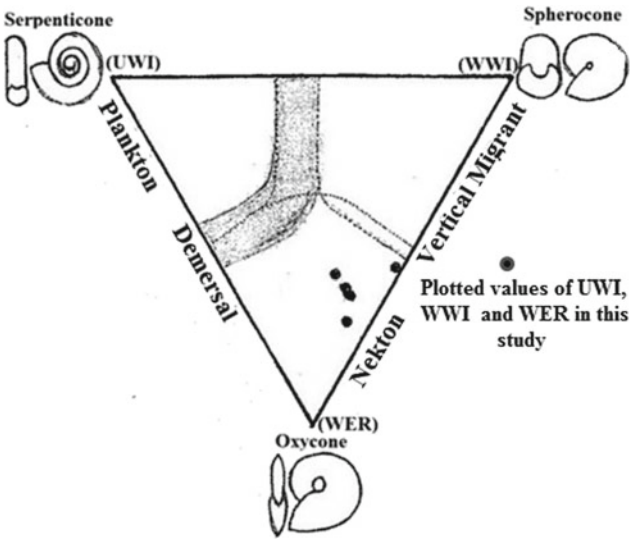

Fig. 5 Plots of values of umbilical width index from Mfamosing, Ekenkpon, and New Netim Formations (UWI)), whorl width index (WWI), and the expansion rate (WER) on Westermann Morphospace ternary diagram (Modified after Westermann, 1996)

3 Results and Discussion

The detailed lithostratigraphic analysis revealed the predominance of limestone lithofacies with shale intercalation in the Mfamosing Formation (e.g., Boboye & Okon, 2014). The present study shows that the Ekenkpon Formation lithologies are mainly shale with intercalation of thin bands of calcareous nodules, limestone and mudstone (e.g., Ukpong et al., 2018). The New Netim Formation lithologies are mostly marl with intercalation of shale and thin bands of limestone (e.g., Ayodele et al., 2017). A total of 32 palynomorphs that comprises 18 pollen, five spores, four marine elements and three miscellaneous elements are recovered from Mfamosing, Ekenkpon and New Netim Formations (Fig. 2a–c). The palynological assemblages in this study suggest shallow to the marginal marine depositional environments (e.g., Itam et al., 2019). Mfamosing and Ekenkpon Formations were dated early Albian to late Cenomanian due to the first occurrences (FOs) of Afro-pollis sp. and Classopollis sp., the last appearance datum (LAD) of Araucariacites sp. and the presence of Triorites africaensis (Jardine & Magloire, 1965; Lawal & Moulade, 1986; Fig. 3). The recorded palynofacies assemblage revealed a dominance of phytoclast with low percentages of AOM and rare occurrence of palynomorphs, which are types I and II of Tyson (1993) and interpreted as type III Kerogen (gas prone). They indicate fluctuation between highly proximal shelf or basin and marginal dysoxic-anoxic basin environments of deposition (Fadiya et al., 2020; Fig. 4). The paleontological analysis revealed sparse occurrence of ammonite taxa that comprised of genera Placenticeras, Coilopoceras and Acompsoceras. This study shows that the ammonite taxa are characterized by low umbilical exposure, low inflation and high whorl expansion similar to what has been previously described and correlated to oxycone shell shape with assumed nektonic life modes, which is associated with pelagic habitat (e.g., Westermann, 1996; Fig. 5).

4 Conclusion

This study has concluded that four lithologies were deposited in Mfamosing, Ekenkpon and New Netim Formations: marl, shale, limestones and sandstone. The palynological assemblage was dominated by terrestrial palynomorphs that helped in dating Mfamosing and Ekenkpon Formations to have ranged from early Albian to late Cenomanian age, and shallow to marginal marine depositional environment were suggested. The palynofacies assemblage was dominated by terrestrial kerogen, which is generally gas prone. The whorl conch shape of the ammonite taxa is characterized by thin to thick discoidal, involute, weakly compressed, low umbilical exposure, low inflation and high whorl expansion rate.

References

Atta-Petters, D., Achaegakwo, C. A., Kwayisi, D., & Garrey, P. (2015). Palynofacies and source rock potential of the ST-7H well, offshore Tano basin, Western region, Ghana. *Earth Sciences, 4*(1), 1–20. https://doi.org/10.11648/j.earth.20150401.11

Ayodele, M. O., Omoboriowo, A. O., & Adiela, U. P. (2017). A geologic field report on the geology of part of the Oban Massif and Calabar Flank, South Eastern Nigeria. *International Journal of Scientific Engineering and Science, 1*(5), 29–34.

Bishop, L. C. (2018). Paleoecology, evolutionary approaches to. *The International Encyclopedia of Anthropology,* 1–4. https://doi.org/10.1002/9781118924396.wbiea1659

Boboye, O. A., & Okon, E. E. (2014). Sedimentological and geochemical characterization of the Cretaceous strata of Calabar Flank, southeastern Nigeria. *Journal of African Earth Sciences*. https://doi.org/10.1016/j.jafrearsci.2014.04.035

Fadiya, S. L., Ogunleye, S. O., Oyelami, A. B., & Aroyewun, F. R. (2020). Palyno-stratigraphic and palynofacies analysis of X and Y wells, offshore Niger Delta, Nigeria. *Ife Journal of Science, 22*(03), 25–45.

Faegri, K., & Iversen, J. (1989). *Textbook of pollen analysis* (4th edn by K. Faegri, P. E. Kaland, & K. Krzywinski) Wiley, p. 328.

Itam, A. E., Una, E. E., Udoh, M. U., Inyang, D. O., Emeka, C. N., Emeka, V. I., & Bassey, E. I. (2019). Palynological evaluation of Cretaceous sediments of Ekenkpon Shale, Calabar Flank, Southeastern Nigeria. *Journal of Scientific and Engineering Research, 6* (7), 156–164.

Jardiné, S., & Magloire, L. (1965). Palynologie et stratigraphie du Crétacé, des bassins de Sénégal et d" Côte De'Ivoire. *Mémoire Bureau Recherche Géologie Et Minéralogie, 32*, 187–245.

Lawal, O., & Moullade, M. (1986). Palynological biostratigraphy of Cretaceous sediments in the Upper Benue Basin, NE Nigeria. *Revue De Micropaléontologie, 29*, 61–83.

Raup, D. M. (1967). Geometric analysis of shell coiling: Coiling in Ammonoids. *Journal of Paleontology, 41*, 43–65.

Schrank, E. (1992). Nonmarine Cretaceous correlation in Egypt and northern Sudan: Palynological and paleobotanical evidence. *Cretaceous Research, 13*, 351–368.

Terry, R. C. (2009). Palaeoecology: Methods. In: *Encyclopedia of Life Sciences (ELS)*. Wiley. https://doi.org/10.1002/9780470015902.a0003274

Tyson, R. V. (1993). Palynofacies analysis. In: Jenkins, D. G. (Ed.), *Applied micropaleontology*. (Ch. 5, pp. 153–191). Kluwer Academic Publishers.

Ukpong, A. J., Dibi, T. I., Okon, E. E., & Iwara, E. E. (2018). Foraminiferal analysis and palaeoenvironmental interpretation of borehole ET (BH-ET) in the Calabar Flank, Southeastern Nigeria. *African Journal of Environmental Science and Technology, 12*(2), 74–83. https://doi.org/10.5897/AJEST2013.1562

Westermann, G. E. G. (1996). Ammonoid life and habitat. In: N. H. Landman, K. Tanabe, & R. A. Davis (Eds.), *Ammonoid paleobiology*. *Topics in Geobiology* (Vol. 13, pp. 607–707). Springer. https://doi.org/10.1007/978-1-4757-9153-2-16

Post-oligocene Tectono-Eustatic Fluctuations and Their Influence on the Stratigraphy of Eastern Arabia: The Fars Group of the Batina Coast, Oman

Osman Salad Hersi, Iftikhar Ahmed Abbasi, Abdulrazak Al-Sayigh, Musaab Al-Sarmi, Mohamed El-Ghali, and Tariq Al-Raisi

Abstract

The Fars Group of the Batina Coast of North Oman lies unconformably over Oligocene Asmari Formation (also known as MAM reefs). The group occurs along the low-lying region between the Al-Hajar Mountains and the coast of the Gulf of Oman. The group is divisible into three tectonostratigraphic successions represented by three formations: Sultan Qaboos University (SQU), Suwadi, and Barzaman, in ascending order. The SQU Formation consists of conglomerates, sandstones, and mudrocks with plant imprints in the muddier facies. The lower boundary of the formation is recognized in a well drilled in the Barka area (~35 km west of the SQU campus). This boundary indicates an erosional unconformable contact. A disconformable contact also defines the upper limit of the formation. The formation represents an alluvial fan to braided river system deposits with interfluvial ponds and flood plains. The Suwadi Formation is a carbonate tongue with abundant corals, calcareous algae, larger benthic foraminifera (LBF), echinoids, and mollusks. The LBF fossils indicate Langhian-Serravalian age. The underlying SQU Formation is envisaged to be early Miocene in age. The Barzaman Formation is dominated by pebble- to cobble-size sandy conglomerates with sandstone and mudrock interbeds. These facies accumulated in a fluvio-deltaic environment connected to lacustrine system. The formation consists of a lower unit with rootlets, imbricated clasts, scour surfaces, normal grading, and minor diagenetic (carbonatized) alterations and an upper unit defined by the typical "Barzamanite facies" (ophiolite detrital grains diagenetically altered to carbonate). The age of the Barzaman Formation is considered to be late Miocene to Pliocene in age. The Fars Group has been affected by Pliocene–Pleistocene uplifting and tilting. This resulted in terrigenous Quaternary deposits with marked erosional surface and angular contact.

Keywords

Fars Group • Miocene • Tectonics • Stratigraphy • Batina Coast • Oman

1 Introduction

The Batina Coastal Plain (BCP) lies along the northeastern flank of the North Oman Al-Hajar Mountains. This low-lying region is mainly covered by Quaternary alluvial deposits, obscuring older stratigraphic successions. The group is recorded throughout the Arabian and Persian regions. It consists of heterogeneous lithologic units, including coarse- to fine-grained siliciclastic, marl, carbonate, and evaporite rocks. In northern Oman, the post-Oligocene Fars Group occurs in two regions, the western/southwestern interior zone (Lacinska et al., 2014; Maizels, 1988) and the BCP (Salad Hersi et al., 2013). The two zones are separated by the Al-Hajar Mountains (Fig. 1). Previous work in the BCP region (Béchennec et al., 1986; Villey et al., 1986) was mainly in the form of regional mapping with little sedimentologic and stratigraphic details. Recent work by Salad Hersi et al. (2013) divided the group into three informal units (I, II, and III) of siliciclastic, carbonate, and siliciclastic strata, respectively. The purpose of this work is to formalize the lithostratigraphic content of the Fars Group of the BCP of Oman. This short paper summarizes the lithostratigraphy of the Fars Group in the BCP of Oman.

O. Salad Hersi (✉)
University of Regina, Regina, SK, Canada
e-mail: osman.salad.hersi@uregina.ca

I. A. Abbasi · A. Al-Sayigh · M. Al-Sarmi · M. El-Ghali
Sultan Qaboos University, Muscat, Oman

T. Al-Raisi
Occidental Petroleum (Oxy), Muscat, Oman

A. Çiner et al. (eds.), *Recent Research on Sedimentology, Stratigraphy, Paleontology, Tectonics, Geochemistry, Volcanology and Petroleum Geology*, Advances in Science, Technology & Innovation,
https://doi.org/10.1007/978-3-031-43222-4_7

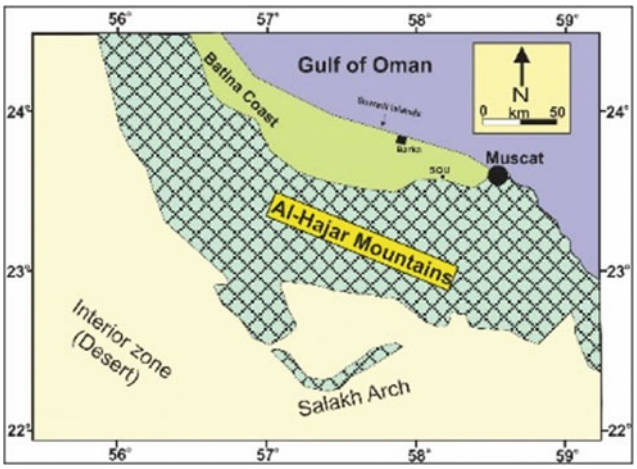

Fig. 1 Location of the Batina Coastal Plain (BCP), Al-Hajar mountains, and the interior zone of northern Oman

2 Geologic Settings

Middle to early late Proterozoic metamorphic and igneous rocks constitute basement rocks unconformably overlain by late Neoproterozoic to Carboniferous sedimentary successions, such as the Huqf and Haima supergroups (Abbasi et al., 2014; Glennie et al., 1974). During the Permian to Cretaceous periods, the region became an extended shelf of the Tethyan Ocean. The shelf was dominated by carbonate deposition represented by the Hajar Supergroup. The divergent tectonic regime of the Tethys Ocean changed to a convergent system in the early Late Cretaceous, followed by an orogenic (early Alpine) event (Hanna, 1995). The converging tectonic setting resulted in the obduction of the Tethyan oceanic crust, along with deep ocean hemipelagic and pelagic sediments of Sumeni and Hamrat Duru groups, on the Arabian platform in Late Cretaceous time. Ophiolite emplacement was followed by tectonic quiescence, sea level rise, and deposition of carbonate-dominated Maastrichtian to Oligocene succession with intermittent depositional hiatuses. A second phase of orogenic activity (late Alpine event) due to the opening of the Red Sea–Gulf of Aden caused northward movement of the Arabian Peninsula, collision with the Eurasian plate, and uplifting of the Zagros Mountains and Al-Hajar Mountains. In the region north of the Al-Hajar Mountains (i.e., the Batina coastal region), post-obduction Maastrichtian to Oligocene clastic and carbonate successions were deposited (Abbasi et al., 2014). As a result, the Fars Group unconformably overlies the Oligocene strata. (Salad Hersi et al., 2013).

3 Lithostratigraphy and Sedimentology of the Fars Group

In ascending order, the Fars Group can be divided into three tectonostratigraphic successions represented by Sultan Qaboos University (SQU), Suwadi, and Barzaman Formations (Fig. 2). These formations are well exposed in road cuts and excavations within the university campus. The SQU Formation comprises a thick succession of normally- and inversely grading conglomerates, sandstones, and mudrocks. Fossilized plant imprints (twigs, leaves, and root casts) are present within the muddier facies. The lower contact of the formation is not exposed within the study area. However, the Barka area's well (~35 km west of SQU) indicates an erosional unconformable contact. The upper contact is a sharp surface followed by conglomeratic lag deposits that define the base of the overlying Suwadi Formation. The SQU Formation represents alluvial fan to braided river system deposits with discrete interfluvial ponds and flood plains. The Suwadi Formation is a thin, highly fossiliferous carbonate tongue. This formation consists of reefal bodies with abundant corals and calcareous algae. It also contains larger benthic foraminifera (LBF), echinoid, and mollusk shells. This formation is well-exposed in the As-Suwadi Islands near Barka, which is much thicker than the section exposed on the SQU campus. Biostratigraphic data (LBF) from this work and previous studies indicate Middle Miocene (Langhian-Serravalian) age for this carbonate unit. This age suggests an early Miocene (pre-Langhian) age for the underlying SQU Formation. The Barzaman Formation is dominated by pebble- to cobble-size sandy conglomerates with sandstone and mudrock interbeds. Sedimentary structures in the formation suggest deposition in a fluvio-deltaic (fan-delta) environment, most likely connected to a lacustrine system. The formation consists of two lithologic units. Rootlets, scoured surfaces, graded beds, imbricated clasts and minor diagenetic (carbonatized) alterations characterize the lower unit of the formation (BZ1). In contrast, the upper unit (BZ2) is defined by the typical "Barzamanite facies" (ophiolite detrital grains diagenetically altered to carbonate, Maizles, 1988; Lacinska et al., 2014). The age of the Barzaman Formation is late Miocene to Pliocene; it documents intensive uplifting of the hinterland and renewal of siliciclastic progradation that followed the withdrawal of the "Suwadi Sea". The Fars Group has been affected by Pliocene–Pleistocene uplifting, faulting, and tilting. This resulted in Quaternary detrital deposits with marked basal erosional surface and angular surface unconformity.

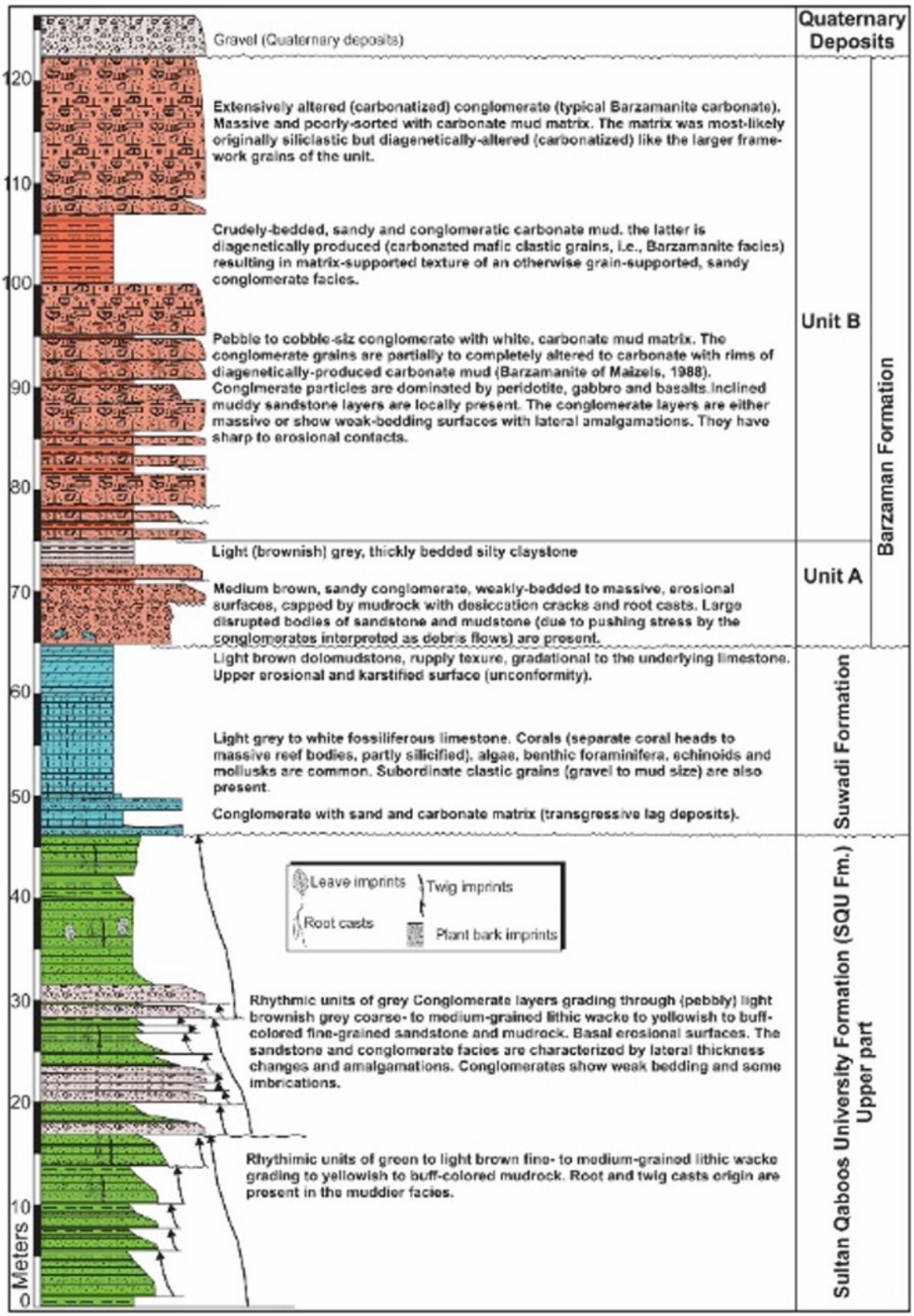

Fig. 2 Lithostratigraphic units and sedimentologic summary of the Fars Group at the SQU campus

4 Discussion

Al-Hajar Mountains preserve and expose extensive rock succession of Precambrian to the Cenozoic age. The stratigraphic stacking nature of the post-Oligocene succession of the BCP reflects tectono-eustatic perturbations that had affected the region. The main uplifting phase of Al-Hajar Mountain was related to the late Neogene Alpine / Zagros deformation (Hanna, 1995). This was followed by intensive erosion and deposition of siliciclastic-dominated strata of the SQU Formation. Middle Miocene tectonic quiescence accompanied by sea level rise resulted in a reduction of the clastic input, establishment of a carbonate platform, and deposition of the Suwadi Formation. Subsequent sea level drop and uplifting of the hinterland rejuvenated weathering and clastic influx represented by the Barzaman Formation. The latter, mainly formed by gravel- to mud-size ophiolite clasts, has been highly altered to carbonate mineralogy, the typical Barzamanite facies of Maizels (1988), Salad Hersi et al. (2013), and Lacinska et al. (2014). This tripartite clastic-carbonate-clastic sequence constitutes the Fars Group of the BCP.

5 Conclusion

Miocene to Pliocene tectonic and marine incursions have shaped the sedimentary succession of the Batina Coast of Oman. The succession constitutes the Fars Group which is well-recognized throughout the Arabian and Persian regions. In the Batina Coastal Plain (BCP), the group is divided into three formations: two siliciclastic units: lower Sultan Qaboos University (SQU) and upper Barzaman formations are intervened by the carbonate strata of the Suwadi Formation. The clastic units were deposited in fluvial, interfluvial, and possibly lacustrine environments. However, the carbonate unit accumulated in a shallow marine setting as suggested by marine fossils (corals, foraminifera, calcareous algae, echinoids, and mollusks). Fossils in the Suwadi Formation indicate middle Miocene age. Thus, the SQU Formation, which unconformably lies over the Oligocene Asmari Formation (or MAM reefs), is inferred to date lower Miocene and the Barzaman Formation as late Miocene to possibly Pliocene in age. The vertical lithostratigraphic pattern of clastic-carbonate-clastic succession reflects two events (early and late Miocene) of tectonic uplifting and intensive weathering of the hinterland. This has resulted in extensive siliciclastic influxes into the basin. These two events are intervened by a middle Miocene period of relatively tectonic quiescence, sea level rise, establishment of a carbonate platform, and deposition of the shallow marine, highly fossiliferous Suwadi Formation.

Acknowledgements This project is supported financially or in-kind by the University of Regina (start-up grant of the senior author by the University of Regina) and Sultan Qaboos University.

References

Abbasi, I. A., Salad Hersi, O., & Al-Harthy, A. (2014). Late cretaceous conglomerates of the Qahlah formation, North Oman. *Geological Society, London, Special Publication, 392*, 325–342.

Béchennec, F., Beurrier, M., Rabu, D., & Hutin, G. (1986). *Explanatory notes, Geological map of Barka, Sheet NF 40–3B, 1:100,000* (p. 33). Ministry of Petroleum & Minerals, Oman.

Glennie, K. W., Boeuf, M. G., Hughes-Clarke, M. H. W., Moody-Stuart, M., Pilaar,W. F., & Reinhardt, B. M. (1974). Geology of the Oman mountains. Verhandelingen Koninklijke Nederlands Geologisch Mijnbouw Kundig Genootschap. Transactions of the Royal Geological and Mining Society of the Netherlands, Vol. 31, p. 423.

Hanna, S. (1995). *Field guide to the geology of Oman. The historical Ass. of Oman* (p. 143).

Lacinska, A. M., Styles M. T., & Farrant, A. R. (2014). Near-surface diagenesis of ophiolite-derived conglomerates of the Barzaman Formation, United Arab Emirates: a natural analogue for permanent CO_2 sequestration via mineral carbonation of ultramafic rocks. In H. R. Rollinson, M. P. Searle, I. A. Abbasi, A. Al-Lazki, & M. H. Al Kindi (Eds.), *Tectonic evolution of the Oman mountains* (The Geological Society London Special Publication, vol. 392, pp. 343–360).

Maizels, J. (1988). Palaeochannels: Plio-Pleistocene raised channel systems of the western Sharqiyah. In R. W. Dutton (Ed.), *The scientific results of the royal geog. society's Oman Wahiba project 1985–1987*. Journal of Oman Studies Special Report l.

Salad Hersi, O., Abbasi, I. A., Ahmed, S., & Al-Raisi, T. (2013). Age of siliciclastic-dominated Fars Group of the Batina Coast, North Oman, inferred from bioclastic-bearing carbonate unit. In *Geologic problem solving with microfossils III conference*. University of Houston, Houston, Texas, USA, Abstract volume, 72–73.

Villey, M., De Gramont, X., & Le Metour, J. (1986). *Explanatory notes, Geological map of Sib, Sheet NF 40–3C, 1:100,000* (p. 48). Ministry of Petroleum and Minerals.

New Time-Expanded Chronostratigraphic Column of Northern Iraq During Cretaceous and Tertiary

Kamal Haji Karim

Abstract

The oil companies worked in Iraq, drew and published the time-expanded chronostratigraphic column (Wheeler diagram) of Iraq in the fifties of the last century. During this long time, the column remained without significant changes. Therefore, the present study tries to modify and update the column according to the recent sedimentological developments and traditional and sequence stratigraphies. Moreover, the modification is based on more than 50 published papers by the author and more than 20 years of fieldwork in northern Iraq. The significant updates include removing previous unconformities between formations, such as Qamchuqa with Dokan and Bekhme, Gulneri with Dokan and Kometan, and the latter Formation with Shiranish Formation. This is true for the unconformity between Tanjero and Kolosh Formations. Thus, the article changed the contacts between the above units to conformable ones, and their boundary is assigned as gradational in the new chronostratigraphic column. The column also includes the lateral merging of the Kolosh Formation and the lower part of the Red Bed Series with the Walash Formation (Group). The study considers these three units as deposits of a large foreland basin, and their sediments derived from a volcanic arc inside Iran during the Paleocene. On the new column, the ophiolites and basaltic rocks are assigned as metamorphosed greywackes (volcaniclastic sandstones) of the Walash Formation. The column manifests the tectonic setting and location of each Formation according to the present tectonic zones (Low and High Folded, Imbricated, Thrust, and Sanandaj-Sirjan Zones) of Iraq instead of the previous general geographic positions of the formations. According to fossils and sedimentary structures, it shows the stratigraphic units in their proper environmental settings, such as the Cretaceous Arabian Platform Margin and the coastal areas of the Zagros Foreland Basin, where the coarse clastic units rested near the source areas during the Tertiary. Similarly, it indicated the deep facies (marls and shales) near the basin plains. The column is associated with models for showing some of the stratigraphic units in their paleogeographic and tectonic settings in basins during the latter two ages. Establishing a new Iraqi time-expanded stratigraphic column has applications in exploring oil and other natural resources. It also enables a better understanding of the stratigraphy and tectonic setting of the Arabian plate and Zagros collisional belt.

Keywords

Wheeler diagram • Northern Iraq stratigraphy • Time-expanded stratigraphic column • Zagros stratigraphy • Arabian Plate stratigraphy

1 Introduction

The time-expanded stratigraphic column (Wheeler diagram) displays graphical geographic extent, period, and the missing ages of many lithostratigraphic units of an area. The missed sediments of ages (unconformity) are expanded in this type of column to manifest their time durations, which are helpful for basin analysis and oil exploration. The missed ages are those that have no representative lithology in the rock column (or in the basin) due to erosion or non-deposition. Geologists can call these columns "wheeler diagrams" in honor of Wheeler (1953). He configured these columns as two axes of time and geographic extent (spatial extent) to represent vertical and horizontal coordinates. He added that it expands or exaggerates the rock bodies and unconformities according to their period. The time-expanded chronostratigraphic column of Iraq was established in the fifties of the last century by Bellen et al. (1959) (Fig. 1a and b). Later, Buday (1980), Jassim and Goff (2006) indicated

K. H. Karim (✉)
University of Sulaimani, Kurdistan, Iraq
e-mail: kamal.karim@univsul.edu.iq

A. Çiner et al. (eds.), *Recent Research on Sedimentology, Stratigraphy, Paleontology, Tectonics, Geochemistry, Volcanology and Petroleum Geology*, Advances in Science, Technology & Innovation,
https://doi.org/10.1007/978-3-031-43222-4_8

most of the missed ages (unconformities) between the formations in their wheeler diagrams. The present study tries to update and modify the column with the aid of recent studies and new developments in the tectonic setting, sequence stratigraphy, and sedimentologic principles of the area. The study is mainly limited to northern Iraq, where the most recent relevant studies are conducted. The present column highly benefited from the column of the latter three works of literature. During this long time, the column was beneficial for teaching and academic purposes in all Iraqi universities and for practical implications by petroleum and other economic activities but remained nearly without main changes.

2 Methodology and Materials

The present study is the result of more than 20 years of field studies in north Iraq (Kurdistan Region), in addition to reviewing the stratigraphy and biozonation of the previous studies. Our study inspected the boundary conditions of all Cretaceous and Tertiary Formations laterally and vertically in northern Iraq. The author revisited all the previous unconformities established in Bellen et al. (1959), Buday (1980), Jassim and Goff (2006) and checked them in tens of sections. In the drawing of the new column, current concepts of sedimentology and sequence stratigraphy are utilized (Fig. 1c, d, e).

3 Result and Discussion: Removal of Several Unconformities

3.1 Problem of Fossils-Based Unconformities

The present column removed several unconformities and changed their statuses to conformable, depending on the absence of conglomerate, erosional surface, paleosoil, and unusual lithologies. Most of the previous unconformities are established depending on the lack of index fossils. Examples of recent studies that used this latter method are the studies of Ameen and Gharib (2014, p. 2708), who attributed missing sediments of Gulneri and Dokan Formations (Middle Cenomanian-Early Turonian) in the majority of the High Folded and Thrust Zone of Iraq to the disappearance of the *R. cushmani* and *H. moremani* subzone. Similarly, Lawa et al. (2013) concluded 4.7 Ma unconformity (as Turonian hiatus) between Qamchuqa and Kometan Formations in the Qamchuqa Gorge section. They justified unconformity by the absence of planktonic foraminiferas such as *Globigerinoides bentonensis* and *Dicarinella hangi, Whitnella archaeocretacea*, *Heterohelix moremani*, and *Helvetotruncana Helvetica*.

Another example is the study of Ghafur et al., 2020), who found unconformity with a period of 25 Ma at the southwestern limb of the Piramagroon anticline, during which the whole Qamchuqa Formation was missed. They do not indicate any direct evidence to estimate the period of this huge unconformity. However, they attributed, indirectly it to the absence of index fossils since they mentioned biostratigraphic age dating of their sections. On the same basis, Farouk et al. (2017) considered the contact between Kometan and Shiranish Formations as unconformable due to the missing sediments of Late Campanian. They observed the absence of CC20-CC21/UC15b-C^{TP} nannofossil zones and equivalent planktonic foraminifera zones *Contusotruncana plummerae* (*Globotruncana ventricosa* Zone), *R. calcarata*, and *G. havanensis*. The present study inspected tens of sections in the field. However, the above three unconformities are not confirmed. The use of the index fossils alone to indicate the unconformity is unsafe since the absence of index fossils depends not only on unconformities but also on diagenesis, environment restrictions, submarine erosion, mass wasting, rate of sedimentation, methods of sampling, and accuracy of identifications. Especially the boundaries of the formations are sensitive to the survival of fauna due to changes in lithologic and nutrients. Taha and Karim (2009), Karim et al. (2018), and Al-Badrani et al. (2012) also refuted the above unconformities, and the present study aids their considerations.

3.2 Fault Breccia Considered as Conglomerate Previously

Wetzel (1950 in Bellen et al., 1959), Al-Qayim et al. (1995) recorded an unconformity represented by 10 m conglomerate between Bekhme (late Campanian) and Qamchuqa (Hautervian-Cenomanian) Formations in Bekhma Gorge, Arbil area. In its type section and the other regions, Al-Mutwali et al. (2008) recorded polygenetic conglomerate too at the base of the Bekhme Formation with variable thickness (3-20 m). According to these authors, this unconformity spanned about 20 million years, during which sediments of the Kometan, Gulneri, and Dokan Formations were missed. Conversely, Ameen and Karim (2008) and Karim (2013) studied this conglomerate in detail and documented much evidence to prove the gradational boundary between the latter two formations. They concluded a fault breccia instead of the claimed conglomerate. They attributed

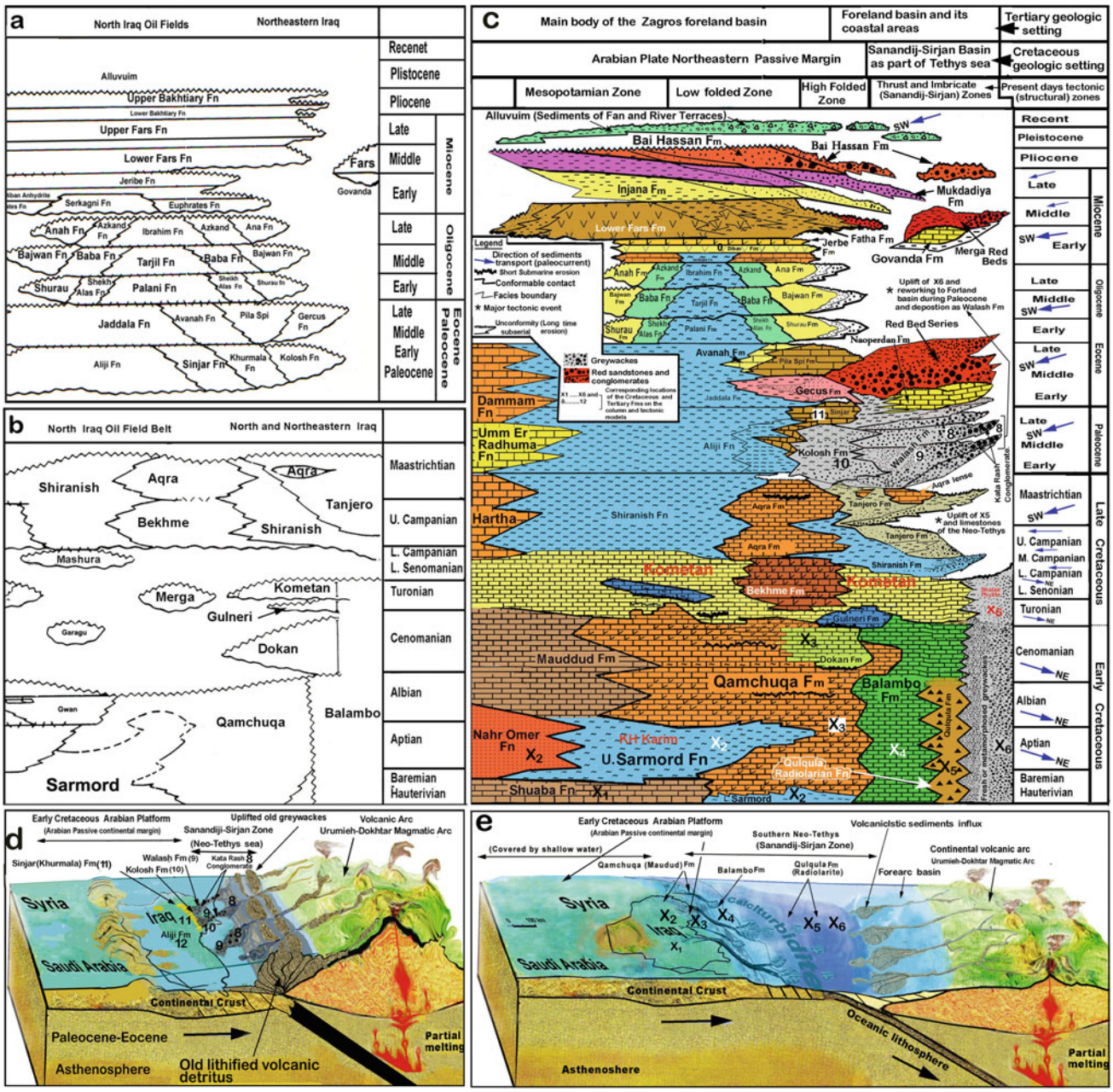

Fig. 1 **a, b** Time-expanded chronostratigraphic column of northern Iraq during Tertiary and Cretaceous by Bellen et al. (1959), **c** similar column of the present study, **d** tectonic and paleographic models during Paleocene and **e** similar model for Cretaceous (modified from Karim, 2020). The corresponding locations of the formations are indicated X1 …X6 for Cretaceous and those of Tertiary by 8 … 12 in the text

it to a reverse fault in the area (Fig. 2). Oil companies recently proved the fault by seismic profiles in the Bekhme gorge. Due to faulting and folding of the type section of the Balambo Fm, Bellen et al. (1959) indicated an unconformity between two deep marine formations (Balambo and Shiranish Fms) in Sirwan valley. It spanned about 10 million years, during which sediments of Coniacian and Santonian were missed. Karim et al. (2016) proved a conformable boundary between the latter two formations and attributed this claimed unconformity to faulting, which was not considered by Bellen et al. (1959).

3.3 Geographic Extension of the Wheeler Diagram to the Sanandaj-Sirjan Zone (SSZ)

Recently, many papers have been published and focused on changing the previous ophiolite and volcanic rocks to

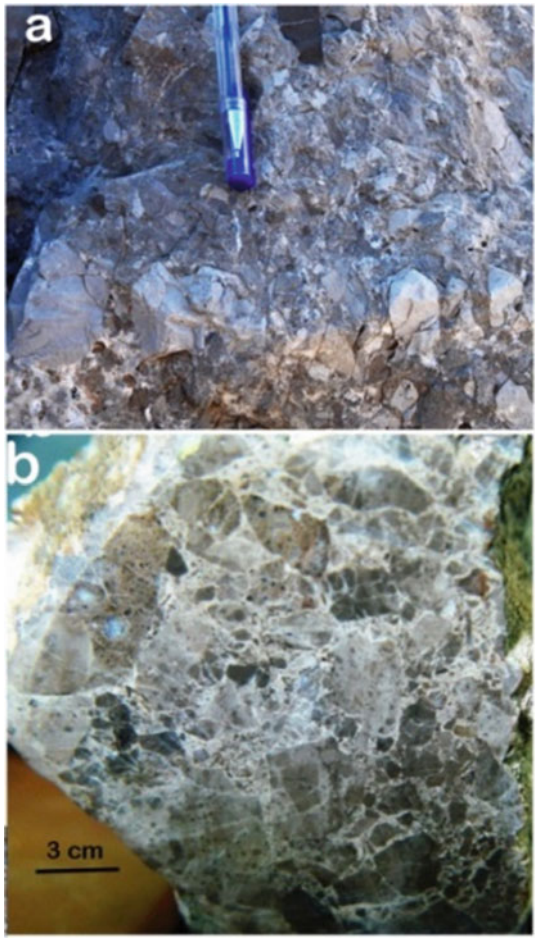

Fig. 2 Outcrop of the fault breccia in the Bekhme gorge at the contact between Bekhme and Qamchuqa Formations. It was considered previously as a conglomerate, **b** a polished surface shows the breccia

metamorphosed sandstones (greywackes and volcanic detritus). These studies are such as Karim and Bidry (2020), Karim and Ghafur (2021), and Karim and Hamza (2021), who refuted the igneous rocks (Ophiolites) and their obduction on the Arabian Continental Plate in the Bulfat, Mawat, Avroman, and Penjween areas. These studies changed the tectonic settings of these areas to metamorphic core complexes and parent rocks to volcaniclastic sandstones, impure limestones and greywackes, which later metamorphosed. In the same context, two other papers were published. The first one is Karim et al. (2020) documented eleven pieces of evidence for the refusal of basaltic intrusion in the Gercus Formation in the Dohuk area and changed to a sedimentary succession of volcaniclastic sandstone. The second one is Karim and Abioui (2021), who refuted ophiolite and basaltic rocks with detailed models and concluded transportation of the volcaniclastic sandstones and greywackes from the Urumieh-Dokhtar Magmatic Arc to the SSZ (Mawat, Bulfat, and Penjween areas as a part of the latter zone). Slightly earlier, Karim (2020) changed the SSZ from a continental block to a deep basin as a part of the Neo-Tethys (Fig. 1d and e). The above papers considered all the previous ophiolite rocks as metamorphosed sediments of the Walash Formation (mainly greywacke and volcaniclastic sediments). The latter Formation is observable in these complexes under the Naopurdan Formation (reefal limestone, see Karim and Ghafur, 2021). In the stratigraphic column, these changes are considered, and the Walash Formation and Kata Rash Conglomerate (as proximal facies) correlated (joined) with Kolosh Formation in the High Folded Zone as distal facies. This correlation is based on the deposition of the three facies in a single foreland basin, aided by present field works. The present study removed many previous unconformities between deep formations but added many new ones on the column in the coastal area of the Tertiary foreland basin (Fig. 1c).

4 Conclusion

This study prepared a new time-expanded stratigraphic column (Wheeler diagram) for northern Iraq during the Cretaceous and Tertiary according to extensive fieldwork. In this column, many previous unconformities are removed, and the new ages and distributions of many units are introduced. The study changed all allochthonous rocks of Northern Iraq to autochthonous ones. This study suggests avoiding using fossil and biozonation for the establishment of unconformities. While using the boundary condition, the field features such as paleosoils, conglomerate, and erosional surfaces, with regional correlation, are more accurate for establishing unconformities.

References

Al-Badrani, O. A., Karim, K. H., & Ismail, K. M. (2012). Nannofossils biozones of contact between Kometan and Shiranish Formations, Chaqchaq Valley, Sulaimanyia, NE-Iraq. *Iraqi Bulletin of Geology and Mining, 8*(1), 19–29.

Al-Qayim, B., & Al-Shaibani, S. (1995). Lithostratigraphy of cretaceous-tertiary transects Bekhme Gorge, NE-Iraq. *Iraqi Geological Journal, 28*(2), 127–136.

Al-Mutwali, M. M., Al-Banna, N. Y., & Al-Ghrear, J. S. (2008). Microfacies and sequence stratigraphy of the late Campanian Bekhme formation in the Dohuk area, N. Iraq. *Journal of GeoArabia, 13*(1), 39–54.

Ameen, B. M., & Karim, K. H. (2008). New sedimentologic and stratigraphic characteristics of the Upper boundary of Qamchuqa formation (Early Cretaceous) Northwest of Erbil, Kurdistan region, NE/Iraq. *Iraqi Bulletin of Geology and Mining, 4*(2), 1–13.

Ameen, F. A., & Gharib, H. (2014). Biostratigraphy of the Tethyan Cretaceous successions from northwestern Zagros fold-thrust belt, Kurdistan region, North east Iraq. *Arabian Journal of Geoscience, 7*, 2689–2710.

Buday, T. (1980). Regional geology of Iraq: Stratigraphy. Kassab, I. I. M., & Jassim, S. Z. (Eds.), GEOSURV, Baghdad, (Vol. 1, 445 p).

Farouk, S., Thibault, N., Jaff, R. B. N., Khashaba, A. (2017). An integrated study of upper Campanian-lower Maastrichtian carbon isotopes and calcareous plankton biostratigraphy of the Kurdistan Region, northeastern Iraq. *Cretaceous Research, 82*. https://doi.org/10.1016/j.cretres.2017.09.020

Ghafur, A. A., Hersib, O. S., Sissakian, et al. (2020). Sedimentologic and stratigraphic properties of early Cretaceous Neo-Tethys shelf margin of Arabia: The Qamchuqa formation of the Zagros folded zone of Iraq. *Marine and Petroleum Geology, 118*, 104421.

Jassim, S. Z., & Goff, G. (2006). *Geology of Iraq, Dolin, Prague and Moravian Museum* (Brno, p. 341).

Karim, K. H. (2013). New geologic setting of the Bekhme Formation. *Journal of Zankoy Sulamani (JZS), 15*(3), 23–38.

Karim, K. H. (2020). Early Cretaceous calciturbidites facies from Zagros Fold-Thrust belt: A key to paleogeography and environment of northeast Arabian platform passive margin, examples from Kurdistan region, Northeast Iraq. *Carbonates and Evaporites, 35*, 19. https://doi.org/10.1007/s13146-019-00544-w

Karim, K. H., & Abioui, M. (2021). Geology of the Zagros basaltic bodies: Examples from the Avroman Mountains, Kurdistan region, Northeast Iraq. *Journal of Sedimentary Environment, 6*(2), 169–188.

Karim, K. H., Al-Barzinjy, S. T., & Khanaqa, P. A. (2018). Geology and critical review of the Upper Cretaceous Zagros chalky limestone (Kometan Formation) from Sulaimani Governorate, Northeastern Iraq. *Bulletin of the Mineral Research and Exploration, 157*, 59–74.

Karim, K. H., & Al-Bidry, M. (2020). Zagros metamorphic core complex: Example from Bulfat mountain, Qala Diza area, Kurdistan region, Northeast Iraq. *Jordan Journal of Earth and Environmental Sciences, 11*(2), 113–125.

Karim, K. H., Al-Khafaf, A. O., Sharbazheri, K. I. (2016). Critical analysis of the type section of the Balambo formation (Valanganian-Turonian), Sirwan valley, Kurdistan Region, NE-Iraq. *Journal of Zankoi Sulaimani,* Special Issue, 189–202.

Karim, K. H., & Ghafur, I. M. (2021). Updated stratigraphy, tectonics and boundary conditions of the Mawat and Bulfat Ophiolite complexes, Kurdistan Region, NE-Iraq. In *The second international & the fourth scientific conference of college of science*. Tikrit University

Karim, K. H., & Hamza, B. J. (2021). Relation between Walash Group and Kolosh formation: A key to the stratigraphy of the Penjween area. In *The 1st International conference (Geo Iraq 1) of Tikrit university, Iraq* (pp. 95–102).

Karim, K. H., Khanaqa, P. A., & Babashekh, S. M. (2020). Revisiting the "Gercus Basalt within the Eocene Gercus formation: Implications for sedimentary origin of a basaltic body, Kurdistan Region, Northern Iraq. *Ore and Energy Resource Geology, 4–5*, 100008. https://doi.org/10.1016/j.oreoa.2020.100008

Lawa, F. A., Koyi, H., Ibrahim, A. (2013). Tectonostratigraphic evolution of the N.W. segment of the Zagros fold-thrust Belt, North, NE Iraq. *Journal of Petroleum Geology, 36*(1), 75–96.

Taha, Z. A., & Karim, K. H. (2009). New ideas about Gulneri Shale formation in Dokan area, Kurdistan Region, NE Iraq. *Iraqi Bulletin of Geology and Mining, 5*(2), 29–39.

Van Bellen, R. C., Dunnington, H. V., Wetzel, R., & Morton, D. (1959). Lexique Stratigraphique, Interntional. Asie, Iraq, Fasc, 10a, Paris, 10a, 333 pp.

Wheeler, H. (1953). Time stratigraphy. *Bulletin of the American Association of Petroleum Geologists, 42*(5), 1047–1063.

Establishment of Geological Age Under the Constraints of Astronomical Cycles in Dongying Sag

Xuwei Luan and Jinliang Zhang

Abstract

The accurate determination of geological age is the key to understanding the evolutionary history and process of earth, but improving the accuracy of geological age has always been a scientific problem. Astronomical cycle analysis is an effective method developed for high-resolution stratigraphic research in recent years. We apply this method to improve the accuracy of the stratigraphic age of the ash-deficient section of lacustrine fine-grained sedimentary rocks in Dongying Sag, which can make up for the lack of isotopic dating. By observing the core (about 198 m thick, well Niu 33), the study interval's petrological characteristics are found. The study interval is divided into four stratigraphic units according to the GR curve and lithology. After the data preprocessing, the results show that these four stratigraphic units all record the Milankovitch cycles of 405 ka eccentricity, 125 ka short eccentricity, 40.1–38.7 ka obliquity, and 18.7 ka precession. Finally, the 38.7 ka obliquity cycle curves are filtered out, and we find about 202.45 cycles of 38.7 ka in the Es3m of the Dongying Sag, with a cumulative deposition time of 7.83 Ma. Taking the volcanic dating 40.1 Ma of the Es3l and the Es3m as the anchor point, a "floating" astronomical age scale is established, and the geologic age of the top of the Es3m is 32.27 Ma.

Keywords

Dongying Sag • Milankovitch cycles • A "floating" astronomical age scale

1 Introduction

Milankovitch hypothesis provides a new perspective for geoscientists. For a long time, it has been considered that the three major factors controlling sedimentation are sea-level rise and fall, tectonic movement, and climatic conditions. These three factors have a particular control effect on sedimentation, but they still encounter some unexplained scientific problems. Therefore, some scholars began to observe the outside of the earth and look for higher-level exogenous control factors. With the deepening of research, people gradually found and extracted the Milankovitch cycle signals from different earth materials, and its application field is more and more extensive. The method of geological dating using the Milankovitch cycle theory is considered the third milestone of time stratigraphy interpretation (Gong et al., 2008). Using the astronomical cycle theory, the age scale is established through the astronomical tuning of high-resolution cycle strata to improve the accuracy of geological age and make up for the shortage of isotopic dating in some time periods (Huang, 2014).

2 Settings and Methods

Dongying Sag is located in the southern part of the Jiyang Depression in the Bohai Bay Basin, eastern China (Fig. 1). The targeted stratum in this study is the third middle member (Es3m) of the Paleogene Shahejie formation. This target interval developed during the rift-filling period. The basin's tectonic movement was relatively stable, and the lake water was deepening because the climate was warm and humid. Therefore, a large set of mudstone deposits developed during this period.

Before spectrum analysis, it is necessary to remove extreme values, obtain evenly spaced data, and then carry out preprocessing processes such as detrending. Therefore, adopt 2Π spectrum analysis of GR logging series by the

X. Luan (✉) · J. Zhang
Faculty of Geographical Science, Beijing Normal University, Beijing, 100875, P. R. China
e-mail: 1419402879@qq.com

A. Çiner et al. (eds.), *Recent Research on Sedimentology, Stratigraphy, Paleontology, Tectonics, Geochemistry, Volcanology and Petroleum Geology*, Advances in Science, Technology & Innovation,
https://doi.org/10.1007/978-3-031-43222-4_9

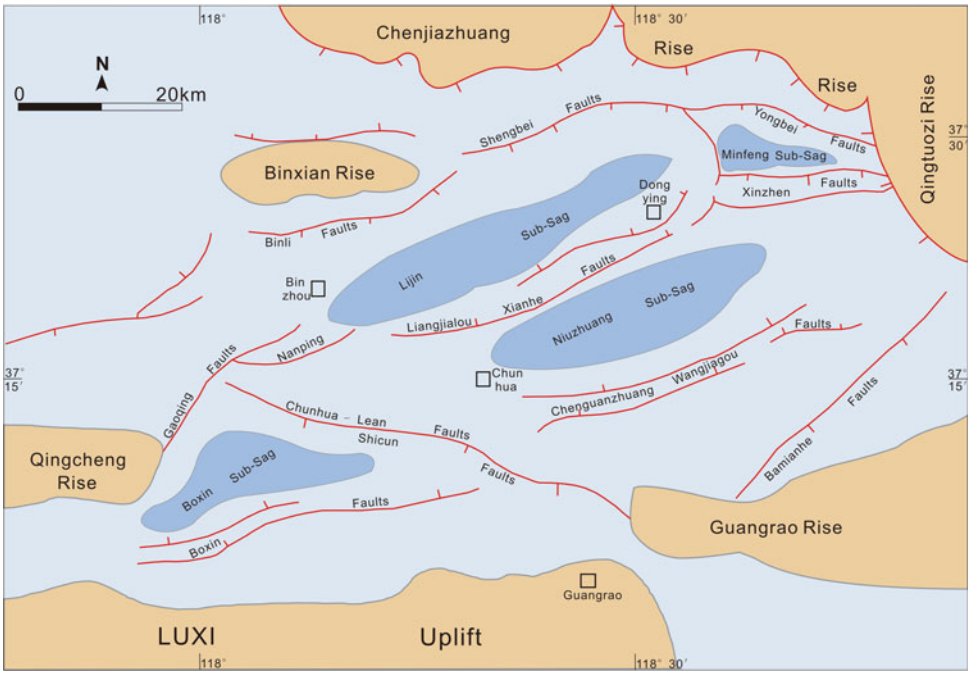

Fig. 1 Geological setting of Dongying Sag

multi-taper method. In addition, the Fast Fourier Transform (FFT) spectrum of the GR logging series is used to track the change of cycle frequency under different sedimentary accumulation rates. The cycle length ratio method determines the relationship between sedimentary cycle and earth orbit parameters. First, the Milankovitch cycles are extracted by the Gaussian bandpass filter, and then the astronomical time scale is established (Hinnov, 2013).

3 Results

3.1 Lithofacies Characteristics

By observing the core (about 198 m thick, well Nui 33), the study interval's petrological characteristics are found. The lithology of the lower section of the Es3m is mainly composed of interbedded silty sandstone and mudstone. The silty sandstone and the light mudstone indicate a shallow lake environment (Fig. 2a). Vertically, the development of the silty sandstone (blue) and the mudstone (red) has the characteristics of periodic (Fig. 2b). The gray mudstone indicates a semi-deep lake environment (Fig. 2c). And the dark gray mudstone indicates the deep lake sedimentary environment (Fig. 2d).

3.2 Time Series Analysis Results

The study interval is divided into four stratigraphic units according to the GR curve. For example, the strata from the

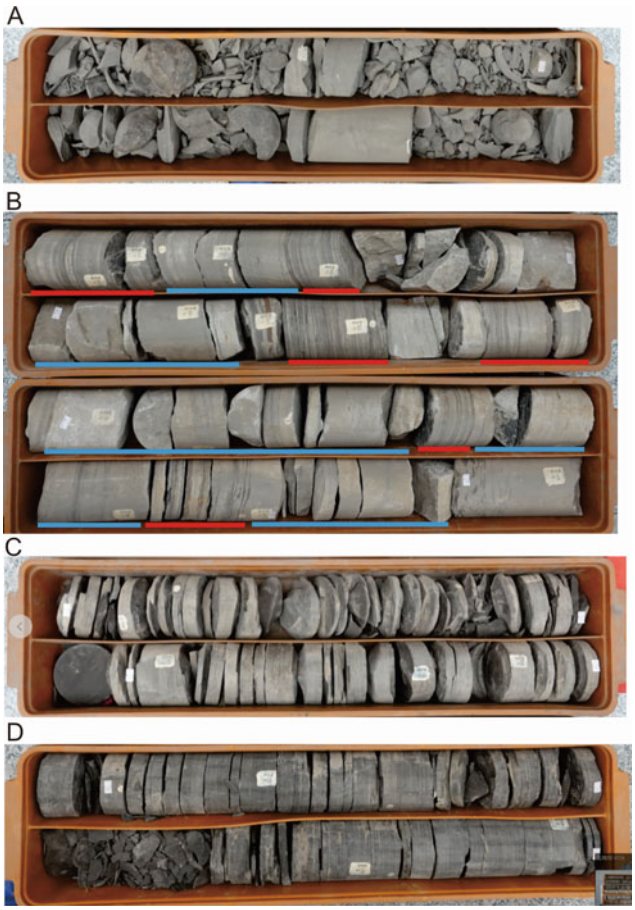

Fig. 2 Core photos of lithofacies in the Dongying Sag. **a** light mudstone, Well Niu 33, 3053.20–3055.20 m; **b** sandstone and mudstone interbed, Well 33, **c** gray mudstone, Well 33, 3138.75–3140.75 m, **d** dark gray mudstone, Well 33, 3211.64–3213.54 m

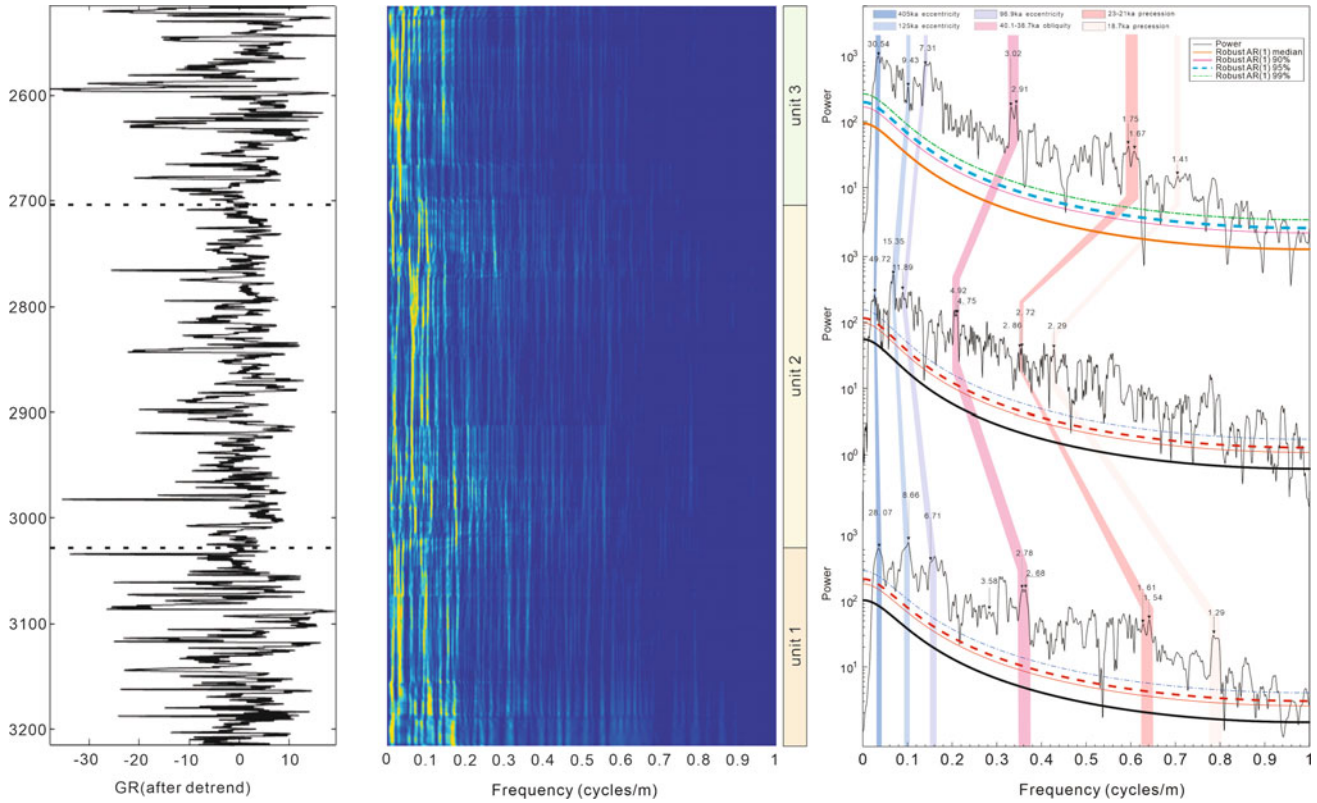

Fig. 3 Spectrum diagram

Es3m in Niu 33 well are divided into three units: 3215–3025 m, 3025–2703 m, and 2703 m–2512 m (Fig. 3.).

The GR logging data are used as a substitute index. After the data preprocessing, the spectrum analysis shows a significant peak value exceeding the 95% confidence level. The results show that these three stratigraphic units all record the Milankovitch cycles of 405 ka eccentricity, 125 ka short eccentricity, 40.1–38.7 ka obliquity, and 23–21 ka, 18.7 ka precession. It proves that lacustrine fine-grained sedimentary rocks can be a sound recorder of Milankovitch cycle signals.

4 Discussion

Comparing the Milankovitch cycle signal identified by the spectrum analysis diagram of the three strata, the astronomical cycle curve with a period of 38.7 ka in each stratum is extracted, respectively. The results show 70 cycles of the 38.7 ka in unit 1 of the Es3m, lasting 2.52 Ma. There are 67.45 cycles of the 38.7 ka in unit 2 of the Es3m, lasting 2.61 Ma. And there are 65 cycles of the 38.7 ka in unit 3 of the Es3m, lasting 2.7 Ma. The volcanic dating 40.1 Ma at the boundary of the Es3l and the Es3m is taken as the anchor point. A "floating" astronomical age scale is established.

5 Conclusions

Lacustrine fine-grained sedimentary rocks can be a sound recorder of Milankovitch cycle signals. About 202.45 cycles of 38.7 ka in the Es3m of the Dongying Sag, with a cumulative deposition time of 7.83 Ma. The geologic age of the top of the Es3m is 32.27 Ma. A "floating" astronomical age scale is established and used to estimate each stage in the study interval.

References

Gong, Y., Du, Y., Tong, J. (2008). Cyclostratigraphy: The third milestone of stratigraphy in understanding time. *Earth Science-Journal of China University of Geosciences, 33*(4), 444–457.

Hinnov, L. A. (2013). Cyclostratigraphy and its revolutionizing applications in the earth and planetary sciences. *Geological Society of America Bulletin, 11*(12), 1703–1734.

Huang, C. (2014). Cyclostratigraphy and astrochronology and their research status in Mesozoic., *21*(2), 49–66.

Well Log Sequence Stratigraphic Analysis of the Upper Carboniferous-Early Permian Haushi Group in South Oman

Ibtisam Nasser Al-Kharusi, Mohamed A. K. El-Ghali, Iftikhar Ahmed Abbasi, and Aleksandar Ilic

Abstract

The Upper Carboniferous-Early Permian Haushi Group is equivalent to the Arabian Plate Megasequence 5 (AP5) and comprises Al-Khlata and Gharif Formations. Wireline sequence stratigraphic analysis from conventional wireline logs in the Dhofar Region, South Oman, has shown that Haushi Group composes of seven third-order system tracts. The Al-Khlata Formation is subdivided into two system tracts, a highstand system tract (HST) followed by a transgressive system tract (TST). The lower Al-Khlata Member is composed of aggrading facies of galciofluvial sand packages and diamictites reflecting an early stage of ice retreat, capped by transgressive fine sediments of the upper Al-Khlata Member. The upper part of the Haushi Group corresponds to the Gharif Formation and is subdivided into four systems in order, transgressive system tract (TST), highstand system tract (HST), transgressive system tract (TST), and finally, the lowstand system tract (LST). The lower Gharif Member deposited consecutively and shared the transgressive system tract (TST) with the upper Al-Khlata Member. This system tract ended with marine shales marking a maximum flooding surface. The middle Gharif reflects a highstand system tract (HST), which comprises progradational calcareous siliciclastics. A sequence boundary marks the end of this system. The upper Gharif Member represents a transgressive system tract in the bottom, shifting to a regressive lowstand system in the top sediment packages of Upper Gharif.

Keywords

Sequence stratigraphy • Gharif formation • Al-Khlata formation • Wireline logs

1 Introduction

Haushi Group in South Oman was studied using subsurface data from conventional wireline logs from five wells in the Dhofar Region, South Oman. The sequence stratigraphy was analyzed using wireline data solely through well-known methods that involve studying log suits' shapes, defining anomalies, cross plots, and correlations. The studied Haushi Group was deposited during Late Carboniferous till the Late Permian period, equivalent to the last Arabian Plate Glaciation (AG3) melt-out (Sharland, 2001). During this period, the Arabian Plate moved from the South Pole toward the equator resulting in an environmental shift from glaciofluvial into marginal marine and fluvial settings (Forbes et al., 2010). The paleogeography of Haushi Group in Rub Al-Khali Basin, South Oman, revealed that the sea-level change influenced the stratigraphic sequence architecture in glacial and fluvial settings (Japex Montasar Report, 1990). Haushi Group in the Rub Al-Khali Basin in southwest Oman was not exposed to public research in the past decades. This study was conducted to fill the research gap in this area and to be used in the future to create sequence-based regional correlation for Haushi Group.

2 Geological Setting and Stratigraphy

The deposition of Haushi Group followed the Hercynian uplift and erosion in the Carboniferous, where the northern terrains of Gondwana drifted apart in response to the opening of the Neo-Tethys Ocean (Abbasi et al., 2012; Forbes et al., 2010; Konert et al., 1999). The first sediments

I. N. Al-Kharusi (✉) · M. A. K. El-Ghali · I. A. Abbasi
Department of Earth Sciences, Sultan Qaboos University, Muscat, Sultanate of Oman
e-mail: Ibtisam.alkharusi@gmail.com

M. A. K. El-Ghali
Earth Sciences Research Center, Sultan Qaboos University, Muscat, Sultanate of Oman

A. Ilic
Tethys Oil AB, Muscat, Sultanate of Oman

A. Çiner et al. (eds.), *Recent Research on Sedimentology, Stratigraphy, Paleontology, Tectonics, Geochemistry, Volcanology and Petroleum Geology*, Advances in Science, Technology & Innovation,
https://doi.org/10.1007/978-3-031-43222-4_10

above the Hercynian Unconformity consist of glacial sediments of the Al-Khlata Formation and are conformably overlayed by the fluvial clastic deposits of the Gharif Formation. The Al-Khlata Formation comprises two members, upper Al-Khlata and lower Al-Khlata, whereas the overlaying Gharif Formation comprises three members, upper Gharif, middle Gharif, and lower Gharif. According to Osterloff (2004), there are two depositional settings developed during the accumulation of the Al-Khlata Formation: glaciofluvial and glaciolacustrine settings. The glaciofluvial deposits are sand-dominated, reflecting channelized glaciofluvial outwash deposits, whereas the glaciolacustrine sediments are massive laminated mud-dominated deposits. The Gharif Formation lithology consists of marginal marine sediments in the lower member and shifting to fluvial sandstones and shales in the middle and upper members (Abbasi et al., 2012; Forbes et al., 2010).

3 Results and Discussion

Conceptual sequence-based depositional models were constructed for Haushi Group using wireline data extracted from five wells located in the Rub Al-Khali Basin (Fig. 1), South

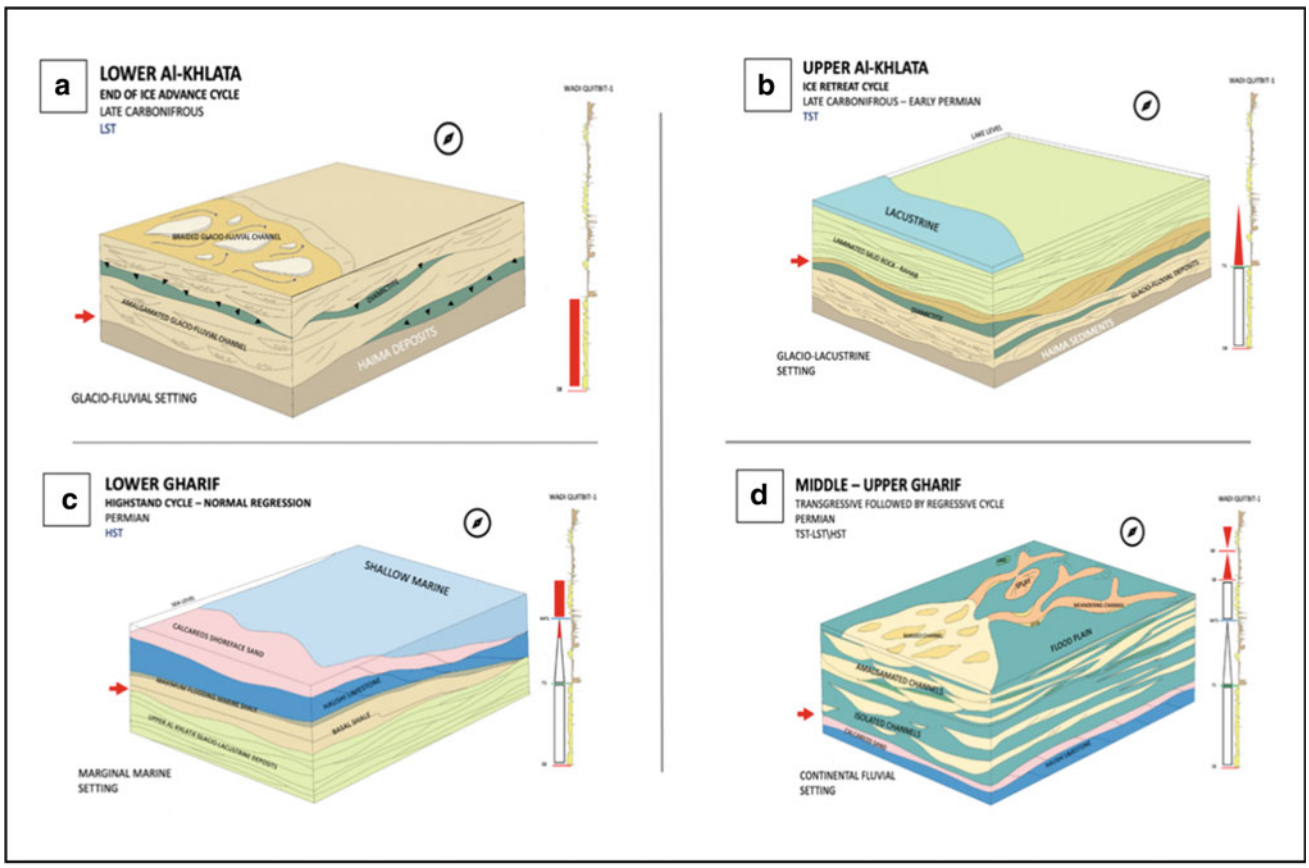

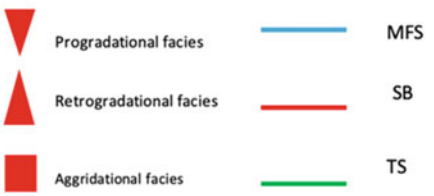

Fig. 1 Conceptual sequence depositional model for Haushi Group, Al-Khlata Formation, and Gharif Formation with the corresponding gamma-ray log shape (red color) from the reference well Wadi Quitbit - 1 South Oman, Rub Al-Khali Basin. **a** Lower Al-Khlata high stand system tract (HST), **b** Upper Al-Khlata transgressive system tract (TST), **c** Lower Gharif transgressive and Highstand system (TST-HST), **d** Upper Gharif transgressive and lowstand system (TST-LST)

Oman (Fig. 1). The findings of this study indicate that the lower Al-Khlata was deposited during the highstand system tract (HST) where glacial melt out began (Fig. 1a). This interpretation is supported by thick packages of diamictites that represent an early stage of ice retreat. This highstand system was developed in a glaciofluvial setting where braided channels formed landward close to source areas (Ghudun-Khasfa high). In this system, the sediment load compared to accommodation space is low. Therefore, amalgamated channels have formed, which reflects in the gamma-ray log as a blocky motif (Fig. 1a). The upper Al-Khlata (Fig. 1b) consists of transgressive sediments (TST) deposited in a glaciolacustrine setting where lakes were formed from ice melt. Fine-laminated sediments dominate the deposits from lakes, namely, Rahab shales (Osterloff, 2004). The gamma-ray log appears in bell shape representing fining upward facies. The beginning of lower Gharif (Fig. 1c) shared the transgressive system tract (TST) with upper Al-Khlata, as there is no evidence of an erosive surface separating the lower Gharif and upper Al-Khlata Members.

However, the sediments of lower Gharif are a mixture of fining upwards sand and shales of marginal marine setting deposited during sea-level increase. Highstand system sediments were detected in the upper layers of the lower Gharif Member, marked by Haushi limestone deposited during the phase where the accommodation space and sediment load formed equally. As a result, an aggregational sedimentary pattern is represented by the blocky shape in the gamma-ray log (Fig. 1 C). The end of this system tract is represented by a sequence boundary that marks the shift from a marginal marine to a continental setting. Following this sequence boundary is a transgressive system tract (TST) characterized by the deposition of isolated channel bodies reflecting a meandering fluvial system (Fig. 1d). The ample space between channels is formed during sea-level increase, which increases the accommodation space. The shaly material reflects the flood plain in between channels. The end of this system tract normally ends with a maximum flooding surface; however, no evidence in the well logs marks an anomaly in the gamma-ray or the other log suits indicating a flooding surface. Therefore, this can be explained by erosion and placement of a sequence boundary (SB). The upper Gharif Formation was deposited during a stage where the accommodation space was lower than the sediment supply due to sea-level fall. This resulted in forming amalgamated channels during the fluvial highstand system (HST) represented by funnel-shaped progradational facies in the gamma-ray log view (Fig. 1d).

4 Conclusion

Haushi Group was deposited in a complex setting. The establishment of sequence stratigraphy for both the Gharif and Al-Khlata formations was affected by sea-level change originating from the melt of glaciers during the last Arabian Plate Glaciation. The third-order sequence architecture was built from seven system tracts. The ice retreat began in lower Al-Khlata, reflecting a highstand system (HST), followed by the formation of a transgressive system by lacustrine from ice melt in upper Al-Khlata. The transgression continued in the overlaying lower Gharif Member by the deposition of marine shales that marks the maximum transgression followed by aggradational highstand limestone facies (HST). Finally, middle and upper Gharif Members were deposited in a transgressive followed by a regressive system in a fluvial setting. This study was conducted using wireline logs as the primary data source. Within this data limitation, the uncertainty of the funding is higher. However, the results were correlatable with Osterloff's (2004) research. This study can be further improved by using a more inclusive data set, including a core study, carbon isotope analysis, etc.

References

Abbasi, I. A., Hersi, O. S., Al-Harthy, A., & Al-Rashdi, I. (2012). Lithofacies attributes, depositional system and diagenetic properties of the Permian Gharif formation from Haushi-Huqf area, Central Oman. *Arabian Journal of Geosciences, 6*(12), 4931–4945.

Al-Belushi, J. (1996). Permo-carboniferous glaciogenic Al Khlata formation, Oman: A new hypothesis for origin of its glaciation. *GeoArabia,* 389–403.

Embry, A. F. (1995). *Sequence boundaries and sequence hierarchies: Problems and proposals*. Norwegian Petroleum Society Special Publications Sequence Stratigraphy on the Northwest European Margin, Proceedings of the Norwegian Petroleum Society.

Forbes, G. A., Jansen, H. S., & Schreurs, J. (2010). *Lexicon of Oman subsurface stratigraphy: Reference guide to the stratigraphy of Oman's hydrocarbon basins*. Manama, Bahrain: Gulf PetroLink.

Heward, & Penney, R. (2014). Al-Khlata glacial deposits in the Oman mountains and their implications. *Geological Society, London, Special Publications,* 392, 281.

Konert, G, Afifi, A. M., & De Groot, K. (1999). Abstract: Paleozoic stratigraphy and hydrocarbon habitat of the Arabian plate. *AAPG Bulletin,* 83.

Osterloff, P. (2004). Depositional sequences of the Al-Khlata formation, subsurface interior Oman. *GeoArabia,* 61–80.

Rider, M., & Kennedy, M. (2018). The geological interpretation of well logs. GeoArabia. Rider-French, pp. 61–80.

Sharland, P. R. (2001). *Arabian plate sequence stratigraphy*. Manama, Bahrain: Gulf PetroLink.

Sequence Stratigraphy and Chemostratigraphy Interpretations Based on Stable Isotope and Gamma Ray: An Example from the Early Triassic Lower Mahil Formation [Upper Khuff Outcrop Equivalent (KS1)], al Jabal Al-Akhdar, North Oman, Sultanate of Oman

Mohamed S. H. Moustafa, Mohamed A. K. El-Ghali, Rasha Al Raqaishi, Iftikhar Ahmed Abbasi, Hezam Al-Awah, Mohammed Farfour, Nada Al Ghafri, and Aaraf Al Humaidi

Abstract

This study aims to integrate facies distribution, stable isotope, spectral and total gamma rays to build high-resolution sequence stratigraphy of the Early Triassic Lower Mahil Formation [Upper Khuff outcrop equivalent (*KS*1)]. The Lower Mahil Formation was deposited on a carbonate ramp in Al Jabal al-Akhdar of North Oman. Saiq Plateau and Wadi Sahtan sections of the Lower Mahil Formation were logged and measured along a depositional dip cross section. A detailed sedimentological description for studied sections was performed using Dunham's classification, isotope samples were taken every 50 cm, and spectral gamma ray measurements were taken every 10 cm. The Lower Mahil Formation is a third-order sequence consisting of inner-ramp and mid-ramp carbonate facies. Several lithofacies were identified, including breccia, packstone/grainstone, and mudstone. The top of the breccia marks the top of the third-order sequence with normal carbon isotope and low gamma rays and shows a sharp change in lithology. However, the base of this sequence is a transition contact with a gradual decrease in the carbon isotope and gamma ray curves. An increasing trend of both carbon isotope and gamma ray curves marks the maximum flooding surface zone.

Keywords

Saiq Plateau • Wadi Sahtan • Lower Mahil • Oman • Third-order sequences • Al Jabal al-Akhdar

1 Introduction

This study presents the stratigraphic framework integrated with high-resolution carbon isotopes for the Early Triassic Lower Mahil Formation (Upper Khuff outcrop equivalent (*KS1*)) within the Al Jabal al-Akhdar of North Oman. The stratigraphic sequence framework presented here builds on the rock-based stratigraphic framework, carbon stable isotope chemostratigraphy, gamma ray, and available biostratigraphic data. Based on the lithology, wireline logs, and faunas, the Khuff Formation has been subdivided into Upper Khuff, Middle Khuff, and lower Khuff. The lower and middle Khuff is equivalent to the Saiq Formation in Jabal al-Akhdar (Alsharhan, 2006). Simultaneously, the upper Khuff is equivalent to the Lower Mahil Formation, which overlies the Saiq Formation (Alsharhan, 2006). The Khuff Formation represents one supersequence, which comprises six transgressive/regressive sequences (*KS*6–*KS*1) (Koehrer et al., 2010). On the Saiq Plateau of the Al Jabal al-Akhdar, Oman, the Upper Saiq Formation is time equivalent to the Lower and Middle Khuff Formation (*K*5–*K*3), and the Lower Mahil Member is the time equivalent to the Upper Khuff Formation (*K*2–*K*1) (Koehrer et al., 2010). This study will focus on the Lower Mahil Formation (upper Khuff outcrop equivalent (*KS*1)). Studying this supersequence may help in

M. S. H. Moustafa (✉) · M. A. K. El-Ghali · R. Al Raqaishi · I. A. Abbasi · M. Farfour · N. Al Ghafri · A. Al Humaidi
Department of Earth Sciences, Sultan Qaboos University, Muscat, Sultanate of Oman
e-mail: m.moustafa@squ.edu.om

M. A. K. El-Ghali
Earth Sciences Research Center, Sultan Qaboos University, Muscat, Sultanate of Oman

H. Al-Awah
Department of Chemistry and Earth Sciences, Qatar University, Doha, Qatar

A. Çiner et al. (eds.), *Recent Research on Sedimentology, Stratigraphy, Paleontology, Tectonics, Geochemistry, Volcanology and Petroleum Geology*, Advances in Science, Technology & Innovation,
https://doi.org/10.1007/978-3-031-43222-4_11

understanding the sequence stratigraphy of the Lower Mahil Formation (upper Khuff outcrop equivalent (*KS*1)). The initial goal of this work is to do a sequence stratigraphic interpretation of the Lower Mahil Formation based on bed-by-bed measured sections (Saiq Plateau and Wadi Sahtan).

2 Geological Setting

The Akhdar Group comprising the Saiq and Mahil Formation in the Al Jebel Akhdar area was deposited due to the initial phase of the breakup of the supercontinent Pangaea. During the lower Paleozoic, Oman was a passive margin. This stable phase ended with the collision of Gondwana and Laurasia during the Carboniferous Hercynian event that created the base Haushi unconformity. Following the widespread Hercynian event, the northern Gondwanan terranes rifted with the opening of the Neo-Tethys Ocean in the Late Carboniferous/earliest Permian. The sediments above the Hercynian unconformity in Oman are represented by the clastics of the Haushi Group. From the middle Permian to middle Cretaceous times (ca. 267–91 Ma), a passive margin developed with extensive carbonate deposition, comprising the Akhdar, Sahtan and Kahmah, and Wasia Groups. The Khuff Formation was deposited on an epeiric carbonate platform under arid conditions dominated by carbonate sedimentation due to a significant transgression.

3 Results

Several lithofacies were identified, including breccia, packstone/grainstone, and mudstone. The Lower Mahil Formation is a third-order sequence consisting of backshoal, shoal, to foreshoal depositional settings. Inside this third-order sequence is fourth- and fifth-order sequences with 23 distinguished parasequences (Fig. 1a–c).

4 Discussion

4.1 Depositional Environment

The Lower Mahil Formation lithofacies were identified, including breccia, packstone/grainstone, and mudstone (Fig. 1c). Studying these facies indicates that the Lower Mahil Formation deposited within shallow ramp setting limited to backshoal, shoal to foreshoal ramp facies, similar to previous studies (Koehrer et al., 2010). The shoal facies dominate the Saiq Plateau section. The source of the breccia is unknown (Koehrer et al., 2010). However, this study shows normal carbon isotope patterns (Fig. 1a) and no indications of subaerial unconformity (Forbes et al., 2010; Koehrer et al., 2012) in response to the breccia facies. These isotopic results confirm that there are no unconformity or diagenetic effects of breccia facies. Therefore, the source of the breccia can be tectonic/syntectonic (?) with no clear evidence from the field.

4.2 Lower Mahil Composite Sequence Duration

The Lower Mahil is Early Triassic, which is time equivalent to the Upper Khuff Formation in the subsurface. However, this study focuses only on the lower member of the Mahil Formation (*KS*1 sequence equivalent), which has been dated previously (Koehrer et al., 2010) as Late Induan. The Lower Mahil was deposited during the late Induan with a $\sim$1 m.y (Gradstein et al., 2012), making it a third-order sequence (Goldhammer et al., 1990). Each of the three sequences of the Lower Mahil Formation has a duration of 0.3 m.y, making them fourth-order sequences. Each of the eight sequences has a duration of 0.1 m.y, making them a fifth-order sequence. In greenhouse times, cycles are likely dominated by high-frequency, low-amplitude sea-level changes driven by precession (Read, 1985, 1998). Therefore, one would expect to find many more parasequences in the one m.y. The duration of parasequences in the Lower Mahil Formation is challenging to evaluate, as they are rarely regionally mappable. The maximum number of parasequences (23) occurs in the Lower Mahil Formation. Given the one m.y. duration of formation, this would suggest that the parasequences are $\sim$43 k.y. The Lower member of the Mahil Formation [(Upper Khuff outcrop equivalent (*KS*1 sequence)] is made up of two-cycle sets composed of 8 fifth-order cycles (Fig. 1a). The maximum flooding surface MFS zone of the Lower Mahil Formation is placed within the wackestones lithofacies (Fig. 1a). The thick brecciated bed defines the upper sequence boundary, which represents the boundary between the Lower Mahil Member (Khuff Formation equivalent) and the overlying Middle Mahil Formation (Sudair Formation equivalent) (Fig. 1a). At the same time, the lower sequence boundary represents the normal contact between *KS*1 and the underlying *KS*2 sequence.

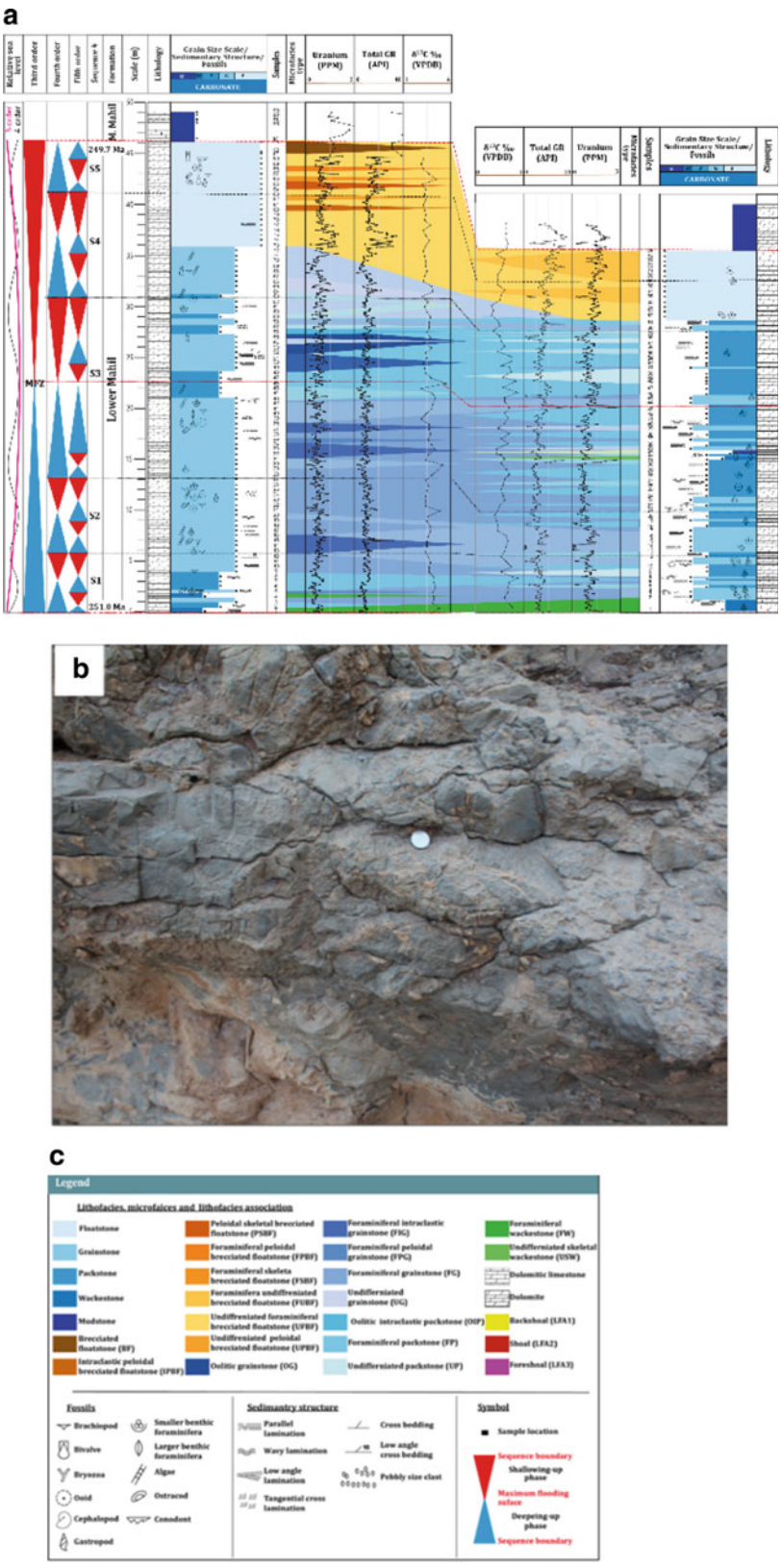

Fig. 1 Third-, fourth-, and fifth-order sequences of the Lower Mahil formation (**a**) and the breccia facies (**b**) with the facies code (**c**)

5 Conclusions

1. The Lower Mahil Formation lithofacies were identified, including breccia, packstone/grainstone, and mudstone. Studying these facies indicates that the Lower Mahil Formation deposited within shallow ramp settings is limited to backshoal–shoal to foreshoal ramp facies.
2. Carbon isotope shows standard patterns and no indication of subaerial unconformity in response to the breccia facies. These isotopic results support the possible tectonic origin of the breccia.
3. The Lower Mahil Formation is a third-order sequence consisting of backshoal, shoal, to foreshoal carbonate facies.

Acknowledgements This study is supported by the Research Council (TRC) Grant Fund # RC/RG-DVC/ESRC/18/01.

References

Alsharhan, A. (2006). Sedimentological character and hydrocarbon parameters of the middle Permian to early Triassic Khuff formation. *United Arab Emirates. Sedimentary Geology, 11*(1–4), 121–156.

Forbes, G.A., Jansen, H. S. M., & Schreurs, J. (2010). Lexicon of Oman subsurface stratigraphy: Reference guide to the stratigraphy of Oman's hydrocarbon basins. *GeoArabia Special Publication* 5, Gulf PetroLink, Bahrain, p 371.

Goldhammer, R. K., Dunn, P. A., Hardie, L. A. (1990). Depositional cycles, composite sea-level changes, cycle stacking patterns, and the hierarchy of stratigraphic forcing: examples from Alpine Triassic platform carbonates.*Geological Society of America Bulletin 102*(5), 535–562.

Gradstein F. M., et al., (2012). (Eds). *The geologic time scale* 2012. Elsevier.

Koehrer, B., Aigner, T., Forke, H., & Pöppelreiter, M. (2012). Middle to upper Khuff (Sequences KS1 to KS4) outcrop-equivalents in the Oman Mountains. *Grainstone architecture on a subregional scale*, *GeoArabia,*59–104.

Koehrer, B., Aigner, T., Poppelreiter, M., Bizarro, P., & Kindy, S. (2010). Outcrop characterization of the Khuff formation from production to exploration scale (Oman Mountains, Sultanate of Oman). Geo.

Read, J. F. (1985). Carbonate platform facies models. *AAPG bulletin 69* (1)1–21.

Read, J. F. (1998). Phanerozoic carbonate ramps from greenhouse, transitional and ice-house worlds: clues from field and modelling studies. *Geological Society, London, Special Publications 149*(1) 107–135.

Spectral Gamma-Ray Variability Within Carbonate Lithofacies: An Example from the Early Triassic Lower Mahil Formation (Upper Khuff-Equivalent) of Al Jabal Al-Akhdar, North Oman

Mohamed S. H. Moustafa, Mohamed A. K. El-Ghali, Iftikhar Ahmed Abbasi, Hezam AL-Awah, Musaab Shakir Al Sarmi, Abdulrazak Al-Sayigh, Arshad Ali, Nada Al Ghafri, Araf Al Humaidi, and Rasha Al Raqaishi

Abstract

This study aims to test the relationship between the elements Potassium (K), Uranium (U), and Thorium (Th) measured by spectral gamma-ray to sedimentary facies. Spectral gamma-ray is widely used in depositional facies and sequence stratigraphic analysis. Here, spectral gamma-ray U, Th, and K measurements from two logged sections of the Early Triassic Lower Mahil Formation (Upper Khuff-equivalent, KS1) of Al Jabal Al-Akhdar (Saiq Plateau and Wadi Sahtan), north Oman, are discussed. A detailed sedimentological description for both logged sections was performed using Dunham's classification, and spectral gamma-ray measurements were taken every 10 cm with an RS-230 BGO Handheld Spectrometer. Several lithofacies were identified, including breccia, packstone/grainstone, and mudstone. Saiq Plateau and Wadi Sahtan lithofacies are grain-dominated facies (e.g., shoals), which indicate that the Lower Mahil Formation was deposited in a shallow carbonate ramp (shoal to foreshoal setting). In all lithofacies in the Lower Mahil Member, the percentage of U exceeds Th and K. This relative enrichment of the U reflects the reduction conditions and high preservation of organic matter.

Keywords

Saiq Plateau • Wadi Sahtan • Lower Mahil • Oman • Al Jabal Al-Akhdar

1 Introduction

Spectral gamma-ray logging has been helpful in some settings, e.g., identifying sediment facies and correlations (Ehrenberg & Svana, 2001; Omidpour et al., 2021). Gamma-ray logs record the radioactivity of the formation and the intensity of gamma-ray signatures controlled by Potassium (K), Thorium (Th), and Uranium (U) contents (Gao et al., 2020). Controls on the absolute and relative contributions of K, Th, and U are complex. They involve the original rock constituents (including depositional and geochemical properties) in addition to the effect of weathering (Cowan & Myers, 1988). The richness of K, Th, and U is a direct product of the mineral composition of the Earth's crust, and the average abundances of K, U, and Th are estimated to be 2–2.5 wt%, 2–3 ppm, and 8–12 ppm, respectively. These are the only elements with radioactive isotopes that show sufficient gamma-ray emission to be adequately measured (Guagliardi et al., 2013).

In general, high U values reflect reducing conditions and high preservation of organic matter. However, low U peaks indicate oxidation conditions and lower organic preservation (Ehrenberg & Svana, 2001; Omidpour et al., 2021). Generally, a high gamma-ray response means fine-grained deposits or clay-rich rock formations, such as shale and

M. S. H. Moustafa (✉) · I. A. Abbasi · M. S. Al Sarmi · A. Al-Sayigh · N. Al Ghafri · A. Al Humaidi · R. Al Raqaishi
Department of Earth Sciences, Sultan Qaboos University, Muscat, Sultanate of Oman
e-mail: m.moustafa@squ.edu.om

M. A. K. El-Ghali · A. Ali
Earth Sciences Research Center, Sultan Qaboos University, Muscat, Sultanate of Oman

H. AL-Awah
Department of Chemistry and Earth Sciences, Qatar University, Doha, Qatar

Department of Chemistry and Earth Sciences, College of Arts and Sciences, Qatar University, Doha, Qatar

A. Al Humaidi
Oil and Gas, Petrogas, Muscat, Muscat, Oman

A. Çiner et al. (eds.), *Recent Research on Sedimentology, Stratigraphy, Paleontology, Tectonics, Geochemistry, Volcanology and Petroleum Geology*, Advances in Science, Technology & Innovation,
https://doi.org/10.1007/978-3-031-43222-4_12

mudstone; lower gamma radiation reflects coarse-grained carbonate rocks (Ehrenberg & Svana, 2001). Diagenesis, such as dolomitization, can result in an uneven distribution in U contents, so there may be no direct correlation between U and organic content. Therefore, U be affected by many other factors, and it shows less correlation with lithofacies than K and Th (Schnyder et al., 2006). In contrast, K and Th concentrations are mainly associated with illite, kaolinite, sericite, and potassium feldspars.

2 Geological Setting

The Akhdar Group comprising Saiq and Mahil formations in Al Jebel Akhdar area was deposited due to the initial phase of the breakup of the supercontinent Pangaea. It covers most of Oman except the site in the South-East due to Cretaceous erosion. The landward (proximal) facies appear in South Oman, and the seaward (distal) facies appears in North Oman. The Permian Saiq Formation and the lowermost part of the Triassic Mahil Formation are the stratigraphic equivalent of the Khuff Formation in the subsurface (Forbes et al., 2010). The lower part of the Akhdar Group is the Khuff Formation (Lower Mahil Formation equivalent, *KS*1). The Lower Mahil Member is time-equivalent to the Upper Khuff Formation.

3 Results

The lithology of both sections is quite similar, showing grain-dominated facies. However, the Saiq Plateau section consists of more grain-dominated facies than the Wadi Sahtan section, leading to a clear shoal setting (oolitic grainstone) in the Saiq Plateau. The spectral gamma-ray data of these lithofacies revealed differences in U, Th, and K measurements (Fig. 1). The Lower Mahil Formation at Wadi Sahtan displays relatively higher U values (0–2.5; av. 1.5 ppm) than the Lower Mahil Formation at the Saiq Plateau (0–2.3; av. 1 ppm). For instance, the U values of the breccia lithofacies range between 1.3 and 2.5 ppm with an average of 1.8 pm in the Wide Sahtan section compared with 0.8–2.3 ppm with an average of 1.2 ppm in Saiq Plateau. Moreover, the average of the U from the packstone/grainstone lithofacies in Wadi Sahtan is 1.2 ppm compared to 0.8 ppm in the Saiq Plateau. The U from mudstone lithofacies in Wadi Sahtan is 1.4 ppm compared to 0.8 ppm in Saiq Plateau.

4 Discussion

In this study, there is evidence that spectral gamma provides more information on lithofacies identification (e.g., grain-dominated vs. mud-dominated). Breccia in both sections are mud-supported, which can be seen directly in the outcrop and indirectly, as indicated by the high U values in these facies (Figs. 1 and 2). Studies have shown that difference in U is a useful indicator of lithofacies. For example, U is concentrated in organic matter (Schnyder et al., 2006), and humid weathering depletes both K and U relative to Th (Parkinson, 1996). In this study, Th and U correlate well in the Saiq Plateau section relative to the Wadi Sahtan section. The Wadi Sahtan section is paleogeographically located more distal (Forbes et al., 2010) than the Saiq Plateau section. It can be the main reason for changes in the U values measured. The high U values at the Wadi Sahtan section are attributed to (1) reduction conditions, (2) diagenetic effects, and (3) relative sea-level rise. The Th values in different lithofacies show low to moderate values (0–1.5; av. 0.5 ppm), which may be due to relative sea-level fall. The K values are nearly zero in all lithofacies, indicating pure carbonate (Omidpour et al., 2021). This study supports that

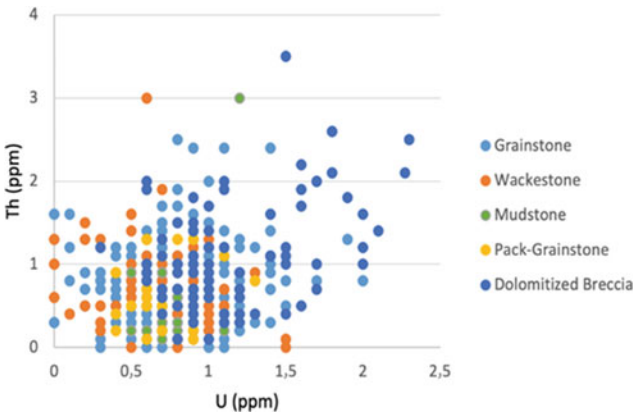

Fig. 1 Scatter plot of Th versus U for each facies from the Saiq Plateau section

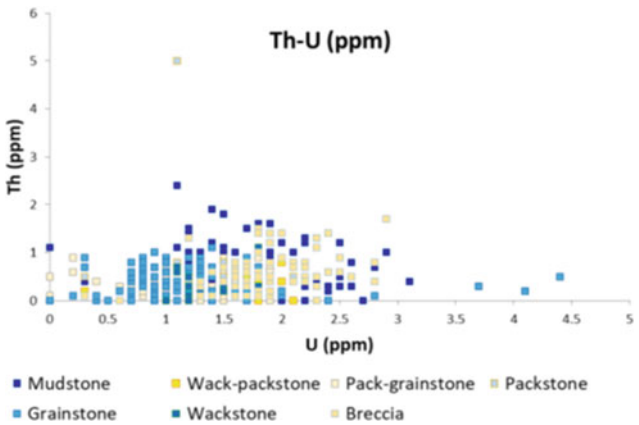

Fig. 2 Scatter plot of Th versus U for each facies from the Wadi Sahtan section. Note that U is higher in the mudstone facies

the Lower Mahil Formation is grain-dominated carbonate. Low spectral gamma-ray values can be seen in both sections, with spikes of mud facies that show relatively higher U values in the Wadi Sahtan section.

5 Conclusions

(1) Spectral gamma-ray (U, Th, and K) measurements from Saiq Plateau and Wadi Sahtan sections of the Early Triassic Lower Mahil Formation (Upper Khuff-equivalent) indicate different concentrations within the facies.
(2) Breccia facies in both sections are mud-supported, as indicated by the high U values.
(3) The Lower Mahil Formation at Wadi Sahtan displays higher U values than in the Saiq Plateau.

Acknowledgements This study is supported by the Research Council (TRC) Grant Fund # RC/RG-DVC/ESRC/18/01.

References

Cowan, D. R., & Myers, K. J. (1988). Surface gamma ray logs: a correlation tool for frontier areas: discussion. *AAPG Bulletin, 72*, 634–636.

Ehrenberg, S., & Svana, T. A. (2001). Use of spectral gamma-ray signature to interpret stratigraphic surfaces in carbonate strata: An example from the Finnmark Carbonate platform (Carboniferous-Permian), Barents Sea. *AAPG Bulletin, 85*, 295–308.

Forbes, G. A., Jansen, H. S. M., & Schreurs, J. (2010). *Lexicon of Oman subsurface stratigraphy: Reference guide to the stratigraphy of Oman's hydrocarbon basins* (371 p). Geoarabia Special Publication 5, Gulf PetroLink.

Gao, Y., Fu, X., Li, Y., Wan, Y., Wang, Z., Song, C., Shen, H., & Lin, F. (2020). Demise of the Middle Jurassic carbonate platform: Responses to sea-level fall in the Qiangtang basin, Eastern Tethys. *Geological Journal, 55*, 7935–7952.

Guagliardi, I., Buttafuoco, G., Apollaro, C., Bloise, A., De Rosa, R., & Cicchella, D. (2013). Using gamma-ray spectrometry and geostatistics for assessing geochemical behavior of radioactive elements in the lese catchment (southern Italy). *International Journal of Environmental Research, 7*, 645–658.

Omidpour, A., Moussavi-Harami, R., Mahboubi, A., & Rahimpour-Bonab, H. (2021). Application of stable isotopes, trace elements and spectral gamma-ray log in resolving high-frequency stratigraphic sequences of a mixed carbonate-siliciclastic reservoirs. *Marine and Petroleum Geology*, *125*, 104854. https://doi.org/10.1016/j.marpetgeo.2020.104854

Parkinson, D. N. (1996) Gamma-ray spectrometry as a tool for stratigraphical interpretation: examples from the western European Lower Jurassic. In S. P. Hesselbo & D. N. Parkinson (Eds.), *Sequence stratigraphy in British geology* (pp. 231–255). Geological Society Special Publication 103.

Schnyder, J., Ruffell, A., Deconinck, J. F., & Baudin, F. (2006). Conjunctive use of spectral gamma-ray logs and clay mineralogy in defining late Jurassic-early Cretaceous palaeoclimate change (Dorset, UK). *Palaeogeography, Palaeoclimatology, Palaeoecology*, *229*, 303–320.

Chemostratigraphy of a Mixed Upper Cretaceous Carbonate-Siliciclastic Succession (Southern Pyrenees): Geochemical Proxies for Sedimentological Interpretations

David Cruset, Mar Moragas, Enric Pascual-Cebrian, Ramon Mercedes-Martín, Anna Travé, and Jaume Vergés

Abstract

The chemostratigraphy of the growth strata related to the growth of the Sant Corneli-Bóixols anticline, reveals the sedimentary environment evolution of these syn-orogenic sediments. The decrease of Y/Ho ratios throughout the succession from typical open marine values to nearshore values indicates the shallowing upward trend of the growth strata and the progressive input of siliciclastic sediments from emerged areas. The depletion in $\delta^{13}C$ and $\delta^{18}O$, the decrease in the Sr and Mg contents, and the Mg/Ca molar ratios reveal the freshwater input into shallower environments. The results correlate well with the previous sedimentological interpretations of the studied succession. They also support the combination of the elemental and isotopic composition of carbonates to interpret depositional environments in non-continuous subsurface reservoirs and seal rocks.

Keywords

Chemostratigraphy • Mixed carbonate-siliciclastic succession • Southern Pyrenees • Sedimentological interpretations

1 Introduction

Core recoveries are often incomplete, hampering sedimentological descriptions and their interpretations. To solve these limitations, chemostratigraphy is a reliable tool that provides information about the evolution of buried sedimentary systems, which can be applied to both continuous conventional core data and drill cuttings. Furthermore, chemostratigraphy offers additional information for core-scan data, facilitating more robust sedimentological interpretations.

We test whether using Y/Ho ratios, combined with standard geochemistry proxies such as $\delta^{13}C$, $\delta^{18}O$, Sr, Mg contents of calcite shells (innoceramids, rudists, oysters, and other bivalves), and bulk rock samples can be used as geochemical proxies of sedimentary environments.

To validate whether sedimentary geochemistry can shed light on environmental conditions of facies deposition, a 1400 m thick well-exposed middle Campanian to upper Maastrichtian syn-orogenic shallowing an upward succession was studied (Sant Corneli-Bóixols anticline, Southern Pyrenees).

2 Geological Setting

The studied growth strata have 1400 m of thickness, are in the southern Pyrenees (Fig. 1), and record the emplacement of the Sant Corneli-Bóixols anticline from the late Santonian to the latest Maastrichtian.

From older to younger, the studied growth strata succession consists of (1) outer platform to slope deposits; (2) prodelta and offshore siltstones and marls; (3) foreshore calcareous sandstones and delta-front sandstones; and (4) lagoonal and littoral limestones and siltstones.

D. Cruset (✉) · M. Moragas · E. Pascual-Cebrian · J. Vergés
Group of Dynamics of the Lithosphere (GDL), Geosciences Barcelona (Geo3Bcn-CSIC), Barcelona, Spain
e-mail: dcruset@geo3bcn.csic.es

R. Mercedes-Martín
Departament de Geologia. Unitat d'Estratigrafia, Universitat Autònoma de Barcelona, Cerdanyola del Vallès, 08193 Barcelona, Spain

A. Travé
Departament de Mineralogia, Petrologia i Geologia Aplicada, Facultat de Ciències de la Terra, Universitat de Barcelona (UB), Barcelona, Spain

A. Çiner et al. (eds.), *Recent Research on Sedimentology, Stratigraphy, Paleontology, Tectonics, Geochemistry, Volcanology and Petroleum Geology*, Advances in Science, Technology & Innovation,
https://doi.org/10.1007/978-3-031-43222-4_13

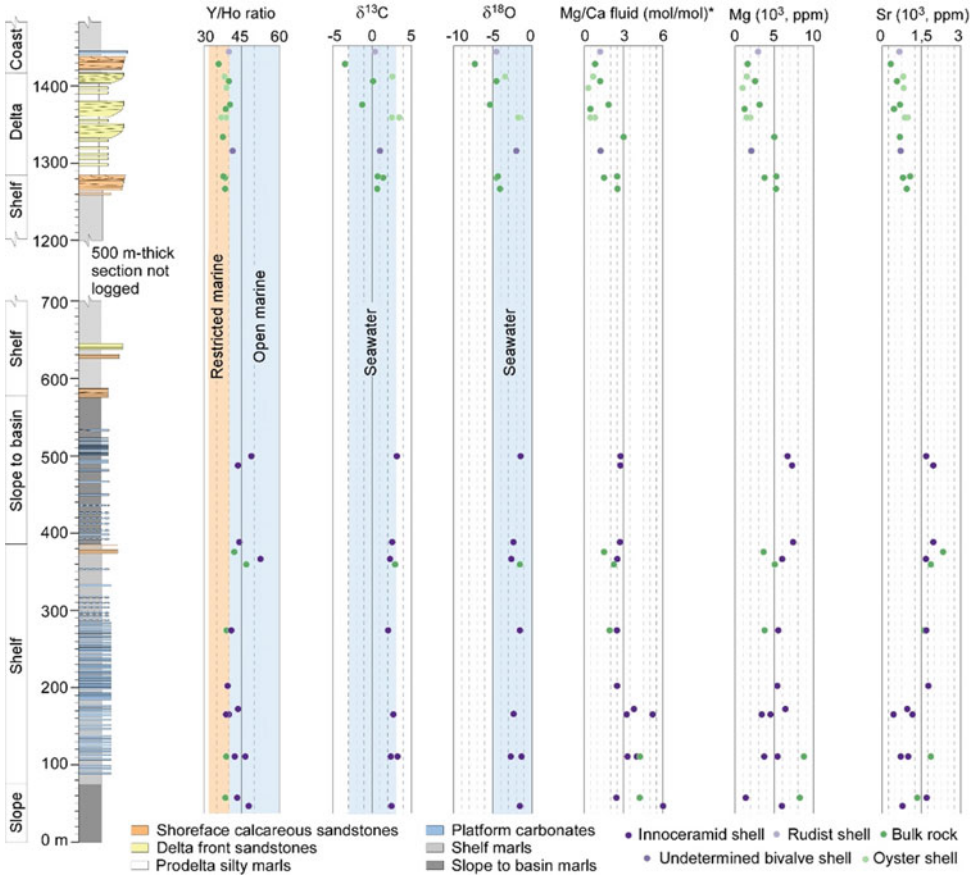

Fig. 1 Stratigraphy, $\delta^{13}C$, $\delta^{18}O$, Y/Ho ratios, Sr and Mg contents, and Mg/Ca molar ratios of the growth strata related to the growth of the Sant Corneli-Bóixols anticline. Mg/Ca molar ratio of parental fluid was calculated using a distribution coefficient of 0.012 for a fluid at 25 °C (Mucci & Morse, 1984)

3 Methodology

Geochemical studies were done in 32 samples of low magnesium calcite shells and bulk rock samples derived from the study of Pascual-Cebrian et al. (2019). For carbon and oxygen isotope analyses of carbonate rocks, an automated Kiel Carbonate Device attached to a Thermal Ionization Mass Spectrometer Thermo Electron (Finnigan) MAT-252 was used. To determine the Sr, Mg, and REE contents, samples were analyzed using High-Resolution Inductively Coupled Plasma Mass spectrometry (HR-ICP-MS), using a Thermo Scientific Model Element XR (Thermo Fisher Scientific, Bremen, Germany).

4 Chemostratigraphy of the Studied Growth Strata

Samples from deeper and older outer platform to slope deposits show $\delta^{13}C$ values between + 2.01 and + 3.19 ‰ VPDB, $\delta^{18}O$ values between −2.72 and −1.25 ‰ VPDB, Y/Ho ratios between 37 and 52.9, Sr contents between 445 and 2278 ppm, Mg contents between 1385 and 8798 ppm and Mg/Ca molar ratios between 1.5 and 5.9. Samples from shallower and younger deposits have lighter $\delta^{13}C$ and $\delta^{18}O$ values between −3.78 and + 3.37 and between −7.27 and −1.72 ‰ VPDB, respectively, lower Y/Ho ratios between 36.46 and 40.8, lower Sr contents between 308 and 1018 ppm, lower Mg contents between 1038 and 5334 ppm and Mg/Ca molar ratios between 0.38 and 3.0.

5 Discussion

Modern seawater contains large positive Y anomaly (calculated as the mass ratio between Y/Ho), with Y anomalies between 40 and 80 in open marine settings decreasing to values between 33 and 40 in nearshore or restricted areas in the studied locality (Nothdurft et al., 2004; Tostevin et al., 2016). Thus, the decrease of Y/Ho ratios throughout the succession, from typical open marine values to lower ratios similar to nearshore settings in shallower deposits, supports the overall upward trend of the growth strata and the progressive input of siliciclastic sediments from emerged areas. The freshwater input into shallower environments could have been responsible for the lighter $\delta^{13}C$ and $\delta^{18}O$ values and the lower Mg/Ca molar ratios and Sr and Mg contents (He & Xu, 2015; Lebrato et al., 2020; Ravelo & Hillaire-Marcel, 2007).

6 Conclusions

The chemostratigraphy of the 1400 m thick Late Santonian to Late Maastrichtian growth strata related to the growth of the Bóixols-Sant Corneli anticline in the Southern Pyrenees reveals a shallowing upward trend that fits with previous sedimentological interpretations. The results support that carbonate's elemental and isotopic composition can be combined as a cost-effective tool for interpreting depositional and environmental conditions in settings where reservoir and seal subsurface data are incomplete.

Acknowledgements Equinor Research Center funded this work, Bergen, Subtetis project (PIECSIC-201830E039), Grup Consolidat de Recerca "Geologia Sedimentària" (2017SGR-824), and DGICYT Spanish Project PGC2018-093903-B-C22. This research is within Grup Consolidat de Recerca "Modelització Geodinàmica de la Litosfera" (2017SGR-847). ICP-MS analyses were done at labGEOTOP of the GEO3BCN. Isotopic analyses were done at CCiTUB of the University of Barcelona. David Cruset acknowledges the Spanish Ministry of Science and Innovation for the "Juan de la Cierva Formación" fellowship FJC2020-043488-I AEI/10.13039/501100011033.

References

He, S., & Xu, Y. J. (2015). Concentrations and ratios of Sr, Ba and Ca along an Estuarine river to the Gulf of Mexico—Implication for sea level rise effects on trace metal distribution. *Biogeosciences Discuss, 2015*, 18425–18461. https://doi.org/10.5194/bgd-12-18425-2015

Lebrato, M., Garbe-Schönberg, D., Müller, M. N., Blanco-Ameijeiras, S., Feely, R. A., Lorenzoni, L., Molinero, J. C., Bremer, K., Jones, D. O. B., Iglesias-Rodriguez, D., et al. (2020). Global variability in seawater Mg:Ca and Sr:Ca ratios in the modern ocean. *Proceedings of the National Academy of Sciences, 117*, 22281. https://doi.org/10.1073/pnas.1918943117

Mucci, A., & Morse, J. W. (1984). The solubility of calcite in seawater solutions of various magnesium concentration, It = 0.697 m at 25 ° C and one atmosphere total pressure. *Geochimica et Cosmochimica Acta, 48*, 815–822. https://doi.org/10.1016/0016-7037(84)90103-0

Nothdurft, L. D., Webb, G. E., & Kamber, B. S. (2004). Rare earth element geochemistry of late devonian reefal carbonates, canning basin, Western Australia: Confirmation of a seawater REE proxy in ancient limestones. *Geochimica et Cosmochimica Acta, 68*, 263–283. https://doi.org/10.1016/S0016-7037(03)00422-8

Pascual-Cebrian, E., Moragas, M., Gallois, A., Belenguer, J., ALmar, Y., Martínez-Doñate, A., Drzewiecki, P., Wright, W. R., Hunnt, D. W., & Vergés, J. (2019). Using Sr isotopes and rare earth elements to correlate sequences in regions with complex facies distributions: Example from the Late Cretaceous of the South-Central Pyrenees. In *Proceedings of Bathurst Meeting, 16th International Meeting of Carbonate Sedimentologists*, Mallorca, Spain.

Ravelo, A. C., & Hillaire-Marcel, C. (2007). Chapter eighteen the use of oxygen and carbon isotopes of foraminifera in paleoceanography. In C. Hillaire–Marcel & A. De Vernal (Eds.), *Developments in marine geology* (Vol. 1, pp. 735–764). Elsevier.

Tostevin, R., Shields, G. A., Tarbuck, G. M., He, T., Clarckson, M. O., & Wood, R. A. (2016). Effective use of cerium anomalies as a redox proxy in carbonate-dominated marine settings. *Chemical Geology, 438*, 146–162. https://doi.org/10.1016/j.chemgeo.2016.06.027

Stratigraphy and Age of the Sahabi Formation, Libya

Moftah El Shawaihdi, Ahmed Muftah, Raymond Bernor, and Noel Boaz

Abstract

New data from lithostratigraphic and biostratigraphic research, sub-surface investigations, and remote sensing studies have allowed the formalization of lithostratigraphic nomenclature in the Sahabi area, North Central Libya. The base of sedimentation is the Late Miocene Benghazi Formation of the Ar Rajmah Group, formerly "Formation M." These sediments were deposited under shallow marine conditions and are of Tortonian age, ranging from biozones NN8 to NNl la, with an age range of 8.23–10.70 Ma. $^{87}Sr/^{86}Sr$ dates from these levels range from 8.99 Ma to 9.36 Ma. The pack of sediments lying unconformably above the Benghazi Formation comprises the Late Miocene Sahabi Formation, the Pliocene Qarat Weddah Formation, and the Pleistocene-Recent "Formation Z." The Sahabi The formation is divided into two members: the "Lower Member," including the gypsiferous former "Formation P" and lower portion of "Member T," and the "Upper Member," including the non-gypsiferous and fossil-rich Units U-1, U-D, and U-2. Vertebrate fossils from U-1 and U-2 represent a highly diverse mosaic of paleohabitats ranging from the steppe, savanna, forest, large river, and estuarine to marine offshore, which makes the Sahabi fauna more valuable for biostratigraphic comparison with a wide variety of penecontemporaneous sites. The open country fauna shows Sahabi to have been a crossroads fauna correlating to European mammalian biozones MN12 and MN13, with a best-fit age estimate of 6.8 Ma for Unit U-1 and 6.0 Ma for Unit U-2. The closed and water-tied faunal elements from Sahabi are more relictual and include a highly endemic anthracothere shared with the essential hominin-bearing site of Toros Menalla, Chad, correlating most closely with the Sahabi U-2 fauna. The Chorora and Adu-Asa Formations in the Awash Basin of Ethiopia, the Qaret El-Muluk Formation of Wadi El-Natrun, Egypt, and the Nawata Formation of Lothagam, Kenya, are close in biostratigraphic age to the "Upper Member" of the Sahabi Formation. Sahabi shows the closest similarity in Eurasia to the MN12/13 site of Baynunah, Abu Dhabi and the MN13 site of Maramena, Axios Valley, Greece. The upper age of the Sahabi U-2 fauna is constrained by the unconformity that forms a Margin Erosion Surface (MES) separating the Messinian-aged Sahabi Formation from the overlying Pliocene Qarat Weddah Formation, dated elsewhere in the Mediterranean Basin to 5.96 Ma to 5.33 Ma.

Keywords

Libya • Messinian • Miocene • Stratigraphy • Sahabi

1 Introduction

Sahabi is located on the northeastern flank of the Sirt Basin and covers an area of ~ 375km^2. It is bounded by longitudes 20° 48′ 08″ to 20° 54′ 45″ E and latitudes 30° 10′ 58″ to 30° 17′ 36″ N (Fig. 1). Strata are exposed along the western edge of the recent Sabkhat Al Qunnayyin, in a general NE-SW trend of elongated intermittent hills (De Heinzelin & El-Arnauti, 1987).

The area is known for both its important Neogene fossil vertebrates (Boaz et al., 1979, 1987) and the discovery of presumed Messinian-aged subsurface channels of over

M. E. Shawaihdi · A. Muftah
Benghazi University, Benghazi, Libya

R. Bernor
Howard University, Washington, DC 20059, USA

R. Bernor · N. Boaz (✉)
International Institute for Human Evolutionary Research, ICSM, Martinsville, VA 24112, USA
e-mail: noeltboaz@integrativemedsci.org

N. Boaz
Virginia Museum of Natural History, Martinsville, VA 24112, USA

A. Çiner et al. (eds.), *Recent Research on Sedimentology, Stratigraphy, Paleontology, Tectonics, Geochemistry, Volcanology and Petroleum Geology*, Advances in Science, Technology & Innovation,
https://doi.org/10.1007/978-3-031-43222-4_14

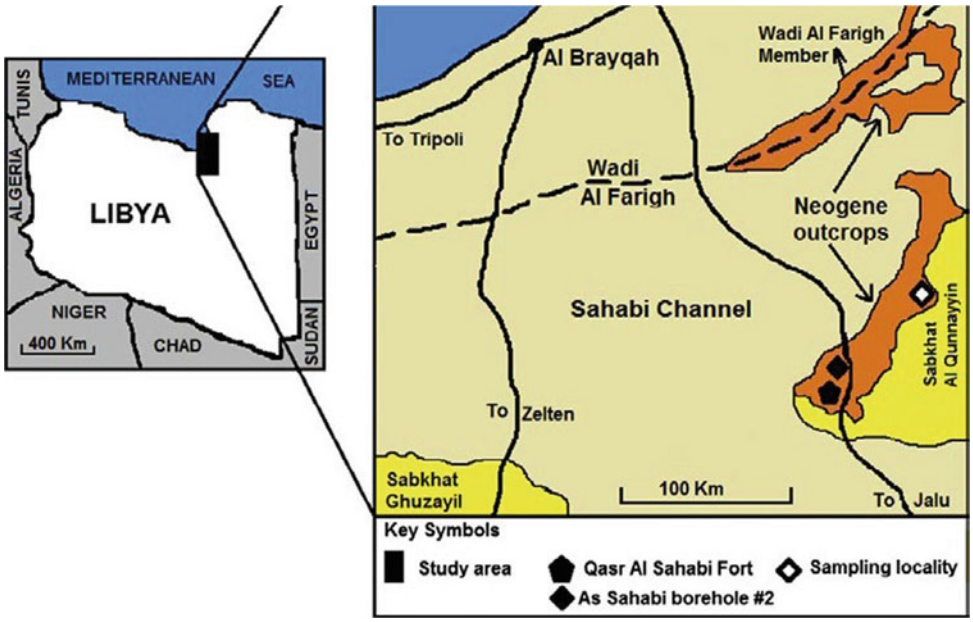

Fig. 1 Location of the Neogene sedimentary deposits in the As Sahabi area, north central Libya

400 m in depth detected by seismic studies (Barr & Walker, 1973). The As Sahabi area is composed of Upper Neogene sediments known as Benghazi Formation, Sahabi Formation, and Qarat Weddah Formation.

2 Materials and Methods

103 stratigraphic exposures were investigated during field seasons between 1977 and 2010. Fieldwork resulted in the lateral tracing of the recognized Sahabi rock units based on lithological descriptions and macro/micropaleontological contents. Standard preparation techniques for age-dating using stable strontium isotopes ($^{87}Sr/^{86}Sr$), foraminifera, and calcareous nannofossils have been followed. Thin sections were studied for petrographical examination. All materials including micropaleontological slides and vertebrate fossils are stored at the Earth Sciences Department and Museum of Vertebrate Paleontology of Benghazi University, Benghazi, Libya. All locality data and specimen identifications are maintained in the master catalog of the East Libya Neogene Research Project (ELNRP) database.

3 Results–Lithostratigraphy of As Sahabi Area

The paper integrates the most recent lithostratigraphic studies by the ELNRP team (El-Shawaihdi et al., 2014, 2016; Muftah et al., 2013, 2018). We identify an unconformable Margin Erosional Surface (MES) (Roveri et al., 2014), dating to 5.33 Ma–5.96 Ma, that resulted from Messinian down-cutting of the Eosahabi paleoriver. This unconformity separates the Miocene Sahabi Formation from the Pliocene Qaret Weddah Formation. This revised lithostratigraphy is supported by vertebrate biostratigraphy, nannoplankton biostratigraphy of intercalated marine sediments, strontium dating, and subsurface studies, and refines earlier studies by De Heinzelin and El-Arnauti (1987) and Giglia (1984) (Fig. 2).

Formerly termed "Formation M," the Benghazi Formation is a ~ 12 m thick dolomitic limestone that forms the lowest stratigraphic level of the sediments exposed in the As Sahabi area. Its lower contact is not exposed, and its upper contact is an unconformity underlying the Sahabi Formation. It consists of highly gypsiferous, halite-containing sandy, and clayey bioclastic sediments. There is a rich marine invertebrate fauna including echinoids, pelecypods, bryozoans, barnacles, foraminifera, and ostracods. The calcareous nannofossils indicate a Tortonian age (ca. 8.23 Ma), supported by $^{87}Sr/^{86}Sr$ isotope studies on a fossilized shell providing ages of 8.99 Ma to 9.36 Ma. The macro/microfossils suggest a depositional environment of transgressive inner neritic marine conditions, indicative of shallow water deposition with a low rate of sedimentation.

The Sahabi Formation is composed of two members. The "Lower Member" is up to 25 m thick and is composed of gypsiferous dark clay and sand, previously termed "Formation P" and the "Member T" portion of the Sahabi Formation. It contains a network of 5 m-deep polygonal cracks filled with selenite gypsum. The upper contact is an unconformity delineated by gypsum-filled cracks. This

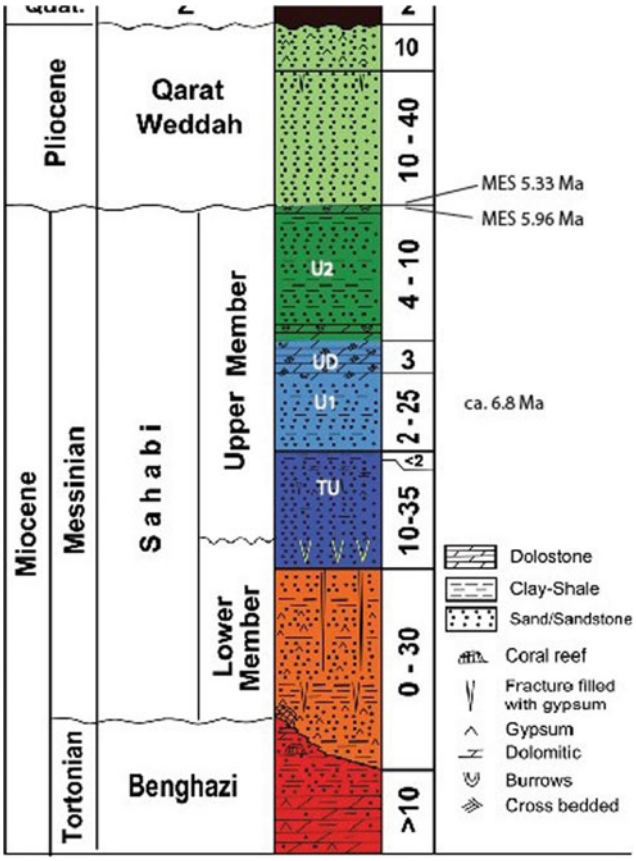

Fig. 2 Chrono/lithostratigraphic columnar section showing the exposed Neogene rock units in the As Sahabi area, northeast Sirt Basin

stratum was interpreted by De Heinzelin and El-Arnauti (1987) to be terminal Miocene in age and correlative to the Messinian Salinity Crisis, but lithologic and fossil content indicate a shallow marine depositional environment and evaporitic conditions within a sabkha or hypersaline lagoon. The age of this Unit is Late Miocene (Messinian Stage) (El-Shawaihdi et al., 2016).

The "Upper Member" of the Sahabi Formation includes the upper part of the member T (TU), and Units U-1, U-D, and U-2. Clay and sands grade upwards into peloidal sandy dolostone, followed by arrhythmic intercalations of sand and clay locally interrupted by thin dolostones. Vertebrate fossils are abundantly preserved in Units U-1 and U-2. This member has been dated to the Late Miocene using benthic foraminifera (*Borelis melo curdica*) and numerous vertebrate taxa at ca. 6.8 Ma (Bernor et al., 2020; Boaz et al., 2008). Depositional environments included a mosaic of paleohabitats, terrestrial (steppe, wooded savanna, and forest) and aquatic (large freshwater river, estuary, and offshore marine). The cross-bedded strata of unit U-D, earlier interpreted as a "dune," constitute a transgressive carbonate barrier bar (Muftah et al., 2008).

The Qarat Weddah Formation formerly termed "Member V," consists of variable white to green sands and sandy mudstones with lenses of gray, gypsiferous dolomite, with frequent clay balls. This unit unconformably overlies the "Upper Member" of the Sahabi Formation, and represents transgressive fluvio-deltaic deposition in tidal channels, fresh to brackish-water marshes, or sabkhas. This formation was deposited during the post-Messinian re-filling of the Mediterranean Basin, and its age is estimated as Early Pliocene based on its stratigraphic position. The upper contact is unconformable with overlying "Formation Z," a brecciated paleosol with root casts of Quaternary age (El-Shawaihdi et al., 2016).

4 Discussion

The regional stratigraphic framework in the As Sahabi area now provides a matrix for documenting earth history events and investigating biotic effects during the Messinian period in northern Africa and the eastern Mediterranean Basin. Among the questions that can be addressed here are the course, timing, and demise of one of Africa's great rivers, the Eosahabi, a significant source of fresh water emptying into the Mediterranean (Barr & Walker, 1973; Griffin, 2006, 2011; Nicolai, 2008). Questions surrounding the timing and origin of the Sahara Desert can also be effectively addressed in unexplored sedimentary deposits along the long Eosahabi valley stretching south to the Mega-Lake Chad Basin. Paradoxical aspects of Neogene As Sahabi, showing attributes of both a "crossroads" and endemic biota, remain to be explained (11).

5 Conclusions

Roveri et al. (2014) note that "a comprehensive stratigraphic scenario of Messinian events is still unavailable because of the difficulties in combining onshore and offshore observations." The Neogene stratigraphic record of sediments exposed at Sahabi represents just such a marine-terrestrial sequence. Reconstructing that record has required a methodical multidisciplinary program of fieldwork and lithostratigraphic correlation. The As Sahabi area holds great promise for interpreting the complex geological and paleoenvironmental phenomena preceding and following the Messinian Salinity Crisis.

References

Barr, F. T., & Walker, B. R. (1973). Late tertiary channel system in northern Libya and its implications on Mediterranean sea-level changes. In Ryan et al. (Eds.), *Initial reports: Deep sea drilling projects* (Vol. 13, pp. 1244–1250).

Bernor, R. L., Boaz, N. T., Cirilli, O., El-Shawaihdi, M., & Rook, L. (2020). Sahabi Eurygnathohippus feibeli: Its systematic, stratigraphic, chronologic and biogeographic contexts. *Rivista Italiana Di Paleontologia e Stratigrafia, 126*(2), 561–581.

Boaz, N. T., El-Arnauti, A., Agusti, J., Bernor, R. L., Pavlakis, P., & Rook, L. (2008). Temporal, lithostratigraphic, and biochronologic setting of the Sahabi Formation, north central Libya. In M. J. Salem et al. (Eds.), *Geology of East Libya* (pp. 233–246). Elsevier.

Boaz, N. T., El-Arnauti, A., Gaziry, A. W., de Heinzelin, J., & Dechant Boaz, D. (Eds.). (1987). *Neogene paleontology and geology of Sahabi Libya*. Liss.

Boaz, N. T., Gaziry, A. W., & El-Arnauti, A. (1979). New fossil finds from the Libyan upper Neogene site of Sahabi. *Nature, 280*, 137–140.

De Heinzelin, J., & El-Arnauti, A. (1987). The Sahabi Formation and related deposits. In N. T. Boaz et al. (Eds.), *Neogene paleontology and geology of Sahabi* (pp. 1–21). Liss.

El-Shawaihdi, M. H., Mozley, P. S., Boaz, N. T., Salloum, F., Pavlakis, P., Muftah, A., & Triantaphyllou, M. (2016). Stratigraphy of the Neogene Sahabi units in the Sirt Basin, northeast Libya. *Journal of African Earth Sciences, 118*(2016), 87–106.

El-Shawaihdi, M. H., Muftah, A. M., Mozley, P. S., & Boaz, N. T. (2014). New age constraints for Neogene sediments of the Sahabi area, Libya (Sirt Basin) using strontium isotope ($^{87}Sr/^{86}Sr$) geochronology and calcareous nannofossils. *Journal of African Earth Sciences, 89*(2014), 42–49.

Giglia, G. (1984). *Geological map of Libya Sheet Ajdabiya (NH34–6) explanatory booklet 1:250,000* (93p). Industrial Research Center (IRC).

Griffin, D. L. (2006). The Late Neogene Sahabi rivers of the Sahara and their climatic and environmental implications for the Chad basin. *Journal of the Geological Society of London, 163*(2006), 905–921.

Griffin, D. L. (2011). The Late Neogene Sahabi rivers of the Sahara and the hamadas of the eastern Libya-Chad border area. *Palaeogeography, Palaeoclimatology, Palaeoecology, 309*(2011), 176–218.

Muftah, A., Triantaphyllou, M., El-Mehaghag, A., Pavlakis, P., & Boaz, N. T. (2018). Late Miocene formations from As Sahabi area, Sirt Basin, Libya in correlation to isochronous SE Europe deposits: A paleoclimatic approach. *Geologica Balcanica, 39*(1–2), 267–268.

Muftah, A. M., Pavlakis, P., Godelitsas, A., Gamaletsos, P., & Boaz, N. (2013). Paleogeography of the Eosahabi River in Libya: New insights into the mineralogy, geochemistry and paleontology of Member U1 of the Sahabi Formation, northeastern Libya. *Journal of African Earth Sciences, 78*, 86–96.

Muftah, A. M., Salloum, F. M., El-Shawaihdi, M. H., & Al-Faitouri, M. (2008). A contribution to the stratigraphy of formations of the As Sahabi area, Sirt Basin, Libya. *Garyounis Scientific Bulletin, 5*, 33–45.

Nicolai, C. (2008). Tracing the As Sahabi channel system in the Ajdabya Trough, Central Sirt Basin. *Garyounis Scientific Bulletin, 5*, 85–94.

Roveri, M., Flecker, R., Krijgsman, W., Lofi, J., Lugli, S., Manzi, V., Sierro, F.J., Bertini, A., Camerlenghi, A., De Lange, G., & Govers, R. (2014). The Messinian Salinity Crisis: Past and future of a great challenge for marine sciences. *Marine Geology, 352*, 25-58. https://doi.org/10.1016/j.margeo.2014.02.002.

Early Pliocene Benthic Foraminifera of the Southeastern Coast of Cap Bon Peninsula (Northern Tunisia)

Syrine Ben Ali and Nadia Gaaloul

Abstract

A study of benthic foraminiferal assemblages was carried out based on the analysis of clay sediment samples collected from the lower Pliocene deposits of the Jrêba section (Nabeul region, southeastern coast of the Cap Peninsula, Tunisia). A diversified micro-faunistic content was documented, consisting of 36 species of benthic foraminiferal belonging to 26 genera and 21 families. Among these species: *Ammonia beccarii*, *Ammonia inflata, Bulimina aculeata, Bulimina costata, Bolivina dilatata*, *Bulimina inflata, Bolivina punctata*, C*ibicides floridani, Elphiduim crispuim, Lobatula lobatula*, *Melonis barleeanum, and Melonis pompiloides.* These species are ecologically characterized by reference to those common to the Mediterranean modern environments, and their distribution is closely related to the seawater dynamics. The obtained results reveal important changes in the composition and the stratigraphic distribution of benthic foraminiferal assemblages indicating, for the study area, an evolution of the paleoenvironment from circalittoral to infralittoral stages during the early Pliocene. Ammonia tepida (species known as tolerant typical coastal lagoons) at the uppermost levels of the Jrêba section within the foraminiferal content denotes a restricted paleoenvironment and a decrease of marine influence from this stratigraphic interval.

Keywords

Benthic foraminifera • Paleoecology • Early Pliocene • Cap Bon Peninsula • Tunisia

1 Introduction

Pliocene deposits are primarily distributed along the Tunisian coasts (Dammak, 2002; Temani & Gaaloul, 2007). On the southeastern coast of Cap Bon Peninsula, the Pliocene transgression favored the deposition of clay sediments with diversified microfossils. Among them, specimens of benthic Foraminifera are well represented. They are unicellular microorganisms colonizing various marine environments and ecosystems (Loeblich & Tappan, 1987), ranging from shallow marine conditions to abyssal plains. Therefore, they are classically used as proxies to evaluate environmental conditions and are applied for environmental reconstructions (Murray, 2001).

The distribution of benthic Foraminifera is influenced by the type of sediments, their grain-size distribution (Armynot du Châtelet, 2009), and the physicochemical parameters of water bodies such as salinity, temperature, and oxygen (Gooday, 2003).

This work aims to investigate the composition and distribution of benthic foraminiferal associations of the southeastern coast of Cap Bon Peninsula, northern Tunisia, and to characterize the paleoenvironmental evolution of this region during the early Pliocene Mediterranean transgression.

2 Materials and Methods

The Cap Bon Peninsula, located on the northeastern coast of Tunisia, covers an area of about 2822 km^2. It is an elongated SW-NE oriented structure called the "Djebel Abdelrahmene" anticline (Fig. 1). The tectonic setting of the region is marked by the Late Cenozoic alpine phase resulting from the collision between African and European plates. The lithostratigraphic succession ranges from Eocene to Quaternary (Ben Salem, 1995) and is represented mainly by alternations of clay, sand, and limestone-rich sediments.

S. B. Ali (✉) · N. Gaaloul
Department of Geology, University of Tunis EL Manar, 1060 Tunis, Tunisia
e-mail: syrine.benali@etudiant-fst.utm.tn

A. Çiner et al. (eds.), *Recent Research on Sedimentology, Stratigraphy, Paleontology, Tectonics, Geochemistry, Volcanology and Petroleum Geology*, Advances in Science, Technology & Innovation,
https://doi.org/10.1007/978-3-031-43222-4_15

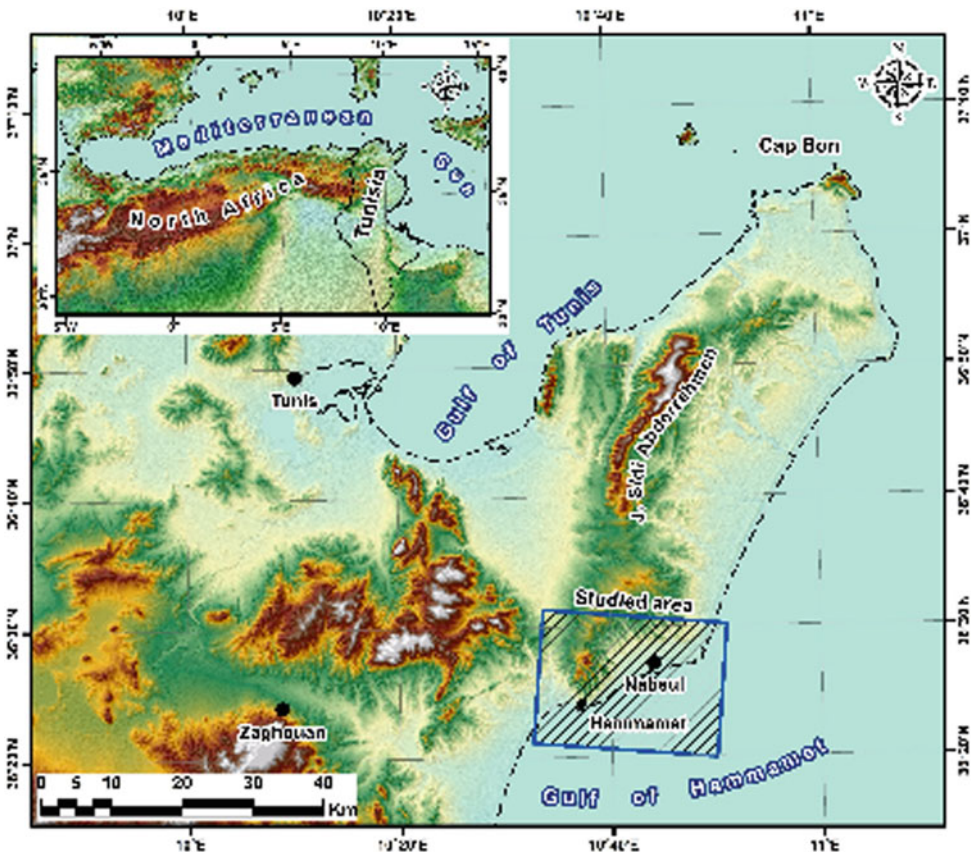

Fig. 1 Geographic localization of the study area

The southeastern coast of Cap Bon Peninsula shows a continuous and thick Pliocene series (Fig. 2a), providing the opportunity to follow the sedimentary record. Therefore, the lower Pliocene section of the Jrêba quarry was selected for this study (Fig. 2a, b). This section, 6 m thick, is located 5 km northwest of Nabeul town. Eighteen samples (codified Ap), spaced 10 to 20 cm, were taken through the section.

Two samples (250 g) replicates were collected from each sampled stratigraphic level and stored in polyethylene bags. A sample was used to study foraminiferal assemblages; a second was kept for further studies. In the laboratory, all samples were washed through 63, 125, 250, and 500 µm sieves. At least three hundred specimens, for all particle size fractions, were observed, picked, counted then studied in slides. The generic taxonomical classification follows that of Loeblich and Tappan (1987). The names of species were checked against the latest name list of the World Register of Marine Species (WORMS). Specimens were photographed by Scanning Electron Microscopy (SEM) of the Tunisian Company of Petroleum Activities and stored in the Laboratory of Sedimentary Basins and Petroleum Geology of the Faculty of Sciences of Tunis (Tunisia).

3 Results

The Jrêba section shows an overall clayey succession containing mollusk shells. Toward the top of the section, sediments are enriched with sandy grains. The micropaleontological study identified 36 species of benthic Foraminifera belonging to 26 genera, 21 families, and six orders.

The occurrence of *Sphaeroidinellopsis* in samples Ap1, Ap2, and *Globorotalia margaritae* in samples Ap3, Ap4, Ap5, AP7, and AP15 allowed us to consider that the sedimentary succession belongs to Zanclean which can be correlated to the MPL1 of Cita (1975).

Benthic foraminiferal assemblages (Fig. 3) were primarily dominated by families: Uvigerinidae, Melonidae, Cibicididae, Ammoniidae, and Buliminidae. Some species, including *Ammonia inflata, Melonis barleeanum, Melonis pompilioides, Pullenia bulloides, Sphaerodina bulloides, Valvulineria glabra,* and *Uvigerina peregrina* were observed in all samples. Species: *Adelosina depressa, Bigenerina nodosaria*, *Bolivina punctata, Lenticulina rotulata, Marginulina* sp., *Neugeborina longiscata, Nonion commune,* and *Plectofrondicularia*

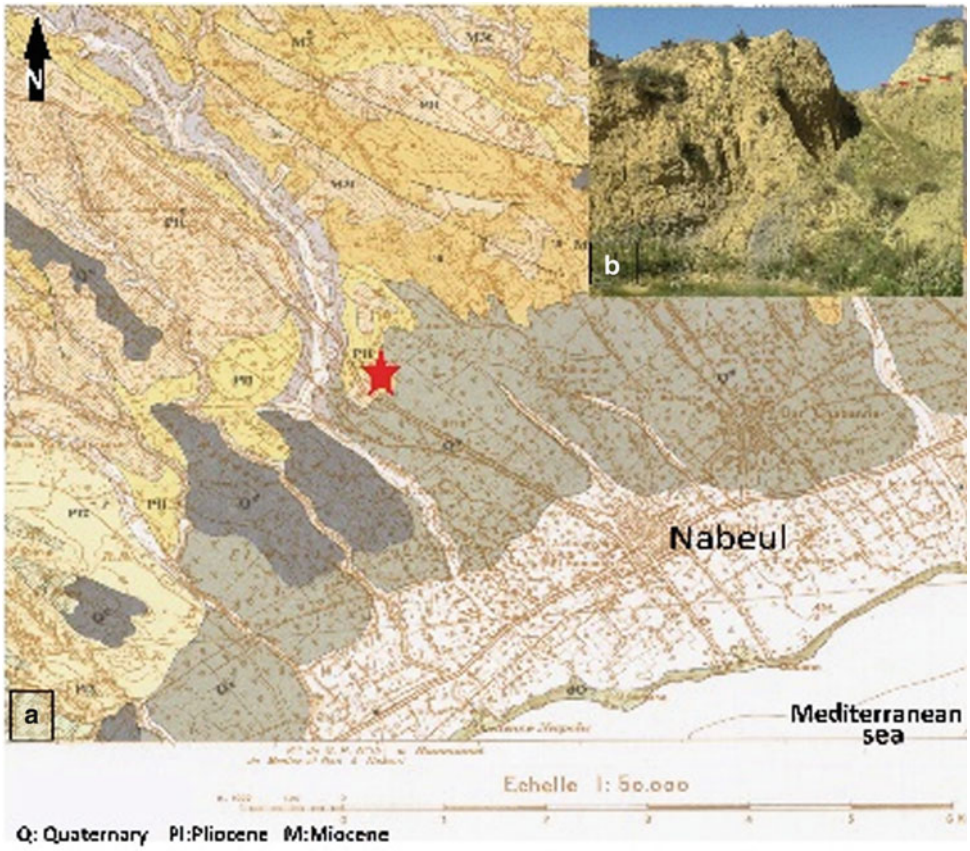

Fig. 2 **a** Geological map of the study area and location of the study section (after geological map of Tunisia 1/50000). **b** General view of the section

inaequalis were restricted to some levels. *Ammonia beccarii, Bulumina aculeata, Bulumina costata, Cancris auriculus, Lobatula lobatula, Planulina arimensis,* and *Uvigerina pygmea* show episodic occurrences. *Melonis pompilioides, Pullenia bulloides, Planulina arimensis,* and *Uvigerina peregrina* reached a maximum abundance (20 to 40%) in the lower part of the section (Ap_1 to Ap_9). The interval from Ap_{10} to Ap_{13} shows the dominance of *Bulimina costata, Bolivina dilatata, Cibicides floridiani,* and *Uvigerina mediterranea.* Species: *Ammonia beccarii, Ammonia inflata,* and *Lenticulina orbicularis* were more frequent in the upper part of the section. The sample Ap_{18} at the top of the section is marked by the presence of *Ammonia tepida*.

4 Discussion

The abundance of benthic foraminiferal taxa provides valuable criteria to determine the habitat type and the faunal assemblage's paleoenvironment for a specific time interval (Bergh et al., 2018). Based on the stratigraphic distribution of benthic foraminiferal species, their abundance throughout the study section, and their ecological preferences, we have distinguished three types of faunal assemblages, indicating three successive paleoenvironments:

A_1, assemblage with typical species of circalittoral stage (interval Ap_1-Ap_{10}). This assemblage contains *M. barleeanum, M. pompilioides, P. arimensis, P. bulloides,* and *U. peregina which* marks the lower part of the section. It is currently present in the East China Sea, the North Atlantic Ocean, the Gulf of Mexico, and the Mediterranean Sea. This assemblage in the Yellow Sea (China) is common in water depths of 32 to 80 m (Lei & Li, 2016). *U. peregrina* is mentioned in the recent sediments of the Bay of Biscay (western France), the Celtic Sea (southern England), the North Atlantic Sea, the continental shelf of North-East U.S., and the Mediterranean Sea. Mohan et al. (2011) reported *M. barleeanum* and *U. peregrina* in the Neogene sediments of Blake Ridge (northeast U.S.). The author links their presence to the early Pliocene warm period. *P. arimensis* characterizes deep marine environments ranging from the circalittoral to bathyal stages (Van Morkhoven et al., 1986). In the Gulf of Cadis (southern Spain), this species is considered an indicator of the Mediterranean Outflow Water.

A_2, Assemblage with infralittoral/circalittoral taxa (interval Ap_{11}-Ap_{13}). Compared to the precedent one, foraminiferal content in this assemblage shows an increase in the abundance of species: *B. costata*, *B. dilatata*, C. *floridiani,* and *U. mediterranea.* According to Jourissen et al. (1995), the genus *Bolivina* is not typical of a particular

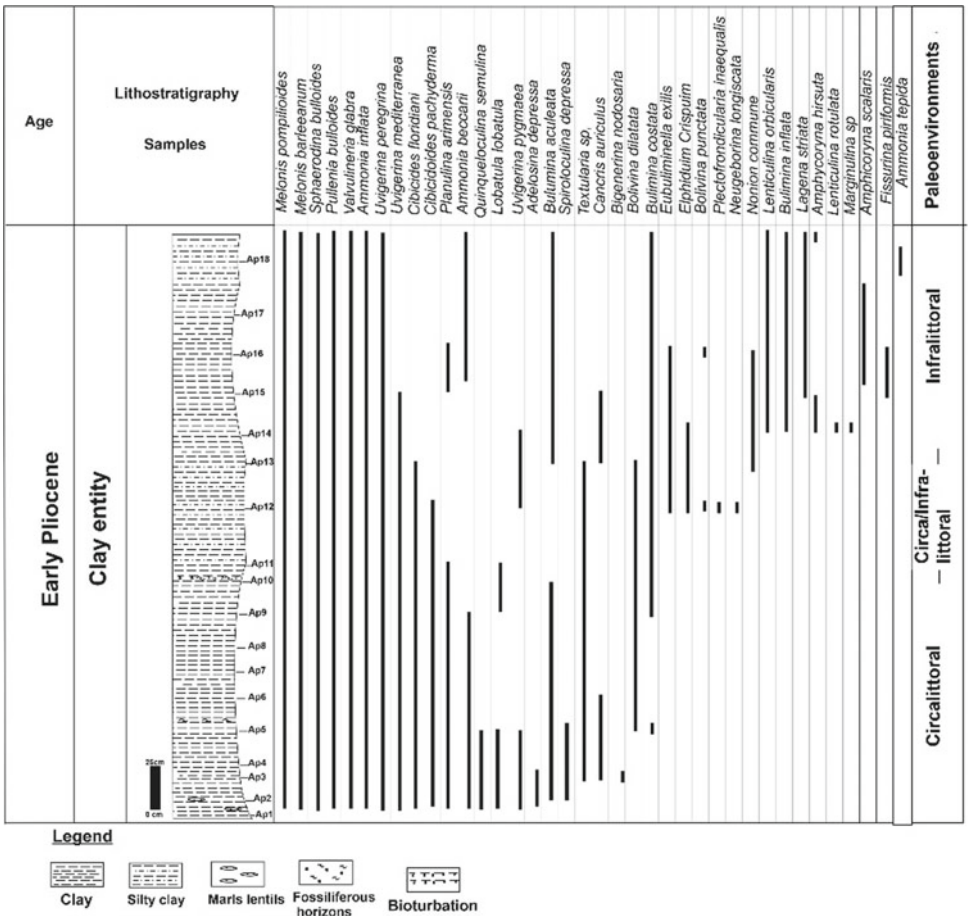

Fig. 3 Distribution of species of benthic Foraminifera in the Jrêba section

bathymetry but seems to indicate a confined marine environment. In addition, these authors consider that the association of genera *Cibicides* and *Bolivina* requires a marine environment with variable input of oxygen and organic matter. The simultaneous presence of circalittoral (*Bulumina*) and intertidal to infralittoral (*Cibicides*) taxa suggest that the median interval of the study section can be linked to an infralittoral/circalittoral environment.

A_3, assemblage with species of infralittoral stage (interval Ap_{14}-Ap_{18}). This assemblage characterizes the upper part of the section. The most abundant species are *A. inflata*, *E. crispuim,* and *L. orbicularis*. Genus *Ammonia* includes species largely common in shallow marine water of transitional environments (Langer and Hottinger, 2000). In addition, *A. beccarii* has been described in the estuarine systems of the whole of Europe and the Mediterranean Sea (Debnay et al., 1996). *Elphiduim* is encountered in the shallowest marine margins of the Iberian coast depth of less than 10 m. In the Ap_{14}-Ap_{18} interval of the study section, foraminiferal benthic association indicates an infralittoral stage showing a great similarity with the associations reported from marginal Mediterranean environments. Our result partially matches with data from Dammak (2002), who reported the Pliocene transgression in the Nabeul region for the first time.

5 Conclusions

This study offers useful information about the relationship between benthic foraminiferal associations and paleoenvironments. The benthic foraminiferal microfauna from the Jrêba section suggests significant paleoenvironmental changes in the southeastern coast of Cap Bon Peninsula during the early Pliocene. In this area, Pliocene paleoenvironments evolve from deep circalittoral conditions, at the base of the section (initiated by the early Pliocene Mediterranean transgression) to shallow infralittoral environments, at the top of the section.

References

Armynot du Châtelet, E. (2009). Sediment grain size and clay mineralogy and organic matter quality control on living benthic Foraminifera. *Revue de Micropaléontologie, 52*(1), 75–84.

Ben Salem, H. (1995). Evolution de la péninsule du cap Bon (Tunisie orientale) au cours du Néogène. *Notes du Service Géologique de laTunisie, 61*, 73–84.

Bergh, E. W., Compton, J. S., & Frenzel, P. (2018). Late Neogene Foraminifera from the northern Namibian continental shelf and the transition to the Benguela Upwelling System. *Journal of African Earth sciences, 141*, 33–48.

Cita, M. B. (1975). Studi sul Pliocene e gli strati di passaggio dal Miocene al Pliocene. VII. Planktonic foraminiferal zonation of the Mediterranean Pliocene deep sea record. *Rivista Italiana di Paleontologia e Stratigrafia, 81*, 527–544.

Dammak, F. (2002). Identification of the mediterranean biostratigraphical zones in the Cap-Bon (Tunisia) Pliocene deposits. *Geobios, 35* (2), 253–264.

Debnay,J. P., Pawlowski, J., & Decrouz, D. (1996). *Les foraminifères actuels.Masson* (p. 329).

Gooday, A. J. (2003). Benthic Foraminifera (Protista) as tools in deep-water palaeoceanography: environmental influences on faunal characteristics. *Advances in Marine Biology, 46*, 1–90.

Jourissen, F. J., DeStigter, H. C., & Widmark, J. G. (1995). A conceptual model explaining benthic formainiferal microhabitat. *Marine Micropaleontology, 26*, 3–15.

Langer, M. R., & Hottinger, L. (2000). Biogeography of selected "larger" Foraminifera. *Micropaleontology, 46*, 105–126.

Lei, Y., & Li, T. (2016). *Atlas of benthic Foraminifera from China seas* (399 p). Science Press Beijing.

Loeblich, A. R., & Tappan, H. (1987). *Foraminifera Genera and their classification* (p. 970p). New York: Van Nostrand Reinhold.

Mohan, K., Gupta, K., & Bhaumik, A. K. (2011). Distribution of deep-sea benthic Foraminifera in the Neogene of Blake Ridge, NW Atlantic Ocean. *Journal of Micropalaeontology, 30*, 33–74.

Murray, J. W. (2001). The niche of benthic Foraminifera, critical thresholds and proxies. *Marine Micropaleontology, 41*(1–2), 1–7.

Temani, R., & Gaaloul, N. (2007). Les paléopeuplements du Messinien et du Pliocène du golfe de Hammamet: Intérêt paléoécologique et événementiel. *Revue Méditerranéenne de l'Environnement, 2*, 130–142.

Van Morkhoven, F. P. C. M., Berggren, W. A., & Edwards, A. S. (1986). *Cenozoic cosmopolitan deep-water benthic Foraminifera* (421 p). Elf Aquitaine.

The Geochemistry of Biotite from TTG Batholiths and A-type Complexes (Silet Region, Hoggar, Algeria): A Marker of Geodynamic Evolution

Sarra Mokaddem, Fatene Bechiri-Benmerzoug, Hamid Bechiri, Nicolas Rividi, and Bernard Bonin

Abstract

This work aims to compare the chemical composition of electron microprobe analysed biotite (n = 245) from four Trondhjemite-tonalite-granodiorite (TTG) batholiths and four A-type complexes. All of them are exposed in the central part of the Silet terrane (western Hoggar, Algeria) and crosscut Pharusian volcano-sedimentary series. According to Nd isotope values, the rocks are geographically arranged in two narrow N-S oriented bands separated by the Tin-Dahar fault. Negative isotopic values characterize all rocks of the narrow eastern band (ENB) ($-2.91 < \varepsilon Nd < -8.10$), and biotite is the only mafic mineral. On the other hand, in the western band, rocks display positive (WPB) isotopic values ($+0.52 < \varepsilon Nd < +4.57$) and amphibole in addition to biotite. WPB biotites are magnesian ($0.50 < Mg < 3.31$) and calc-alkaline, while ENB biotites are ferroan ($0.31 < Mg < 2.55$) and alkali-calcic to alkaline. ENB biotites are relatively poor in $Altot_{ot}$ ($2.58 < Altot_{ot} < 2.89$) compared with WPB biotites ($2.72 < Altot_{ot} < 3.10$). On the other hand, a-type biotites have high Al tot values in the WPB rocks ($2.67 < Al_{tot} < 4.18$) compared to ENB ($2 < Al_{tot} < 3.18$). The distinctive features of the studied biotites evidence the Tin-Dahar fault as a major regional feature.

Keywords

Biotite chemistry • TTG batholiths • A-complex granite • Tin-Dahar fault • Silet • Hoggar • Algeria

1 Introduction

Like 25 other terranes in Hoggar, the Silet Terrane is located within the Tuareg shield (Liégeois, 2019). The Silet terrane considered a composite island arc (Bechiri-Benmerzoug, 2009), was accreted to the eastern margin of the LATEA meta craton during the late stage of pan-African orogeny (650–630 Ma). It comprises Neoproterozoic volcano-sedimentary series (Pharusien I and II), crosscut by TTG batholiths (870–639 Ma). The last phase of the cycle is marked by the emplacement of A-type granitic complexes of the "Taourirt" suite (Azzouni-Sekkal et al., 2020, and references therein). According to Nd whole-rock and Hf zircon isotopic ratios, rocks of the central region of the Silet terrane are geographically arranged into two narrow bands roughly oriented N-S, separated by the Tin-Dahar fault. Rocks of the eastern band (ENB) yield negative εNd ($-2.91 < \varepsilon Nd < -8.10$), while those of the western band (WPB) yield positive εNd/εHf ($+0.52 < \varepsilon Nd < +4.57$). We compared biotite chemical compositions from eight massifs, including four TTG-type batholiths: Tin-Tekadiouit, Ahambatou, Silet, and Eheli, and four A-type granitic complexes: Tin-Erit, Tioueïne, Teg-Orak, and Inedjaren (Fig. 1). The main geological, petrographic, geochemical, and geochronological features are summarized in Tables 1 and 2.

2 Materials and Methods

We selected two hundred and forty-five (245) chemical compositions of biotite, of which 44 analyses were carried out at the Museum of Natural History of Paris (Teg-Orak and Tioueine) and 201 new analyses were carried out at the

S. Mokaddem (✉) · F. Bechiri-Benmerzoug
Laboratoire Didactique Des Sciences, École Normale Supérieure de Kouba Bachir El Ibrahmi, B.P. 91, 6308 Kouba, Algeria
e-mail: sarra.mokaddem@g.ens-kouba.dz

H. Bechiri
Faculté Des Sciences de Terre Géographie Et Aménagement du Territoire, USTHB, Algiers, Algeria

N. Rividi
Sorbonne Université, Campus Pierre Et Marie Curie 4 Place Jussieu Tour 46, 3Ème Étage, Couloir 46-00, 75005 Paris, France

B. Bonin
'GEOPS', Université Paris-Sud, CNRS UMR8148, Université Paris-Saclay, Rue du Belvédère, 91405 Orsay Cedex, France

A. Çiner et al. (eds.), *Recent Research on Sedimentology, Stratigraphy, Paleontology, Tectonics, Geochemistry, Volcanology and Petroleum Geology*, Advances in Science, Technology & Innovation,
https://doi.org/10.1007/978-3-031-43222-4_16

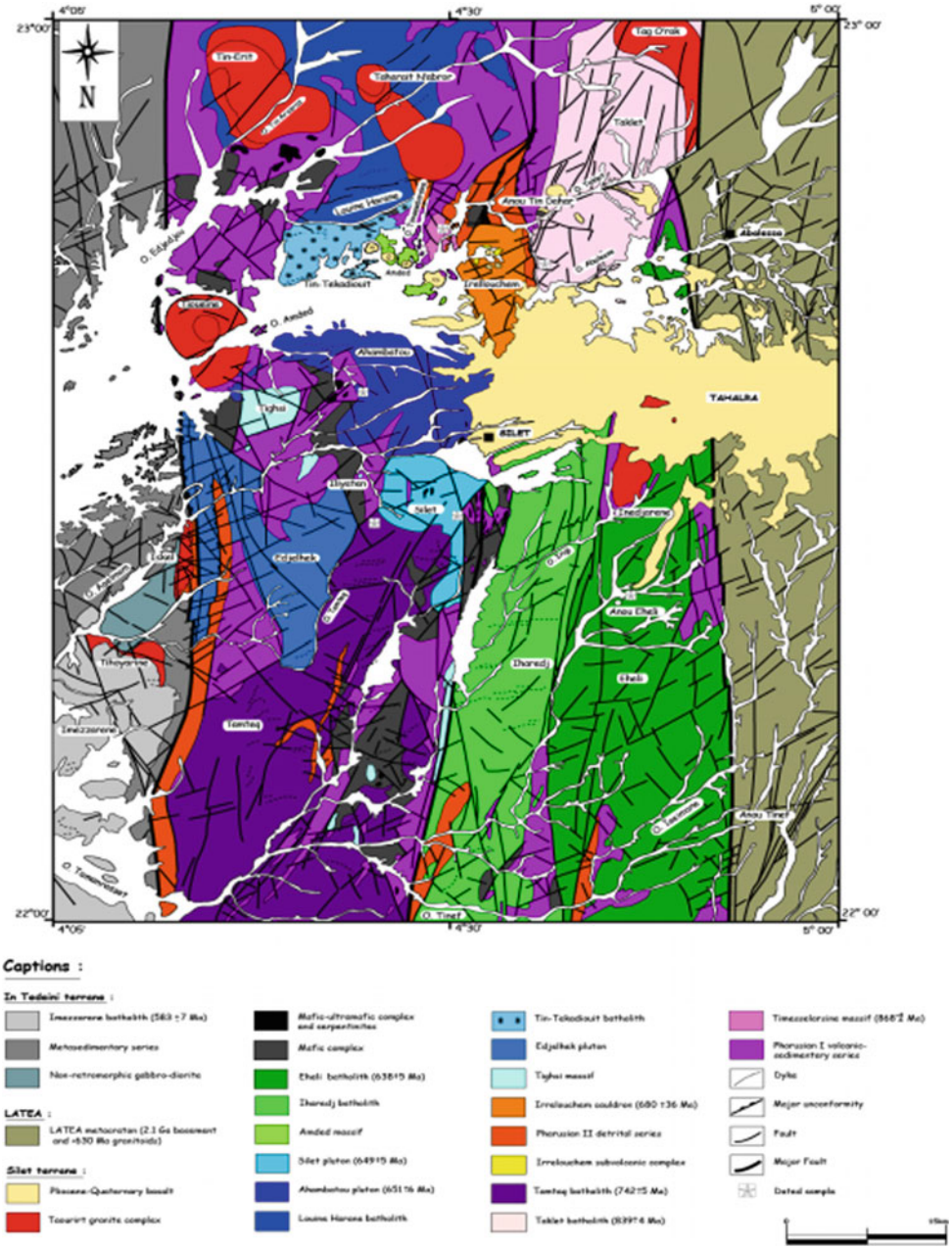

Fig. 1 Geological map of Silet area (Bechiri et al., 2016)

OSU UPMC-INSU (Sorbonne University–Paris-France) with CAMECA SX-100 microprobe for four TTG batholiths (Eheli, Ahambatou, Tin-Tekadiouit, and Silet) and two A-type granites (Tin-Erit and Inedjaren). The structural formulas, based on 22 oxygen anions, and the distribution of Fe^{2+} and Fe^{3+} were calculated using the software of Li et al.

3 Results

Black mica is a hydrated ferromagnesian silicate common in all plutonic rocks of the TTG and A-type batholiths of the western positive isotope signature (WPB): Eheli (TTG) and Inedjaren and Teg-Orak (A-type) and the biotite of the TTG (Tin-Tekadiouit, Ahambatou, and Silet) and A-type (Tin-Erit and Tioueïne) batholiths, located in the eastern band negative isotopic signature (ENB) is associated with amphibole.

Comparative results of the chemical compositions of biotites conducted in the two bands (ENB, WPB) show a distinct geochemical contrast between the biotites of the two bands, the element Mg is decreased from the biotites of the ENB granites ($0.57 < Mg < 4.20$) to the biotites of the WPB band ($0 < Mg < 2.88$). In contrast, Fet shows the opposite trend $2.14 < Fet < 6.05$ (WPB) and $1.80 < Fet < 4.23$ (ENB).

In the Feal [Fe + Mn + Ti-AlVI] vs. Mgli (Mg-Li) diagram (modified from Tischendorf et al., 1997), the

Table 1 Main petrographic and geochemical characters of the TTG batholiths

Band position	Eastern negative band	Western positive band		
Batholith age	Eheli (638 ± 5 Ma)	Silet (649 ± 5 Ma)	Tin-Tekadiouit (undated)	Ahambatou (651 ± 6 Ma)
TTG type	Sodic Low-HREE	Potassic	Potassic	Sodic Low-HREE
Rock types	Granodiorite—Monzogranite	Monzodiorite—Quartz monzonite—Syénogranite	Granodiorite	Tonalite—Granodiorite—Monzogranite
Major felsic minerals	Quartz + Oligoclase + K-feldspar		Quartz + Oligoclase-Andesine + K-feldspar	
Major mafic minerals	Biotite	Biotite ± Mg-Hornblende		
Accessory minerals	Zircon + Allanite + Titanite + Apatite + Ilmenite + Titanomagnetite			
A/CNK	Peraluminous			
Chemical affinity	Calc-alkaline to calcic	Calc-alkaline to Alkali-calcic	Calc-alkaline	
Geodynamic context	Volcanic arc granites			
εNd(t)	−2.91 < εNd < −8.30	+ 0.2 < εNd < + 3.27	+ 1.92 < εNd < + 4.57	−0.09 < εNd < + 1.22

Table 2 Main petrographic and chemical characters of A-type granites (Silet area)

Band position	Eastern negative band		Western positive band	
Complex age	Teg-Orak (519 ± 18 Ma)	Inedjarene (Undated)	Tin-Erit (584 ± 2 Ma)	WTioueïne (561 ± 1 Ma)
Taourirt type	GI – GIIa	GIIa – GIIb	GIIa – GIII	GI – GIII
Rock types	Monzogranite—Syenogranite	Alkali feldspar Granite—Syenogranite	Monzogranite—Syenogranite—Hypersolvus granite	Monzogranite—Syenogranite—Hypersolvus granite—Syenite
Major felsic minerals	Quartz + K-feldspar + Plagioclase			
Major mafic minerals	Biotite		Biotite ± Mg-hornblende	
Accessory minerals	Zircon + Allanite + Titanite + Ilmenite + Magnetite + Apatite			
A/CNK	Metaluminous to peraluminous	Metaluminous	Metaluminous to peralkaline	Metaluminous
Alkali-calcic Alkaline	Alkali-calcic—Alkaline	Alkali-calcic	Alkali-calcic—Alkaline	Alkali-calcic—Peralkaline
Geodynamic site	Syn-kinematic within-plate granite	Within-plate granite	Syn-kinematic within-plate granite	Syn-kinematic within-plate granite
εNd(t) / εHf(t)	$-5.18 < \varepsilon Nd < -8.38$	/	$+5.54 < \varepsilon Hf < +11.99$	$+2.2 < \varepsilon Hf < +7.1$

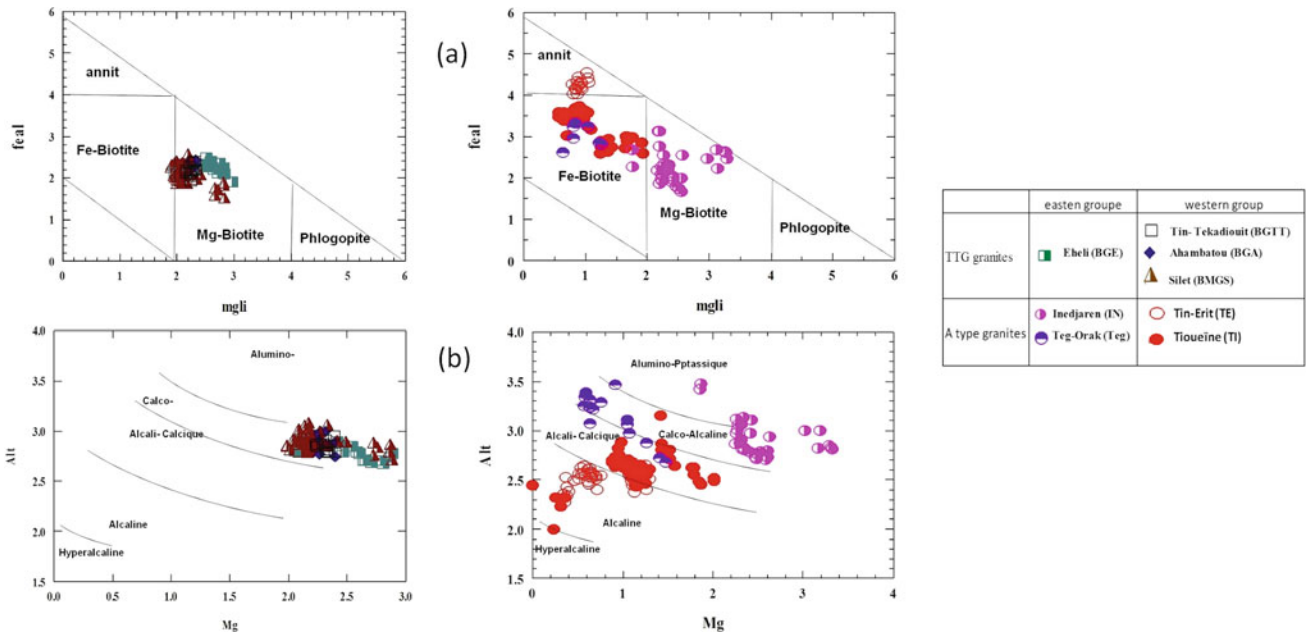

Fig. 2 Chemical compositions of TTG and A-type granite biotites of the Silet area **a** feal (Fe + Mn + Ti–AlVI) versus mgli (Mg–Li) (Tischendorf et al., 1997) and **b** Mg versus Al_{tot}

compositions of the black micas of TTG and A-type granites show an evolution from the ENB band group (Mg-biotite,) except the Teg-Orak batholith biotite which is less magnesian and lies in the Fe-biotite field, to the WPB band group where the biotite is more ferriferous which straddles the Fe-biotite field for TTG granites and approaches the annite pole for A-type granites (Fig. 2a).

In the Alt/Mg magmatic affinity diagram of Nachit et al., we find a certain similarity between the different micas of the granites studied in the two bands as regards the evolution from the most magnesian biotites of the eastern band (TTG and A-type) which are similar to the Calco-Alkaline to Alkali-Calcic to the least magnesian biotites which characterizes the Western band (A-type) draw a trend going from the domain Alkali-Calcic towards the domain Alkaline for the granite of A-type, on the other hand, the biotites of granite of Type TTG are registered in the same line with the other biotites of the Eastern band (Calco-Alcaline) (Fig. 2b).

4 Discussion

Major oxides, FeO, MgO, Al_2O_3, and TiO_2 (not discussed here) enable the characterization of biotites (Foster, 1960, etc.). Biotite of Eheli TTG batholith is more magnesian and less alumina-rich than Tin-Tekadiouit, Ahambatou, and Silet batholiths. Biotite of Inedjaren and Teg-Orak A-type complexes show the same features, pointing to a siderophyllite end-member, while biotite of Tin-Erit and Tioueïne A-type complexes are ferroan (Azzouni-Sekkal et al., 2003). Magnesian and aluminous characteristics of Teg-Orak and Inedjaren may reflect an orogenic character, though they are anorogenic (Fig. 3).

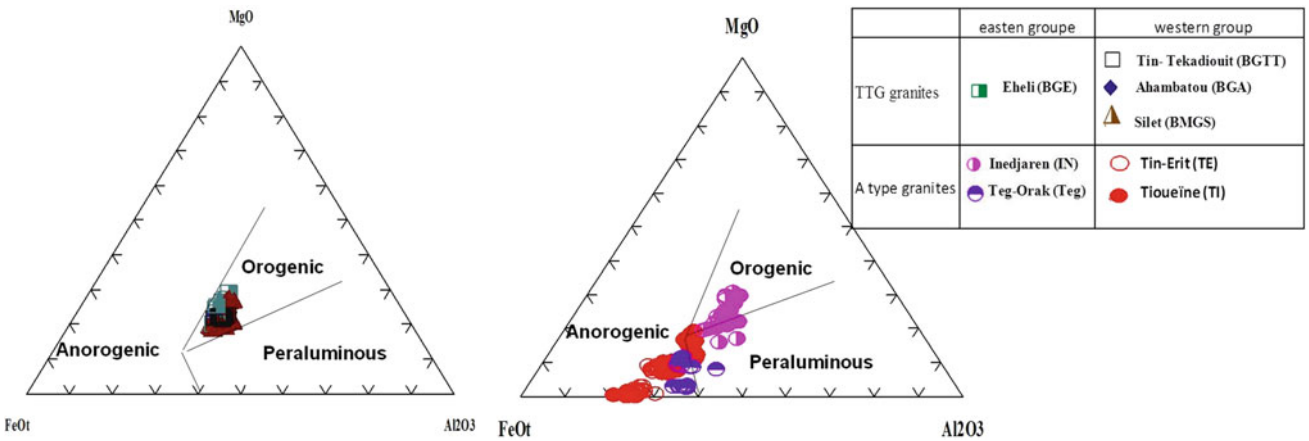

Fig. 3 Silet biotites on FeOt-MgO-Al_2O_3 discrimination ternary diagrams

5 Conclusions

The eastern band's juvenile rocks (TTG + A-type) may reflect an ocean-ocean subduction context. In contrast, those of the western band suggest a crustal contribution in their parent magmas emplaced in an ocean-continent context. This result is supported by the studied rocks' biotite compositions (Mg-biotite and Fe-biotite).

References

Azzouni-Sekkal, A., Bonin, B., Bowden, P., Bechiri-Benmerzoug, F., & Meddi, Y. (2020). Zircon U-Pb and Lu–Hf isotopic systems in Ediacaran to Fortunian "Taourirt" granitic ring complexes (Silet and In Tedeini terranes, Tuareg shield, Algeria). *Journal of African Earth Sciences, 168*, 103865.

Azzouni-Sekkal, A., Liégeois, J.-P., Bechiri-Benmerzoug, F., Belaidi-Zinet, S., & Bonin, B. (2003). The, "Taourirt" magmatic province, a marker of the closing stage of the Pan-African orogeny in the Tuareg Shield: A review of available data and Sr-Nd isotope evidence. *Journal of African Earth Sciences, 37*, 331–350.

Bechiri, H., Azzouni-Sekkal, A., Béchiri-Benmerzoug, F., Bonin, B., Liégeois, J. P., Kheloui, R., Matukov, D. I., & Sergeev, S. A. (2016). La faille de Tin-Dahar, un élément clé dans la structuration du bloc de Silet (ex Iskel) Hoggar occidental, Algérie. In *1st Arab geoscience union international conference (AIC-1)* (p. 4). Algiers, Algeria.

Bechiri-Benmerzoug, F. (2009). Pétrologie, géochimie isotopique et géochronologie des granitoïdes Pan-africains de type TTG de Silet: contribution à la connaissance de la structuration du bloc d'Iskel (Silet, Hoggar occidental) Algérie, Thèse Doctorat, Université des Sciences et Techniques Houari-Boumedienne, Alger, 398p.

Bechiri-Benmerzoug., F., Bonin, B., Bechiri, H., Khéloui, R., Talmat-Bouzeguela, S., & Bouzid, K. (2017). Hoggar geochronology: A historical review of published isotopic data. *Arabian Journal of Geosciences, 10*, 351.

Foster, M. (1960). *Interpretation of composition of trioctaheral micas* (Geological Survey Professional Paper 354-B) (pp. 1–49). United States Department of the Interior.

Liégeois, J. P. (2019). A new synthetic geological map of the Tuareg Shield: An overview of its global structure and geological evolution, the geology of the arab world—An overview, springer geology.

Mokaddem, S. et al. (2019). Classification des biotites de la région de Silet (Hoggar Occidental, Algérie): Exemple d'un TTG (Tin-Tekadiouit), d'un complexe annulaire (Taharait N'abror) et d'un granite à deux micas. 1er séminaire National en Géosciences et Environnement- Centre Universitaire de Tamanrasset. 23–24 octobre 2019.

Rieder, M., Cavazzini, G., D'Yakonov, Y. S., Frank-Kamenetskii, V. A., Gottardi, G., Guoggenheim, S., Koval, P. V., Müller, G., Neiva, A. M. R., Radoslovich, E. W., Robert, J. L., Sassi, F. P., Takeda, H., Weiss, Z., & Wones, D. R. (1998). Nomenclature of the micas. *Canadian Mineralogist, 36*, 905–912.

Tishendorf, G., Gottesmann, B., Forster, H. J., & Trumbull, R. B. (1997). On Li-bearing micas: Estimating Li fromelectron microprobe analysis and an improved diagramfor graphical representation. *Mineralogical Magazine, 61*, 809–834.

U–Pb Age Dating for Carbonate Sequences: An Example from Late Neoproterozoic Kharus Formation, Al Jabal Al-Akhdar, Northern Oman

Mohamed A. K. El-Ghali, Osman Salad Hersi, Iftikhar Abbasi, Hezam Al-Awah, and Mohamed S. H. Moustafa

Abstract

Outcrops of the late Neoproterozoic carbonate Kharus Formation are time-equivalent to the subsurface Buah Formation in Oman Interior Basin. Kharus Formation belongs to the Nafun Group, overlying the Mu'aydin Formation with a transitional contact, and is overlain conformably by the late Neoproterozoic to early Cambrian Fara Formation, or unconformably (i.e., angular unconformity) by the Permian Saiq Formation. However, precise age dating of the Kharus Formation is not constrained yet due to the lack of fossils and absolute age results. Herein, we report results to constrain the Kharus Formation age using the direct in-situ U–Pb technique on carbonate samples. The samples were collected from the outcropped Kharus Formation at Wadi Bani Awf, Jabal Akhdar. The samples collected from the lower part of the Kharus Formation close to the contact with the Mu'aydin Formation yielded an age of 573 ± 28 Ma. In contrast, the samples from the uppermost part close to the Fara Formation provided a period of 564 ± 4.5 Ma. These ages are relatively comparable with the reported speculative age of the Kharus Formation (ca. 575–550 Ma) in the literature based on the dated overlying Fara Formation (ca. 544 ± 3.3 Ma) using zircon age dating. However, further refinement of the obtained results using the direct in-situ U–Pb age dating of carbonate successions is required. This can be achieved by analyzing samples not affected or less affected by diagenetic processes.

Keywords

Late Neoproterozoic carbonate • Kharus Formation • U–Pb age dating • Geochronology

1 Introduction

The late Neoproterozoic Kharus Formation carbonate unit is well-exposed along deeply cut valleys (wadis) on the flanks of Jabal Akhdar in northern Oman (Fig. 1a–c; Cozzi, 2000; Cozzi et al., 2004a, b; Cozzi & Al-Siyabi, 2004; Tiley et al., 2000). The Formation belongs to the Nafun Group and is an outcrop-equivalent of the subsurface, hydrocarbon-producing Buah Formation (Fig. 1c). The Kharus Formation lies unconformably over the Mu'aydin Formation and underlies either the latest Neoproterozoic-early Cambrian Fara Formation conformably or Permian Saiq Formation with an angular unconformity (Fig. 1c; Cozzi et al., 2004a, b). Direct age dating of the Kharus Formation is not constrained yet, biostratigraphically and/or radiometrically. Yet, the age of the Kharus Formation is speculated between ca. 575 and 550 Ma based on zircon dating (ca. 544 ± 3.3 Ma) of the overlying Fara Formation (Amthor et al., 2003; Brasier et al., 2000; Le Guerroué et al., 2006). The current research aims to decipher the age of the Kharus Formation by using direct in-situ U–Pb carbonate age dating on selected carbonate samples from Kharus Formation.

M. A. K. El-Ghali (✉) · I. Abbasi · M. S. H. Moustafa
Department of Earth Sciences, College of Science, Sultan Qaboos University, Muscat, Oman
e-mail: melghali@squ.edu.om

M. A. K. El-Ghali
Earth Sciences Research Center, Sultan Qaboos University, Muscat, Oman

O. S. Hersi
Department of Geology, University of Regina, Regina, SK, Canada

H. Al-Awah
Department of Chemistry and Earth Sciences, Qatar University, Doha, Qatar

A. Çiner et al. (eds.), *Recent Research on Sedimentology, Stratigraphy, Paleontology, Tectonics, Geochemistry, Volcanology and Petroleum Geology*, Advances in Science, Technology & Innovation,
https://doi.org/10.1007/978-3-031-43222-4_17

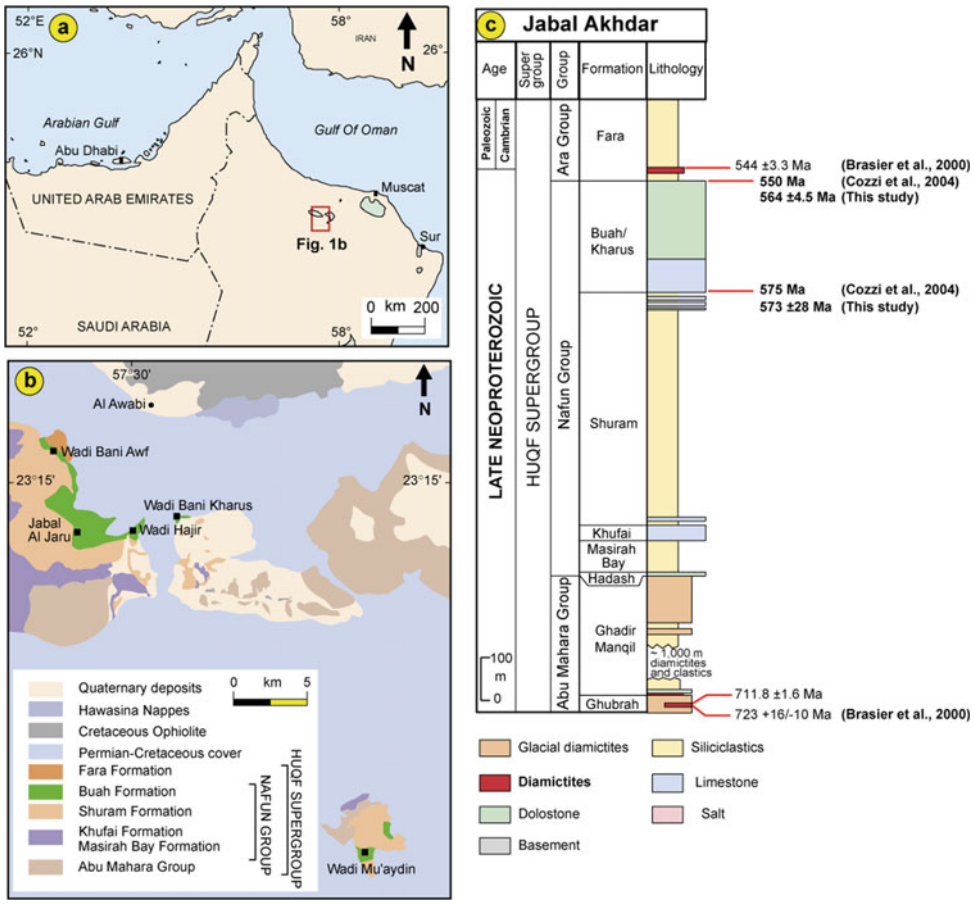

Fig. 1 **a** Location and **b** geological map of the study area showing the position of Jabal Akhdar [red square] in northern Oman and position of studied wadis; Wadi Bani Awf and Wadi. Bani Kharus, where Kharus/Buah Formation is exposed, and **c** stratigraphic section from Jabal Akhdar (northern Oman) to Huqf region (central Oman) and subsurface (South Oman Salt Basin) depicting the reported absolute age from Brasier et al. (2000), Cozzi et al. (2004a, b), and this study

2 Materials and Methods

To achieve the aim of this current study, carbonate samples were collected from two logged sections of the outcropped Kharus Formation in Wadi Bani Kharus and Wadi Bani Awf in Jabal Akhdar of northern Oman (Fig. 1a–c). The samples were collected from the lowermost layers of the Formation, close to the Mu'aydin Formation, and the uppermost part of the Formation, close to the Fara Formation contact (Fig. 1c). The samples were thin-sectioned and polished (1 µm) to increase the ability to view the sample. In-situ U–Pb carbonate dating was performed on the collected samples at the University of New Brunswick, Department of Earth Sciences, Canada, using a Resonetics S-155-LR 193nm Excimer laser ablation system coupled to an Agilent 7700 × quadrupole ICP MS. Forty spots with a 112-µm-diameter crater and a 30-s ablation time following 30 s of background collection for each collected sample, and a standard sample was used to measure and calculate the 207Pb/206Pb and 238U/206Pb ratio and age.

3 Results

Herein, we report the preliminary results of an in-progress study to decipher the age of the Kharus Formation using direct in-situ U–Pb technique on carbonate samples. LA-ICP-MS results show that samples collected from the lowermost layers of the Kharus Formation, close to the contact with the Mu'aydin Formation (Fig. 1c), yielded an age of 573 ± 28 Ma (Fig. 2a). On the other hand, the results from the uppermost part of the Formation, close to the contact with Fara Formation (Fig. 1c), provided an age of 564 ± 4.5 Ma (Fig. 2b).

4 Discussion

The obtained ages (573 ± 28 Ma to 564 ± 4.5 Ma) using in-situ U–Pb carbonate age-dating technique on the selected carbonate samples from Kharus Formation in Jabal Akhdar are relatively comparable with the previously reported

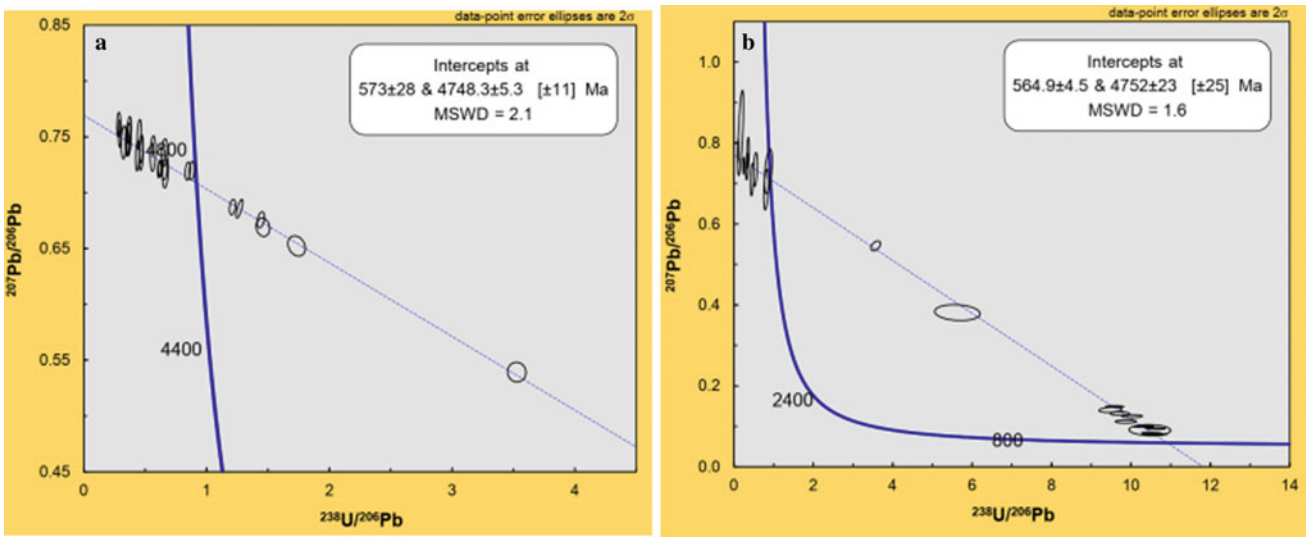

Fig. 2 Laser ablation ICP-MS results of U–Pb carbonate geochronology of samples collected from **a** the base and **b** the top of Kharus Formation in Jabal Akhdar, north Oman

speculative age range (ca. 575–550 Ma; Amthor et al., 2003; Brasier et al., 2000; Le Guerroué et al., 2006) for the Kharus Formation in Jabal Akhdar and the subsurface. However, although the obtained age range for Kharus Formation is comparable, the top age (ca. 564 ± 4.5 Ma) is somehow not a good match with the previously reported ages in the literature. Reported ages were based on a single zircon in Jabal Akhdar (ca. 544 ± 3.3 Ma; Brasier et al., 2000) and on a single zircon for each of the two selected intervals in the subsurface (ca. 542.0 ± 0.6 Ma and 542.6 ± 0.3 Ma; Amthor et al., 2003) from the overlying middle part of Fara Formation. Cozzi et al. (2004a, b) estimated the age of the top Kharus Formation to be about 550 Ma. However, this estimated age is about 15 Ma, different from the reported age in this study. This poor match could be related to the effect of diagenesis. It is reported through former studies that the upper part of the Kharus Formation is severely dolomitized (Cozzi et al., 2004a, b) or possibly the presence of a time gap between the Kharus and Fara formations. The presence of such a time gap between the two formations is not reported geologically yet. On the other hand, the constrained age of the base of Kharus (ca. 573 ± 28 Ma) is in good agreement with the interpolated age (ca. 575 Ma) by Le Guerroué et al. (2006). To constrain the Kharus Formation's age using direct in-situ carbonate age-dating technique, more samples are required from other exposed sections in Jabal Akhdar and Huqf region and from the subsurface, taking into consideration that samples with minimal diagenetic modifications are to be selected.

5 Conclusions

This study aimed to use the in-situ U–Pb carbonate age-dating technique to constrain the age of the Kharus Formation in Jabal Akhdar. This study revealed that:

1. The lower part of the Kharus Formation, close to the contact with the underlying Mu'aydin Formation, yielded an age of 573 ± 28 Ma, and
2. The uppermost part of the Kharus Formation, close to the contact with the overlaying Fara Formation, yielded an age of 564 ± 4.5 Ma.

Acknowledgements This study is supported by Sultan Qaboos University Internal Grant Fund # IG/SCI/ETHS/18/04.

References

Amthor, J. E., Grotzinger, J. P., Schroder, S., Bowring, S. A., Ramezani, J., Martin, M. W., & Matter, A. (2003). Extinction of cloudina and namacalathus at the precambrian-cambrian boundary in Oman. *Geology, 31*, 431–434.

Brasier, M., McCarron, G., Tucker, R., Leather, J., Allen, P., & Shields, G. (2000). New U-Pb zircon dates for the neoproterozoic ghubrah glaciation and for the top of the Huqf supergroup, Oman. *Geology, 28*, 175–178.

Burns, S. J., & Matter, A. (1993). Carbon isotopic record of the latest proterozoic from Oman. *Eclogae Geologicae Helvetiae, 86*(2), 595–607.

Burns, S. J., Haudenschild, U., & Matter, A. (1994). The strontium isotopic composition of carbonates from the late precambrian (~560–540 Ma) Huqf Group of Oman. *Chemical Geology (isotope Geoscience Section), 111*, 269–282.

Cozzi, A. (2000). Facies analysis of a precambrian carbonate gas reservoir: the buah formation, huqf supergroup, North-Central Oman. In *4th middle east geosciences conference, GEO 2000* (v. 5, no. 1, p. 73). GeoArabia, Abstract.

Cozzi, A., & Al-Siyabi, H. A. (2004). Sedimentology and play potential of the late neoproterozoic buah carbonates of Oman. *GeoArabia, 9*, 11–36.

Cozzi, A., Grotzinger, J. P., & Allen, P. A. (2004a). Evolution of a terminal neoproterozoic carbonate ramp system (buah formation, sultanate of Oman): Effects of basement paleotopography. *Geological Society of America Bulletin, 116*(11/12), 1367–1384.

Cozzi, A., Allen, P. A., & Grotzinger, J. P. (2004b). Understanding carbonate ramp dynamics using δ13C profiles: Examples from the neoproterozoic buah formation of Oman. *Terra Nova, 16*, 62–67.

Le Guerroué, E., Allen, P. A., Cozzi, A., Etienne, J. L., & Fanning, C. M. (2006). 50Myr recovery from the largest negative D13C excursion in the Ediacaran ocean. *Terra Nova, 18*, 147–153.

Tiley, G., Billing, I., Muggli, R., Al-Rawahi, S., Ghulam, J., Jones, A. M., Mattner, J., Strauss, J., Ozkaya, I., Koehler, V., Rawanchaikul, M., Sams, M., & Shanor, G. (2000). Makarem: tighter integration for tighter gas. In *4th middle east geosciences conference, GEO 2000* (v. 5, no. 1, p. 186–187). GeoArabia, Abstract.

Diagenetic Alterations of the Outcropped Lower Triassic Mahil Formation (KS-1 Khuff-Equivalent) in the Oman Mountains, North Oman

Mohamed A. K. El-Ghali, Mohamed S. H. Moustafa, Iftikhar Ahmed Abbasi, Hezam Al-Awah, Musaab Shakir Al Sarmi, Arshad Ali, Abdulrazak Al-Sayigh, Rana Al Rab'ani, Basma Al Kindi, Najiya Al Subhi, and Sankaran Rajendran

Abstract

The Lower Triassic Mahil Formation in North Oman is the outcrop time-equivalents to the hydrocarbon-bearing reservoir, Upper Khuff Formation (referred to as KS-1 cycle). The studied sections of the KS-1 cycle in the Saiq Plateau and Wadi Sahtan of North Oman are ca. 50 m thick. They are dominated by dolomitized grainstones, less commonly dolomitized mudstones, and brecciated dolostone. The detailed petrographic analyses revealed various diagenetic alterations affecting pore types, pore throats, and pore size distributions. The identified diagenetic alterations include (i) near-surface to shallow burial (eodiagenesis), fine- to medium-crystalline dolomite, mostly with non-planer texture, through prevalent dolomitization of carbonates (allochems and matrix) via modified marine pore waters (δ18OVPDB = −4.2 to + 0.2‰), (ii) shallow burial (eodiagenesis), mechanical compaction as indicated by closely packed carbonate allochems grains, (iii) chemical compaction and stylolite development at the onset of deep burial (mesodiagenesis), (iv) precipitation of deep burial (mesodiagenesis), various types of coarse-crystalline dolomite cement, e.g., saddle texture cement (typically for deep burial) and rarely calcite cement via evolved marine pore waters, (v) fracture-filled calcite and dolomite cement with saddle texture, which is typical for deep burial (mesodiagenesis) and/or with equant drusy texture, which is typical for meteoric water diagenesis indicating its formation during telodiagenesis, and (vi) carbonate allochems grains and cement dissolution during progressive burial (eo- to mesodiagenesis) and/or during telodiagenesis. This study revealed that the Lower Triassic Mahil Formation in North Oman is deeply buried. Consequently, the porosity is destructed by extensive cementation and compaction through near-surface and progressive burial. However, on the other hand, porosity is enhanced by fracturing and dissolution of allochems grains during progressive burial and subsequent uplifting.

Keywords

Carbonate diagenesis • Lower triassic • Lower Mahil formation • Oman

1 Introduction

The assessment of reservoir quality and heterogeneity in sandstone and carbonate reservoirs, which is essential for hydrocarbon exploration, appraisal, production, and enhanced hydrocarbon recovery, relies on better identification and quantification of diagenetic processes products (El-Ghali et al., 2006; El-Ghali et al., 2019; El-Khatri et al., 2015; Lucia & Ruppel, 1996). Dolomitization, cementation, compaction, and dissolution are common diagenetic processes in carbonate reservoirs and have profound effects on the final reservoir quality and heterogeneity (Ehrenberg et al., 2007; Lucia & Ruppel, 1996; Moradpour et al., 2008).

The Permian–Triassic Saiq and lower Mahil formations in North Oman are the outcrop time-equivalents to the hydrocarbon-bearing reservoir of the Khuff Formation (referred to as KS-7 to KS1 cycles). The Saiq and lower Mahil

M. A. K. El-Ghali (✉) · M. S. H. Moustafa · I. A. Abbasi · M. S. Al Sarmi · A. Al-Sayigh · R. Al Rab'ani · B. Al Kindi · N. Al Subhi
Department of Earth Sciences, College of Science, Sultan Qaboos University, Muscat, Oman
e-mail: melghali@squ.edu.om

M. A. K. El-Ghali · A. Ali
Earth Sciences Research Center, Sultan Qaboos University, Muscat, Oman
e-mail: melghali@squ.edu.om

H. Al-Awah
Environmental Science Center, Qatar University, Doha, Qatar

S. Rajendran
Department of Chemistry and Earth Sciences, Qatar University, Doha, Qatar

A. Çiner et al. (eds.), *Recent Research on Sedimentology, Stratigraphy, Paleontology, Tectonics, Geochemistry, Volcanology and Petroleum Geology*, Advances in Science, Technology & Innovation,
https://doi.org/10.1007/978-3-031-43222-4_18

formations (Khuff-equivalent) were deposited on a low-relief epeiric carbonate platform under arid climatic conditions during the opening of the Neotethys Ocean (Baud et al., 2001). Therefore, understanding the depositional environment, palaeoclimate, and tectonic history of Saiq and lower Mahil formations will help better understand the operating diagenetic processes and, thus, reservoir quality evolution.

This study aims to outline the type and distribution and decipher the origin of diagenetic alterations of the Lower Mahil Formation (KS-1 cycle) in North Oman (Fig. 1).

2 Methods

To achieve the main objective of this study, 170 rock samples were collected from two logged sections, namely the Saiq Plateau section and the Wadi Sahtan section located in Oman Mountains, northern Oman. The samples were thin-sectioned after impregnating with blue epoxy for porosity recognition, defining and describing the diagenetic alterations, and constructing their paragenetic sequence. The thin sections were half-stained with Alizarin Red-S better to

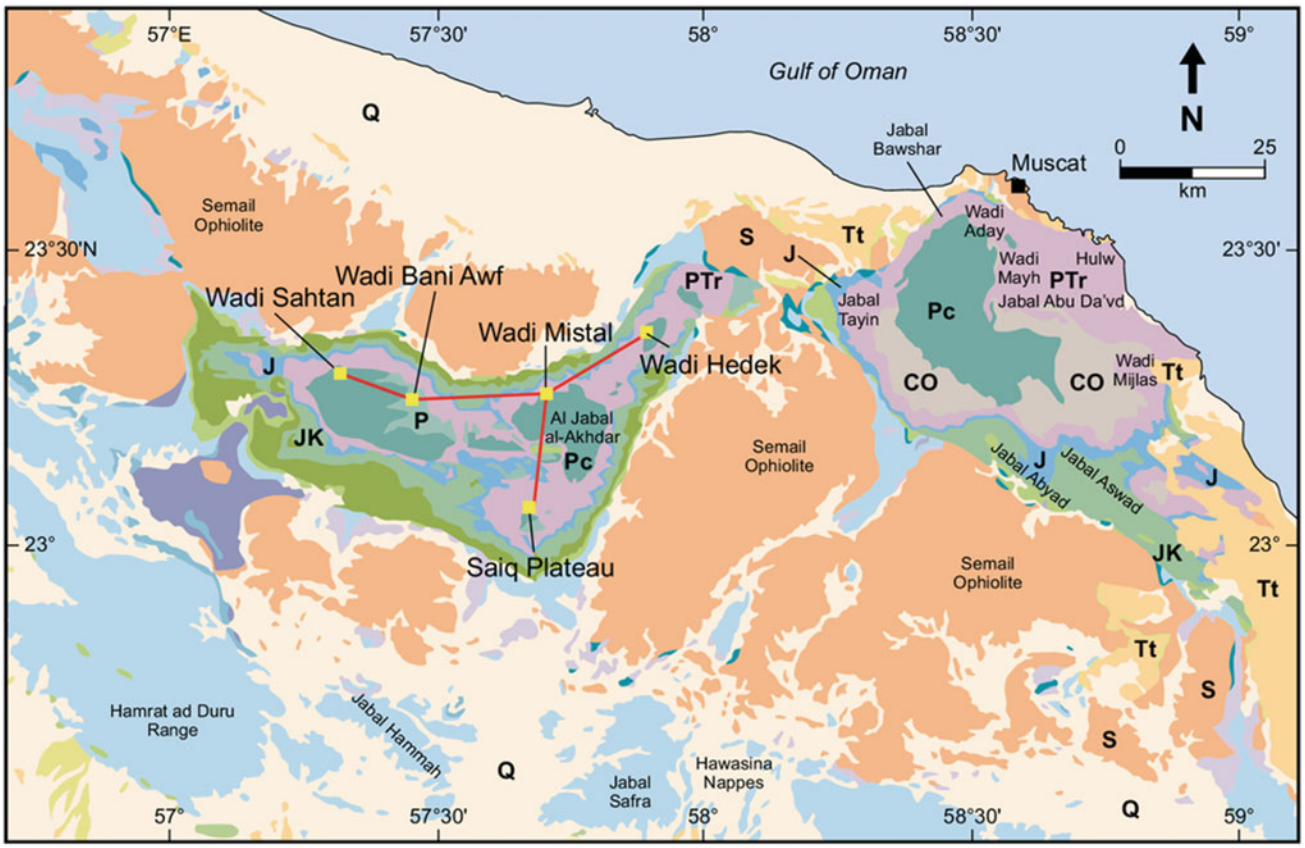

(Q) Quaternary
(Tt) Tertiary
(J) Sahtan Group (Jurassic)
(JK) Kahmah Group (end Jurassic – mid-Cretaceous)
Baid Formation (Late Permian – Jurassic)
(PTr) Akhdar Group (Late Permian – Triassic)
(CO) Haima Group (Cambrian – Ordovician)
(P) upper Huqf Group (Proterozoic – Cambrian)
(Pc) lower Huqf Group (Proterozoic)
Kawr Group (Triassic – Cretaceous)
Al Aridh Group (Triassic – Late Cretaceous)
Umar Group (Triassic – Cretaceous)
Hamrat Duru Group (Late Permian – Late Cretaceous)
Wasia Group (mid-Cretaceous)
Muti Formation (mid-Late Cretaceous)
Aruma Group (end Cretaceous)
(S) Semail Ophiolite (mid-Late Cretaceous)
Metamorphic sole (mid-Late Cretaceous)

Fig. 1 Geological map showing the distribution of Permian–Triassic rocks including Saiq and Mahil formations (Khuff-equivalent) and the logged sections' locations in Saiq Plateau and Wadi Sahtan areas (After Béchennec et al., 1993)

recognize calcite and dolomite and their ferroan types using an optical microscope. Stable O- and C-isotope analyses were performed on selected samples for various diagenetic carbonate cement. O- and C-isotope results were reported in the δ notation relative to the Vienna PDB (PeeDee Belemnite) and Standard Mean Ocean Water (SMOW) standards.

3 Results and Discussion

Several diagenetic processes have been recognized and described, including dolomitization, cementation, compaction, and dissolution (Fig. 2a–i). Dolomite is the most dominant diagenetic alteration in the studied Lower Mahil Formation. Dolomite is extensively replacing diagenetic minerals of the preexisting carbonate matrix and grains (i.e., ooids, peloids, etc.) (Fig. 2a,b). This dolomite is highly variable in size, occurring as fine- to medium-sized crystals (ca. 10–200 µm across). The fine-crystalline dolomites are characterized by non-planar to sub-planar texture. Medium-crystalline dolomites are characterized by non-planar texture. This dolomite is characterized by $\delta^{18}O_{VPDB}$ between −2.5 and + 0.2‰ and $\delta^{13}C_{VPDB}$ between + 1.4 and + 2.6‰, reflecting their marine and modified marine pore water origins, knowing that the original oxygen isotope signatures of the Lower Triassic ocean are ca. −3.9 to −0.6 and the carbon isotope signatures of the Lower Triassic ocean are ca. + 1 to + 4.2‰ (Korte et al., 2005; Veizer et al., 1999). Various types of coarse-crystalline dolomite with variable crystal sizes between 300 and 2000 µm across occur as overgrowths, intergranular pore-filling between grains, and vug pore-filling, e.g., blocky and saddle textures (Fig. 2c–e). These dolomites are characterized by $\delta^{18}O_{VPDB}$ between −4.2 and −2.8‰ and $\delta^{13}C_{VPDB}$ between −2.3 and −0.2‰, reflecting their modified marine pore waters during progressive burial, i.e., shallow to deep at higher temperatures. Calcite is a rare diagenetic alteration in the (Fig. 2g) studied samples. It occurs as a fine-

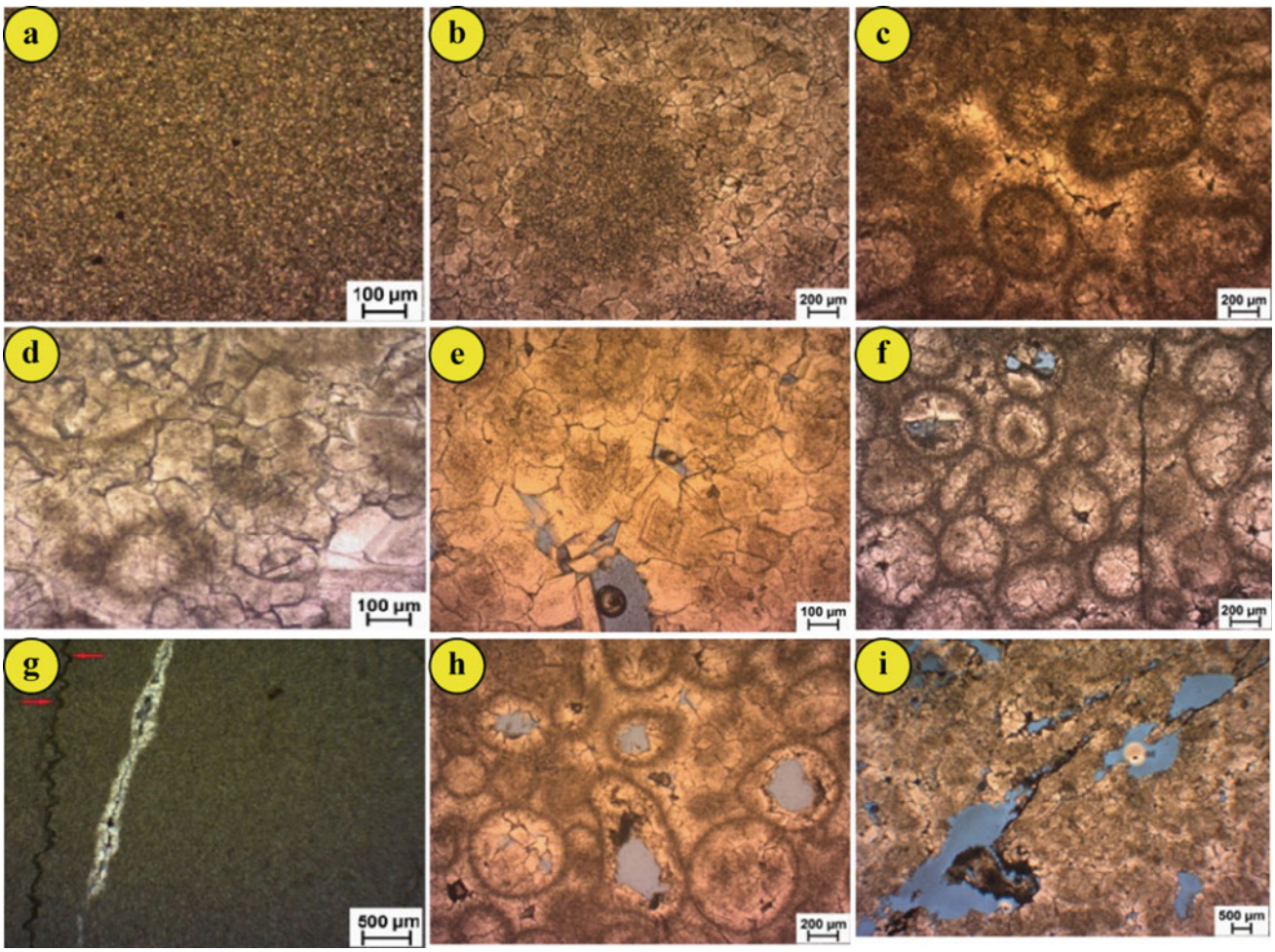

Fig. 2 Microphotographs showing **a** dolomitized matrix, **b** dolomitized grains, **c** intergranular pore filling dolomite, **d** grain-coating dolomite, **e** dolomite overgrowths, **f** coarse-crystalline dolomite replacing grains and mechanical compaction evidenced by grain-to-grain and concave–convex contact, **g** development of stylolite and calcite filling fractures, **h** intragranular porosity, and **i** vug porosity

to coarse-crystalline depicting, in some cases, sparry and equant drusy texture, filling vugs, fractures, and intergranular pores. The origin of these calcites is enigmatic due to the lack of isotope analysis. However, the vug filling calcite with an equant drusy texture may reflect their meteoric water origin, possibly during telodiagenesis. Compaction is a common diagenetic process, including both the mechanical and chemical types of compaction. Mechanical compaction is indicated by closely packed carbonate allochems grains (Fig. 2f), reflecting their development at shallow depths during progressive burial. Chemical compaction, as evidenced by the presence of concave–convex and straight contact along the interface of the ooid grains and the development of stylolite (Fig. 2f,g), reflects the onset of deep burial diagenesis. Dissolution is relatively rare in the studied samples, resulting in vugs and melodic, intragranular, and intercrystalline pores (Fig. 2h,i). Dissolution may occur during progressive burial and/or after uplift.

4 Conclusions

In conclusion, petrographic and stable oxygen and carbon isotopic analyses helped better understand the prevalent diagenetic processes and products of the Lower Mahil Formation. This study revealed that Lower Mahil Formation exposed to various diagenetic processes resulted in the formation of prevalent dolomitization of grains and matrix and filling vug, inter- and intragranular pores, and fractures with various textures. These various types of dolomites reflect their development under various diagenetic regimes, i.e., near-surface diagenesis, shallow to deep burial, and subsequent uplift. Mechanical and chemical compaction is relatively common, reflecting the development during shallow and deep burial. Pervasive dolomitization and compaction caused a severe reduction in porosity and permeability. However, dissolution, although rare, resulted in secondary porosity.

Acknowledgements This study is supported by the Research Council (TRC) Grant Fund # RC/RG-DVC/ESRC/18/01.

References

Baud, A., Bechennec, F., Cordey, F., Krystyn, L., Le Metour, J., Marcoux, J., Maury, R., & Richoz, S. (2001). Permo-Triassic deposits: From the platform to the basin and seamounts. Conference on the Geology of Oman, Field Guidebook, Muscat, Oman.

Béchennec, F., Le Métour, J., Platel, J.-P., & Roger, J. (1993). Explanatory notes to the geological map of the sultanate of Oman, scale 1:1,000,000. In *Directorate General of Minerals, Oman, Ministry of Petroleum and Minerals* (p. 93).

Ehrenberg, S. N., Nadeau, P. H., & Aqrawi, A. A. M. (2007). A comparison of Khuff and Arab reservoir potential throughout the Middle East. *AAPG Bulletin*, *91*(3), 275–286.

El-Ghali, M. A., Mansurbeg, H., Morad, S., Al-Aasm, I., & Ramseyer, K. (2006). Distribution of diagenetic alterations in glaciogenic sandstones within a depositional facies and sequence stratigraphic framework: Evidence from the Upper Ordovician of the Murzuq Basin, SW Libya, Marine and Petroleum geology (vol. 23, pp. 323–351).

El-Ghali, M. A. K., Al-Hinai, N., Mandhari, K., & Khan, J. (2019). Diagenesis and reservoir quality of glacio-lacustrine sandstones: An example from the upper carboniferous-lower permian Al Khlata formation in Wadi Daiqa, Northern Oman: In M. Boughdiri, B. Bádenas, P. Selden, E. Jaillard, P. Bengtson, & B. Granier (Eds.), *Paleobiodiversity and tectono-sedimentary records in the mediterranean tethys and related eastern areas. CAJG 2018: Advances in science, technology & innovation (IEREK interdisciplinary series for sustainable development)* (pp. 151–153). Springer, Cham.

El-Khatri, F., El-Ghali, M., Mansurbeg, H., Morad, S., Ogle, N., & Kalin, R. (2015). Diagenetic alterations and reservoir quality evolution of lower cretaceous fluvial sandstones: Nubian Formation, Sirt Basin, North-Central Libya. *Journal of Petroleum Geology*, *38* (2), 217–239.

Korte, C., Kozur, H.W., & Veizer, J. (2005). $\delta^{13}C$ and $\delta^{18}O$ values of Triassic brachiopods and carbonate rocks as proxies for coeval seawater and palaeotemperature. *Paleogeography Paleoclimatolgy Paleoecolgy*, *226*, 287–306.

Lucia, F. J., & Ruppel, S. C. (1996). Characterization of diagenetically altered carbonate reservoirs, South Cowden Grayburg Reservoir, West Texas. In *SPE Annual Technical Conference and Exhibition, 6–9 October 1996, Denver, Colorado*.

Moradpour, M., Zamani, Z., & Moallemi, S. A. (2008). Controls on reservoir quality in the lower Triassic Kangan Formation, Southern Arabian Gulf. *Journal of Petroleum Geology*, *31*(4), 367–386.

Veizer, J., Ala, D., Azmy, K., Bruckschen, P., Buhl, D., Bruhn, F., Carden, G. A. F., Diener, A., Ebneth, S., Goddéris, Y., Jasper, T., Korte, C., Pawellek, F., Podlaha, O. G., & Strauss, H. (1999). $^{87}Sr/^{86}Sr$, ^{13}C and ^{18}O evolution of phanerozoic seawater. *Chemical Geology, 161*(59–88), 1999.

Geochronologic Constraints on the Rubidium Deposit of Guiren Peak, Guangdong, China

Su Zhou, Ruizhao Qiu, Bingjing Xie, Lei Qiu, Cui Liu, and Dan Lin

Abstract

A rubidium deposit has been recently discovered in Jiaoling county, Guangdong province, China. MC-LA-ICP MS zircon U–Pb yields ages 141.7–133.7 Ma for barren rocks, while two ore-bearing granites are 128.1 ± 2.6 Ma and 128.6 ± 1.0 Ma, respectively. Petrographic, mineralogical, and geochemical observations suggest that granites may be classified as aluminous A-type. It also indicates that the rubidium ore deposit was formed during the late magmatism of the district. The tectonic environment of the deposit formation was extensional, related to slab rollback in the oblique subduction of the paleo-Pacific plate under Eurasia.

Keywords

Geochronology • A-type granite • Rubidium deposit

1 Introduction

The rubidium element is generally associated with alkali feldspar granite containing lepidolite, granite pegmatite, and salt deposits. An Rb deposit has been recently discovered in the Guiren peak, Jiaoling County, Guangdong province, China, and is predicted to produce about 1.7 Mton of rubidium (Noferrous Metals Geological Bureau of Guangdong Province 935 Battalion, 2015). The orebodies were hosted in metasedimentary and granitic rock, with the cutoff grades mainly occurring in the upper part of Louziba formation of Upper Sinian (Z_2lz). A small portion appeared in the contact intersects between the middle part of the formation and the hidden granite rock. The preliminary geological survey showed that the strike of the ore body is roughly consistent with the relief form of the intrusive rock (Zhang, 2016). Thus, studies of it are important to understand when and how this unique ore deposit was formed.

2 Geological Background

The Meizhou area is situated in the southern margin of the Cathaysia block on the outer margin of the E-W Nanling metallogenic belt and the N-E Wuyi metallogenic belt, belonging to the regionally Yongmei depression within northeastern-central Guangdong, south China. Its northwest and southeast sides are adjacent to Jiulianshan uplift and the eastern Guangdong uplift. The geological background of the study area is shown in Fig. 1. Magmatic rocks there were assigned to the third Yanshanian epoch by previous geological surveys (corresponds to the late Jurassic), while hypabyssal dikes were granite porphyry, quartz porphyry, aplite, and diorite-porphyrite, compositionally variated, multistage, and successive to intrusions (Zhang, 2016). However, there is a lack of reliable isotopic data on these intrusive acids. The Rb-bearing minerals in the metamorphic rocks include alkaline feldspar and biotite, which contain an average content of 0.09% and 0.19% Rb_2O, respectively. In contrast, the ones in granite are alkaline feldspar, with an average Rb_2O content of 0.16%.

One granite sample was collected from a drilling core (ZK808 T1-5, about 400 m in depth), and other granites were collected from the outcrops of Huangyoubi (HY-12) and Shangcunzi (HY-17) intrusion. Moreover, sample HY-14 was collected in the NW trending granite porphyry dike (Fig. 1).

S. Zhou (✉)
State Key Laboratory of Geological Processes and Mineral Resources, China University of Geosciences, Beijing, 100083, China
e-mail: zhousu@cugb.edu.cn

S. Zhou · B. Xie · L. Qiu · C. Liu · D. Lin
China University of Geosciences, Beijing, 100083, China

R. Qiu
Development and Research Center, China Geological Survey, Beijing, 100037, China

A. Çiner et al. (eds.), *Recent Research on Sedimentology, Stratigraphy, Paleontology, Tectonics, Geochemistry, Volcanology and Petroleum Geology*, Advances in Science, Technology & Innovation,
https://doi.org/10.1007/978-3-031-43222-4_19

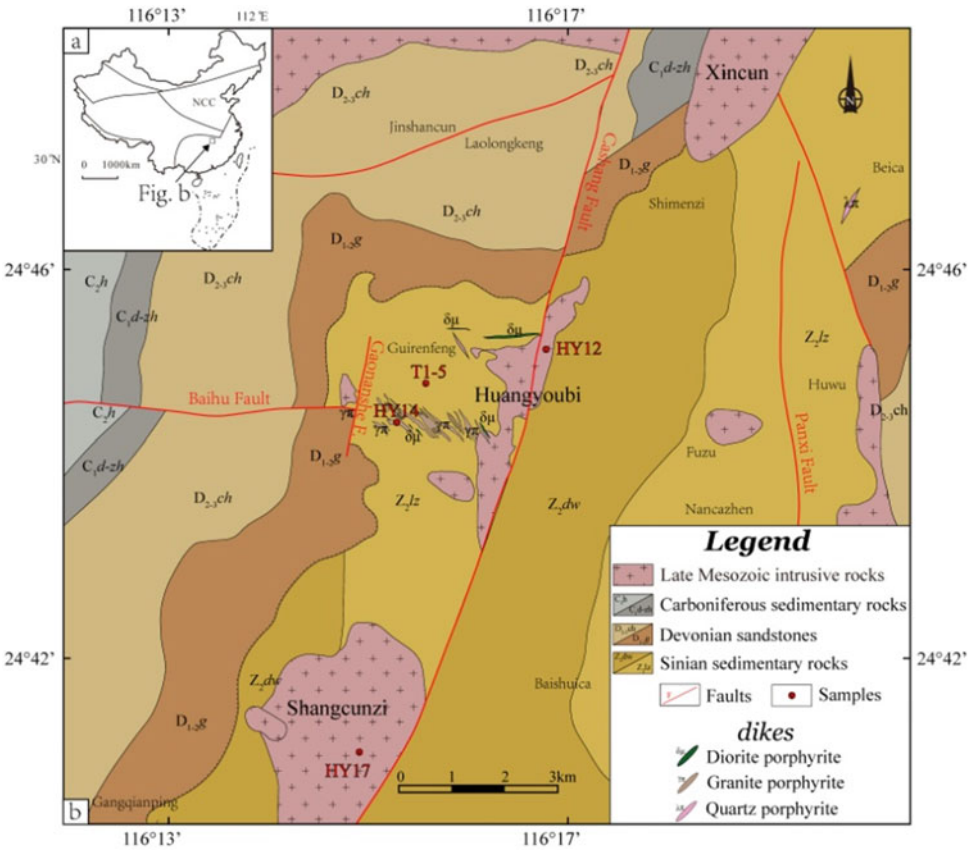

Fig. 1 Simplified geological map of research area (modified after (Noferrous Metals Geological Bureau of Guangdong Province 935 Battalion, 2015)). SCB = the South China Block; NCC = the North China Craton

3 Results

3.1 Petrography

Granites (T1-5, HY-12, and HY-17) are medium- to coarse-grained with hypidiomorphic equigranular textures and consist of quartz, alkaline feldspar, plagioclase, and biotite, along with accessory minerals such as magnetite, pyrite, topaz, and fluorite (Fig. 2). The granite porphyry (HY-14) is pale red and shows porphyritic texture, with mineral assemblage similar to the plutons. No hornblende has been identified in them. The analyses of the mineral composition by Electron probe show that all plagioclase from the granite and granite porphyry are more enriched in sodium with albite composition, indicating late-stage, highly evolved magmas; the biotites are siderophyllite (Fe-rich annite). Some sub-idiomorphic flaky muscovites occur between feldspar crystals or interact with biotite.

3.2 Zircon U–Pb Geochronology and Whole-Rock Nd Isotopes

One hundred and twenty-six zircon U–Pb ages are obtained by MC-LA-ICP-MS, which yield four groups of weighted mean $^{206}Pb/^{238}U$ ages on concordia diagrams. The data of dating and whole-rock Nd isotopes of samples are as Table 1.

4 Discussion

4.1 Ages of the Granitoid Crystallization and Rb Mineralization

U–Pb dating of granites and porphyry from Jiaoling, Guangdong, reveals that granitic intrusions were emplaced in a major phase from 128.1 to 141.7 Ma (Table 1). The borehole where the ZK808T1-5 sample is located is the

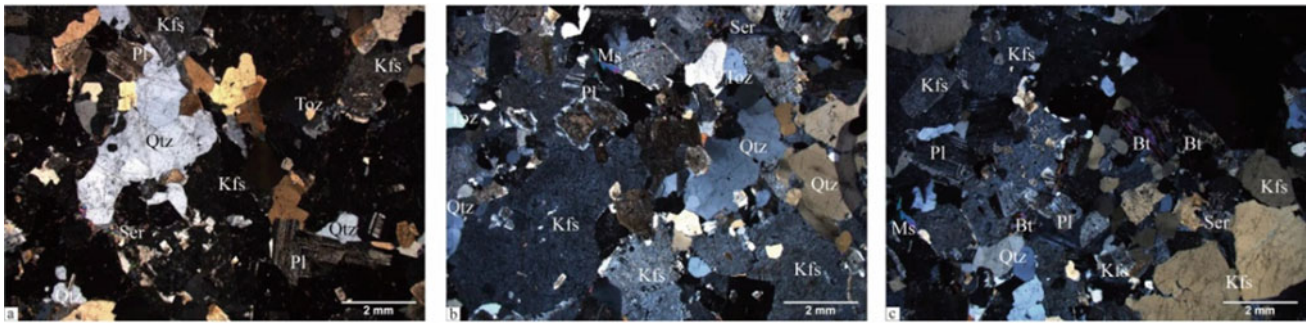

Fig. 2 Photomicrographs of HY-012 **a** and ZK808T1-5 **b** and **c** under cross-polarized light. Abbreviations: Bt-biotite; Kfs- alkaline-feldspar; Pl-plagioclase; Ms-muscovite; Qz-quartz. Ser- sericite; Toz- topaz

Table 1 Representative data of granitic samples from Jiaoling, China

Sample	Age (Ma)	SiO_2 wt.%	Rb (ppm)	*F* (ppm)	T_{Zr} (°C)	ε_{Nd} (t)
HY-12	128.1 ± 2.6	75.10	412	3420	754	−6.3
T1-5	128.6 ± 1.0	75.30	410	3220	764	−6.4
HY-17	133.7 ± 1.2	75.96	384	363	768	−6.5
HY-14	141.7 ± 1.5	77.69	296	580	802	−8.0

The initial Nd isotopic ratios rocks were calculated based on the crystallization age of 130 Ma

hidden ore-forming body with an average content of Rb_2O of higher than 0.06%. Thus, the isotopic dating of the sample T1-5 indicates the metallogenic age of 128.6 ± 1.0 Ma. On the other hand, the isotopic age of Huangyoubi pluton, which is also enriched in rubidium, is 128.1 ± 2.6 Ma; that identical age strongly suggests that ore-formation might have occurred in the late stage of magma activity in this period.

4.2 Petrogenetic Type of Granitoid: I-, S-, or A-type?

As the granitoid plutons in this study are highly fractionated rocks with elevated SiO_2 concentration (up to 75.96 wt %) and near-horizontal ``Seagull'' REE patterns (tetrad effect), it is hard to classify them as I-, S- or A-type. The rocks are weakly peraluminous (molar ratios $Al_2O_3/(CaO + Na_2O + K_2O)$ of 1.03–1.07) and show low P_2O_5 contents (about 0.01 wt %), which are different from the highly felsic, strongly peraluminous S-type, but similar to the I-type granites in the Lachlan Fold Belt. However, our samples contain neither amphibole nor pyroxene, independent from typical I-type granite. Moreover, it is noteworthy that these granites have higher HFSE contents (Zr + Nb + Ce + Y > 343 ppm) and FeO^T/MgO (total iron as FeO), contain topaz, siderophyllite and show Nb–Ta positive anomaly, similarly to typical A-type. In highly fractionated magma, zircon crystallization separation may decline the Zr content and zirconium saturation temperature of rocks (Table 1). Therefore, we prefer that our rocks belong to A_2-subtype suites (Liu et al., 2003).

4.3 Rb-Metallogenic Model

The Jiaoling granitoid was enriched in Rb, with the highest rubidium and fluorine contents in the later stages of the magmatic period (Table 1). We speculate that both magma and strata supplied the ore-forming material (Rb). The slab rollback in the process of the oblique subduction of the paleo-Pacific plate under Eurasia provided large amounts of volatile (fluorine) to the source of the granite. It lowered its solidus temperature and viscosity (Liu et al., 2003). It also facilitated transforming plagioclase to albite, which is more compatible with rubidium in the form of isomorphism, subsequently generating metallogenic granite. The ascending rubidium-rich magma caused the metamorphism of the overlying sandstone and shale, forming iron and magnesia biotite, which benefited rubidium enrichment and mineralization.

5 Conclusions

A study on petrography and geochemistry for these granitoid suggests that they may be classified as aluminous A-type granites and that the tectonic environment of the formation

of granites was extensional. Zircon MC-LA-ICPMS U–Pb dating yields the emplacement ages of 141.7–128.1 Ma, indicative of an Early Cretaceous age rather than a Late Jurassic. The Rb mineralization occurred about 128 Ma, about 13 Ma later than the emplacement ages for the Shangcunzi pluton (barren rock).

Acknowledgements This study was financially supported by the project of geological survey (DD20190370) and ISTCP (2011DFA22460). In addition, we are grateful to the reviewers for their modifications and valuable comments.

References

Liu, C.S. et al. (2003). subdivision, disctrimination criteria and genesis for a type rock suites. *Geological Journal of China Universities, 4*, 573–591 (Chinese with English abstract).

Noferrous Metals Geological Bureau of Guangdong Province 935 Battalion. (2015). Periodic geological report of Gurenfeng molybdenum deposit, Wenfu Town, Jiaoling County, Guangdong Province (Chinese ,Unpublished).

Zhang, M. (2016). Analysis of geological characteristics of elegant peak rubidium deposit in Jiaoling of Guangdong province. *World Nonferrous Metals, 1*, 40–41 (Chinese with English abstract).

Sandstone Petrography and Geochemistry of the Pre-albian Awi Formation, Calabar Flank, Southeast Nigeria

Emmanuel Etim Okon, Nse Udo Essien, Oluwaseye Peter Oyetade, Ebenezer Agayina Kudamnya, Ama Otele, and Betty Ikporukpo

Abstract

A combined petrographic and geochemical study of the pre-Albian Awi Formation, Calabar Flank, was carried out to characterize their provenance history and tectonic setting. Ten (10) samples were collected and subjected to petrographic analysis and whole rock geochemistry (major oxides, trace, and rare earth elements). The petrographic analysis showed that the sandstones are poor to moderately sorted, with evidence of angular to sub-angular grains. The sandstones are arkosic–sub-arkosic arenites with quartz ranging from 57 to 66% and feldspar generally greater than 25% (26–35). Predominantly polycrystalline quartz with sutured contacts exhibiting undulose extinction constitutes most grains. The geochemical analysis reveals SiO_2 (53.56–80.03 wt. %) as the predominant major oxide in sandstone. A close variation was observed between the major oxides of this study and the upper continental crust composition (UCC). There is a positive correlation between Al_2O_3 and K_2O, and Na_2O suggesting abundant clay mineral contribution to major oxides during the weathering process. Ratios of Fe_2O_3/K_2O, SiO_2/Al_2O_3, Na_2O/K_2O, and $/Al_2O_3$ reveal the sandstone is non-calcareous and chemically immature. Enriched high field strength elements and bivariate plots of TiO_2 against $Fe_2O_3 + MgO$ reflect contributions from more felsic provenance for the sediments, with only a few contributions from mafic sources in tectonic settings typical of a passive margin. This suggests deposition within a passive/rifted tectonic province (continental block provenance). This study re-affirms the suitability of an integrated approach using petrography and geochemical composition in evaluating provenance as well as the tectonic setting of the sandstones.

Keywords

Awi formation • Polycrystalline quartz • Provenance • Undulose extinction • Whole rock geochemistry

1 Introduction

The Awi Formation (Neocomian–Aptian) is exposed as the oldest formation unconformably overlying the crystalline basement complex in the Calabar Flank, far southeastern part of the Southern Benue Trough. It has been the focus of many researchers since the late 1970s when Adeleye and Fayose (1978) defined it as a separate lithological unit from the Odukpani Formation of Reyment (1965).

Studies involving age, stratigraphy, sedimentological characteristics, sedimentary geochemistry, and its applications to provenance determination (Boboye & Okon, 2014; Boboye et al., 2021; Nton, 1999; Okon, 2015; Okon et al., 2017) using exposed outcrop sections are well documented in the literature. In their study, Nton (1999) and Okon (2015) emphasized the sandstones' arkosic nature and the fluvio-deltaic settings within which the sediments were deposited. Therefore, based on this, it is true that information about the compositions and post-depositional modifications (especially of the provenance materials) and tectonic settings are recorded in the sediments (Fedo et al., 1995; Okon, 2015; Okon et al., 2017). Framework components of clastic rocks are suitable for classification and lend clues into the

E. E. Okon (✉) · O. P. Oyetade · E. A. Kudamnya
Geology Department, University of Calabar, Calabar, Cross River State, Nigeria
e-mail: etyboy911@yahoo.com

N. U. Essien
Akwa Ibom State University, Mkpat Enin, Akwa Ibom State, Nigeria

A. Otele
Federal Polytechnic, Ekowe, Bayelsa State, Nigeria

B. Ikporukpo
Federal University of Petroleum Resources, Effurun, Delta State, Nigeria

A. Çiner et al. (eds.), *Recent Research on Sedimentology, Stratigraphy, Paleontology, Tectonics, Geochemistry, Volcanology and Petroleum Geology*, Advances in Science, Technology & Innovation,
https://doi.org/10.1007/978-3-031-43222-4_20

paleoclimatic settings, provenance, and paleotectonic setting during deposition (Dickinson et al., 1983; Johnsson, 1993). As a complement to the modal compositions, the geochemical signatures of parent source materials are pre-recorded in the sediments, with only slight modifications depending on the intensity of diagenesis. Some elements are known to be less fractionated and, therefore, insoluble in transporting fluids during sedimentary processes making the analyses of major, trace, and rare earth elements a suitable complement to modal analysis during provenance and tectonic setting determinations (Fedo et al., 1997; Wronkiewicz & Condie, 1989; Ibe & Okon, 2021). This research aims to integrate the data derived from petrological modal analysis and sediment geochemistry to assess and characterize the provenance and tectonic setting of the pre-Albian Awi Formation.

2 Methods

Petrographic analysis and whole rock geochemical analysis were carried out on ten (10) sandstone samples using the LOGITECH PM6 autoprecision lapping/polishing machine and inductively coupled plasma mass spectrometer (ICP-MS), respectively. The analyses facilitated thin section description (XP 213C petrographic microscope) of mineralogy using the modified Glagolov Chayes methods to evaluate the framework elements and void fillers (Chayes, 1949) and characterization of multi-elements in the sediments. The choice of ICP-MS was due to its high accuracy and low detection limit, and details of the methodological approach are outlined in Ibe & Okon (2021).

3 Results

Petrographic analysis showed that the sandstones are poorly to moderately sorted, with evidence of angular to sub-angular grains (Fig. 1a–b). Predominantly polycrystalline quartz with sutured contacts exhibiting undulose extinction constitutes most grains. The geochemical analysis of Awi Sandstone reveals SiO_2 (53.56–80.03 wt. %) as the predominant oxide in sandstone. A close variation was observed between the major oxides of this study and upper continental crust composition (UCC). Observed positive correlation between Al_2O_3 and K_2O, and Na_2O suggests abundant clay mineral contribution to major oxides during the weathering process. Depletion of CaO indicates that the sandstone sediments are not calcareous (Table 1).

4 Discussion

The sandstones are arkosic–sub-arkosic arenites (Fig. 2a), with quartz ranging from 56 to 80%; and feldspar generally greater than 25%. The petrographic analysis suggests that the sediments are immature, poorly sorted arkoses derived from a nearby continental (uplifted fault) block setting typical of the Oban Massif (Fig. 2b). The absence of evaporites and volcanic sediments precludes any marine and active arc setting. The abundance of polycrystalline quartz exhibiting undulose extinction admixed with monocrystalline quartz and altered feldspar grains points to mix metamorphic and igneous provenance within a humid setting as the most probable source for sediments (Boboye et al., 2021; Okon, 2015). The geochemistry of the sediments results from the

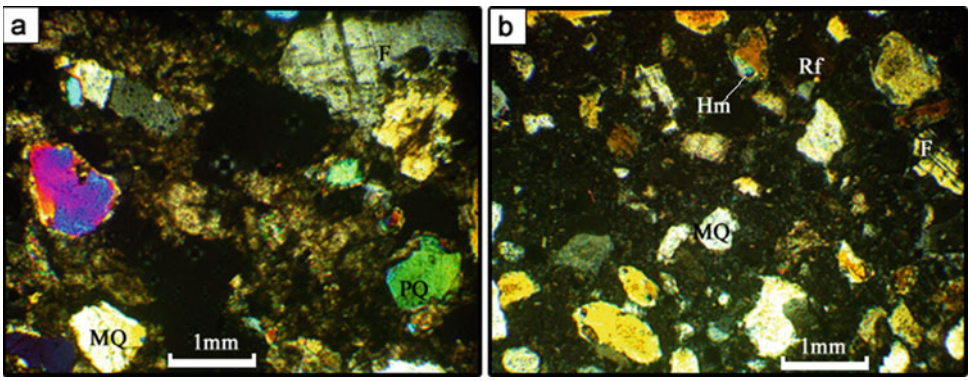

Fig. 1 Photomicrographs of selected pre-Albian Awi sandstones, illustrating: **a** poorly sorted, sub-rounded grains with point and sutured contacts; **b** matrix-supported sandstone with heavy mineral included in quartz (*MQ-Monocrystalline quartz; PQ-Polycrystalline quartz; F-Feldspar; Hm-Heavy mineral; Rf-Rock fragment*)

Table 1 Pearson correlation matrix for the major oxides

	SiO_2	TiO_2	Al_2O_3	Fe_2O_3	MgO	CaO	Na_2O	K_2O
SiO_2	1							
TiO_2	0.359	1						
Al_2O_3	−0.898	−0.271	1					
Fe_2O_3	−0.071	−0.444	−0.302	1				
MgO	0.389	0.408	−0.583	0.136	1			
CaO	0.017	−0.612	−0.178	0.442	0	1		
Na_2O	0.539	0.304	−0.724	0.304	0.745	0	1	
K_2O	−0.75	0	0.52	0.238	0.7	−0.349	−0.052	1

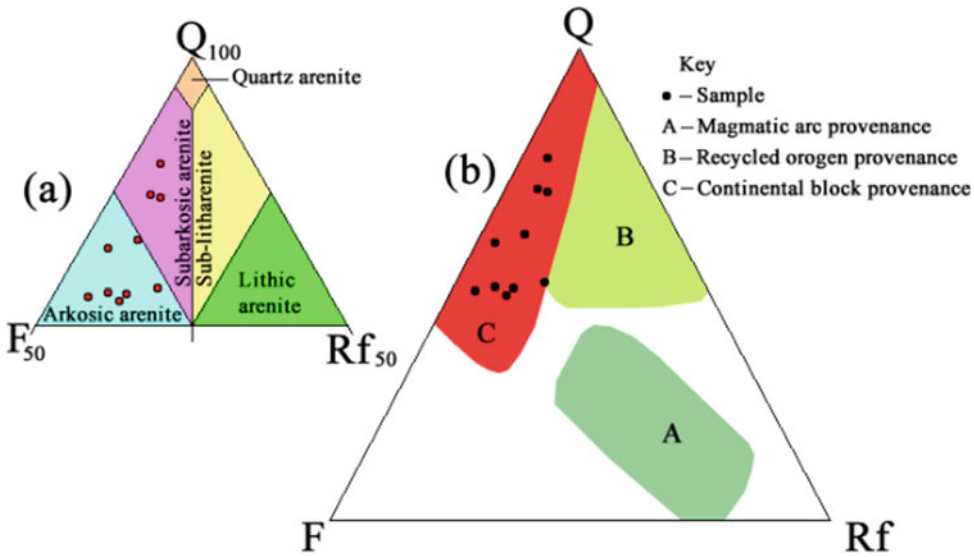

Fig. 2 **a** Sandstone classification; **b** Provenance of Awi Sandstone

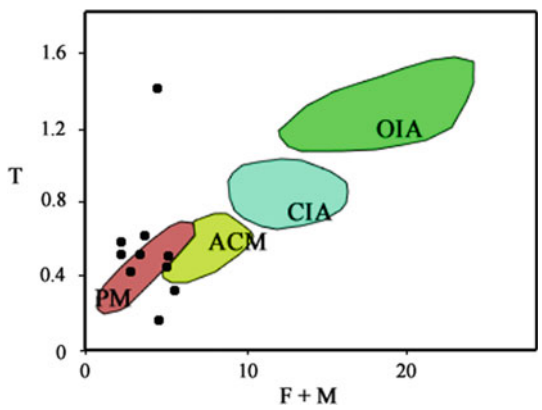

Fig. 3 Tectonic discrimination diagrams for Awi sandstone using T (TiO_2) versus F + M (Fe_2O_3 + MgO) (fields after Bhatia, 1983) [PM-passive margin; ACM-active continental margin; CIA-continental island arc; OIA-ocean island arc]

composition of the parent materials, prevalent climatic settings during transportation and deposition, and tectonic history (McLennan, 1989). During sedimentary processes, it has been observed that certain elements (e.g., Zr, Ti, Al) remain immobile and are not affected by weathering processes (Okon, 2015).

Enrichment in HFSE typifies felsic source rocks. Tectonic imprints derived from the sediment studied were from transitional and cratonic settings. Furthermore, the geochemical plot of TiO_2 against Fe_2O_3 + MgO was used to constrain the tectonic setting and suggest passive margin settings for the sandstones (Fig. 3).

5 Conclusions

The sandstones in the study area contain abundant quartz grains of monocrystalline and polycrystalline affinities, with a few metamorphic rock fragments and heavy minerals. They are arkosic and poorly sorted with sub-angular to sub-rounded grain morphologies. Integrating geochemistry with mineralogy further enhanced the characterization of the sediments hinging on the nature of the source rock's provenance as well as the tectonic setting of the sandstones. Data from immobile traces and REEs indicated the parent materials (source rocks). They suggested felsic sources dominated the provenance area of the sandstone with deposition in the continental (uplifted and faulted) block cratonic settings typical of a passive margin. This study supports the significance of an integrative approach using petrography and geochemistry to characterize provenance and tectonic settings, especially in clastic rocks.

References

Adeleye, D. R., & Fayose, E. A. (1978). Stratigraphy of the type section of Awi formation, Odukpani area Southeastern Nigeria. *Journal of Mining and Geology, 15*, 33–37.

Bhatia, M. R. (1983). Plate tectonics and geochemical composition of sandstones. *Journal of Geology, 91*, 611–627.

Boboye, O. A., & Okon, E. E. (2014). Sedimentological and geochemical characterization of the Cretaceous strata of Calabar Flank, Southeastern Nigeria. *Journal of African Earth Sciences, 99*, 427–441.

Boboye, O. A., Jaiyeoba, O. K., & Okon, E. E. (2021). Sedimentological characteristics and mineralogical studies of some Cretaceous sandstones in Nigeria: Implications for depositional environment and provenance. *Journal of Sedimentary Environments, 6*, 531–550.

Chayes, F. (1949). A simple point counter for thin section analysis. *American Mineralogist, 34*, 1–11.

Dickinson, W. R., Beard, L. S., Brakenridge, G. R., Erjavec, J. L., Ferguson, R. C., Inman, K. F., Knepp, R. A., Lindberg, F. A., & Ryberg, P. T. (1983). Provenance of North American Phanerozoic sandstones in relation to tectonic setting. *Geological Society of America Bulletin, 94*(2), 222–235.

Fedo, C. M., Nesbitt, H. W., & Young, G. M. (1995). Unravelling the effects of potassium metasomatism in sedimentary rocks and paleosols with implication for paleoweathering conditions and provenance. *Geology, 23*, 921–924.

Fedo, C. M., Young, G. M., & Nesbitt, H. W. (1997). Paleoclimatic control on the composition of the Paleoproterozoic Serpent formation, Huronian Supergroup, Canada: A greenhouse to ice-house transition. *Precambrian Research, 86*, 210–223.

Floyd, P. A., Winchester, J. A., & Park, R. G.: Geochemistry and tectonic setting of Lewisian clastic metasediments from the early Proterozoic Loch Maree Group of Gairloch, N.W. Scotland. *Precambrian Research, 45*(1–3), 203–214.

Fralick, P. W., & Kronberg, B. I. (1997). Geochemical discrimination of clastic sedimentary rock source. *Sedimentary Geology, 113*, 111–124.

Ibe, C. U., & Okon, E. E. (2021). Provenance and tectonic settings of the Eze-Aku sandstone (Turonian) in Awajir and adjoining areas, Southern Benue trough, Nigeria: Evidence from petrography and geochemistry. *Journal of Sedimentary Environments, 6*, 237–254.

Johnsson, M. J.: The system controlling the composition of clastic sediments. (1993). In: Johnsson, M. J., & Basu, A., (Eds) *Processes controlling the composition of clastic sediments*. Geological Society of America, Special Papers (Vol. 284, pp 1–19).

McLennan, S. M.: Rare earth elements in sedimentary rocks: Influence of provenance and sedimentary processes. (1989). In Lipin, B. R., & McKay, G. A., (Eds.), *Geochemistry and mineralogy of rare earth elements* (Vol. 21, pp 169–200).

Nton, M. E. (1999). Sedimentology and depositional environment of Awi formation, Calabar Flank, Southeastern Nigeria. *Journal of Mining and Geology, 33*(1), 23–36.

Okon, E. E. (2015). Sedimentologic characteristics and provenance studies of Awi formation, Calabar Flank, SE Nigeria. *Journal of Mining and Geology, 51*(2), 121–138.

Okon, E. E., Essien, N. U., & Adeyemi, G. O. (2017). Geochemistry of sandstones of Awi formation, Southeastern Nigeria: Implications for weathering, provenance and tectonic settings. *International Journal of Science and Technology, 6*(4), 742–755.

Reyment, R. A. (1965). *Aspects of the geology of Nigeria*. Ibadan University Press.

Wronkiewicz, D. J., & Condie, K. C.: Geochemistry and provenance of sediments from the Pongola Supergroup, South Africa: Evidence for a 3.0-Ga-old continental craton. *Geochimica et Cosmochimica Acta, 53*, 1537–1549

Trace Element Geochemical Analysis and Depositional Environment of Lokoja-Basange Sandstone at Imiegba Area, Southwestern Nigeria

S. O. Obaje and B. Alli

Abstract

This study uses trace element geochemistry to establish the paleodepositional environment of sediments from the study area. Although granulometric and petrological assessments have been extensively carried out and published by several researchers in the study area, the application of trace element geochemistry for paleodepositional environmental interpretation of the sediments is grossly absent. Eight sandstone surface samples were collected from the Campanian Lokoja-Basange Formation in the western part (Benin Flank) of the Anambra Basin situated at Imiegba, southwestern Nigeria, and investigated using standard procedures of trace element geochemical analysis to infer their depositional environment. The trace element geochemical analysis of the field samples was done using the X-ray fluorescence technique. The Lokoja-Basange Formation is conformably overlain by the Mamu Formation and underlain by the Igarra Schist Belt Basement Complex. The sandstones from the study area originated from highly altered igneous/metamorphic rocks, and they are compositionally immature and deposited in a tectonically stable cratonic environment. Lokoja-Basange sediments are composed of fine- to coarse-grained, highly ferruginous sandstones: litharenite (50%), greywacke (25%), and arkose (25%). Using the average values in parts per million, W is < 0.01 ppm; Cr, Cu, Pb, Ni, V, and Zn have an average concentration of < 0.01 to 0.04 ppm; Sb, Sn, Mo, and Zr have an average value > 0.04 to 0.4 ppm, while Co has an average concentration of 2.12 ppm. The computed trace element ratios for the Lokoja-Basange sediments are Cu/Zn, Ni/Co, V/Cr, V/Ni, V/(Ni + V), and V/(V + Cr). Cu/Zn ranged between 0.33 and 1.00, with an average of 0.52; Ni/Co varied between 0.00 and 0.01, with an average of 0.01; V/Cr ranged from 0.00 to 0.33, with an average of 0.21; V/Ni ranged between 0.00 and 1.00 with an average of 0.69; V/(Ni + V) ranged between 0.00 and 0.50 with an average of 0.38 and V/(V + Cr) ranged between 0.00 and 0.25 with an average of 0.17. Using six trace element ratios such as Cu/Zn, Ni/Co, V/Cr, V/Ni, V/(Ni + V), and V/(V + Cr) suggests an oxic fluvial paleoenvironment for the sandstones from the study area.

Keywords

Sandstone • Geochemistry • Depositional environment • Anambra basin • Lokoja-Basange formation

1 Introduction

The geochemistry of sedimentary rocks in a basin reflects its tectonic setting and insight into the environment of their deposition (McLennan et al., 1993). The study area is the Campanian Lokoja-Basange Formation in the western part (Benin Flank) of the Anambra Basin situated at Imiegba, southwestern Nigeria, on latitude 07°12′49″N and longitude 06°27′33″E.

This study uses trace element geochemistry to establish the paleodepositional environment of sediments from the study area. Although granulometric and petrological assessments have been extensively carried out and published by several researchers in the study area, the application of trace element geochemistry for paleodepositional environmental interpretation of the sediments is grossly absent.

2 Regional Geological Setting

The Anambra Basin had received geological attention since 1903, when coal exploration started in the basin. The basin is adjacent to the lower Benue Trough, which is intracratonic.

S. O. Obaje (✉) · B. Alli
Department of Earth Sciences, Faculty of Science,
Adekunle Ajasin University, P.M.B. 001 Akungba-Akoko,
Ondo State, Nigeria
e-mail: solomon.obaje@aaua.edu.ng

A. Çiner et al. (eds.), *Recent Research on Sedimentology, Stratigraphy, Paleontology, Tectonics, Geochemistry, Volcanology and Petroleum Geology*, Advances in Science, Technology & Innovation,
https://doi.org/10.1007/978-3-031-43222-4_21

Consequently, there are numerous research publications on the stratigraphy, age, paleoenvironment, paleogeography, sedimentary tectonic, granulometric assessments, the origin of the Anambra Basin, and component formations (Agagu et al., 1985; Arua, 1988; Ladipo, 1988; Lucas & Ebahili, 2017; Obaje, 2019).

Anambra Basin is stratigraphically made up of the Enugu and the Nkporo Shales representing the brackish marsh and fossiliferous pro-delta facies of the Late Campanian-Early Maastrichtian depositional cycle. The coal-bearing Lower Maastrichtian Mamu Formation and the Upper Maastrichtian Ajali Sandstone were deposited during the overall regression of the Nkporo Shale cycle. Mamu Formation has continental and marginal marine influence, while Ajali Formation is entirely continental. The Imo Shale and Nsukka Formation were deposited at the onset of another transgression episode during the Paleocene. The shales contain a significant amount of organic matter and may be a potential source of the hydrocarbons in the northern part of the Niger Delta. Finally, the Eocene Nanka and Ameki Sandstones mark the return to regressive conditions in the basin (Nwajide & Reijers, 1996).

Lokoja-Basange Formation is made up of sediments composed of fine- to coarse-grained highly ferruginous sandstones: litharenite (50%), graywacke (25%), and arkose (25%). Lokoja-Basange Formation is the oldest Formation in the Benin Flank of Anambra Basin. It is the chronostratigraphic lateral equivalent of the Nkporo Formation and Enugu Shales in the Eastern portion of the Anambra Basin. It is siliceous and conformably overlain by the Mamu Formation and underlain by the Igarra Schist Belt Basement Complex (Alli, 2021).

Figure 1 shows a map of Nigeria, the stratigraphy of the Anambra Basin, the Study Area, and Samples Locations.

3 Materials and Methods

Eight representative surface samples, which consist of fine- to coarse-grained highly ferruginous indurated sandstones, were collected from the study area. Major and trace element compositions of the samples were assessed with Energy Dispersive X-Ray Fluorescence (ED-XRF) machine (PANalytical model) at the Engineering Material Development Institute (EMDI) in Akure, Nigeria.

The samples were pulverized to 63 µm (230 mesh) and divided into two portions. One portion produced glass beads for significant oxides analysis, while the second was used to make pellets for trace element analysis. The assessment of duplicate samples and industrial standards/reference materials ascertained the accuracy of the results. The instrumental error of analysis is < 2.5% compared to industry-certified standards/reference materials. The detection limit of ED-XRF is 0.1 ppm for trace elements and 100% for significant components. The elemental range is Be to Am.

4 Result

Table 1 gives the primary (weight percent) and trace (parts per million (ppm)) elemental concentrations of the samples from the study area.

5 Discussion

The major oxides results show SiO_2(73.49–79.85 wt. %; average77.33 wt.%), Al_2O_3(11.07–13.00 wt. %; average 12.09 wt.%), Fe_2O_3(1.74–3.41 wt. %; average 2.75 wt.%), MgO (0.03–0.09 wt. %; average 0.06 wt.%) LOI (0.28–

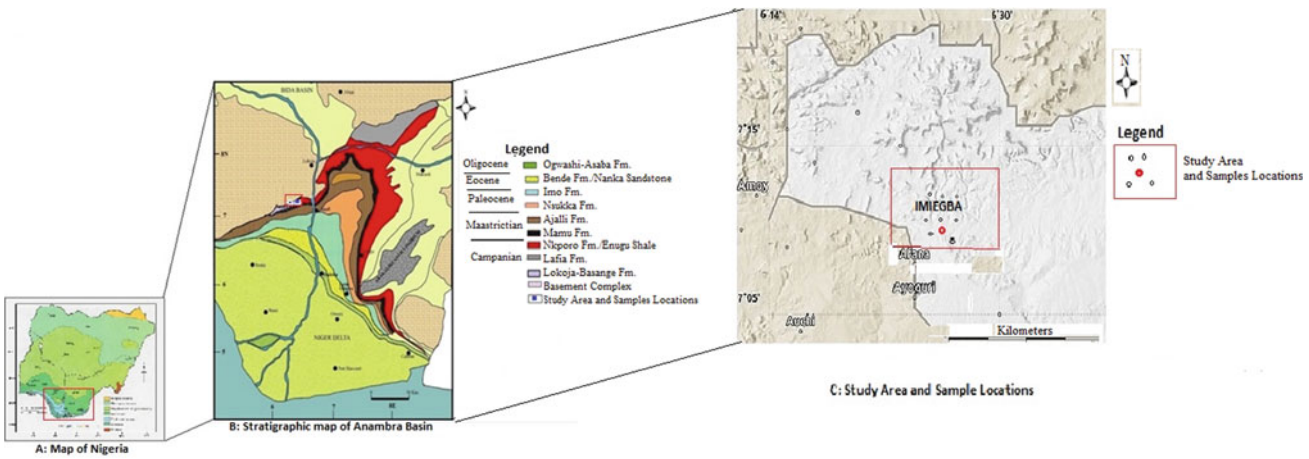

Fig. 1 Map of Nigeria, stratigraphy of Anambra Basin, study area and samples locations (modified after Nwajide & Reijers, 1996)

Table 1 Major (wt.%) and trace (ppm) elements compositions of Lokoja-Basange sandstone samples

Element (wt.%)	SOBA1	SOBA2	SOBA3	SOBA4	SOBA5	SOBA6	SOBA7	SOBA8
SiO_2	75.41	73.49	77.83	79.22	78.15	77.57	77.14	79.85
TiO_2	0.81	0.82	0.82	0.95	1.15	0.91	1.14	0.84
Al_2O_3	11.46	12.5	12.12	11.07	12.52	13	12.31	11.72
Fe_2O_3	3.41	3.22	2.56	2.51	2.43	2.84	3.32	1.74
MnO	0.02	0.03	0.59	0.04	0.03	0.05	0.07	0.06
MgO	0.05	0.03	0.04	0.09	0.06	0.05	0.04	0.09
CaO	0.85	0.76	0.91	1.12	1.11	0.87	0.86	1.04
Na_2O	1.29	1.06	1.67	2.00	1.71	1.75	2.10	2.08
K_2O	2.16	2.52	2.53	2.59	2.39	2.55	2.70	2.07
P_2O_5	0.01	0.01	0.02	0.01	0.02	0.01	0.01	0.01
LOI	4.54	5.56	0.91	0.37	0.37	0.41	0.28	0.40
Total (ppm)	100.01	100.00	100.00	99.97	99.94	100.01	99.97	99.90
Co	1.71	1.81	1.90	2.14	2.53	2.22	2.49	2.19
Cr	0.03	0.04	0.05	0.05	0.05	0.04	0.04	0.04
Cu	0.02	0.01	0.01	0.01	0.01	0.01	0.01	0.01
Mo	0.24	0.24	0.19	0.21	0.2	0.15	0.2	0.17
Ni	0.02	0.02	0.01	0.01	0.01	0.01	0.01	0.02
Pb	0.03	0.04	0.05	0.06	0.06	0.02	0.02	0.04
Sb	0.51	0.37	0.24	0.15	0.19	0.28	0.43	0.35
Sn	0.54	0.32	0.24	0.15	0.19	0.26	0.34	0.39
V	0.01	0.01	0.01	0.01	0.01	0.01	0.00	0.01
W	0.00	0.00	0.00	0.00	0.00	0.00	0.00	0.00
Zn	0.03	0.03	0.02	0.02	0.02	0.01	0.03	0.03
Zr	0.19	0.16	0.21	0.21	0.23	0.22	0.20	0.20
log (SiO_2/Al_2O_3)	0.82	0.77	0.81	0.85	0.80	0.78	0.80	0.83
log (Fe_2O_3/K_2O)	0.20	0.11	0.01	−0.01	0.01	0.05	0.09	−0.08
*CIA	72.72	74.23	70.34	65.97	70.61	71.55	68.50	69.31
*ICV	0.67	0.61	0.63	0.74	0.62	0.62	0.76	0.58
Cu/Zn	0.67	0.33	0.50	0.50	0.50	1.00	0.33	0.33
Ni/Co	0.01	0.01	0.01	0.00	0.00	0.00	0.00	0.01
V/(Ni + V)	0.33	0.33	0.5	0.5	0.5	0.5	0.00	0.33
V/(V + Cr)	0.25	0.2	0.17	0.17	0.17	0.2	0.00	0.20
V/Cr	0.33	0.25	0.20	0.20	0.20	0.25	0.00	0.25
V/Ni	0.50	0.50	1.00	1.00	1.00	1.00	0.00	0.50

* CIA = $(Al_2O_3/(Al_2O_3 + CaO + Na_2O + K_2O)) \times 100$

* ICV = $((Fe_2O_3 + K_2O + Na_2O + MgO + TiO_2)/Al_2O_3)$

5.56wt.%;average 1.61 wt.%). The Index of Compositional Variability (ICV) was used to determine the provenance and compositional maturity of the sandstones in the study area. ICV is computed using $((Fe_2O_3 + K_2O + Na_2O + MgO + TiO_2)/Al_2O_3)$. According to Cox et al. (1995), ICV > 1 infers matured sandstones in a tectonic active first cycle setting, while ICV < 1 suggests sandstones in a tectonically quiescent or cratonic environment. The ICV values for Lokoja-Basange Sandstones are 0.58 to 0.76, with an average of 0.65 indicative of compositionally immature sandstones deposited in a tectonically quiescent or cratonic environment. Also, the Chemical Index of Alteration (CIA) was used to ascertain the degree of weathering of the source rocks of the Lokoja-Basange Sandstones. CIA is calculated using $[(Al_2O_3/(Al_2O_3 + CaO + Na_2O + K_2O)) 100]$. The CIA values for the samples are 65.97–74.23%, with an average of 70.40%. According to Nesbitt and Young (1982), The CIA values for the study area sandstone indicate highly altered igneous and metamorphic source rocks. The binary plot of log (SiO_2/Al_2O_3) versus log $(Fe_2O_3 + K_2O)$

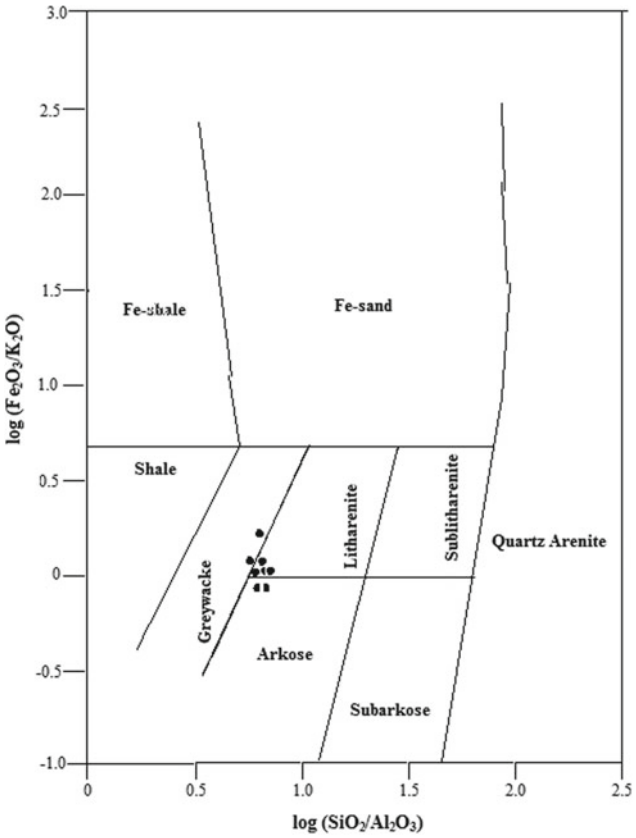

Fig. 2 Binary plot for characterisation of Lokoja-Basange sandstone (after Herron, 1988)

(Fig. 2) shows that 50% of the samples are litharenite, while graywacke and arkose are 25% each.

Co, Cr, Cu, Ni, V, and Zn are redox-sensitive indicators of the prevalence of paleodepositional conditions of sediments. Trace element ratios such as Cu/Zn, Ni/Co, V/(Ni + V), V/(V + Cr), V/Cr, and V/Ni were used to infer paleo-redox depositional environments of sandstones from the study area. Eighteen trace elements were assessed in the samples; however, Ag, As, Au, Cd, Nb, and Rb have detection limits far below the ED-XRF. They were excluded from the trace elements analysis result accordingly. On the other hand, the average values in parts per million for the rest twelve trace elements are as follows: W has < 0.01 ppm; Cr, Cu, Pb, Ni, V, and Zn have an average concentration of < 0.01 to 0.04 ppm; Sb, Sn, Mo, and Zr have an average value > 0.04 to 0.4 ppm, while Co has an average concentration of 2.12 ppm (Table 1). The low Cu/Zn ratio depicts oxic, while high values infer a reducing environment (Hallberg, 1976). Ni/Co ratio < 5 indicates an oxic environment, while values in the range of 5 to 7 show a reducing atmosphere. V/Cr ratio < 2 is oxic, while > 2 to 4.25 is reducing environment (Jones & Manning, 1994; Nagarajan et al., 2007). According to Hatch and Leventhal (1992), V/(Ni + V) ratio < 0.46 is oxic, while values >0 0.46 to > 0.84 are a reducing environment. V/Ni ratio < 3 is oxic, while > 3 is reducing habitat; V/(V + Cr) < 0.6 is toxic, and > 0.6 is reducing environment of deposition (Brumsack, 2006; Pi et al., 2014).

The computed trace element ratios for the Lokoja-Basange sediments show that low Cu/Zn ratios ranged between 0.33 and 1.00 with an average of 0.52; Ni/Co varied between 0.00 and 0.01 with an average of 0.01; V/Cr ranged from 0.00 to 0.33, with an average of 0.21; V/Ni ranged between 0.00 and 1.00 with an average of 0.69; V/(Ni + V) ranged between 0.00 and 0.50 with an average of 0.38 and V/(V + Cr) ranged between 0.00 and 0.25 with an average of 0.17. The interpretation of the six trace element ratios established that the sediments were deposited in the oxic fluvial paleoenvironment.

6 Conclusion

The sandstones from the study area originated from highly altered igneous/metamorphic rocks, and they are compositionally immature and were deposited in a tectonically stable cratonic environment. Lokoja-Basange Formation is composed of fine- to coarse-grained highly ferruginous sandstones: litharenite (50%), graywacke (25%), and arkose (25%). Using six trace element ratios such as Cu/Zn, Ni/Co, V/Cr, V/Ni, V/(Ni + V), and V/(V + Cr) suggests an oxic fluvial paleoenvironment for the sandstones from the study area.

References

Agagu, O. K., Fayose, E. A., & Petters, S. W. (1985). Stratigraphy and sedimentation in the Senonian Anambra Basin of Eastern Nigeria. *Journal of Mineralogy and Geology, 22*, 25–36.

Alli, B. (2021). *Trace element geochemical analysis and depositional environment of Lokoja-Basange Sandstone at Imiegba, Southwestern Nigeria* (pp. 1–97). Unpublished B.Sc. degree project. Adekunle Ajasin University Akungba-Akoko.

Arua, I. (1988). Episodic sedimentation: An example from the Nkporo Shale (Campano-Maastrichtian) Nigeria. *Journal of African Earth Sciences, 7*, 759–762.

Brumsack, H. J. (2006). The trace metal content of recent organic carbon-rich sediments: Implications for Cretaceous black shale formation. *Paleogeography, Paleoclimatology and Paleoecology, 232*, 344–361.

Cox, R., Lowe, D. R., & Culler, R. L. (1995). The influence of sediment recycling and basement composition on evolution of mudrock chemistry in the Southwestern United States. *GeochimCosmochim Acta, 59*(14), 2919–2940.

Hallberg, R. O. (1976). A geochemical method for investigating paleoredox conditions in sediments. *Ambio Spec Rep, 4*, 139–147.

Hatch, J. R., & Leventhal, J. S. (1992). Relationship between inferred redox potential of the depositional environment and geochemistry of the Upper Pennsylvanian (Missourian) Stark Shale Member of

the Dennis Limestone, Wabaunsee County, Kansas, U.S.A. *Chemical Geology*, *99*, 65–82

Herron, M. M. (1988). Geochemical classification of terrigenous sands and shales from core or logs data. *Journal of Sedimentary Petrology, 58*, 820–829.

Jones, B., & Manning, D. A. C. (1994). Comparison of geological indices used for the interpretation of paleoredox conditions in ancient mudstones. *Chemical Geology, 111*, 111–129.

Ladipo, K. O. (1988). Paleogeography, sedimentation and tectonics of the Upper Cretaceous Anambra Basin Southeastern Nigeria. *Journal African Earth Sciences, 7*, 815–821.

Lucas, F. A., & Ebahili, E. O. (2017). Lithofacies palynology and paleoenvironmental study of campanian to late Maastrichtian deposits of Ogbabu-1 well Anambra Basin, Southeastern Nigeria. *Journal Applied Sciences Environment Management, 21*(1), 137–153.

McLennan, S. M., Hemming, S., McDanniel, D. K., & Hanson, G. N. (1993). Geochemical approaches to sedimentation, provenance, and tectonics. In Johnsson, M.J., & Basu, A. (Eds.), *Processes controlling the composition of clastic sediments, Geological Society of America, Special Paper* (Vol. 285, pp. 21–40).

Nagarajan, R., Madhavaraju, J., Nagendral, R., Armstrong-Altrin, J. S., & Moutte, J. (2007). Geochemistry of neoproterozoic shales of the Rabanpalli formation, Bhima Basin, Northern Karnataka, southern India: Implications for provenance and paleoredox conditions. *Revista Mexicana Ciencias Geologicas, 24*, 150–160.

Nesbitt, H. W., & Young, G. (1982). Early proterozoic climates and plate motions inferred from major element chemistry of lutites. *Nature, 299*, 715–717.

Nwajide, C. S., & Reijers, T. J. A. (1996). Geology of the Southern Anambra Basin. In Reijers, T. J. A. (Ed.), *Selected chapters on geology* (pp. 133–148). SPDC, Warri.

Obaje, S. O. (2019). Granulometric and geochemical assessment of Ajali Sandstone in Fugar area in BeninFlank of Anambra Basin, Nigeria. *Fulafia Journal of Science and Technology, 5*(2), 78–87.

Pi, D.–H., Jiang, S.–Y., Luo, L., Yang, J.–H., Ling, H.–F. (2014). Depositional environments for stratiform witherite deposits in the Lower Cambrian black shale sequence of the Yangtze Platform, southern Qinling region, SW China: Evidence from redox-sensitive trace element geochemistry. *Palaeogeography, Palaeoclimatology, Palaeoecology, 398*, 125–131. ISSN 0031-0182, https://doi.org/10.1016/j.palaeo.2013.09.029.

Gold in Silicified Structures Related to the Quartz Diorite-Serpentinite Contact of Taghouni Prospect in the Bou Azzer Mining District (Central Anti-Atlas, Morocco)

Hamid Dani, Abdelhafid El Fels El Alaoui, Mustapha El Ghorfi, and Lhou Maacha

Abstract

The Taghouni deposit is part of the Bou Azzer mining district, where the mineralization is of a "cross-cutting" type, as cobalt arsenide veins hosted in quartz diorites. The district is mined for Cobalt, Nickel, and Chromium, but the mining activities provide significant concentrations of gold and silver. Based on the study of quartz diorite alteration, they appear to correspond to a metasomatic system involving the quartz diorites, serpentinites, and hydrothermal fluids. The reactions are ensured by the interface quartz diorite-serpentinite and by the fractures which intersect these two components. In this alteration system, the quartz diorites have recognized mineralogical modifications. Essentially, the albite and sericite replace the potassic feldspars and the quasi-totality of the plagioclases, and the ferromagnesians are transformed into chlorite and muscovite. The hydrothermal manifestation is summarized in three stages. Only the last one has been studied in detail: (i) a chlorite breccia which are associated with the Co–Ni phases; (ii) carbonatization, leading to the development of a stockwerk of dolomite, siderite, and ankerite; (iii) auriferous silicification, expressed in polyphasic quartz-filled veinlets, and we distinguish Quartz I (Q1) well-crystallized toward the outskirts of the veinlet; Quartz II (Q2) microcrystalline in the middle; Quartz III (Q3) as geodes within Q2. These last two silifications carry the explored gold as native grains and electrum.

Keywords

Serpentinites • Quartz diorite • Ophiolite • Hydrothermal alterations • Gold mineralization • Cobalt arsenide • Taghouni deposit • Bou Azzer • Anti-Atlas

1 Introduction

The Anti-Atlas deposits are the leading suppliers of Moroccan gold production, in addition to some deposits of the High Atlas such as the one of Tamlalt–Menhouhou, and the Tighza deposit in the Moroccan central massif. Furthermore, the reports recently published by the National Office of Hydrocarbons and Mines "ONHYM" highlight the gold potential of the southern province of Morocco (Sahara), which will increase the ambitions of Morocco in this field.

2 Geological Background

The Bou Azzer inlier records a stacking of Precambrian crustal rocks, which outcrop as tectonic units testifying to a subduction environment (Leblanc, 1975, 1981; Leblanc & Lancelot, 1980; Bodinier et al., 1984; Triantafyllou, 2016). The lithostratigraphy of Bou Azzer extends from Tonian to Cambrian. The basement includes the Tachdamt–Bleida formation and Assif n'Bougmmane–Takroumt metamorphic complex. The Tachdamt–Bleïda unit represents a vestige of a platform, constituted of sandstones, quartzites, carbonates, and tholeïtic basalt veins (Bouougri et al., 2020; Clauer, 1976), while the metamorphic complex forms a discontinuous band, covered by the upper Neoproterozoic cover, and exhumed in the massifs of Bou Azzer, Tazegzaout, Oumlil, and in the main outcrop of central El Graara (Bougemmane massif in the Takroumt area). Their lithology includes Augen orthogneiss, métagabbros, amphibolites, and mica schists (Blein et al., 2014; D'lemos et al., 2006; El Hadi

H. Dani (✉) · A. E. F. E. Alaoui · M. E. Ghorfi
Faculté Des Sciences Et Technique (FST Guéliz), Laboratoire L3G, Université Cadi Ayyad, Marrakech , Morocco
e-mail: danihamid266@gmail.com

M. E. Ghorfi
Mohamed VI Polytechnic University, Mining Environment and Circular Economy EMEC, Ben Guerir, Morocco

L. Maacha
Managem, Twin Center, Tour A, angle Bd Zerktouni Et Abdelkarim Khattabi Casablanca, Casablanca, Morocco

A. Çiner et al. (eds.), *Recent Research on Sedimentology, Stratigraphy, Paleontology, Tectonics, Geochemistry, Volcanology and Petroleum Geology*, Advances in Science, Technology & Innovation,
https://doi.org/10.1007/978-3-031-43222-4_22

et al., 2010; Hefferan et al., 2014). In the northern part of the inlier outcrops, the Tichibanin–Ben-Lgrad back arc suite, formed by basalts, microgabbros, rhyolites, acid, and dacitic ash tuffs, as well as sandstone silts, whose arc affinity dated to 760Ma- is well established (Bodinier et al., 1984; El Hadi et al., 2010; Naidoo et al., 1991; Saquaque et al., 1989; Triantafyllou et al., 2018). The Ophiolite is exposed in the axial part of the inlier and is expressed as serpentinites, gabbros, sheeted dykes complex, and pillow basalts. This sequence is intruded by diorite, quartz diorite, and monzodiorite, indicating the Cryogenian–Ediacaran transition (Blein et al., 2014; Leblanc, 1975; Samson et al., 2004; Triantafyllou et al., 2020). The cover comprises the Ediacaran terranes as Bou-Lbarod, Tiddiline, and Ouarzazate groups. They are respectively composed of mafic volcanic rocks, terrigenous sediments (overlying unconformably the Ophiolite), and high-K volcanic rocks as ignimbrite and tuffs (Blein et al., 2014; Chbani, 2001; Choubert, 1963; Choubert & Faure-Muret, 1970; Hefferan et al., 2014; Inglis et al., 2004; Leblanc, 1975). The terranes described above lie under a Paleozoic sedimentary cover. The Precambrian–Cambrian transition is marked by a carbonate formation known as the Adoudou formation, recently attributed to the Taroudant group (Bouchta et al., 1997; Gasquet et al., 2005).

3 Petrographic Analysis of Quartz Diorites

The samples studied are quartz diorites taken from the walls of Co-mineralized structures at the contact between these diorites and the serpentinites. They are brittle and deformed, whereas the phyllitic minerals (chloritized biotite) exhibit a ductile deformation. These samples present several features of alteration successive in time. The sericitization seems the earliest because it is affected by all the deformation stages. It concerns only the primary minerals of the rock, essentially the potassic feldspars and the plagioclases. These are characterized by neoformation of epidote in their cleavages and often in patches on them. The accentuation of alteration caused the albitization of neoformed sericite and epidote (Fig. 1a). The primary epidote is completely leached from the rock (Garcia, 1979). On the other hand, the alteration system, which appears to be important in mineralization, is initiated by a chlorite (occasionally penninite) brecciation carrying a cobalt arsenides mineralization, specifically skutterudite. The chlorite and mineralization are intersected by a network of waste carbonate veinlets, such as dolomite, siderite, and probably ankerite (Fig. 1b).

Silicification is the most common alteration. Our investigations lead to distinguishing between two types. Comb quartz mineralized by automorphic Fe-Co-arsenides materializes the first type. This quartz intersects the chlorite breccia, but no relationship is observed with the carbonate veins (Fig. 1c). The second type is interpreted as a polyphase mobilization of silica. We believe this phase is the last of all previously described stages, giving the argument of the erythrine particles hosted in the silicified veins, which means that this silicification was set up only after the oxidation of the primary cobalt mineralization to erythrine (Fig. 1d).

The auriferous phases have been identified at the second-type silicification. The textural examinations of these silicified structures reveal three generations of quartz: (1) large quartz crystals in the borders of the veins (Q1); (2) microcrystalline quartz in the middle of the veins (Q2); (3) the geodic quartz within the microcrystalline (Q3). The gold has been recognized only in these last two stages. The native gold occurs as small grains within microcrystalline quartz (Fig. 1e), while the geodes contain electrum particles (Fig. 1f).

4 Discussion

To characterize the precious metals associated with cobalt in the Taghouni area, we have studied the alteration of quartz diorites, the main host rock of these mineralizations. Mineralogically, the studied rocks have undergone polyphase modifications, starting with the total leaching of their primary epidote, then the sericitization of feldspars. First, the plagioclase is affected by saussuritization leading to the genesis of epidote patches on the minerals or in their cleavages. Next, the albite appears in the proximity of mineralized structures replacing the feldspars. We also notice the formation of muscovite near these structures. Then, another tectonic-hydrothermal event is triggered and expressed in a chlorite breccia associated with Co-Fe arsenides. This chlorite, and sometimes in the form of penninite. The chlorite–penninite association is intersected by carbonate veinlets (ankerite, siderite). We have distinguished here between two types of silicifications: the type materialized by quartz comb-bearing iron and cobalt arsenides, and the type of polyphase silicifications, composed of three stages, which correspond to a series of mobilizations of silica in the veinlets. The destruction of the whole primary epidote and the replacement of the feldspars (K-feldspar + plagioclase) by sericite + muscovite + albite is a piece of evidence about the highly active behavior of calcium (Ca) under these conditions and also alkalis, concluding the departure of calcium and the entrance of sodium in the form of albite and potassium incorporated in sericite and muscovite. This stage matches the spilitization phenomenon in the tonalite massifs of Bou-Zben, and Oumisden described by Besson (1980).

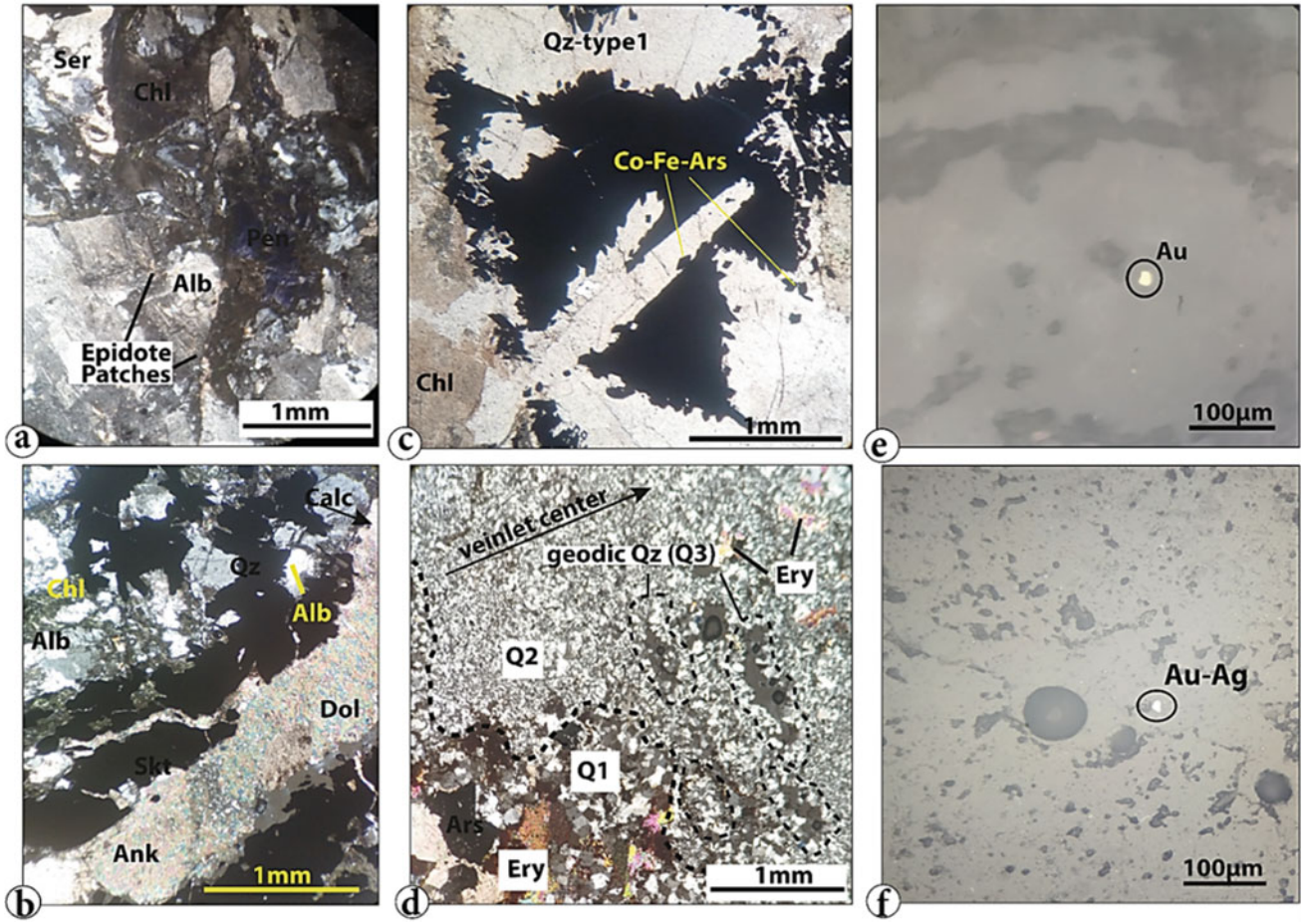

Fig. 1 Microphotography of the alterations affecting the quartz diorites (photos **a**, **b**, **c**, and **d** are under transmitted light, while e and f are under reflected light): **a** sericitized potassic feldspars and plagioclases with saussuritization of the plagioclases and the posterior chlorite (Chl)–penninite (Pen) breccia; **b** the carbonate vein cross-cutting the chlorite breccia; **c** silicification type-1 as comb quartz bearing iron and cobalt arsenides (Co-Fe-Ars); **d** silicification type-2 with the three quartz generations; **e** native gold (Au) in microcrystalline quartz (Q2); **f** electrum (Au–Ag) in geodic quartz (Q3) *(Ser: sericite, Alb; albite, Ank: ankerite; Dol: dolomite, Ery: erythrite, Skt: skutterudite; Ars: arsenides)*

The chloritization corresponds to the activation of the Mg-Fe system. The presence of the penninite refers to an Mg-high bring. The iron is supposed to be varied in the opposite trend like in the Bou-Zben tonalite, and to be accumulated until its incorporation in the carbonates veinlets (siderite, ankerite) to explain those carbonate's Fe-high content. Native silver was identified by Leblanc and Lbouabi (1989) in the Tizi deposit, not far to the east of our study area. Based on the results provided by the fluid inclusions, the authors link these mineralizations to the phenomenon of diorite rodingitization, resulting from the Na–K-rich fluid metasomatism. This study highlights that gold mineralization occurs as small grains of native gold in microcrystalline quartz (Q2) veins and electrum (Au–Ag) in the geodes (Q3). We link the auriferous event to the last paragenetic stage, a series of silicifications, and mainly to the last two stages of silicification.

5 Conclusions

We draw two main conclusions from the petrographic analysis of the Taghouni quartz diorites and the comparison with previous studies:

- The quartz diorites studied are the result of Na–K-metasomatism, causing the subtraction of almost all rock calcium as well as that the chloritization is related to a high bringing of Mg, which derives from the serpentinites, whereas the carbonatization controls the iron.
- The auriferous phase is observed in silicified structures of the last paragenetic stage. The native gold is directly linked to the microcrystalline quartz (Q2), and the electrum is observed in silicified geodes.

References

Besson, M. (1980). *Wall rock alteration of cobalt ore bodies in Bou-Azzer district*, Morocco.

Blein, O., Baudin, T., Chevremont, P., Soulaimani, A., Admou, H., Gasquet, P., ... & Gombert, P. (2014). Geochronological constraints on the polycyclic magmatism in the Bou Azzer-El Graara inlier (central Anti-Atlas Morocco). *Journal of African Earth Sciences, 99*, 287–306.

Bodinier, J. L., Dupuy, C., & Dostal, J. (1984). Geochemistry of precambrian ophiolites from Bou Azzer Morocco. *Contributions to Mineralogy and Petrology, 87*(1), 43–50.

Bouchta, R., Boyer, F., Routhier, P., Saadi, M., & Salem, M. (1997). L'aire cuprifère de l'Anti-Atlas (Maroc); permanence et arêtes riches. *CR Academie Sciences Paris, 284*, 503–506.

Bouougri, E. H., Lahna, A. A., Tassinari, C. C., Basei, M. A., Youbi, N., Admou, H., ... & Maacha, L. (2020). Time constraints on early Tonian Rifting and Cryogenian Arc terrane-continent convergence along the northern margin of the West African craton: Insights from SHRIMP and LA-ICP-MS zircon geochronology in the Pan-African Anti-Atlas belt (Morocco). *Gondwana Research, 85*, 169–188.

Chbani, B. (2001). Géodynamique sédimentaire de bassins sur la bordure nord du craton ouest africain: exemple du PII, PIII et de l'Adoudounien de la boutonnière de Bou Azzer El Graara (Anti-Atlas central, Maroc) (Doctoral dissertation, Thèse Doctorat d'Etat, Université Cadi Ayyad, Faculté des Sciences Semlalia, Marrakech, Maroc (pp. 282).

Choubert, G. (1963). Histoire géologique du précambrien de l'Anti--Atlas. Notes et Mémoire de Service Géologique du Maroc. n 162 (Doctoral dissertation, Thèse sciences) (pp. 352).

Choubert, G., & Faure-Muret, A. (1970). Les corrélations du Précambrien, Anti-Atlas occidental et central. *Notes et Mémoires Services Géologique Maroc, 229*, 259.

Clauer, N. (1976). Strontium isotope geochemistry of sedimentary environments. Application to the geochronology of the West African craton cover (Vol. 45(1). Persée-Portail des revues scientifiques en SHS).

D'lemos, R. S., Inglis, J. D., & Et Samson, S. D.: A newly discovered orogenic event in Morocco: Neoproterozic ages for supposed Eburnean basement of the Bou Azzer inlier, Anti-Atlas Mountains. *Precambrian Research, 147*(1–2), 65–78.

Garcia, D. (1979). Host rocks alterations of cobalt-bearing deposits in the Bou-Azzer district (Anti-Atlas, Morocco) (Doctoral dissertation, Ecole Nationale Supérieure des Mines de Paris).

Gasquet, D., Levresse, G., Cheilletz, A., Azizi-Samir, M. R., & Mouttaqi, A. (2005). Contribution to a geodynamic reconstruction of the Anti-Atlas (Morocco) during Pan-African times with the emphasis on inversion tectonics and metallogenic activity at the Precambrian-Cambrian transition. *Precambrian Research, 140*(3–4), 157–182.

El Hadi, H., Simancas, J. F., Martínez-Poyatos, D., Azor, A., Tahiri, A., Montero, P., ... & González-Lodeiro, F. (2010). Structural and geochronological constraints on the evolution of the Bou Azzer Neoproterozoic ophiolite (Anti-Atlas, Morocco). *Precambrian Research, 182*(1–2), 1–14.

Hefferan, K., Soulaimani, A., Samson, S. D., Admou, H., Inglis, J., Saquaque, A., ... & Heywood, N. (2014). A reconsideration of Pan African orogenic cycle in the Anti-Atlas Mountains, Morocco. *Journal of African Earth Sciences, 98*, 34–46.

Inglis, J. D., MacLean, J. S., Samson, S. D., D'Lemos, R. S., Admou, H., & Hefferan, K. (2004). A precise U-Pb zircon age for the Bleïda granodiorite, Anti-Atlas, Morocco: Implications for the timing of deformation and terrane assembly in the eastern Anti-Atlas. *Journal of African Earth Sciences, 39*(3–5), 277–283.

Leblanc M. (1975). Precambrian ophiolites and arsenized cobalt deposits: Bou-Azzer (Morocco). Doctoral thesis, University of Paris VI.

Leblanc, M. (1981). The late Proterozoic ophiolites of Bou Azzer (Morocco): Evidence for Pan-African plate tectonics. In *Developments in precambrian geology* (Vol. 4, pp. 435–451). Elsevier.

Leblanc, M., & Lancelot, J. R. (1980). Geodynamic interpretation of the pan-African (Precambrian terminal) domain of the Anti-Atlas (Morocco) based on geological and geochronological data Canadian. *Journal of Earth Sciences, 17*(1), 142–155.

Leblanc, M., & Lbouabi, M. (1989). Native silver mineralization along a rodingite tectonic contact between serpentinite and quartz diorite (Bou Azzer, Morocco). *Economic Geology, 83*(7), 1379–1391.

Naidoo, D. D., Bloomer, S. H., Saquaque, A., & Hefferan, K. (1991). Geochemistry and significance of metavolcanic rocks from the Bou Azzer-El Graara ophiolite (Morocco). *Precambrian Research, 53*(1–2), 79–97.

Samson, S. D., Inglis, J. D., D'lemos, R. S., Admou, H., Blichert-Toft, J., & Hefferan, K.: Geochronological, geochemical, and Nd–Hf isotopic constraints on the origin of Neoproterozoic plagiogranites in the Tasriwine Ophiolite, Anti-Atlas orogen, Morocco. *Precambrian Research, 135*(1–2), 133–147.

Saquaque, A., Admou, H., Karson, J., Hefferan, K., & Reuber, I. (1989). Precambrian accretionary tectonics in the Bou Azzer-El Graara region, Anti-Atlas, Morocco. *Geology, 17*(12), 1107–1110.

Triantafyllou, A. (2016). Geodynamic evolution of a neoproterozoic island arc of the Moroccan Anti-Atlas: characterization of the processes of intra-oceanic growth and accretion (Doctoral dissertation, Nantes).

Triantafyllou, A., Berger, J., Baele, J. M., Bruguier, O., Diot, H., Ennih, N., ... & Watlet, A.: Intra-oceanic arc growth driven by magmatic and tectonic processes recorded in the Neoproterozoic Bougmane arc complex (Anti-Atlas, Morocco). *Precambrian Research, 304*, 39–63.

Triantafyllou, A., Berger, J., Baele, J. M., Mattielli, N., Ducea, M. N., Sterckx, S., ... & Ennih, N.: Episodic magmatism during the growth of a Neoproterozoic oceanic arc (Anti-Atlas, Morocco). *Precambrian Research, 339*, 105610.

Geology and Geodynamic Setting of the Chadak Epithermal Au–Ag Deposit in Middle Tien Shan (Uzbekistan)

Bakhtiar Nurtaev and Svetlana Kirezidi

Abstract

The Kurama ore region in the east of Uzbekistan is located in the eastern part of the extended Beltau-Kurama volcano-plutonic belt of the Middle Tien Shan. This mining district exemplifies unique deposits with perfectly preserved characteristic features of Au–Cu porphyry and epithermal Au–Ag occurrences. This paper briefly summarizes original and published data on the Chadak deposit, including its geological features, ore characteristics, and primary mineral assemblages. The event of syenite, trachydolerite, lamprophyre, and leucogranite dikes at the upper parts of the formation of plutons simultaneously with mineralization is interesting since they fit into the ore-forming process and make it possible to trace its evolution unambiguously. Significant differences in REE and trace element patterns of analyzed porphyry intrusions and dikes were reported in the study area. On this basis, the trachydolerites, syenites, and leucogranites have not formed by fractional crystallization from a common parental magma. The stage of magmatism closest to ore genesis is represented here by mafic dikes. The emergence of the hydrothermal system, which caused the final formation of gold-silver ore bodies, should be associated with the activity of a deep source, the magmatic derivatives of which are basic dikes.

Keywords

Kurama ore region • Epithermal deposit • Deep faults • Geochemical features • Genesis

1 Introduction

The Kurama ore region in the east of Uzbekistan is located in the eastern part of the extended Beltau-Kurama volcano-plutonic belt—a structural component of the Middle Tien Shan (Cheng et al., 2018; Dolgopolova et al., 2017; Rudniye mestorozhdeniya Uzbekistana [Ore deposits of Uzbekistan], 2001). This mining district exemplifies unique deposits with perfectly preserved characteristic features of Au–Cu porphyry and epithermal Au–Ag occurrences (Nurtaev & Mamarozykov, 2021; Rudniye Mestorozhdeniya Uzbekistana [Ore deposits of Uzbekistan], 2001). The section is composed of diverse blocks and volcanic structures. It shows widespread manifestations of intrusive magmatism ranging from Devonian, Middle and Late Carboniferous, and Early Permian in age. The geological driving force of these processes was tectonic activity in the Chatkal–Kurama zone. Extensive factual evidence (Dolgopolova et al., 2017; Kovalenker et al., 1995; Rudniye Mestorozhdeniya Uzbekistana [Ore deposits of Uzbekistan], 2001) indicates that this activity was accompanied by the multiple restyling of the local topography and hydrothermal activity younger than 290 Ma. The igneous rocks in the area are associated in space and time with the large epithermal deposits of the Kochbulak (Au–Ag–Te) and Lashkerek (Ag–Pb–Zn) ore fields, the Kyzylalmasai and Chadak (Au–Ag), and Aktepe (Ag-As-Co–Ni-U) deposits as well as several occurrences of Au, Ag, Cu, Pb, Zn, and Bi occurrences (Kovalenker et al., 1995; Rudniye Mestorozhdeniya Uzbekistana [Ore deposits of Uzbekistan], 2001).

This paper briefly summarizes original and published data on the Chadak deposit, including its geological features and ore characteristics, the sequence of the mineral paragenesis, and the primary ore mineral assemblages. The Chadak ore field is one of Uzbekistan's oldest gold and silver deposits, industrially developed since 1970 by two still operating mines—Pirmirab and Guzaksai (Kovalenker et al., 1995; Rudniye Mestorozhdeniya Uzbekistana [Ore deposits of

B. Nurtaev (✉) · S. Kirezidi
Institute of Geology and Geophysics, University of Geological Sciences, Tashkent, Uzbekistan
e-mail: nurtaev@ingeo.uz

A. Çiner et al. (eds.), *Recent Research on Sedimentology, Stratigraphy, Paleontology, Tectonics, Geochemistry, Volcanology and Petroleum Geology*, Advances in Science, Technology & Innovation,
https://doi.org/10.1007/978-3-031-43222-4_23

Uzbekistan], 2001). The most important Au- and Ag-bearing phases are electrum of highly variable fineness, acanthite, and Ag–Cu sulfides (jalpaite, mckinstryite). The average grades range between 5.6 and 6.0 ppm for Au and from 26 to 80 ppm for Ag. Previous mineralogical and fluid inclusion studies revealed that the mineralization was formed during three hydrothermal stages: an early hydrothermal stage of Upper Carboniferous age, skarn-hydrothermal, and late hydrothermal stages of Upper Permian age (Rudniye Mestorozhdeniya Uzbekistana [Ore deposits of Uzbekistan], 2001). Gold and silver mineralization occurs during the later mineral stages associated with skarn-like Ag-Bi-Pb-Cu-bearing mineralization**.** In the Chadak ore field, syenitoid dikes, together with trachydolerites and lamprophyres, form a group of dike bundles that developed along parallel-oriented fractures. Understanding the genesis of these ore deposits and their relations with intrusions of different ages remains uncertain.

2 Materials and Methods

The petrography, chemical composition of dikes, and their petro- and ore-generating role during the gold-silver mineralization are provided in this research. This will help reveal the petrogenesis of intrusive and associated dikes responsible for forming the Chadak fluid-magmatic system. In this regard, petrographic and mineralogical studies of igneous rocks were performed using the Nikon Optiphot 2Pol multifunctional polarizing microscope. In addition, the form of occurrence and composition of rock forming, accessory ore minerals were determined using an ***electron*** probe ***microanalyzer*** JXA-8800R. Finally, the chemical compositions and abundances of ore elements were determined by applying the ICP-MS-7500 series mass spectrometer.

3 Results

According to satellite and geophysical imagery data, the ore field is located in the conjugate system of northwest-southeast-trending strike-slip Kumbel-Ugam and north-dipping reverse North Fergana faults where Late Carboniferous supra-subduction and Permian intraplate magmatism actively occurred. In terms of geochemical characteristics, the dikes of the Chadak deposit belong to the K-Na series: syenitoids (Na_2O/K_2O–0.1–1.3, on average −0.9), trachydolerites dikes (0.4–2.2, on average −1.3), leucogranites (0.4–1.5, on average −0.9), as well as high aluminous. In a spider diagram (Pearce, 1983) normalized to MORB (Fig. 1a), trachydolerites and syenitoids show a consistent pattern characterized by substantial depletion in Ti and Zr and high Rb, Ba, and Th. A chondrite-normalized REE pattern with enrichment of light REE relative to REE and fragile Eu anomalies characterizes the REE diagram. In the MORB-normalized trace element spider diagrams, the leucogranites (Fig. 1a) display Sr, Ti, Zr, and La depletion and enrichment of HFSE, including Nb, Ta, and Hf. The REE diagram of leucogranites (Fig. 1b) is characterized by positive anomalies of Pr, Sm, Eu, Er, and Lu, typical for shallow depths of the magmatic source. Significant differences are noted between the two groups, indicating that they cannot have formed by a fractional crystallization process from a common parental magma. It is also necessary to report the general antidromic sequence of dikes from acidic rhyolitic to olivine dolerite, one of the specific features of the late orogenic stage of the region's development.

4 Discussion

The petrogenesis and tectonic setting of trachydolerites suggests that they are unfractionated, meta-aluminum, calc-alkaline to sub-alkaline formations of volcanic arcs, while lamprophyres belong to the intraplate environment. Narrow dikes of spherulite trachytes cropped out with geochemical affinities for gold and silver rare earth elements. Syenitoid dikes are accompanied by quartz-hematite, quartz-carbonate, and quartz-adularia hydrothermal veins, in which gold and silver mineralization is associated with Bi, W, and REE. The concentration of the last three elements in these veins is associated with increased fluorine in their fluid phases. The basic dikes are more silver-bearing than syenitic ones. So we assumed that Chadak deposits belong to the volcanic-hosted low-sulfidation gold deposits with an anomalous regime of fluid evolution, e.g., high temperature jumps after the main stage of epithermal ore formation. The age of gold-silver mineralization was determined by many researchers and has not received an unambiguous interpretation. According to the data of the absolute age determinations by the K–Ar dating, at least two age groups of metasomatized similar to their petrological features were distinguished: I (272–253) ± 11 Ma—Permian and II (239–220) ± 9 Ma—Triassic (Rudniye Mestorozhdeniya Uzbekistana [Ore deposits of Uzbekistan], 2001).

The stage of magmatism closest to ore genesis is represented here by mafic dikes. Therefore, it seems that the emergence of the hydrothermal system, which caused the final formation of gold–silver ore bodies, should be associated with the activity of a deep source, the magmatic derivatives of which are basic dikes. One of the main reasons for the formation of the ore field we assume a vertical channel for magmatic and ore bodies associated with the northwestern influence of the Tarim plume, which was active at about the same time (Gao et al., 2014).

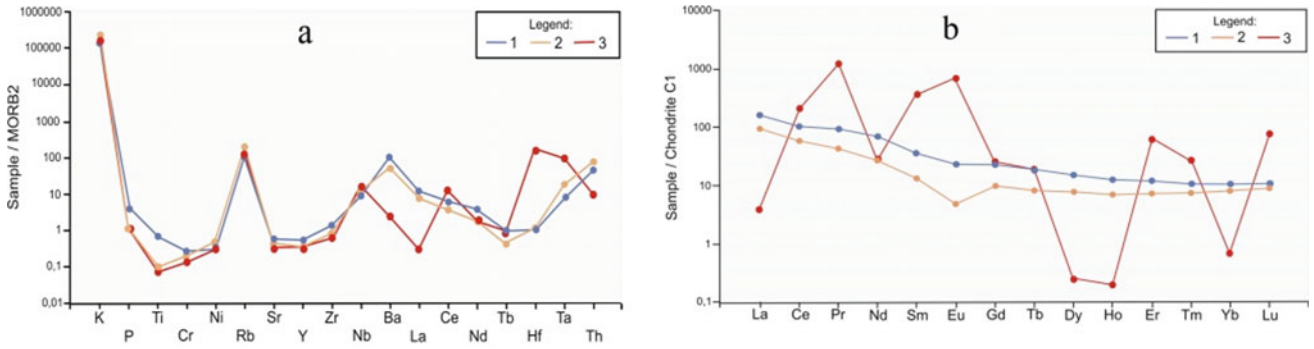

Fig. 1 MORB-normalized trace element **a** and chondrite-normalized REE pattern spider diagram **b** (1) trachydolerites and lamprophyres, (2) syenitoids, (3) leucogranites (average values)

5 Conclusions

The stage of magmatism closest to ore genesis is represented here by mafic dikes. However, it is hardly possible to consider them as a source of ore-bearing fluids. Therefore, it seems that the emergence of the hydrothermal system, which caused the final formation of gold-silver ore bodies, should be associated with the activity of a deep source, the magmatic derivatives of which are basic dikes. The drainage systems provided deep tectonic zones for the ascending mantle material at the intersection of the Kumbel-Ugam zone of deep faults with the North Fergana fault. It is hoped that a better understanding of the nature of epithermal Au–Ag mineralization will assist in evaluating the prospects for the placement of polymetallic mineralization with gold, silver, and platinum group elements in the zone of Kumbel-Ugam deep faults.

References

Cheng, Z., Zhang, Z., Turesebekov, A., Nurtaev, B. S., Xu, L., & Santosh, M. (2018). Petrogenesis of gabbroic intrusions in the Valerianov-Beltau-Kurama magmatic arc, Uzbekistan: The role of arc maturity controlling the generation of giant porphyry Cu-Au deposits. *Lithos, 320–321*, 75–92.

Dolgopolova, A., Seltmann, R., Konopelko, D., Biske, Yu. S., Shatov, V., Armstrong, R., Belousova, E., Pankhurst, R., Koneev, R., & Divaev, F. (2017). Geodynamic evolution of the western Tien Shan, Uzbekistan: Insights from U-Pb SHRIMP geochronology and Sr-Nd-Pb-Hf isotope mapping of granitoids. *Gondwana Research, 47*, 76–109.

Gao, R., Xiao, L., Pirajno, F., Wang, G.-C., He, X.-X., Yang, G., & Yan, S.-W. (2014). Carboniferous-Permian extensive magmatism in the West Junggar, Xinjiang, Northwestern China: Its geochemistry, geochronology, and petrogenesis. *Lithos, 204*, 125–143.

Kovalenker, V. A., Rusinov, V. L., Kabo, A. E., & Jambor, J. L. (1995). The Aktepe silver-arsenide deposits, Uzbekistan. *Exploration Mining Geology, 4*(2), 111–119.

Nurtaev, B. S., & Mamarozykov, U. D. (2021). On the genesis of the Aktepa-Chadak fluid-magmatic ore-generating system with multimetal specialization (Western Tien Shan). *Geology and Subsoil Protection, 2*, 44–56. (in Russian).

Pearce, J. (1983). Role of the sub-continental lithosphere in magma genesis at active continental margins. In Hawkesworth, C. J., & Norry, M. J., (Eds.), *Continental basalts and mantle xenoliths*. (pp. 230–249). Shiva Publishing, Nantwich.

Rudniye Mestorozhdeniya Uzbekistana [Ore deposits of Uzbekistan]. (2001). Responsible Akhmedov, N. A. (Ed.), Tashkent, IMR (pp. 660). (in Russian).

Zhao, X.-B., Xue, C.-J., Chi, G.-X., Mo, X.-X., Nurtaev, B., & Zhang, G.-Z. (2017). Zircon and molybdenite geochronology and geochemistry of the Kalmakyr porphyry Cu–Au deposit, Almalyk district, Uzbekistan: Implications for mineralization processes. *Ore Geology Reviews, 86*, 807–824.

Fluid Evolution of the Fe-Zn Skarn Deposits in the Çiftehan (Ulukışla-Niğde) Area, South-Central Turkey

Emmanuel Daanoba Sunkari, Abdurrahman Lermi, and Yılmaz Demir

Abstract

This study investigated the compositional variations of fluid inclusions in the different stages of mineralization at the Esendemirtepe and Horoz Fe-Zn skarns, south-central Turkey. The skarn zones in the study area consist of volcano-sedimentary sequences intruded by intrusive bodies and marble–schist in contact with granitoids. The primary ore minerals in both locations are magnetite and hematite, with subordinate sphalerite, chalcopyrite, pyrite, and pyrrhotite. The Esendemirtepe Fe-Zn skarn deposit is a typical deep exoskarn characterized by irregular disseminated hematite and magnetite assemblages with blebs of chalcopyrite, accompanied by calcite, quartz, and epidote at the contact between the volcano-sedimentary units and the skarn. The Horoz Fe-Zn skarn deposit is also a relatively deep endoskarn characterized by massive garnet crystals. Rhythmic banded crystallization of sporadic nodular-shaped sphalerite, quartz, and calcite developed along with the marble–schist skarn contact. Two-phase liquid-rich (L + V) fluid inclusions were observed in garnet, epidote, quartz, calcite, and sphalerite mineral assemblages. The average homogenization temperatures and calculated salinities in all stages of mineralization range from 155 to 600 °C and 0.53 to 23.1 wt.% NaCl equ., respectively. The eutectic temperatures also range from −66.2 to −21.2 °C, implying that the early stages were dominated by fluids that reflect an H_2O-NaCl-$CaCl_2$ system and become an H_2O-NaCl system in the later stage. The continuous evolution history of the fluids reveals a gradual change from early high-temperature-salinity magmatic fluids to late relatively low-temperature-salinity mixed magmatic fluids due to interaction with meteoric-derived fluids.

Keywords

Fluid inclusions • Skarn deposits • Esendemirtepe and Horoz Fe-Zn Skarns • Magmatic-derived fluids • Meteoric-derived fluids

1 Introduction

Skarn deposits are an essential class of mineral deposits in Turkey that formed between the Late Cretaceous and Oligo-Miocene periods during the collision between the Afro-Arabia and Eurasia plates (Kuşcu, 2019). The Fe-Zn skarn deposits in the Çiftehan (Ulukışla-Niğde) area are located in the eastern part of the Bolkar Mountains. In this area, several large- and small-scale mines exist, but only a small number are currently in operation (Çiftçi et al., 2014). The geology of the region, stratigraphic relations between the lithologies, formation mechanisms of the units, kinematics of the Ecemiş Fault, constraints on the geotectonic position of the Horoz granitoids, geology and mineralogy of other deposits in the region have already been studied. However, studies on the fluid evolution of the Fe-Zn skarn deposits in the region are limited. Therefore, this study aims to determine the compositional variation of fluid inclusions in the different stages of mineralization so that the formation

E. D. Sunkari (✉) · A. Lermi
Department of Geological Engineering, Faculty of Engineering, Niğde Ömer Halisdemir University, 51240 Niğde, Main Campus, Turkey
e-mail: emmanueldaanoba.sunkari@mail.ohu.edu.tr

E. D. Sunkari
Department of Geological Engineering, Faculty of Geosciences and Environmental Studies, University of Mines and Technology, P.O. Box 237 Tarkwa, Ghana

Department of Geology, Faculty of Science, University of Johannesburg, Auckland Park 2006, Kingsway Campus, P.O. Box 524 Johannesburg, South Africa

Y. Demir
Department of Geological Engineering, Faculty of Engineering, Recep Tayyip Erdoğan University, 53100 Rize, Main Campus, Turkey

A. Çiner et al. (eds.), *Recent Research on Sedimentology, Stratigraphy, Paleontology, Tectonics, Geochemistry, Volcanology and Petroleum Geology*, Advances in Science, Technology & Innovation,
https://doi.org/10.1007/978-3-031-43222-4_24

conditions of the Fe-Zn skarns in the study area can be properly understood.

2 Materials and Methods

The ore textures as observed in the various lithologies were described prior to the fluid inclusion studies. In total, 30 doubly-polished sections were prepared for fluid inclusion petrography and microthermometry. Microthermometric data were obtained using a LINKAM THMG600 heating-freezing stage coupled to an OLYMPUS microscope housed in the Department of Geological Engineering, Recep Tayyip Erdoğan University, Turkey. The equipment has a sensitivity rate of 0.01–150 °C/min heating with temperature control from −196 to 600 °C.

3 Results

3.1 Textural Properties of the Skarn Deposits

The Esendemirtepe skarn includes a variety of macroscopic-scale prograde patterns. Irregular disseminated hematite and magnetite assemblages with blebs of chalcopyrite are accompanied by garnet, calcite, and quartz at the contact between the volcano-sedimentary rocks and the skarn zone. Epidote and chalcopyrite inclusions are observed around fracture-filling textures and retrograde-stage magnetite. In the Horoz skarn, the early prograde-stage garnets are represented by massive textures. Sporadic nodular-shaped sphalerite and irregular quartz developed along the marble–schist skarn contact. Coarse-grained garnet crystals surrounded by smaller fine-grained garnet crystals are also common, representing the late prograde stage of garnet formation closer to the ore zone and may suggest reactive infiltration (Demir et al., 2017).

3.2 Classification of Fluid Inclusions

Fluid inclusion studies were performed on garnet, epidote, quartz, calcite, and sphalerite mineral assemblages. Liquid- and vapor-bearing (L + V) two-phase fluid inclusions were identified in the investigated minerals. The fluid inclusions were generally polygonal and irregular in shape, while lesser amounts of the rounded, elliptical, tube- and pear-shaped morphologies were also present. Fluid inclusions observed in the samples were generally two-phase (L + V) Type I inclusions, which are liquid-rich at room temperature. Most of these inclusions are present in garnet, calcite, epidote, and sphalerite from all stages of mineralization. A NaCl crystal was found in Type I inclusion of garnet. The Type I fluid inclusions have vapor–liquid ratios of approximately 10–30%, and homogenization commonly occurs in the liquid phase. Clathrate formation was observed in Type I calcite inclusions during the microthermometric measurements. Also, the Type I inclusions in sphalerite are CO_2-bearing in a few samples. The CO_2 phase was so small that it was difficult to define CO_2 in the inclusions by the microscopic investigations. But during the microthermometric measurements, CO_2 melting temperature (Tm-CO_2) and CO_2 homogenization temperature (ThCO_2) were easily defined.

Type II inclusions are vapor-rich, characterized by 30–40% vapor–liquid ratios, and homogenized in the vapor phase. The Type II inclusions were identified in only the early stages of garnet and quartz formation. The Type II inclusions found in garnet are characterized by clathrate melting temperatures, which imply that there may be a limited amount of CO_2 and/or CH_4 in the system, but not as much as the formation of CO_2-bearing separate phases.

3.3 Microthermometric Properties of the Fluid Inclusions

The eutectic temperatures (Te) were measured in Type I and Type II fluid inclusions in garnet, epidote, quartz, calcite, and sphalerite minerals. The Te of fluid inclusions studied in garnet minerals scattered in a large range of −59.1 to −29.7 °C (Fig. 1a), and the final ice melting (Tm-ice) temperatures vary from -20.8 to −4.00 °C. Calculated salinities of the fluid inclusions entrapped in garnet according to Bodnar (1993) and based on the Tm-ice values vary in the range of 6.45–23.1 wt% NaCl equ (Fig. 1a). The homogenization temperatures (Th) of fluid inclusions in garnet were very high (280–600 °C; Fig. 1a) when compared with the other minerals. Clathrate melting temperatures were measured in the range of 1.1 and 2.8 °C. The salinity (12.2–14.3 wt% NaCl equ.) of these clathrate bearing inclusions was calculated according to Darling (1991). For epidote, the Te changed from −66.2 to −36.2 °C (Fig. 1b) with Tm-ice values from −20.9 to −10.0 °C. The salinity values range from 13.9 to 23.0 wt% NaCl equ. (Fig. 1b). The Th values also varied from 298 to 469 °C (Fig. 1b). The Te measured in quartz ranged from −54.3 to −21.2 °C (Fig. 1c) with Tm-ice values in the range of −17.9 to −3.8 °C. In addition, the salinity and Th values of fluid inclusions in quartz ranged from 6.16 to 20.9 wt% NaCl equ. and 155 to 491 °C, respectively (Fig. 1c). For calcite, the Te scattered in a narrow range of −47.9 to 31.5 °C (Fig. 1d) with Tm-ice values ranging from −15.5 to 0.30 °C. Relatively lower salinity values (0.53–19.6 wt% NaCl equ.) and Th values (192–378 °C) were recorded in the fluid inclusions in calcite (Fig. 1d). Clathrate melting temperatures in the fluid inclusions found in calcite are in the range of 1.50–2.00 °C with

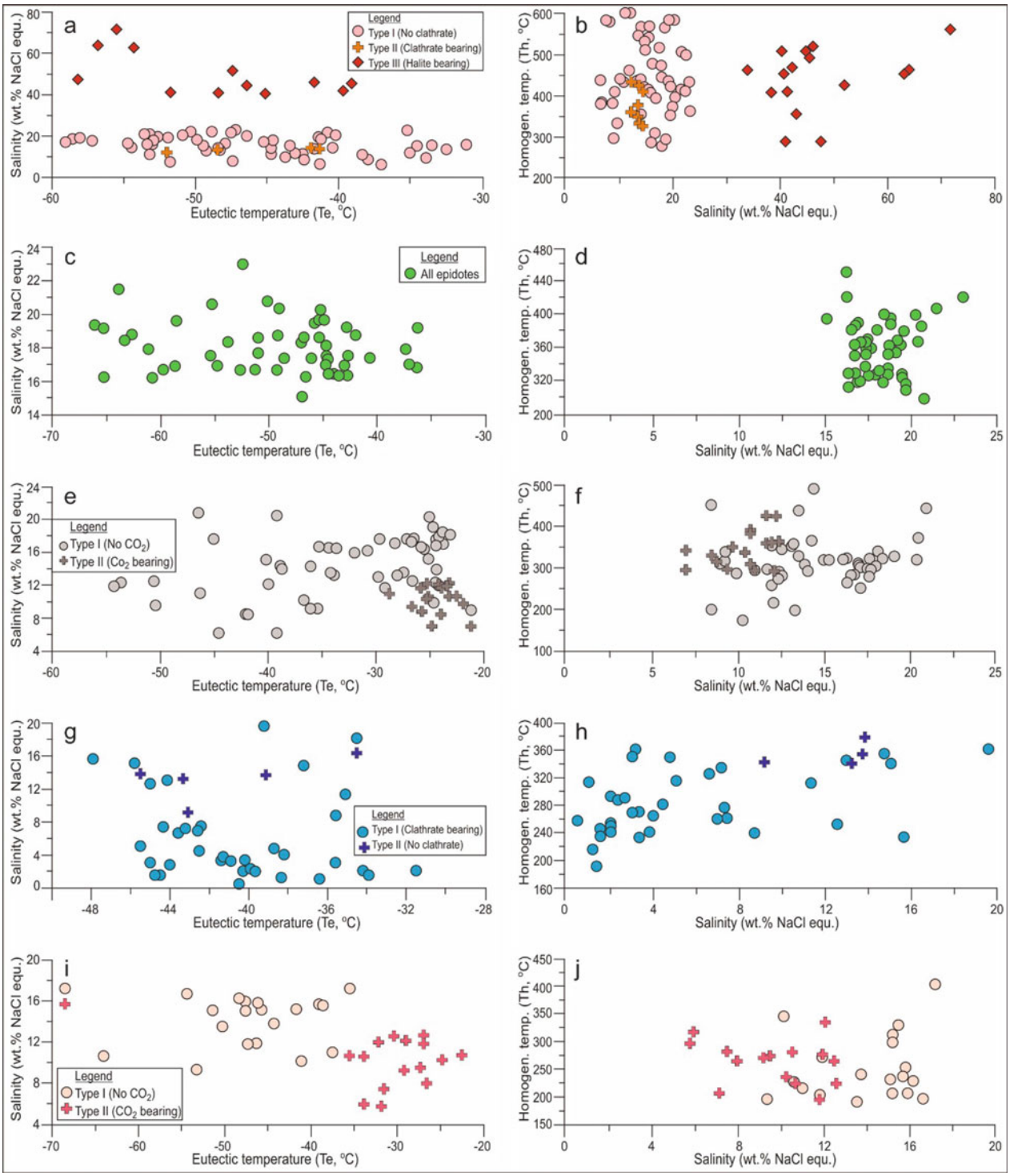

Fig. 1 Microthermometric measurements of the fluid inclusions (a) eutectic temperature versus salinity in garnet, (b) homogenization temperature versus salinity in garnet, (c) eutectic temperature versus salinity in epidote, (d) homogenization temperature versus salinity in epidote, (e) eutectic temperature versus salinity in calcite, (f) homogenization temperature versus salinity in calcite, (g) eutectic temperature versus salinity in quartz, (h) homogenization temperature versus salinity in quartz, (i) eutectic temperature versus salinity in sphalerite, and (j) homogenization temperature versus salinity in sphalerite

salinity values ranging from 9.19 to 13.86 °C. Also, the Te of fluid inclusions in sphalerite varied from −64.0 to −22.5 °C (Fig. 1e) with Tm-ice values from −12.9 to −6.1 °C. The salinity values (9.34–17.2 wt% NaCl equ.) are lower than that of all the other minerals except calcite. The Th values are also lower (192–404 °C) (Fig. 1e). Clathrate formed in some fluid inclusions of sphalerite has melting temperatures and salinity values varying from 2.50 to 7.00 °C and 5.76 to 12.6 °C, respectively. The CO_2 phase in the sphalerite is characterized by CO_2 melting temperatures ($TmCO_2$) and CO_2 homogenization ($ThCO_2$) temperatures in the range of −57.1 to −56.1 °C and 17.7 to 30.6 °C, respectively.

4 Discussion

Skarn deposits commonly form along the contact between intrusive bodies and carbonate host rocks. In this regard, diverse metasomatic processes that involve fluids derived from magmatic, metamorphic, meteoric, and marine sources have been suggested for skarn formation (Baker & Lang, 2003). These studies indicate that high salinity fluid inclusions are mostly derived from magmatic sources, whereas low salinity fluid inclusions are typically derived from a mixture of magmatic and other reservoir solutions. Furthermore, the lower salinity values of the fluid inclusions in all the investigated minerals of samples from the skarn deposits in the study area indicate that the fluids evolved from a magmatic origin and later mixed with meteoric fluids during their ascent.

Comparing the Te temperatures of fluid inclusions with the specific salt combination and according to Hein (1989), it was found that the fluid composition was predominantly H_2O-NaCl-$CaCl_2$. The volcano-sedimentary sequences dominated by limestone and dolomite units are the only reason for the $CaCl_2$-rich early-stage inclusions. The change from $CaCl_2$-rich first-stage inclusions to a mixture of salt solutions in the later stages indicates that the interaction of the hydrothermal solutions with the carbonate host rocks was high at the onset of skarnization. The continuous evolution of the fluids in the skarn deposits also indicates that the hydrothermal solutions contain relatively higher Th and salinity values at the early stages of skarn formation due to interaction between fluids derived from magmatic sources and carbonaceous limestones and dolomites. However, the Th and salinity values gradually reduced as the system was opened to influence from meteoric water infiltration during the later stage (prograde to retrograde stage) (Wilkinson, 2001).

5 Conclusions

From the fluid inclusion studies, it is proposed that the formation of the skarn deposits started with the exsolution of relatively high saline fluids (up to 600 °C) from a deep-seated pluton. Then, the magmatic fluids from the deep-seated pluton ascended along major faults and began interacting with the host limestones, dolomites, and marble–schist rocks to form the skarn. Later, reactivation of the faults redirected ore-forming fluids through the same pathways to replace the skarn and host rocks under a moderately high oxidation state to form magnetite–sphalerite-dominated Fe-Zn ore bodies in the area.

References

Baker, T., & Lang, J. R. (2003). Reconciling fluid inclusion types, fluid processes, and fluid sources in skarns: An example from the Bismark deposit Mexico. *Mineralium Deposita, 38*, 474–495.

Bodnar, R. J. (1993). Revised equation and table for determining the freezing point depressionof H_2O-NaCl solutions. *Geochimica et Cosmochimica Acta*, *57,* 683–684.

Çiftçi, E., Lermi, A., Gosh, N., & Basu, A. (2014). Carbonate-hosted gallium-bearing lead-zinc deposits of tauride belt (Turkey): Genetic implications. *Acta Geologica Sinica* (*English Edition*), *88*(2), 147–147.

Darling, R. S. (1991). An extended equation to calculate NaCl contents from final clathrate melting temperatures in H_2O-CO_2-NaCl fluid inclusions: Implications for P-T isochore location. *Geochimica et Cosmochimica Acta*, *55*(12), 3869–3871.

Demir, Y., Uysal, I., Kandemir, R., & Jauss, A. (2017). Geochemistry, fluid inclusion and stable isotope constraints (C and O) of the Sivrikaya Fe-skarn mineralization (Rize, NE Turkey). *Ore Geology Reviews, 91*, 153–172.

Hein, U. F. (1989). Microthermometry. Compact course and exercises, IGDL, University of Göttingen, 52 p.

Kuşcu, İ. (2019). Skarns and Skarn deposits of Turkey. In *Mineral resources of Turkey* (pp. 283–336). Springer.

Wilkinson, J. J. (2001). Fluid inclusions in hydrothermal ore deposits. *Lithos, 55*, 229–272.

Effect of Different Basis Sets on the Theoretical Calculation of Zinc Isotope Fractionation of Zn Complexes

Yang Zhao and Yongbing Li

Abstract

Isotope fractionation of zinc between $Zn(H_2O)_6^{2+}$, $ZnCl(H_2O)_5^{+}$, $ZnCl_2(H_2O)_4$, $ZnCl_3(H_2O)^{-}$, $ZnCl_4^{2-}$, $ZnHCO_3(H_2O)_3^{+}$, $ZnCO_3(H_2O)_3$, $Zn(OH)_2(H_2O)_4$, and $ZnSO_4(H_2O)_5$ was explored by DFT method in this study, as well as the optimized structures, vibrational frequencies. These complexes were calculated by mixed basis sets LanL2DZ/6–311 + G(d, p) and def2-TZVP/6–311 + G(d, p). The results show that the optimized bond lengths calculated by mixed basis sets are more extensive than previous data, and the calculated vibrational frequencies are smaller than experimental values. Furthermore, the mixed basis sets lead to larger reduced partition function rations (RPFR) than 6–311 + G(d, p) basis set. Therefore, combining the calculated vibrational results with previous studies and experimental data, the def2-TZVP/6–311 + G(d, p) basis set may be more suitable for calculating Zn isotope fractionation.

Keywords

Zn complexes • Zn isotope fractionation • Density functional theory • Basis sets

1 Introduction

Zinc complexes, such as Zn hydrate, chloride, carbonate, hydroxide, and sulfate, are essential inorganic complexes in nature. The Zn isotope fractionation in these complexes plays an important tracing role in geochemistry fields (e.g., hydrothermal fluids, seawater, and soil–plant systems). Therefore, it has been studied experimentally and theoretically in recent years. However, the effect of different basis sets on the theoretical calculation of Zn isotope fractionation has not been studied. Here, we aimed to explore the impact of varying basis sets on the structures, vibrational frequencies, and reduced partition function rations (RPFR) of selected Zn complexes (Tables 1 and 2).

2 Theory and Methods

Density functional theory (DFT) was used to study the isotope fractionation of Zn complexes, $Zn(H_2O)_6^{2+}$, $ZnCl(H_2O)_5^{+}$, $ZnCl_2(H_2O)_4$, $ZnCl_3(H_2O)^{-}$, $ZnCl_4^{2-}$, $ZnHCO_3(H_2O)_3^{+}$, $ZnCO_3(H_2O)_3$, $Zn(OH)_2(H_2O)_4$,and $ZnSO_4(H_2O)_5$. Here, the Gaussian 09 (Dennington et al., 2009; Frisch et al., 2009) was used to calculate the geometries optimization, vibrational frequencies, and isotope fractionation of Zn complexes. Becke-style 3-parameter (B3) with the Lee–Yang–Parr (LYP) correlation functional (Lee et al., 1988; Becke, 1993a, 1933b) and mixed basis sets (LanL2DZ/6–311 + G(d, p) and def2-TZVP/6–311 + G(d, p)) was used, where LanL2DZ is effective core potential (ECP) basis set, and def2-TZVP and 6–311 + G(d, p) are all-electron basis sets. LanL2DZ or def2-TZVP basis sets were used for Zn, and 6–311 + G(d, p) was used for other elements.

3 Results

Tables 1 and 2 give the optimized bond lengths of Zn complexes. The results show that most of the bond lengths calculated by LanL2DZ/6–311 + G(d, p) are larger than that by def2-TZVP/6–311 + G(d, p), and the results calculated by the two mixed basis sets are larger than the previous study calculated by 6–311 + G(d, p).

Table 3 gives the totally symmetric vibrational frequencies of Zn aqueous and chloride complexes. According to

Y. Zhao · Y. Li (✉)
College of Earth and Planetary Sciences, University of Chinese Academy of Sciences, Beijing, 100049, China
e-mail: yongbingli@ucas.ac.cn

A. Çiner et al. (eds.), *Recent Research on Sedimentology, Stratigraphy, Paleontology, Tectonics, Geochemistry, Volcanology and Petroleum Geology*, Advances in Science, Technology & Innovation,
https://doi.org/10.1007/978-3-031-43222-4_25

Table 1 Optimized bond lengths (Å) of Zn aqueous and chloride complexes

Basis sets	$Zn(H_2O)_6^{2+}$	$ZnCl(H_2O)_5^{+}$		$ZnCl_2(H_2O)_4$		$ZnCl_3(H_2O)^{-}$		$ZnCl_4^{2-}$
	Zn–O	Zn–O	Zn–Cl	Zn–O	Zn–Cl	Zn–O	Zn–Cl	Zn–Cl
LanL2DZ/ 6–311 + G(d, p)	2.15	2.21,2.16,2.20,2.22	2.30	2.24	2.36	2.30	2.35,2.29	2.42
def2-TZVP/ 6–311 + G(d, p)	2.13	2.21,2.14,2.20,2.24	2.24	2.26	2.30	2.37	2.30,2.24	2.37
6–311 + G(d, p)[a]	2.13	2.21, 2.13	2.23	2.25	2.30	2.39	2.29,2.23	2.37

[a] Fujii et al. (2010)

Table 2 Optimized bond lengths (Å) of Zn sulfate and hydroxide complexes

Basis sets	$ZnSO_4(H_2O)_5$		$Zn(OH)_2(H_2O)_4$		$ZnHCO_3(H_2O)_3^{+}$		$ZnCO_3(H_2O)_3$	
	Zn–O	Zn–S	Zn–OH	$Zn–OH_2$	Zn–O	Zn–C	Zn–O	Zn–C
LanL2DZ/6–311 + G(d, p)	2.12, 2.23, 2.17, 2.07	3.10	2.02	2.02, 2.25, 2.30	2.10, 2.09, 2.07	2.40	2.09, 1.97, 2.13,2.14	2.46
def2-TZVP/6–311 + G(d, p)	2.10, 2.24, 2.16, 2.03	3.05	1.97	2.26, 2.36, 2.36	2.09, 2.08, 2.07	2.39	2.07, 1.94, 2.12,2.13	2.44

Table 3 Totally symmetric vibrational frequencies of Zn $(H_2O)_6^{2+}$ and $ZnCl_4^{2-}$ complexes

Species	Basis sets	Frequency	Reference
Zn $(H_2O)_6^{2+}$	LanL2DZ/6–311 + G(d, p)	327.04	This study
	def2-TZVP/6–311 + G(d, p)	336.64	This study
	6–311 + G(d, p)	333.4	Fujii et al. (2010)
	Raman	379 ± 5	Yamaguchi et al. (1989)
$ZnCl_4^{2-}$	LanL2DZ/6–311 + G(d, p)	218.61	This study
	def2-TZVP/6–311 + G(d, p)	233.45	This study
	6–311 + G(d, p)	230.9	Fujii et al. (2010)
	Raman	279–289	Yamaguchi et al. (1989)

Table 3, the theoretically calculated values are smaller than the experimental ones. For example, the frequencies of Zn $(H_2O)_6^{2+}$ and $ZnCl_4^{2-}$ calculated by the two mixed basis sets are 327.04 cm^{-1} and 218.61 cm^{-1}, 336.64 cm^{-1} and 233.45 cm^{-1}, respectively. This means that the vibrational frequencies calculated by LanL2DZ/6–311 + G(d, p) are smaller than that by def2-TZVP/6–311 + G(d, p), and the vibrational frequencies results calculated by 6–311 + G (d, p) are in the middle of the two mixed basis sets.

Table 4 gives the calculated RPFR values of Zn complexes at 298K computed using 6–311 + G(d, p), LanL2DZ/6–311 + G(d, p), and def2-TZVP/6–311 + G(d, p) basis sets. The results show that the RPFR values of Zn species calculated by mixed basis sets are larger than previous results calculated by 6–311 + G(d, p) basis set, and the RPFR values of $Zn(H_2O)_6^{2+}$, $ZnCl(H_2O)_5^{+}$, $ZnCl_2(H_2O)_4$, $ZnSO_4(H_2O)_5$, $ZnHCO_3(H_2O)_3^{+}$ calculated by LanL2DZ/6–311 + G(d, p) are larger than those by def2-TZVP/6–311 + G(d, p). In addition, the orders of isotope fractionation calculated by different basis sets are also different.

4 Discussion

Different basis sets may cause the deviation of the optimized structures, vibrational frequencies, and RPFR values. Comparing the calculated results of selected Zn species by this study with the previous theoretical results and experimental data shows that the optimized bond lengths calculated by the mixed basis sets are larger than previous results calculated by the 6–311 + G(d, p) basis set. Furthermore, the theoretical vibrational frequencies are smaller than experimental values, and the vibrational frequency results calculated by 6–311 + G(d, p) are in the middle of the two mixed basis sets. Frequency is one of the most affected factors that may cause errors in the calculated RPFR values. Thus, the deviation of calculated vibrational frequencies and experimental data may lead to an error between theoretical and experimental results. For RPFR values, the mixed basis sets lead to larger results than the 6–311 + G(d, p) basis set, even in different RPFR order.

Table 4 Calculated $10^3\ln(\beta_{66-64})$ for Zn complexes at 298 K calculated by 6–311 + G (d, p), LanL2DZ/6–311 + G (d, p) and def2-TZVP/6–311 + G(d, p) basis sets

Species	Basis sets		
	6–311 + G(d, p)[a]	LanL2DZ/6–311 + G(d, p)[b]	def2-TZVP/6–311 + G(d, p)[b]
$Zn\ (H_2O)_6^{2+}$	3.263	3.572	3.369
$ZnCl\ (H_2O)_5^{+}$	3.136	3.332	3.230
$ZnCl_2(H_2O)_4$	2.950	3.143	3.020
$ZnCl_3(H_2O)^{-}$	2.952	2.894	3.062
$ZnCl_4^{2-}$	2.293	2.339	2.450
$ZnSO_4(H_2O)_5$	3.527	3.776	3.642
$Zn(OH)_2(H_2O)_4$	3.567	3.585	3.637
$ZnHCO_3(H_2O)_3^{+}$	3.877	4.059	3.981
$ZnCO_3(H_2O)_3$	4.199	4.257	4.287

[a] Fujii et al. (2014)
[b] This study

5 Conclusions

Our calculated results show that setting different basis sets for Zn complexes can cause differences in optimized structures, vibrational frequencies, and isotope fractionation. For example, comparing the three kinds of frequencies calculated by three basis sets with the experimental ones shows that def2-TZVP/6–311 + G(d, p) basis set may be more suitable for calculating Zn isotope fractionation.

References

Becke, A. D. (1993). A new mixing of Hartree-Fock and local densityfunctional theories. *The Journal of Chemical Physics, 98*, 1372–1377.

Becke, A. D. (1993a). Density-functional thermochemistry. III. The role of exact exchange. *Journal of Chemical Physics, 98*, 5648–5652.

Dennington, R., Keith, T., & Millam, J. (2009). GaussView, Version 5.0.8. SemichemInc., Shawnee Mission, KS.

Frisch, M. J., Trucks, G. W., & Schlegel, H. B., et al. (2009). Gaussian 09, Revision A.01. Gaussian, Inc., Wallingford, CT.

Fujii, T., Moynier, F., Telouk, P., & Abe, M. (2010). Experimental and theoretical investigation of isotope fractionation of zinc between aqua, chloro, and macrocyclic complexes. *Journal of Physical Chemistry A, 114*(7), 2543–2552.

Fujii, T., Moynier, F., Blichert-Toft, J., & Albarède, F. (2014). Density functional theory estimation of isotope fractionation of Fe, Ni, Cu, and Zn among species relevant to geochemical and biological environments. *GeochimCosmochim Acta, 140*, 553–576.

Lee, C., Yang, W., & Parr, R. G. (1988). Development of the Colle-Salvetti correlation-energy formula into a functional of the electron density. *Physical Review B, 37*, 785–789.

Yamaguchi, T., Hayashi, S., Ohtaki, H. (1989) X-ray diffraction and raman studies of zinc(II) chloride hydrate melts, $ZnCl_2/RH_2O$ (R≈1.8, 2.5, 3.0, 4.0, and 6.2). *Journal of Physical Chemistry, 93*, 2620.

Lead Mineralization in Carbonate Rocks Jamrud, District Khyber, Pakistan

Asghar Ali, Sajid Ali, Salman Akbar, Aamir Azad, Aasim Danish, Rafique Ahmad, and Liaqat Ali

Abstract

Sulfide vein, fluorite vein, brecciated wall rock, and host rock were analyzed using X-ray Diffraction (XRD). The XRD qualitative analyses of samples collected from brecciated wall rock and sulfide vein consist of goethite, dolomite, calcite, quartz, and galena. The host rock contains dolomite and calcite. A fluorite vein NW of the lead sulfide mineralization zone consists of fluorite, calcite, sodalite, quartz, and localized well-crystalline malachite grains. Lead sulfide mineralization is largely controlled by vein and brecciated wall rocks, with less lateral extension in the host Khyber Limestone. Petrological, geochemical, micro to mesoscopic structures, carbonate host rocks, and associated fluorite suggest that this mineralization agrees with the characteristics of Mississippi Valley Type (MVT) deposits.

Keywords

Sulfide • Fluorite • Khyber limestone • MVT

1 Introduction

Ore genesis occurs in strata-bound, magmatic, skarn, sedimentary, and metamorphic environments. Metal enrichment in these deposits takes place through different types of hydrothermal circulation. Due to ore-laden fluid circulation within sedimentary basins, the strata-bound deposits are confined to a particular stratigraphy and region. These deposits preserve in dilation sites, including veins, brecciated stratigraphic units, pipes, and flats. An MVT deposit is an epigenetic ore deposit that forms in sedimentary basins by hydrothermal fluid flow. The sedimentary diagenetic or syngenetic ore deposits are usually called sedimentary exhalative deposits. The Mississippi Valley sphalerite, galena, fluorite, and barite deposits are worldwide mined from the Phanerozoic carbonate rocks. However, an insufficient quantity or number is reported in Precambrian rocks (Edwards & Atkinson, 1986; Stanton, 1972). The MVT deposits association with coral debris suggests that these deposits form at low latitudes and warmer climates. The coral debris provides initial high porosity and permeability to fluid circulation within sedimentary basins (Badham, 1981; Dunsmore & Shearman, 1977). The MVT deposits commonly contain more sphalerite than galena, fluorite, and barite. However, sometimes galena concentration increases from sphalerite. Therefore, Evans (1993) included all carbonate-hosted low-temperature epigenetic sulfides, barite, and fluorite in the MVT deposits. These deposits are the most significant source of the world's lead and zinc production. Around 85% of lead in the USA is mined from Mississippi Valley Type deposits (Vineyard, 1977). Therefore, these deposits are appealing and lucrative for large- and small-scale metal-based industries worldwide. The Silurian–Devonian Khyber Limestone contains sporadic galena, barite, and fluorite occurrences. This research focuses on understanding the nature of sulfide mineralization in the Khyber Limestone through geochemical and petrographic investigations.

2 Regional Geology

The E–W trending Himalayan mountain belt culminated at the northernmost plate margin of the Indian Plate. This gigantic orogenic belt formed due to the collision of the

A. Ali (✉) · S. Ali · S. Akbar · A. Azad · A. Danish
Department of Geology, University of Peshawar, Peshawar, Pakistan
e-mail: asghar.ali@uop.edu.pk

R. Ahmad
Department of Geology, Bacha Khan University Charsadda, Charsadda, Pakistan

L. Ali
National Center of Excellence in Geology, University of Peshawar, Peshawar, Pakistan

A. Çiner et al. (eds.), *Recent Research on Sedimentology, Stratigraphy, Paleontology, Tectonics, Geochemistry, Volcanology and Petroleum Geology*, Advances in Science, Technology & Innovation,
https://doi.org/10.1007/978-3-031-43222-4_26

Indian Plate with the Kohistan Island Arc during the Cenozoic (Larson et al., 2018). It extends from Bhutan in the east through Nepal, India, and Pakistan into Afghanistan to the west (Gansser, 1981). The Khyber Range, where the current research has been taken, forms the western portion of the Higher Himalaya (Fig. 1). It is bounded by the Main Mantle Thrust in the north and Khairabad/Panjal Thrust in the south. Concordant and discordant dolerite intrusions in the Khyber Ranges are associated with the Permian rifting before the Indian plate separation from the Gondwanaland.

3 Materials and Methods

3.1 Petrography

Detailed petrographic analyses were carried out on 25 specimens to understand rocks composition, depositional environment, alteration around epigenetic mineralization, and primary to secondary textures. These specimens were collected from carbonate rocks, dolerite dikes, sulfide-laden veins, fluorite veins, and sulfide-mineralized wall rocks (Fig. 2). Systematically collected samples from the sulfide vein walls confirm opaque minerals enrichment toward the vein axis. The wall rocks are mesoscopically brecciated. Sulfide nucleation in the brecciated mass indicates hydrothermal solution flow in the more porous medium of the host rock.

3.2 X-ray Diffraction (XRD)

Qualitative analyses of different mineral phases in sulfide-mineralized zone, host, and brecciated wall rocks are carried out using XRD. S 17, BG 3, BG 7, S 22, SF 9, and SF 10 were analyzed with XRD operating conditions of generator voltage 45 V, tube current 40 A, anode material Cu, monochromator absent, K-Alpha wavelength 1.542512. The results of XRD analyses are shown in Fig. 3.

4 Results and Discussion

4.1 Lead Mineralization Associated with Carbonate Rocks

The MVT deposits that mainly occur in the foreland basins are globally reported from the Middle to Late Paleozoic rocks of the supercontinent Pangaea reaching 61% of lead and zinc content in the dated MVT deposits (Leach et al., 2001). In these period rocks, the MVT deposits are commonly associated with fluorite and barite mineralization (Leach, 1980). The occurrence of lead sulfide mineralization in the form of galena in Khyber Limestone of Devonian age and its association with fluorite and barite indicates that the ore body most probably belongs to the MVT deposit. Barite mined from Ali Masjid region located at ~ 5–6 km NW of the lead mineralized zone (Fig. 1). The Khyber limestone

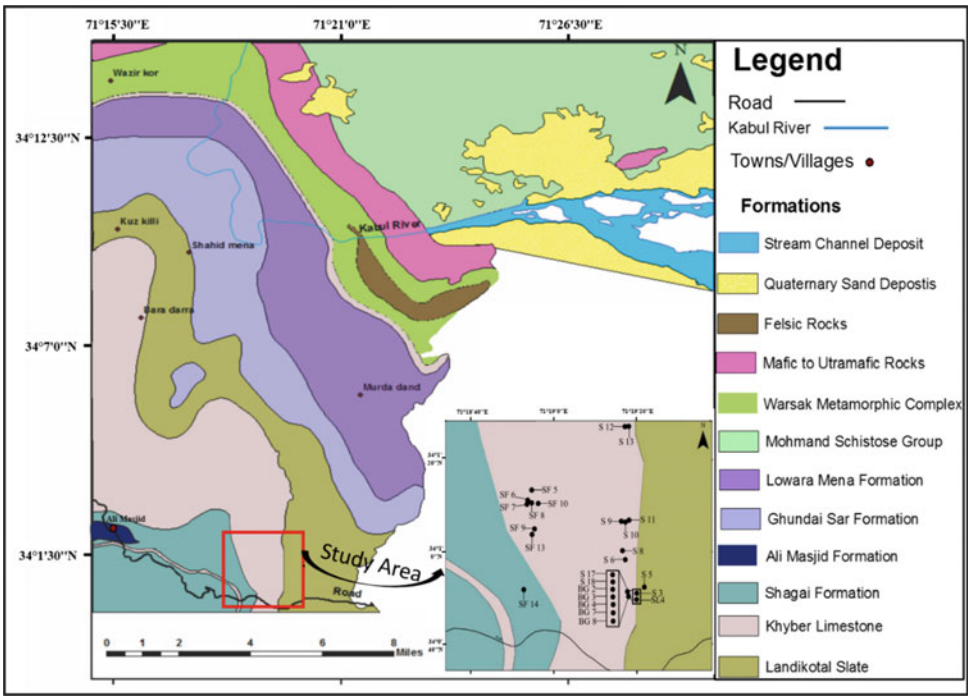

Fig. 1 Regional geological map of the Paleozoic rocks exposed in Khyber and Mohmand districts. Red square and black dots show the study area and sample locations (modified after the Geological Survey of Pakistan, 1995)

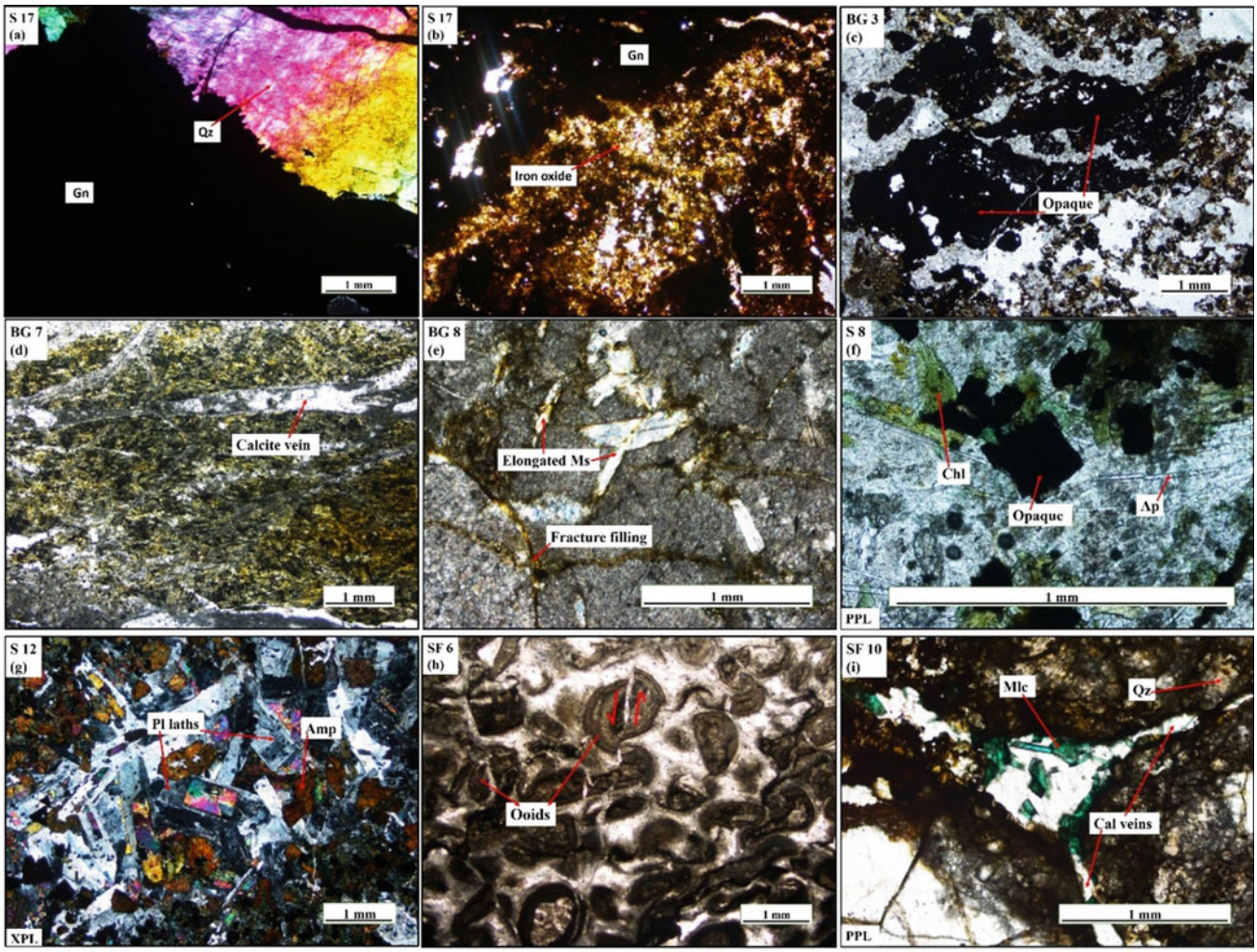

Fig. 2 Photomicrographs showing galena mineralization hosted within Khyber Limestone in a brecciated wall rock, relative changes in sulfide mineralization along the wall rocks of galena vein, mineral phases in dolerite dikes, ooids, and malachite crystals. The concentration of galena decreases away from the main mineralized fracture zone. **a** galena surrounded by quartz grains. The tiny white dots in the galena are quartz inclusions; **b** iron oxides crystallized into hematite around the mineralized zone; **c** sample BG 3, representing the immediate left side of wall rock, is altered more and contains a greater number of opaque minerals as compared to rest of wall rock samples; **d**, **e** BG 7 and BG 8 showing fracture filled by calcite and elongated muscovite around the mineralized zone; **f** chlorite nucleated in pyroxene and amphibole grains, elongated apatite needle growth in the matrix. Apatite grew in a groundmass of the rock and protruded to pyroxene, amphibole, and plagioclase grains; **g** photomicrograph showing well-developed ophitic texture, large crystals of pyroxene and amphibole enclosed randomly oriented euhedral plagioclase laths. Note the ophitic texture characteristically occurs in dolerite phaneritic intrusion; (h) photomicrograph showing different shapes of ooids present within the carbonate matrix. Some dislocation can also be observed, which has divided ooids into two parts and moved them apart; (i) photomicrograph showing green-colored malachite crystals along veins, calcite, and malachite-filled fractures. Malachite crystals grow from wall rocks to the fracture cavity

grades into marble at several horizons, which indicates recrystallization of limestone. It overlies the Shagai Formation argillaceous rocks with a faulted contact. The Ghundi Sar reef complex lies in its north (Fig. 1). The MVT deposits form at low latitudes, and warmer climates often occur close to reefal carbonates (Dunsmore & Shearman, 1977). The occurrence of ooids in the Khyber limestone also indicates a shallow marine environment and warmer climate. The MVT ores are deposited along lithological transitions where vertical and lateral permeability variations exist in the carbonate sequence, common in reef and barrier complexes. It also includes facies transition from shale to carbonate, sandstone to carbonates, and limestone to dolostone. Argillaceous units act as barriers to fluid migration within a stratigraphic sequence. The presence of shallow marine carbonates, coral reefs, and intercalated shales in the Silurian to Devonian rocks of Jamrud, district Khyber confirms the presence of suitable rock variations in the region for hosting MVT deposits.

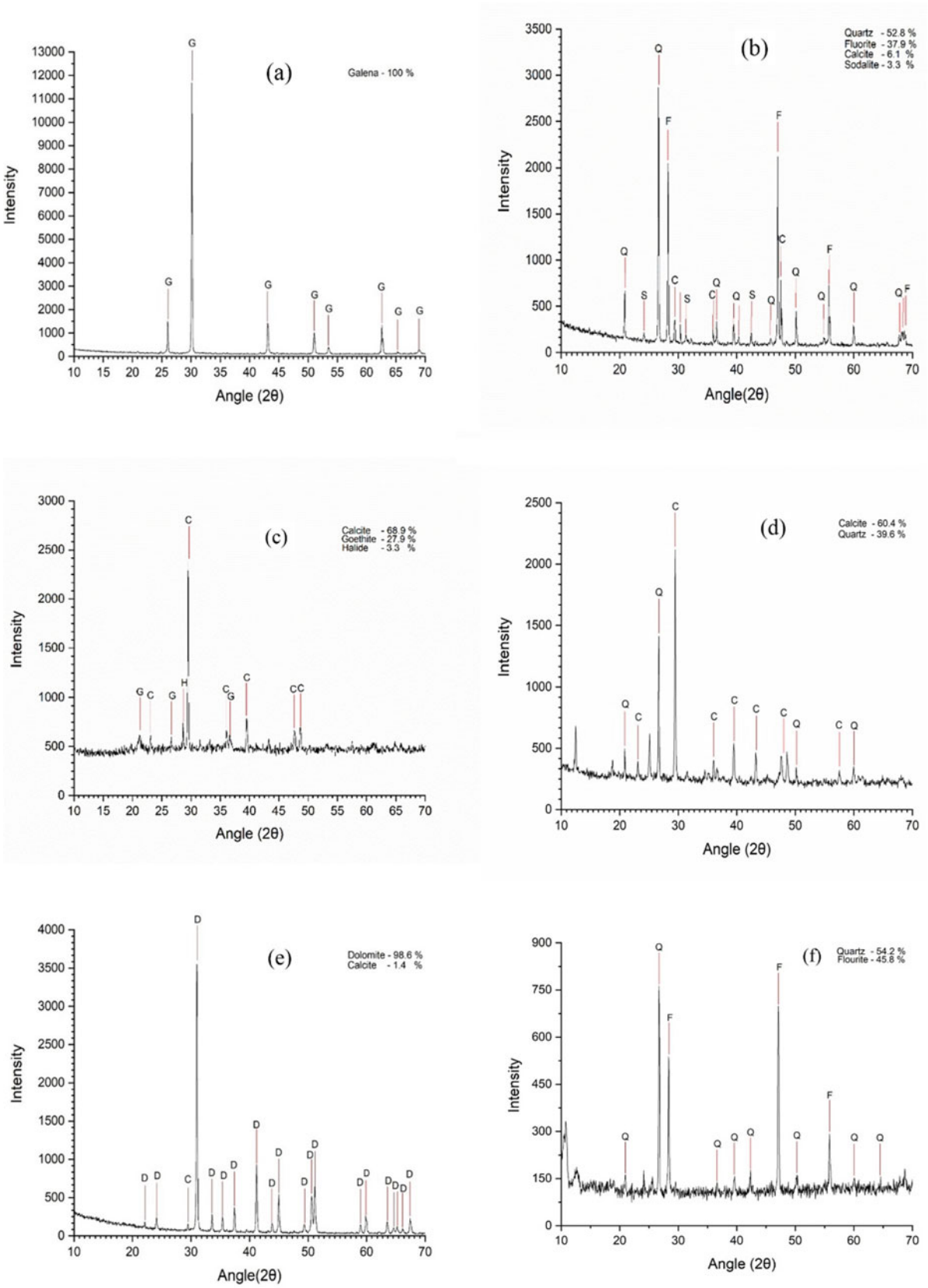

Fig. 3 XRD graphs **a** sample S 17 collected from a galena mineralized zone representing galena (G), **b** sample SF 10 obtained from a fluorite mineralized zone contains fluorite (F), quartz (Q), calcite (C), and sodalite (S), **c** sample BG 3 taken from the brecciated wall rocks showing goethite (G), calcite (C) and halide (H), **d** sample BG 7 collected from wall rock showing calcite (C) and quart (Q). In addition, the presence of quartz gives a siliceous limestone signature to the rock, **e** sample S 22 collected from host carbonate showing dolomite (D) and calcite (C), **f** sample SF 9 collected from fluorite mineralized zone showing fluorite (F) and quartz (Q) peaks

4.2 Carbonate Host Rocks

The Khyber Limestone hosted MVT deposit occurs in a very high micro to mesoscopic fractured and brecciated structure. The deposit contains very high-grade galena as indicated by XRD qualitative peaks (Fig. 3a). The XRD analyses of samples SF 9 and SF 10 collected from fluorite mineralized zones show quartz, fluorite, and quartz, fluorite, calcite, and sodalite, respectively (Fig. 3b, f). Samples BG 3 and BG 7 collected from lead sulfide wall rock indicate high-intensity peaks of calcite (Fig. 3c, d). The XRD analysis of S 22 gives dolomite high-intensity peaks with minor calcite (Fig. 3e), which geochemically indicates that some part of the host rock has been altered to dolomite. The same has been reported by McKnight and Fischer (1970) from the Tri-State district, where the host limestone rocks crystallized to dolomite. Fractured and brecciated carbonates near coral reefs with both secondary and primary porosity and permeability are highly favorable sites for MVT ore bodies. MVT is often restricted to dolomite compared to limestone (Leach et al., 2005). Extensive dolomite is determined in XRD graphs (Fig. 3e). MVT deposits are usually characterized by dolomite and calcite alterations (McKnight & Fischer, 1970). These alterations were frequently observed across and along the sulfide-mineralized zone through changes in color, composition, and texture (Fig. 2).

4.3 Source of Sulfur

Sulfur-rich organic materials, connate seawater, SO_4 bearing evaporates, H_2S reservoir gas, diagenetic sulfate, and reduced sulfur in anoxic waters of stratified basins are considered sources for sulfur in MVT deposits (Deng et al., 2017; Leach et al., 2005; Ohmoto & Rye, 1979; Sangster, 1990). Recent field investigations during this study have identified organic-rich shale beds in the Khyber Limestone. The sulfur-rich organic shale bed is at ~ 2 km NW of the lead mineralized zone. It has been presumed that sulfur preserved in the organic shale beds could be one of the potential sources of sulfur for lead sulfide mineralization in the region. The sulfur from the source could be transported as part of the basinal brines deposited along the fractures and brecciated zone (cf. Leach et al., 2005).

5 Conclusions

Very similar in characteristics to many studied MVT deposits in the world, Jamrud sulfide deposits of this study constitute dominantly galena, whereas sphalerite is absent. We conclude these studied sulfide deposits by referring to them as MVT ore deposits based on the following evidence:

(1) Hosted by a fractured and brecciated part of carbonate rocks. (2) Presence of coral reef and ooids in the north of the sulfide-mineralized zone. (3) In the vicinity of these sulfide deposits, fluorite, barite, and traces of copper in malachite are associated closely with MVT ore deposits. (4) Presence of lithological transitions in the studied area from shale to limestone and limestone to dolostone adds more focus to calling studied sulfide mineralization an MVT deposit. (5) Host rocks belong to the geological time frame where about 61% of MVT ore deposits formed. (6) The organic-rich shale bed located at ~ 2 km NW of the lead mineralized zone indicates that it might have provided sulfur for forming this sulfide ore mineralization in Khyber district, one of the critical factors for MVT ore deposition.

References

Badham, J. P. N. (1981). The origins of ore deposits in sedimentary rocks. In D. H. Tarling (Ed.), *Economic geology and geotectonics* (pp. 149–191). Blackwell Scientific Publications.

Deng, J., Wang, C., Bagas, L., Selvaraja, V., Jeon, H., Wu, B., & Yang, L. (2017). Insights into ore genesis of the Jinding Zn–Pb deposit, Yunnan Province, China, Evidence from Zn and in-situ S isotopes. *Ore Geology Reviews, 90*, 943–957.

Dunsmore, H. E., & Shearman, D. (1977). Mississippi Valley-type lead-zinc orebodies, a sedimentary and diagenetic origin. In P. Garrard (Ed.), *Forum on oil and ore in sediments* (pp. 189–201). Imperial College.

Edwards, R., & Atkinson, K. (1986). *Ore Deposit Geology, and its influence on mineral exploration.* London and New York.

Evans, A. M. (1993). In ore geology and industrial minerals: An introduction. In A. M. Evans (Ed.), (Vol. 3, pp. 403). Blackwell.

Gansser, A. (1981). The geodynamic history of the Himalaya. In *Zagros Hindu Kush Himalaya geodynamic evolution*, 3rd edn. pp. 111−121.

Regional geological map of the Jamrud quadrangle, Khyber agency, NWFP, Pakistan.

Larson, K., Ali, A., Shrestha, S., Soret, M., Cottle, J. M., & Ahmad, R. (2018). Timing of metamorphism and deformation in the Swat valley, Northern Pakistan, Insight into garnet-monazite HREE partitioning. *Geoscience Frontiers, 10*, 849–861.

Leach, D. L. (1980). Nature of mineralizing fluids in the barite deposits of central and southeast Missouri. *Economic Geology, 75*, 1168–1180.

Leach, D. L., Bradley, D., Lewchuk, M. T., Symons, D. T., Marsily, G. D., & Brannon, J. (2001). Mississippi Valley-Type lead-zinc deposits through geological time, implications from recent age-dating research. *Mineralium Deposita, 36*, 711–740.

Leach, D. L., Sangster, D. F., Kelley, K. D., Large, R. R., Garven, G., Allen, C. R., Gutzmer, J., & Walters, S. (2005). Sediment-hosted lead-zinc deposits: A global perspective. *Society of Economic Geologists, Economic Geology One Hundredth Anniversary, 1905–2005*, 561–607.

McKnight, E. T., & Fischer, R. P. (1970). Geology and ore deposits of the Picher Field, Oklahoma and Kansas: US Geological Survey Professional Paper, Report P 0588. 165.

Ohmoto, H., & Rye, R. O. (1979). Isotopes of sulfur and carbon. In H. L. Barnes (Ed.), *Geochemistry of hydrothermal ore deposits* (2nd ed., pp. 509–567). Wiley.

Sangster, D. F. (1990). Mississippi Valley-type and Sedex lead zinc deposits—A comparative examination. *Applied Earth Science: Transactions of the Institutions of Mining and Metallurgy: Section B, 99*, 21–42.

Stanton, R. L. (1972). *Ore petrology*. McGraw-Hill.

Vineyard, J. D. (1977). In preface to the issue devoted to the Viburnum Trend SE Missouri. *Economic Geology, 72*(3), 337–338.

Microfaciological Characterization of Calcareous Crusts of Pleistocene Moghrebian Strata in the Coastal Basin of Tarfaya (Morocco): Paleoclimatic Implications

Fatima Jira and Abdallah Lakhouili

Abstract

The Pleistocene Moghrebian strata in the Tarfaya (Morocco) coastal basin comprise alternating beds of conglomerate, lumachelle, sandstone, calcarenite, and a calcareous crust on the surface. The diagenetic evolution of the Moghrebian strata is very precocious. It is characterized by the dissolution of bioclasts, the crystallization of microsparitic calcite, and the corrosion of quartz in the crust due to the over-saturation of the medium with calcium carbonate. Supersaturation of the environment with calcium carbonate has promoted the development of a calcareous crust on the surface of the Mogrebian strata by isovolumetric epigeny of the initially deposited detrital material. This calcification has occurred in a climate of alternating wet and dry seasons, where wet seasons are characterized by the dissolution of quartz and dry seasons are characterized by intense evaporation, the crystallization of calcite in quartz corrosion concavities, and the neoformation of palygorskite and sepiolite. The fine fraction of the different beds are characterized by the following clay minerals: chlorite, illite, kaolinite, smectite, interlayered clay (chlorite-smectite, chlorite-vermiculite, vermiculite-smectite), and fibrous clay (palygorskite and sepiolite) of detrital origin. Palygorskite and sepiolite occur as detrital clays in all the studied beds and as newly formed clays in the superficial calcareous crusts.

Keywords

Moghrebian • Palygorskite • Crystallization • Crust • Neoformation • Tarfaya • Epigeny • Pleistocene

1 Introduction

The coastal basin of Tarfaya is located on the western margin of the Sahara platform in North Africa. The Atlantic Ocean borders the basin to the North-West and West, the South Atlas Range to the East and South-East, and the Sebkha Et-Tah to the south (Fig. 1). Lower Pleistocene conglomerate, sandstone, lumachelle, and limestone beds are collectively called the Moghrebian strata (Choubert, 1957).

The lithostratigraphic data (Choubert et al., 1966) from the Tarfaya coastal basin show a Precambrian basement overlain by strata ranging in age from Paleozoic to Quaternary (Choubert et al., 1966). Most outcrops are of Cretaceous strata with a monocline structure (Abou ali et al., 2005). The tabular shape of the Tarfaya coastal basin results mainly from (1) sediment progradation toward the west; and (2) positive vertical movements during the Late Cretaceous belonging alpine tectonic phase (Kabbachi et al., 2001). In Morocco, Moghrebian strata of Lower Pleistocene age were defined in the Rabat region, consisting of detrital deposits lying unconformity over Pliocene strata (Arambourg & Choubert, 1965; Choubert, 1957) characterized by the coexistence of Pliocene and Quaternary fauna (Lecointre, 1966) In the Tarfaya coastal basin, the Moghrebian strata are represented by sub-horizontal biodetritic series of marine and continental origin. At most locations, this series overlies an unconformity on Cretaceous marls, although in a few places in the southwest part of the basin, the Moghrebian series overlies Pliocene sandstone. The Pleistocene age of the Moghrebian is assigned based on lithological and paleontological comparisons (Choubert et al., 1966; Lecointre, 1966) and palynological determinations (Ortlieb, 1975). The development of a calcareous crust at the top of the biodetritic series gives it the name Moghrebian Dalle (Bouab, 2001).

This manuscript presents new data on the lithology and microfacies of Moghrebian strata and their clay mineral content. These data are used for the microfaciological characterization of calcareous crusts and subsequently for

F. Jira (✉) · A. Lakhouili
Faculty of Sciences and Techniques Settat, Hassan First University of Settat, B.P. 577 Settat, Morocco
e-mail: fatima.jira@uhp.ac.ma

A. Çiner et al. (eds.), *Recent Research on Sedimentology, Stratigraphy, Paleontology, Tectonics, Geochemistry, Volcanology and Petroleum Geology*, Advances in Science, Technology & Innovation,
https://doi.org/10.1007/978-3-031-43222-4_27

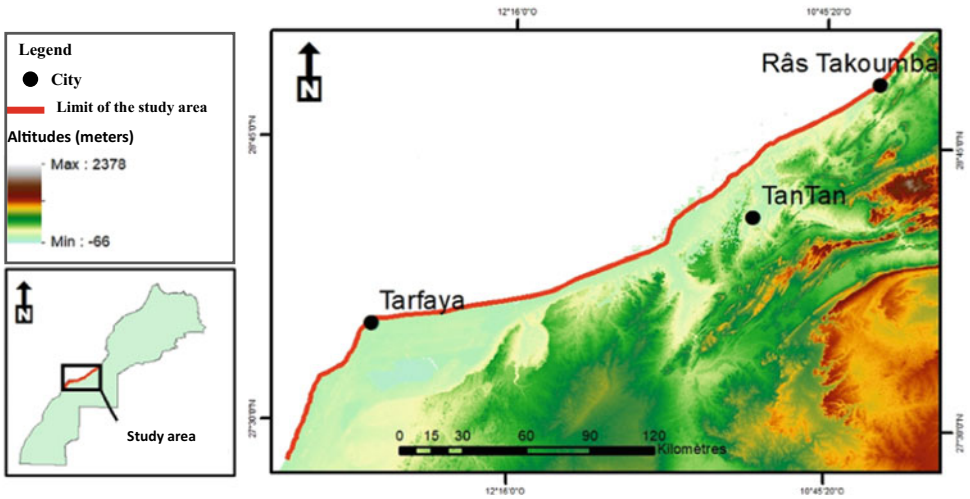

Fig. 1 Location of the studied area (coastal basin of Tarfaya, Morocco)

reconstructing the climatic conditions that prevailed in the coastal basin of Tarfaya during post-Moghrebian times.

2 Methods

Two kinds of studies were carried out to clarify the crust development modalities: the microfacies study and the X-ray diffractometry of fine fractions. In addition, stratigraphic surveys were carried out in the field to make the lithostratigraphic logs representative of the area (Figs. 2 and 3).

Forty-seven samples were selected for the clay mineral study and were leached for 12 h. When the clay fraction (< 2 μm) was separated from the obtained stable suspension, it was spread on oriented sections that were analyzed using an X-ray diffractometer. This analysis consisted of recording the following three diagrams for each sample after their preparation;

- A "normal" diagram (without treatment);
- A "heating" diagram produced by heating the sample for 4 h at 490 °C;
- An "ethylene–glycol" diagram was produced by placing the slides in a vacuum overnight in the presence of ethylene–glycol.

For the study of microfacies, thin sections were made for lumachelle, calcarenites, sandstones, and surface crusts. These slides were microscopically studied using a polarizing microscope.

3 Results

The Moghrebian strata are present along a 350 km-long stretch of the coast between Râs Takoumba and Tarfaya (Fig. 2). The lithostratigraphic logs show that the Moghrebian strata range in thickness from 5 to 30 m and comprise conglomerate, lumachelle, sandstone, and calcarenite beds (Fig. 3). The uppermost bed of the Moghrebian strata is a remarkably developed calcareous crust rich in terrestrial gastropods. In addition, many beds are characterized by diagenetic features such as the dissolution of bioclasts and the crystallization of microsparitic calcite in dissolution pores and drusic cement in intergranular pores.

The calcareous crust is characterized by micritic veins and nodules, grains with ooids, and an accentuated corrosion of the detrital elements, especially quartz grains. Furthermore, diffractograms of the fine sediment fraction in the different beds of the lithostratigraphic logs indicate the following assemblage of clay minerals: chlorite, kaolinite, illite, smectite, interlayered clay (chlorite-smectites, chlorite-vermiculite, vermiculite-smectite), and fibrous clay (sepiolite and palygorskite). The latter is especially abundant in the superficial crust. The percentage of the various clay minerals in the logs is listed in Table 1.

4 Discussion

Pliocene–Pleistocene strata are not common in the coastal basin of Tarfaya. However, Pleistocene marine strata are represented there by the Moghrebian and Uljian strata, which denote the classic last stage of the stratigraphy of the Quaternary marine units in North Africa (Brebion & Ortlieb, 1976).

The Moghrebian strata show significant variability in lateral extent and thickness. The thickness variability is explained by the alternation of sediment deposition/erosion phases that can be related to regional variations in sea level. The diagenetic evolution of these strata is very precocious and characterized by bioclast dissolution. This dissolution

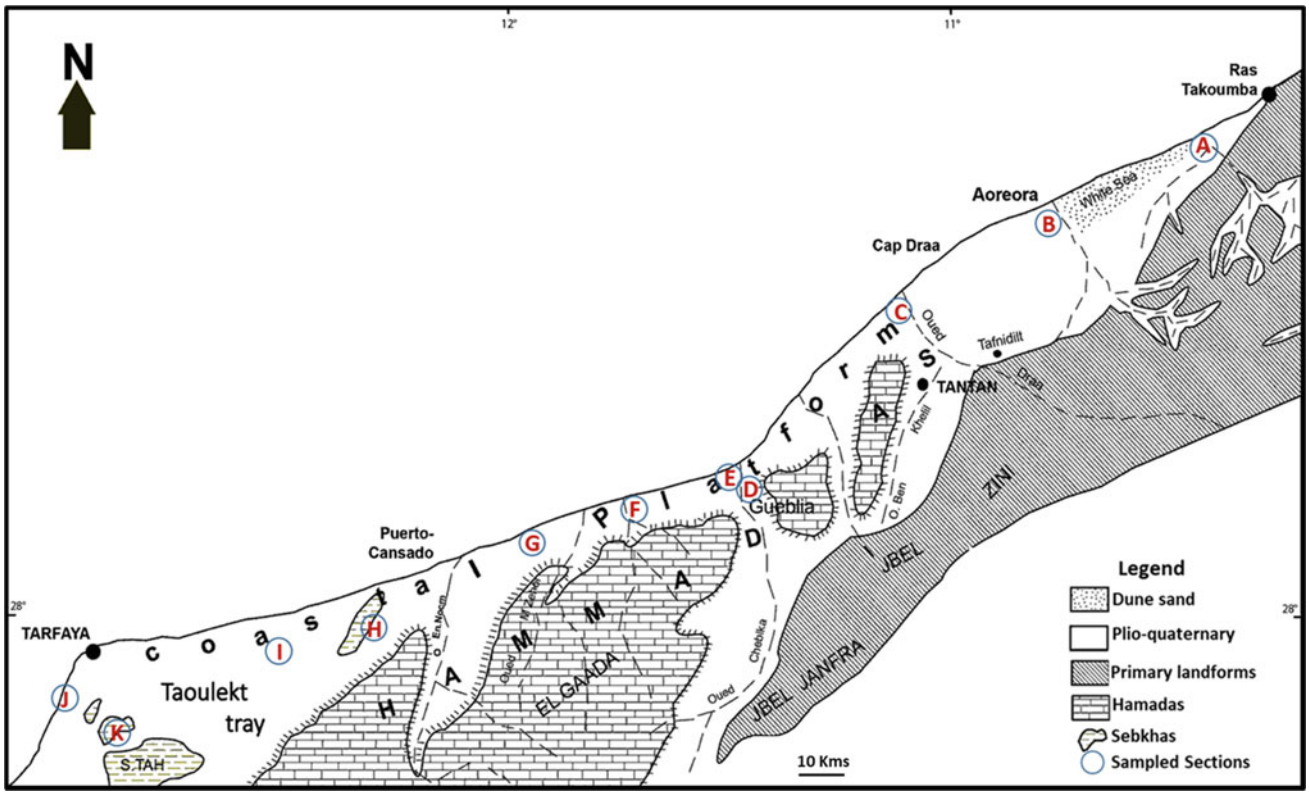

Fig. 2 Geomorphological and geological sketch of the studied area according to Arambourg (1952). The stars indicate the location of sampled sections: A: Bou Issafen; B: Aoreora; C: Draa; D: Chebeika North; E: Chebeika South; F: El Waar; G: Sidi Akhfennir; H: Sebkha Tazra; I: Carriere Shell; J: Sidi Aila; K: Sebkha Tisfourine

increased the rock's porosity and enriched the environment in calcium carbonate, thus promoting the precipitation of microparticle calcite in the form of drusic cement. As a result, the surface crust is characterized by strong quartz grains corrosion and calcite precipitation in the corrosion concavities. This corrosion occurs either by developing concavities on the quartz grain's surface until it is completely replaced by calcite or by the bursting of the quartz grain before its dissolution and its total replacement by calcite. This process corresponds to isovolumetric calcareous epigeny (Millot et al., 1977) (Fig. 4).

The presence of continental gastropods and the nodular appearance of the superficial calcareous crusts indicate that the phenomenon affects the upper section of previously deposited detrital sediment. In addition to the abundance of palygorskite and sepiolite, such calcification can only occur in a climate of alternating wet and dry seasons. During the wet season, the supersaturation of carbonate solutions creates destabilization of the silica and, subsequently, the dissolution of quartz and the release of silica in the medium.

During dry seasons, evaporation becomes significant. Solutions are oversaturated, the pH increases, and calcite precipitates. The epigenesis of quartz also marks dry seasons by calcite and by the neoformation of magnesian fibrous clays (palygorskite and sepiolite). The abundance of clay mineral types (illite, kaolinite, chlorite, smectite, interlayered clay, palygorskite, and sepiolite) in the studied beds is unrelated to the sample lithology. In addition, the burial diagenesis of these strata is negligible, which confirms the detrital origin of these clays.

Fibrous magnesian clays (palygorskite and sepiolite) often develop in calcareous crusts formed in arid climates (Guettouch et al., 2006; Paquet, 1983). Their presence in the calcareous crusts surmounts the Moghrebian strata of the Tarfaya coastal basin which could be explained by their neoformation from the hydrolysis of silicates in a basic medium (Millot, 1964). In addition to their neoformation in the superficial crusts, which is associated with massive drought and evaporation, these clays seem to be derived from the Lower Eocene strata of the Tarfaya basin, where they are very abundant. Similar fibrous clays (palygorskite and sepiolite) in dry coastal climatic conditions have been reported in the northeast Atlantic, Mediterranean, and Indian basins (Sajid et al., 2019).

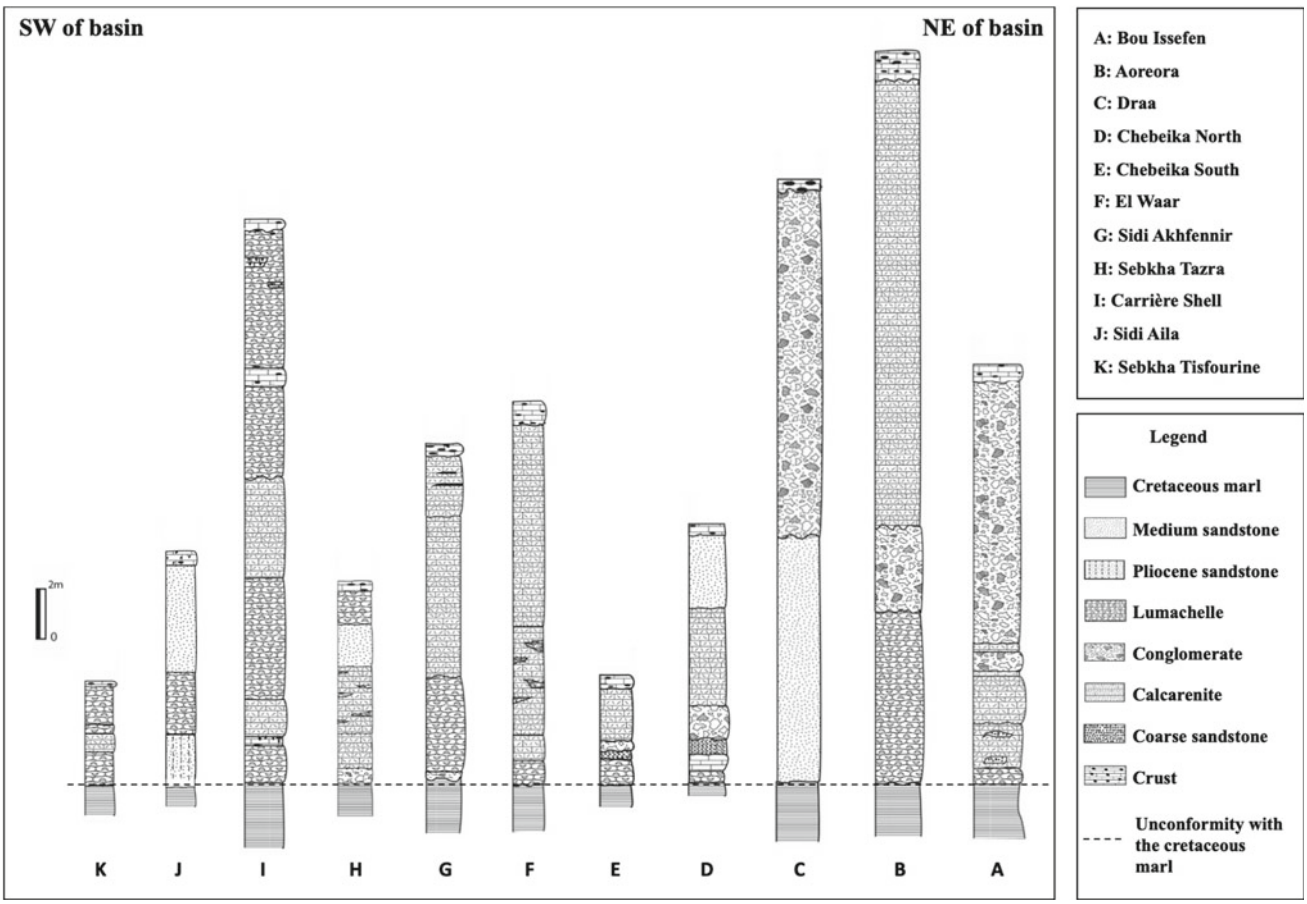

Fig. 3 Lithostratigraphic logs of Pleistocene Moghrebian strata in the coastal basin of Tarfaya

Table 1 Clay mineral data (weighted average by log) from the Pleistocene Moghrebian strata in the coastal basin of Tarfaya

Log	Kaolinite (%)	Illite (%)	Chlorite (%)	Smectite (%)	Palygorskite (%)	Sepiolite (%)	Chl/Verm (%)	Verm/Smect (%)	Chl/Smec (%)
Bou Issafen	10	42	46	0	2	0			
Aoreora	39	23	13	15	9	0	1		
Draa	10	7	24	48	11	0	0	0	
Chébeika N	3	21	26	23	27	0			
Chébeika S	7	35	11	0	26	21			
EL Waar	11	14	15	32	10	9			9
S Akhfennir	1	26	7	0	49	17			
Sebkha Tazra	25	21	15	23	14	0		1	
Carr Shel	15	35	20	25	4	1	0		
Sidi Aila	17	47	25	4	6	0			
Tisfourine	7	45	32	0	15	0			

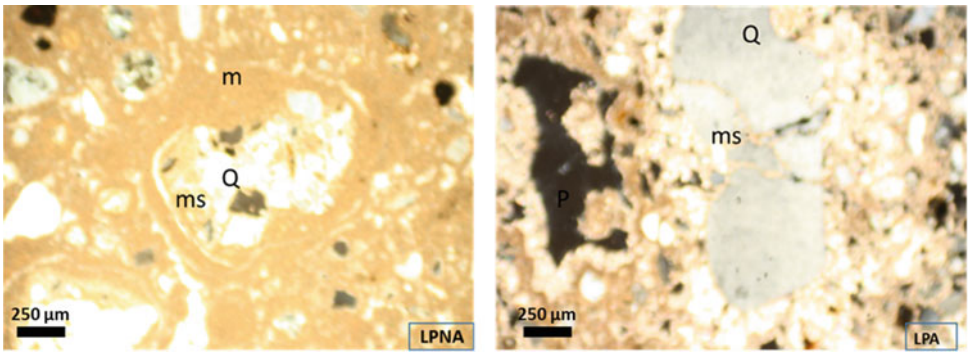

Fig. 4 Thin section photographs of calcareous crusts that form the uppermost bed of the Moghrebian strata in the coastal basin of Tarfaya. LPA: Polarized Light Analyzed; LPNA: Polarized Light not Analyzed; m: micrite; ms: microsparite; P: pore; Q: quartz

5 Conclusion

The diagenetic evolution of the Pleistocene Moghrebian strata of the coastal basin of Tarfaya is very precocious. The dissolution of bioclastic debris and the beginning of drusic cementation characterizes this evolution. The development of calcareous crusts by the isovolumetric epigeny of quartz by calcite at the top of the Moghrebian strata and the richness of these crusts in palygorskite sepiolite imply that the climate during post-Moghrebian times has been marked by the alternation of wet and dry seasons. Wet seasons favor the mobility of ions in solution, whereas dry seasons favor the neoformation of magnesian clays, calcareous epigenesis, and the crystallization of micritic calcite into microsparite.

References

Abou ali, N., et al. (2005). Structure de socle, sismostratigraphie et héritage structural au cours du rifting au niveau de la marge d'Ifni/Tan-Tan (Maroc sud-occidental): Comptes Rendus Géoscience, (Vol. 337, No. 14, pp. 1267–1276). Arambourg.

Arambourg, C., & et Choubert, G. (1965). Les faunes de mammifères de l'étage moghrébien du Maroc occidental. *Notes du service géologique du Maroc, 25*(185), 29–33, Rabat (1965).

Arambourg, C. (1952). Eustatisme et isostasie. *Comptes rendus de l'Académie des Sciences, 234*(2), 226–227 (Paris, France).

Bouab, N. (2001). Application des méthodes de datation par luminescence optique à l'évolution des environnements désertiques- Sahara Occidental (Maroc) et les Iles Canaries Orientales (Espagne). Thèse, Univ. de Québec, 253p.

Brebion, P., & Ortlieb, L. (1979). Nouvelles recherches géologiques et malacologiques sur le Quaternaire de la Province de Tarfaya (Maroc méridional): Geobios, no. 9, f. 5, pp. 529–550.

Choubert, G., Faure-muret, A., & Hottinger, L. (1966). Le bassin côtier de Tarfaya (Maroc méridional). *Notes et Mémoire du Service Géologique (Maroc) 1*(175), (STRATIGRAPHIE).

Choubert, G. (1957–65b). L'étage Moghrébien dans le Maroc Occidental. *Notes et Mémoires du Service Géologique, 25*(185), 47–55.

Guettouch, M., Guendouz, S., & Boutiba, M. (2006). Sur existence d'un model-type d'encroûtement des sols arides et semi-aride en Algérie : Étude comparative entre la Tafna (Algérie nord-occidentale), les Hauts Plateaux Sétifiens et le bassin hodéen (Algérie nord-orientale). *Journal des Sciences Pour l'Ingénieur, Numéro 6/2006*, 65–80.

Kabbachi, B., EL Youssi, M., Ezaidi, A., & Rognon P. (2001). Physiostratigraphie et dynamique sédimentaire actuelle dans la marge atlantique sud-ouest marocaine (Le bassin de Tan-Tan-Cap Juby) *Quaternaire, 12*(3), 139–148.

Lecointre, G. (1966). Néogène récent et quaternaire du Bassin Côtier de Tarfaya. *Notes Et Mémoires Du Service Géologique Du Maroc, 175*, 256–328.

Millot, G. (1964). Géologie des argiles, Altération, Sédimentation, Géochimie. Edition Masson et Cie, 491p.

Millot, G., Nahon, D., & Paquet, H. (1977). L'épigenèse calcaire des roches silicatées dans les encroûtements carbonatés en pays subarides (Anti-Atlas, Maroc). *Sciences Géologiques Bulletin, Strasbourg, 30*, 129–152.

Ortlieb, L. (1975). «Recherches sur les formations plio-quaternaires du littoral Ouest-saharien: 28030'-20040'lat. N,» IRD Edition, Vol. 48.

Paquet, H. (1983). Stability, instability and significance of attapulgite in the calcretes of Mediterranean and tropical areas with marked dry season. Coll. CNRS. `Petrology of weathering and soils', Paris, July 1983. In Sciences Geologies. Mémoire n°72, pp.131–140.

Sajid, A., Karl, S., Zhifei, L., Khelifi, N., & Wolfgang, K. (2019). Paleoclimatic and paleoenvironmental reconstruction at Tarfaya Atlantic coastal basin (Morocco) based on clay mineral records from Upper Cretaceous to Quaternary. *Arabian Journal of Geosciences 12–6*, 12p.

Chlorides' Concentration Assessment in the Waters of the Sila Massif (Calabria, Southern Italy)

Ilaria Guagliardi, Tommaso Caloiero, Ernesto Infusino, Simona Gaglioti, and Nicola Ricca

Abstract

In this study, 63 water samples were collected and analyzed using UV spectrophotometry for chloride (Cl^-) contents inside the Sila Massif (Calabria region, Italy). In addition, the spatial distribution of chlorides in the study area was performed through the geostatistical approach. Results showed a good quality status of the spring waters in the Sila Massif, considering that their Cl^- content was lower than the permissible levels of chloride for safe drinking water. Furthermore, the observed Cl^- concentrations are strongly affected by the geological nature of the rocks of the aquifers of the study area. Therefore, the knowledge of chloride sources may help decision-makers identify the presence of contaminants that can disturb drinking.

Keywords

Chloride • Water • Geochemistry • Geostatistics • Mediterranean

1 Introduction

Chloride (Cl^-) is a major anion in all-natural waters (Granato et al., 2015). Since most chloride naturally present in water comes from dissolved rocks and minerals, the natural chloride content for an area varies considerably according to its geology. Upon contacting the land surface, Cl^- concentrations in water increase due to the interaction with soils, rocks, and biota (waste products) and the atmospheric contributions (Gaglioti et al., 2019; Mullaney et al., 2009). Although chloride is a relatively minor contaminant, it is non-toxic to humans (however, elevated levels make water unpotable due to the salty taste), and it is deleterious to some plants and aquatic biota (Scott et al., 2019). Furthermore, various anthropogenic sources (e.g., wastewater, fertilizer, and animal waste) increase the chloride concentrations in many receiving waters (Kelly et al., 2019). This investigation aimed to determine the chloride concentrations in the Sila Massif (Calabria, southern Italy) and to relate these concentrations with local geology to identify the source(s) of Cl^-. These aims have also been obtained using geostatistical methods, an essential tool for most scientists (Buttafuoco et al., 2017). It is important to conduct this survey in the selected area because the Sila Massif is sufficiently representative of more expansive territories in the Mediterranean setting.

2 Materials and Methods

Spring waters were collected from 63 sites inside the Sila Massif, located in the central-northern area of the Calabria region (Fig. 1). The study area consists of an igneous-metamorphic complex with acidic mineral associations. The Mesozoic and tertiary sedimentary soils have a modest extension and are formed by Calabrian sediments, i.e., sands and conglomerates (Iovine et al., 2018). The study area presents a high climatic variability due to its position in the Mediterranean and its mountainous nature (Buttafuoco et al., 2016, 2018; Coscarelli et al., 2004; Pellicone et al., 2019). The sampling was carried out from February to May 2020, during which the spring's maximum flow rates are generally recorded. The chloride contents were analyzed by UV Spectrophotometry. The quality control results were within accepted international standards (< 5%). The valuation of Cl^- content in water was performed by analyzing

I. Guagliardi (✉) · T. Caloiero · N. Ricca
National Research Council of Italy—Institute for Agricultural and Forest Systems in the Mediterranean (CNR-ISAFOM), 87036 Rende (CS), Italy
e-mail: ilaria.guagliardi@isafom.cnr.it

E. Infusino · S. Gaglioti
Department of Environmental Engineering (DIA), University of Calabria, 87036 Rende (CS), Italy

A. Çiner et al. (eds.), *Recent Research on Sedimentology, Stratigraphy, Paleontology, Tectonics, Geochemistry, Volcanology and Petroleum Geology*, Advances in Science, Technology & Innovation,
https://doi.org/10.1007/978-3-031-43222-4_28

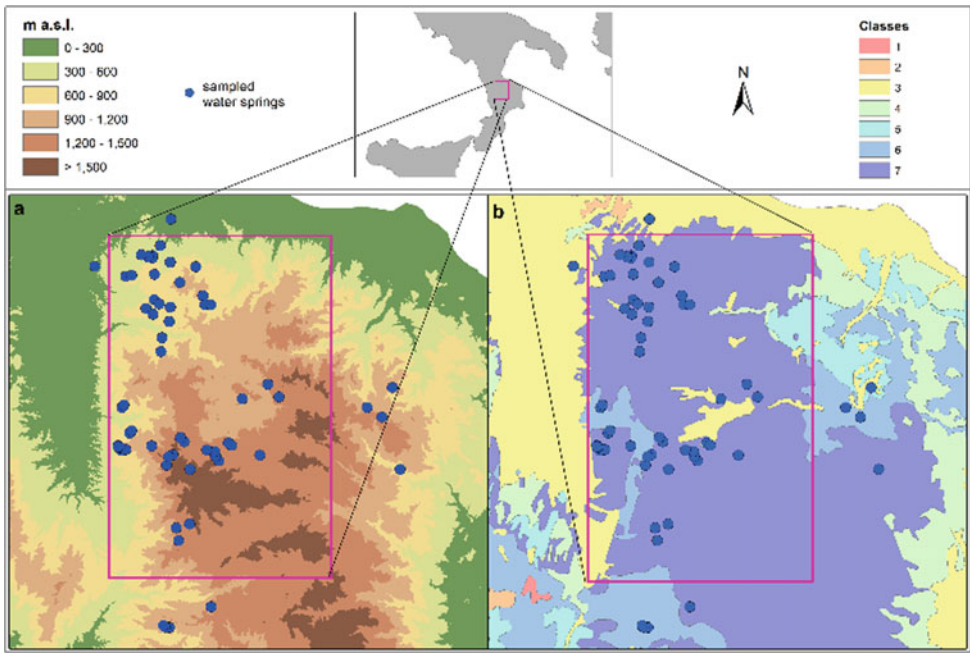

Fig. 1 **a** Sila Massif with the water sample locations in the square. **b** Lithological map of the study area: (1) limestones and dolostones, (2) metamorphic rocks with ophiolites, (3) sand, clay, and gravel, (4) clayey and marly terranes, (5) flysch, (6) sandstones, conglomerates, and limestone banks, and (7) intrusive metamorphic complex

its spatial distribution through geostatistical methods (Matheron, 1971), precisely by using ordinary kriging (Chilès & Delfiner, 2012; Webster & Oliver, 2007).

3 Results

Basic statistics for Cl^- in waters sampled are reported in Table 1. Results highlighted that the Cl^- maximum concentration in mg l^{-1} was 85.12, the minimum was 7.80, and the mean was 17.97 (st. dev. 11.63). A nested model was tested to fit the shape of the experimental variogram for Cl-content, whose goodness was checked by cross-validation. The results were acceptable for the statistics used, i.e., the mean of the raw estimation errors was close to 0, while the variance of the standardized error was close to 1.

Figure 2 shows the spatial distribution map of Cl^- content produced by the ordinary kriging technique.

4 Discussion

Chloride concentrations suitable for human consumption and agricultural and industrial water use are commonly on the order of 10–1000 mg per liter. In the present study, the chloride level recorded in the whole sampling point of the spring waters was lower than the permissible chloride levels for safe drinking water set by WHO in 250 mg l^{-1} (WHO, 2003). Furthermore, the distribution map of the chlorides shows higher concentrations in the northern-western part of

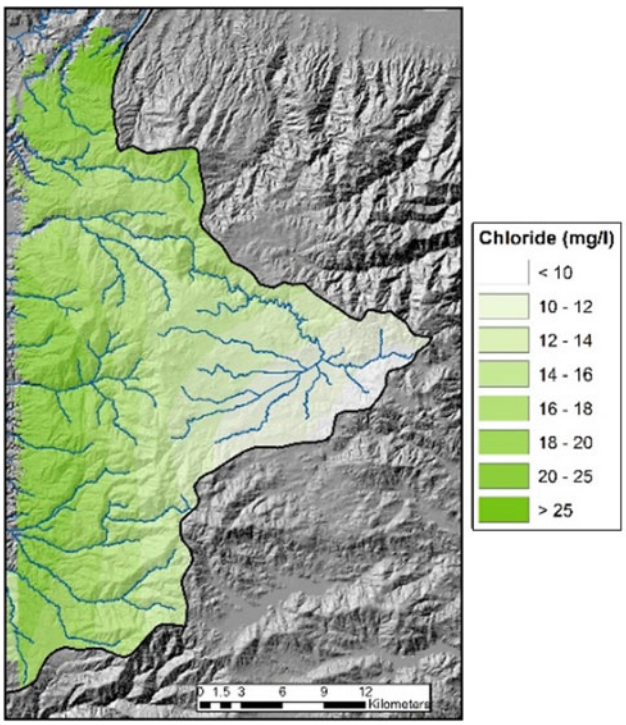

Fig. 2 Spatial distribution of chloride concentration in Sila Massif waters

Table 1 Basic statistics for Cl^- water content

	Min	Max	Mean	Standard deviation	Kurtosis	Skewness
Cl^-	7.80	85.12	17.97	11.63	18.48	3.72

the study area, where the intrusive metamorphic complex occurs, than in the eastern one, where the lithology also includes flysch, sandstones, conglomerates, and limestone banks. Indeed, the recorded Cl^- contents in the Sila Massif waters can be ascribable to the area's geology, whose mineralogical composition of the rocks and soil permeability strongly affected the waters' geochemistry. Conversely, no human activities were individuated as responsible for the chloride increase in the spring waters.

5 Conclusions

The study in the Sila Massif (Calabria, Southern Italy) on spring water samples confirms that the chloride ion concentration was within the limit. Furthermore, a correspondence between Cl^- content and local geology has been observed. This outcome complies with the geochemistry of the study area waters, which are relatively shallow, coming from intrusive aquifers. Furthermore, the geochemical and climatic characteristics of the study area are common to other wide Mediterranean regions. Therefore, relevant considerations could be applied in similar contexts.

References

Buttafuoco, G., Guagliardi, I., Tarvainen, T., & Jarva, J. (2017). A multivariate approach to study the geochemistry of urban topsoil in the city of Tampere. *Journal of Geochemical Exploration, 181*, 191–204.

Buttafuoco, G., Caloiero, T., Ricca, N., & Guagliardi, I. (2018). Assessment of drought and its uncertainty in a southern Italy area (Calabria region). *Measurement, 113*, 205–210.

Buttafuoco, G., Caloiero, T., Guagliardi, I., & Ricca, N. (2016). Drought assessment using the reconnaissance drought index (RDI) in a southern Italy region. In *6th IMEKO TC19 Symposium on Environmental Instrumentation and Measurements 2016*, pp. 52–55.

Chilès, J. P., & Delfiner, P. (2012). *Geostatistics: Modelling Spatial Uncertainty* (2nd ed.). Wiley.

Coscarelli, R., Gaudio, R., Caloiero, T. (2004). Climatic trends: an investigation for a Calabrian basin (southern Italy). In *Proceedings International Symposium Basic Civil Water Science Total*, pp 255–266.

Gaglioti, S., Infusino, E., Caloiero, T., Callegari, G., & Guagliardi, I. (2019). *Geochemical characterization of spring waters in the crati ziver Basin.* Calabria (Southern Italy). Geofluids. https://doi.org/10.1155/2019/3850148

Granato, G.E., DeSimone, L.A., Barbaro, J. R., & Jeznach, L.C. (2015). Methods for evaluating potential sources of chloride in surface waters and groundwaters of the conterminous United States. US Geological Survey, Report 2015–1080, 89p.

Iovine, G., Guagliardi, I., Bruno, C., Greco, R., Tallarico, A., Falcone, G., Lucà, F., & Buttafuoco, G. (2018). Soil-gas radon anomalies in three study areas of Central-Northern Calabria (Southern Italy). *Natural Hazards, 91*, 193–219.

Kelly, V. R., Findlay, S. E., Hamilton, S. K., et al. (2019). Seasonal and long-term dynamics in stream water sodium chloride concentrations and the effectiveness of road salt best management practices. *Water, Air, and Soil Pollution, 230*, 13.

Matheron, G. (1971). The theory of regionalised variables and its applications, in *Les Cahiers du Centre de Morphologie Mathématique de Fontainebleau, Chateau Fontainebleau, Paris*.

Mullaney, J. R., Lorenz, D. L., & Arntson, A. D. (2009). Chloride in groundwater and surface water in areas underlain by the glacial aquifer system, northern United States. US Geological Survey Scientific Investigations Report 2009-5086, 41p. .

Pellicone, G., Caloiero, T., & Guagliardi, I. (2019). The De Martonne aridity index in Calabria (Southern Italy). *Journal of Maps, 15*(2), 788–796.

Scott, R., Goulden, T., Letman, M., Hayward, J., & Jamieson, R. (2019). Long-term evaluation of the impact of urbanization on chloride levels in lakes in a temperate region. *Journal of Environmental Management, 244*, 285–293.

Webster, R., & Oliver, M. A. (2007). *Geostatistics for environmental scientists* (2nd ed.). Wiley.

WHO (World Health Organization). (2003). Background document for development of WHO Guidelines for Drinking-water Quality: Chloride in Drinking-water. World Health Organization.

Geothermal Supply System for a Winery on a Volcanic Island (Lanzarote, Canary Islands)

Juan C. Santamarta, Giovanni Lemes Pacheco, Jesica Rodríguez-Martín, Mª del Cristo Expósito, Alejandro García-Gil, and Noelia Cruz-Pérez

Abstract

Geothermal energy comes in many different forms depending on the specific conditions of the resource. For example, in volcanic areas (such as the Canary Islands) or with subduction of tectonic plates, deposits of water/steam of very high energy and temperatures (150°–350 °C) are sometimes produced, known as high enthalpy resources. Due to their high quality, these can be used for electricity production in binary cycles. The design of a geothermal heat pump system to replace conventional cæold and heat production systems in a winery on the island of Lanzarote (Canary Islands, Spain) is presented. First, a calculation system based on the Matlab program was designed to review the influences of the winemaker's decisions on the cold and heat consumption of the winery. After calculating hot and cold water consumption and heat pump requirements, a field of geothermal probes was designed using available software. Subsequently, the dimensions of the liquid impulsion equipment were estimated, and an electrical installation was created for the whole system. The data considered are related to winery logistics, must properties, environment, tank dimensions, and energy needs (cooling and heating). Finally, it was decided to use a reversible heat pump with exhaust heat recovery. This system allows heat extracted by the cooling system to be partly used to produce hot water instead of all of it being discharged to the ground. The cooling system will be operated for 18 h daily as a design criterion. The pump selected for the final project installed has an exhaust heat recovery system that allows domestic hot water to be produced in cooling mode. Hot water generation, when the heat pump is cooling, is 15 kW, and the temperature provided is 60 °C, which is adequate to meet the hot water needs of the winery. In addition, the heat pump's heat sink is in the ground, which remains in practically constant conditions throughout the year, so the effect of outside temperature is minimized. In general, the main advantages of installing a geothermal system are energy savings and reduction in CO_2 emissions.

Keywords

Geothermal energy • Low-enthalpy • Heat pump • Refrigeration • Winery

1 Introduction

The energy accumulated on earth represents an opportunity to address energy supply and efficiency issues. Conventional energy resources, such as oil, natural gas, coal, and uranium, which are increasingly consumed in the world, originate from finite energy resources extracted from the earth's crust. Moreover, only one energy resource from the crust is renewable, namely geothermal energy (Drahansky et al., 2016).

The ground possesses high heat storage capacity and low thermal conductivity. In fact, at a depth of 15–20 m, the temperature remains practically constant throughout the year (Muñoz et al., 2015). These conditions can provide renewable energy to supply the heating and cooling needs of a room throughout the year and even generate a certain amount of hot water. The equipment most used for this

J. C. Santamarta (✉) · N. Cruz-Pérez
Departamento de Ingeniería Agraria y del Medio Natural, Universidad de La Laguna (ULL), Tenerife, Spain
e-mail: jcsanta@ull.es

G. L. Pacheco
Instituto de Carboquímica (ICB-CSIC), Zaragoza, Spain

J. Rodríguez-Martín · M. del Cristo Expósito
Departamento de Técnicas y Proyectos en Ingeniería y Arquitectura, Universidad de La Laguna (ULL), Tenerife, Spain

A. García-Gil
Geological Survey of Spain (IGME-CSIC), C/ Ríos Rosas 23, 28003 Madrid, Spain

A. Çiner et al. (eds.), *Recent Research on Sedimentology, Stratigraphy, Paleontology, Tectonics, Geochemistry, Volcanology and Petroleum Geology*, Advances in Science, Technology & Innovation,
https://doi.org/10.1007/978-3-031-43222-4_29

purpose is the geothermal heat pump, capable of extracting heat from the ground and injecting it into a room or, working in a reverse cycle, removing heat from the room and injecting it into the ground. In cooling mode, heat extracted from the building is transferred to the ground. In heating mode, heat extracted from the earth is moved to the structure (Márquez et al., 2016).

2 Materials and Methods

Winemaking is a seasonal process, and production is concentrated in a short period, which may vary depending on the climatic conditions of each year. Much of the energy consumed is used for refrigeration due to the importance of operating below climatic temperatures to ensure product quality (Carlos et al., 2009). The temperature has a significant influence on oenological processes. An increase in temperature accelerates the dissolution of solids, the volatilization of gases and liquids, and the speed of chemical reactions. On the other hand, a decrease in temperature decreases the solubility of gases and exerts a complex action on the development of microorganisms (at first favorable and then inhibitory) and on the products of their metabolism (Blouin & Maron, 2006). The distribution of energy consumption is not homogeneous since the consumption of refrigerated energy is produced, especially during white vinification and in different auxiliary operations. In general, refrigeration needs vary throughout the day, as many of the processes occur intermittently at other times of the day. In addition, energy consumption depends on the time of year, with a peak toward the middle of the harvest period, when the arrival of the grapes overlaps with the fermentation process (Carlos et al., 2009).

Refrigeration and heating needs vary throughout the winemaking processes, concentrating on the harvest stage, when the procedures with the highest thermal demands are carried out. For this reason, computer tools have been used to calculate the needs in different scenarios and to verify that the size of the facilities follows these assumptions. The processes studied and measured refrigeration for desludging and its thermal losses, refrigeration for fermentation and its thermal losses, and losses associated with the distribution of the cooling fluid. In addition, other cooling and heating processes are carried out, whose impact on the size of the facilities is minor. These include temperature-controlled maintenance of elaborated wines, generation of domestic hot water for various uses, production of hot water for tank cleaning, and production of hot water for disinfection of the bottling line.

3 Results

3.1 Refrigeration Needs

The winery's refrigeration equipment is designed to meet the refrigeration needs during the harvest season. Therefore, all the starting conditions for performing the calculations were entered in a Matlab function that calculates energy demand autonomously and has the following sections: (a) Start data (logistics data, must characteristics, temperature and humidity, fermentation tank, and refrigerant distribution); (b) Racking; (c) Losses per wall during desludging; (d) Needs for fermentation refrigeration; (e) Wall losses during fermentation; (f) Losses in the cold water distribution line; (g) Unification.

The usual method in the winery consists of working in batches, with tanks at different stages of fermentation and generating different amounts of heat at each harvest stage. To quantify the effect of these tanks, it has been assumed that all batches of must are equal in quantity, acidity, and sugar content and that they will ferment at the same temperature. Therefore, they are generated periodically, typically one batch each day.

The effect of climate is only influential when using a heat pump whose heat sink is the ambient air (López & Secanell, 1992). Therefore, in this facility, it was decided to use a heat pump in which the heat sink is in the ground and remains in practically constant conditions throughout the year. Hence, the effect of the external temperature is minimal.

3.2 Heating Requirements

The facility also needs hot water for the disinfection of the bottling line, the cleaning of the tanks, and domestic hot water (DHW) for the services of the workers. Considering a demand of 15 L per person and day, and knowing that in its moment of maximum production, the winery has 15 workers, the need for domestic hot water will be 225 l/d.

Additionally, the bottling machine must be rinsed before use. Each wash consumes 500 L of water at 90 °C for disinfection of all its pipes, which takes place twice a month. The facility has been designed, so that the bottling tank is filled with hot water produced by the heat pump at a temperature of 60 °C. The additional energy needed to reach 90 °C is obtained using electric resistance incorporated in the accumulator. The tanks can be washed with cold or hot water. However, the advantage of hot water is that it has greater descaling power, achieving savings in using cleaning products. Therefore, whenever it is available, hot water is used to wash the tanks.

4 Discussion

The energy consumed in wine production is mainly due to lighting, grape processing, pumping filtration and mixing, bottling, thermal conditioning, sterilization, cleaning, wine moving machinery, and miscellaneous (Smyth & Nesbitt, 2014). Calculations have shown that cold water requirements are more significant than hot water requirements and that refrigeration will be necessary every day of the year. Therefore, it was decided to use a reversible heat pump, as this system allows heat extracted by the cooling system to be partly used to produce hot water instead of being sent into the ground.

Since there are no wells around the winery, it was decided to construct a closed geothermal circuit with vertical probes. The facility costs depend on the depth of the reservoir, the various applications, the type of technology used, and the maintenance required (Xydis et al., 2013).

5 Conclusions

Low-temperature geothermal facilities applied to buildings are cost-effective and adapt to the thermal needs of different facilities and uses. Low-enthalpy projects are viable due to the following: Less dependence on primary energy, which is one of the objectives sought when using renewable energies; geothermal energy is clean energy and reduces CO_2 emissions to the atmosphere, and it is very efficient as it comes from an inexhaustible source of energy. It is also an excellent alternative to conventional heating systems and residential air conditioning; monitoring inside the facility through an intelligent control system makes it much more profitable in system maintenance and energy efficiency.

References

Blouin, J., & Maron, J. (2006). *Control de las temperaturas y calidad de los vinos*. ACRIBIA.

Carlos, A., Stella, M., Rosa, A., Carlos, A., Stella, M., & Rosa, A. (2009). Modelo matemático para la predicción de las necesidades de frío durante la producción de vino. *Ciencia, Docencia y Tecnología, 20*(38), 205–226.

Drahansky, M., Paridah, M., Moradbak, A., Mohamed, A., Owolabi, F., Taiwo, A., Asniza, M., & Abdul Khalid, S. H. (2016). We are IntechOpen, the world's leading publisher of Open Access books Built by scientists, for scientists. https://doi.org/10.5772/57353

López, A., & Secanell, P. (1992). A simple mathematical empirical model for estimating the rate of heat generation during fermentation in white-wine making. *International Journal of Refrigeration*, 276–280.

Márquez, J. M. A., Bohórquez, M. Á. M., & Melgar, S. G. (2016). Ground thermal diffusivity calculation by direct soil temperature measurement. application to very low enthalpy geothermal energy systems. *Sensors (Switzerland), 16*(3). https://doi.org/10.3390/s16030306

Muñoz, M., Garat, P., Flores-Aqueveque, V., Vargas, G., Rebolledo, S., Sepúlveda, S., Daniele, L., Morata, D., & Parada, M. Á. (2015). Estimating low-enthalpy geothermal energy potential for district heating in Santiago basin-Chile (33.5°S). *Renewable Energy, 76*, 186–195.https://doi.org/10.1016/j.renene.2014.11.019

Smyth, M., & Nesbitt, A. (2014). Energy and English wine production: A review of energy use and benchmarking. *Energy for Sustainable Development, 23*(1), 85–91. https://doi.org/10.1016/j.esd.2014.08.002

Xydis, G. A., Nanaki, E. A., & Koroneos, C. J. (2013). Low-enthalpy geothermal resources for electricity production: A demand-side management study for intelligent communities. *Energy Policy, 62*, 118–123. https://doi.org/10.1016/j.enpol.2013.08.012

Origin of Çardak Tephra, SW Turkey

Rengin Özsoy, Erkan Aydar, and Orkun Ersoy

Abstract

The origin of the Çardak tephras remains a mystery. Two different remarks on this issue were presented by Kazancı et al. in Glob Planetary Change 80–81:36–50 (2012), Sulpizio et al. in J Quaternary Sci 28:329–335 (2013). Kazancı et al. in Glob and Planetary Change 80–81: 36–50 (2012) reported that the Çardak tephras were formed by the eruption of the Yalı-Nisyros volcano, while Sulpizio et al. in J Quaternary Science 28:329–335 (2013) associated them with the Minoan eruption. By solving this enigma, we aim to contribute to future studies on the distribution of tephra belonging to the Aegean Islands' volcanism. Using SEM-EDS, we performed chemical analyses on volcanic glass, minerals, and xenoliths. Moreover, whole-rock geochemical analysis (major, trace, and rare earth elements), XRD, and grain size analysis are reported in this contribution. During the analysis of the tephras, the predominance of xenoliths/xenocrystals belonging to different basement rock groups was noted. Moreover, albite and quartz peaks were observed in XRD results. We believe that the xenoliths significantly influence our geochemical analysis. Consequently, we found these chemical analyses irrelevant to compare with volcanic sources. Instead, we think that using the chemistry of volcanic glasses to investigate the origin of tephra will give more accurate results. The volcanic glass analyses of the Çardak tephras exhibit a rhyodacitic/rhyolitic composition. After comparing the major oxides values are obtained from the glass analysis of the Çardak tephras with the glass analysis of the volcanic eruptions in different Aegean islands, the glass chemistry is similar to the Minoan Eruption of Santorini, as was already claimed by Sulpizio et al. in J Quaternary Science 28:329–335 (2013).

Keywords

Çardak tephra • Minoan eruption • Acıgöl graben • Ash dispersal • Contamination

1 Introduction

Throughout history, the Mediterranean has hosted many volcanic events caused by subduction-related processes (Dilek & Sandvol, 2009; Sengör & Yilmaz, 1981; Yilmaz et al., 1998). One of the most destructive and well-known eruptions is the Minoan (Druitt et al., 1989; Hamann et al., 2010; Karátson et al., 2020; Stock et al., 2020). The volcanic products of the Minoan eruption are widely distributed (Aksu et al., 2008; Eastwood et al., 1999; Goodman-Tchernov et al., 2009; Guichard et al., 1993). Previous studies have reported that tephras of the Minoan eruption have been observed in different regions of Turkey (Aksu et al., 2008; Aydar et al., 2021; Guichard et al., 1993). The Çardak tephras, found within the Acıgöl Graben of Western Anatolia, are also tephra levels associated with volcanic eruptions in the Aegean Arc volcanism (Kazancı et al., 2012; Sulpizio et al., 2013). This study's characterization of the Çardak tephras was approached from a new perspective. Different researchers have reported two separate studies on the Çardak tephras. While Kazancı et al. (2012) stated that the tephras were produced due to Yali-Nisyros volcanism, Sulpizio et al. (2013) reported that the eruption that caused the formation of Çardak tephras was related to the Minoan eruption of Santorini. We tried to solve this mystery and shed light on the origin of the Çardak tephras with our work.

R. Özsoy
Graduate School of Science and Engineering, Hacettepe University, 06800 Beytepe, Ankara, Turkey

Department of Earth Sciences, Sapienza - University of Rome, P.le Aldo Moro 5, 00185 Roma (RM), Italy

E. Aydar (✉) · O. Ersoy
Department of Geological Engineering, Hacettepe University, 06800 Beytepe, Ankara, Turkey
e-mail: eaydar@hacettepe.edu.tr

A. Çiner et al. (eds.), *Recent Research on Sedimentology, Stratigraphy, Paleontology, Tectonics, Geochemistry, Volcanology and Petroleum Geology*, Advances in Science, Technology & Innovation,
https://doi.org/10.1007/978-3-031-43222-4_30

2 Methodology

Microscopy analysis of volcanic ash samples taken from the Çardak Formation was performed at Hacettepe University by using a Zeiss EVO 50-EP Scanning Electron Microscope (SEM) equipped with a Bruker XFlash 3001 Energy Dispersive Spectrometer (EDS) operating in backscattered electron (BSE) mode and secondary electron (SE) at beam conditions of 15–20 keV accelerating voltage. Whole-rock major and trace element compositions of Bozkurt-4 and Bozkurt-2 samples were carried out in ACME laboratories. The ICP-ES (emission spectrometry) method performed major element analyses, and trace element contents were obtained by ICP-MS (mass spectrometry). X-ray diffraction (XRD) analyses were performed for Bozkurt-2 and Bozkurt-4 samples using Empyrean, Malvern Panalytical, Worcestershire, UK, at Niğde Ömer Halisdemir Central Research Laboratory. Classification diagrams of whole rock and glass analyses were made using PetroGram (Gündüz & Asan, 2021).

3 Results

The chemistry of the Çardak tephras was determined to be rhyolitic and rhyodacitic (Fig. 1), according to the classification diagram of Le Bas et al. (1986). Alkali feldspar, albite, andesine, labradorite, bytownite and anorthite oligoclase, augite, diopside, pigeonite, enstatite, olivine, and quartz are found in free form in the Çardak tephras. Xenoliths are predominantly of magmatic origin. However, dolomite, calcite, and some xenoliths/xenocrystals of metamorphic origin were also observed in the samples. Moreover, the XRD analysis results show quartz and albite peaks.

4 Discussion

The Mediterranean region has hosted many volcanic activities throughout the Neogene (Aydar & Gourgaud, 1998) and Quaternary, with the effect of the Hellenic arc formed by subduction (Dilek & Sandvol, 2009; Palladino et al., 2008; Sengör & Yilmaz, 1981). The products of the eruptions in the Mediterranean show a wide spread of ash (Hamann et al., 2010; Tomlinson et al., 2015; Wulf et al., 2020). One of these dangerous and devastating eruptions is the Minoan eruption of Santorini (Aydar et al., 2021; Druitt et al., 1989). The volcanic products of the Minoan eruption were observed at locations in Western Anatolia (Aksu et al., 2008; Aydar et al., 2021). Kazancı et al. (2012) and Sulpizio et al. (2013) provided two different hypotheses on the origin of the Çardak tephras that can be found within the colluvial fan of the Acıgöl Graben of Western Anatolia. Kazancı et al. (2012) stated that these tephras belong to the Yali-Nisyros volcanism. Considering that both the minerals belonging to the different basement rock revealed by XRD analysis affect the whole rock composition and the chemical analyses taken from the volcanic glasses, the origin of the Çardak tephras has been determined as the Minoan eruption, as previously reported by Sulpizio et al. (2013).

5 Conclusion

This study focused on the origin of the Çardak tephras within the colluvial fan of the Acigöl Graben of Western Anatolia. Considering the major oxide values of the Çardak tephras, it has been observed that the composition of the Çardak tephras is compatible with the Minoan eruption of Santorini. Xenoliths of different origins encountered during

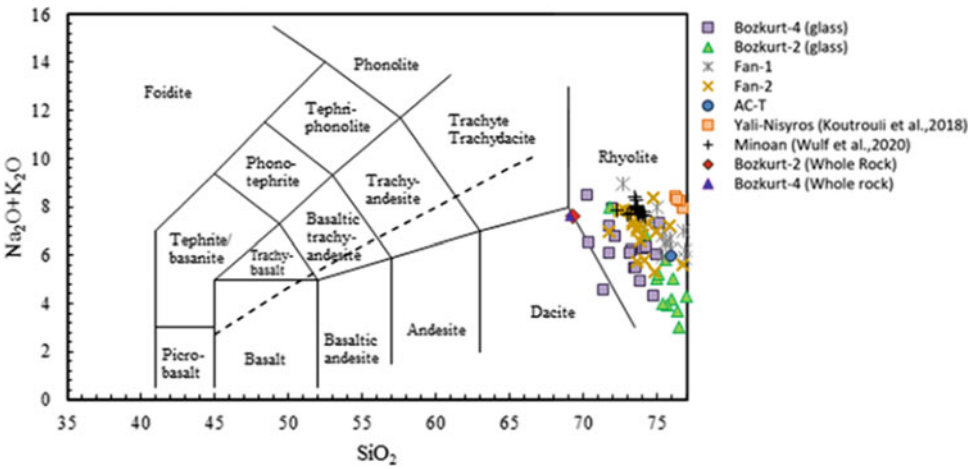

Fig. 1 TAS diagram of Çardak tephras (Le Bas et al. 1986). Data are from; Minoan (Wulf et al. 2020), Yali-Nisyros (Koutrouli et al. 2018)

the investigation made with SEM-EDS and quartz and albite minerals observed in the XRD results indicate contamination in the samples.

Acknowledgements We thank Prof. Dr. Nizamettin Kazancı for providing samples. In addition, we thank the three anonymous reviewers.

References

Aksu, A. E., Jenner, G., Hiscott, R. N., & Işler, E. B. (2008). Occurrence, stratigraphy and geochemistry of Late Quaternary tephra layers in the Aegean Sea and the Marmara Sea. *Marine Geology, 252*(3–4), 174–192.

Aydar, E., Çiner, A., Ersoy, O., ÉCochard, E., & Fouache, E. G. (2021). Volcanic ash and tsunami record of the Minoan Late Bronze Age Eruption (Santorini) in a distal setting, southwestern Turkey. *Journal of Quaternary Science, 36*(4), 586–597.

Aydar, E., & Gourgaud, A. (1998). The geology of Mount Hasan stratovolcano, central Anatolia Turkey. *Journal of Volcanology and Geothermal Research, 85*(1–4), 129–152.

Dilek, Y., & Sandvol, E. (2009). Seismic structure, crustal architecture and tectonic evolution of the Anatolian-African Plate Boundary and the Cenozoic Orogenic Belts in the Eastern Mediterranean Region. *Geological Society Special Publications, 327*, 127–160.

Druitt, T. H., Mellors, R. A., Pyle, D. M., & Sparks, R. S. J. (1989). Explosive volcanism on Santorini. *Greece. Geol Mag., 126*(2), 95–126.

Eastwood, W. J., Pearce, N. J. G., Westgate, J. A., Perkins, W. T., Lamb, H. F., & Roberts, N. (1999). Geochemistry of Santorini tephra in lake sediments from Southwest Turkey. *Global and Planetary Change, 21*(1–3), 17–29.

Goodman-Tchernov, B. N., Dey, H. W., Reinhardt, E. G., McCoy, F., & Mart, Y. (2009). Tsunami waves generated by the Santorini eruption reached Eastern Mediterranean shores. *Geology, 37*(10), 943–946.

Guichard, F., Carey, S., Arthur, M. A., Sigurdsson, H., & Arnold, M. (1993). Tephra from the Minoan eruption of Santorini in sediments of the Black Sea. *Nature, 363*(6430), 610–612.

Gündüz, M., & Asan, K. (2021). PetroGram: An excel-based petrology program for modeling of magmatic processes. *Geoscience Frontiers, 12*(1), 81–92.

Hamann, Y., Wulf, S., Ersoy, O., Ehrmann, W., Aydar, E., & Schmiedl, G. (2010). First evidence of a distal early Holocene ash layer in Eastern Mediterranean deep-sea sediments derived from the Anatolian volcanic province. *Quaternary Research, 73*(3), 497–506.

Karátson, D., Telbisz, T., Gertisser, R., Strasser, T., Nomikou, P., Druitt, T., et al. (2020). Constraining the landscape of Late Bronze Age Santorini prior to the Minoan eruption: Insights from volcanological, geomorphological and archaeological findings. *Journal of Volcanology and Geothermal Research, 401*, 106911.

Kazancı, N., Boyraz, S., Özkul, M., Alçiçek, M. C., & Kadöoğlu, Y. K. (2012). Late Holocene terrestrial tephra record at western Anatolia, Turkey: Possible evidence of an explosive eruption outside Santorini in the eastern Mediterranean. *Global and Planetary Change, 80–81*, 36–50.

Koutrouli, A., Anastasakis, G., Kontakiotis, G., et al. (2018). The early to mid- Holocene marine tephrostratigraphic record in the Nisyros-Yali-Kos volcanic center, SE Aegean Sea. *Journal of Volcanology and Geothermal Research, 366*, 96–111. https://doi.org/10.1016/j.jvolgeores.2018.10.004

Le Bas, M. J., Le Maitre, R. N., Streckeisen, A., & Zanettin, B. (1986). A chemical classification of volcanic rock based on total silica diagram. *Journal of Petrology [Internet], 27*(3), 745–750. Available from: http://petrology.oxfordjournals.org/

Palladino, D. M., Simei, S., & Kyriakopoulos, K. (2008). On magma fragmentation by conduit shear stress: Evidence from the Kos Plateau Tuff, Aegean Volcanic Arc. *Journal of Volcanology and Geothermal Research, 178*(4), 807–817.

Sengör, A. M. C., & Yilmaz, Y. (1981). Tethyan evolution of Turkey: A plate tectonic approach. *Tectonophysics, 75*(3–4).

Stock, F., Laermanns, H., Pint, A., Knipping, M., Wulf, S., Hassl, A. R., et al. (2020). Human-environment interaction in the hinterland of Ephesos—As deduced from an in-depth study of Lake Belevi, West Anatolia. *Quaternary Science Reviews, 244*.

Sulpizio, R., Alçiçek, M. C., Zanchetta, G., & Solari, L. (2013). Recognition of the Minoan tephra in the Acigöl Basin, western Turkey: Implications for inter-archive correlations and fine ash dispersal. *Journal of Quaternary Science, 28*(4), 329–335.

Tomlinson, E. L., Smith, V. C., Albert, P. G., Aydar, E., Civetta, L., Cioni, R., et al. (2015). The major and trace element glass compositions of the productive Mediterranean volcanic sources: Tools for correlating distal tephra layers in and around Europe. *Quaternary Science Reviews, 118*, 48–66.

Wulf, S., Keller, J., Satow, C., Gertisser, R., Kraml, M., Grant, K. M., et al. (2020). Advancing Santorini's tephrostratigraphy: New glass geochemical data and improved marine-terrestrial tephra correlations for the past ~360 kyrs. *Earth-Science Rev.,* 200, 102964.

Yilmaz, Y., Güner, Y., & Şaroglu, F. (1998). Geology of the quaternary volcanic centres of the east Anatolia. *Journal of Volcanology and Geothermal Research, 85*(1–4), 173–210.

Distal Pyroclastic Current Deposits of the 79 AD Vesuvius Eruption on the Mountains Adjacent to the Campanian Plain

Ileana Santangelo, Claudio Scarpati, Annamaria Perrotta, Lorenzo Fedele, and Giulia Chiominto

Abstract

Literature data show that the two most widespread Vesuvius 79 AD pyroclastic density currents (PDCs) have been traced over a large area around the volcano throughout the Campanian plain. Here, we present stratigraphic and volcanological evidence for 79 AD PDC deposits on higher elevated areas bordering the Campanian plain. More specifically, a sequence of ash deposits, with erosive basal contacts, interstratified with lithic-rich lapilli fall layers (D, G1, G3, I, and X2), has been observed above a thick pumice blanket that has been associated with the Plinian phase on the Lattari mountains between 50 and 300 m asl. We use fall layers as guide levels that allow the correlation of the distal ash deposits with the proximal/medial stratigraphic sequences. The ash PDC sequence ranges in thickness from 22 cm (where local debris flows partially erode it) to 150 cm (where it thickens against anthropic structures). This study demonstrates that most PDC units recognized in medial areas, including the final phreatomagmatic events, are traceable on mountain slopes about 20 km from the vent. The discovery of PDC units at altitudes as high as 300 m asl adjacent to the Campanian plain suggests an inflated and turbulent nature of the parental pyroclastic currents and a limited shielding effect of the mountains to the spread of the PDCs.

Keywords

AD 79 vesuvius eruption • Distal pyroclastic current deposits • Post-plinian phase

1 Introduction

Plinian eruptions are characterized by buoyant plumes, widespread fall deposits, and total or partial collapse regimes emplacing pyroclastic density currents (PDCs) (Cioni et al., 2015). Although, most of the volume of magma emitted is usually associated with a sustained column phase, the generation and propagation of PDCs cause the greatest damage to the territory and the resident populations (Neri, 2015). One of the most important examples in this sense is represented by the 79 AD Plinian eruption of Vesuvius, during which several PDCs destroyed and buried the Roman cities of Pompeii and Herculaneum and many suburban villas (Cioni et al., 2004; Luongo et al., 2003; Sigurdsson et al., 1985). The destructive impact is mostly observed 10 km from the vent, even if a PDC probably killed the famous Pliny the Elder near Stabiae, ca. 15 km south of Vesuvius (Sigurdsson et al., 1985). PDCs were generated during and after the Plinian phase by a partial to entirely collapsing plume (Shea et al., 2011). The two most energetic PDCs inundated the Campanian Plain south of Vesuvius (Tadini et al., 2021).

Here, we present stratigraphic and volcanological evidence for 79 AD PDC deposits on the mountains bordering the Campanian plain.

2 Methods

The composite stratigraphy of the 79 AD Vesuvius eruption deposits, illustrated here, follows the naming scheme proposed by Scarpati et al. (2020). The relationship between this stratigraphy and previously published data is described in Scarpati et al. (2020). Lithofacies were described using non-genetic terms based on the lithological characteristics of the deposits (e.g., internal structures, grain size, sorting, component variations, and welding intensity).

I. Santangelo · C. Scarpati (✉) · A. Perrotta · L. Fedele · G. Chiominto
Department of Earth, Environmental and Resources Sciences, University of Napoli Federico II, Napoli, Italy
e-mail: claudio.scarpati@unina.it

A. Çiner et al. (eds.), *Recent Research on Sedimentology, Stratigraphy, Paleontology, Tectonics, Geochemistry, Volcanology and Petroleum Geology*, Advances in Science, Technology & Innovation,
https://doi.org/10.1007/978-3-031-43222-4_31

3 Results

3.1 Stratigraphy

In distal areas, beyond 15 km from the vent, ash deposits are observed at altitudes between 50 and 300 m asl on the Lattari mountains (Fig. 1). They are not interbedded with the Plinian pumice fall deposit but lie above it (Fig. 1). The lowermost ash deposit, unit E, which is poorly sorted ($\sigma\phi$ = 2.15–2.73), exhibits a massive structure with gray pumice clasts at the base and rare armored lapilli. It thickens toward obstacles. Unit F is poorly sorted ($\sigma\phi$ = 2.18–3.02), stratified, and shows diffuse accretionary lapilli. Unit H is a massive ash deposit with accretionary lapilli. Locally, it thickens in small depressions, and accretionary lapilli concentrate at the top. Unit L is an accretionary lapilli-bearing horizon. Unit N is a thin, very fine ash deposit. It is overlain by unit X1, a poorly sorted, lithic-rich, coarse ash deposit documented here for the first time. Finally, above the uppermost lithic-rich fall deposit (X2), a stratified ash deposit, unit O, is observed. Accretionary lapilli are diffused in the whole unit and concentrates at the base and in the middle. Lithic clast content increases from 14 to 40 wt% from E to X1, while the overlying unit O has 5–15 wt%.

3.2 Lithofacies

Lithofacies recognized in the distal 79 AD PDC deposits are described, and their emplacement mechanisms are discussed in Table 1. Facies description indicates that the depositional system shows spatial and temporal variability in many parameters (e.g., concentration and components). Massive facies are generally overlain by accretionary lapilli-bearing tuff, indicating an increasing involvement of external water in the eruptive dynamics. Large-scale lateral facies variation, from proximal to distal locations, shows a substantial decrease in grain size and lithic content and few types of facies in distal areas. These sedimentological variations generally reflect a depletive competence and nonuniform behavior of all post-Plinian AD 79 PDCs.

4 Conclusions

Most of the 79 AD PDC units recognized in medial locations above the pumice lapilli Plinian deposit are recognized on the elevated areas bordering the Campanian plain, interstratified with lithic-rich lapilli fall layers. The presence of PDC units at 300 m asl in distal locations suggests the

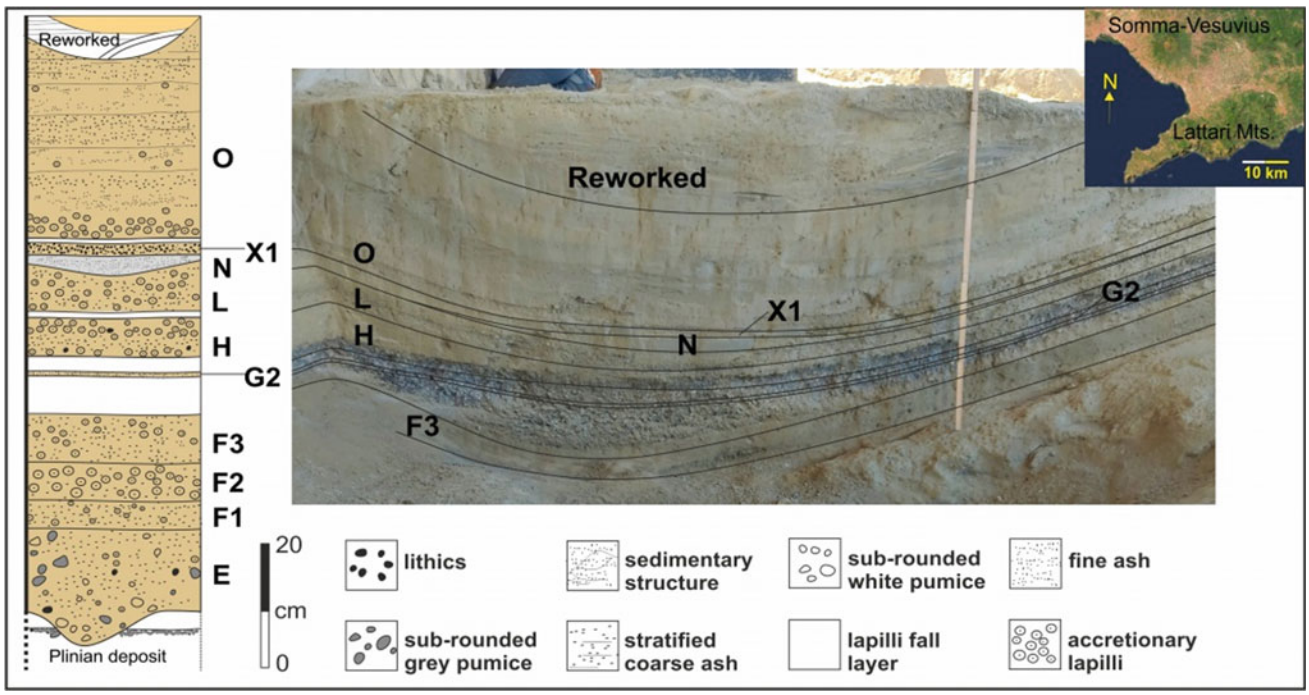

Fig. 1 Stratigraphic column showing the AD 79 distal deposits. On the right is a field photograph of AD 79 PDC layers. Inset shows the location of the PDCs facies on the Mts. Lattari

Table 1 Summary description and interpretation of AD 79 PDC lithofacies

Lithofacies	Description	Unit	Interpretation
Massive tuff or massive lapilli tuff (mLT)	Massive, coarse ash matrix-supported, and very poorly sorted deposits containing rounded pumice lapilli, white and gray (up to 20 mm in diameter) with subordinate sub-centimeter lithic fragments (mainly lava and rare limestone) and rare accretionary lapilli set into the matrix. The basal contact is strongly erosive Sorting: $2.96 < \sigma\varphi < 3.43$; Thickness: 6 to 124 cm	E, G2, N	Aggradation from highly concentrated, fluid-escape dominated flow-boundary zone without directional grain fabric
Accretionary lapilli-bearing tuff (accT)	Poorly-sorted coarse ash beds are rich in accretionary lapilli (between 4 and 30%) with concentric layers or an armored structure around a lithic or pumice clast. Accretionary lapilli are up to 10 mm in diameter and are randomly distributed in the deposits or arranged in layers Sorting: $2.49 < \sigma\varphi < 3.02$; Thickness: 4–21 cm	F, H, L	Explosive phase involving external water consistent with a phreatomagmatic origin
Lithic-rich massive tuff (lmT)	Massive, poorly-sorted, fine ash matrix-supported deposit with abundant rounded mm-sized lithic clasts predominantly composed of lava fragments. Very rare limestone and tuff clasts are found Sorting: 2.31; Thickness: 2 cm	X1	Lithic-rich deposits are related to the segregation of heavy components
Stratified tuff (sT)	Stratified deposits with sub-parallel millimeter to centimeter scale stratifications are defined by sharp changes in matrix grain size, from fine to coarse ash. Most individual layers are laterally impersistent, and low-angle erosional truncations are observed. Locally, massive and clast-supported lenses composed of very fine lithic fragments occur between the layers Sorting: $2.24 < \sigma\varphi < 2.76$; Thickness: 25–37.5 cm	O	Low-concentrated, traction-dominated flow-boundary zone in a highly unsteady current

turbulent behavior of the parental pyroclastic currents and the limited shielding effect of the mountains on the spread of the PDCs.

References

Cioni, R., Gurioli, L., Lanza, R., & Zanella, E. (2004). Temperatures of the AD 79 pyroclastic density current deposits (Vesuvius, Italy). *Journal of Geophysical Research Solid Earth*, *109.*

Cioni, R., Pistolesi, M., & Rosi, M. (2015). Plinian and subplinian eruptions. In *The encyclopedia of volcanoes* (2nd edn., pp. 519–535), Elsevier, Amsterdam.

Luongo, G, Perrotta, A., & Scarpati, C.: Impact of AD 79 explosive eruption on Pompeii I: Relations amongst the depositional mechanisms of the pyroclastic products, the framework of the buildings and the associated destructive events. *Journal of Volcanology and Geothermal Research, 126*, 201–23 (2003)

Neri, A., Esposti Ongaro, T., Voight B., & Widiwijayanti, C. (2015). Pyroclastic density current hazards and risk. In *Volcanic hazards, risks and disasters* (pp. 109–140), Elsevier, Amsterdam.

Scarpati, C., Perrotta, A., Martellone, A., & Osanna, M. (2020). Pompeian hiatuses: New stratigraphic data highlight pauses in the course of the AD 79 eruption at Pompeii. *Geological Magazine, 157*, 695–700.

Shea, T., Gurioli, L., Houghton, B. F., Cioni, R., & Cashman, K. V. (2011). Column collapse and generation of pyroclastic density currents during the AD 79 eruption of Vesuvius: The role of pyroclast density. *Geology, 39*, 695–698.

Sigurdsson, H., Carey, S., Cornell, W., & Pescatore, T. (1985). The eruption of vesuvius in AD 79. *National Geographic Research, 1*, 1–55.

Tadini, A., Bevilacqua, A., Neri, A., Cioni, R., Biagioli, G., de'Michieli Vitturi, M., & Esposti Ongaro, T. (2021). Reproducing pyroclastic density current deposits of the 79CE eruption of the Somma–Vesuvius volcano using the box-model approach. *Solid Earth, 12*, 119–139.

Fallout Events During the Post-plinian Phase of the AD 79 Vesuvius Eruption

Giulia Chiominto, Claudio Scarpati, Annamaria Perrotta, Lorenzo Fedele, and Ileana Santangelo

Abstract

The AD 79 Vesuvius eruption is characterized by two main phases: a sustained column phase, which deposited a thick white–gray pumice lapilli deposit, followed by a column collapse phase, which emplaced several pyroclastic density currents. Here, we present stratigraphic and volcanological evidence for five lithic-rich lapilli fall layers (D, G1, G3, I, and X2, from base to top) interstratified with pyroclastic density current deposits, which have been emplaced after the collapse of the AD 79 Plinian column. These are distributed south of the Vesuvius, at distances between 5 and 20 km from the vent. All sections were sampled to quantify lateral and vertical changes in grain size, and sedimentological parameters were determined. Clasts were separated into three main categories: juvenile, lithic, and crystals. The coarser layers, D and G1, have median diameters similar to those of the finer part of the Plinian deposit at the same locations, indicating a significant plume height during these later sustained column pulses. Our study suggests that the resumption of a sustained column was repeatedly established during the post-Plinian phase of the AD 79 eruption, similar to the ignimbrite phase of the Novarupta and Bishop Tuff Plinian eruptions. The lithic-rich nature of all these late fall phases suggests changes in eruption style (with respect to the magmatic Plinian phase), possibly associated with instabilities in the conduit-vent system.

Keywords

Vesuvius • AD 79 eruption • Lithic-rich fall layers

1 Introduction

High, sustained plumes characterize plinian eruptions, often collapsing and generating pyroclastic density currents (PDC). This 'classical' behavior is well represented by the AD 79 Vesuvius eruption that produced two main eruptive phases: a sustained column phase, which deposited a thick white to gray pumice lapilli deposit, followed by a column collapse phase, which emplaced several PDCs (Cioni et al., 1992; Sigurdsson et al., 1985). In addition, single or multiple grain-supported lapilli fall layers, interstratified with PDC ash deposits, were described at the Pompeii archeological site (Cioni et al., 1992; Luongo et al., 2003). This paper reports the stratigraphy and distribution of the lithic-rich fall deposits accumulated during late resumption of the eruptive column. These results have been obtained from detailed descriptions and measurements of AD 79 sequences found within a wide area south of Mt. Vesuvius.

2 Methods

Several stratigraphic sections, located 5 and 20 km from Mt Vesuvius, have been studied in detail and extensively sampled. Samples were collected in the unconsolidated layers to characterize them from a sedimentological point of view. Samples were dry-sieved down to 4φ (0.063 mm) at 1φ intervals. Clasts were separated into three main categories: (1) juvenile: gray phono-tephritic pumice clasts; (2) lithic: fragments of lavas, subordinate limestones, and rare syenitic subvolcanic rocks and marbles; (3) crystals: predominantly clinopyroxene and minor amounts of sanidine and biotite.

G. Chiominto · C. Scarpati (✉) · A. Perrotta · L. Fedele · I. Santangelo
Department of Earth, Environmental and Resources Sciences, University of Napoli Federico II, Napoli, Italy
e-mail: claudio.scarpati@unina.it

A. Çiner et al. (eds.), *Recent Research on Sedimentology, Stratigraphy, Paleontology, Tectonics, Geochemistry, Volcanology and Petroleum Geology*, Advances in Science, Technology & Innovation,
https://doi.org/10.1007/978-3-031-43222-4_32

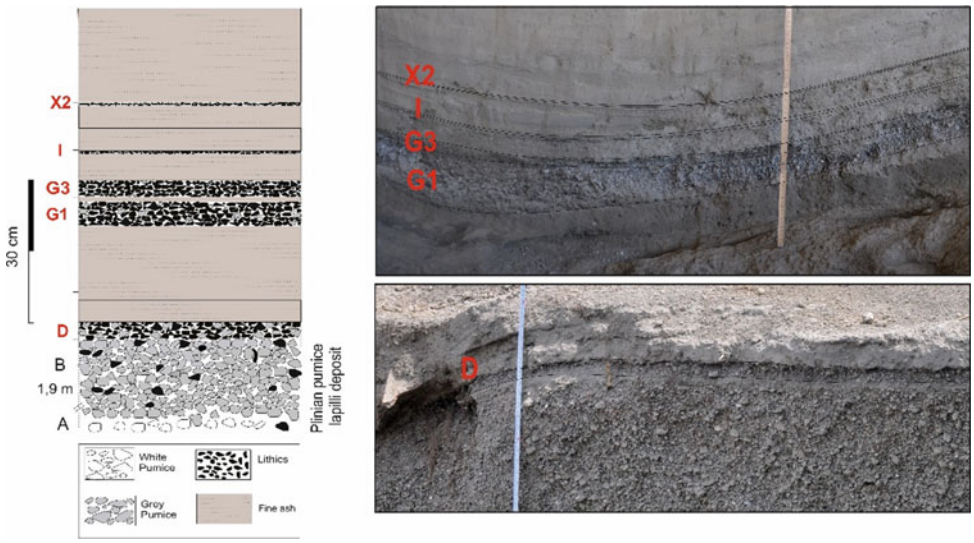

Fig. 1 Stratigraphic column showing the AD 79 deposits 20 km south of Vesuvius. On the right field are photographs of the lithic-rich layers

3 Results

3.1 Stratigraphy and Lithology

Thin, lithic-rich horizons, named layers D, G1, G3, I, and X2 from base to top, were found interstratified with the PDC units accumulated after the collapse of the AD 79 Vesuvius Plinian eruptive column (Fig. 1). The maximum thicknesses are 7 cm, 7 cm, 4 cm, 1.5 cm, and 1.5 cm, respectively, and were measured 6–15 km south of Mt. Vesuvius. Many of these layers gradually thin and become coarser toward the proximal sections, where they may be absent. These lithic-rich layers exhibit massive mantling structures and are generally well sorted (σ_ϕ = 1.05–1.55). Successive layers at a given outcrop show a decreasing trend in size. Grain size and component data of a selected location on Mt. Lattari, 15 km from the source, are reported in Table 1. Mdϕ ranges from 2 mm (unit D) to almost 0.5 mm (unit G3). High lithic contents characterize all these layers. Layer D has 61 wt% of lithics and 23 wt % of juvenile clasts. The upper layers show 70–83 wt% of lithics and less than 1.5 wt% of juvenile material.

3.2 Distribution

A sufficient number of outcrops were identified to reconstruct the distribution for the thicker units D and G1 (Fig. 2). Both distributions show a SE trend even if the azimuth of the dispersal axis of layer G1 seems to be rotated by 10°–20° relative to that of D1. Lithic-rich layers dispersion is similar to those of the basal lapilli Plinian deposit (see Sigurdsson et al., 1985 for comparison), including rotation of the dispersal axis.

4 Discussion

Some of the layers described here (D, G1, G3, and I) were previously identified in some archeological sites (e.g., Pompeii, Oplontis) (Cioni et al., 1992; Luongo et al., 2003; Scarpati et al., 2020), and their emplacement mechanisms attributed to sedimentation from a turbulent surge (Cioni et al., 1990; Sigurdsson et al., 1982) or fall from a sustained column (Cioni et al., 1992; Luongo et al., 2003; Scarpati et al., 2020). All five recognized lithic-rich layers show a wide dispersal and mantle bedding and are interpreted to be fall deposits that repeated resumptions of a sustained eruption column have produced. This occurred during the post-Plinian phase of the AD 79 eruption, comparable to the ignimbrite phase of the Novarupta and Bishop Tuff Plinian eruptions (Fierstein & Hildreth, 1992; Wilson & Hildreth, 1997). The main difference with the basal pumice lapilli deposit is the strong enrichment in lithic clasts, possibly associated with instabilities in the conduit-vent system. The coarser layers, D and G1, have median diameters similar to those of the finer part of the Plinian deposit at the same

Table 1 Grain size data and componentry at different stratigraphic heights in the AD 79 deposit 15 km from the Vesuvius, Mt. Lattari. J: juvenile clasts; L: lithic clasts; C: crystals

Layers	Mdϕ	$\sigma\phi$	J (wt%)	L (wt%)	C (wt%)
X2	−0.2	1.4	0.00	75.41	10.41
I	0.5	1.6	0.00	70.71	10.01
G3	0.5	1.05	0.02	79.39	16.48
G1	−1.0	1.25	1.49	83.02	11.25
D	−1.3	1.55	23.41	61.22	15.58

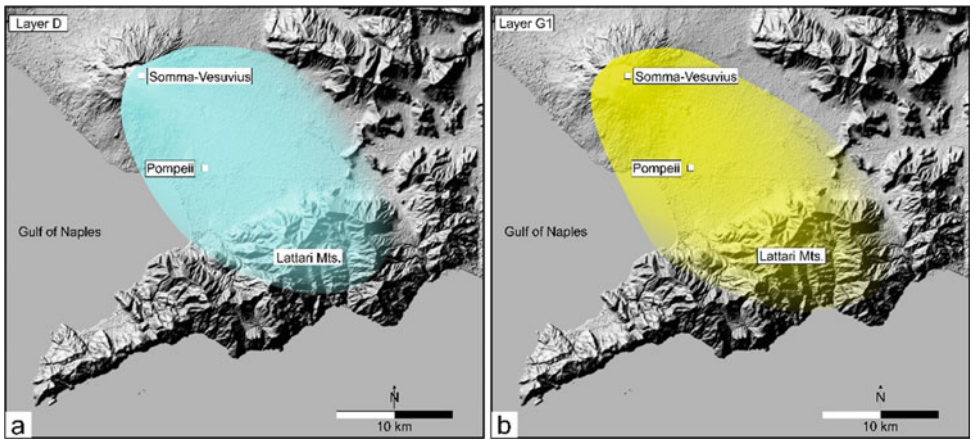

Fig. 2 Distribution of the thicker lithic-rich layers, D and G1. Note the slight clockwise rotation of the dispersal axis

locations, indicating a significant plume height during these later sustained column pulses.

5 Conclusions

Five lithic-rich fall layers have been recognized in the PDC post-Plinian sequences of the Vesuvius AD 79 eruption cropping out at various locations from the Vesuvius slopes to the edge of the Campanian Plain, 20 km from the source. They record pulses of a sustained column during a predominantly collapsing phase and could help better to constrain the timing of late AD 79 PDC events.

References

Cioni, R., Marianelli, P., & Sbrana, A. (1992). Dynamics of the AD 79 eruption: Stratigraphic, sedimentologic and geochemical data on the successions of the Somma-Vesuvius southern sector. *Acta Vulcanologica, 2*, 109–123.

Cioni, R., Marianelli, P., & Sbrana, A. (1990). L'eruzione del 79 dC: stratigrafia dei depositi ed impatto sugli insediamenti romani nel settore orientale e meridionale del Somma-Vesuvio. *Rivista di Studi Pompeiani, 4*, 179–198

Fierstein, J., & Hildreth, W. (1992). The plinian eruptions of 1912 at Novarupta, Katmai National Park, Alaska. *Bulletin of Volcanology, 54*, 646–684.

Luongo, G., Perrotta, A., & Scarpati, C. (2003). Impact of AD 79 explosive eruption on Pompeii I: Relations amongst the depositional mechanisms of the pyroclastic products, the framework of the buildings and the associated destructive events. *Journal of Volcanology and Geothermal Research, 126*, 201–223.

Scarpati, C., Perrotta, A., Martellone, A., & Osanna, M. (2020). Pompeian hiatuses: New stratigraphic data highlight pauses in the course of the AD 79 eruption at Pompeii. *Geological Magazine, 157*, 695–700.

Sigurdsson, H., Cashdollar, S., & Sparks, R. S. J. (1982). The eruption of Vesuvius in AD 79: Reconstruction from historical and volcanological evidence. *American Journal of Archaeology, 86*, 39–51.

Sigurdsson, H., Carey, S., Cornell, W., & Pescatore, T. (1985). The eruption of vesuvius in AD 79. *National Geographic Research, 1*, 1–55.

Wilson, C. J. N., & Hildreth, W. (1997). The Bishop Tuff: New insights from eruptive stratigraphy. *The Journal of Geology, 105*, 407–439.

The Composition of Fly Ash and Bottom Ash (FABA) from Indonesian Coal Power Plant: A Case Study from Batam

Iqbal Iqbal, Ferian Anggara, and Himawan Tri Bayu Murti Petrus

Abstract

Fly ash and bottom ash (FABA) are inorganic and organic components from coal combustion residue. Samples of FABA were collected from the combustion of the power plant in Ecogreen Oleochemical, Batam. This study aims to examine the composition of FABA in the study area. The organic and inorganic components of FABA are determined by petrographic analysis. The mineralogy composition of FABA was determined by XRD analysis. In addition, ICP-AES and ICP-MS analyses were also conducted to determine the geochemistry components. The results show that the inorganic components of FABA consist of amorphic materials and minerals. The amorphic materials of FABA in the form of glass were classified by their morphological properties: cenospheres and pleiospheres. The other inorganic FABA components in the form of minerals consist of glass, quartz, Fe-spinel, Mg-spinel, hematite, magnetite, mullite, feldspar, and kaolinite. The most abundant inorganic component in FABA is quartz and iron oxide minerals. Organic components of FABA consist of unburned coal, which is unburned inertinite maceral. The geochemistry composition of major oxide compounds mainly found on FABA consists of SiO_2, Al_2O_3, and Fe_2O_3. SiO_2 compounds are distributed in the components of glass, quartz, mullite, and k-feldspar. Al_2O_3 compounds are distributed to mullite, Mg-Fe spinel, and k-feldspar. Fe_2O_3 compounds are distributed to hematite, magnetite, and Fe-spinel.

Keywords

FABA • Unburned coal • Glass

1 Introduction

1.1 Background

Sources of fossil fuels, coal, and renewable energy generally supply energy needs in Indonesia. One form of national energy needs is electrical energy. To prepare for national energy demand, the government has issued Presidential Regulation of the Republic of Indonesia Number 22 of 2017, which regulates the General National Energy Plan to be implemented in 2017–2025. Based on this, the government plans to generate 135.5 GW of electricity, of which 30% of the energy will be produced from burning coal. The use of coal as a fuel for power plants at PLN from 2000–2010 was 49.1% (Cahyadi, 2011), and the total fly ash and bottom ash (FABA) produced was even greater in the coming year. Electrical energy in PLTU is formed through burning coal to produce hot steam, which drives turbines in power generators. However, the use of excessive production could have an impact on the environment. One of them is the ash produced from coal combustion at PLTU, which requires management to avoid environmental problems such as air pollution or a decrease in ecosystem quality. This study aims to determine the components of FABA produced from coal combustion in PLTU Batam. The benefits of this research can be used to determine the processing of FABA based on their constituent elements to increase the value of coal combustion waste products.

I. Iqbal
Undergraduate Program, Department of Geological Engineering, Universitas Gadjah Mada, Yogyakarta, Indonesia

F. Anggara (✉)
Department of Geological Engineering, Faculty of Engineering, Unconventional Geo-Resources Research Group, Universitas Gadjah Mada, Yogyakarta, Indonesia
e-mail: ferian@ugm.ac.id

H. T. B. M. Petrus
Department of Chemical Engineering, Faculty of Engineering, Unconventional Geo-Resources Research Group, Universitas Gadjah Mada, Yogyakarta, Indonesia

A. Çiner et al. (eds.), *Recent Research on Sedimentology, Stratigraphy, Paleontology, Tectonics, Geochemistry, Volcanology and Petroleum Geology*, Advances in Science, Technology & Innovation,
https://doi.org/10.1007/978-3-031-43222-4_33

1.2 Research Area

Research locations of FABA where the samples were taken is PLTU Ecogreen Oleochemicals, Batam, located in Batam Special Industrial Zone, Riau Islands. The PLTU unit is located in the eastern part of Batam Island (Fig. 1).

2 Method

The samples taken were fly ash and bottom ash. The sample was taken at the PLTU Ecogreen Oleochemicals unit, Batam. The total number of samples was 12, consisting of 10 samples of fly ash (FA) and two samples of bottom ash (BA). All samples were then analyzed in the laboratory according to the research objectives. The analysis carried out in this study includes petrographic analysis, XRD analysis, and geochemical analysis. Sample recapitulation, and the type of analysis performed on each sample, can be seen in Table 1.

2.1 Petrographic Analysis

Petrographic analysis on FABA polished incisions was carried out to identify the type and abundance of organic and inorganic components. FABA polish incisions were made using the SpeciFix-20 Kit and the Struers Labo System. The FABA polished incisions were analyzed using the point counting method with 550 points under a reflecting microscope with 40 times magnification. Identifying inorganic and organic components that makeup FA and BA is based on Hower's (2012) classification.

2.2 XRD Analysis

XRD analysis was performed to determine the mineralogical composition of FABA samples that could not be observed microscopically, such as altered minerals produced from the coal combustion process. The sample used for XRD analysis was only 5 g of the finely grounded sample of FABA. Eight FA samples were analyzed using XRD test with bulk analysis method referring to the United States Geological Survey (USGS) standard.

2.3 Geochemical Analysis

The geochemical analysis carried out in this study is the ICP-AES analysis. ICP-AES tested FABA samples to determine the type and concentration of the major oxide compounds. The preparation of the two types of samples was carried out by finely grinding the samples. This analysis uses borate fusion and diluted acid at the ALS Geochemistry Laboratory, Kamloops, Canada.

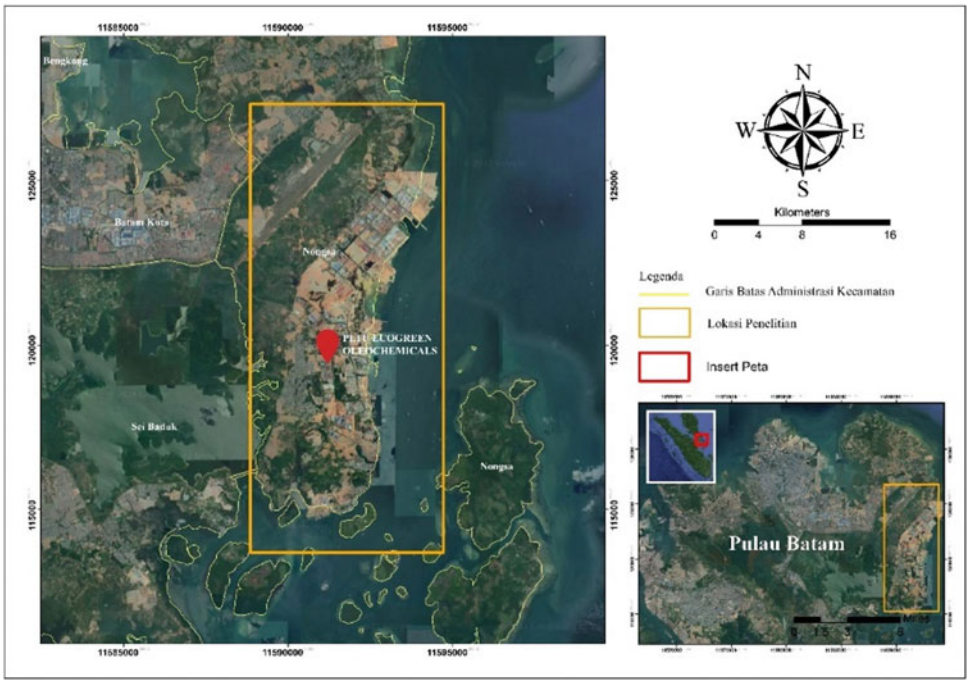

Fig. 1 Map of the study area

Table 1 Table of samples

No.	Sample code	Proksimat	XRD	Petrografi	ICP-MS and ICP-AES
1	FA-01	–	v	v	v
2	FA-02	–	v	v	v
3	FA-03	–	v	v	v
4	FA-04	–	v	v	v
5	FA-05	–	v	v	v
6	BA-01	–	v	v	v
7	BA-02	–	v	v	v
8	FA-06	–	v	v	v
9	FA-07	–	v	v	v
10	FA-08	–	v	v	v
11	FA-09	–	v	v	v
12	FA-10	–	v	v	v

3 Results and Discussion

FABA components of coal burning in PLTU not only produce steam but also produce coal ashes. Coal ashes can be divided into two groups based on the size of their constituent particles, namely FA and BA. According to Wardani (2008), FA or fly ash is a particle resulting from coal combustion which is fine and light in size, so exhaust gases easily carry it away. Meanwhile, BA is ash from coal combustion, which is coarser in size than FA. The composition of maceral and mineral matter in the original coal generally influences variations in the constituent components of FA and BA. Hower (2012) showed that, in general, FA is composed of inorganic and organic components from coal combustion residues and new materials formed in boilers and flue gas streams. The mineral matter contained in coal can change either totally or partially during combustion to produce new types of minerals that are different from the minerals in the original coal. The constituent components of FA obtained based on XRD in the samples studied were dominated by inorganic components in quartz with an abundance of 34.44%. Other inorganic components that makeup FA are Fe-spinel (2.79%), mullite (13.56%), Mg-spinel (5.48%), hematite (28.82%), magnetite (8.09%), feldspar (5.93%), and kaolinite (0.87%) were found in small amounts. The organic component found in FA based on petrographic analysis was unburned coal (UC), with an abundance of 12.8%. In contrast, the constituent components of BA obtained based on petrographic analysis in the sample studied were also dominated by inorganic components, with quartz, an abundance of 45.1%. Other inorganic components that makeup BA are glass (4.9%) and iron oxide minerals (9.95%). Meanwhile, the organic elements found in BA based on petrographic analysis was UC, with an abundance of 40.4%. The principal oxides in FA and BA are SiO_2, Al_2O_3, and Fe_2O_3. SiO_2 compounds are distributed in glass, quartz, mullite, and k-feldspar. Al_2O_3 compounds are distributed to mullite, Mg–Fe spinel, and k-feldspar. Fe_2O_3 compounds were distributed to hematite, magnetite, and Fe-spinel.

3.1 Inorganic Components

The results of petrographic analysis on polished incision samples showed that FABA was composed of inorganic components such as glass, quartz, Fe-oxide minerals, mullite, and spinel. Variations of inorganic components that make up FABA based on XRD analysis are quartz, Mg-spinel, Fe-spinel, mullite, hematite, magnetite, feldspar, and kaolinite minerals. Differences in the variation of inorganic components make up FABA based on data from petrographic and XRD analysis. The mullite mineral was identified by petrographic observation only in fly ash samples (FA-02, FA-04, FA-05, FA-06, FA-08, and FA-10) with minor amounts. The type of iron oxide minerals (Fe-oxide minerals) in FABA could not be identified in detail on petrographic analysis. In contrast, on XRD analysis, it was known that iron oxide minerals in FABA samples were hematite and magnetite. Hematite and magnetite minerals are almost found in all FABA samples. In addition, from the XRD analysis, it is also known that there are two types of spinel in the FA studied, namely Fe-spinel and Mg-spinel. The two kinds of spinels cannot be distinguished when conducting petrographic observations using a reflecting microscope because they have very similar optical characteristics and textures. Mg-spinel and Fe-spinel were found in all FABA samples studied, but the abundance in bottom ash samples ranged from 1.48 to 13.6% for Mg-spinel, while there was only 0.57–0.88% in the bottom ash sample. Mg-spinel in fly ash samples ranged from 4.98 to 6.94%,

while Fe-spinel in fly ash samples ranged from 0.06 to 6.29%. The following is a detailed explanation of the inorganic components that make up FABA:

- Quartz (SiO_2)

Quartz minerals in FABA generally come from quartz minerals in the original coal (Dai et al., 2010). Quartz in crystalline form can be found in the inorganic component of FABA because quartz does not melt when the coal combustion temperature does not exceed 1400–1500 °C (Hower, 2012). Quartz is one of the most common inorganic components found in abundance in FABA. The abundance of quartz on FA in petrographic observations ranged from 25.7 to 35.6%, and XRD ranged from 31.95 to 37.12%, while in BA in petrographic observations, it ranged from 40.9 to 49.3% and XRD ranged from 55.49 to 63.25%. A colorless–white color characterizes quartz on petrographic observations with an angular–subrounded shape.

- Mullite ($Al_6O_{13}Si_2$)

Mullite in FABA is generally derived from kaolinite in the original coal (Dai et al., 2010). The abundance of mullite in FABA positively correlates with the abundance of clay minerals in the original coal. The petrographic analysis showed the characteristic of mullite, which was black with a needle shape. The needle form of mullite results from the initial melting of kaolinite when coal combustion takes place at high temperatures (Dai et al., 2010). The abundance of mullite was only identified in FA samples (FA-02, FA-04, FA-05, FA-06, FA 08, and FA-10) ranging from 0.3 to 0.6% and not specified in BA. Based on XRD analysis, the abundance of mullite in FA ranged from 10.93 to 18.14%, and in BA, it ranged between 6.8 and 8.98%. The abundance of mullite was identified as more dominant in FA because of its finer particle size than BA.

- Glass (amorphous SiO_2)

Glass is a constituent component of FABA composed of SiO_2 compounds and amorphous. The abundance of glass in FA samples ranged from 1.30 to 11.70%, and in BA, it ranged from 4.3 to 5.5%. The petrographic analysis of FABA samples showed that the glass could be distinguished based on its morphology, namely in the cenosphere and pleiosphere. The cenosphere is characterized by the glass with a perfectly spherical appearance resembling a sphere. On the other hand, a pleiosphere is a glass with a morphology that is not perfectly round. Glass is interpreted to be formed when clay minerals composed of aluminasilic compounds are burned at high temperatures, resulting in some of the SiO_2 compounds being released and developing amorphous SiO_2 materials.

- Spinel

Spinel is formed from coal-rich in Fe and is sometimes found with magnetite (Hower, 2012). The results of the petrographic analysis show that the spinel characteristics found in FA and BA are bright mineral appearances and generally are spheres composed of white crystals with a dendritic texture which can be seen in Fig. 6.4. The spinel found in FABA is Fe-spinel ($FeAl_20_4$) and Mg-spinel ($MgAl_2O_4$). The two types of spinels cannot be distinguished under a microscope because the optical characteristics and texture of the minerals observed are very similar. Mg-spinel and Fe-spinel were found in all FABA samples. The abundance of Mg-spinel in FA ranged from 4.59 to 6.94%, while in BA samples, it ranged from 1.48 to 13.6%. The abundance of Fe-spinel in FA ranged from 0.06 to 6.29%, while Fe-spinel in BA ranged from 0.57 to 0.88%. The main oxide compounds affect the inorganic or mineral components formed in FABA. SiO_2 compounds are distributed in glass, quartz, mullite, and feldspar. Al_2O_3 compounds were distributed in Mg-spinel, Fe-spinel, and mullite. Fe_2O_3 compounds are distributed in Fe-spinel, and iron oxide minerals include hematite and magnetite. MgO compounds are distributed in Mg-spinel minerals, while K_2O compounds are distributed in feldspars. Feldspar minerals were found in all FABA samples. The abundance of feldspar in FA ranges from 2.22 to 9.90%, while in BA, it ranges from 4.36 to 6.86%.

- Iron oxide minerals

The petrographic analysis shows the characteristics of the iron oxide minerals (Fe-oxide minerals) in FABA which are red with a relatively angular-subrounded shape. Iron oxide minerals are produced from burning coal rich in Fe (Dai et al., 2010). The element Fe in the coal samples studied was present as the mineral pyrite. Pyrite minerals undergo oxidation when coal is burned and produce iron oxide minerals. The types of iron oxide minerals found in FABA samples based on XRD analysis were hematite (Fe_2O_3) and magnetite (Fe_3O_4). Based on XRD analysis, the abundance of hematite in the FA sample ranged from 21.72 to 32.57%. It ranged from 5.87 to 10.78% for BA samples, while the abundance of 86 magnetite in the FA sample ranged from 2.62 to 12.79%, and the BA sample ranged from 10.20 to 10.82%.

3.2 Organic Components

The results of the petrographic analysis on the polished incision showed that the FABA sample was also composed of organic components in the form of unburned coal (UC) or inertinite maceral groups that did not burn out. The maceral composition of coal can significantly influence the proportion of UC produced in FABA. In various coal grades, the inertinite maceral group is more difficult to burn when compared to the vitrinite and liptinite maceral groups. Thus, it tends to be present in FABA with relatively the same conditions as the original coal or in the form of unburned carbon or unburned coal (Nandi et al., 1977; Shibaoka, 1985; Vleeskens et al., 1993 in Hower, 2012). The abundance of inertinite maceral groups in the coal samples ranged from 44 to 45% (Table 5.4). The appearance of UC in FABA samples can be seen in (Fig. 6.5). The abundance of UC based on FA samples ranged from 11.15 to 13.65%, and on BA, it ranged from 40.1 to 40.7%.

4 Conclusion

The components that makeup fly ash (FA) in the samples studied are dominated by inorganic components in the form of iron oxide minerals, with 47.48%. The other inorganic components of FA are quartz (30.99%), spinel (2.25%), and glass (6.21%), while bottom ash (BA) is dominated by inorganic components in the form of quartz, with a percentage of 45.1%. Other inorganic components that makeup BA are glass (4.9%) and iron oxide minerals (9.95%).

Based on XRD analysis, the mineralogical components of FA were dominated by quartz with a percentage of 34.44%, with other components in the form of feldspar (5.93%), mullite (13.56%), Fe-spinel (2.79%), Mg-spinel (5.48%), hematite (28.82%), magnetite (8.09%), and kaolinite (0.87%), and for the components that make up BA are also dominated by quartz with a percentage of 59.37% with other components in the form of feldspar (5.61%), mullite (7.89%), Fe-spinel (0.72%), Mg-spinel (7.54%), hematite (8.32%), magnetite (10.51%), and kaolinite (0.02%). The organic components found in FA and BA are unburned coal, with an abundance of 12.8% and 40.4%.

References

Cahyadi. (2011). Kajian Teknis Pembangkit Listrik Berbahan Bakar Fossil. *Ilmiah Teknologi Energi, 1*, 21–32.

Dai, S., Zhao, L., Peng, S., Chou, C. L., Wang, X., Zhang, Y., Li, D., & Sun, Y. (2010). Abundances and distribution of minerals and elements in high-alumina coal fly ash from the Jungar Power Plant Inner Mongolia, China. *International Journal of Coal Geology, 81*, 320–332.

Hower, J. C. (2012). Petrographic examination of coal-combustion fly ash. *International Journal of Coal Geology, 92*, 90–97.

Wardani, S. (2008). *Pemanfaatan Limbah Batu Bara (Fly Ash) Untuk Stabilitas Tanah Maupun Keperluan Teknik Sipil Lainnya Dalam Manggurangi Pencemaran Lingkungan* (pp. 1–71). Pengukuhan Guru Besar Fakultas Teknik Universitas Diponogoro.

Forensic Fingerprinting of Biomarkers for the Geochemical Characterization of Oil Spills and Soil Contamination in the Coastal Area of Bizerte, Tunisia

Cyrine Belhadj, Anis Belhaj Mohamed, and Noamen Rebai

Abstract

This research deals with oil contamination of the surface sediments of the various sites in the southwest of the Mediterranean Sea distributed over the coastal region of Bizerte (depth: 0–20 m), northern Tunisia. This work was carried out according to a geochemical approach combining the sedigraph method, gravimetric analyzes, rock–eval pyrolysis, and chromatographic techniques based on molecular biomarkers (n-alkanes, steranes, terpanes, and hopanes). This approach made it possible to highlight the substantial contamination by petroleum hydrocarbons and, in particular, by polycyclic aromatic hydrocarbons (PAHs) of the surface sediments (0–25 cm) of the Bay of Bizerte (∑PAHs: 1539.24 ng/g. dry sed). In addition, it also indicates an anthropogenic crude origin and a state of biodegradation for all the oils, the bases of organic materials (terrestrial, lake, and marine origin), and different responsible sources (maritime traffic for the contamination of northeastern Tunisia).

Keywords

Oil contamination • Surface sediments • Mediterranean Sea • Molecular biomarkers • PAHs

1 Introduction

The marine environment represents a considerable stake in terms of socio-economic development. In recent decades, ocean pollution has become a subject of international scientific concern.

The Mediterranean Sea is considered a representative model of the world ocean. The region includes a vast array of marine and coastal ecosystems that provide essential benefits to all coastal dwellers. Nevertheless, it also registers various signals of strong enthronization and pressure from neighboring countries and industrialized countries in Northern Europe (Zaghden et al., 2005) . A large part of these anthropogenic or natural micropollutants are absorbed by suspended particles and then accumulated in the sediments (Soclo et al., 2000). Sedimentary matrices constitute genuine filters and reservoirs for organic contaminants such as petroleum hydrocarbons.

In this context, a large number of actors in the marine environment are interested in the development of new approaches and new tools in geochemistry. The use of molecular biomarkers is an essential tool in examining the contamination levels of surface marine sediments by petroleum hydrocarbons (n-alkanes, polycyclic aromatic hydrocarbons PAHs) and taking into account the environmental risk associated with the petroleum contamination (Burgess et al., 2003). Despite the ban on using some of these pollutants in Europe and Tunisia since the 1980s, they continue to pose problems due to their toxicity following their intentional or accidental release into the environment. Let us cite the example of the fuel oil leak accident of October 4, 2018, by the Tunisian Company of Refining Industries (Zarzouna, Bizerte), which resulted in solid contamination by petroleum hydrocarbons in the coastal region of Bizerte, deeply affecting its matrices sedimentary (Bejaoui et al., 2018).

2 Materials and Methods

The Bay of Bizerte is at the northeastern end of Tunisia (37° 17′38″ N, 9° 56′20″ E). Different geological formations characterize the stratigraphic context of the study area from the Eocene to the Quaternary. The Oligocene occurs

C. Belhadj (✉) · N. Rebai
National Engineering School of Tunis (ENIT), University of Tunis El Manar, 1002 Tunis, Tunisia
e-mail: Cyrin.belhaj@gmail.com

A. B. Mohamed
Petroleum Research and Development Center, Tunisian Petroleum Activities Company (ETAP), 2035 Tunis, Tunisia

A. Çiner et al. (eds.), *Recent Research on Sedimentology, Stratigraphy, Paleontology, Tectonics, Geochemistry, Volcanology and Petroleum Geology*, Advances in Science, Technology & Innovation,
https://doi.org/10.1007/978-3-031-43222-4_34

locally in the Bay of Bizerte from the quarries near Zarzouna with variable thickness in the form of alternating marl and sandstone locally rich in glauconite (Bejaoui et al., 2018). The sea trips and the sampling companions were carried out in two sites of the bay, distributed along the north and north-east coast of the Tunisian coasts Zarzouna and Cape Zebib located between the parallels 35° 15′29″ and 37° 17′15″ North and meridians 9° 42′55″ and 10° 04′05″ East.

Ten surface sediment samples were taken at a layer depth of 25 cm, using underwater dives (depth: 0–20 m), a manual corer, a hammer, and a spatula at two stations in the Bay of Bizerte. At each sampling station, three cores were driven and enclosed with a cork stopper, and a preliminary reduction of sediment aggregates (to <2 mm fragments) was performed to separate coarse elements.

2.1 In Situ Conservation and Sample Preparation

For in situ conservation, the soil samples were transported to the speaking laboratory in a refrigerated cooler at 4 °C, wrapped with aluminum foil, and stored in the freezer at −20 °C until analysis. The samples were manually homogenized and lyophilized.

2.2 Textural Characterization of Sediments

The textural characterization of the sediments collected from the Bay of Bizerte was carried out by sedigraphic analysis. All samples were analyzed by liquid (in solution) using a Malvern 2000 laser particle size analyzer. Data processing software represented the percentage of particle size populations. The results of the laser particle sizer were represented as cumulative curves in a semi-logarithmic diagram. The determination of different types of sedimentary facies was carried out according to the shape of the curves and to Folk's (1957) diagram (Folk, 1957), allowing the classification of the sediments according to the percentages of the three particle size fractions (clay, lemon, and sand).

2.3 Geochemical Approach

2.3.1 Pyrolytic Analysis: Determination of TOC

The determination of the petroleum hydrocarbon (TPH) content and the calculation of the TOC and HI content were carried out using the rock–eval 6 pyrolysis method and applying the following formula [7]:

$$\%\,\mathrm{TOC\,(Total\ Organic\ Carbon)} = \mathrm{PC}\,(\%\,) + \mathrm{RC}\,(\%\,)$$

With PC: Particular carbon, RC: Residual carbon.

2.3.2 Extraction and Fractionation of Hydrocarbon Compounds

The extraction of the hydrocarbon compounds in 1 g dry-weight sediment was carried out using the Randall extraction method with 100 ml of dichloromethane. After evaporation by the rotary steamer, the extract was fractionated into aliphatic (SH) and aromatic hydrocarbons (AH) using solid-phase extraction (SPE). The extract constituted the mobile phase of SPE. To extract these compounds, the polar SPE supports (virgin silicas and Florisil) and the hexane/dichloromethane mixture were selected.

2.3.3 Identification and Detection of Hydrocarbons

The analytical procedure based on HPLC chromatographic analysis coupled with ultraviolet (UV) detection was used to assess qualitatively and quantitatively the polycyclic aromatic hydrocarbons (PAHs) contained in the surface sediment samples collected from the bay of Bizerte. The standards, injected into the HPLC, had concentrations of 25 ng/ml, and the columns were tested in 30 min with an acetonitrile/water solution in proportions varying between (50/50 to 70/30, v/v) in the initial state and (100/00, v/v) in the final form.

2.3.4 Molecular Biomarkers

After purification and fractionation of the hydrocarbons, the saturated compounds were analyzed by gas chromatography coupled with mass spectrophotometry (GC/MS) to identify the origins, evaluate the temporal evolution, and characterize the contaminations in Bizerte bay using molecular biomarkers (n-alkanes: from *n*-C12 to *n*-C40, isoprenoids: pristane (Pr) and phytane (Ph), aditerpenoids, cyclic terpenoids, steranes, hopanes, and aromatics.

2.4 Statistical Analysis

A principal Component analysis (PCA) was applied to the matrix of correlations obtained from the ratios of biomarkers measured at the ten stations in the Bay of Bizerte during the sampling periods. To classify the samples based on the similarities and differences between the properties of the biomarkers, the psych, FactoMineR, and factoextra packages of the R software were used.

3 Results and Discussions

3.1 Sedimentological Study

Analysis by laser sedigraph of the fraction less than 63 µm and the texture of the surface sediments made it possible to record a heterogeneous particle size distribution from the shape of the cumulative curves from one sampling station to another. Moreover, percentages of sand varying between 0 and 99.34%, clay between 0 and 72.3%, and silt between 0 and 49.44% were noted for the samples collected from the Bay of Bizerte. In addition, the collected soil samples' granulometric classification of Folk (1957) allowed underlining the following sedimentary texture (Fig. 1): A coarse sand-clay facies dominating the stations of Cape Zebib (S7, S8, S9), a fine facies with a sandy-silty texture covering the western part of the discharge zone, particularly at point S5, a silt–clay-sand type facies at point S0 (Bizerte channel), and a sandy facies characterizing the discharge zone (SR), the eastern part and the other stations of the Bay of Bizerte (S1, S2, S3, S4).

3.2 Geochemical Characterization of Soils Contaminated by Hydrocarbons

3.2.1 Result of the Pyrolytic Analysis

The examination of the results of the rock–eval 6 pyrolysis (reservoir mode) of surface sediment samples relating to the coastal region of Bizerte revealed a variation in the contents (low to very high) of total organic carbon (TOC) oscillating between 0.04 and 52.19% sediment. Moreover, a maximum of TOC was recorded in the sediments of Cape Zebib (52.19%), representing the top of the series. Our results also bear witness to the heavy soil contamination by petroleum hydrocarbons.

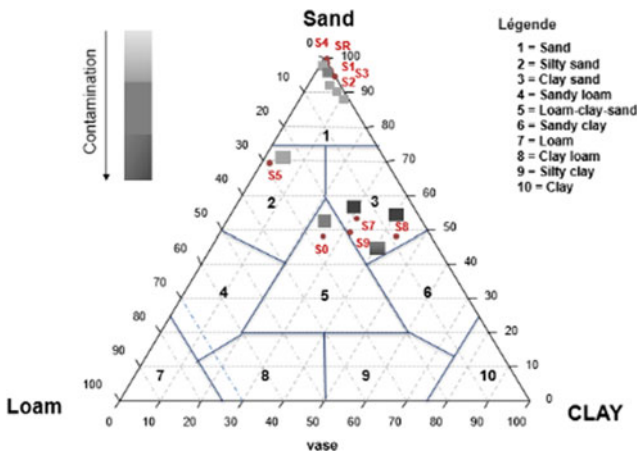

Fig. 1 Ternary diagram by Folk (1957) showing the sedimentary classes of samples from the Bay of Bizerte (Folk, 1957)

3.2.2 Solid-Phase Extraction (SPE) Result

The gravimetric results of the SPE made it possible to note that:

- The sediments collected from the Zarzouna and Cape Zebib stations are very rich in hydrocarbons, respectively, with averages of 262 and 5090 µg g^{-1} dry residues, compared to the Tunisian standard (Decree n° 2018-315), which sets a limit for TPHs at ten µg g^{-1} dry sediment.
- The most contaminated stations in the Zarzouna region (S0, SR, S1) are located near the discharge zone and have total hydrocarbon concentrations varying between 194 and 1760 µg g^{-1} dry sediments.
- The most contaminated stations in the Cape Zebib region are those, which coincide with the extent of the contamination (S7 and S8), showing total hydrocarbon concentrations varying between 4900 and 8260 µg g^{-1} dry sediment.
- The most potent hydrocarbon contamination in the Bay of Bizerte is recorded at the stations where the clay fraction forms the sedimentary facies. This result testifies that the latter represents the sedimentary texture most likely to trap the hydrocarbons compared to the other sedimentary fractions.

3.2.3 HPLC–UV Signaling of Pollutants

The results of the chromatographic analysis by HPLC–UV of the various samples of sediments located in the Bay of Bizerte showed concentrations of total PAHs higher than the reference values set by Decree 2018-315. The highest total ∑PAHs concentrations were recorded in site S7 with values between 10.19 and 225.66 ng/g dry weight. The S3, S4, and S5 sites exhibited the lowest concentrations of total PAHs, with values ranging from 3.12 to 7.25 ng/g dry weight. Our results showed the predominance of high molecular weight PAHs of 4–6 cycles (ranging from pyrene to benzo [g, h, i] perylene) over low molecular weight PAHs of 2–3 cycles (ranging from naphthalene fluoranthene) for all samples analyzed.

3.2.4 Forensic Fingerprinting of Biomarkers in Identifying the Origin of Contamination

The chromatograms (m/z) corresponding to the stations in the Bay of Bizerte (Fig. 2) demonstrated the natural origin of the oils. Moreover, signs of a developed unresolved complex mixture (UCM) were also identified in all chromatograms (m/z = 85), generally indicative of crude contamination. In addition, a regular distribution with a predominance of odd n-alkanes (*n*-C13-*n*-C35) was noted, indicating

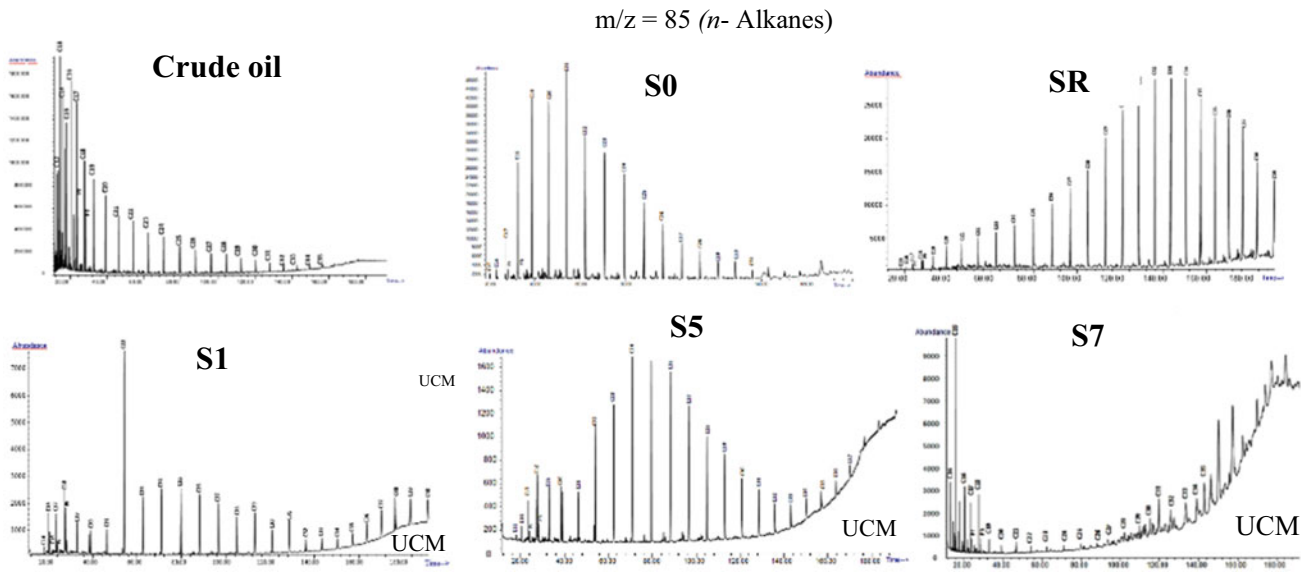

Fig. 2 Chromatograms obtained by GC/MS of the aliphatic fraction of the Bay of Bizerte stations

contamination by oil inputs or the presence of complex mixtures of biodegraded hydrocarbons.

Projection of Oil Indices and Biomarker Reports

The gas chromatography results coupled with mass spectrometry (GC/MS) and the projection of indices calculated from the ratios in Pr/*n*-C17 and Ph/*n*-C18 showed a variation in the nature of organic matter as well as in the evolution of the states of biodegradation of oils contaminating the sediments of the Bay of Bizerte.

A marine origin of the contamination of the Cape Zebib station (S7) was recorded, which differs from most of the oils collected from the other stations in the Bay of Bizerte. The contamination of the Bizerte canal (S0) showed a less critical state of biodegradation than that of Cape Zebib and a type of organic matter of terrestrial origin. Furthermore, the approximate age of fuel oil spills is proportional to their biodegradation conditions. These trends led to the conclusion that this contamination is more recent than the Cape Zebib extent and cannot be a reliable source of oil pollution. In addition, lake and terrestrial origins were noted, respectively, for the oils in the sediments collected from the fishing port (S5) and El Rimel station (S1), and less advanced biodegradation states were recorded. All these results have shown that these cannot be the origins of the contamination of the Cape Zebib site.

3.3 Statistical Analysis

Correlations between oil indices allowed samples to be classified based on similarities and differences between the properties of biomarkers: N-alkanes (*n*-C17/Pr, *n*-C18/Ph), tricyclic terpanes (T24/T25), hopanes (Tm/Ts, H29/H30, H31/H32), homohopanes (H31R/H31S, H32R/H23S), and steranes (C27αβR/C27αβS, C28αβR/C28αβS, C29αβR/C29αβS).

The result of the stadiagram based on biomarkers ratios showed negative correlations between the studied oil indices. Moreover, a negative correlation between the contaminations of Cape Zebib and the STIR oil release zone was noted. This trend made it possible to conclude that the oils are dissimilar and do not have the same origin, to confirm the hypothesis related to the source of the contamination of Cape Zebib from maritime traffic, and to deny the idea linking it to the oil leakage accident by the STIR, which dates from October 4, 2018. The results of the PCA revealed two class groups for the Bay of Bizerte. The first group corresponds to the SR (STIR oil release zone) and S7 (Cape Zebib contamination extent) stations. This trend proves that these stations are very close to the age of contamination by hydrocarbons and have pretty similar physicochemical characteristics. The second group corresponds to the stations relating to S0, S1, S2, S3, S4, and S5.

4 Conclusion

Our geochemical study based on the forensic fingerprints of biomarkers carried out on the surface sediments in the coastal region of Bizerte made it possible to identify contamination of the surface sediments by the crude associated mainly with the loads' anthropogenic inputs vastly exceeding the Tunisian standards Decree No. 2018-315 and Decree of December 5, 2008, related to sediment management. The sedimentary texture study (0–25 cm) highlighted the dominance of the sandy soil in our study area, with the highest hydrocarbon contamination found in soil with a clay fraction. The correlations of the relationships between the biomarkers demonstrated the origin of the maritime traffic of the contamination and not of the oil spill accident by the Tunisian Company of Refining Industries (STIR). A state of biodegradation was also noted for all the oils contaminating the coastal zone of Bizerte.

References

Bejaoui, B., Chouba, L., Mastouri, A., Akrout, F., Afli, A., & Harki, M. (2018). *Prospection du déversement accidentel de pétrole Au niveau du port d'accostage à Zarzouna/Bizerte* (pp. 12–14). Institut National des Sciences et Technologies de la Mer (INSTM).

Burgess, R. M., Athrens, M. J., & Hickey, C. W. (2003). *Geochemistry of PAHs in aquatic environnements: Source, persistence and distribution* (45 pp). Wiley.

Folk, R. L. (1957). Brazors river bar: A study in a signification of grain size parameters. *Journal of Sedimentary Petrology, 1*(27), 3–26.

Soclo, H. H., Guariguess, P., & Ewald, M. (2000). Origin of polycyclic aromatic hydrocarbons (PAHs) in coastal marine sediments: Case studies in Cotonou (Benin) and aquitaine (France) areas. *Marine Pollution Bulletin, 40*(5), 387–396.

Zaghden, H., Kallel, M., Louati, A., Elleuch, B., Oudot, J., & Saliot, A. (2005). Hydrocarbons in surface sediments from the Sfax coastal zone, (Tunisia) Mediterranean Sea. *Marine Pollution Bulletin, 50*, 1287–1294.

Structural Geology, Tectonics, Geodynamics

New Geochemical and Age Data on the Bajgan Complex (Makran Accretionary Prism, SE Iran): Implications for the Redefinition of Its Tectonic Setting of Formation from a Paleozoic Continental Basement to a Cretaceous Oceanic Domain

Edoardo Barbero, Morteza Delavari, Asghar Dolati, Antonio Langone, Luca Pandolfi, Michele Marroni, and Emilio Saccani

Abstract

The Bajgan Complex (BC) in the North Makran Domain (Makran Accretionary Prism, SE Iran) has been considered a remnant of a Paleozoic metamorphic continental basement detached from the southernmost edge of the Lut Block. We present here new geochronological and petrological data on metamorphic rocks from this Complex, intending to assess the age and tectonic–magmatic setting of the formation of their magmatic protoliths. The BC consists of meta-ophiolitic tectonic slices, including meta-peridotites, meta-gabbros, meta-plagiogranites, and meta-basaltic lavas. Whole rock geochemical data show that their magmatic protoliths include: (1) magmatic rocks showing both normal (N-) and enriched (E-) MORB affinities, as those formed at mid-ocean ridge settings; (2) basalts showing alkaline ocean island (OIB) chemistry similar to those formed in seamounts. Zircon U-Pb dating indicates magmatic ages of the protoliths from 161–114 Ma (Late Jurassic–Early Cretaceous). Our new data suggest that the interpretation of the BC as a Paleozoic continental ribbon should be abandoned. Instead, it represents a long-lived (at least ~50 My) Cretaceous oceanic lithosphere whose composite chemistry and petrogenesis indicate that it was characterized by mantle plume activity and plume–ridge interaction processes. Similar rock associations and procedures have been documented in many other Cretaceous ophiolites of the North Makran, suggesting that the magmatic protoliths of the Bajgan meta-ophiolites were most likely formed in the same oceanic basin.

Keywords

Meta-ophiolite • Geochemistry • Plume–ridge interaction • Cretaceous • Makran accretionary prism • Iran

1 Introduction

The North Makran Domain (NMD) in the Makran Accretionary Prism (SE Iran) consists of a stack of primarily ophiolitic tectonic units, which record the Cretaceous tectonic evolution of the Neotethys Ocean—Eurasia realm (Fig. 1). According to the existing interpretations, the Cretaceous tectonic shift of the NMD implies the subduction of the Neotethyan lithosphere beneath the Lut Block and the opening of an Early Cretaceous marginal basin (North Makran Ocean) that led to the separation of a continental ribbon (the Bajgan–Durkan microplate) from the southernmost edge of the Lut Block. In this view, the Bajgan Complex has been considered as remnants of a Paleozoic metamorphic continental basement (Burg, 2018; McCall & Kidd, 1982; Saccani et al., 2018). However, our field observations have revealed that the Bajgan Complex primarily consists of meta-ophiolitic tectonic slices, including meta-peridotites, meta-gabbros, meta-plagiogranites, and meta-basaltic lavas. Therefore, this study aims to present new petrological and geochronological data on the Bajgan meta-ophiolites to define the age and tectonic–magmatic setting of formation of their magmatic protoliths to compare them with other ophiolitic units in the NMD.

E. Barbero · E. Saccani (✉)
Ferrara University, Ferrara, Italy
e-mail: sac@unife.it

M. Delavari · A. Dolati
Kharazmi University, Tehran, Iran

A. Langone
IGC-CNR, Pavia, Italy

L. Pandolfi · M. Marroni
Pisa University, Pisa, Italy

A. Çiner et al. (eds.), *Recent Research on Sedimentology, Stratigraphy, Paleontology, Tectonics, Geochemistry, Volcanology and Petroleum Geology*, Advances in Science, Technology & Innovation,
https://doi.org/10.1007/978-3-031-43222-4_35

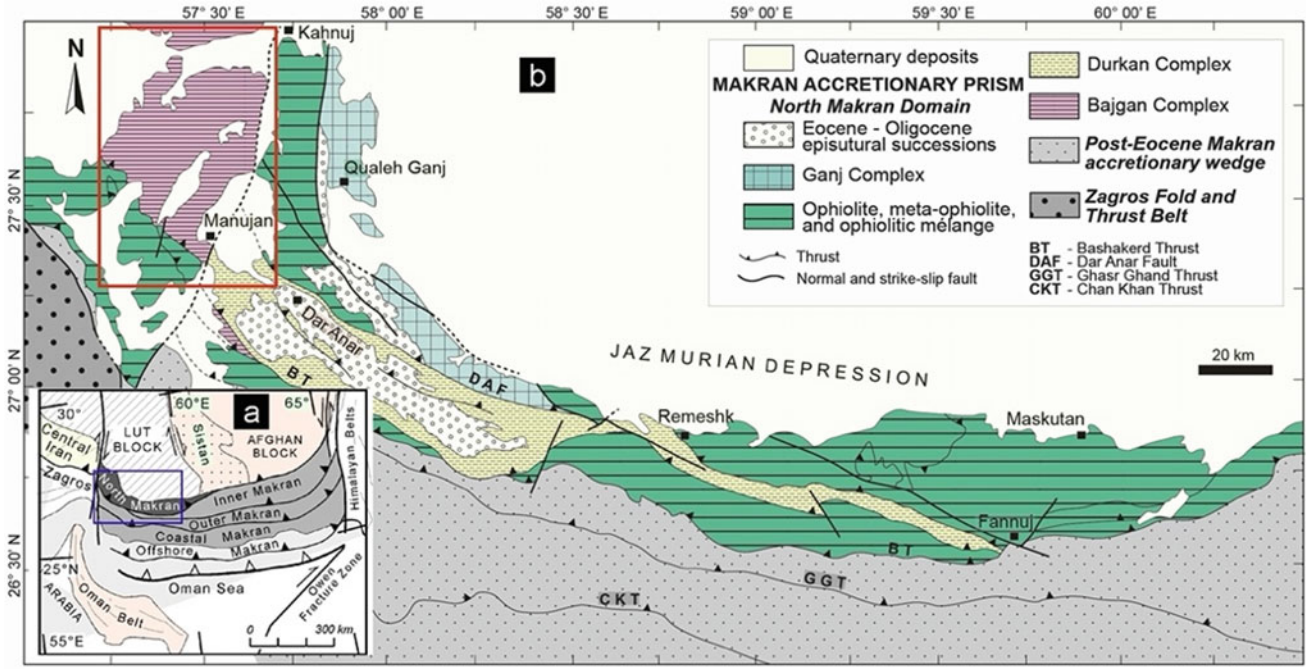

Fig. 1 **a** Simplified tectonic sketch map of the Makran Accretionary Prism and surrounding areas; **b** simplified geological map of the North Makran Domain. Both figures are modified from Burg (2018), Allahyari et al. (2014), Barbero et al. (2020)

2 Materials and Methods

Geochemical investigations were focused on mafic rocks (meta-gabbros and meta-basalts). They were performed by X-ray fluorescence spectrometry (XRF) and inductively coupled plasma-mass spectrometry (ICP-MS) at Ferrara University. In addition, geochronological studies for determining the magmatic age of the protoliths were carried out on meta-gabbros and meta-plagiogranites by ^{238}U-^{206}Pb geochronology on zircons using a laser-ablation ICP-MS at the CNR of Pavia.

3 Results

Based on geochemical data, three main groups of mafic protoliths can be identified (Fig. 2): (1) rocks showing normal (N-) MORB affinity with low contents of Nb (1.3–3.3 ppm) and Th (0.10–0.24 ppm), Nb/Yb ratios, and LREE depletion compared to Yb (La_N/Yb_N = 0.5–0.7); (2) rocks showing enriched (E-) MORB affinity with moderate enrichment in Nb (9.7–11.4 ppm), Th (1.04–1.07 ppm), and Nb/Yb ratios, coupled with LREE enrichment compared to Yb (La_N/Yb_N = 2–3); (3) rocks showing an apparent alkaline affinity with high contents of Nb (19–65 ppm), Th (2.9–9.6 ppm), and TiO_2 (1.8–2.3 wt%), high Nb/Yb ratios, and significant enrichment in LREE compared to Yb (La_N/Yb_N = 8–20). Geochronological analyses gave ages of formation of magmatic protoliths of 156 ± 6 and 136 ± 3 Ma for a plagiogranite and a gabbro associated with E-MORB rocks and an age of 112 ± 4 Ma or a gabbro associated with N-MORB rocks.

4 Discussion

Figure 2a shows that the magmatic protoliths of the Bajgan meta-ophiolites were formed in a subduction-unrelated oceanic setting. They show compositions (Fig. 2a, b) and ages that are very similar to those of many other NMD ophiolitic units (Barbero et al., 2020, 2021; Saccani et al., 2018). Figure 2b shows that OIB protoliths were generated by deep partial melting of an enriched, "plume-type" mantle source. A comparison with similar NMD ophiolites (Barbero et al., 2021) points out eruption in a seamount setting. N-MORB and E-MORB compositions are compatible with shallow partial melting of a sub-oceanic mantle in a mid-ocean ridge setting (Fig. 2b). Petrogenetic models (not shown) and regional-scale evidence (Barbero et al., 2020; Saccani et al., 2018) suggest that N-MORBs derived from a depleted MORB-type mantle source, whereas E-MORBs derived from a depleted MORB-type mantle metasomatized by OIB-type components because of plume–ridge interaction processes. Similar petrogenetic mechanisms and plume–ridge interaction processes have been documented in the

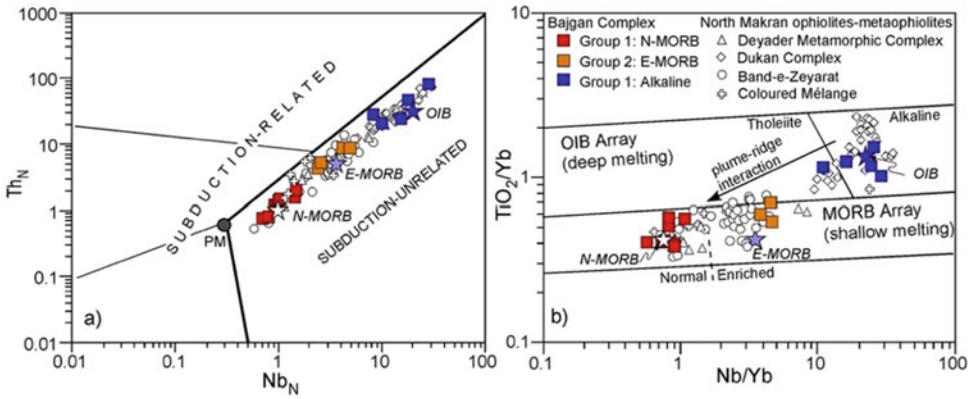

Fig. 2 **a** Th versus Nb discrimination diagram of Saccani (2015) and **b** TiO_2/Yb versus Nb/Yb diagram of Pearce (2008) for mafic meta-ophiolitic rocks from the Bajgan Complex. Abbreviations, MORB: mid-ocean ridge basalt; N-: normal type; E-: enriched type; OIB: ocean island basalt. Data for comparison are from Saccani et al. (2018), Barbero et al. (2020), Barbero et al. (2021)

Band-e-Zeyarat and colored Mélange units (Barbero et al., 2020).

5 Conclusions

Our new data indicate that the interpretation of the Bajgan Complex as a Paleozoic continental ribbon should be abandoned. Instead, this Complex represents a long-lived (>50 My) oceanic lithosphere. The chemically composite nature of the Bajgan meta-ophiolites with N-MORBs, E-MORBs, and OIBs suggests that they represent an oceanic lithosphere characterized by mantle plume activity and plume–ridge interaction processes. Similar rock associations and procedures have been documented in many other Cretaceous ophiolites of the NMD, suggesting that the magmatic protoliths of the Bajgan meta-ophiolites were most likely formed in the same oceanic basin in which other NMD ophiolites were generated.

References

Allahyari, K., Saccani, E., Rahimzadeh, B., & Zeda, O. (2014). Mineral chemistry and petrology of highly magnesian ultramafic cumulates from the Sarve-Abad (Sawlava) ophiolites (Kurdistan, NW Iran): New evidence for boninitic magmatism in intra-oceanic fore-arc setting in the Neo-Tethys between Arabia and Iran. *Journal of Asian Earth. Sciences, 79*, 312–328.

Barbero, E., Delavari, M., Dolati, A., Vahedi, L., Langone, A., Marroni, M., Pandolfi, L., Zaccarini, F., & Saccani, E. (2020). Early cretaceous plume–ridge interaction recorded in the band-e-zeyarat ophiolite (North Makran, Iran): New constraints from petrological, mineral chemistry, and geochronological data. *Minerals, 10*. https://doi.org/10.3390/min10121100

Barbero, E., Zaccarini, Delavari, M., Dolati, A., Saccani, E., Marroni, M., & Pandolfi, L. (2021). New evidence for Late Cretaceous plume-related seamounts in the Middle East sector of the Neo-Tethys: Constraints from geochemistry, petrology, and mineral chemistry of the magmatic rocks from the western Durkan Complex (Makran Accretionary Prism, SE Iran). *Lithos,* 396–397. https://doi.org/10.1016/j.lithos.2021.106228

Burg, J.-P. (2018). Geology of the onshore Makran accretionary wedge: Synthesis and tectonic interpretation. *Earth-Science Reviews, 185*, 1210–1231.

McCall, G. J. H., & Kidd, R. G. W. (1982). The Makran southeastern Iran: the anatomy of a convergent margin active from Cretaceous to present. In J.K. Leggett (Ed.), *Trench-forearc geology: sedimentation and tectonics of modern and ancient plate margins* (Vol. 10, pp. 387–397). Geological Society of London Special Publication, vol. 10, pp. 387–397.

Pearce, J. A. (2008). Geochemical fingerprinting of oceanic basalts with applications to ophiolite classification and the search for Archean oceanic crust. *Lithos, 100*, 14–48.

Saccani, E. (2015). A new method of discriminating different types of post-Archean ophiolitic basalts and their tectonic significance using Th-Nb and Ce-Dy-Yb systematics. *Geoscience Frontiers, 6*, 481–501.

Saccani, E., Delavari, M., Dolati, A., Marroni, M., Pandolfi, L., Chiari, M., & Barbero, E. (2018). New insights into the geodynamics of Neo-Tethys in the Makran area: Evidence from age and petrology of ophiolites from the Coloured Mélange Complex (SE Iran). *Gondwana Research, 62*, 306–327.

Tectonic-Diagenesis Interaction from Carbonate Veins Studies in Guelma Basin (Eastern Constantine Unit-Algeria)

Amira Ouddah, Abdelkader Khiari, and Badreddine Saadali

Abstract

In studying sedimentary basins, deciphering tectonics and related diagenesis features leads to a better understanding of involved processes in their geological history. This work investigated the impact of tectonic reactivation cycles and synchronous fluid flow events on the sedimentary evolution of the Late Jurassic to Cretaceous carbonates bedrock sequence in the Guelma basin (Constantine Unit- NE Algeria). Based on their petrographic and geochemical characteristics, two major stages of fractures and associated filling types of cement were identified: 1) Tectonic veins (F1), entirely affecting Constantine neritic-carbonate bedrock sequence, displaying several generations of thin (10 µm to 5 cm) bedding parallel and perpendicular sets of veins, dominantly infilled by sparite calcite crystals and; 2) fault-related hydraulic breccia, with saddle dolomite, calcite, pyrite, Fe-oxides, and Quartz. Furthermore, trace elements and REE patterns indicate precipitation of calcite cement from deeply circulating meteoric water. In contrast, dolomite cement has precipitated from mixed shallower meteoric and deeper basinal fluids in epithermal conditions.

Keywords

Veins • Breccia • Fluid flow • REE • Guelma basin • Algeria

1 Introduction

The study of fracture development and sealing mechanisms can provide insightful information that significantly improves the understanding of diagenetic evolution in sedimentary basins (Bons et al., 2012; Laubach et al., 2010). However, in the Guelma region, no previous detailed diagenetic work has been carried out on the neritic carbonates belonging to the Constantine unit. For this reason, we have examined these carbonates using petrographic and structural analysis, major, trace, and rare earth element (REE) geochemistry. This was made to identify their diagenetic parasequence and associated circulating fluids characteristics and examine tectonic deformations possible role in their evolution.

Guelma basin is located in the eastern part of the Algeria Alpine system. This basin is oriented roughly N10˚E and started to develop as a pull-apart type during Miocene. The basin is defined to the north by Debbagh major Strike-slip fault and normal active faults by the east and west (Vila, 1980; Yelles-Chaouche et al., 2006). The neritic carbonates of the Constantine unit, as exposed in the Guelma basin, contain thick-bedded Late Jurassic to Cenomanian limestone and dolostone sequences (Dareste de la Chavanne, 1910; Vila, 1980), with a rich fauna of benthic foraminifera and molluscs (Dareste de la Chavanne, 1910).

2 Materials and Methods

Structures were examined first in the field, allowing the detection of fractures in different scales. Samples were available from outcrops and drill cores provided by the Algerian geological and mining research office (ORGM).

Fifty (50) thin sections were used to describe the microstructures and diagenesis features via conventional and cathodoluminescence (CL) petrography.

A. Ouddah (✉) · A. Khiari · B. Saadali
Department of Geology, Faculty of Earth Sciences, University of Oum El Bouaghi, 4000 Oum El Bouaghi, Algeria
e-mail: amira.ouddah@univ-oeb.dz

A. Ouddah · A. Khiari · B. Saadali
Natural Resources and Management of Sensitive Environments Laboratory (RNAMS), University of Oum El Bouaghi, 4000 Oum El Bouaghi, Algeria

A. Çiner et al. (eds.), *Recent Research on Sedimentology, Stratigraphy, Paleontology, Tectonics, Geochemistry, Volcanology and Petroleum Geology*, Advances in Science, Technology & Innovation,
https://doi.org/10.1007/978-3-031-43222-4_36

CL images were taken using a technosyn 8200MK II Luminoscop fitted with a Polaroid (DMC-1) camera under an accelerating voltage of 10–18 kV and a gun current of 500–800 mA.

Chemical analysis for major and trace elements was carried out using Inductively Coupled Plasma Optical Emission Spectroscopy (ICP-OES) Varian 720ES at the Division of Geology of the Catholic University of Leuven (KUL)–Belgium.

3 Results

3.1 Petrographic and Structural Features

Neritic carbonates that regionally belong to the Constantine unit of the Guelma region show a complicated style of structure-related diagenesis, including compaction and pressure solution, multiple crack-seal-like fracture generations, and fault-related hydraulic breccia development.

Two stages of fractures likely controlled by tectonic pulses are distinguished:

1. a set of veins affecting the whole stratigraphic section with multiple cross-cutting fracture generations cemented by coarse crystalline calcite;
2. a fault-related breccia measuring approximately 4 m wide, with polygenic clasts cemented by blocky white calcite crystals at the marginal part and saddle dolomite at the center.

Both normal and lateral slip components characterize fault-controlling breccia development.

Cathodoluminescence images revealed bright orange and yellow sector zonation within sparry calcite cement, whereas breccia cement shows dull luminescence red and purple colors of non-zoned saddle-shaped dolomite crystals.

3.2 Geochemical Features

Rare earth element (REE) patterns of basin carbonates bedrock and fractures filling material revealed variations of the geochemical nature of circulating fluids during basin structuration stages. For example, PAAS-normalized REE profiles are similar to host rocks in calcite veins with flat to slightly uniform LREE-depleted patterns. However, in breccia dolomite cement, patterns show LREE enrichment with a marked positive Eu anomaly.

4 Discussion

The combination of petrographic observations and geochemical data indicates that over the history of carbonates evolution in the Guelma basin, tectonic fractures and fluid flow were the major controls on diagenesis evolution.

REE behavior in calcite cement indicates a low fluid-rock interaction and their precipitation from dominantly shallower meteoric fluids. In contrast, breccia cement reveals the involvement of hotter fluid, as evidenced by sulfides and silica cement precipitation, commonly occurring under epithermal conditions in sedimentary environments (Davies & Smith, 2006; Tostevin, et al., 2016).

Dissolution and recrystallization features along breccia wells are observed, with the replacement of saddle dolomite by calcite crystals and micritization of breccia clasts, as a result of the circulation of infiltrating shallower water.

5 Conclusions

Petrographic study and chemical data of veins and hydraulic breccia from Guelma basin formations show that different minerals have precipitated during fluid circulations.

The fractures development and fillings show at least two fracturing stages in the neritic carbonates of the Guelma basin.

Multi-stage fluid circulations are evidenced by the nature of fillings, especially in the breccia, where the saddle dolomite crystals were deposited as a result of the circulation of a relatively hot fluid followed by cooler fluid depositing calcite cement.

References

Bons, P. D., Elburg, M. A., & Gomez-Rivas, E. (2012). A review of the formation of tectonic veins and their microstructures. *Journal of Structural Geology, 43*, 33–62.

Dareste de la Chavanne, J. (1910). *La région de Guelma, étude spéciale des terrains tertiaries*. Bull. du service de la carte géologique de l'Algérie.

Davies, G. R., & Smith, L. B. (2006). Structurally controlled hydrothermal dolomite reservoir facies: An overview. *AAPG Bulletin, 90*(11), 1641–1690.

Laubach, S. E., Eichhubl, P., Hilgers, C., & Lander, R. H. (2010). Structural diagenesis. *Journal of Structural Geology, 32*(12), 1866–1872.

Tostevin, R., et al. (2016). Effective use of cerium anomalies as a redox proxy in carbonate-dominated marine settings. *Chemical Geology, 438*, 146–162.

Vila, J. M. (1980). La chaîne alpine d'Algérie orientale et des confins Algéro-Tunisiens [*The Alpine chain in eastern Algeria and the Algerian-Tunisian border*] (*Sciences thesis*) (p. 450). Paris: Pierre et Marie Curie University.

Yelles-Chaouche, A., Boudiaf, A., Djellit, H., & Bracene, R. (2006). La tectonique active de la région nord-algérienne. *Comptes Rendus Geoscience, 338*(1–2), 126–139.

Possible Causes of the Late Cenozoic Global Activation of the Earth's Tectonomagmatic Processes

Evgenii Sharkov

Abstract

The Late Cenozoic global activation of the Earth's tectonomagmatic processes, which continues to this day, occurred unexpectedly at ~ 30 Ma. It covered almost the entire globe, leading to new orogens and numerous areas of intraplate magmatism associated with the ascension of mantle plumes. However, its nature and mechanism of implementation remain a mystery. According to modern concepts, the origin of mantle plumes occurs at the boundary of the liquid outer core and the mantle due to the penetration of fluids from the core into its bottoms (Maruyama in J Geol Soc Jpn 100(1):24–49, 1994; Dobretsov et al., Deep geodynamics. GEO Publ, 2001; French and Romanowicz Nature 525:95–99, 2015, etc.). Accordingly, the number of mantle plumes—the main drivers of tectonomagmatic processes—directly depends on the fluids coming from the irreversibly solidifying core. We believe that the reason for the considered global tectonomagmatic activation of the Earth was a sharp increase in the content of core's fluids in the cooling high-Fe liquid of the outer core due to a decrease in their solubility at one of the bifurcation points. The mechanism for implementing this activation was most likely a massive ascent of mantle plumes.

Keywords

Global activation • Liquid outer and solid inner cores • Fluids • Mantle plumes • Bifurcation point

1 Introduction

One of the most critical events in the recent history of the Earth is the Late global Cenozoic (Neogene-Quaternary) activation of tectonomagmatic processes, which unexpectedly began ~ 30 Ma in the middle Miocene and continues nowadays (Stille, 1924; Dineley, 2000; Potter & Szatmari, 2009, etc.). This activation resulted in a sharp intensification of tectonomagmatic processes and covered almost the globe. However, despite numerous studies, the causes and mechanism of this activation remain a mystery. It is only clear that this activation is global and continues to exist today, although there seem to be no obvious external or internal reasons for this.

In our opinion, a sharp increase in magmatism's intraplate (mantle plume related) intensity is particularly interesting. Many areas of this magmatism have appeared all over the Earth: on continents and in oceans, from the Arctic to the Antarctic, most of which are still active (Sharkov & Bogatikov, 1987).

The considered tectonic–magmatic activation of the Earth occurred almost simultaneously on the entire planet. This implies the existence of a single homogeneous global source of energy and matter and some event that triggered the process. From our point of view, only the outer liquid core of the Earth, the composition of which is constantly maintained uniformly by convection, can serve as such a source. Therefore, it seems appropriate to consider the structure of the Earth's core in general.

2 The Earth's Core

The Earth's core is located at depths from ~ 2900 km to the center of the Earth (~ 6400 km). Therefore, there are no direct data on the composition of the Earth's core. Nevertheless, the shock compression data of metals and their compounds make it possible to assume with a high degree of

E. Sharkov (✉)
Institute of Geology of Ore Deposits, Petrography, Mineralogy and Geochemistry (IGEM) RAS Moscow, Moscow, Russia
e-mail: esharkov@mail.ru

A. Çiner et al. (eds.), *Recent Research on Sedimentology, Stratigraphy, Paleontology, Tectonics, Geochemistry, Volcanology and Petroleum Geology*, Advances in Science, Technology & Innovation,
https://doi.org/10.1007/978-3-031-43222-4_37

probability that the Earth's core is 90% formed by iron (Al'tshuler et al., 1968). In that case, the outer (liquid) core cannot consist of just pure Fe or, even more, of its mixture with Ni since the density of iron and nickel–iron of the meteorite composition at pressures prevailing in the Earth's core is approximately 10–15% higher than the density of matter the outer core of the Earth, which requires lighter additions. According to (McDonough, 2014), the most probable candidates are elements such as S and O, widespread on the Earth, and Si, Mn, Cr, Co, Ni, C, and P. In addition, we believe that Ti, K, and Na, as well as H_2O and CO_2, which are part of the fluid components of the modern mantle thermochemical plumes (see below), can also play a particular role in the composition of the present-day outer core of the Earth.

In this regard, the unusual properties of a natural high-Fe liquid revealed in the study of crystallization products of moderate alkaline Fe-Ti picrobasalts of plume origin are noteworthy. This refers to the coronite structures in the ferrogabbroids of Ti-bearing intrusions, particularly the Elet'ozero syenite-gabbro complex in North Karelia (Sharkov & Chistyakov, 2017a, 2017b). These corones formed mainly by amphibole (kaersutite), biotite, and olivine, appeared around solidifying drops of high-Fe liquid released during the crystallization of the initial picrobasaltic melt. Judging by the composition of the coronite structures, the total content of impurity components dissolved in this liquid (Si, Ti, Al, Mg, Ca, Na, and K, as well as water, Cl, and F) could reach 10–15% weight. Moreover, this intrusion formed at a pressure of ~ 0.55 Gpa. Suppose high-Fe liquids retain their properties even under conditions of ultra-high core pressures. In that case, there is a high probability that the Earth's liquid outer core may contain such components and be a source of fluids feeding mantle plumes.

The upper margin of the solid inner core (~ 5% mass and ~ 4% volume of the entire core) is located at a depth of 5080 km. It is assumed that the solid core consists of a Fe–Ni alloy close in composition to the iron meteorites identified in the study of crystallization products, possibly with additions of stishovite and diamond. Moreover, the structure of the inner core is not uniform. Special studies in the inner core have established the presence of compositional stratification (Labrosse, 2014), which makes the inner core similar to solidification products of large volumes of silicate melts, such as layered intrusions.

In addition, an important recent achievement was the discovery of the center of the modern solid core of the remains of an ancient solid core with an independent structure, which is its oldest part (Wang et al., 2015). In our opinion, these are relics of the primary iron core of the Earth, one the evidence of the secondary origin of the modern core (Sharkov et al., 2020), but this problem is not discussed in this work. According to (Labrosse et al., 2001), the solid inner core appeared no earlier than 2.5 Ga and no later than 1.0 Ga, most likely, between 2.0 and 1.7 Ga.

3 Cooling and Solidification of the Earth's Core

Mantle plumes constantly carry away heat and fluids from the core, which should inevitably lead to its cooling and solidification. As it was shown by (Jeffries, 1959), two independent factors control the solidification of molten planets (the liquid core in the case under consideration): (a) the adiabatic gradient (the minimum temperature difference for the beginning of convection) and (b) the melting point gradient (the slope of the liquidus line in P–T coordinates) (Fig. 1). Since the adiabatic gradient is significantly lower than the melting temperature gradient, the main volume of the melt remains superheated relative to the liquidus temperature, and the solidification of the molten planets (and their cores) should occur gradually from the bottom up, i.e., from the center to the surface.

The crystallization zone mainly consists of the highest temperature (liquidus) crystalline phases. As the intrusive chamber cools down, this zone moves steadily from bottom to top, burying the previously precipitated crystalline phases and leaving behind a solidified part of the intrusion. Thus, its highest temperature components are constantly withdrawn from the original melt, and the remaining melt is enriched with low-temperature components. As a result, the melt following the cotectics of the corresponding physicochemical systems enters the bifurcation points where the mineral phases released at the solidification front are changed by lower-temperature ones, which leads to the appearance of primary magmatic layering (Sharkov, 2006). Thus, the formation of such layering (stratification) results from the

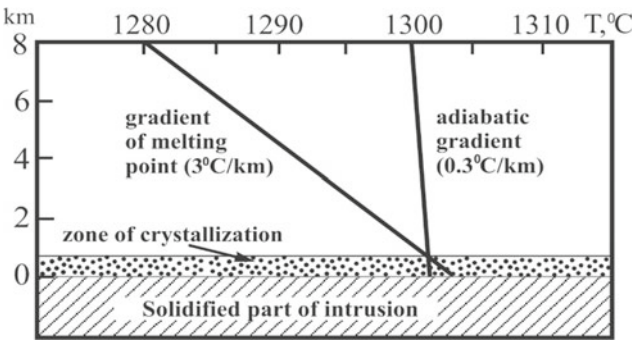

Fig. 1 Relationship between the adiabatic gradient and the melting point temperature gradient determining the directional solidification of large volumes of silicate magma

natural course of events during the directional solidification of large volumes of the melt and does not carry any other information.

3.1 The Earth's Core Solidification

Let us consider the situation with the Earth's core from such a position. Obviously, in the case of a spherical liquid core, solidification should begin in its center with the appearance and growth of a solid inner core, an already solidified part of the entire core. It follows from this that the structure of the modern core is the result of the continuing process of solidification of the initially liquid core of the Earth from its center to the periphery, and is in good agreement with the layered (stratified) structure of the solid inner core (Labrosse, 2014), which resembles the structure of the above-mentioned layered intrusions. Such a structure of the core presupposes the presence between the inner and outer parts of a low-power crystallization zone constantly moving upward, forming at the temporary bottom of the core's liquid (outer) part. There, like cumulates in layered intrusions, crystalline solid phases of iron should precipitate at the front of the beginning of solidification, gradually growing the solid inner core.

3.2 Mantle Plumes

As shown by the study of the evolution of the LIPs in the history of the Earth, the composition of intraplate magmas has remained practically unchanged over the past 2.3 Ga (Sharkov et al., 2020). This means that the composition of the fluid components that provided the rise of mantle plumes did not change. Such a situation could arise only when the fluids play the role of the residual melt during the solidification of a high-Fe liquid. Then, the excess of these components, which appeared in the process of core solidification, passed in transit through the still-saturated liquid part of the core and left it together with newly formed mantle plumes. Accordingly, the number of mantle plumes, the main movers of tectonomagmatic processes, directly depends on the fluids coming from the core.

What do we know about the material of modern mantle plumes? Important information about this is contained in mantle xenoliths in Neogene-Quaternary intraplate basalts of plume origin. Two independent groups represent these xenoliths: (1) spinel ultramafic rocks of the green series, which represent the mantle matrix of the plume, and (2) veins of kaersutite- and phlogopite-bearing rocks of the "black series". The "black series" of mantle xenoliths developed due to the fluid-dependent melting of mantle plume heads. Geochemical data indicate that incompatible elements are contained mainly in fluids that participated in the decompression melting of mantle plume heads (Ma et al., 2015). We believe that these fluids are the "contribution" of the Earth's core to the formation of these plumes.

4 Discussion and Conclusions

What could have caused such an unpredictable increase in the scale of mantle plumes' development originating at the boundary between the liquid core and the mantle?

This indicates a sharp increase in the volume of mantle fluids necessary for forming mantle plumes. As already mentioned, the mantle plays a passive role here, and the required heat and fluids arrival from the core.

From our view, the reason for the global Neogene-Quaternary tectonomagmatic activation of the Earth was most likely a noticeable decrease in the solubility of fluid components in the high-Fe liquid of its outer core during cooling, and the mechanism of this activation was the massive rise of thermochemical mantle plumes. The "energy heart" of the modern Earth is its outer core, which produces mantle plumes—generators of tectonomagmatic processes in its upper geospheres.

References

Al'tshuler, L. V., Simakov, G. V., Trunin, R. F. (1968). On the question of the chemical composition of the Earth's core. Izv. Academy of Sciences of the USSR. Physics of the Earth (1), 3–6 (1968) (in Russian).

Dineley, D. L. (2000). Miocene. In P. L. Hancock & B. J. Skinner (Eds.), *Oxford Companion to the Earth* (pp. 694–695). Oxford University Press.

Dobretsov, N. L., Kirdyashkin, A. G., & Kirdyashkin, A. A. (2001). *Deep geodynamics*. GEO Publ. (in Russian).

French, S. W., & Romanowicz, B. (2015). Broad plumes rooted at the base of the Earth's mantle beneath major hotspots. *Nature, 525*, 95–99.

Jeffries, H. (1959). *The Earth, its origin, history, and physical constitution*. Cambridge University Press.

Labrosse, S., Poirier, J.-P., & Le Mouel, J.-L. (2001). On the age of the inner core. *Earth and Planetary Science Letters, 190*, 111–123.

Labrosse, S. (2014). Thermal and Compositional Stratification of the Inner Core. In *Abstract of AGU 2014 Fall Meeting. 15–19 December. San Francisco, USA*. DI31A-4257.

Ma, G. S.-K., Wang, K.-L., Malpas, J., Iizuka, Y., Xenophontos, C., Turkmani, A. A., Chan, G. H.-N., Usuki, T., Chan, Q.H.-S. (2015). Melt-pockets and spongy clinopyroxenes in mantle xenoliths from the Plio-Quaternary Al Ghab volcanic field, NW Syria: implications for the metasomatic evolution of the lithosphere. In A. Khan & F. Deschamps (Eds.), *The Earth's heterogeneous mantle* (pp. 205–257). Springer International Publishing.

Maruyama, S. (1994). Plume tectonics. *The Journal of the Geological Society of Japan, 100*(1), 24–49.

McDonough, W. F. (2014). Compositional model for the Earth's core. In *Treatise on geochemistry. The mantle and core* (2nd Ed., pp. 559–576). Elsevier.

Potter, E., & Szatmari, P. (2009). Global Miocene tectonics and the modern world. *Earth-Science Reviews, 96*, 279–295.

Sharkov, E. V. (2006). *Formation of layered intrusions and their ore mineralization*. Scientific World. (in Russian).

Sharkov, E. V., & Bogatikov, O. A. (1987). Late Cenozoic global activation of geological processes in the Earth—Tectono-magmatic aspects. *International Geology Review, 29*(10), 1135–1149.

Sharkov, E. V., Bogina, M. M., Chistyakov, A. V., & Zlobin, V. L. (2020). The evolution of large igneous Provinces in the Earth's History: The Eastern Baltic Shield. *Journal of Volcanology and Seismology, 148*(5), 327–340.

Sharkov, E. V., & Chistyakov, A. V. (2017a). Coronitic textures in the Ferrogabbroids of the Elet'ozero intrusive complex (Northern Karelia, Russia) as evidence for the existence of Fe-rich Melt. 1. Types of Coronas. *Geochemistry International, 55*(6), 535–547.

Sharkov, E. V., & Chistyakov, A. V. (2017b). Coronitic textures in the Ferrogabbroids of the Elet'ozero intrusive complex (Northern Karelia, Russia) as evidence for the existence of Fe-rich Melt. 2. Origin of Fe-rich liquid. *Geochemistry International, 55*(7), 621–628.

Stille, H. (1924). *Grundfragen der vergleichenden Tektonik*. Gebrüder Borntraeger.

Wang, T., Song, X., & Xia, H. H. (2015). Equatorial anisotropy in the inner part of Earth's inner core from autocorrelation of earthquake coda. *Nature Geoscience, 8*, 224–227.

New Tectonic and Topometric Evidence of Modern Transtensional Tectonics in the Low Nekor Basin (NE Morocco)

Morad Taher, Taoufik Mourabit, Ali Errahmouni, and Abdelhak Bourjila

Abstract

The Nekor basin is located in the northeastern part of the RIF at the heart of the border between the African and Eurasian plates. It is characterized by tectonic and seismic activities. This area was affected by powerful seismic events, such as the Mw 6.0 earthquake of May 26, 1994, the Mw 6.4 earthquake of February 24, 2004, and the Mw 6.4 earthquake of January 25, 2016. We propose, in our work, the tectonic and topometric studies to confirm the transtensional tectonic regime of the low Nekor basin. The topometric measurements in the study area indicate a horizontal movement of 5.33 ± 2 mm per year through the Trougout fault in the NE-SW direction. This suggests a sinistral movement calculated at 3.76 mm/year and an E-W distension of the same value. In addition, the Ajdir-Imzouren fault field study shows a dextral activity. These movements confirm the transtensional tectonic regime of the lower Nekor basin.

Keywords

Ajdir-Imzouren fault • Nekor basin • Transtensional • Topometric • Trougout spot

1 Introduction

The geological history of the western Mediterranean is made up of several geodynamic events that have shaped the border area between the African plate and the Eurasian plate. The Rif chain, where our study area is located, which results from the N-S convergence of the two plates, is made up of three main areas, from North to South: internal zones, flysch layers, and external zones (Flinch, 1993). Our study area, the lower basin of Oued Nekor (Fig. 1), is located on the southern shore of the Alboran Sea. It is bounded to the south by the Kétama unit, to the east by the Temsamane massif and the Neogene volcanic massif of Ras Tarf, and to the west by the Bokoya massif and the flysch zones. Morphologically, it is a triangular graben basin constituting the alluvial plain of Oued Nekor open to the bay of Al Hoceima (Tahayt, 2008). The lower Nekor basin corresponds to an N-S collapse ditch, the result of E-W extension associated with N-S compression (Hatzfeld et al., 1993). It is delimited by two active conjugate normal faults: Imzouren-Ajdir (NNW-SSE) to the west and Trougout (N-S) to the east (Medina, 1995; Poujol et al., 2014; Tahayt, 2008).

2 Materials and Methods

The study of active tectonics in the lower Nekor basin is the goal of this paper. We looked for geomorphological features that suggest an apparent shift in landforms or geological formations over the study area that extends between the Ajdir region to the west of the Nekor basin and the Trougout region to the east of the bay. We used different sources of information (satellite optical images, aerial photos, and geological and topographic maps) and field work to study the faults that limit the lower Nekor basin. The topometric technique (Fig. 2) is used to monitor the horizontal movement of the Trougout fault. The active Trougout fault is morphologically clearly visible (Poujol et al., 2014; Tahayt, 2008) and is even considered to be the boundary between the two plates in the western Mediterranean (Fig. 3).

M. Taher (✉) · T. Mourabit · A. Errahmouni · A. Bourjila
Abdelmalek Essaadi University, B.P. 2117, Tétouan, Morocco
e-mail: m.taher@uae.ac.ma

A. Çiner et al. (eds.), *Recent Research on Sedimentology, Stratigraphy, Paleontology, Tectonics, Geochemistry, Volcanology and Petroleum Geology*, Advances in Science, Technology & Innovation,
https://doi.org/10.1007/978-3-031-43222-4_38

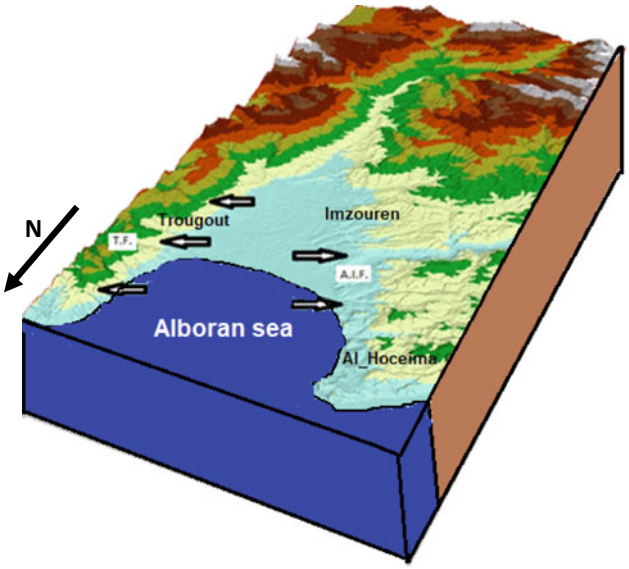

Fig. 1 Study area in 3D showing the position of TF (Trougout fault) and AIM (Ajdir-Imzouren fault)

3 Results

The results (Table 1) show that the Trougout fault's horizontal activity is 5.33 ± 2 mm/year in the NE-SW direction. This indicates the existence of a sinistral component calculated at 3.76 mm/year and an E-W distension (Fig. 4) of the same value.

The Ajdir-Imzouren fault in the northern part presents a fault mirror (N164, 56 E) poorly preserved. The height of this escarpment (Fig. 5) plan varies between 1 and 2 m, and its length exceeds 50 m. Two zones that have undergone further erosions are visible on the Ajdir-Imzouren fault plane (Fig. 6). The upper part of the fault plane (black coloration) is the most altered. In contrast, the lower part of this planar surface (brown coloration) is less qualified or presents a recent alteration. This means that the top of the escarpment is older than its lower part. The linear structures on this fault mirror have been affected by the alteration of the limestone formation that gates them. Still, fortunately, we have found streaks and tectonic clues, such as tearing niches, useful to measure and interpret them. Furthermore, the measurements of the striations on the fault plane (N100, 40SE) indicate a normal transtensive dextral movement of the fault. From these field observations, we can say that the Ajdir-Imzouren fault is normal-dextral (Fig. 7).

4 Conclusion

The total station confirmed the conjugate movement of the Trougout normal fault and an E-W distension movement. In addition, the fieldwork in the north of Ajdir-Imzouren's normal fault confirmed the existence of conjugate movement. The activities thus determined to agree with the results of previous work and ensure the transtensional character of the tectonic regime of the lower Nekor basin.

Fig. 2 Total station device used in our study-Leica TS02

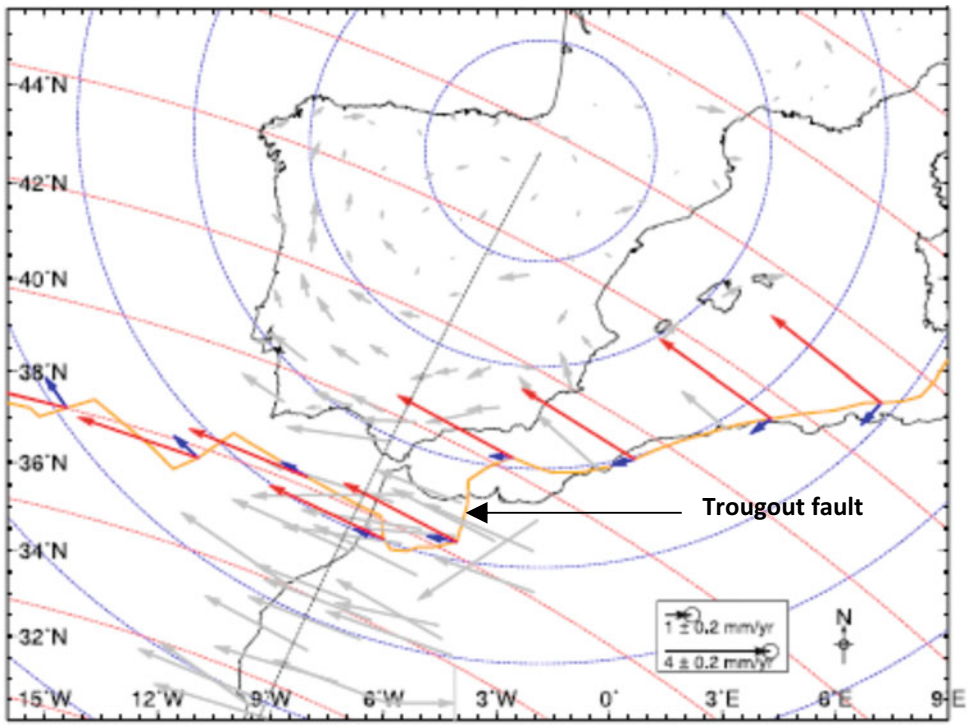

Fig. 3 Trougout fault is part of the boundary between the Eurasian and African plates (Palano et al., 2015)

Table 1 Result of the measurement

Measurement of variation in mm				
Fault	08/2017	08/2018	08/2019	08/2020
Trougout	00	10 ± 2	01 ± 2	05 ± 2

Fig. 4 Image Google Earth shows the result obtained by total station

Fig. 5 The escarpment of Ajdir fault

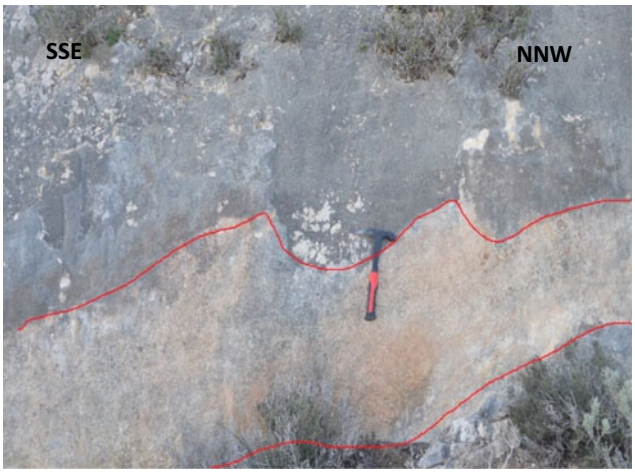

Fig. 6 Two different zones at the level of the fault plane

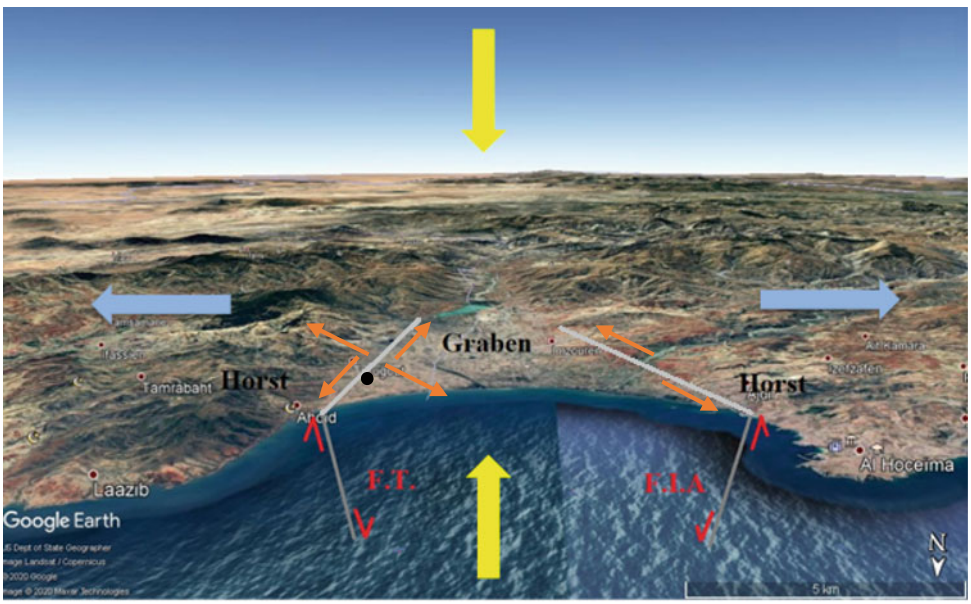

Fig. 7 Google Earth image modified to show the phenomenon that controls the study area. Orange arrows indicate the results of topometric and field studies. T.F. (Trougout fault), A.I.F. (Ajdir-Imzouren fault). The black point shows the position of the total station

Acknowledgements We want to express our special thanks for the valuable comments from anonymous reviewers that significantly improved this short paper's text.

References

Flinch, J. (1993). *Tectonic evolution of the Gibraltar arc*, Ph.D. thesis: Rice University.

Hatzfeld, D., Caillot, V., Cherkaoui, T. E., Jebli, H., & Medina, F. (1993). Microearthquake seismicity and fault plane solutions around the Nekor-slip fault, Morocco. *Earth and Planetary Science Letters, 120*, 31–41.

Medina, F. (1995). Present-day state of stress in northern Morocco from focal mechanism analysis. *Journal of Structural Geology, 17*, 1035–1046.

Palano, M., González, P. J., & Fernández, J. (2015). The diffuse plate boundary of Nubia and Iberia in the Western Mediterranean: Crustal deformation evidence for viscous coupling and fragmented lithosphere. *Earth and Planetary Science Letters, 430*, 439–447.

Poujol, A., Ritz, J. F., Tahayt, A., Vernant, P., Condomines, M., Blard, P. H., & Billant, J. (2014). Active tectonics of the Northern Rif (Morocco) from geomorphic and geochronological data. *Journal of Geodynamics*. https://doi.org/10.1016/j.jog.2014.01.004

Tahayt, A. (2008). Apport des mesures de la géodésie spatiale dans l'étude des déformations tectoniques actuelles dans la Méditerranée occidentale. Université Abdelmalek Essaadi, Faculté des Sciences, Tetouan. Thèse du doctorat, pp. 10–22–38–45.

The Mila 2020 Seismic Sequence in North-East Algeria: Seismotectonic Context and Geohazard Consequences

Yahia Mohammedi, Abdelkarim Yelles-Chaouche, and Seifeddine Adjiri

Abstract

The Mila region in northeastern Algeria was shaken recently by a moderate (Mw $\leq$ 5) seismic sequence between July and August 2020. The second mainshock (Mw 4.9) was followed by a massive landslide ($\approx$ 2 $\times$ 1 km), leading to dramatic destruction in the El Kherba locality in the western part of Mila city. The landslide occurred a few hours after the mainshock. This is the first time a critical landslide has occurred after a moderate seismic event. Although this sequence follows the general trend of seismicity in northern Algeria, it caused a vital panic among the population and the authorities that it occurred near the essential water reservoir in Algeria (i.e., Beni Haroun dam). This paper aims to investigate the seismotectonic context of this earthquake, focusing on mapping potential active faults and discussing the triggered associated landslide. To this end, we accomplished a geologic field investigation, where the observations covered an area of 15 km around the epicenter. Remotely sensed data helped to identify potential lineaments in this area and oriented the field investigation and analysis. The results show that the El Kherba landslide (situated 15 km south-west of the epicenter) was triggered by many factors, including topography, soft-rock lithology, underwater, loading due to the building, and finally, the successive seismic events, which were a secondary factor. From a seismotectonic point of view, the sequence occurred on the northwestern border of the Miocene Constantine basin, underlined by a heavy network of faults. The most important is the Mcid-Aïcha Debbagh EW strike-slip fault and many transverse segments. The source faults are discussed based on the geomorphic, geologic, and seismologic aspects.

Y. Mohammedi (✉) · A. Yelles-Chaouche · S. Adjiri
Centre de Recherche en Astronomie, Astrophysique et Géophysique, Bp 63 route de l'observatoire, Algiers, Algeria
e-mail: yahyouhe@yahoo.com

Keywords

Mila earthquake • Landslide • Active faults • Miocene basin • Neotectonics

1 Introduction

The eastern part of the Tell Atlas belt (Northern Algeria) has recently experienced several small to moderate seismic events located mainly on the northern edge of the Constantine-Mila Miocene basin (Bendjama et al., 2021). The most recent sequence (with two mainshocks) has affected the Mila region between July and August 2020. A massive landslide followed the second mainshock of 17 August 2020 at the western part of Mila city, significantly damaging houses and infrastructures. In addition, the Algerian Digital Seismic Network has recorded several aftershocks.

This paper gives an overview of the geologic and seismotectonic setting of the zone shaken by this sequence and investigates the potential causative faults using geologic, seismic, and remotely sensed data. The paper also briefly describes the triggered landslide, focusing on its geometry and structure and analyzing the factors leading to its activation.

2 Setting

The study area is part of the Miocene Constantine-Mila basin formed mainly by upper Miocene Lacustrine, continental and evaporitic deposits. The actual shortening of the Nubia-African plate is expressed by strikes-slip faulting, which is the actual regime in northeastern Algeria (Bougrine et al., 2019). Many earthquakes in the Constantine-Mila zone occurred along strike-slip faults that border the basin. Recently, many minor to moderate seismicity occurred along the EW Mcid Aïcha Debbagh fault zone (MAD) between

A. Çiner et al. (eds.), *Recent Research on Sedimentology, Stratigraphy, Paleontology, Tectonics, Geochemistry, Volcanology and Petroleum Geology*, Advances in Science, Technology & Innovation,
https://doi.org/10.1007/978-3-031-43222-4_39

Guelma and Sidi Driss (Bendjama et al., 2021). This fault is at least 80 km EW strike-slip shear zone with a long deformation history, including Miocene normal faulting, Upper Miocene thrusting and folding, and Pleistocene transpression.

In the epicentral area of the 2020 Mila sequence, the MAD fault zone (Fault 3 in Fig. 1) cuts along the Mcid Aïcha Debbagh mountain (1482 m) and probably continues to the west toward the Babor chain (Boulahia et al., 2021). Many neotectonic deformations have been observed and mapped at the southern foot of the Mcid Aïcha mountain (the epicentral area), including thrusting and folding events (Coiffait, 1992). Besides its active tectonic character, this zone is known for its slope instability, making the geohazard greater (Merghadi et al., 2018).

3 Results

3.1 Potential Causative Faults

The seismic sequence occurred South of Mcid Aïcha mountain, East of the Beni Haroun Dam. The focal mechanisms and the distribution of the aftershocks exclude the implication of the EW MAD fault zone. However, we could select two potential active faults using remotely sensed data, including high-resolution Google Earth imagery and EO-Ali multispectral images combined with field observations and analysis. The first one corresponds to a NE-SW fault zone (Fault 1 in Fig. 1) composed of many segments that affect the upper Miocene folded formations north of Grarem Gouga municipality. Many observations show displaced

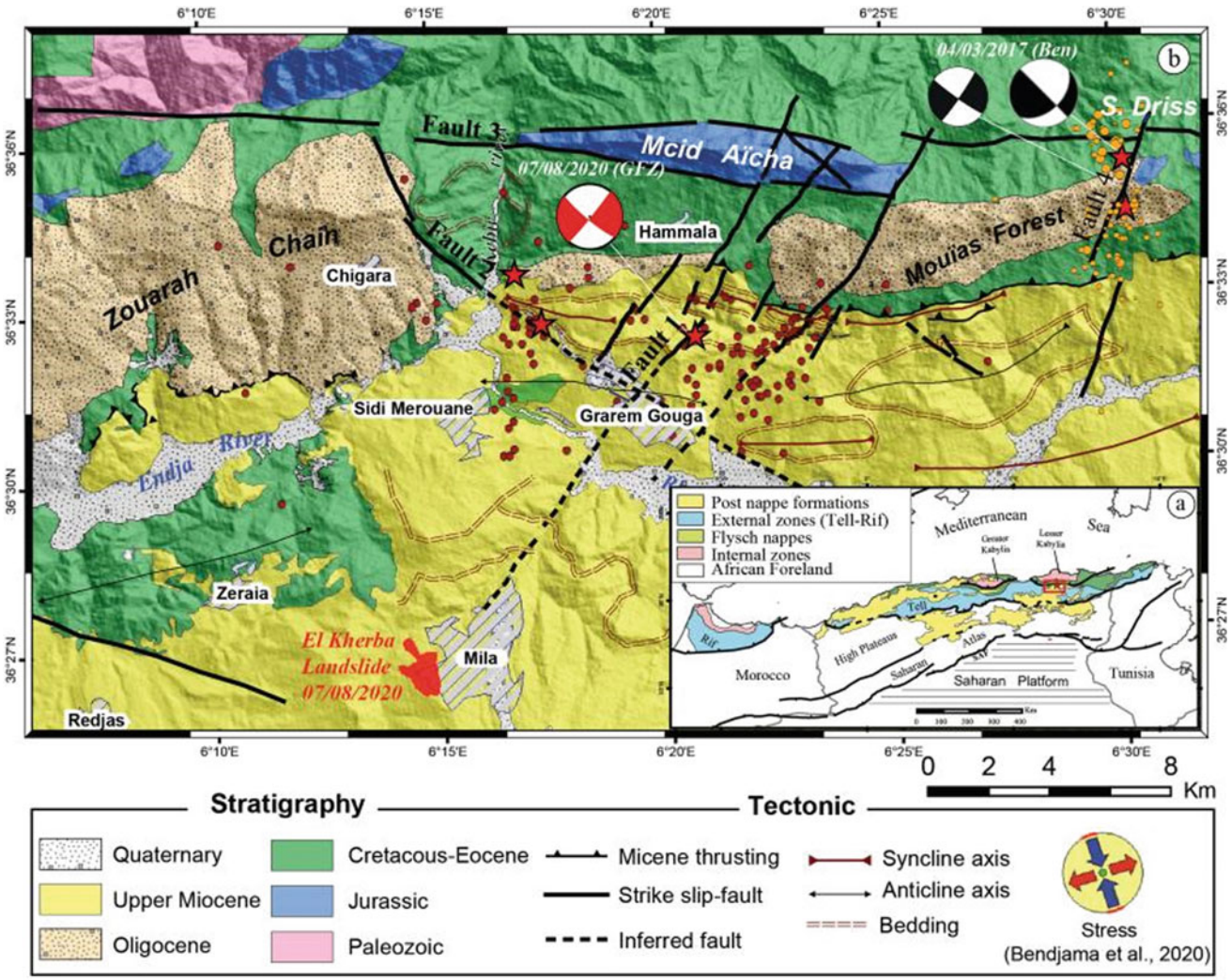

Fig.1 Seismotectonic context of the Mila zone. **a** General tectonic map of the Algerian Tell Atlas. **b** The local tectonic map of the epicentral area of the 2020 Mila sequence shows the main geologic and seismotectonic features. Red stars and dots correspond to the Mainshock-Aftershock sequence of the Mila 2020 earthquake (from ADSN-CRAAG). Orange circles show the Sidi Driss 2017 sequence (Bendjama et al., 2021)

strata along these faults (Fig. 1b). The second mapped fault has a NW–SE orientation and cuts through the Dam of Beni Haroun (Fault 2 in Fig. 1). Observations show that this fault has a critical breccia zone with multiple slickensides that are different in orientation and slip direction, the most recent slickenside is in agreement with the actual stress regime.

3.2 The Triggered Landslide

Two hours after the second mainshock of 08 August 2020 (Mw = 5), a massive landslide affected El Kherba City at the western part of Mila (15 km southeast of the epicenter, Fig. 1). It led to significant damage to the infrastructure. Fortunately, no human losses were reported. Field observations and pre- and post-landslide analyses using high-resolution Google Earth imagery led to the map of Fig. 2a, where the principal features of this landslide have been reported. The observations show that this complex mass movement combines slumping at the upslope and earthflow at the downward slope (Slump-Earth flow movement). The length of the displaced mass reached 2 km, and its width could reach 1.3 km. The upper part of the slide is characterized by curved ruptures with exposed vertical scarps (Fig. 2b). At the left flank, these ruptures could reach 6 m of height and are characterized by well-preserved oblique slickensides (Fig. 2c). Many less important secondary scarps are observed as we go down toward the center of the slide. The downslope, however, is formed by a transverse ridge, especially in the eastern part, and by an

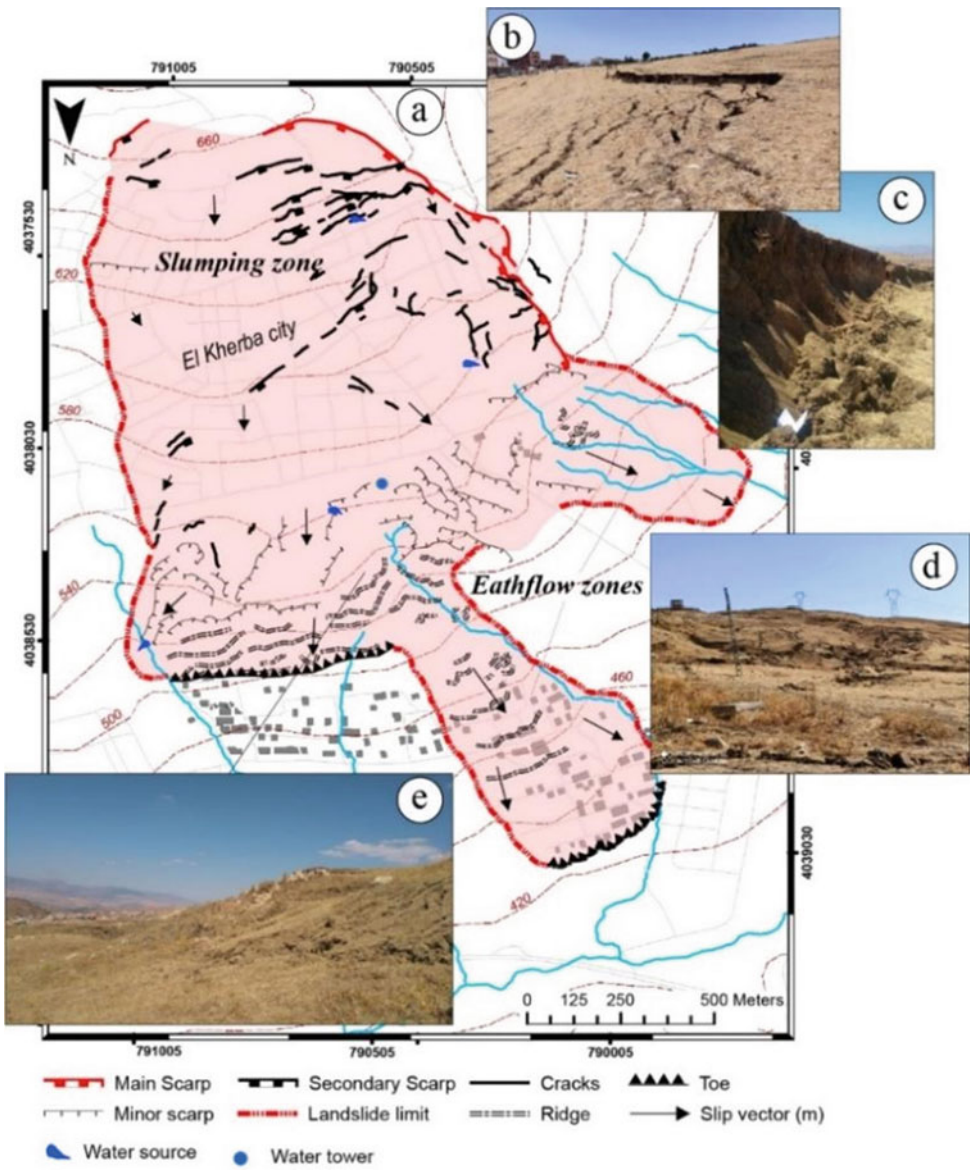

Fig. 2 Map showing the El Kherba 2020 Landslide with its principal features. For explanations of the associated photos, see the text

important earthflow in the western part (Fig. 2d, e). The top of this earthflow coincides with a slope break at 550 m, where many secondary scarps and slumping occurred.

By analyzing pre- and post-Google imagery from 07/2020 to 03/2021, we were able to map the different horizontal slip vector within the displaced mass (black arrows in Fig. 2a). The main mass has a displacement vector to NNW in the upper part then it spreads out in all directions in the down position. The movement at the upslope is about 4 m, and at the downslope increases significantly to reach 30–40 m within the earthflow mass.

4 Discussion

The 2020 seismic sequence of Mila proves again that the Algerian Tell and particularly the post-thrust sheet basins are active areas even though there are no historical records. The causative faults hadn't been mapped before, and they likely were inactive for the spending of the historic period. Although the mainshock focal mechanism and the aftershock distribution exclude the direct implication of the MAD fault, it seems that some transverse faults are causative. This sequence is similar to the 2017 Sidi Driss sequence [(Bendjama et al., 2021) 12 km East of the actual sequence, Fig. 1b]. Both sequences have occurred at the northwestern border of the basin and have a similar distribution similarity. Therefore, the tow sequences should belong to the same fault network that affects the basement of the basin (Fault 1 and Fault 4 in Fig. 1).

The triggered landslide is 15 km away from the epicentral zone. This distance/magnitude ratio is beyond the upper limit of Keefer (1984), indicating that the slope had almost reached its threshold stability before the earthquake. Many factors are at the origin of this landslide, including topography, clay-bearing lithology with bedding parallel to the slope, water content and groundwater flow, and human excavation/loading at the downslope and upslope, respectively. Among these factors, the role of water is likely to be primordial, especially at the downslope where the earthflow behaved as a viscous fluid. The rupture planes are found to be very wet, which agrees with water percolation along the rupture surface. In addition, seismic shaking seemed to trigger the earth flow at the downslope, which led to slope instability and slumping at the upslope.

5 Conclusions

The present study provides evidence of two new potential active faults affecting the NW border of the Constantine-Mila basin. The first belongs to a NE-SW network that cuts through the western part of Mcid Aïcha mountain, and the second with NW–SE direction cuts near the Beni Haroun dam.

The landslide hazard is one of the direct consequences of seismic hazards in the Mila zone, and any attempt to assess this hazard should consider the area's seismotectonic context. Here we show that the triggered landslide is a complex slumping-earthflow movement. Many factors are combined to accelerate the movement, water, and human activities which are the principal factors.

References

Bendjama, H., Yelles-Chaouche, A., Boulahia, O., et al. (2021). The March 2017 earthquake sequence along the E-W-trending Mcid Aïcha-Debbagh Fault, northeast Algeria. *Geosciences Journal*, 1–17.

Bougrine, A., Yelles-Chaouche, A. K., & Calais, E. (2019). Active deformation in Algeria from continuous GPS measurements. *Geophysical Journal International, 217*(1), 572–588.

Boulahia, O., Abacha, I., Yelles-Chaouche, A., et al. (2021). Recent seismic activity in the Bejaia-Babors Region (Northeastern Algeria): The case of the 2012–2013 Bejaia Earthquake Sequences. *Pure and Applied Geophysics, 178*(4), 1253–1279.

Coiffait, P. E. (1992). Un bassin post-nappes dans son cadre structural: l'exemple du bassin de Constantine (Algérie nord-orientale). Thèse de doctorat, Université de Nancy I.

Keefer, D. K. (1984). Landslides caused by earthquakes. *Geological Society of America Bulletin, 95*(4), 406–421.

Merghadi, A., Abderrahmane, B., & Tien Bui, D. (2018). Landslide susceptibility assessment at Mila Basin (Algeria): A comparative assessment of prediction capability of advanced machine learning methods. *ISPRS International Journal of Geo-Information, 7*(7), 268.

Petroleum and Energy Engineering, Petroleum Geology

Overcoming the Crude Oil Emulsion Problem Through the Utilization of Organic Additive De-emulsifier from Olea Europaea: Effect of Additive Volume, Temperature, and Composition

Novrianti Novrianti, Idham Khalid, Sri Setia Ningsih, and Adi Novriansyah

Abstract

The existence of crude oil emulsion (COE) leads to some portion of the crude-containing brine, which aggravates the crude oil quality. To overcome this problem, the addition of a de-emulsifier will be effective. However, commercial de-emulsifiers are mostly harmful to the environment. Through this study, the de-emulsifier product is synthesized from the oil product of Olea europaea (Olive oil), which is categorized as an organic and environmentally safe product. This study consists of two procedures, additive production by saponification process and bottle test, to observe the effectiveness of olive oil de-emulsifier (OOD) in vanishing the COE under 50, 70, and 80 °C temperatures. This study utilizes two kinds of OOD with different component compositions: the OODA and the OODB component. This study will also investigate the effect of de-emulsifier composition and volume. The bottle test results indicate that OOD positively impacts the separating oil and brine from the emulsion phase. On the other hand, oil–water easily separates from the emulsion phase at a higher volume of OOD and higher temperature but consumes more time. Comparing two kinds of OOD at 5 ml volume and 80 °C yields a slight difference in separation volume, whereby samples containing OODA separate the emulsion more than OODB. However, the sample with OODB consumes less time to achieve maximum separation volume. OODB, derived from olive oil using more potassium oxide (KOH), water, and less glycerin, tends to disappear COE at a lower time and higher separation volume.

Keywords

Crude oil emulsion • Olive oil • De-emulsifier • Separation time • Separation volume

1 Introduction

It is widely known for its de-emulsifier role in the oil and gas industry, especially for overcoming crude oil–water emulsion issues (1). Rapid encouragement of eco-friendly materials in oil and gas operations triggers us to look for alternative ingredients commonly used in daily activities as raw materials for replacing or even complimenting oil and gas additives. We introduce an optional de-emulsifier through this experimental work derived from the Olea europaea, which is known as olive oil. Global utilization of olive oil products is doubtless from the supply and demand sector (2). However, its contribution to oil and gas, i.e., storage and pipe transportation, is still vague and requires room for further development. We hope that through the findings of this study, we may find another approach to valorize the olive oil product as a de-emulsifier product in the oil and gas sector. Furthermore, this kind of utilization may increase the economic value of this product. This study investigates the effect of additive content, temperature, and composition on the breaking emulsion ability.

2 Settings Up Experiments

This study utilizes virgin olive oil from the Bertolli company. Moreover, glycerin ($C_3H_8O_3$) and potassium oxide (KOH) are purchased as ingredients to prepare de-emulsifier products. The first step is adding 50 ml olive oil into the 100 ml beaker glass and heating it until reaching 70 °C temperature for 30 min. Next, pour KOH and de-ionized

N. Novrianti · I. Khalid · S. S. Ningsih · A. Novriansyah (✉)
Universitas Islam Riau, Pekanbaru, Riau, Indonesia
e-mail: anba11181@gmail.com

A. Çiner et al. (eds.), *Recent Research on Sedimentology, Stratigraphy, Paleontology, Tectonics, Geochemistry, Volcanology and Petroleum Geology*, Advances in Science, Technology & Innovation,
https://doi.org/10.1007/978-3-031-43222-4_40

Table 1 De-emulsifier composition

Composition (unit)	OODA	OODB
Olive oil (ml)	50	50
DI water (ml)	12.5	19.6
KOH (ml)	25	50
$C_3H_8O_3$ (ml)	4	2

(DI) water slowly and stir with 800 rpm velocity with magnetic stirrer apparatus. As a result, there are two samples of de-emulsifier products (OODA) and (OODB) which are prepared, where one sample is more enriched by KOH but more minor in $C_3H_8O_3$, compared to another (Table 1). Finally, put glycerin into the solution and continuously stir until forming homogeneous solutions.

The next step is the bottle test experiment, which utilized 50 ml crude–brine emulsion and olive oil de-emulsifier sample A (OODA). The crude–brine emulsion contains medium gravity crude (21° API) and DI water with the same proportion, i.e., one to one ratio. Accomplish the mixing process inside the 100 ml bottle. Locate 1 ml of OODA into the bottle, and put the bottle into the water bath apparatus. Maintain the water bath temperature at 50 °C, and observe and record the oil–water separation volume every 30 min until 2.5 h elapsed. Perform the same procedure as OODB. To investigate the effect of additive volume, perform a similar process for 3- and 5-ml OODA and OODB de-emulsifier. Furthermore, examine both samples for 70 and 80 °C temperatures.

3 Results

Figure 1 depicts the effect of additive volume (Fig. 1a), temperature (Fig. 1b), and composition (Fig. 1c) on the separated water volume for 3 h of observation time. Figure 1a indicates that increasing the volume of the de-emulsifier in the crude–water emulsion yields a larger volume of separated water. The highest amount of separated water occurs for a 5 ml OODA additive sample at 50 °C water bath temperature. The sample with 5 ml de-emulsifier shows effective results; we compare it for each water bath temperature. Figure 1b yields that the temperature parameter positively impacts the water–crude separation process where higher temperature separates more water from the emulsion. To investigate the effect of the component in the de-emulsifier, we compare the capability of OODA and OODB in breaking the crude–water emulsion. Figure 1c reveals that the OODA de-emulsifier can separate more water after 3 h than OODB. However, OODB requires less time to yield a peak-separated water volume than OODA. Conclusively, OODA can break the emulsion more but consumes more time than OODB.

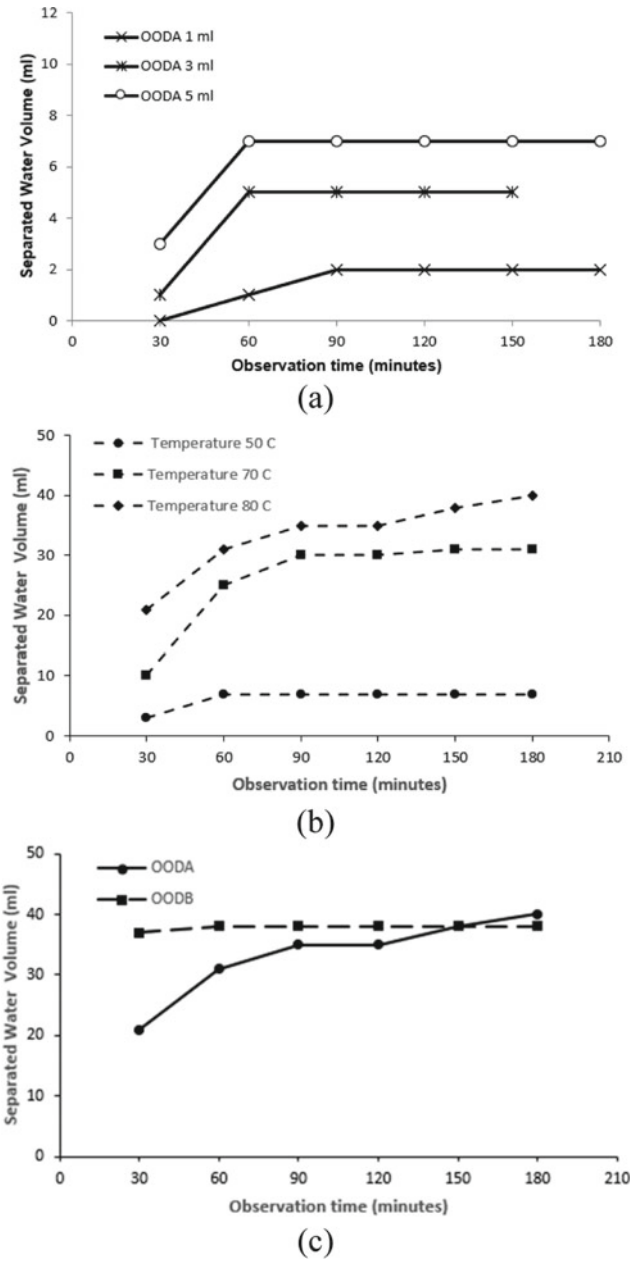

Fig. 1 Effect of **a** de-emulsifier volume; **b** water bath temperature; **c** de-emulsifier type to separated water volume under 3 h observation time

4 Discussion

The bottle test results show how effectively olive oil is used as a de-emulsifier product due to its high fatty acid content (3). KOH triggers surfactant generation, which affects the stability of the oil, water, and interfacial film. Surfactants' primary function as agents for reducing surface tension disrupts emulsion stability and accelerates the water–oil separation process. Higher emulsifier volume increases the

surfactant component in the oil–water emulsion, inducing a higher volume of separated water. Elevating the temperature also contributes positively to breaking the oil–water emulsion. Higher temperature gives thermal energy to water droplets and affects the stability of the interfacial film layer. OODB, which contains more KOH than OODA, has a higher possibility of generating surfactants through the saponification process. The existence of more surfactants may potentially break the crude–water emulsion.

5 Conclusions

This study proves the alternative utilization of olive oil as a raw material for an emulsion breaker additive. We determine the capability of the OODA and OODB products under various additive volumes, temperatures, and the composition of the de-emulsifier parameters. The result from the bottle test indicates that applying a high volume of de-emulsifier at elevated temperatures may break the emulsion more. The appearance of KOH at higher concentrations in OODB may rapidly break the water–crude emulsion, inducing low requirement time. Meanwhile, OODA successfully separates more aqueous phases from the emulsion but needs longer to achieve that. There is still room to develop an economical product from olive oil use.

A Practical Recipe to Reconstruct Fluid Composition from Limited Sample or Data

Abhijit Dandekar

Abstract

Reservoir fluid composition is essential in simulation studies, evaluating reserves, enhanced oil recovery (EOR) processes, production, and flow assurance. However, engineers are often faced with the challenge of incomplete information on fluid composition, which is quite frequently due to limited sample size, age, data, HSE, and economic considerations. This was precisely the case when an Alaskan oilfield (Umiat), potentially containing large recoverable reserves, was being considered for development. Unfortunately, the only physical sample was a weatherized dead oil ($\sim$ 50 cm^3) collected in the 1940s. Using this limited physical sample and other available data, a systematic and practical novel methodology was developed to successfully reconstruct the fluid composition by replenishing the lost components. PVT laboratory tests, fluid property measurements, and Equations of State (EOS) modeling were successfully carried out using the reconstructed fluid sample. The data was used in reservoir simulation studies to screen different EOR methods. The robustness and versatility of this methodology are further demonstrated by successfully recreating a stock tank condensate from Norway and oil from Saudi Arabia from severely weatherized samples and minimal data. The key takeaway from this paper—the novel methodology successfully demonstrated—has a universal appeal in that it can be applied to reconstruct any fluid composition in sample or data-constrained cases.

Keywords

Fluid composition • PVT • Fluid characterization • Equations of state • Live oil

A. Dandekar (✉)
Department of Petroleum Engineering, University of Alaska Fairbanks, Fairbanks, AK 99775, USA
e-mail: adandekar@alaska.edu

1 Introduction

Fluid composition, normally expressed in mole fraction or mole%, is the signature/identity or DNA of a given reservoir fluid. It is the backbone of Equations of State (EOS) modeling, which is used in multiple applications such as reservoir simulation, material balance, enhanced oil recovery processes, and flow assurance. The most reliable method of obtaining fluid composition and the PVT data is laboratory analysis of bottom hole or reconstituted fluid samples. However, that is not always the case due to various reasons such as limited sample or data, its age, Health Safety Environment (HSE), and most importantly, economic considerations. In addition, although some numerical approaches to estimate fluid composition or relate them to other properties exist (Ovalle et al., 2007; Paredes et al., 2014; Spivey & McCain, 2013), they tend to be data intensive. Moreover, given the unique nature of every reservoir fluid and composition (especially gas condensates and volatile oils), empirical correlations and others may have a limited range of applicability. Finally, proper definition or characterization of the plus fraction is also a prerequisite.

The above conundrum means incomplete information on fluid composition, which thus constitutes a major challenge faced by petroleum engineers that need it for the purposes mentioned above. This was precisely the case when a unique oilfield (broadly known as Umiat) in Alaska was considered for development circa 2008–2009, following interest and funding (DE-FC26-08NT0005641) by the US Department of Energy and Industry (Renaissance Alaska LLC). Unfortunately, notwithstanding the initial exploration conducted by the US Department of Navy, and despite drilling 11 wells, the field was never developed during that period due to its techno-economic challenges. One of the significant obstacles in the development plan was the insufficient information, including the lack of bottom hole or recombined fluid samples, that was needed in fluid studies. What was available at the time was: (1) $\sim$ 50cm^3 of severely weatherized

A. Çiner et al. (eds.), *Recent Research on Sedimentology, Stratigraphy, Paleontology, Tectonics, Geochemistry, Volcanology and Petroleum Geology*, Advances in Science, Technology & Innovation,
https://doi.org/10.1007/978-3-031-43222-4_41

physical Umiat oil sample stored in a plastic container (at Alaska Geological Materials Center, GMC) and (2) sparse, dated physical property data. So, the challenge at the time was to put the puzzle pieces together and construct the physical and numerical Umiat fluid sample. Motivated by this case study, we devised a creative approach and a practical recipe (see next section) to address this challenge. First, we recreated the physical fluid sample and the composition from limited data and samples. The developed methodology's robustness was also tested on two other liquid cases.

2 Methodology

A self-explanatory Fig. 1 outlines the workflow and the analytical instruments used in accomplishing the methodology. Specific details can be found elsewhere (Shukla, 2011). The Pedersen characterization method for limited data (Danesh, 1998) is applied. Umiat dead (stock tank) oil is assumed as represented by C_{7+}. Using available distillation data from 1958 (Baptist, 1960) and generalized specific gravity (γ) and molecular weight (MW) of SCNs, γ_{C7+} and MW_{C7+} are calculated, and the method (Danesh, 1998) is applied to characterize the supposedly *original* Umiat (dead) oil from C_7 through C_{25+} (adequate given the oil is light),

$$\sum_{C_7}^{C_{25+}} Z_{C_n} M_{C_n} = \sum_{C_7}^{C_{25+}} \mathrm{EXP}(A + BM_{C_n}) M_{C_n} = Z_{C_{7+}} M_{C_{7+}} \quad (1)$$

$$A = \mathrm{LN}\left(Z_{C_{7+}}\right) - \mathrm{LN}\left(\sum_{C_7}^{C_{25+}} e^{BM_{C_n}}\right) \quad \text{and} \quad \sum_{C_7}^{C_{25+}} \left(M_{C_n} - M_{C_{7+}}\right) e^{BM_{C_n}} = 0 \quad (2)$$

Finally, based on the methodology, the "lost components" due to weatherization were replenished by using n-alkanes first to recreate the physical and numerical "pseudo-representative" dead oil sample and, subsequently, the live oil sample (also see next section on Results). A similar methodology was applied for the other two external gas condensate and light oil cases.

3 Results

A comparison of γ_{API}, viscosity, and MW of the limited Umiat oil sample with other data confirmed weatherization, e.g., 29.7° API (this work) versus 36.6° API (Baptist, 1960). Additionally, lost components-based weatherization is evident in Fig. 2.

After adding n-alkanes (right bar graph, Fig. 2), the matched Umiat dead oil composition was achieved. The methodology was also tested on a gas condensate (Sørheim & Andreassen, 2011) and a light oil (Wang et al., 2003); both represent the severest form of weatherization. Therefore, experimental data are taken from these sources. In both cases, the fluid composition is reconstructed entirely based on only the un-weatherized stock tank liquid gravity (even more limited data than Umiat), using additional correlations developed by this author's unpublished work. Figure 3 shows the recreated stock tank liquid compositions for Umiat, the gas condensate, and the light oil.

4 Discussion

To obtain additional verification that the practical recipe works, the density (API), viscosity, and molecular weight also were compared, which resulted in a perfect match with the limited old data (Collins, 1958). This is yet another demonstration of successfully recreating a representative Umiat dead oil sample. The recreated dead oil sample was recombined with the Umiat gas using the 70.6 scf/stb GOR to produce the Umiat live oil sample. Obviously, no physical sample of Umiat solution gas existed; hence, it was blended by a commercial gas company based on values reported elsewhere (Masterson, 2001). The CCE conducted on the recreated live oil sample resulted in bubble points at the range of Umiat reservoir temperatures that matched very

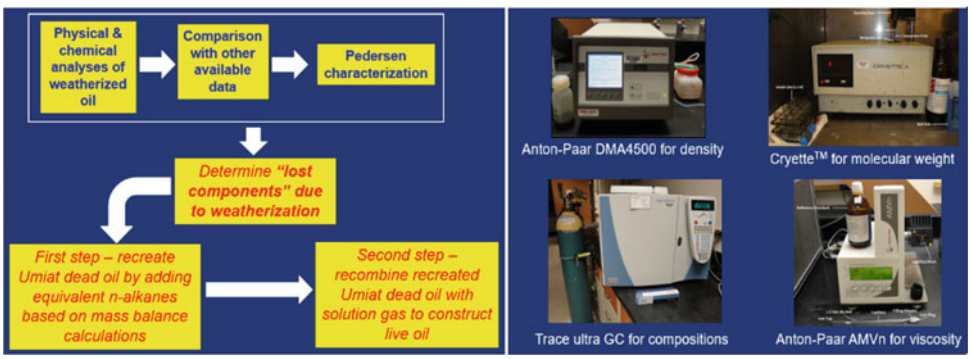

Fig. 1 Workflow and analytical instruments used for constructing Umiat fluid sample from limited sample and data

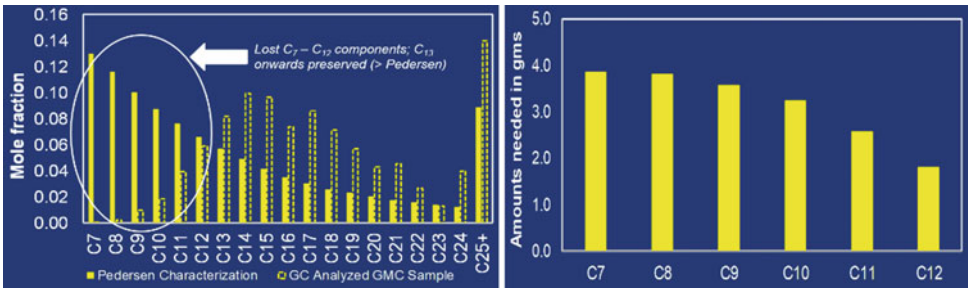

Fig. 2 Lost components due to weatherization and their replenishment by equivalent n-alkanes based on mass balance on the total mass of weatherized Umiat oil available, 39 g (50 cm^3)

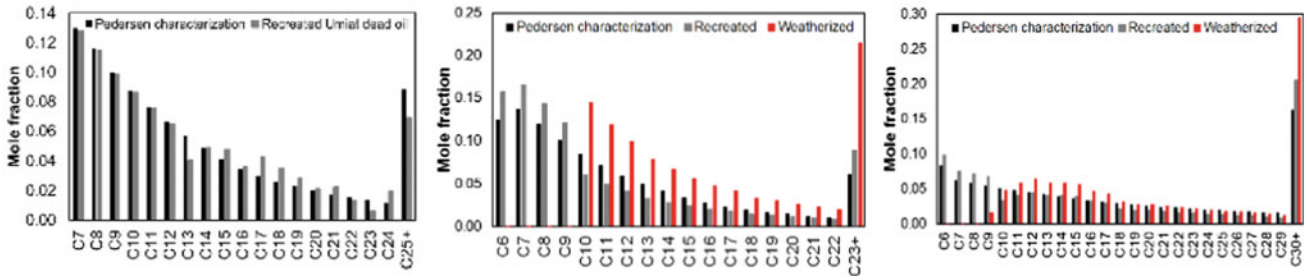

Fig. 3 Recreated Umiat, gas condensate, and light oil stock tank liquids

well with well-known empirical correlations and the PR EOS model (Robinson & Peng, 1978).

As mentioned in the results, the two external cases represented almost an acid test of the practical recipe, given the extreme case of weatherization. In addition to the molar composition distribution achieved, shown in Fig. 3, the γ values of the stock tank liquids were compared, for which the differences were within 2%.

Finally, a small caveat that is in order here is that the creative approach is perhaps the best way to solve the problem of missing sample and data information; however, it should not be construed as a substitute for nature (geochemistry).

5 Conclusions

The following main conclusions or takeaways are based on this work:

- This work shows the application of well-established experimental and modeling techniques to a real practical problem to fill in the gaps in the reservoir data.
- The adopted approach has a universal appeal in that it can be easily applied to recreate any fluid composition in sample and data-constrained cases.
- Finally, the demonstrated technique is simple, practical, and can be used by any petroleum engineer.

References

Baptist, O. C. (1960). *Oil recovery and formation damage in permafrost, Umiat field*, Alaska, report of investigation 5642, US Department of Interior, Bureau of Mines, Available online at http://www.dggs.alaska.gov/webpubs/usbm/ri/text/ri5642.PDF

Collins, F. R. (1958). *Test wells, Umiat area*, Alaska, US. Geological Survey professional paper 305-B, 71-206. Available online at http://www.dggs.alaska.gov/webpubs/usgs/p/text/p0305b.PDF

Danesh, A. (1998). *PVT and phase behavior of petroleum reservoir fluids*. Elsevier.

Masterson, IV, W. D. (2011). *Petroleum Filling History of Central Alaskan North Slope Fields*, Ph.D. Thesis, The University of Texas at Dallas.

Ovalle, A. P., Lenn, C. P., & McCain, W. D. (2007). Tools to manage gas/condensate reservoirs; novel fluid-property correlations on the basis of commonly available field data. *SPE Reservoir Evaluation and Engineering, 10*, 687–694.

Paredes, J. E., Perez, R., Perera Perez, L., & Larez, C. J. (2014). Correlations to estimate key gas condensate properties through field measurement of gas condensate ratio. In *SPE Annual Technical Conference and Exhibition, Amsterdam*.

Robinson, D. B., & Peng, D. Y. (1978). The characterization of the heptanes and heavier fractions for the GPA Peng-Robinson programs. In *GPA Research Report 28*, Tulsa.

Shukla, C. (2011). *Fluid characterization and phase behavior studies for frozen reservoir of Umiat oil field*, Alaska, MS Thesis, University of Alaska Fairbanks.

Sørheim, K. R., & Andreassen, I. (2011). Weathering properties of the Trym condensate, SINTEF Materials and Chemistry. In *Marine Environmental Technology Report*.

Spivey, J. P., & McCain, W. D. (2013). Estimating reservoir composition for gas condensates and volatile oils from field data.

In *SPE Annual Technical Conference and Exhibition New Orleans, Louisiana, USA*.

Wang, A., Hollebone, B. P., Fingas, M., Fieldhouse, B., Sigouin, L., Landriault, M., Smith, P., Noonan, J., & Thouin, G. (2003). *Characteristics of spilled oils, fuels, and petroleum products: 1. Composition and properties of selected oils*. Emergencies Science and Technology Division, Environmental Technology Centre Report, EPA/600/R-03/072.

Numerical Investigation of Wettability Alteration and Well Configuration Effects on Oil Recovery in Waterflooding Operations

Palang Moronke Guful and Serhat Canbolat

Abstract

This work studied the effects of wettability alteration and well configuration on waterflooding recovery. This was assessed by creating nine models on a commercial black oil simulator with the properties of the Bonga oilfield in Nigeria. These models had three different wettability (water-wet, oil-wet, and mixed-wet) and three different well configurations [vertical injectors and vertical producers (VIVP), vertical injectors and horizontal producers (VIHP), and horizontal injectors and horizontal producers (HIHP)], which gave a total of nine models. The results showed that water-wet cases generally performed the best in oil recovery in waterflooding operations (63.6–53.6%) with the same amount of injected water in each scenario. Mixed-wet cases gave the second-best performance (43.1–33%), and the oil-wet cases yielded a minor recovery (34.2–32.1%). For the well configurations, the VIHP cases (63.6–34.2%) gave the best results and were closely followed by the HIHP cases (63.2–33.9%), while the VIVP yielded the least recovery of the three (53.6–32.1%). Moreover, analysis of the injected water to produced oil ratio showed wettability variation as the primary determinant. The water-wet cases were seen to have the best results (3–4), the mixed-wet issues to have the following best ratio (4–6), and the oil-wet case yielded the least (5–7) among the different wettability types. In the Bonga oilfield of Nigeria, it is strongly recommended to implement the VIHP well scenario to improve oil recovery while simultaneously reducing water injection (and resultant water production).

Keywords

Waterflooding • Bonga field • Numerical simulation • Wettability • Well configuration

1 Introduction

While in most studies, water-wet systems have been seen to give better waterflood performance than either oil-wet or mixed-wet systems (Anderson, 1987), some studies have shown that mixed-wet performed better than water-wet and oil-wet systems (Xiao et al., 2017). Similarly, well configuration has also been seen to significantly affect the performance of waterflooding operations. For example, in some cases, pairing vertical wells with horizontal wells have been seen to give better recovery values than both horizontal injectors and producers (Lee, 2012).

In this study, the good orientation and wettabilities are changed to check their effect on water injection, while the amount of water injected was kept at a minimum. The properties of a field in Nigeria—Bonga oilfield—were used for this investigation, and the best-case scenario for this field was proposed.

2 Methodology

The reservoir model was a block centered, uniform grid size, a homogeneous, non-fractured, and three-dimensional model with grid dimensions of 20 by 20 by 4. The model was simulated with the properties of the Bonga oilfield, which are given in Table 1. However, to capture the difference in the performance of the waterflood, it was simulated with two injection wells and two production wells in all cases to represent a simple basic form of the waterflood (Fig. 1). The injection wells were constrained to a maximum surface water rate of 300 MSTB/D to keep the amount of injected

P. M. Guful · S. Canbolat (✉)
Department of Petroleum and Natural Gas Engineering, Near East University, Nicosia, Mersin 10, Turkey
e-mail: serhat.canbolat@neu.edu.tr

A. Çiner et al. (eds.), *Recent Research on Sedimentology, Stratigraphy, Paleontology, Tectonics, Geochemistry, Volcanology and Petroleum Geology*, Advances in Science, Technology & Innovation,
https://doi.org/10.1007/978-3-031-43222-4_42

Table 1 Reservoir model characteristics

Parameter (unit)	Value
Area (acres)	14,826
Thickness (ft)	90
Horizontal permeability (md)	2500
Vertical permeability (md)	250
Porosity (decimal)	0.32
Initial temperature (F)	°F
Initial Pressure (psi)	4550
Oil gravity (lbm/ft^3)	47.45
Depth to top of the reservoir (ft)	6000
Irreducible water saturation (decimal)	0.3

Table 2 Recovery results of wettability systems and well configurations

Parameter (unit)	Cumulative oil recovery (bbl) (MM)	Recovery factors (%)
VIVP (water-wet)	768	53.9
VIHP (water-wet)	912	63.6
HIHP (water-wet)	906	63.2
VIVP (oil-wet)	419	35.0
VIHP (oil-wet)	447	34.2
HIHP (oil-wet)	443	33.9
VIVP (mixed-wet)	391	32.5
VIHP (mixed-wet)	517	43.1
HIHP (mixed-wet)	510	42.4

water to economic levels and to a maximum bottom hole pressure (BHP) of 6000 psi to prevent accidental fracturing of the formation. The optimal well length was decided by changing the length of the laterals to see which gave the best results.

Three different wettability models were used—water-wet, oil-wet, and mixed-wet and three different well configurations were used—vertical injector and vertical producers (VIVP), vertical injector, and horizontal producers (VIHP), and horizontal injectors and horizontal producers (HIHP). These made a total of 9 case studies: VIVP water-wet model, VIHP water-wet model, HIHP water-wet model, VIVP oil-wet model, VIHP oil-wet model, HIHP oil-wet model, VIVP mixed-wet model, VIHP mixed-wet model, and HIHP mixed-wet model (Fig. 1).

3 Results and Discussion

3.1 Effect of Wettability Alteration

Water-wet systems cause water to preferentially adhere to the formation body, which causes oil to flow more quickly through the pores. This led to low ratios of cumulative water injected to cumulative oil produced, making the water-wet systems the most economically feasible of all three. The oil-wet systems are the direct opposite of the water-wet systems. From the definition of oil-wet systems, the lack of favorability of this system to oil production is obvious. The mixed-wet systems have recovery results that are in between the water-wet and the oil-wet values. This is because, for mixed-wet systems, the smaller pores are water-wet, and the larger pores are oil-wet. This mixed behavior of mixed-wet reservoirs made some parts of the reservoir act as water-wet systems and others act as oil-wet systems (Table 2; Fig. 2).

3.2 Effect of Well Configuration

Horizontal wells generally are expected to produce more oil than vertical wells (Table 2; Fig. 2). This was the case in the simulations performed. Regardless of wettability, horizontal producers performed better than vertical producers. This is because horizontal wells open larger areas of the formation to flow than vertical wells, which means more oil production can be realized. However, the injectors' results depended on the type of producer used. For example, in the VIHP scenario, better results were realized than in the HIHP scenario, while the VIVP scenario performed the least. Other studies have seen this behavior and can be attributed to sweeping efficiency (Claridge & Qui, 1991).

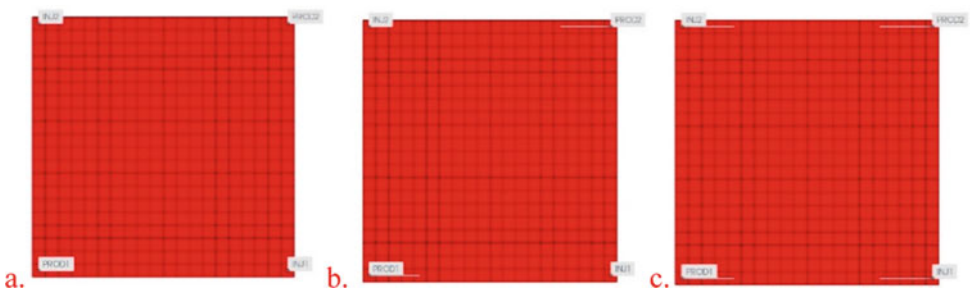

Fig. 1 Well configurations used in the reservoir model for all wettability systems **a** VIVP, **b** VIHP, **c** HIHP

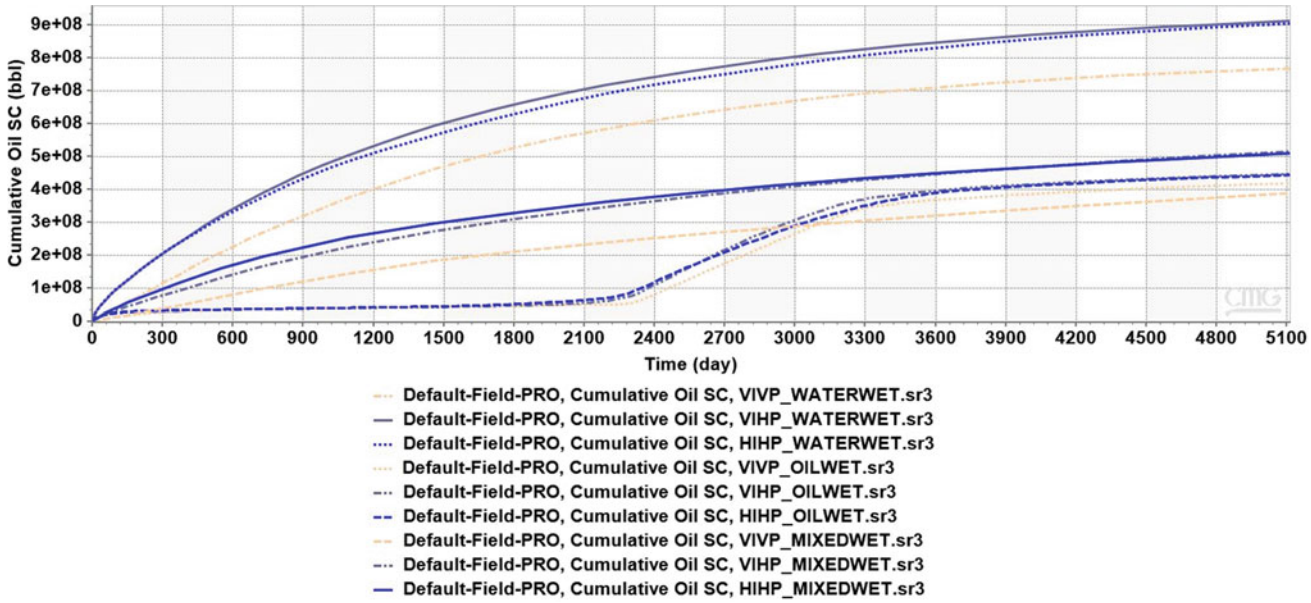

Fig. 2 Cumulative oil production for all wettability systems and well configurations

4 Conclusions

This study showed that horizontal producers led to more oil recovery than vertical producers. However, pairing vertical injectors with horizontal producers could give better results than pairing horizontal injectors with horizontal producers. Also, wettability was seen to have a more significant effect on recovery than well configuration. In terms of the impact of wettability on oil recovery, water-wet systems gave better results than all the other wettability systems, followed closely by the mixed-wet systems and then the oil-wet systems.

It is strongly recommended that the VIHP well scenario be implemented in the Bonga oilfield to improve oil recovery while simultaneously reducing water injection (and resultant water production).

References

Anderson, W. (1987). Wettability literature survey-part 6: The effects of wettability on waterflooding. *Journal of Petroleum Technology, 39*(12), 1605–1622.

Claridge, E., & Qui, S. (1991). Sweep efficiency comparisons of horizontal and vertical wells. *Journal of Canadian Petroleum Technology, 30*(04).

Lee, K. S. (2012). Efficiency of horizontal and vertical well patterns on the performance of micellar-polymer flooding. *Energy Procedia, 16*, 889–894.

Xiao, P., Leng, X., Xiao, H., Sun, L., Zhang, H., Mei, S., & Zhang, H. (2017). Investigation effect of wettability and heterogeneity in water flooding and on microscopic residual oil distribution in tight sandstone cores with NMR technique. *Open Physics, 15*(1), 544–550.

Well Deliverability Assessment of Libyan Near-Critical Gas Condensate Field

Raghd Gadrbouh and Mohsen Khazam

Abstract

Optimizing gas condensate reservoirs requires an adequate understanding of the flow behavior changes under various depletion cases and accurate estimates of reservoir properties of zones bearing condensate gas systems. The main objective of this study is to assess the well deliverability of a Libyan near-critical gas condensate field by simulating the actual pressure transient test and investigating the impact of various production scenarios on future well performance. Well, test data were evaluated using conventional interpretation techniques to estimate the average reservoir permeability, composite skin, and absolute open flow potential. A Cartesian compositional single well model was constructed to simulate the well A3 pressure transient test and design the field's relative permeability curves with a detailed description of the geological features near the wellbore and the rock and fluid properties. The well was then projected to different production scenarios, including various completion schemes, natural depletion, and gas cycling, to identify the optimum development option. Interpretation results indicated a considerable skin value mainly due to formation damage and reservoir heterogeneity rather than a condensate blockage. Formation damage was found to duplicate the effect of other skin components. The simulated vertical natural depletion case cannot sustain a plateau rate of 15 MMscf/d due to the damage around the well. However, this target plateau rate can be maintained for 11 years by stimulating the well primary production. Condensate recovery can be significantly enhanced to 58% by performing gas cycling at the initial pressure for ten years. This recovery can reach 64% using makeup gas.

Keywords

Near-critical fluid • Gas condensate • History matching • Well deliverability • Gas cycling

1 Introduction

The condensate blockage is the crucial factor in influencing the productivity of gas condensate reservoirs as it decreases relative gas permeability and well deliverability.

Much research has been conducted over the years to understand the effect of condensate buildup around the wellbore on well productivity. For example, Hinchman and Barree (1985) showed in their study that the well productivity is mainly affected by condensate accumulation around the wellbore; this accumulation depends on relative permeability and liquid viscosity and is defined as condensate banking blockage.

Usually, simulation models are used to understand the behavior of condensate accumulation near the. However, dynamic validation before deliverability prediction is preferred to determine the proper parameters for future investigations. Various scenarios can be conducted to mitigate the effect of condensate blockage on well deliverability and increase the well productivity. While Miller et al. (2010) suggested that horizontal wells can improve well deliverability, Zaitsev et al. (1996) showed that gas injection helped to remove the condensate "plug" and improved well performance.

In this study, we assess the well deliverability of a Libyan near-critical gas condensate field by simulating the actual pressure transient test and then investigate the impact of various production scenarios on future well performance.

R. Gadrbouh (✉) · M. Khazam
University of Tripoli, 13275, RoadSidy Almasry, Tripoli, Libya
e-mail: raghadgaderboh44@gmail.com

A. Çiner et al. (eds.), *Recent Research on Sedimentology, Stratigraphy, Paleontology, Tectonics, Geochemistry, Volcanology and Petroleum Geology*, Advances in Science, Technology & Innovation,
https://doi.org/10.1007/978-3-031-43222-4_43

2 Methodology

Well A3–located in the field's crest—was chosen to be the target well in this study. Since well A3 fluid composition varies with depth from a near-critical gas condensate fluid to volatile oil in the deeper sections, the p-approximation method was preferred for interpreting the well test as it treats the gas as a pseudo-liquid.

A Cartesian single well compositional model was constructed. The model consists of a reservoir fluid model simulated by the tuned PR-EOS and a fluid rock petrophysical model describing the nine geological layers identified from the log data and the routine core analyses conducted on the well. The model was used to regenerate the actual well test conducted on well A3. To capture the condensate behavior around the wellbore, the grids were distributed exponentially, and the parameters used to generate the preliminary relative permeability curves were then varied to investigate the effect of gas relative permeability endpoint (k_{rgmax}) and critical condensate saturation (S_{cc}) on the history matching to select the most appropriate curve to impose in the prediction cases.

To reduce the complexity of the accurate model and obtain a better understanding of various parameters' impact on the flow behavior, the geological features near the wellbore and assessing the skin parameters to achieve a match, the initial runs were conducted with a simple averaged model of one layer and single relative permeability curve. A sophisticated model with the actual rock petrophysical data (of the nine layers) was then used to describe the reservoir adequately.

3 Results

The interpretation of the pressure buildup indicates an infinite acting system (i.e., open system) with probably good pressure support. The main results are summarized in Table 1.

The assessed average simple model relative permeability endpoints of 0.72 from the gas relative permeability and 0.6 for the condensate relative permeability was again used in the sophisticated model and achieved the most suitable match (Fig. 1).

An additional pressure drop during the drawdown period is observed. To understand this, the critical condensate saturation is assumed to be zero to reduce the effect of condensate blockage skin (Sb $\sim$ 0). Both the average and the sophisticated models were compared. The comparison results indicated an additional pressure drop due to reservoir heterogeneity and are proportional to the gas rate during the drawdown periods. As the response was correlated to permeability variation, the composite skin equation is recommended to incorporate additional skin due to permeability heterogeneity (S_h).

Two scenarios of natural depletion versus gas cycling were compared. First, the natural depletion case was simulated with a target production rate of 15 MMscf/d for 30 years. The production scenario was conducted for both with and without damage cases. Considering the mechanical skin effect, the well showed almost no plateau period at the target flow rate of 15 MMscf/d. The well was then assumed to undergo a cleaning process, and no damage was encountered; a relatively reasonable plateau period of 11 years was projected. Therefore, the well life is predicted to be 18 years. However, condensate accumulates immediately as the reservoir pressure falls below the saturation pressure creating a blockage area near the wellbore, restricting the flow and choking the reservoir from producing the desired amount of gas and condensate. Hence, condensate production declines sharply, and its recovery does not exceed 30%, with an ultimate gas recovery (EUR) estimated to be around 73%.

During gas cycling processes, dry gas is injected from four injectors—a five-spot pattern—into the reservoir. The results show that increasing the cycling duration from 5 to 10 years enhances condensate production and recovery from 47 to 58%.

4 Discussion

The critical condensate saturation seems to have no significant effect on the simulated derivative curve, but assuming no critical condensate saturation (S_{cc} = 0%) will tend to increase the drawdown pressure profile. This shows that the test duration is not long enough for a condensate blockage to affect the flow behavior significantly.

A sharp decline in the reservoir pressure associated with the high skin due to damage was observed, and the target plateau rate could not be sustained. However, this period can be extended by lowering the gas production rate and stimulating the well before production. Furthermore, gas cycling maintains the reservoir pressure and enhances condensate production.

The shortage in displacement ratio (VRR < 1.0) is believed to prevent achieving high condensate recovery.

Table 1 Well, test interpretation results

Slope (m_{SL}), psi/cycle	Q_g, MMscf/d	Permeability, mD
46.06	13.33	13.35

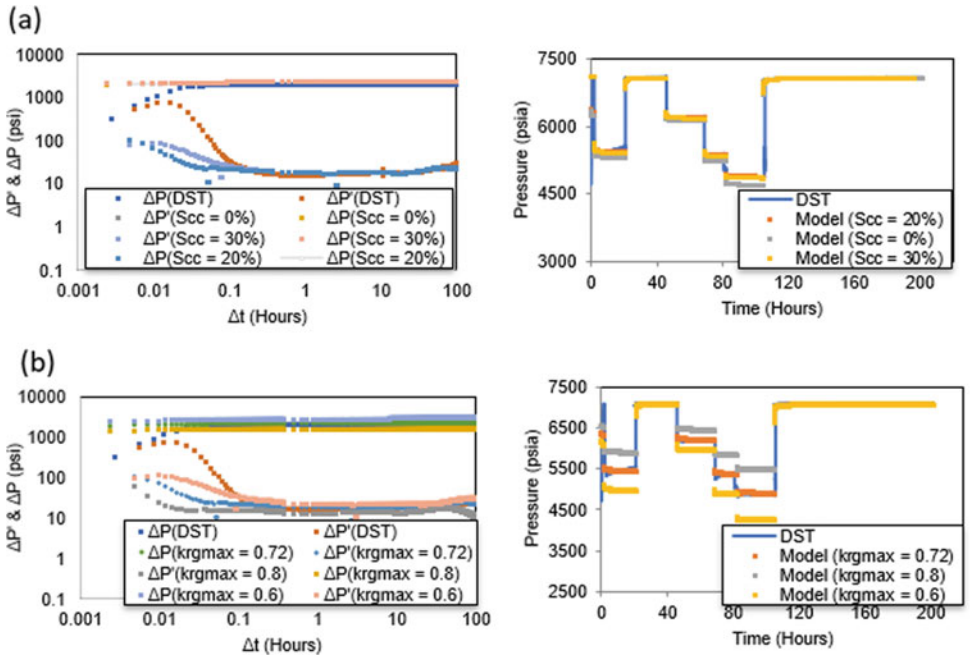

Fig. 1 Impact of critical condensate saturation S_{cc} **a** and gas relative permeability endpoint k_{rgmax} **b** on test log–log derivative and test sequence match

However, makeup gas can bring this ratio to unity and significantly improve condensate recovery by 6%.

5 Conclusions

Analysis of well A3 DST indicated a considerable skin value (~46) and a relatively low effective permeability (~13 mD). Furthermore, the single well compositional simulation model confirmed that the sizeable composite skin is mainly contributed by the well damage/perforation skin and reservoir heterogeneity skin, and the formation damage skin is found to have a compounding effect on other skin factors.

A history match of well A3 test data was used to generate the pseudo gas condensate relative permeability that reasonably represents the average dynamic flow of gas and condensate around well A3 area.

The simulated natural depletion case of well A3 cannot sustain a plateau rate of 15 MMscd/d due to the extensive damage around the well. However, if the well undergoes a stimulation process before the production scheme, this target rate is expected to be sustained for 11 years. Condensate recovery can be significantly enhanced by performing gas recycling up to 58% for ten years of cycling duration. In addition, using makeup gas can enhance this recovery (64%).

References

Hinchman, S. B., & Barree, R. D. (1985). Productivity loss in gas condensate reservoirs. *Proceedings-SPE Annual Technical Conference and Exhibition*. https://doi.org/10.2118/14203-ms

Miller, N., Nasrabadi, H., & Zhu, D. (2010). Application of horizontal wells to reduce condensate blockage in gas condensate reservoirs. In *SPE-international oil and gas conference and exhibition in China 2010, IOGCEC*. https://doi.org/10.2118/130996-ms

Zaitsev, I. Y., Dmitrievsky, S. A., Norvik, H., Yufin, P. A., Bolotnik, D. N., Sarkisov, G. G., & Schepkina, N. E.: Compositional modeling and PVT analysis of pressure maintenance effect in gas condensate field: Comparative study. https://doi.org/10.2118/36923-ms

Experimental and Visual Assessments of Artificially/Naturally Fractured Cores During Improved Oil Recovery

Serhat Canbolat

Abstract

Artificially and naturally fractured cores were utilized in this study. Experimental and visual assessments were performed to understand the physical properties of the cores properly. Computer tomography (CT) scanner images were used to determine matrix porosity. A polymer gel treatment was applied to reduce the impact of fracturing and boost oil recovery. The permeability values were assessed before and after the polymer gel injection. Furthermore, estimated CT porosity was used to evaluate each core's CT permeability. Microscope measurements of fracture apertures were compared to cubic law-based analytical calculations. In oil-saturated and water-saturated core studies, homogeneous core recovery surpassed heterogeneous core recovery due to natural fracture. Using experimental measurements, the relative error percent and absolute error distributions were acceptable for CT porosity and CT permeability estimates. However, for the equivalent fracture apertures (EFA) calculated by cubic law (CL) and visual measurements done with the microscope, the relative errors ranged from 13.44 to 31.93%. The homogeneous cores #5 and #8 have higher relative errors, indicating no fracture in the cores. The estimated relative error percent distributions for the apertures in fractured cores were 15.84%. The high relative errors were caused by the fractures being assumed to be smooth plates, ignoring the roughness and tortuosity visible during microscope views.

Keywords

Natural fracture • Artificial fracture • Equivalent fracture aperture • Polymer gel • Computer tomography • Microscope

1 Introduction

CT scanning images were used to determine matrix porosity (Canbolat & Parlaktuna, 2019a). A polymer gel treatment is used to reduce the fracture's impact and increase oil recovery. The matrix and fracture permeability were assessed before and after the polymer gel injection. Microscope measurements of fracture apertures were compared to cubic law-based analytical computations (Canbolat & Parlaktuna, 2019b). Furthermore, estimated CT porosity was used to evaluate each core's CT permeability.

2 Methodology

All cores' porosity and permeability values used in this work are shown in Table 1. The porosity of the cores was assessed by saturating the dry cores in de-ionized water and measuring the permeability with a helium permeameter. Core #2 has a higher permeability than the other cores as a result of a natural fracture observed in it (Fig. 1). Cores #3, #6, and #7 were artificially fractured (AF) during the study by cutting them in half longitudinally (Fig. 2). After the cutting procedure, the porosity and permeability of those cores were determined again. The findings are presented in Table 1.

S. Canbolat (✉)
Department of Petroleum and Natural Gas Engineering, Near East University, Nicosia, Mersin 10, Turkey
e-mail: serhat.canbolat@neu.edu.tr

A. Çiner et al. (eds.), *Recent Research on Sedimentology, Stratigraphy, Paleontology, Tectonics, Geochemistry, Volcanology and Petroleum Geology*, Advances in Science, Technology & Innovation,
https://doi.org/10.1007/978-3-031-43222-4_44

Table 1 Experimentally measured porosity and permeability of cores

Core	#2	#3	#5	#6	#7	#8	AF#3	AF#6	AF#7
Permeability (md)	207	81	41	87	116	74	285	301	293
Porosity (%)	34	34	31	32	31	32	34	34	34

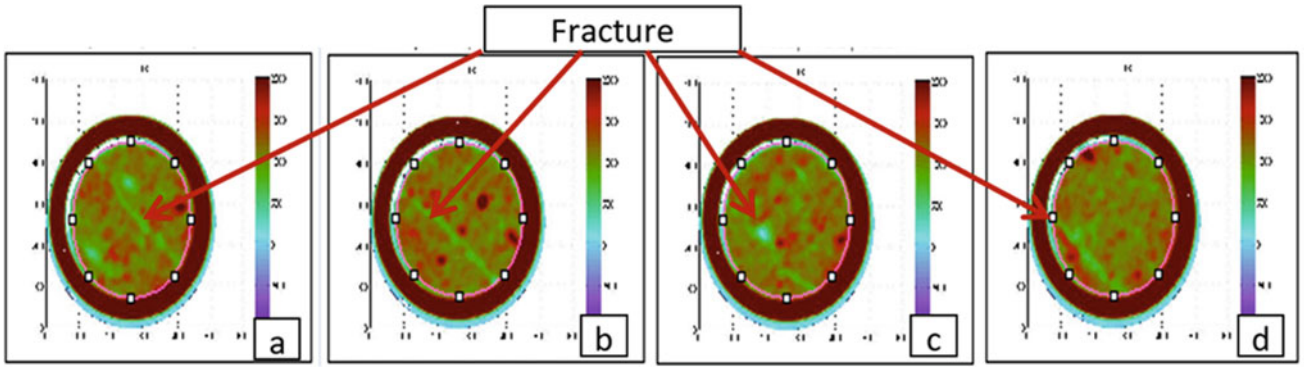

Fig. 1 CT thin section view of natural fracture in Core #2 **a** 19 mm, **b** 14 mm, **c** 9 mm, **d** mm from the outlet, respectively

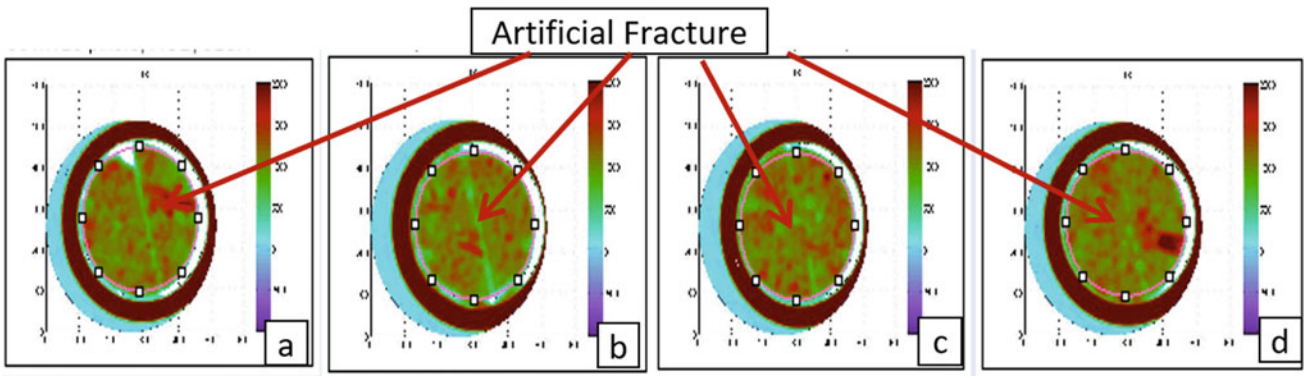

Fig. 2 CT thin section view of artificial fracture in Core#3 **a** 2 mm, **b** 5 mm from the inlet, **c** 5 mm, and **d** 2 mm from the outlet

3 Results and Discussion

3.1 CT Porosity of Cores

The porosity of each thin section was determined using CT numbers (Table 2). Next, the average porosity of all non-fractured, naturally fractured (NF), and artificially fractured cores was calculated using appropriate equations (Canbolat & Parlaktuna, 2019a).

3.2 Analysis of Polymer Gel Injection

Before the fracturing operation, the permeability of core #7 was measured as 115.86 md by de-ionized water injection. The permeability was eventually confirmed to be 292.63 md when an artificial fracture was created on core #7. Finally, the polymer gel-treated core permeability was determined to be 21.33 md. The injection of polymer gel for fracture plugging resulted in a considerable reduction in permeability (Table 3).

Table 2 CT porosity calculations

Core	#3	#5	#6	#7	#8	NF#2	AF#3	AF#6	AF#7
Φ_{CT} (%)	34	30.4	32	32	32.5	33.3	34.3	34	32

Table 3 Average permeability measurements of treated and untreated cores

Core	#5	AF#3	AF#7
k (md)	41.13	81.26	115.86
k_{AF} (md)	–	284.55	292.63
$k_{\text{Polymer Gel Treated}}$ (md)	7.79	15.32	21.33

3.3 CT Permeability of Cores

The Navier–Stokes equation solution, as reported by Narsilio et al. (2009), was used to calculate the system permeabilities and for CT permeability calculations and listed in Table 4. Equation 1 is as follows:

$$k_{(N-S)} = ((-\emptyset_{\text{CT}}/A) * L_z * \int_A v.\text{d}A)/(\Delta P/\eta) \quad (1)$$

where k_{N-S}, permeability (md); $\varnothing_{\text{CT}}$, sample's CT porosity; A, fluid flow area; η, fluid's dynamic viscosity; v, velocity, and ΔP, pressure difference through the inlet/outlet of the sample in the flow direction. L_z is the length of the core in the z direction (Narsilio et al., 2009). As reported in Table 4, the results were compatible with permeability measurements.

The absolute error was also evaluated. For error calculation, it was assumed that the experimentally measured permeability (Table 1) was the true value of the core permeability. The steady-state solution to the Navier–Stokes equations for laminar viscous flow between two smooth parallel plates is commonly used in fractured reservoirs to describe the effect of aperture on flow. This is known as the cubic law (CL). The authors mostly agree upon the estimations of the apertures with CL (Canbolat & Parlaktuna, 2019b; Narsilio et al., 2009). If the measured quantities (flow rate: Q, inlet and outlet pressures: ΔP, viscosity of flowing fluids: μ, the length of the fracture: L) are inserted in Eq. (2) and the EFA, b can be estimated (Canbolat & Parlaktuna, 2019a).

$$Q = b^3/12\mu\,(\Delta P/L) \quad (2)$$

Table 4 Error calculations of CT calculated and the experimentally measured average porosity and permeability of the cores

Core	#3	#5	#6	#7	#8	NF#2	AF#3	AF#6	AF#7
k_{CT} (md)	80.5	39.9	85	118	77	196	290	298	291
Φ_{CT} (%)	34	30.4	32	32	32.5	33.3	34.3	34	32
Δk (%)	0.62	2.68	2.30	1.72	4.05	5.31	1.75	1.00	0.68
$\Delta\Phi$ (%)	0.00	1.94	0.00	3.23	1.56	2.06	0.88	0.00	0.00

Table 5 Error calculations of numerical and visual EFA by CL and microscope

Core	#5	#8	NF#2	AF#3	AF#7
EFA numerical, (mm)	0.143	0.191	0.186	0.250	0.235
EFA visual, (mm)	0.103	0.130	0.161	0.202	0.200
ΔEFA error, (%)	27.97	31.93	13.44	19.20	14.89

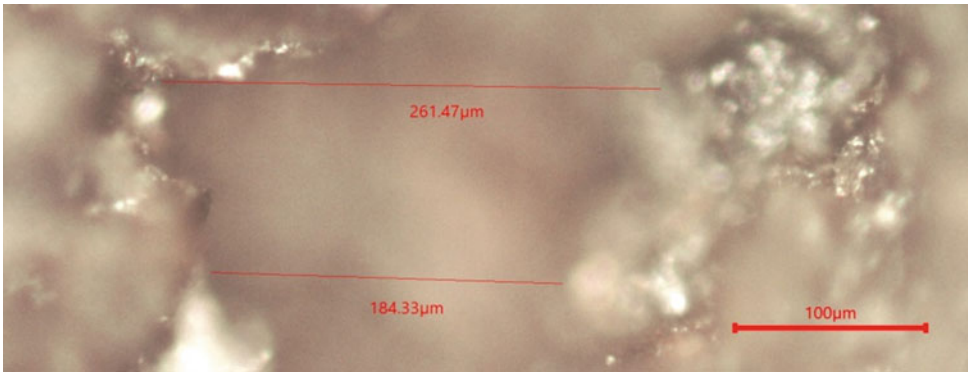

Fig. 3 Fracture aperture measurement of artificial fracture in Core#7 by microscope

Table 5 illustrates the differences between NF core #2, AF cores #3, and #7, based on calculated EFA using cubic law (CL) and observed apertures from different points across the fracture by microscope (Fig. 3). CL calculated the EFA and visual measurements and the relative errors ranged from 13.44 to 31.93%. The estimated relative error distributions for the apertures in fractured cores were 15.84%.

4 Conclusions

The permeability of the rock caused the high absolute error in the instance of NF in core #2. The homogeneous cores' EFA calculations showed higher relative errors, indicating no fracture in the cores. EFA calculations using CL showed high relative errors because the fractures were assumed to be a smooth plate, ignoring the roughness and tortuosity. Thus, the CL formula requires a correction factor (constant).

References

Canbolat, S., & Parlaktuna, M. (2019a). Analytical and visual assessment of fluid flow in fractured medium. *Journal of Petroleum Science and Engineering, 173*, 77–94.

Canbolat, S., & Parlaktuna, M. (2019b). Polymer gel conformance on oil recovery in fractured medium: Visualization and verification. *Journal of Petroleum Science and Engineering, 182*, 106289.

Narsilio, G., Buzzi, O., Fityus, S., Yun, T., & Smith, D. (2009). Upscaling of Navier-Stokes equations in porous media: Theoretical numerical and experimental approach. *Computers and Geotechnics, 36*(7), 1200–1206.

Optimization of Multi-stage Fracturing Cluster Space and Perforation Parameters of Deep Shale Horizontal Well

Jinbo Li, Suling Wang, and Kangxing Dong

Abstract

Deep shale needs multi-stage fracturing of horizontal wells to achieve efficient development, and cluster space is the core parameter of fracturing design. Currently, the optimization of cluster spacing is studied to fix the flow rate, and the pressure drop of the perforating hole is not considered. Therefore, there exists a difference between the results and the actual situation on interference between the fractures. Based on the fluid–solid coupling basic equations and damage mechanics principles, a three-dimensional model of multi-stage fracturing in horizontal wells was established using the finite element method to realize the dynamic distribution of the injection flow of each fracture through subroutine programming. The perforation friction force is calculated by embedding the perforation element, and the pressure flow friction force curve is used to verify its rationality. According to the shale geological conditions of the Lucaogou formation in Jimusaer, the local optimal cluster spacing design and the variation of different geological and construction parameters on the spacing optimization were studied. The results showed that the fracture morphology significantly differs due to flow distribution and friction effects. Large drainage volume is beneficial to open natural fractures and increase crack volume. But large inject volume and high brittle geology need to increase the spacing to avoid sand plugging. Deep shale reservoirs generally have large in situ stress differences. Small spacing should utilize beneficial inter-fracture interference to activate natural fractures. At the same time, adjusting the perforation parameters based on the flow-limiting method of fracturing can effectively control the uniform propagation of multiple clusters of fractures and make full use of the reservoir to achieve safe and efficient development.

Keywords

Deep shale • Multi-stage fracturing of horizontal wells • Dynamic flow distribution • Cluster spacing optimization • Flow limiting fracturing • Perforation parameters

1 Introduction

As the development of oil and gas resources fully advances to deep oil and gas reservoirs, it has become essential for realizing production succession. The Ministry of Natural Resources defines shale oil and gas reservoirs with a buried depth of more than 3500 m as deep shale oil and gas resources. 39% of the remaining oil and 57% of my country's remaining natural gas resources are buried deep, and the development prospects are broad. The deep shale storage environment has the "three highs" geological characteristics of high temperature, high confining pressure, and high pore pressure; horizontal wells and hydraulic fracturing technology are the key technologies for development. In order to achieve efficient reservoir development, it is necessary to use horizontal well-staged fracturing to generate multiple cross-cut fractures to expand the discharge area. Still, production logging data shows that 30% or more perforation clusters do not contribute to production. Therefore, it is necessary to strengthen the understanding of the influence of cluster spacing on the crack propagation law.

2 Numerical Calculation Model of Staged Fracturing for Deep Shale Horizontal Wells

The shale oil of the Lucaogou Formation in the Jimsar Sag has become a large-scale developed terrigenous clastic sedimentary shale oil reservoir. Based on the above theory and modeling technology, this paper uses the cohesive element to establish a multi-cluster synchronous fracturing

J. Li (✉) · S. Wang · K. Dong
Northeast Petroleum University, Daqing, 163318, China
e-mail: 459182649@qq.com

A. Çiner et al. (eds.), *Recent Research on Sedimentology, Stratigraphy, Paleontology, Tectonics, Geochemistry, Volcanology and Petroleum Geology*, Advances in Science, Technology & Innovation,
https://doi.org/10.1007/978-3-031-43222-4_45

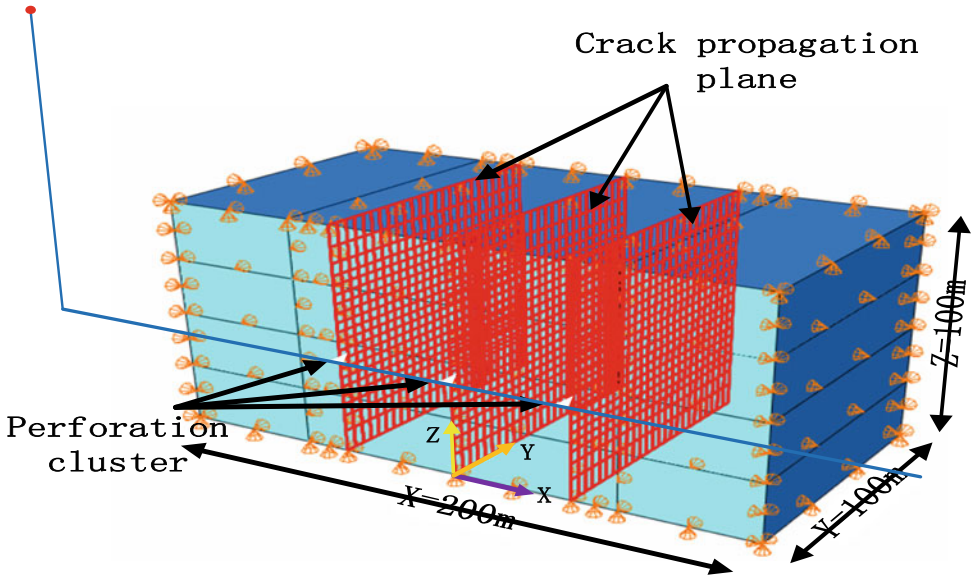

Fig. 1 Finite element model of multi-stage fracturing in horizontal wells

three-dimensional numerical model, such as Fig. 1. The model's material parameters are based on data from the burial depth of 3500–3800 m from the Lucaogou Formation in Jimsar. The elastic modulus and Poisson's ratio are about 15 GPa and 0.26, and the permeability and porosity are 0.1md and 6.1%, respectively. The tensile strength is about 6 MPa. The filter loss coefficient is $1e^{-14}$ m/Pas, the fracture energy is 4000 m•Pa, and the horizontal maximum, minimum ground, and vertical stress are 85 MPa, 70 MPa, and 78 MPa. Moreover, the reservoir pore pressure is 40 MPa, based on hydrostatic pressure. The system calculates that the three-dimensional stress of the reservoir is applied as the effective stress, the displacement boundary around the model is fixed, the ground stress is balanced before fracturing to simulate the initial occurrence state, and then the fracturing fluid whose dynamic viscosity of 1.01 mpa.S is injected at a displacement of $9m^3$/min (Fig. 2).

3 Results

3.1 Optimal Cluster Spacing Selection

Based on the selected well section formation parameters, the optimal cluster spacing design is comprehensively selected through multi-fracture shape and fracture volume. As a

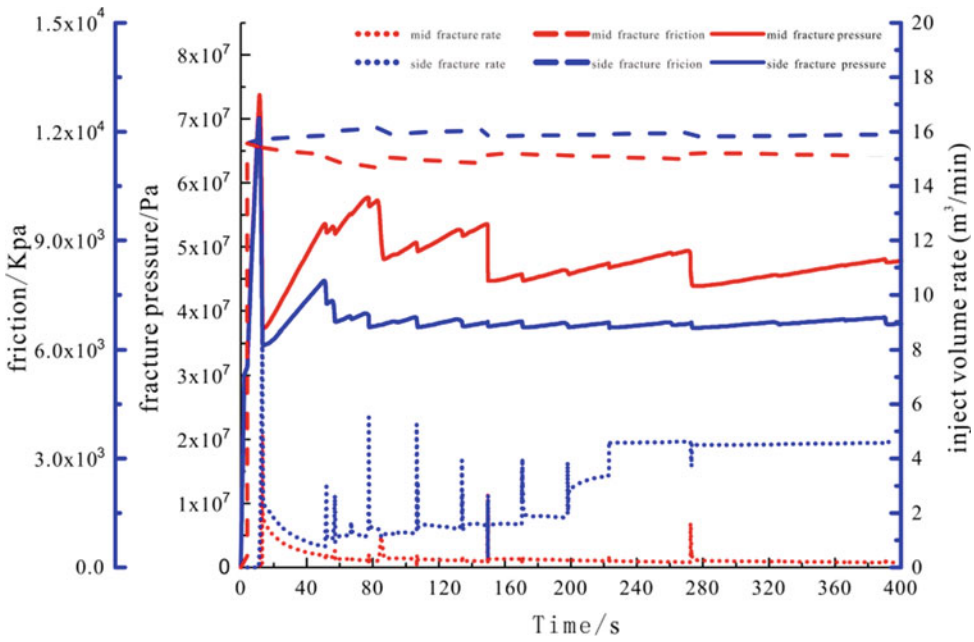

Fig. 2 Pressure flow friction curve

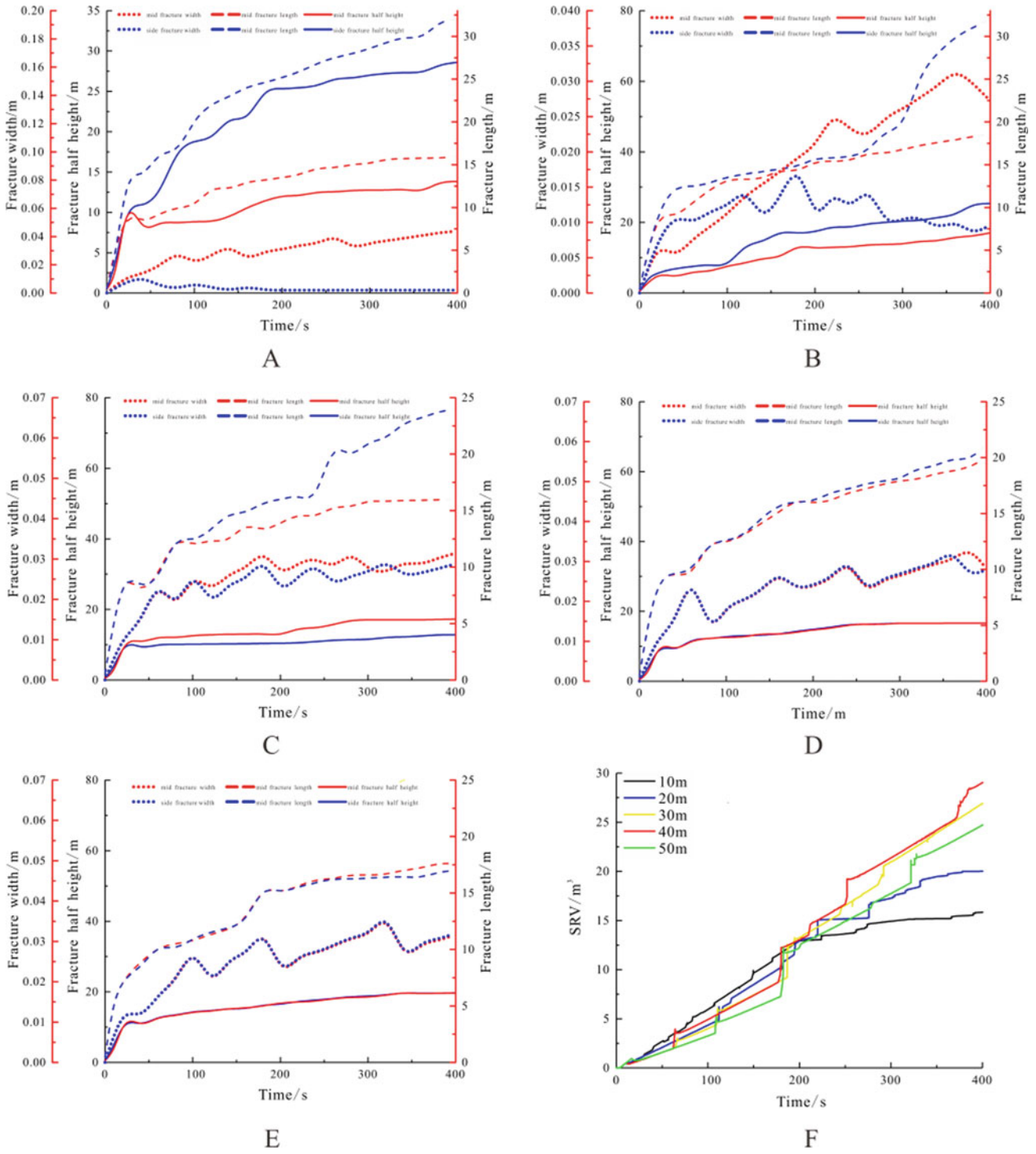

Fig. 3 Comparison of fracturing effect in different cluster spacing

result, the cluster spacing is 10 m (A), 20 m (B), 30 m (C), 40 m (D), and 50 m (E).

When multiple cracks are spread in close spacing due to the inter-fracture interference stress, the middle crack is restrained in the length and height direction under the influence of the cracks on both sides. As the cluster spacing increases, the interference between fractures weakens, the high-pressure stress area at the front end of the middle fracture and the extrusion stress area on the outer side gradually disappears, and multiple fractures show a uniform

expansion pattern. As a result, the fracture shape of 40 and 50 m is the same. At the same time, based on the principle of reservoir utilization, the fracturing effect of 50 m cluster spacing is not ideal. In summary, 40 m should be selected as the optimal cluster spacing under this well section's formation conditions and construction parameters.

3.2 Analysis of Influencing Factors

Based on the benchmark example, the controlled variable method was used to study the influence of the horizontal stress difference coefficient, elastic modulus, and displacement on the optimal cluster spacing and the fracture height difference, fracture width difference, and fracture length of the inner and outer cracks were extracted. The difference can visually compare the cracks' uniform expansion degree and shape difference (Fig. 3).

4 Conclusions

During the staged fracturing of deep shale horizontal wells, the outer cracks expand rapidly in the length and height directions. The combined effect leads to differences in the crack propagation morphology.

Aiming at the geological conditions of a well section within the buried depth of 3600–3800 m in the Lucaogou Formation in Jimsar, the optimal cluster spacing is selected as 40 m.

Large spacing needs to be designed. In formations with high-stress differences, the cluster spacing can be appropriately reduced, and the beneficial inter-fracture interference can be fully utilized to open natural fractures. By increasing the number of perforations in the middle cluster, the flow distribution can be balanced to achieve uniform liquid inflow and increase the crack volume.

Fracture Initiation Mechanism Study of Circulating Pump Injection Hydraulic Fracturing

Kangxing Dong, Annan Zhao, Suling Wang, Jinbo Li, and Wei Liu

Abstract

To explore the fracture initiation mechanism of pulse hydraulic fracturing in a tight reservoir, based on the theory of rock mechanics and fluid–solid coupling, a fracture initiation calculation model of pulse hydraulic fracturing in a tight reservoir is established, and the fracture initiation is simulated by the plastic damage finite element method. The results show that as the number of pulses increases, the perforation surface's damage value increases gradually. The larger the pulse amplitude, the fewer the number of pulse cycles needed to reach the condition of fracture initiation. At the same injection pressure, the sine pulse needs the least number of cycles, followed by a triangle and rectangle pulse. Compared with hydrostatic fracturing, the maximum fracture initiation pressure of pulse fracturing can be reduced by 27%. Therefore, compared with conventional fracturing, pulse hydraulic fracturing can effectively reduce the fracturing pressure and the cost of fracturing.

Keywords

Tight reservoir • Pulse fracturing • Damage accumulation • Numerical simulation • Initiation pressure

1 Introduction

Due to the low porosity, low permeability, and burial depth of tight reservoirs, hydraulic fracturing is required for commercial development. At present, the fracturing of tight reservoirs mainly draws on the volumetric fracturing technology of shale reservoirs. Still, compared with shale reservoirs, the natural fractures in tight reservoirs are underdeveloped, and the volumetric fracturing effect is not good (Wu et al., 2011, 2012; Yonggang & Jianqiu, 2010; Yunsheng et al., 2017). Pulsating hydraulic fracturing is to pump the fracturing fluid into the reservoir with a particular frequency of dynamic load so that the rock mass can undergo multiple dynamic load damage effects, such as impact failure, fatigue failure, and so on, to continuously produce micro-fractures, which gradually penetrate through to form macro fractures and eventually form an extensive range of volume fracture network. Pulsating hydraulic fracturing has been applied in coalbed methane mining. Field practice shows that pulsating hydraulic fracturing can effectively reduce fracture initiation pressure and produce a wide range of volumetric fracture networks near the wellbore more easily than static fracturing (Jiang-zhan et al., 2017; Pingya, 2013).

When Li Xianzhong studied the anti-reflection mechanism of high-pressure pulsating hydraulic fracturing, he concluded that there might be reflection, superposition, and reciprocation of pulsating pressure waves in the propagation process pulsating pressure, and the pulsating pressure causes pressure fluctuation in the gap. Applying sinusoidal pulsating wave fracturing in coal seam gas drainage has achieved good results (Xianzhuong, 2013). Youping et al. (2011), Quangui et al. (2013), and other scholars studied the anti-reflection mechanism of coal seam pulsation hydraulic fracturing and the action characteristics of briquette pulsation parameters and clarified the advantages of pulsation hydraulic fracturing in industrial applications compared with static fracturing. Pulsation hydraulic fracturing can destroy coal rock under small water injection pressure, and the lower the frequency, the smaller the peak pressure. Xie (2014); (Wenqing & Haitao, 2014); Wenchao et al. (2015) proved in field tests that the post-pressure flow of pulsating hydraulic fracturing significantly increased compared with conventional hydraulic fracturing. Frash et al. (n.d.) conducted a

K. Dong (✉) · A. Zhao · S. Wang · J. Li · W. Liu
Noreast Petroleum University School of Mechanical Science and Engineering, Daqing, 163318, Heilongjiang, People's Republic of China
e-mail: dongkangxing@163.com

A. Çiner et al. (eds.), *Recent Research on Sedimentology, Stratigraphy, Paleontology, Tectonics, Geochemistry, Volcanology and Petroleum Geology*, Advances in Science, Technology & Innovation,
https://doi.org/10.1007/978-3-031-43222-4_46

feasibility study on implementing secondary pulsating hydraulic fracturing after conventional fracturing with granite as the laboratory object. They found that: After the second pulsating hydraulic fracturing, the permeability of granite is significantly improved, the secondary fractures develop, and the main fractures further extend and intersect and form through fractures. The anti-reflection effect is better than that of conventional repeated fracturing.

This paper discusses the effects of pulse fracturing parameters on fracture initiation and propagation of tight reservoirs through laboratory experiments and numerical simulation.

2 Experiment

2.1 Experimental Method

The experiment uses a 300 × 300 × 300 mm cubic cement block as the hydraulic fracturing specimen. The cement specimen is made by mixing 50 mesh quartz sand and 425 cement at a weight ratio of 1:1 and pouring them into a 300 × 300 × 300 mm mold. After curing for 15 days, the casted specimens are formed, and the resulting specimens are shown in Fig. 1.

In this test, true triaxial hydraulic fracturing equipment was used to simulate the influence of cyclic load on the initiation pressure, and acoustic emission technology was used to monitor the crack propagation law. The test equipment is shown in Fig. 2, and the specific structure of the fracturing test machine system is shown in Fig. 3.

Fig. 1 Test specimens

Fig. 2 Triaxial hydraulic fracturing equipment

2.2 Experimental Results

The specimen after fracturing is shown in Fig. 4. The pressure curves of conventional fracturing and circulating pump injection are shown in Fig. 5.

Comparing the pressure curves of conventional hydraulic fracturing and circulating pump hydraulic fracturing, it can be seen that the maximum initiation pressure of circulating pump hydraulic fracturing is 20 Mpa. In contrast, the initiation pressure of conventional hydraulic fracturing is close to 28 Mpa. Therefore, it is possible to use a circulating pump injection for hydraulic fracturing to reduce the initiation pressure of the specimen by about 28%.

3 Mathematical Model of Pulse Hydraulic Fracturing

3.1 Constitutive Model with Damage

This paper uses the strain equivalence hypothesis to calculate the elastic model with damage (Xinpu & Shengji, 2014). If E is the elastic model of the material in the initial no-damage state, Hooke's law can be expressed in the unidirectional tension and compression state.

$$\sigma_t = (1 - d_t)E\left(\varepsilon_t - \overline{\varepsilon}_t^{pl}\right) \quad (1)$$

$$\sigma_c = (1 - d_c)E\left(\varepsilon_c - \overline{\varepsilon}_c^{pl}\right) \quad (2)$$

where σ_t is stress; As the strain; $\overline{\varepsilon}$ Is equivalent strain; d Is the damage value; Subscript t represents the mechanical quantity related to tensile; Subscripts c represent mechanical

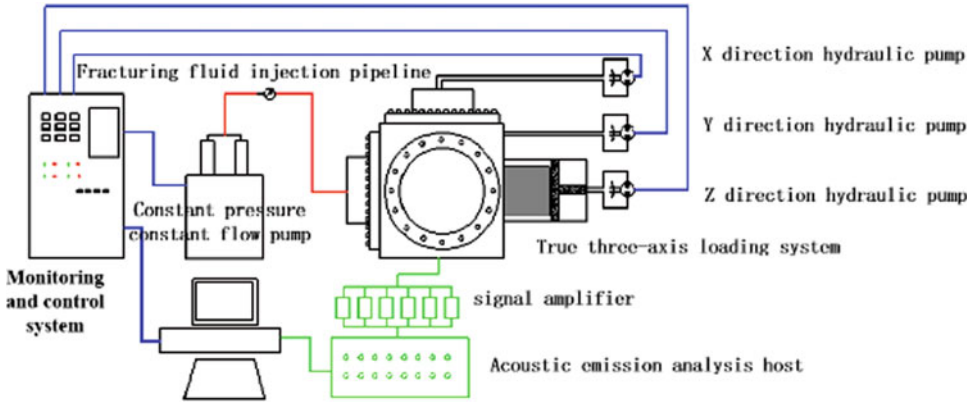

Fig. 3 Schematic diagram of the test device composition system

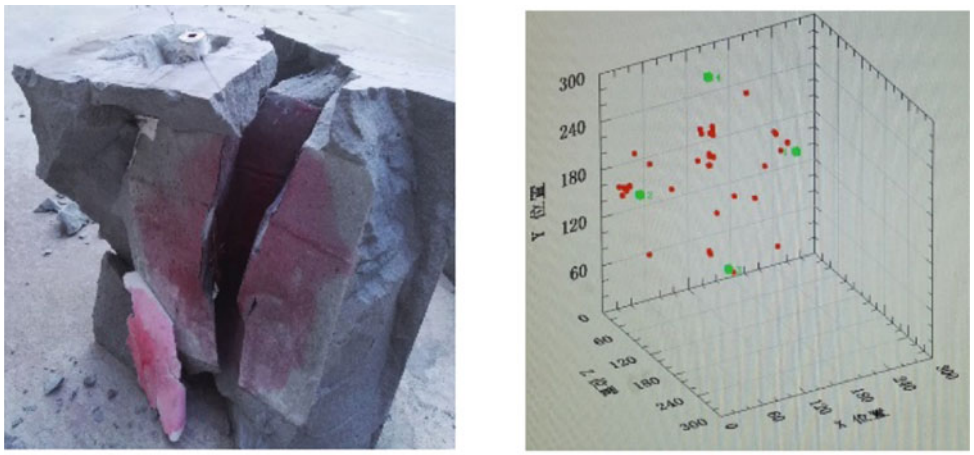

(a) (b)

Fig. 4 **a** Specimen after compression **b** acoustic emission event

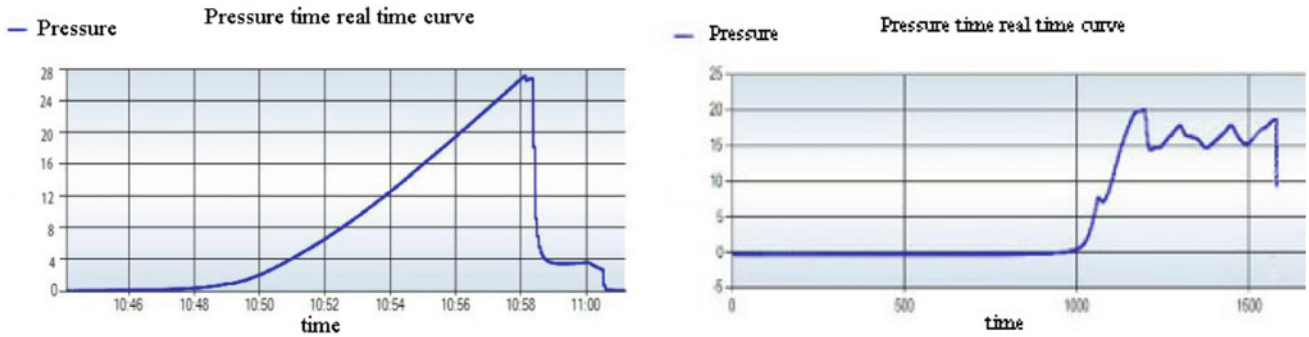

(a) Conventional hydraulic fracturing (b) Circulating pump injection hydraulic fracturing

Fig. 5 Injection pressure curve

quantities related to compression; The superscript *pl* indicates shaping.

The elastic modulus after material damage is expressed as

$$E' = (1 - d)E \tag{3}$$

3.2 Seepage Model

According to previous studies (Frash et al., n.d.), the seepage equation of fracturing fluid in tight rock can be expressed as

$$\alpha \frac{\partial \varepsilon_v}{\partial t} + \left(\frac{\phi}{\beta_1} + \frac{1-\phi}{K_s}\right)\frac{\partial p}{\partial t} = \nabla\left(\frac{k}{\mu}\nabla p\right) \tag{4}$$

where ε_v is the volumetric strain; ϕ Is porosity; β_1 Is the volume modulus of fluid, Pa; K_s Is the effective volume modulus of solid particles, Pa; k Is permeability; μ Is the hydrodynamic viscosity coefficient, N s m^{-2}.

3.3 Rock Damage Accumulation Model

Tight rock has a damage accumulation effect under cyclic impact. Based on the cyclic impact test of rock (Jin et al., 2014), the rock damage accumulation evolution model is

$$d = \alpha - \beta \ln\left(\frac{\kappa}{n} - \eta\right) \tag{5}$$

where α, β, and η are the cumulative rate factor at different loading stages, which is measured experimentally; κ Is the axial load, N; n Is the number of cyclic impacts.

4 Numerical Calculation Model

To simplify the model, the stress state at the perforation can be simplified for complex formations as a two-dimensional plane strain problem. Take the cross section of the perforation as a model to analyze the rock damage. According to the assumptions and working conditions used in the damage plastic model, a two-dimensional shell element simulation is adopted to establish the model, as shown in Fig. 6.

Displacement constraints in the X and Y directions are, respectively, applied around the model. The initial porosity is 0.2, and the pore pressure is 0 MPa; the principal stress in the Y direction is the largest.

After repeated trial calculation, when the injection pressure is greater than 64.5 MPa, the perforating surface appears damaged, and the greater the pressure, the greater the damage. To analyze the influence of different frequencies on damage, the influence rule of pulse number on damage value is calculated when the pressure is 65 MPa, 70 MPa, 75 MPa, 80 MPa, and 85mpa, respectively.

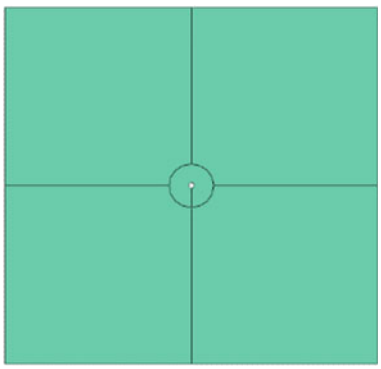

Fig. 6 Finite element model

4.1 Triangle Pulse Pressure Influence Law

Figure 7 shows the triangular pulse pressure loading curve, and Fig. 8 shows the variation rule of damage value in the loading process.

As can be seen from Figs. 7 and 8, when the pulse pressure changes in a triangular form, the damage value of the perforating surface gradually accumulates and increases

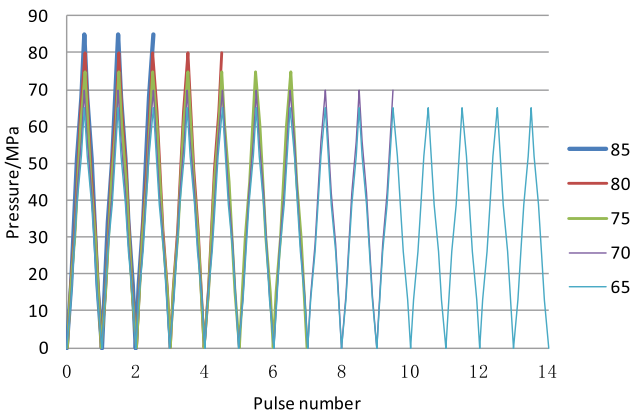

Fig. 7 Triangle pulse pressure loading curve

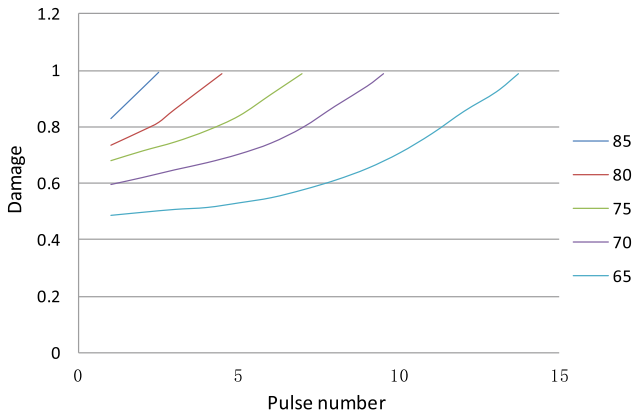

Fig. 8 Damage change value during loading

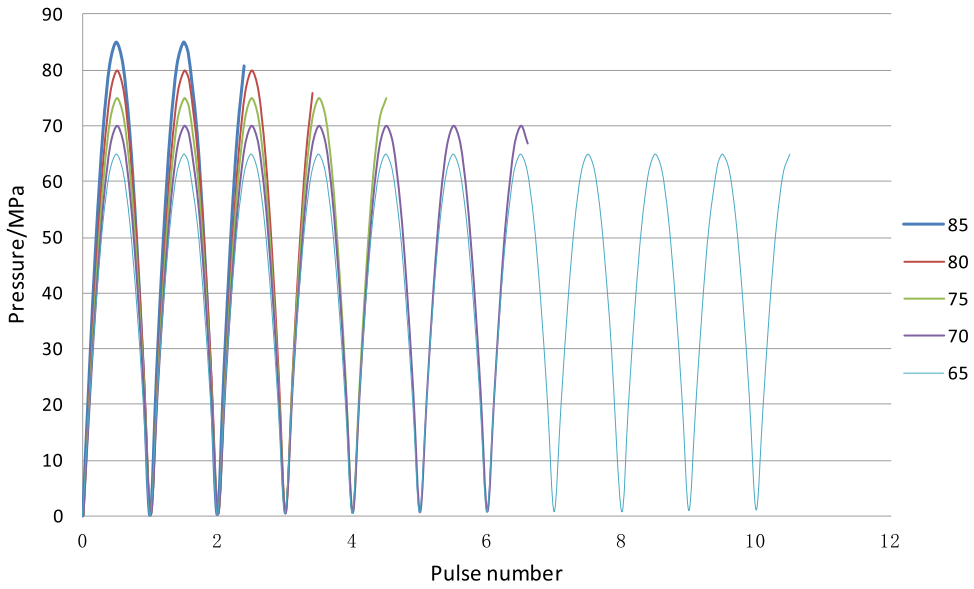

Fig. 9 Sine pulse pressure loading curve

with the application of the pulse pressure until the damage value reaches 1. When the pulse pressure varies from 0 to 85 MPa, and the pulse cycle number is 2.62 times, the maximum damage value of perforating surface reaches 1. This leads to the fact that rock fracture produces macroscopic fractures. When the pulse pressure varies from 0 to 65 MPa, and the pulse frequency is 13.7 times, the maximum damage value of perforating surface reaches 1. The larger the pulse pressure amplitude, the fewer pulse times are needed for fracture initiation.

4.2 Influence Law of Sinusoidal Pulse Pressure

Figure 9 shows the sinusoidal pulse pressure loading curve, and Fig. 10 shows the variation rule of damage value in the loading process.

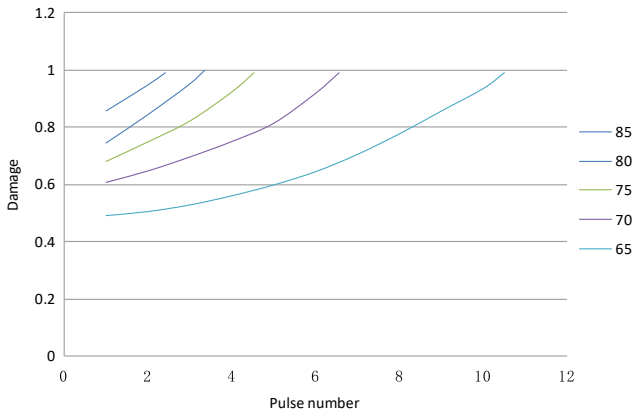

Fig. 10 Damage change value during loading

As can be seen from Figs. 9 and 10, when the pulse pressure changes in a sinusoidal form, the damage value of the perforating surface gradually accumulates and increases with the application of the pulse pressure until the damage value reaches 1. When the pulse pressure varies from 0 to 85 MPa, and the pulse cycle number is 2.22 times, the maximum damage value of perforating surface reaches 1; rock fracture produces macroscopic fractures. When the pulse pressure varies from 0 to 65 MPa, and the pulse number is 13.13 times, the maximum damage value of perforating surface reaches 1. The larger the pulse pressure amplitude, the fewer pulse times are needed for fracture initiation.

4.3 Rectangular Pulse Pressure Affects the Law

Figure 11 shows the rectangular pulse pressure loading curve, and Fig. 12 shows the variation rule of damage value in the loading process.

As can be seen from Figs. 11 and 12, when the pulse pressure changes in a sinusoidal form, the damage value of the perforating surface gradually accumulates and increases with the application of the pulse pressure until the damage value reaches 1. When the pulse pressure varies from 0 to 85 MPa, and the pulse cycle number is 2.99, the maximum damage value of perforating surface reaches 1; rock fracture produces macroscopic fractures. When the pulse pressure varies from 0 to 65 MPa, and the pulse number is 15.51, the maximum damage value of perforating surface reaches 1. The larger the pulse pressure amplitude, the fewer pulse times are needed for fracture initiation.

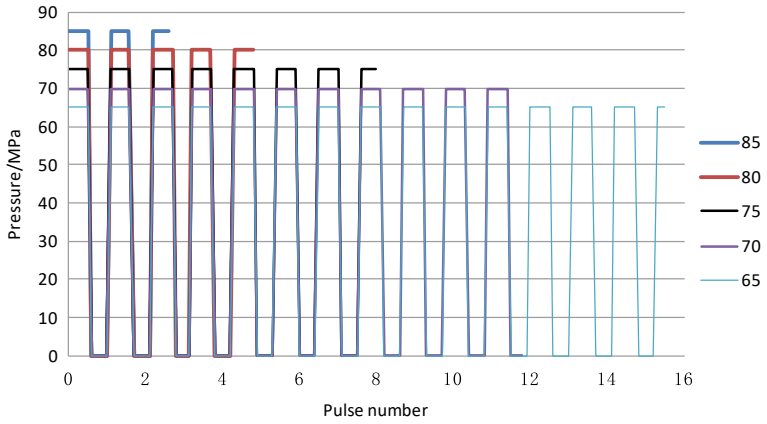

Fig. 11 Rectangular pulse pressure loading curve

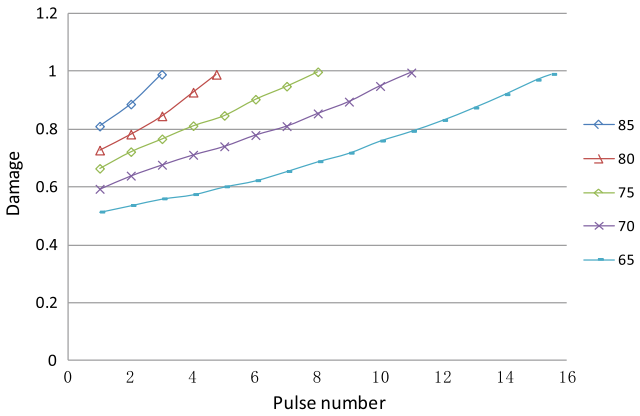

Fig. 12 Damage change value during loading

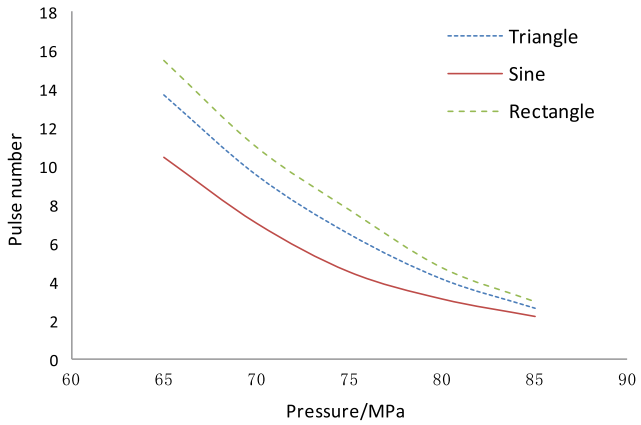

Fig. 13 Comparison of loading times for crack initiation in different pulse forms

4.4 Different Pulse Forms Affect the Law

Figure 13 shows the comparison curves of pulse times under different injection pressures under triangular, sinusoidal, and rectangular pulse forms.

As seen from Fig. 13, with the increase of injection pressure on the perforating surface, the number of pulses required when the damage value reaches one gradually decreases. As a result, the sinusoidal pulse needs the least number of cycles at the same injection pressure for the three different pulse forms, followed by a triangular pulse and a rectangular pulse.

For the three pulse forms, when the number of pulse cycles is increased and the maximum injection pressure is 68.25mpa, the damage value of perforating surface can reach 1; that is, the condition of crack initiation is reached. Therefore, the fracture initiation pressure of the tight reservoir decreases from 93.5 Mpa during injection fracturing to 68.25 Mpa, a decrease of 30.48%.

5 Conclusions

(1) As the number of pulses increases, the damage value of the perforation surface gradually increases. The larger the pulse amplitude, the fewer pulse cycles are required to reach the crack initiation condition. At the same injection pressure, the sinusoidal pulse requires the least number of cycles, followed by triangular and rectangular pulses.

(2) With the pulse number increase, the damage value of perforating surface increases gradually. The larger the pulse amplitude is, the less cycle number is needed to reach the initiation condition. When the injection pressure is the same, the cycle number of sinusoidal pulses is the least, followed by triangular and rectangular pulses.

(3) Compared to conventional hydraulic fracturing, pulse hydraulic fracturing reduced initiation by 30.48% under the same conditions.

Acknowledgements The project is supported Petro China Innovation Foundation (Number: 2020D-5007-0206).

References

Frash, L. P., Gutierrez, M., Hampton, J. (n.d.). Laboratory-scale-model testing of well stimulation by use of mechanical-impulse hydraulic fracturing. *SPE Journal*, 173186.

Jiang-zhan, C., Han, C., & Ping-he, S., et al. (2017). Mechanisms of fracture extending in coal rock by pulse hydralic fracturing under triaxial loading. *Rock an Soil Mechanics*, *38*(04), 1023–1031.

Jin J. F., Li, X., Qiu, C. (2014). Evolution model for damage accumulation of rock under cyclic impact loadings and effect of static loads on damage evolution. *Chinese Journal of Rock Mechanics and Engineering*, *33*(8), 1662–1671.

Pingya, L. (2013). A discussion on how to significantly improve the single-well productivity of CBM gas wells in China. *Natural Gas Industry, 33*(6), 1–6.

Quan-gui, L. I., Bai-quan, L. I. N., Cheng, Z. H. A. I., et al. (2013). Experimental study on action characteristic of pulsating parameters incoal seam pulse hydraulic fracturing. *Journal of China Coal Society, 38*(7), 1185–1190.

Wang, W., Li, X., & Lin, B., et al. (2015). Pulsating hydraulic fracturing technology in low permeability coal seams. *International Journal of Mining Science and Technology*, *25*, 681–685.

Wen-qing, Z., & Haitao, L. (2014). Study and application of high voltage pulse hydraulic fracturing technology to increase permeability in Changping Company. *Coal Mine Modernization*, *5*, 4–6.

Wu, Q., Xu, Y., & Wang, T., et al. (2011). The revolution of reservoir stimulation: An introduction of volume fracturing. *Natural Gas Industry*, *31*(4), 7–12.

Wu, Q., Xu, Y., & Wang, X., et al. (2012). Volume fracturing technology of unconventional reservoirs: Connotation, optimization design and implementation. *Petroleum Exploration and Development*, *39*(3), 352–358.

Xianzhuong, L. (2013). The mechanism and technology of permeability enhancements in coal seam based on high pressure pulsating hydraulic fracturing. China University of Mining and Technology

Xie Z. (2014). High-pressure pulsating hydraulic fracturing and permeability enhancement technology and its application. *Coal Safety, 9*, 97–101.

Xinpu, S., & Shengji, J. (2014). Numerical method and application example of stimulation damage mechanics for fracture of reservoir formation. *Journal of Shenyang University of Technology, 036* (003), 341–346.

Yonggang, D., & Jianqiu, L., et al. (2010). Transient pressure analysis of infinite conductivity fractured wells for shale gas. *Natural Gas Industry*, *30*(10), 30–32.

You-ping, X., Bai-quan, L., & Cheng, Z., et al. (2011). Analysis on dynamic characteristics of cracks extension in directional hydraulic fracturing and its application. *China Safety Science Journal*, *21*(07), 104–110.

Yunsheng, W. E. I., Ailin, J., & Dongbo, H. E., et al. (2017). Comparative analysis of development characteristics and technologies between shale gas and tight gas in China. *Natural Gas Industry*, *37*(11), 43–52.

Pseudopotential Method of Hydrocarbon Contacts Resolution in Reservoirs with Poor and Insufficient Pressure Data. Case Study of Feji Offshore Field, Eastern Niger Delta Basin (Nigeria)

Godwin Oboh, Eliseus Akpunonu, Solomon Okeke, Onochie Okafor, and Daniel Okolo

Abstract

Hydrocarbon contact resolution in reservoirs with poor and insufficient pressure data was determined with a pseudopotential method using the Feji offshore field, Eastern Niger Delta, as a case test. The work aims to solve the difficulty encountered while determining fluid contacts in reservoirs that have fluid phase mix and are characterized by dearth of good and adequate (pressure) data, especially in old fields. The study was designed to bridge the gap associated with other methods of hydrocarbon contact determination. The study area is located offshore Eastern Niger Delta Basin and lies within one of Nigeria's offshore Oil Mining Lease (OML). The Feji field comprises six isolated compartments (A-F) and thirteen isolated levels with several separate fluid contacts. With a manometer, the notion is that wells in the same compartment have the same head/ height or the same magnitude of pressure at the same stratigraphic level and are thus located in a shared pressure compartment. However, direct pressure measurements are scanty, poorly available in the wells, and grossly inadequate in some instances (wells 1/ − 2/ − 3). The pseudopotential plots were used to define fluid gradients, fluid contacts, pressure communications, possible large-scale pressure differences, and reservoir compartmentalization. Twenty-one (21) hydrocarbon contacts (GOC, OWC and ODT) were established. Eleven (11) were pseudopotential derived for OWC, and ten (10) were derived from PVT studies for GOCs. All the contacts (GOC, OWC, ODT, and FWL) were defined and determined using the pseudopotential method and authenticated/ corroborated by the PVT studies' results. From the study, the formation pressure is no longer hydrostatic below 2315 mSL, implying an overpressure condition. This method will help in the subsequent well-planned field management and production life for geological and economic gains because hydrocarbon contacts and volumes will be accurately determined.

Keywords

Pseudopotential • Hydrocarbon contacts • Compartmentalization • Fluid gradients • Pressure communication

1 Introduction

Feji field is located offshore Eastern Niger Delta Basin and lies within one of Nigeria's offshore Oil Mining Lease (OML). It comprises six isolated compartments (A-F) and thirteen isolated levels with several separate fluid contacts. Niger Delta Basin situates in the Gulf of Guinea and extends through the Niger Delta Province (Klett et al., 1997). The Niger Delta Province contains one major petroleum system (Kulke, 1995; Ekweozor and Daukoru, 1994). This system is called the Tertiary Niger Delta (Akata–Agbada Petroleum System). The total extent of the petroleum system is defined by the areal extent of fields and contains known resources of 34.5 billion barrels of oil (BBO) and 93.8 trillion cubic feet of gas (TCFG) (Petroconsultants, 1996).

The evolution of the Niger Delta Basin has been controlled by pre- and syn-sedimentary tectonics Ejedawe, (1981), Evamy et al., (1978), Knox and Omatsola (1989). As a result, the stratigraphy of the Niger Delta is made up of three lithostratigraphic units, namely: Akata Formation (Paleocene), Agbada Formation (Eocene), and Benin Formation (Post-Miocene to recent) (Short and Stauble (1967).

Defining the depths of the fluid contacts, gas/water contact (GWC), oil/water contact (OWC), and gas/oil contact (GOC), or defining both of the latter in some reservoir situations is essential for volumetric calculations and important

G. Oboh · E. Akpunonu (✉) · S. Okeke · O. Okafor · D. Okolo
Department of Geological Sciences, Faculty of Physical Sciences, Nnamdi Azikiwe University, Awka, Nigeria
e-mail: akpunonu@unizik.edu.ng

A. Çiner et al. (eds.), *Recent Research on Sedimentology, Stratigraphy, Paleontology, Tectonics, Geochemistry, Volcanology and Petroleum Geology*, Advances in Science, Technology & Innovation,
https://doi.org/10.1007/978-3-031-43222-4_47

for detailed petrophysical calculations. This is achievable with enough pressure data and no fluid-phase mix. Pressure versus depth plots and dated pressure plots demonstrate clear vertical pressure barriers (Reynolds, 2005). "Traditionally," the pressure versus depth plot is used to determine fluid contacts and fluid formation gradients, which is further translated and interpreted based on the range either in specific gravity (sg) or in pounds per square inch (psi/ft):

This work attempts to define a "new and more robust method" in using formation pressures to determine fluid formation contacts in the well bore. This research aims to use the pseudopotential method to resolve hydrocarbon contacts in reservoirs with poor and insufficient pressure data using Feji field as a case study. Using the pseudopotential method, difficult and closed fluids can be separated and determined.

2 Materials and Methods

2.1 Materials

The data for the study comprised RFT data from the wells, logs, master-logs, PVT samples, fluid modeling data, and reports. In addition, validated and quality-checked (QC) data obtained from main results and report(s), geological reports, and final composite logs of the wells were also used (Table 1).

2.2 Methods

2.2.1 Derivation of Pseudopotential Equation

The method of study involves deriving the pseudopotential formulas from Eq. 1 of Feynman (2011) and modified from Hubbert, Willis (1982).

$$\mathrm{PE}(\Phi) = mgh \tag{1}$$

where PE = Potential energy (Φ), m = mass of the object/substance in kilograms, g = Acceleration due to gravity (9.8 m/s^2 at the surface of the earth), and h = height of the object/substance in meters.

$$\begin{aligned} &\text{Since} \qquad \mathrm{PE}(\Phi) = mgh \\ &P_{\mathrm{bar}} = \varrho_w \times g \times h \end{aligned} \tag{2}$$

where P_{bar} = Pressure measured in bars, ϱ_w = Density of water in g/cc, g = Acceleration due to gravity (0.09806 bar/m), z = Vertical height of the fluid (TVDss), H = Water head (Pseudopotential above or below mean sea level-mSL), $h = (z + H)$ is the fluid height above mean sea level (z) (see Fig. 1).

$$P_{\mathrm{bar}} = \varrho_w \times g \times (z+H) \tag{3}$$

Equation 3 is expressed as same below:

$$\begin{aligned} \varrho_w \times g \times (z+H)\mathrm{P}_{\mathrm{bar}} \\ (z+H) = P_{\mathrm{bar}}/(\varrho_w \times g) \\ H = (P_{\mathrm{bar}}/(\varrho_w \times g) - z \\ H = [P_{\mathrm{bar}}/(\varrho_w \times g)] - z \end{aligned} \tag{4}$$

Since g = 0.09806; therefore,

$= [P_{\mathrm{bar}}/(\varrho_w \times 0.09806)] - Z$

$= [10.197162 \times \mathrm{P}_{\mathrm{bar}}/(\varrho_w)] - Z$

Hence,

$$\mathrm{Pseudo-Pot}(H) = \left[P_{a(\mathrm{Bar})} - 1\right]/0.0981] - \mathrm{TVDss}(m) \tag{5}$$

Or

$$\mathrm{Pseudo-Pot}(H) = 0.197162\left[P_{a(\mathrm{Bar})} - 1\right] - \mathrm{TVDss}(m) \tag{6}$$

Following the above explanations and the various unit conversions and expressions, and introducing Eq. 6, which is the original equations of and Willis (1982), we thus re-expressed the equation for use in this project as:

Table 1 Number of pressure data acquired per well

RFT / MDT Data Acquired								
Well	Nº of attempts	Excellent to VG	Good	Low Perm	Tight	Seal Failure	Total acceptable	Sampling
		(> 300mD/cp*)	(10-300mD/cp)	(0.1-10mD/cp)	<0.1 mD/cp			
FEJI-1	1		1				1	1 sample
FEJI-2	2		2				2	2 samples R7
FEJI-3	3		3				3	3 samples
FEJI-4	57	14	32	2	4	5	46	7samples/2 PVT R6 to R14
FEJI-5	41	20	10	1	5	5	30	3 samples : R5/R8
FEJI-6	55	12	18	8	11	6	30	6 samples / 2PVT
FEJI-7	NIL	-	-	-	-	-	-	-

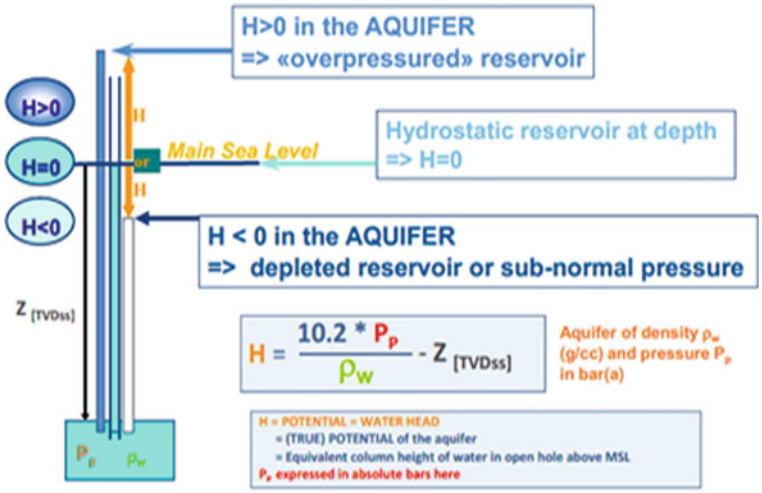

Fig. 1 Relationship between water head and pressure to demonstrate the potential considering the height at which water will rise in an open-topped manometer whose base terminates at the point at which the potential is measured (modified after Willis, 1982)

$$h = (p - 1/g) + z \tag{7}$$

Expressing Eq. 7 in functional form gives:

$$\text{Pseudo} - \text{Pot}(H) = 10.197162\left[P_{a(\text{Bar})} - 1.013\right] - \text{TVDss}(m) \tag{8}$$

where, H = **Pseudopotential** (pseudopotentiometric head in meters), Z = Elevation of point of interest (below MSL, hence −ve)…TVDSS, p = Pressure (Bar) less atmospheric pressure (1Atm = 1.013 Bar), ϱ = Density of water (1gm/cc, already expressed in Eq. 7 and taken out), g = Inverse of Acceleration due to gravity ($1/g$ = 1/0.0981 = 10.197).

2.2.2 Pseudopotential Plots

Setting up the p-pot plots goes through three main steps: data syntheses, the plots, interpretations, and determinations. First, the calculated pseudopotential "h" values were plotted against depth (TVSSS).

3 Results

All the wells penetrated all the levels, and the pseudopotential "h" was determined for all: R5 to R21 (Fig. 2).

A comparison of fluid gradients from pseudopotential plot versus PVT (laboratory) derived values is presented in Fig. 2 and Table 2, while a summary of fluid contacts derived from pseudo-pot plots and PVT (laboratory) is given in Table 3.

4 Discussion

A composite pressure plot (Fig. 2) of all the available data shows a general pressure regime within the Feji field structure to be above hydrostatic except for the shallower reservoirs of R5 and R6, which are hydrostatic. A formation pressure convergence was noted at 2315 mSL on both plots to increase formation pressure above hydrostatic in the field. Below this depth, formation pressure is no longer hydrostatic, implying an overpressure condition. The potential, hence the height (h) calculated from the pseudopotential formula, indicates a close to zero value up to a depth of 2315 mSL. The reservoirs below this depth return value greater than zero, thus showing higher than hydrostatic or normal pressures.

FEJI-2, FEJI-4, and FEJI-6 encountered water in R5. However, R5 is found oil bearing in FEJI-1, FEJI-3, and FEJI-5. From log and pseudopotential plot interpretations, FEJI-1 and FEJI-3 are in the same oil pool. R5 OWC for FEJI-1 and ODT for FEJI-3 are the same at 1814mSL, respectively, supporting the pseudopotential method's higher accuracy and validity over the normal depth vs pressure plot. The normal plot (method) clearly shows no fluid gradient intersection and hence cannot be used to decide hydrocarbon fluid contact for any of the layers in R5.

Fluid gradient definition is quite difficult using the data acquired in the R8 level from FEJI-4, which encountered R8.01 in compartments B and E as subdivided by the faults F2—F3. The PVT report indicates that a GOC is anticipated in the fluid column of level 8.1—compartment A (FEJI-4) around 2403.5 m/MSL. Therefore, it is difficult to determine the fluid gradient using the normal pressure plot in R8. Fluid contacts were, however, determined using the pseudopotential plots. However, an ODT exists for this level at 2411mSL with two (2) GOC possibilities: PVT estimated GOC at 2403.5 and GOC at 2406.5mSL and derived from the pseudopotential plot.

In compartment F, where FEJI-5 encountered R8.1, a clear oil gradient of 0.65 g/cm^3 was established with a corresponding PVT fluid gradient of 0.648 g/cm^3 from the sample at 2517mRT/ 2298mSL. No contact could be found

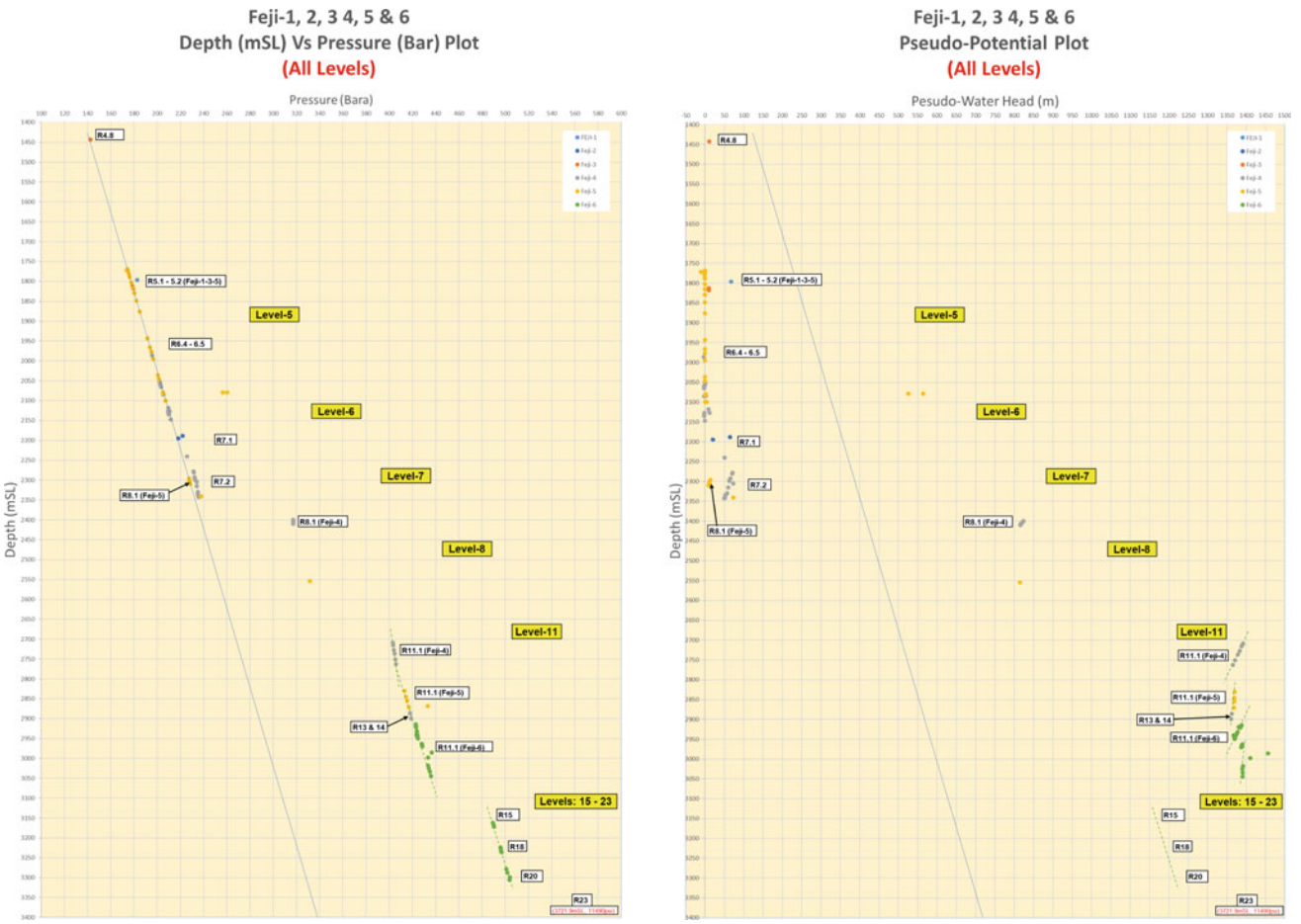

Fig. 2 Feji field general pressure regime (Formation pressure versus depth plot and pseudopotential)

from RFT data/ plot as the sands are seen to be filled with hydrocarbon, and only an ODT is established at 2311mSL from logs. In R8.1, compartment F penetrated by FEJI-5 is different and independent of compartment B/ E (F2-F3) penetrated by FEJI-4, as evidenced by the different fluid gradients derived from the wells FEJI-4 and FEJI-5. Based on the available PVT report syntheses for compartment F, a GOC is reported at 2297.9mSL in the FEJI-5 well.

The normal pressure versus depth plot cannot effectively determine fluid gradient or contact for R8.1. The pseudopotential plot, however, clearly creates the possibility for the fluid gradient to be determined, hence fluid contact. The fluid gradient determined for R8.1 is 0.65 g/cm^3, and a PVT-measured fluid gradient of 0.648 g/cm^3.

Three wells encountered R11.1: FEJI-4, FEJI-5, and FEJI-6. R11 in FEJI-6 are completely water wet, as seen in logs and further proved by the formation pressure gradient of 0.96 g/cm^3. An ODT (oil down to) exists at 2951mSL. R11 in FEJI-4 and FEJI-5 are on different pressure regimes, as proven by the fluid gradients, so there is no fluid communication between both.

A comparison of fluid gradients from the pseudopotential plots versus PVT (laboratory) derived values is displayed in Table 2 and Fig. 2. It shows clearly that the pseudopotential method, in addition to determining contacts under challenging conditions, can also be used as a suitable replacement for the PVT laboratory-derived results and values for fluid gradient and hence hydrocarbon fluid types. The comparison of the results shows clearly that the pseudopotential method gives values that can be the same or very comparable to PVT laboratory-determined results and can be an adequate replacement.

A summary of fluid contacts as determined using the pseudopotential method is given in Table 3. It also captures the GOCs as determined by PVT laboratory analyses. The contacts were determined mainly from wells FEJI-1, -3, -4, -5, and -6. Twenty (21) hydrocarbon contacts (GOC, OWC, and ODT) were established. Eleven (11) were p-pot derived for OWC and ODT, and ten (10) were derived from PVT studies for GOC. The GOCs were PVT-derived because the pressure data sampling was carried out mainly in the reservoirs' oil leg. Hence, there was no data or very

Table 2 Comparison of fluid gradients from pseudo-pot plots versus PVT (laboratory) derived values

Well	Levels	Sub Levels	RFT (This Study)	PVT (Report/ Study)	Comments/ Remarks
FEJI-1-3-5	5	5.01-5.04	0.91	0.88	PVT report
FEJI -4	6	6.02	0.68	0.65	PVT report
		6.05	0.64		No PVT
		6.08-6.09	0.63	0.62	PVT report
FEJI -4	7	7.01-7.02	0.62	0.625	PVT report
		7.03	0.61		No PVT
		7.04	0.6		No PVT
FEJI-4	8	8.01	0.42	0.525	PVT report
		8.01	0.65	0.648	PVT report
FEJI-4 & 6	11	11.1	0.49	0.475	PVT report
		11.1	0.44	0.439	PVT report
FEJI-4	13	13		No sample	No PVT
FEJI-4	14	14		No sample	No PVT
FEJI-6	21	21	No data		No PVT report
FEJI-6	23	23	No data	(?) Gas	PVT report

Table 3 Summary of fluid contacts derived from pseudo-pot plots and PVT (laboratory)

FEJI WELLS CONTACT SUMMARY																					
LEVEL	COMPT- A				COMPT- B				COMPT- C			COMPT- D			COMPT- E			COMPT- F			WELL
	OWC		ODT	GOC	OWC		GOC	GWC	OWC		GOC	OWC		GOC	OWC		GOC	OWC		GOC	
5.02 - 5.04									1814	1817								1774			FEJI-1, 3, 5
6.2																					
6.4	2060			2054																	FEJI-4
6.5	2129			2118																	FEJI-4
6.06																					
6.8-6.9			2239	2213				2119.5													FEJI-4
7.01-7.03			2302	2278																	FEJI-4
7.04			2344	2266																	FEJI-4
8.1						2411	2403.5												2311	2298	FEJI-4, 5
11.1 - 11.6									2768		2706		2951	2915							FEJI-4, 6
																					FEJI-4

scanty recorded data for the upper parts of the reservoirs (gas) sections which were not enough to be used for the GOC determination. The contacts and the compartments within the highly compartmentalized structure of the field in which the contacts are located are also indicated (Table 3). Compartment A has eleven (11) contacts. R5, R6, and R7 have hydrocarbons in wells FEJI-1, -3, -4, and -5. Compartment E has no hydrocarbon shows. Hence, no contact

was seen in any of the wells. Further exploration may unlock hydrocarbons in this compartment since it has the potential.

5 Conclusion

Although the Feji wells have some levels that have clear fluid contacts (OWC) that could have been derived from the "normal" depth versus pressure method, the pseudopotential method was used in this study to determine all the hydrocarbon fluid contacts, including the identified difficult fluid contacts.

The superiority of the pseudopotential method as derived and applied to the reservoirs of the Feji field has been demonstrated. The consequence of not using the pseudopotential method may increase the cost of determining hydrocarbon fluid contacts using other methods and tools. Since the industry and the economy are generally profit-driven, the pseudopotential method comes quickly in handy to help drive capital expenditure (CAPEX) down, thus increasing profitability and revenue.

References

Ejedawe, J. E. (1981). Patterns of incidence of oil reserves in Niger delta basin. *American Association of Petroleum Geologists Bulletin, 65*, 1574–1585.

Ekweozor, C. M., & Daukoru, E. M. (1994). Petroleum source-bed evaluation of Tertiary Niger Delta; discussion and reply. *American Association of Petroleum Geologists Bulletin, 68*, 387–394.

Evamy, B. D., Haremboure, J., Kamerling, P., Knaap, W. A., Molloy, F. A., & Rowlands, P. H. (1978). Hydrocarbon habitat of Tertiary Niger Delta. *American Association of Petroleum Geologists Bulletin, 62*, 1–39.

Feynman, R. P. (2011). Work and potential energy. *Physics, 1*, 13 ISBN 978-0-465-02493-3

Klett, T. R., Ahlbrandt, T. S., Schmoker, J. W., & Dolton, J. L. (1997). Ranking of the world's oil and gas province by known petroleum volumes. US. Geological Survey Open-file Report 97-463, CD-ROM.

Knox, G. J., & Omatsola, E. M. (1989). Development of the Cenozoic Niger delta in terms of the "escalator regression" model and impact on hydrocarbon distribution: Proceedings KNGMG Symposium. *Coastal Lowlands, Geology and Geotechnology*, *111*, 181–202

Kulke, H. (1995). Nigeria. In H. Kulke (Ed.) *Regional petroleum geology of the world. Part II: Africa, America, Australia, and Antarctica* (pp. 143–172)

Petroconsultants. (1996a). Petroleum exploration and production database: Houston, Texas, TX Petroconsultants, Inc, (*database available from Petroconsultants*, Inc, PO Box 740619, Houston 77274-0619)

Reynolds, T. (2005). Pressure data in the development of a giant oilfield: Acg Azerbaijan Bp, Middlesex, England. *AAPG Publication*

Short, K. C., & Stauble, A. I. (1967). Outline of geology of Niger-delta. *AAPG Bulletin, 51*, 761–779.

Willis. (1982). Entrapment of Petroleum in traps and seals1, structural/fault-seal and hydrodynamic traps. In: N. H. Foster, & E. A. Beaumont

Thermodynamic and Kinetic Characterization of the Formation Process for Improving the CO_2 Capture Efficiency into Hydrates

Alberto Maria Gambelli and Federico Rossi

Abstract

This article deals with carbon dioxide hydrate production in the presence of freshwater and silica-based sand from the Mediterranean seafloor. Three tests were carried out and described both thermodynamically and kinetically. Hydrate equilibrium was defined by observing pressure trends over temperature and was then compared with equilibrium values already present in the literature. Results proved that sand acted as an inhibitor for the process. The kinetic process was described via the hydrate formation rate, which allowed us to distinguish hydrate nucleation from the massive growth phase. Finally, differences in pressure between tests and equilibrium values were used to evaluate the CO_2 capture efficiency, which was found to increase with temperature, thus proving that the inhibiting action provided by sand became more intense in the presence of more severe thermodynamic conditions.

Keywords

Gas hydrates • CO_2 capture • Equilibrium • Hydrate formation rate

1 Introduction

Natural gas hydrates (NGH) are ice-like crystalline compounds consisting of a hydrogen-bonded three-dimensional network of water molecules, which includes gas molecules to remain stable. Gas hydrate formation mainly depends on the availability of gas and water molecules and the presence of relatively high pressures and low temperatures; in addition, the presence of impurities may significantly affect the process (Gambelli et al., 2021).

Concerning porous media, it was previously defined that particle size strongly affects gas hydrate formation and plays a role similar to chemical additives (Daryayehsalameh et al., 2021; Gambelli & Rossi, 2021). Kamath and co-workers (1984) deepened the heat transfer characteristics of the dissociation interface for propane hydrates and, thanks to it, they found similarities between hydrates dissociation and nucleate boiling of liquids; thus, they defined it as a heat transfer limited process. Several studies were focused on detecting the inhibiting action of chemical additives to counteract issues as hydrates formation in pipelines (Hosseini & Vaferi, 2021). During hydrates dissociation, free water molecules are produced, forming an adhesive layer over the existing hydrate structures. Such a layer hinders heat transfer and reduces the hydrate dissociation rate (Kamath & Holder, 1987).

In the present work, CO_2 hydrates were formed and dissociated in the presence of natural silica-based sand picked up from the Mediterranean seafloor. Equilibrium for CO_2 hydrates in the presence of such a medium was first defined and then compared with data present elsewhere in the literature. Thermodynamic and kinetic parameters were used to determine the CO_2 capture efficiency, via hydrate formation, in the presence of that specific porous medium and, in particular, its correlation with temperature.

2 Materials and Methods

Carbon dioxide hydrates were formed in a small-scale experimental apparatus, appositely designed to simulate offshore hydrate reservoirs. A detailed description of the reactor is available elsewhere in the literature (Gambelli, 2012; Gambelli & Rossi, 2020; Gambelli et al., 2020). It consists of a small-scale 316SS apparatus, with an internal cylindrical volume equal to 949 cm^3, inserted in a thermostatic bath and used to control temperature.

A. M. Gambelli (✉) · F. Rossi
Engineering Department, University of Perugia, Via G. Duranti 93, 06125 Perugia, Italy
e-mail: albertomaria.gambelli@unipg.it

A. Çiner et al. (eds.), *Recent Research on Sedimentology, Stratigraphy, Paleontology, Tectonics, Geochemistry, Volcanology and Petroleum Geology*, Advances in Science, Technology & Innovation,
https://doi.org/10.1007/978-3-031-43222-4_48

Table 1 Chemical composition and grain size of the natural silica-based sand were used to perform experiments

Compound	Concentration [%]	Grain size [mm]	Concentration [%]
SiO_2	99.1	> 1	Negligible
Al_2O_3	0.25	1–0.8	1
Fe_2O_3	0.045	0.8–0.6	7
TiO_2	0.03	0.6–0.4	22
CaO	0.06	0.4–0.3	22
MgO	0.05	0.3–0.2	22
K_2O	0.11	0.2–0.1	22
Na_2O	0.05	< 0.1	4

Ultra-high-purity (≈ 99.99%) CO_2 was used for experiments, together with pure demineralized water (0.236 l was inserted inside the reactor). Besides them, natural sand from Tunisian coasts was used (0.744 l were inserted). Table 1 describes the sand composition and dimensions of its grains.

Hydrates were formed according to previous works (Gambelli & Rossi, 2020). The internal temperature was firstly lowered till reaching 1–3 °C; contemporarily, a weak gas stream was provided to remove air (if present). Then, the ejection valve was closed, and the rector was filled with carbon dioxide. When the target pressure value was reached, the injection valve was closed, and the reactor was left free to operate in batch conditions. Hydrate formation is an exothermic reaction that produces heat, especially during the initial nucleation phase. As soon as pressure stopped decreasing and stabilized around a constant value, the process ended. Besides pressure and temperature, which were directly measured, the hydrate formation rate was calculated to provide a complete description of the process, according to Eq. 1 (Gambelli et al., 2021):

$$\frac{d_{CO_{2g}}}{dt} = -CO_{2g0} k e^{-kt} \quad (1)$$

where "k" is the rate constant and CO_{2g0} is the initial quantity of gas injected inside the reactor.

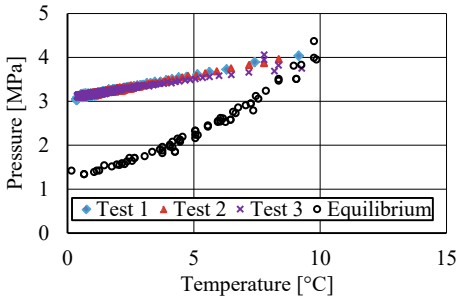

Fig. 1 Pressure–temperature trend observed during experiments and comparison with equilibrium data for CO_2 hydrates

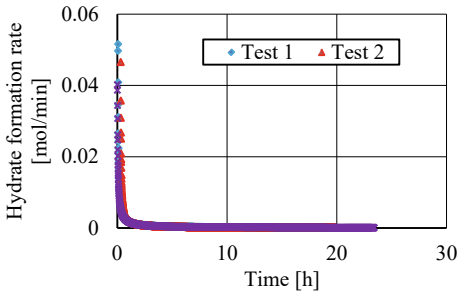

Fig. 2 Hydrate formation rate calculated during hydrate formation

3 Results

Three experiments were carried out, and the results will be shown in the following pages. Figure 1 describes thermodynamically the hydrate formation trend observed in all tests. Conversely, the same process was described kinetically in Fig. 2, which shows the hydrate formation rate over time.

All experiments led to similar trends, proving high accuracy of results. The equilibrium diagram was drawn by considering results produced in the last decades and already present in the literature (Rossi & Gambelli, 2021). Sand used during experiments acted as an inhibitor for the process (Fig. 1 proved it). However, the difference between actual and ideal values seemed to decrease with temperature. In correspondence with the lowest temperature values achieved during experiments, such difference is over 1.5 MPa, while it completely disappeared at temperatures higher than eight °C.

The present parameter may be used to distinguish hydrate nucleation from the massive growth phase: the formation of the first nuclei produced a sudden peak; conversely, the following enormous growth required more time and was uniform. Equilibrium values produced during experiments were then compared with the ideal ones, used to represent the equilibrium curve in Fig. 2. Finally, those values were used to define the CO_2 capture efficiency, which was calculated according to the following Eq. 2 (Gambelli et al., 2021):

Table 2 CO_2 capture efficiency vs. temperature, calculated according to Eq. 2

T [°C]	ηCO_{2cap} [%]	T [°C]	ηCO_{2cap} [%]	T [°C]	ηCO_{2cap} [%]	T [°C]	ηCO_{2cap} [%]	T [°C]	ηCO_{2cap} [%]	T [°C]	ηCO_{2cap} [%]
0.7	43.08	2.2	48.62	3.7	55.56	5.2	62.17	6.7	74.20	8.2	87.15
0.8	43.13	2.3	49.08	3.8	54.81	5.3	63.06	6.8	75.86	8.3	88.24
0.9	43.22	2.4	50.15	3.9	55.65	5.4	64.27	6.9	76.19	8.4	89.03
1	43.67	2.5	52.13	4	55.43	5.5	65.75	7	76.25	8.5	89.59
1.1	43.99	2.6	51.22	4.1	56.29	5.6	66.48	7.1	76.58	8.6	90.40
1.2	44.80	2.7	51.51	4.2	59.60	5.7	67.31	7.2	76.90	8.7	91.18
1.3	44.51	2.8	51.50	4.3	59.03	5.8	67.95	7.3	77.43	8.8	91.73
1.4	45.31	2.9	51.50	4.4	61.43	5.9	68.21	7.4	78.80	8.9	92.50
1.5	45.96	3	51.49	4.5	60.51	6	68.65	7.5	79.64	9	92.79
1.6	46.58	3.1	52.40	4.6	61.86	6.1	68.92	7.6	80.21	9.1	93.05
1.7	46.61	3.2	53.27	4.7	61.97	6.2	70.35	7.7	81.30	9.2	93.81
1.8	47.06	3.3	54.01	4.8	61.73	6.3	70.70	7.8	82.38	9.3	93.84
1.9	47.68	3.4	54.73	4.9	62.29	6.4	71.59	7.9	83.72		
2	47.84	3.5	55.16	5	62.29	6.5	72.00	8	87.39		
2.1	48.30	3.6	55.13	5.1	62.40	6.6	72.80	8.1	85.83		

$$\eta_{CO_2cap} = \left(1 - \left(\frac{P_{exp} - P_{eq}}{P_{exp}}\right)\right) * 100 \qquad (2)$$

The values obtained are given in Table 2.

Values obtained for ηCO_{2cap} were plotted in Fig. 3.

This last diagram proved how the CO_2 capture efficiency increased with temperature. Temperatures up to 9 °C led to efficiency higher than 90%, while in the presence of the lowest temperature values, the efficiency remained below 45%. The experimental analysis carried out in this work allowed us to affirm that environmental elements, like sand, water, and others, may strongly affect hydrate formation (Gambelli et al., 2019). In this case, sand acted as an inhibitor for the process, and its effect varied in function of thermodynamic conditions.

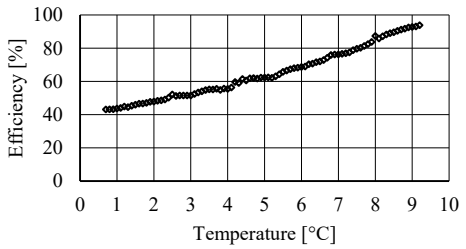

Fig. 3 Efficiency versus temperature for CO_2 capture in the form of a hydrate

4 Conclusions

Carbon dioxide hydrates were formed in a small-scale experimental apparatus, and the presence of natural quartz came from the Mediterranean seafloor. Equilibrium values were compared with how to present in literature, and differences between observed and ideal values were used to evaluate the CO_2 capture efficiency, which was found to increase with temperature, thus proving that environmental elements can modify the process and their effect depends on thermodynamic conditions.

References

Daryayehsalameh, B., Nabavi, M., & Vaferi, B. (2021). Modeling CO_2 capture ability of [Bmim][BF4] ionic liquid using connectionist smart paradigms. *Environmental Technology & Innovation, 22*, 101484.

Gambelli, A. M. (2012). An experimental description of the double positive effect of CO_2 injection in methane hydrate deposits in terms of climate change mitigation. *Chemical Engineering Science, 233*, 116430.

Gambelli, A. M., Castellani, B., Nicolini, A., & Rossi, F. (2020). Water salinity as potential aid for improving the carbon dioxide replacement process' effectiveness in natural gas hydrate reservoirs. *Processes, 8*, 1298. https://doi.org/10.3390/pr8101298

Gambelli, A. M., Filipponi, M., Nicolini, A., & Rossi, F. (2019). Natural gas hydrate: Effect of sodium chloride on the CO_2 replacement process. *International Multidisciplinary Scientific GeoConference Surveying Geology and Mining Ecology Management, 19*, 333–343.

Gambelli, A. M., & Rossi, F. (2020). The use of sodium chloride as strategy for improving CO_2/CH_4 replacement in natural gas hydrates promoted with depressurization methods. *Arabian Journal of Geosciences, 13*, 898. https://doi.org/10.1007/s12517-020-05879-6

Gambelli, A. M., & Rossi, F. (2021). Experimental investigation on the possibility of defining the feasibility of CO_2/CH_4 exchange into a natural gas hydrate marine reservoir via fast analysis of sediment properties. *Chemical Engineering Research and Design, 171*, 327–339.

Gambelli, A. M., Tinivella, U., Giovannetti, R., Castellani, B., Giustiniani, M., Rossi, A., Zanotti, M., & Rossi, F. (2021). Observation of the main parameters influencing the formation of gas hydrates. *Energies, 14*, 1803.

Hosseini, S., & Vaferi, B. (2021). Determination of methanol loss due to vaporization in gas hydrate inhibition process using intelligent connectionist paradigms. *Arabian Journal for Science and Engineering*. https://doi.org/10.1007/s13369-021-05679-4

Kamath, V. A., & Holder, G. D. (1987). Dissociation heat-transfer characteristic of methane hydrates. *Aiche Journal, 33*, 347–350.

Kamath, V. A., Holder, G. D., & Angert, P. F. (1984). 3 phase interfacial heat-transfer during the dissociation of propane hydrates. *Chemical Engineering Science, 39*, 1435–1442.

Rossi, F., & Gambelli, A. M. (2021). Thermodynamic phase equilibria of single-guest hydrate and formation data of hydrate in presence of chemical additives: A review. *Fluid Phase Equilibria*. https://doi.org/10.1016/j.fluid.2021.112958

Numerical Assessment of CO_2-Circulated Geothermal Production from a Closed Reservoir System

Mingjie Chen, Mohammad Mahdi Rajabi, Ali Al-Maktoumi, and Azizallah Izady

Abstract

Renewable energy is becoming more attractive to meet energy demands due to increasing concerns about carbon dioxide (CO_2) emission, environmental pollution, and exhaustion of oil/gas reserves. In addition to oil and solar energy sources, Oman also has abundant low-enthalpy geothermal energy resources in the northern mountain region to be explored and utilized. In the past decade, CO_2 has been proposed and studied as the working fluid mining low-enthalpy geothermal energy owing to its favorable thermodynamic properties. The purpose of this study is to numerically evaluate the technical feasibility of CO_2-circulated geothermal production from depleted oil reservoirs in North Oman, which are usually thin-layered, relatively homogeneous and low-permeable, inclined, compartmentalized, and sealed by faults. A numerical reservoir model is developed to simulate CO_2 circulation and heat transfer in a geothermal prospect in North Oman. The reservoir is assumed to have experienced CO_2-enhanced oil recovery and was initially flooded by CO_2 and residual brine. A triplet horizontal well placement, one central injection well, and two parallel production wells are horizontally placed in the thin-layered reservoir to circulate CO_2. Produced thermal energy capacity is quantitatively assessed based on the model simulation. The findings could provide useful guidance for constructing similar closed geothermal reservoir systems in North Oman and worldwide.

M. Chen (✉) · A. Al-Maktoumi · A. Izady
Water Research Center, Sultan Qaboos University, Muscat, Oman
e-mail: mingjie@squ.edu.om

M. M. Rajabi
Department of Civil and Environmental Engineering, Tarbiat Modares University, Tehran, Iran

A. Al-Maktoumi
Department of Soils, Water and Agricultural Engineering, Sultan Qaboos University, Muscat, Oman

Keywords

Geothermal energy • Carbon dioxide • Low enthalpy • Closed reservoir

1 Introduction

The ready availability of oil and gas reserves in Oman seems to reduce the necessity for exploring and utilizing renewable energy, such as solar, wind, wave, and geothermal energy. Fossil energy is non-renewable and will eventually be depleted. Oman's crude oil production has dropped since 2007 due to the depletion of the oil fields. Although the production decline has been arrested successfully by applying enhanced oil recovery (EOR) techniques in the past years, improved recovery enabled by EOR practice accelerates the exhaustion rate of the limited oil reserve. Moreover, extensive utilization of fossil energy can cause severe environmental pollution and climate change. Exploring potential renewable energy resources, therefore, is strategically significant to Oman's economy, in addition to the demonstrated environmental benefits over fossil fuels. Compared with solar and wind systems, geothermal energy has many advantages, including being impervious to weather changes, providing stable base load power, and high thermal efficiency (Axelsson, 2012). In Oman, low-enthalpy (< 100 °C) geothermal resources are abundant but have received little attention. The potential geothermal prospect is north of the PDO concession toward the Oman Mountains, and the maximum temperature is reached in the vicinity of the Oman Mountains due to the tectonic movements (Al-Lamki & Terken, 1996).

CO_2 has been used as a working fluid to extract oil from petroleum reservoirs (e.g., EOR) and heat from low-permeable hot, dry rock (Pruess, 2008). Recently, CO_2-circulated geothermal production has been considered an effective approach to harvesting low-enthalpy geothermal energy

A. Çiner et al. (eds.), *Recent Research on Sedimentology, Stratigraphy, Paleontology, Tectonics, Geochemistry, Volcanology and Petroleum Geology*, Advances in Science, Technology & Innovation,
https://doi.org/10.1007/978-3-031-43222-4_49

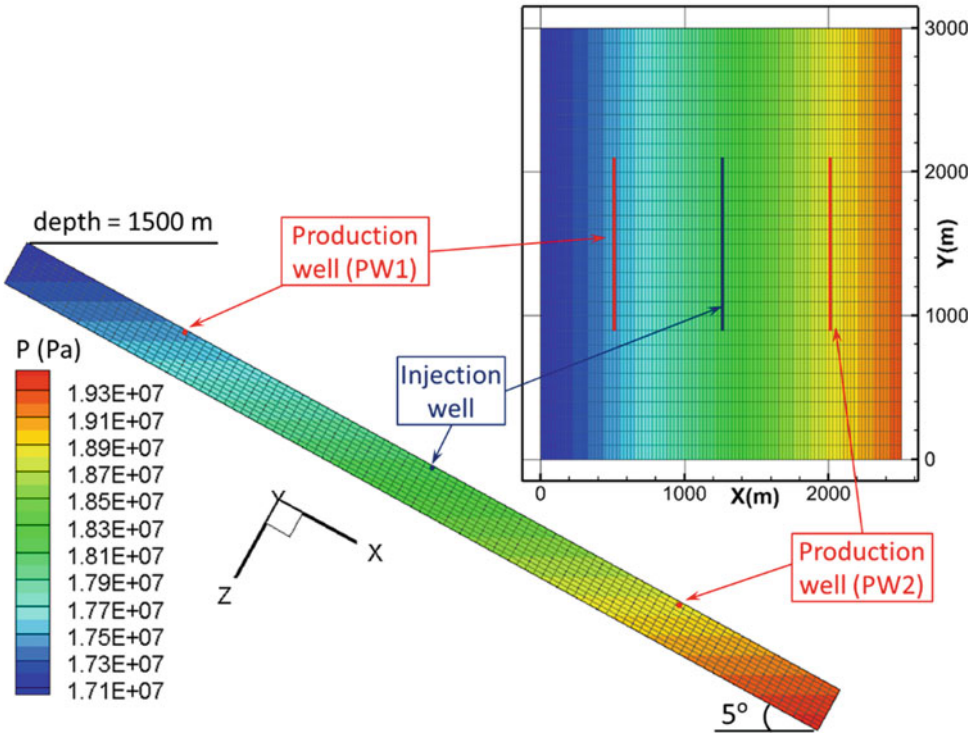

Fig. 1 Reservoir model domain, grid, well placement, and initial pressure distribution. A horizontal injection well (blue line) is placed in the center, and two parallel production wells (red lines) are placed 750 m away on both sides. The exaggerated scale of *Z* is 6.25

from saline aquifers due to CO_2's favorable hydrothermal dynamics (Adams et al., 2014). This study aims to numerically assess CO_2-circulated geothermal production from a fault-sealed oil reservoir which is oil-depleted after CO_2-EOR in North Oman.

2 CO_2 Circulation Model

Figure 1 shows the numerical model domain simplified from reservoir Block *B* of the Daleel oil field in North Oman (Zhang et al., 2007). The xyz dimension of the 5°-inclined reservoir is 2500, 3000, and 20 m, respectively, discretized into $25 \times 100 \times 2$ m^3 cells. The important hydro-geothermal reservoir properties are given in Table 1. The left top is at 1500 m, and the initial pressure is distributed according to hydrostatic equilibrium. Initial temperatures are calculated according to 30 °C of surface temperature and 39.7 °C/km of the vertical thermal gradient. The domain is a fully closed system without fluid or heat crossing the boundaries, except that a constant 75 mW/m^2 geothermal heat source is applied to the bottom boundary. The reservoir pores are initially saturated by 70% CO_2 in volume and 30% 180 ppt (parts per thousand) brine. A 1.2-km horizontal injection well is placed in the middle top of the domain, and two parallel production wells are placed 750 m away on both sides. A 5 MPa overpressure is specified at the injection well (linearly increased to 5 MPa in first year and remained thereafter), and pressures are fixed as initial at both production wells. The numerical model is developed using NUFT software (Nitao, 1998) and simulated for 50 years.

Table 1 Important hydro-geothermal properties of the reservoir

Parameter	Values
Porosity (−)	0.25
Permeability (m^2)	8.95×10^{-15}
Residual brine saturation (−)	0.3
Residual CO_2 saturation (−)	0.05
van Genuchten α (1/Pa)	5.1×10^{-5}
van Genuchten m (−)	0.455
Specific heat (J/kg-°C)	1000
Thermal conductivity (W/m-°C)	2.1

3 Results and Discussion

Overpressure on the injection well increased to 5 MPa in the first year and remained thereafter. Under the pressure gradient between the injection and production wells, CO_2 is extracted at 20 to 17 kg/s from PW1 and 15 kg/s from PW2 (Fig. 2a). After the first five years, the injected CO_2 is stabilized and slightly decreases from 38 to 33 kg/s, a little (1–2 kg/s) more than the total produced CO_2. This supplemental CO_2 injected is necessary to compensate for the freed volume caused by produced brine with CO_2 to support the fixed

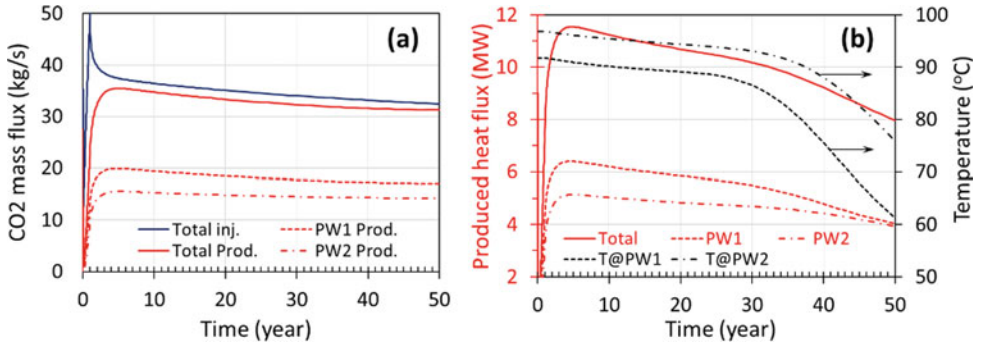

Fig. 2 Simulated **a** CO_2 injection (blue line) and extraction rates (red lines) from two wells and **b** produced thermal energy flux (red lines) and temperature (black lines) at two production wells during 50 years of CO_2 circulation

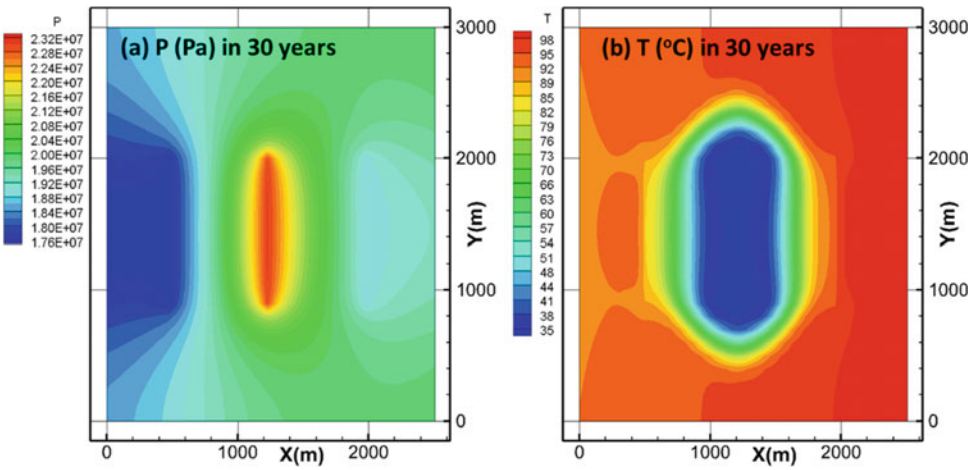

Fig. 3 Simulated **a** pressure and **b** temperature distribution after 30 years of CO_2 circulation

5 MPa overpressure at the injection well. The initial temperature of PW1 is about 10 °C lower than that of PW2 due to their vertical space in the inclined reservoir. However, the produced energy from PW1 is still higher than that from PW2 because of the larger mass flux of PW1. As shown in Fig. 2b, the total produced thermal energy capacity is increased to a maximal 11.5 MW after four years. It decreases gradually to 10 MW in the 30th year, the typical lifespan of a geothermal reservoir. After 30 years of circulation, the temperature is higher than 85 and 90 °C at PW1 and PW2, respectively, sufficient to operate CO_2 gas turbine.

Figure 3 presents pressure and temperature distribution on the top layer in 30 years. It should be noted that the spatial pressure pattern is relatively stable since pressures at the three wells are fixed after the first year. Still, the low-temperature area is expanding to the production wells with the continuous cold CO_2 injection.

4 Conclusions

A numerical reservoir model is developed to simulate CO_2-circulated geothermal production from a thin, low-enthalpy, and fault-sealed reservoir block. Simulated results show that produced thermal energy capacity is above 10 MW in a typical 30-year lifespan. The findings suggest that the proposed triplet horizontal well placement is technically feasible to harvest low-enthalpy geothermal energy from similar oil-depleted reservoirs in the North Oman region, considering existing infrastructure and rich field hydrogeological knowledge gained during decades of oil recovery.

Acknowledgements BP Oman supported this research with project #BP-DVC-WRC-18-01. Authors extend their appreciation to SQU research Group DR/RG/17.

References

Adams, B. M., Kuehn, T. H., Bielicki, J. M., Randolph, J. B., & Saar, M. O. (2014). On the importance of the thermosiphon effect in CPG (CO_2 plume geothermal) power systems. *Energy, 69*, 409–418.

Al-Lamki, M., & Terken, J. M. (1996). The role of hydrogeology in petroleum development Oman. *GeoArabia, 1*(4), 495–510.

Axelsson, G. (2012). The physics of geothermal energy. In C.A. Sayigh (Ed.), *Comprehensive Renewable Energy* (Vol. 7, Chapter 7.02, pp. 3–50). Elsevier.

Nitao, J. J. (1998). *Reference manual for the NUFT flow and transport code, version 2.0*. Technical Report UCRL-MA-130651, Lawrence Livermore National Laboratory.

Pruess, K. (2008). On production behavior of enhanced geothermal systems with CO_2 as working fluid. *Energy Conversion & Management, 35*, 1446–1454.

Zhang, L., Zhou, L., Al-Mugheiry, M. A., & Xu, K. (2007). Horizontal waterflooding in shuaiba carbonate reservoir of daleel field in Oman: From pilots performance to development era. *Society of Petroleum Engineers*.

Efficiency Analysis of the European Oil Pipeline Systems Between 2007 and 2017

Corrado lo Storto

Abstract

This paper presents the results of a benchmarking study that compared the efficiency and productivity of 25 oil pipelines in Europe. The Global Malmquist Productivity Index using Slack-Based Measure-Data Envelopment Analysis was calculated to measure productivity changes between 2007 and 2017. Findings may help governments and utility operators to improve the performance of the national energy infrastructure.

Keywords

Oil pipeline industry • Europe • Efficiency • Data envelopment analysis • Global Malmquist productivity index

1 Introduction

The availability of modern energy infrastructure is a crucial resource to effectively integrate the energy markets, guarantee the security of the energy supply, and meet sustainability targets. Hence, one of the main goals of the national authorities is to develop this infrastructure and keep it fully effective to grasp the greatest possible value from its usage. An important infrastructure component is the systems to transport oil and gas.

Since time, pipelines have been a safe and efficient means for transporting crude oil for short and long distances. Furthermore, pipelines have environmental advantages compared to trucks and ships as they have lower polluting emissions and allow transporting of large quantities of oil. Therefore, benchmarking and efficiency studies may help governments and utility operators better understand the real value generated by using oil pipelines to develop the energy infrastructure. This paper presents the results of a benchmarking study aimed at measuring the efficiency and productivity changes in the European oil pipeline industry from 2007 to 2017. The Global Malmquist Productivity Index (GMPI) was calculated to measure productivity changes using Slack-Based Measure (SBM)-Data Envelopment Analysis (DEA).

2 Method

The MPI under the DEA framework was calculated following the approach suggested by Färe et al. (1992). In addition, to avoid the problems of infeasibility and lack of circularity, the method to calculate the Global Malmquist Productivity Index (GMPI) proposed by Pastor and Knox Lovell (2005) was implemented. In the GMPI calculation, the output distance is measured against a global benchmarking frontier rather than a frontier relative to a single period. For the Decision-Making Unit (DMU) k, the GMPI is defined as follows:

$$M_k^G\left(x^{t+1}, y^{t+1}, x^t, y^t\right) = \frac{D_k^G\left(x^{t+1}, y^{t+1}\right)}{D_k^G\left(x^t, y^t\right)} \tag{1}$$

The GMPI can be decomposed into two components, measuring the efficiency change (EC) and technology change (TC), respectively, as follows:

$$M_k^G\left(x^{t+1}, y^{t+1}, x^t, y^t\right) = \frac{D_k^{t+1}\left(x^{t+1}, y^{t+1}\right)}{D_k^t\left(x^t, y^t\right)} \times \left[\frac{D_k^G\left(x^{t+1}, y^{t+1}\right)}{D_k^{t+1}\left(x^{t+1}, y^{t+1}\right)} \times \frac{D_k^t\left(x^t, y^t\right)}{D_k^G\left(x^t, y^t\right)}\right] \tag{2}$$

where

$$EC = \frac{D_k^{t+1}\left(x^{t+1}, y^{t+1}\right)}{D_k^t\left(x^t, y^t\right)}, \qquad TC = \frac{D_k^G\left(x^{t+1}, y^{t+1}\right)}{D_k^{t+1}\left(x^{t+1}, y^{t+1}\right)} \times \frac{D_k^t\left(x^t, y^t\right)}{D_k^G\left(x^t, y^t\right)} \tag{3}$$

C. lo Storto (✉)
University of Naples Federico II, 80125 Piazzale V. Tecchio 80, Naples, Italy
e-mail: corrado.lostorto@unina.it

A. Çiner et al. (eds.), *Recent Research on Sedimentology, Stratigraphy, Paleontology, Tectonics, Geochemistry, Volcanology and Petroleum Geology*, Advances in Science, Technology & Innovation,
https://doi.org/10.1007/978-3-031-43222-4_50

In this study, the distance functions D_k^t, D_k^{t+1}, D_k^G have been calculated by employing the Slack-Based Measure (SBM) DEA suggested by Tone (2001), assuming an output orientation to maximize the output level keeping constant the input quantities as these cannot be easily changed. Furthermore, the GMPI was computed considering two scenarios, constant returns to scale (crs) and variable returns to scale (vrs).

For DMU k, the distance measurement can be calculated by solving a linear program. Let us suppose that there are n DMUs having the input and output matrices $X = (x_{ij}) \in R^{m \times n}$ and $Y = (y_{rj}) \in R^{p \times n}$. The values $s^- \in R^m$ indicate the input surplus, whereas the values $s^+ \in R^p$ indicate output shortage. The solution of the following linear program provides the DMU k distance measurement:

$$\begin{aligned} &\min \ \rho = \frac{1}{1 + \frac{1}{p}\sum_{r=1}^{p} \frac{s_r^+}{y_{rk}}} \\ &\text{st} \quad x_k - X\lambda - s^- = 0 \quad \text{and} \quad Y\lambda - y_k - s^+ = 0 \\ &i = 1, 2, \ldots, m \quad r = 1, 2, \ldots, p \quad j = 1, 2, \ldots, k, \ldots n \quad \lambda_j, s_i^-, s_r^+ \geq 0 \end{aligned} \tag{4}$$

3 Sample and Variables

The sample includes 25 pipelines that transport oil in countries belonging to the European Union (EU) and the EFTA area and current EU candidates: AT, BE, BG, HR, CZ, DK, FR, DE, EL, HU, IT, LV, LT, NL, MK, NO, PL, PT, RO, RS, SK, ES, CH, TR, UK.

The pipeline was conceptualized as a production function consuming two inputs and generating one output. As in other studies measuring efficiency in the energy industry, the number of employees and oil pipeline network length was included in the DEA model specification as inputs (Ertürk & Türüt-Aşık, 2011; Goncharuk & lo Storto, 2017; lo Storto, 2018; Zorić et al., 2009), while the oil transport within the national territory was used as the unique output of the model (Goncharuk & lo Storto, 2017; Yardımcı et al., 2015). Table 1 presents major variable statistics. For the sake of brevity, only data relative to the year 2017 are shown.

Table 1 Input and output description and statistics (the year 2017)

Variable	Type	Measurement unit	Mean	Max.	Min.
Employees	Input	Number of units	1191.86	6094	27
Pipeline network length	Input	km	1643.46	7142	53
Oil transport	Output	Mio tkm	6788.56	52,095.25	13

4 Results

Figure 1 displays the graphs of pipeline mean efficiencies from 2007 to 2017 estimated under the crs and vrs assumptions. The efficiency graphs differ over time to a large extent, although both indexes have a decreasing trend.

Over the period, mean efficiencies scores are 0.298 and 0.486, respectively, under the crs and vrs assumptions. This indicates that oil pipelines were generally inefficient, and scale economies were an important factor determining such an efficiency drop. The mean vrs-efficiency is 64.15% higher than crs-efficiency. In 2014, the difference between the two efficiency scores was very large.

Figure 2 presents the productivity analysis results. For the sake of brevity, only results relative to the vrs assumption are reported. The GMPI behavior emphasizes the productivity fluctuations between 2007 and 2017. The GMPI score slightly greater than one indicates some minor productivity improvements in 2007–08, 2011–12, 2013–14, and 2016–17. However, there was a relevant productivity increase in 2012–13 and a more moderate one in 2009–10. An incredible positive change in pipeline efficiency determined such a remarkable productivity improvement.

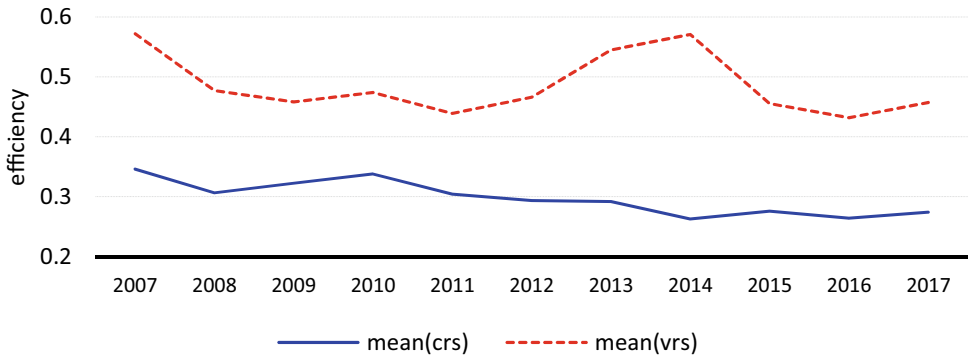

Fig. 1 Pipelines mean efficiency scores from 2007 to 2017

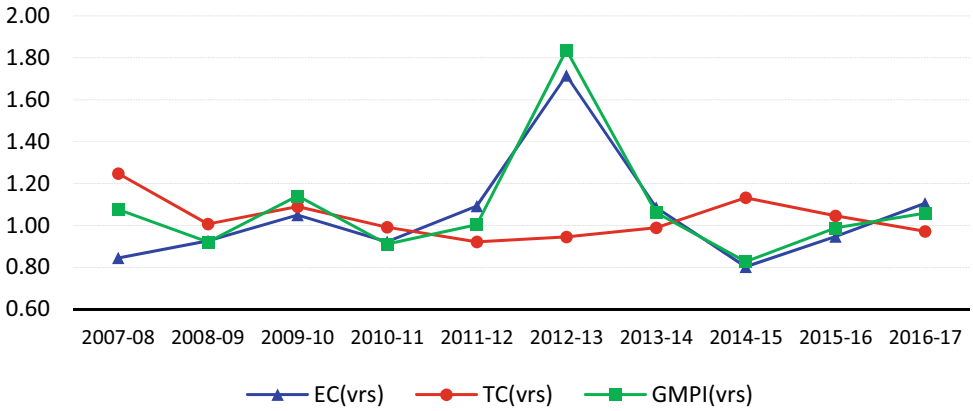

Fig. 2 Mean scores of GMPI, TC, and EC indicators from 2007 to 2017 (vrs assumption)

5 Conclusions

Results from the benchmarking analysis showed that between 2007 and 2017, the oil pipeline industry in Europe had a low average operational efficiency. Scale diseconomies are an important key determinant of scarce efficiency. From 2007 to 2017, operational efficiency improvements largely affected productivity gains.

References

Ertürk, M., & Türüt-Aşık, S. (2011). Efficiency analysis of Turkish natural gas distribution companies by using data envelopment analysis method. *Energy Policy, 39*(3), 1426–1438.

Färe, R., Grosskopf, S., Lindgren, B., & Roos, P. (1992). Productivity change in Swedish pharmacies 1980–1989: A non-parametric Malmquist approach. *Journal of Productivity Analysis, 3*, 85–102.

Goncharuk, A. G., & lo Storto, C. (2017). Challenges and policy implications of gas reform in Italy and Ukraine: Evidence from a bench-marking analysis. *Energy Policy, 101*, 456–466.

lo Storto, C. (2018). A nonparametric economic analysis of the US natural gas transmission infrastructure: Efficiency, trade-offs and emerging industry configurations. *Energies, 11*, 519.

Pastor, J. T., & Knox Lovell, C. A. (2005). A global Malmquist productivity index. *Economics Letter, 88*, 266–271.

Tone, K. (2001). A slacks-based measure of efficiency in data envelopment analysis. *European Journal of Operational Research, 130*, 498–509.

Yardımcı, O., & Karan, M. B. (2015). Efficiency and service quality analyses of the natural gas distribution companies: A case study of Turkey. In A. Dorsman, W. Westerman, & J. L. Simpson (Eds.), *Energy technology and valuation issues, part III* (pp. 165–198). Springer International Publishing.

Zorić, J., Hrovatin, N., & Scarsi, G. (2009). Gas distribution bench-marking of utilities from Slovenia, the Netherlands and the UK: An application of data envelopment analysis. *South East European Journal of Economics and Businesses, 4*(1), 113–124.

Assessment of Geological Risks in the Search for Oil and Gas Fields in the Eastern Arctic

Rustam Mamedov, Yulia Scherbina, and Maria Frolova

Abstract

The paper assesses geological risks and the probability of discovering oil and gas fields in the Eastern Arctic water zones using the methodology widely used by oil companies. Three promising sedimentary complexes are predicted in the water zones of the Eastern Arctic: Aptian-Upper Cretaceous, Paleogene, and Neogene. As a result, the probability of geological success in the Aptian-Upper Cretaceous deposits is associated with high risks. On the other hand, the likelihood of discovering hydrocarbon (HC) in the Paleogene and Neogene complexes is higher and corresponds to a moderate risk. The results helped identify the most promising areas for further geological exploration.

Keywords

Eastern Arctic • Geological risk • Probability of discovery • Resources • Traps • Hydrocarbons • Geochronology • Reservoirs

1 Introduction

Geological risk is the probability of a negative result when searching for a deposit in the license area. The value of geological risk is defined by estimating the likelihood of success ratio (POS). The creation of reliable models of hydrocarbon systems, consisting of four elements: a hydrocarbon trap, a reservoir rock, conditions for the formation and migration of hydrocarbons, and sealing horizons, contributes to the reduction of geological risks during geological prospecting works for oil and gas. Geological risks are assessed as the product of the probabilities of the following four independent factors: the likelihood of an oil source rock (P_{source}), the possibility of a reservoir availability ($P_{reservoir}$), the probability of a trap availability (P_{trap}), and the probabilities of the favorable time factor $P_{dinamics}$. The likelihood of detecting HC accumulation is estimated on a scale from 0.01 to 0.99.

2 Method

Assessment of geological risks and the probability of field discovery was performed using a method widely used by oil companies. The methodology comprehensively analyzes geological information about oil and gas source rocks, reservoirs, and seals (Guliyev et al., 2017). Based on empirical data, geological risks are divided into the following categories:

(1) shallow risk (0.5 ÷ 0.99)—all factors of the object are assessed as "favorable";
(2) low risk (0.25 ÷ 0.5)—all factors are assessed as "reassuring" and "favorable";
(3) moderate risk (0.125 ÷ 0.25)—two or three factors are from "reassuring" to "favorable", one or two are from "reassuring" to "neutral";
(4) high risk (0.063 ÷ 0.125)—one or two factors are "reassuring", two or three "neutral", or from "neutral" to "reassuring";
(5) very high risk (0.01 ÷ 0.063) from two to three factors not more elevated than "neutral" with one or two—"doubtful" or "neutral".

3 Results

In the water zones of the Eastern Arctic, three promising sedimentary complexes are predicted: Aptian-Upper Cretaceous, Paleogene (Paleocene-Eocene), and Neogene

R. Mamedov (✉) · Y. Scherbina · M. Frolova
Sergo Ordzhonikidze Russian State University for Geological Prospecting, Moscow, Russia
e-mail: mamedovra@mgri.ru

A. Çiner et al. (eds.), *Recent Research on Sedimentology, Stratigraphy, Paleontology, Tectonics, Geochemistry, Volcanology and Petroleum Geology*, Advances in Science, Technology & Innovation,
https://doi.org/10.1007/978-3-031-43222-4_51

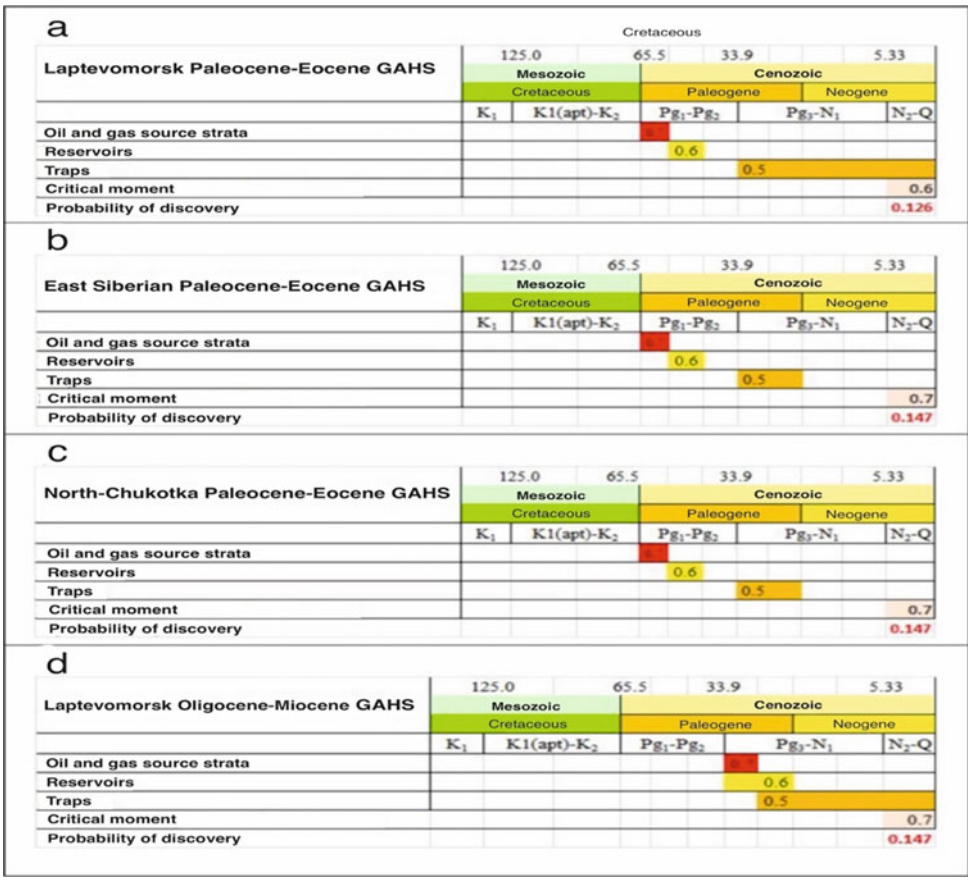

Fig. 1 Geological risk diagrams: **a** Laptevomorsk Paleocene-Eocene GAHS; **b** East Siberian Paleocene-Eocene GAHS; **c** North Chukotka Paleocene-Eocene GAHS; **d** Laptevomorsk Oligocene–Miocene GAHS

(Oligocene–Miocene). The results of assessing the probability of geological success of the studied generation-accumulation HC systems (GAHS) of the East Arctic water zones are shown in Fig. 1.

The modeling results performed using the variable-based approach showed that regardless of the type of kerogen, at average C_{org} values in sediments, potential oil and gas source strata (OGSS) are capable of saturating HCs of bright objects. Therefore, the factor "Assessment of OGSS" was assessed as "reassuring" (0.7). However, the seal quality rating cannot be higher than 0.5 ("neutral"). Accordingly, the overall risk for the "Trap Assessment" factor was assessed by the minimum criterion—0.5.

The unfavorable ratio of the time of the critical moment and the formation of traps for the Aptian GAHS led to high risks in terms of the conservation of deposits. Therefore, the factor "Geochronology" was assessed as "unfavorable" with a value of 0.3 for all HC systems of the Aptian-Upper Cretaceous complex (Gordadze et al., 2017; Guliev et al., 2018). On the other hand, for the GAHS of the Cenozoic part of the section, depending on the relationship between the critical moment and the established folding stages in sedimentary basins, the "Geochronology" factor is assessed as "favorable" with values of 0.6 ÷ 0.7 (Fig. 5.13 ÷ 5.21).

Thus, the probability of geological success for Cretaceous deposits is associated with high risks (Pg = 0.063). On the other hand, the likelihood of discovering HC in the Cenozoic part of the section is higher (from 0.126 to 0.147), which corresponds to a moderate risk (Kerimov & Rachinsky, 2016).

4 Discussion

HC systems of the Cretaceous age passed the critical moment long before the end of tectonic activity in the region. This negatively affected the filling of traps formed at the later stages of tectonic movements and the destruction of previously created HC accumulations. The high maturity of the organic matter of the oil and gas source rocks of the studied GAHS and the widespread development of secondary cracking processes led to a high proportion of gaseous HCs in the composition of the predicted deposits (Kerimov et al., 2019a; Lapidus et al., 2018). This is especially typical for the Laptevomorsk GAHS. However, the initial type of kerogen is the main factor determining the phase composition of the predicted HC accumulations (Kerimov et al., 2018a). Therefore, the most significant

initial geological HC resources are expected (in descending order) in the East Siberian, North Chukotka, and Laptevomorsk Aptian-Upper Cretaceous HC systems. At the same time, the North Chukotka, East Siberian, and Dremkhedskaya GAHS are in the lead regarding HC-specific densities (land perspectivity).

The HC systems of the Paleogene sedimentary complex are characterized by high maturity. In this case, the maximum coefficients are noted for the North Chukotka and East Siberian GAHS—the minimum for the Laptevomorsk one. However, despite these unfavorable factors, the maximum initial geological resources of HCs are predicted in the traps of the Laptevomorsk GAHS (Mustaev et al., 2016). The second largest resource potential is the North Chukotka HC system. The presence of marine-type organic matter in the oil and gas source rocks determines the predominance of liquid HCs. By the volume of the initial geological resources of HCs, the systems are ranked in the following order (in descending order): Laptevomorsk, North Chukotka, and East Siberian, according to the perspectivity of lands, respectively: North Chukotka, East Siberian, and Laptevomorsk GAHS.

The mature organic matter at the base of the Neogene (Oligocene/Miocene) sedimentary complex is predicted within the Laptevomorsk and the North Chukotka trough (Kerimov et al., 2019b). More favorable conditions for the formation of the necessary elements of HC systems exist within the Laptevomorsk water zone: a higher maturity of the OGSS, rapid subsidence, and a tectonic condition favorable for the formation of anticlinal traps (Kerimov et al., 2018b; Zaicev et al., 2017). Traps of the non-anticlinal type were formed here under the needs of the gradual progression of the sedimentary wedge, predominantly in the northern direction. The hydrocarbon potential of this part of the section requires further study.

5 Conclusions

Based on the results obtained, the most promising areas recommended for licensing were identified, and recommendations were given for further exploration in these areas to clarify their HC potential and reduce geological risks.

References

Gordadze, G., Kerimov, V., Gaiduk, A., & Romanyuk, T. (2017). Hydrocarbon biomarkers and diamondoid hydrocarbons from late Precambrian and lower Cambrian rocks of the Katanga saddle (Siberian Platform). *Geochemistry International, 55*, 360–366.

Guliev, S., Mustaev, R., Kerimov, V., & Yudin, M. (2018). Degassing of the Earth: Scale and implications. *Gornyi Zhurnal, 11*, 38–42. https://doi.org/10.17580/gzh.2018.11.06.

Guliyev, I., Kerimov, V., Osipov, A., & Mustaev, R. (2017). Generation and accumulation of hydrocarbons at great depths under the Earth's crust. *SOCAR Proceedings, 1*, 4–16.

Kerimov, V., Gordadze, G., Mustaev, R., & Bondarev, A. (2018a). Formation conditions of hydrocarbon systems on the Sakhalin shelf of the sea of Okhotsk based on the geochemical studies and modeling. *Oriental Journal of Chemistry, 34*(2), 934–947. https://doi.org/10.13005/ojc/340243.

Kerimov, V., Mustaev, R., & Osipov, A. (2018b). Peculiarities of hydrocarbon generation at great depths in the crust. *Doklady Earth Sciences, 483*(1), 1413–1417.

Kerimov, V., Leonov, M., Osipov, A., Mustaev, R., & Hai, V. (2019a). Hydrocarbons in the basement of the South China Sea (Vietnam) shelf and structural-tectonic model of their formation. *Geotectonics, 53*(1), 42–59.

Kerimov, V., Osipov, A., Mustaev, R., Minligalieva, L., & Huseynov, D. (2019b). Conditions of formation and development of the void space at great depths. *Neftyanoe Khozyaystvo—Oil Industry, 4*, 22–27.

Kerimov, V., & Rachinsky, M. (2016). Geofluid dynamic concept of hydrocarbon accumulation in natural reservoirs. *Doklady Earth Sciences, 471*(1), 1123–1125.

Lapidus, A., Kerimov, V., Mustaev, R., Movsumzade, E., & Zakharchenko, M. (2018). Caucasus Maykopian kerogenous shale sequences: Generative potential. *Oil Shale, 35*(2), 113–127.

Mustaev, R., Kerimov, V., Shilov, G., & Dmitrievsky, S. (2016). Modeling of thermobaric conditions formation of the shale hydrocarbon accumulations in low-permeability reservoirs khadum formation Ciscaucasia. In *Geomodel 2016—18th Science and Applied Research Conference on Oil and Gas Geological Exploration and Development*.

Zaicev, V., Kerimov, V., Mustaev, R., & Dmitrievskij, S. (2017). Geomechanical modeling of low permeability shale strata of the maikop series Ciscaucasia. In *EAGE/SPE Joint Workshop on Shale Science 2017: Prospecting and Development*.

Geochemical Evidence of Deep Source Rocks—Adamantanes in Oils from the Absheron Archipelago, South Caspian Basin, Azerbaijan

Arzu Javadova and Galina Martinova

Abstract

Oil samples taken from various depths and stratigraphic formations of the fields in the Absheron archipelago were analyzed to evaluate the composition of adamantane hydrocarbons, its derivatives, and other biomarkers using gas-chromatography and gas-chromatography-mass-spectrometry. Reservoirs in the study area are Middle Pliocene age stacked fluvial-deltaic sandstone units that contain hydrocarbons generated by organic-rich shales of deep-water Oligocene–Miocene and Diatom formations. s organic matter matures, the total amount of the biomarkers in the hydrocarbons decreases. It happens due to the thermodynamic equilibrium that builds between certain types of biomarkers, suggesting that in the case of highly mature oils, it is more beneficial and diagnostic to apply thermally highly resistant structures, such as adamantanes. Adamantanes and their homologs have been identified in the oil samples analyzed. The number of adamantanes and their methyl substitution compounds are present in the sequence of increasing their thermodynamic resistances. This indicates the formation of the adamantine as a result of thermal transformations of normal alkanes. It is known that the amount of adamantane hydrocarbons in oils depends on the oil's chemical nature. Data clearly show a direct relationship between the number of naphthenic hydrocarbons and adamantanes in oils. It indicates that the degree of transformation of the polycyclic hydrocarbons into adamantanes and their isomers is much higher in the naphthenic type of oils. Unique geological setting–rapid sedimentation and low to moderate geothermal gradients suggest the presence of deeper source rock that can support geochemical features, which we observe in the oil samples analyzed, including a high abundance of adamantanes hydrocarbons.

Keywords

South Caspian Basin • Hydrocarbons • Biomarkers • Adamantanes • Source rock

1 Introduction

South Caspian Basin is one of the wealthiest hydrocarbon provinces in the world, with more than 100 years of oil and gas production history. It contains more than 20 km of Mesozoic and Tertiary sediments deposited on oceanic or thinned continental crust. The primary production in the basin is from the Pliocene productive series of fluvial-lacustrine, deltaic sandstones deposited after the Miocene base level fall that caused the isolation from the global ocean. Principal source rocks for the oil and gas fields are organic-rich Oligocene–Miocene Maykop and Diatomaceous shales deposited in deep water environments. Raw data on source rocks predominantly come from the onshore well penetrations and natural outcrops. This work aims to share preliminary results from the geochemical work done on the oil samples collected from the various oil fields in the Absheron archipelago. The focus was on the composition and distribution of adamatanes, their homologs, and other biomarkers, as well as evaluating the role of adamantanes in hydrocarbon formation. Adamantane is the chemical name for "diamond-type hydrocarbons." It is a bridged hydrocarbon of the $C_{10}H_{16}$ composition, consisting of three cyclohexane rings in the "armchair" conformation. An essential feature of adamantane hydrocarbons is their thermodynamic stability, which helps a lot in the case of studying highly mature or biodegraded oils.

A. Javadova (✉)
Oil and Gas Institute of the Azerbaijan National Academy of Science, F. Amirov 9, Baku, AZ1000, Azerbaijan
e-mail: ajavadova@yahoo.com

G. Martinova
Institute of Geology and Geophysics of the Azerbaijan National Academy of Science, H. Cavid 119, Baku, AZ1143, Azerbaijan

A. Çiner et al. (eds.), *Recent Research on Sedimentology, Stratigraphy, Paleontology, Tectonics, Geochemistry, Volcanology and Petroleum Geology*, Advances in Science, Technology & Innovation,
https://doi.org/10.1007/978-3-031-43222-4_52

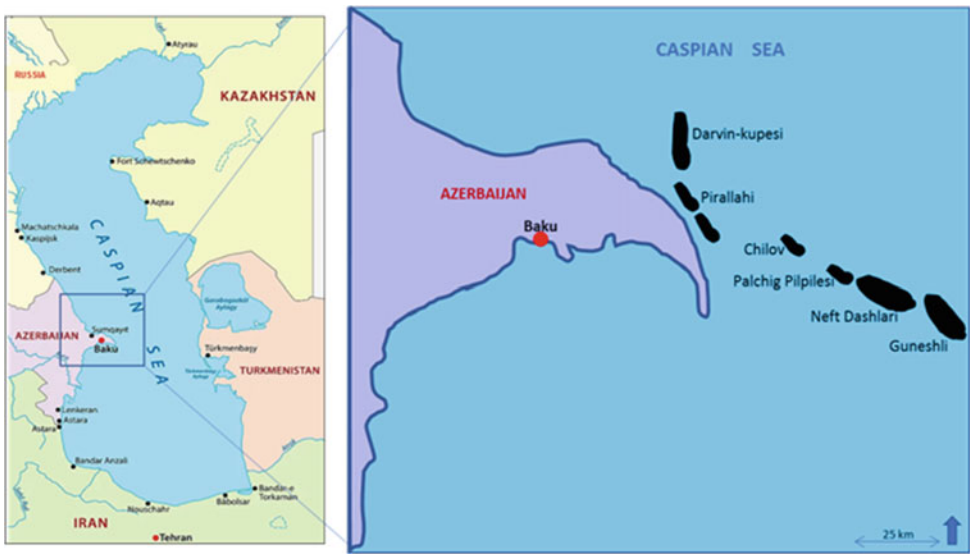

Fig. 1 Study area location map

Oil samples from various depths and stratigraphic formations of the fields in the Absheron archipelago, such as Darvin-kupesi, Pirallahi, Palchig Pilpilesi, Neft Dashlari, Guneshli, Chilov, and Sangachal-Deniz fields are the subjects of the current study (Fig. 1).

2 Materials and Methods

Gas-chromatography-mass-spectrometry (Perkin-Elmer Clarus 680) was used to analyze the oil samples selected: carrier gas—helium, 60 m capillary column/0.25 mm diameter. Temperature programming steps 2 °C/min from 80 to 300 °C, and source temperature is 250 °C. Chromatograms of hydrocarbons were obtained by total ion current (TIC) and specific ion fragments (SIR). The individual hydrocarbons were identified through a computer search of the National Institute of Standards NIST-08 library (more than 130,000 mass-spectrums of organic compounds), according to published data and based on the reconstruction of ion fragments that have been identified. Adamantane hydrocarbons were detected by scanning fragmented ions m/z 136, 135, 149, and 163.

3 Results

More than 250 individual hydrocarbons have been identified in the oil samples analyzed. The important ones are the biomarkers—terpenes, steranes, hopanes, and adamantanes (Peters & Moldowan, 1993). In addition to adamantanes, their homologs with C_{11}–C_{15} composition have also been identified in the oil samples. It should be noted that the samples analyzed represent oils of different stratigraphic ages. The distribution of adamantanes in the oil samples from the Guneshli field is given as an example in Table 1.

The distribution of adamantanes C_{10}–C_{13} in oils from the Guneshli and Neft Dashlari fields shows that the highest amount of alkyl-adamantanes corresponds to its dimethyl-transitioned homologs. In contrast, the concentration of the adamantanes that have not been transformed is the lowest. We also observe high content of 2-monomethyl-adamantanes (2-MAd) in C_{12}. Generally, there is the following trend in the distribution of adamantane hydrocarbons in oils analyzed: 2-MAd > 1-MAd > 3-MAd > Ad., i.e., we see a higher concentration of thermodynamically stable adamantanes.

4 Discussion

It is known that the amount of adamantanes in oils directly depends on their chemical composition. The highest content of adamantane is typical for the naphthenic type of oils. Our data clearly show a direct relationship between the concentration of the naphthenic hydrocarbons and adamantanes in oils, i.e., naphthenic oils have a higher amount of adamantanes. It indicates that the degree of transformation of the polycyclic hydrocarbons into adamantanes and their isomers is much higher in a naphthenic type of oil. A high concentration of adamantanes in some of the samples could be due to intensive transformations due to thermal destructions or biodegradation. The correlation of the distributions of adamantane hydrocarbons and their isomers from various oil samples shows a good relationship between individual isomers that could suggest common mechanisms for forming adamantanes in the study area. As per the formation of adamantanes, there could be different mechanisms to

Table 1 Biomarkers in oils—guneshli field, absheron archipelago

Well #	Adamantanes, % C10:C11:C12:C13	C11/C10	C12/C11	C13/C12	C11/C13	C12/C13
135	10:35:40:25	3.6	1.14	0.63	1.4	1.6
250	7:31:36:27	4.43	1.16	0.75	1.15	1.33
136	5:27:40:27	5.4	1.48	0.67	1	1.48
293	23:29:30:17	1.26	1.03	0.56	1.7	1.76
244	5:37:25:33	7.4	0.68	1.32	1.12	0.76
212	3:19:37:37	6.3	1.94	1	0.51	1

consider here, including thermal cracking of n-alkanes, saturated hydrocarbons, and polar components (Chen et al., 1996; Giruts & Gordadze, 2007; Giruts et al., 2014; Goodwin et al., 2020). This will require high temperatures and thus deep-buried source rocks in the cold South Caspian Basin case. The formation of adamantanes could occur during the migration of hydrocarbon fluids from the deeper strata due to chemical transformations and isomerization processes. The presence of acid catalysts (clays) is an important criterion here. This subject requires further analytical work and modeling.

5 Conclusions

- Adamantanes and their homologs have been identified in soil samples from various depths, stratigraphic ages, and locations in the Absheron archipelago and South Caspian Basin fields.
- Chromato-mass spectrometry data show the following distribution of the adamantane and its methyl substitutions: 2–MAd > 1-MAd > 3-MAd > Ad. The such distribution suggests the formation of adamantanes due to thermal transformations of normal alkanes.
- A high amount of adamantanes, low geothermal gradients, and potential formation mechanisms of adamantanes described above suggest the presence of deeper buried source rocks (deeper than 8 km in the case of the cold South Caspian Basin) to support temperatures enough to form mature source rocks that generate hydrocarbon fluids accumulated in the study area.

References

Chen, J., Fu, J., Sheng, G., Liu, D., & Zhang, J. (1996). Diamondoid hydrocarbon ratios: Novel maturity indices for highly mature crude oils. *Organic Geochemistry, 25*, 179–190.

Giruts, M. V., & Gordadze, G. N. (2007). Generation of adamantanes and diamantanes by thermal cracking of polar components of crude oils of different genotypes. *Petroleum Chemistry, 47*(1), 12–22.

Giruts, M. V., Gordadze, G. N., Stroeva, A. R., Stokolos, O. A., Bogatyrev, S. O., & Koshelev, V. N. (2014). Generation of hydrocarbons having adamantine structure from bacterial biomass. *Chemistry and Technology of Fuels and Oils, 50*(4), 290–298.

Goodwin, N., Abdullayev, N., Javadova, A., Volk, H., & Riley, G. (2020). Diamondoids and basin modeling reveal one of the world's most profound petroleum systems, the South Caspian basin. *Azerbaijan. Journal of Petroleum Geology, 43*(2), 133–150.

Peters, K. E., & Moldowan J. M. (1993). *The biomarker guide: interpreting molecular fossils in petroleum and ancient sediments* (p. 363). Prentice Hall.

Geological Resources and Prospects of Oil- and Gas-Bearing Capacity of Low-Permeability Shale Strata of the Tersko-Caspian Basin

Vagif Kerimov, Rustam Mustaev, and Uliana Serikova

Abstract

An assessment of the initial geological resources of hydrocarbons of the Khadum and Batalpashinsk low-permeability shale strata of the Tersko-Caspian basin is presented. Due to the difficulty of expulsion from predominantly argillaceous deposits, the Khadum and Batalpashinsk oil source rocks are also oil bearing. The degree of hydrocarbon saturation of sediments is determined by the value of the initial generation potential and the degree of its implementation, i.e., by the importance of the pyrolytic parameter S1, which characterizes the number of free hydrocarbons in the parent stratum at the current stage of catagenetic transformation. The volumetric method can calculate the oil and gas deposits and prospective structures. On the territory of the Tersko-Caspian oil and gas basin, according to the degree of prospects of the Maikop deposits, highly promising, medium-promising, low-promising, and unpromising zones are distinguished.

Keywords

Oil • Gas • Resources and reserves • Oil- and gas-bearing capacity • Generation • Migration • Tersko-Caspian oil • Gas-bearing basin

1 Introduction

The Maikop deposits in most of the Tersko-Caspian oil- and gas-bearing basin, covering the Prikumskiy arch, the East Stavropol basin, the Nogai step, and the Tersko-Caspian trough, are characterized by the most remarkable stratigraphic completeness, significant depths of cover (up to 5–6 km), and thicknesses (up to 2 km and more). Natural reservoirs in the Maikop strata (primarily in the Khadum and Batalpashinsk deposits) are represented by horizons of decompacted thinly laminated thin-slabby clays and carbonate rocks (thin interlayers of marls, dolomites, and limestones), interspersed with layers of dense impermeable clays and marls, which serve as hydrodynamic screens.

2 Research Method

To assess the geological resources and oil- and gas-bearing capacity potential of the low-permeability shale strata of the Tersko-Caspian basin, a methodology for modeling hydrocarbon systems was used (Guliev et al., 2018).

3 Results

In the Tersko-Caspian oil- and gas-bearing basin, the Maikop generation-accumulation hydrocarbon system (GAHS) was identified, and the elements of this system were studied. According to laboratory and hydrodynamic studies, the oil reservoirs in the Maikop deposits are thinly laminated claystone-like clays, mudstones of the Batalpashinsk suite, and thin-slabby to thinly laminated mudstones of the Morozkina gully horizon, a characteristic feature of which is decompaction. In the interval of the greatest decompaction of rocks (the boundary of the Batalpashinsk and Khadum suits), fracture porosity ranges from 0.1 to 4.1%, open porosity—up to 22.6% (Gordadze et al., 2017; Kerimov & Rachinsky, 2016).

The Khadum and Batalpashinsk deposits in the geochemical plan are characterized by a more "precious," mainly sapropelic organic matter composition. The share of the sapropelic component in organic matter in the eastern regions of Eastern Ciscaucasia reaches up to 90%. In terms of C_{org} content in the predominant part of this territory, the

V. Kerimov (✉) · R. Mustaev · U. Serikova
Sergo Ordzhonikidze Russian State University for Geological Prospecting, Moscow, Russia
e-mail: vagif.kerimov@mail.ru

A. Çiner et al. (eds.), *Recent Research on Sedimentology, Stratigraphy, Paleontology, Tectonics, Geochemistry, Volcanology and Petroleum Geology*, Advances in Science, Technology & Innovation,
https://doi.org/10.1007/978-3-031-43222-4_53

studied deposits can be classified as "rich" and "very rich" (more than 3%) oil source rocks (Kerimov et al., 2019a). According to the degree of catagenetic transformation, the Khadum deposits are located here within the "main zone of oil formation."

For potentially oil-bearing lands, a ranking was performed according to the degree of prospectivity, emphasizing highly promising, medium-promising, low-promising, and unpromising zones (Fig. 1).

Zones and areas of maximum correspondence (combination) of the most favorable values (characteristics) of parameters (criteria) that determine the conditions for the generation, accumulation, and preservation of hydrocarbon accumulations are allocated to the rank of highly promising lands (Lapidus et al., 2018). As the degree of compliance decreased and the characteristics of the parameters deteriorated, the rest of the territory was ranked with the allocation of medium-promising, low-promising, and unpromising lands.

The central part of Eastern Ciscaucasia, covering most of the Prikumskiy zone of uplifts and the Nogai step, is classified as highly promising for oil. The up-and-coming area includes the discovered oil fields Ozek-Suat, Ozek-Suat Yuzhnoye, Kraevoe, Yuzhnoye, Lesnoye, and Achikulakskoye (Kerimov et al., 2018a). In this part of the territory of the Eastern Ciscaucasia, Khadum deposits are represented by carbonate-argillaceous rocks and contain humic-sapropelic organic matter with TOC concentrations $\geq$ 3% ("very rich"), converted to MK1 and higher grades ("main oil formation zone"); the values of the total generation potential reach 6 mg HC/g of rock and more ("oil source rocks with high generation potential").

The medium-promising territory for oil covers almost the entire rest of the platform part of Eastern Ciscaucasia and most of the Tersko-Caspian forethought. It surrounds the highly promising zone (Mustaev et al., 2016). The western boundary of the distribution of medium-promising lands is the line of demarcation of the sapropelic-humic and humic-sapropelic

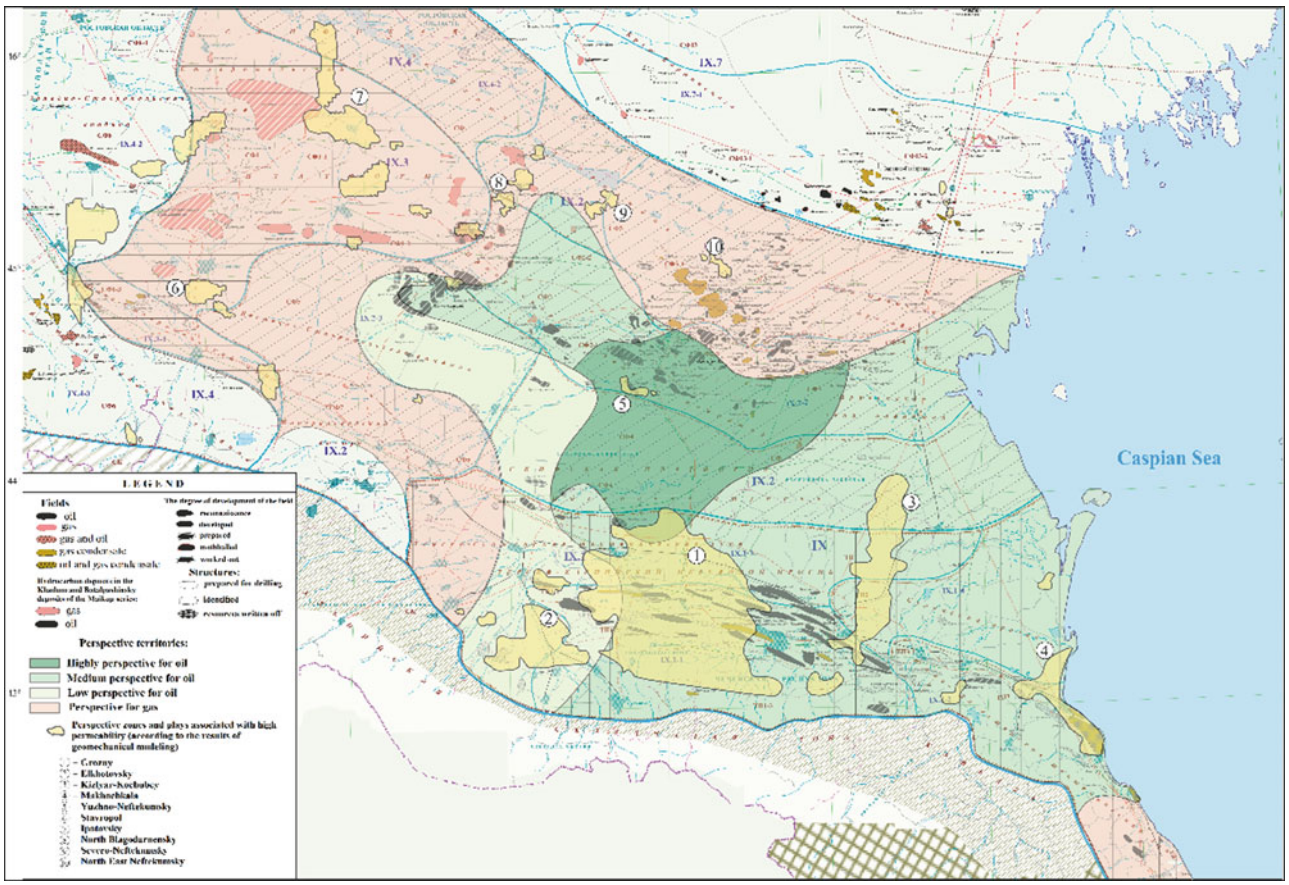

Fig. 1 Map of the perspectivity for oil- and gas-bearing capacity of the Khadum deposits

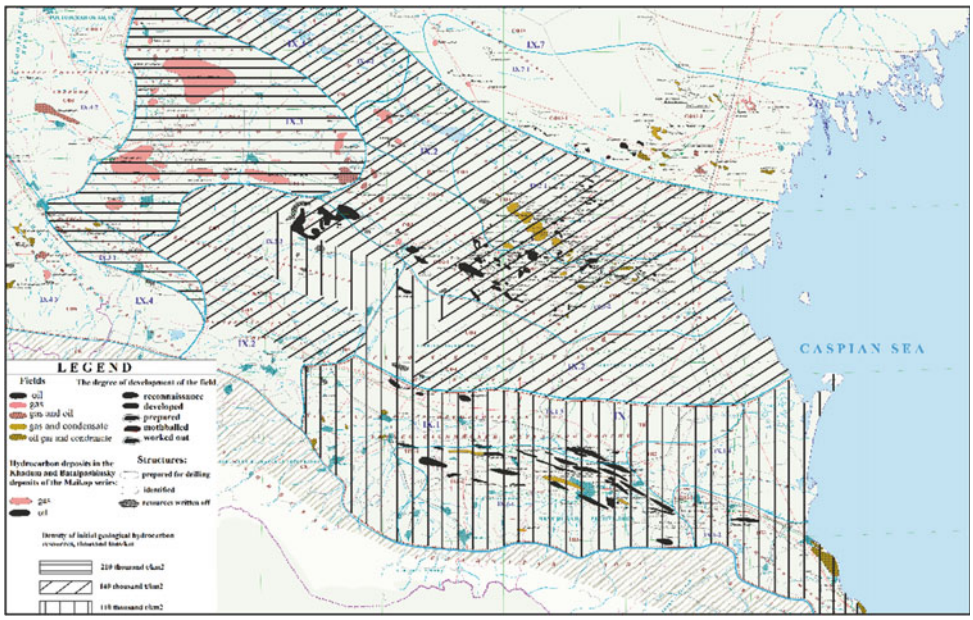

Fig. 2 Density map of the initial geological oil resources of the Khadum suite with differentiation according to zones

subtypes of organic matter of the Khadum deposits. To the east of this line, the content of sapropelic components (more than 50%) prevails in the particulate organic matter of the studied sediments, and to the west, humic components. In the north, medium-promising lands' territory covers the Manych troughs' zone. It is limited by the structural contour T_{max} = 422 °C, corresponding to the PK3/MK1 catagenetic boundary, i.e., the beginning of the "main zone of oil formation" in the considered deposits (Kerimov et al., 2019b). In the eastern direction, it opens into the water zone of the Middle Caspian. The medium-promising area includes the discovered deposits Zhuravskoye, Vorobyevskoye, Pasholkinskoye, Yuzhno-Spasskoye, Iskrinskoye, Kumskoye, Prasko-veyskoye, Mozdokskoye, Shamkhal-Bulak, Benoyskoye, and Karabulak-Achalukskoye.

The volumetric method can calculate deposits' and prospective structures' oil and gas reserves. Moreover, when calculating gas reserves, it is advisable to use a modified version of the volumetric method, which considers the amount of free and adsorbed gas (Kerimov et al., 2018b; Zaicev et al., 2017). Thus, the initial geological resources of hydrocarbons in the Khadum and Batalpashinsk oil source suits within the studied region are 22.8 billion tons, including the Khadum suit—18.4 billion tons, the Batal-pashinsk suite—4.4 billion tons (Fig. 2).

4 Conclusions

On the territory of the Tersko-Caspian oil- and gas-bearing basin, according to the degree of prospectivity of the Maikop deposits, highly promising, medium-promising, low-promising, and unpromising zones are distinguished. The initial total geological resources of hydrocarbons of low-permeability shale strata of the Maikop series—the Khadum and Batalpashinsk oil source suits within the study region—are 22.8 billion tons, including the Khadum suit—8.4 billion tons, the Batalpashinsk suite—4.4 billion tons.

References

Gordadze, G., Kerimov, V., Gaiduk, A., & Romanyuk, T. (2017). Hydrocarbon biomarkers and diamondoid hydrocarbons from late Precambrian and lower Cambrian rocks of the Katanga saddle (Siberian Platform). *Geochemistry International, 55*, 360–366.

Guliev, S., Mustaev, R., Kerimov, V., & Yudin, M. (2018). Degassing of the earth: Scale and implications. *Gornyi Zhurnal, 11*, 38–42. https://doi.org/10.17580/gzh.2018.11.06

Kerimov, V., & Rachinsky, M. (2016). Geofluid dynamic concept of hydrocarbon accumulation in natural reservoirs. *Doklady Earth Sciences, 471*(1), 1123–1125.

Kerimov, V., Gordadze, G., Mustaev, R., & Bondarev, A. (2018a). Formation conditions of hydrocarbon systems on the Sakhalin shelf of the sea of Okhotsk based on the geochemical studies and modeling. *Oriental Journal of Chemistry, 34*(2), 934–947. https://doi.org/10.13005/ojc/340243

Kerimov, V., Mustaev, R., & Osipov, A. (2018b). Peculiarities of hydrocarbon generation at great depths in the crust. *Doklady Earth Sciences, 483*(1), 1413–1417.

Kerimov, V., Leonov, M., Osipov, A., Mustaev, R., & Hai, V. (2019a). Hydrocarbons in the basement of the South China Sea (Vietnam) shelf and structural-tectonic model of their formation. *Geotectonics, 53*(1), 42–59.

Kerimov, V., Osipov, A., Mustaev, R., Minligalieva, L., & Huseynov, D. (2019b). Conditions of formation and development of the void space at great depths. *Neftyanoe Khozyaystvo—Oil Industry, 4*, 22–27.

Lapidus, A., Kerimov, V., Mustaev, R., Movsumzade, E., & Zakharchenko, M. (2018). Caucasus Maykopian kerogenous shale sequences: Generative potential. *Oil Shale, 35*(2), 113–127.

Mustaev, R., Kerimov, V., Shilov, G., & Dmitrievsky, S. (2016). Modeling of thermobaric conditions formation of the shale hydrocarbon accumulations in low-permeability reservoirs Khadum formation Ciscaucasia. In *Geomodel 2016—18th Science and Applied Research Conference on Oil and Gas Geological Exploration and Development*.

Zaicev, V., Kerimov, V., Mustaev, R., & Dmitrievskij, S. (2017). Geomechanical modeling of low permeability shale strata of the Maikop series Ciscaucasia. In *EAGE/SPE Joint Workshop on Shale Science 2017: Prospecting and Development*.

Results of Modeling the Hydrocarbon Systems of the Bering Sea

Elena Lavrenova, Sanan Guryanov, Vadim Kosyanov, and Vagif Kerimov

Abstract

Based on the results of modeling hydrocarbon systems, regional features of generation, migration, and accumulation of hydrocarbons within the marine part of the Gulf of Anadyr of the Bering Sea have been determined. Based on the obtained modeling and basin analysis results, hydrocarbon generation-accumulation system (HGAS) maps were created for all studied sedimentary complexes using Schlumberger's PetroMod and QGIS software systems. The studied hydrocarbon systems differ in the area and size of the generation center and hence in the volumes of produced hydrocarbons. Therefore, the maximum specific volumes of generated hydrocarbons are predicted in the Mainitsko-Sobolkovskaya HGAS of the East Anadyr basin.

Keywords

Modeling • Hydrocarbon system • Bering Sea • Oil • Gas • Generation • Accumulation

1 Introduction

Within the framework of this project, HGAS, located in the water zones of the Anadyr Trough, is considered. In the sediments of the Paleogene-Lower Miocene, the following HGAS are found: Mainitsko-Sobolkovskaya HGAS of the East Anadyr basin, Nikolaev Mainitsko-Sobolkovskaya HGAS, Mainitsko-Sobolkovskaya HGAS of the Lagunny Trough, Solomatin Mainitsko-Sobolkovskaya HGAS, Uelkal Mainitsko-Sobolkovskaya HGAS, Kurimskaya Mainitsko-Sobolkovskaya HGAS, Enmelen Mainitsko-Sobolkovskaya HGAS (Guliev et al., 2018; Guliyev et al., 2017).

All systems are characterized by synchronous oil-and-gas source strata of the Mainitskaya strata, reservoirs of the Sobolkovskaya suite, and impermeable seals of the Lower Miocene following the given model conditions, as well as the same period of trap formation, which is determined by the peculiarities of the development of the Anadyr Trough and phases of tectonic activation in the region.

2 Research Method

Based on the obtained modeling and basin analysis results, HGAS maps were created for all studied sedimentary complexes using Schlumberger PetroMod and QGIS software systems (Gordadze et al., 2017).

3 Results

The studied hydrocarbon systems differ in the area and size of the generation center and hence in the volumes of produced hydrocarbons (Zaitsev et al., 2017). The maximum specific (per unit area of HGAS) volumes of generated hydrocarbons are predicted in the Mainitsko-Sobolkovskaya HGAS of the East Anadyr basin, Nikolaev Mainitsko-Sobolkovskaya HGAS, and Mainitsko-Sobolkovskaya HGAS of the Lagunny Trough. However, even in the most promising areas, good lands are at the level of category V due to the low quality of kerogen and a low accumulation coefficient.

4 Discussion

In the majority of HGAS, the maturity of the organic matter of the oil and gas source strata does not exceed the level of the "oil window" (Fig. 1). In the most submerged parts of

E. Lavrenova · S. Guryanov (✉) · V. Kosyanov · V. Kerimov
Sergo Ordzhonikidze Russian State University for Geological Prospecting, Moscow, Russia
e-mail: guryanov_1996@inbox.ru

E. Lavrenova
ASAP «Service», Gelendzhik, Russia

A. Çiner et al. (eds.), *Recent Research on Sedimentology, Stratigraphy, Paleontology, Tectonics, Geochemistry, Volcanology and Petroleum Geology*, Advances in Science, Technology & Innovation,
https://doi.org/10.1007/978-3-031-43222-4_54

the generation centers of the systems of the Mainitsko-Sobolkovskaya of the East Anadyr basin and the Nikolaev Mainitsko-Sobolkovskaya, oil and gas source strata are in the area of predominant generation of gaseous hydrocarbons.

Accordingly, the degree of organic matter depletion of the parent rocks also differs. The shortage of the HGAS kerogen of the Krest Trough does not exceed 40%. In the hydrocarbon systems of the Nikolaev Mainitsko-Sobolkovskaya HGAS, the Mainitsko-Sobolkovskaya HGAS of the Lagunny Trough, and the Solomatin Mainitsko-Sobolkovskaya HGAS, the degree of the generation potential of kerogen approaches to 60%. In the central part of the Mainitsko-Sobolkovskaya HGAS of the East Anadyr basin, the potential is almost entirely implemented (Kerimov et al., 2018a).

The different degree of implementation of the generation potential of hydrocarbon systems determines the differences in the period of critical moment occurrence, which varies from 8 million years (Mainitsko-Sobolkovskaya HGAS of the East Anadyr basin) to 3 million years (Solomatinskaya Mainitsko-Sobolkovskaya HGAS) (Kerimov & Rachinsky, 2016). In general, the temporal relationship between the periods of formation of traps and the occurrence of the critical moment is favorable for all hydrocarbon systems in the water zone of the Anadyr Trough.

In most of the HGAS, the maturity of the organic matter of the oil and gas source strata does not exceed the level of early oil generation. Only the parent rocks of the Koryakskaya Gagarinsko-Avtatkulskaya system and the Gagarinsko-Avtatkulskaya HGAS of the Lagunny Trough reached the oil window level.

All Neogene HGAS are characterized by a meager degree of implementation of the generation potential of their oil and gas source strata—not exceeding mainly 10%, which is due to the low maturity of the organic matter of the rocks (Kerimov et al., 2018b). Only in the Gagarinsko-Avtatkulskaya HGAS of the Lagunny Trough, the generation potential of the parent rock is realized at 20–30%, and in the Koryakskaya Gagarinsko-Avtatkulskaya one—about 40%.

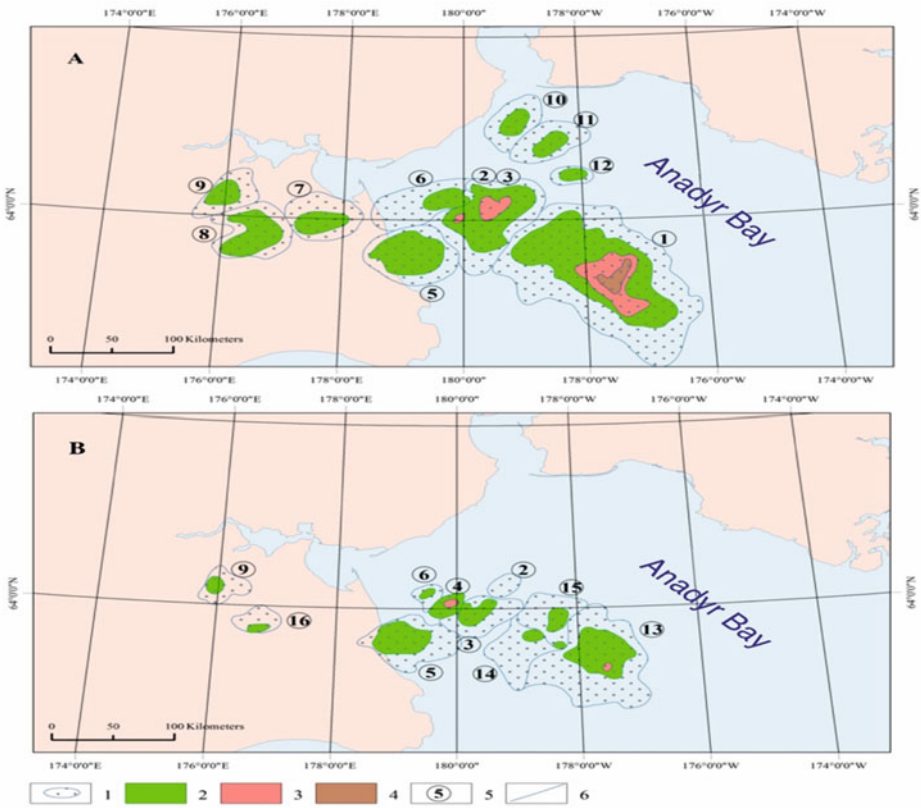

Fig. 1 Hydrocarbon generation and accumulation systems (HGAS) of the Anadyr oil and gas field according to the modeling results (generalized): A—Eocene-lower Miocene, Mainitsko-Sobolkovskaya deposits, B—lower-middle Miocene, Gagarinsko-Avtatkulskaya deposits. 1—the area of development of HGAS, 2—the area of predominant generation of oil in the center, 3—the area of predominant generation of gas, 4—the area of development of overmature rocks, 5—the index of HGAS, and 6—coastline. Numbers in circles (HGAS): 1—East Anadyr, 2—North Nikolaev, 3—South Nikolaev, 4—West Nikolaev, 5—Lagunny Trough, 6—Solomatinskaya, 7—Oleninskaya, 8—Mainitskiy Trough, 9—Velikorechenskaya, 10—Uelkal, 11—Kurimskaya, 12—Enmelen, 13—Koryakskaya, 14—South Chukotka, 15—North Chukotka, and 16—Protochnyi Trough

The low degree of implementation of the generation potential of the considered oil and gas source strata determines the low value of the generation and expulsion potential—about 70 billion tons of hydrocarbons in total for all HGAS (Mustaev et al., 2016).

5 Conclusions

The hydrocarbon systems of the Paleocene-Lower Miocene part of the sedimentary section differ in the area and size of the generation center and, accordingly, in the volumes of hydrocarbons produced. The most promising is the Nikolaev Mainitsko-Sobolkovskaya HGAS. On the other hand, all the Lower–Upper Miocene hydrocarbon systems of the Gulf of Anadyr are characterized by a shallow degree of implementation of the generation potential of their oil and gas source strata, which is due to the low maturity of the organic matter of the rocks. This fact determined the shallow hydrocarbon potential of the Miocene part of the sedimentary section.

References

Gordadze, G. N., Kerimov, V. Yu., Gaiduk, A. V., ... Romanyuk, T. V. (2017). Hydrocarbon biomarkers and diamondoid hydrocarbons from late Precambrian and lower Cambrian rocks of the Katanga saddle (Siberian Platform). *Geochemistry International, 55*, 360–366.

Guliyev, I. S., Kerimov, V. Y., Osipov, A. V., & Mustaev, R. N. (2017). Generation and accumulation of hydrocarbons at great depths under the earth's crust. In *SOCAR Proceedings* (Vol. 1, pp. 4–16).

Guliev, S., Mustaev, R. N., Kerimov, V. Y., & Yudin, M. N. (2018). Degassing of the earth: Scale and implications. *Gornyi Zhurnal, 11*, 38–42.

Kerimov, V. Y., & Rachinsky, M. Z. (2016). Geofluid dynamic concept of hydrocarbon accumulation in natural reservoirs. *Doklady Earth Sciences, 471*(1), 1123–1125.

Kerimov, V. Y., Mustaev, R. N., & Osipov, A. V. (2018a). Peculiarities of hydrocarbon generation at great depths in the crust. *Doklady Earth Sciences, 483*(1), 1413–1417.

Kerimov, V. Y., Gordadze, G. N., Lapidus, A. L., Zhagfarov, F. G., ... Zakharchenko, M. V. (2018b). Physicochemical properties and genesis of the asphaltites of Orenburg Oblast. *Solid Fuel Chemistry, 52*(2), 128–137.

Mustaev, R. N., Kerimov, V. Y., Shilov, G. Y., & Dmitrievsky, S. S. (2016). Modeling of thermobaric conditions formation of the shale hydrocarbon accumulations in low-permeability reservoirs khadum formation Ciscaucasia. In *Geomodel 2016—18th Science and Applied Research Conference on Oil and Gas Geological Exploration and Development*.

Zaitsev, V. A., Kerimov, V. Y., Ryabukhina, S. G., & Bondarev, A. V. (2017). Modern geodynamics and its influence on the secondary filtration properties of the reservoirs of the northeastern part of the Sakhalin Shelf. *Moscow University Geology Bulletin, 72*(6), 391–398.

Integrated Technique on Static and Dynamic Properties Estimation: An Application of Probabilistic Neural Network and Seismic Inversion

Chukwuemeka Abbey, Chukwudi Meludu, Adetola Sunday Oniku, Abraham Sebastian, and Mohammed Aminu

Abstract

This research work used well logs and 3D seismic volume to extract the dynamic and static properties. First, the analyzed reservoir was identified from the well log using the gamma-ray log and resistivity at the low gamma interval corresponding to a high resistivity value. Next, a synthetic seismogram was generated, which was used in tying the wells to the seismic data to identify events (the mapped reservoir) from the seismic volume. This was done by convolving the generated reflectivity series, derived from approximated Zeoppritz reflectivity with a zero-phase wavelet generated from the seismic volume. Finally, a nonlinear statistical relationship, the probabilistic neural network (PNN), was used to define the weight factor to estimate the artificial log from the seismic traces in connection with the seismic attribute. This process makes it easy for the system to recognize the systematic training pattern for the prediction and transforms the seismic attribute into well log data in areas where there are no dill wells. This process is then transformed with the seismic volume and well logs into static and dynamic properties initial-based model used for the seismic inversion. The properties estimated from the seismic volume correspond to the petrophysical analysis performed from the well log at the interval penetrated by the log. These properties include porosity, water saturation, the volume of shale, permeability, pressure, and facies classification. A correlation analysis performed on these properties shows the process's great predictive and estimation ability. This gives a clear insight into the heterogeneity within the formation as it concerns petrophysical properties, fluid flow, and a secondary recovery plan.

Keywords

Seismic inversion • Reservoir • Well logs • Petrophysical properties • Probabilistic neural network

1 Introduction

A reservoir's static and dynamic properties characterize the productivity and producibility of the reservoir, and they are determinant factors in field optimization and recovery planning. These properties comprise the porosity, volume of shale and water saturation, permeability, formation pressure, and, most times, the facies composition of the reservoir. While the porosity and volume of shale give more details on the static properties, pressure and permeability provide insight into its dynamic attributes.

The approach involved in reservoir characterization has a direct implication in its quantification. Over time, the reservoir's productivity and producibility are either underestimated or overestimated due to the adopted approach in properties characterization. This process evolves with time, from the population of reservoir properties estimated from the well log into the mapped seismic volume to seismic inversion, where the acoustic impedance is constrained with a multi-linear transform to characterize reservoirs. This approaches mentioned its shortcomings, with the latter having a bit estimation advantage over the former. Furthermore, the formation heterogeneity makes it impossible to establish a linear relationship between the seismic inversion attributes and reservoir properties.

This calls for a nonlinear approach in estimating these properties from the formation. A probabilistic neural network (PNN) is a nonlinear approach used to estimate artificial logs from seismic traces. The process defines a weight

C. Abbey (✉) · M. Aminu
Department of Petroleum Chemistry and Physics, American University of Nigeria, Yola, Nigeria
e-mail: chukwuemeka.abbey@aun.edu.ng

C. Meludu · A. S. Oniku · A. Sebastian
Department of Physics, Modibbo Adama University of Technology, Yola, Njobbore, Nigeria

A. Çiner et al. (eds.), *Recent Research on Sedimentology, Stratigraphy, Paleontology, Tectonics, Geochemistry, Volcanology and Petroleum Geology*, Advances in Science, Technology & Innovation,
https://doi.org/10.1007/978-3-031-43222-4_55

factor with the seismic attributes in a nonlinear approach to recognize the systematic training pattern used for the prediction (Hampson et al., 2001; Haris et al., 2016). This approach will determine the properties of the seismic volume. And as expected, it will give a clear insight into the heterogeneity within the formation as it concerns petrophysical properties and fluid flow.

2 Materials and Methods

The study area is the Ataga oil field of the Niger Delta. The delta comprises one petroleum system called the Agbada-Akata petroleum system. Petroleum in the Niger Delta is produced from sandstones and unconsolidated sands predominantly in the Agbada Formation (Okpogo et al., 2018), which is from Eocene to Pliocene geologic age. From this field, 3D post-stack seismic data and four wells were provided for the research through the Department of Petroleum Resources (DPR). The data were Qc and loaded into the HR software.

The petrophysical properties were calculated in the wells, with permeability and pore pressure carried out using the Coates empirical formula (Coates & Dumanoir, 1973) and Eatons (Eaton, 1972) depth-dependent formula. A synthetic seismogram was generated, which was used to tie the wells to the seismic data to identify events (the mapped Horizons) from the seismic volume, the analysis interval. This was done by convolving the generated reflectivity series, derived from approximated Zeoppritz reflectivity with a zero-phase wavelet generated from the seismic volume. The acoustic impedance was derived using the model-based seismic inversion approach. PNN was employed in training the multi-attributes and the inverted seismic volume with nonlinear transforms (natural log, exponential, square, inverse, and square root) to establish a training pattern for the process. The desired networks were derived and validated by correlating natural logs and the inverted derived logs from the volume. This transforms the acoustic impedance and the derived reservoir properties in seismic volume within the interval of horizons 1 and 2.

3 Results

The figures below show the predicted properties and the inserted well verifications from the seismic section. Figure 1a is the model of acoustic impedance from the

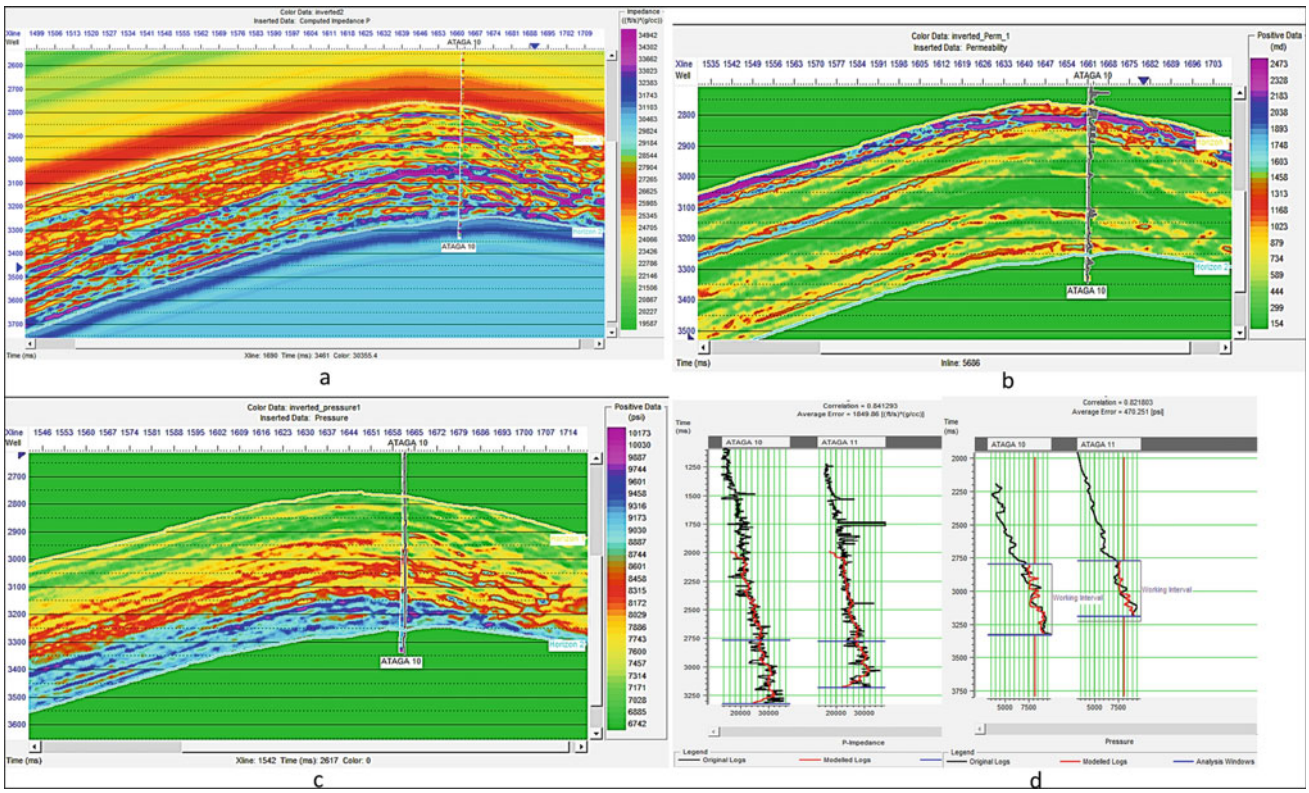

Fig. 1 **a** Acoustic impedance section overlaid with well ten acoustic impedance. **b** Estimated permeability from the section of inline overlaid with the well permeability. **c** Derived formation pressure with the inserted log calculated. **d** correlation of the PNN modeled log derived from the seismic and the original log from the well

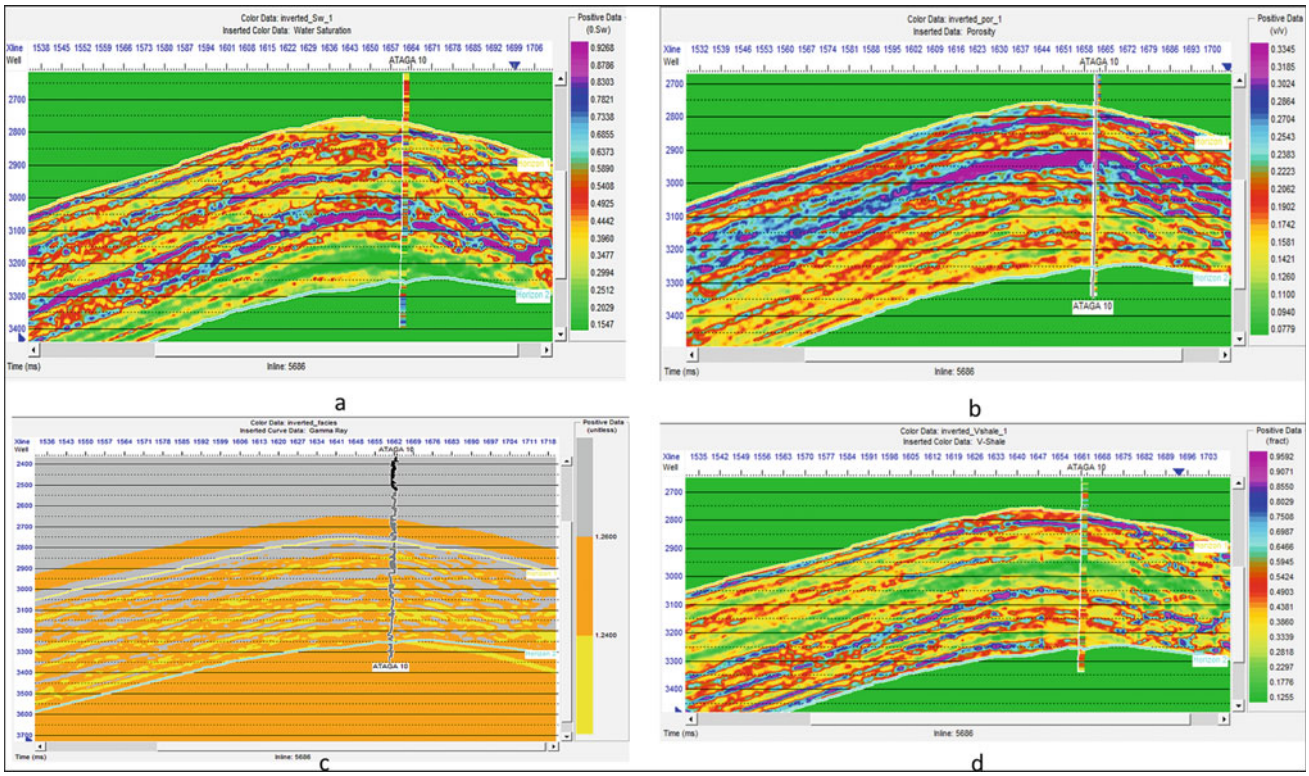

Fig. 2 **a** Estimated Sw in the inline section and the overlaid log Sw from the well, **b** derived porosity in section, **c** the determined facies in the section overlaid with the gamma-ray log, **d** estimated V-shale from the seismic section overlaid with V-shale log from the well

section with an overlay of acoustic impedance from the well. Figure 1b–d are the permeability, formation pore pressure, and the correlation result of the PNN acoustic impedance and the formation pore pressure. Figure 2a–d are the seismic section of water saturation, porosity, faces, and volume of shale, respectively, overlaid by their corresponding logs from the well. The correlation coefficient from the modeled and original logs in the water saturation and V-shale are 0.81 and 0.79, respectively. The porosity is 0.83, and permeability is 0.6. The correlation of the acoustic impedance and formation pore pressure are 0.84 and 0.82, respectively, as shown in Fig. 1d. As shown in Fig. 2c, facies were calibrated using the V_p/V_s ratio with the knowledge of Niger Delta lithology of sand and shale with the Agbada formation to sand, shaly-sand, and shale.

4 Discussion

The results obtained from this integration give a clear insight into the petrophysical properties of the field. The acoustic impedance (AI) volume in Fig. 1a shows an increase in impedance with an increase in burial depth, corresponding with the well-computed impedance. As the depth of burial increases, the density and p-velocity, which are the product of AI of the formation, increase due to compaction in normal compacted sediment. The studied interval, which is then mapped horizons, is believed to be in the region of the Agbada formation of the Niger Delta. This formation mainly consolidated sandstones with intercalation of shales.

The mapped interval comprises reservoirs and non-reservoir sands, and shales. There is a potential reservoir within 2950–3050 ms penetrated by well 10. This interval reveals a low shale volume (0.12–026 v/v), moderate to good porosity (0.1–0.28 v/v), Sw of 0.26–0.63 v/v, and permeability of 197–713 md. The facies within this range are sand and shaly-sand. This interval corresponds to a high resistivity from the well log, making it a hydrocarbon zone of interest. Also, at an interval of 3150–3250 ms, there is a potential hydrocarbon reservoir with Sw range from 0.14 to 0.32 v/v, V-shale, 0.27 to 0.6 v/v, porosity 0.13 to 0.18 v/v, and permeability 236–1486 md. This interval also corresponds to a high resistivity value from the log. From the results estimated at these intervals, the variations in values result from sand and intercalation of sand and shale within these analyzed units. The lateral variation in reservoir properties is conspicuous, and fluid flow can be worked out. More so, the interval of the high volume of shales (2800–

2850 ms) corresponds to high water saturation and indicates shale, as seen in the facie section, also having a high acoustic impedance.

The variations observed in the figures inform the heterogeneity of the formation, which is a characteristic of deposition. The formation pressure shows that pressure increases with depth, with a normal trend of increased pressure through the Agbada to Akata formations. And the formation pressure at these intervals mentioned is suitable for hydrocarbon drive and recovery.

5 Conclusions

The application of PNN in transforming the multi-attributes and the acoustic impedance volume derived from seismic inversion as an external constraint in multi-attribute analysis has proven to be a good approach. This approach extracts the nonlinear relationship between natural logs, seismic inversion, and other multi-attributes in estimating reservoir properties from the seismic volume, as shown in this work. The result obtained from the correlation of the natural logs and modeled logs confirms that PNN is a reliable tool in reservoir properties estimation from the seismic volume.

References

Coates, G. R., & Dumanoir, J. L. (1973). A new approach to improved log derived permeability. In *Proceedings of the SPWLA 14th Annual Logging Symposium held in Lafayette* (pp. 1–28).

Eaton, B. A. (1972). The effect of overburden stress on geopressure prediction from well logs. *Journal of Petroleum Technology, 24* (08), 929–934. https://doi.org/10.2118/3719-pa

Hampson, D. P, Schuelke, J. S., & Quirein, J.A. (2001). Use of multiattribute transforms to predict log properties from seismic data. *Geophysics, 66*(1), 220–236.

Haris, A. Sitorus, R. J., & Riyanto, A. (2017). Delineating chalk sand distribution of Ekofisk formation using probabilistic neural network (PNN) and stepwise regression (SWR): case study Danish North Sea Field. In *Proceeding South East Asian Conference on Geophysics, Bali, 2016 (IOP Conference Series: Earth and Environmental Science*) (Vol. 62, pp. 012021).

Okpogo, E. U., Chukwuemeka, P. A., & Atueyi, I. O. (2018). Reservoir characterization and volumetric estimation of Orok Field, Niger Delta hydrocarbon province. *Egyptian Journal of Petroleum, 27*(4), 1087–1094. https://doi.org/10.1016/j.ejpe.2018.03.014

Assessment of Geological Risks and the Probability of Discovering Oil and Gas Fields in the Bering Sea

Sanan Guryanov, Vagif Kerimov, and Vadim Kosyanov

Abstract

Increasing the efficiency of geological exploration at different stages is associated with improving accounting methods and minimizing geological risks. This requires an analysis of hydrocarbon systems and their elements (oil source strata, container rocks, impermeable seals, and traps) and dynamic processes (generation, migration, and accumulation of hydrocarbons). The presence of an active hydrocarbon generation-accumulation system (GAHS). The Anadyr trough is confirmed by numerous oil and gas shows and fields identified in its land part. The Anadyr trough is located in the Bering Sea. Geochemical studies of sedimentary rocks and fluids have shown that deposits of the Upper Cretaceous, Paleogene, and Neogene can be the source of these hydrocarbons. The results of seismic-geological correlation and the performed paleogeographical reconstructions showed that the area of development of probable source rock would spread to the area of the water zone, where an improvement in their generation properties is predicted. An assessment of geological risks was performed in the search and exploration of hydrocarbon deposits. The paper has tested a methodology for assessing geological risks for geological exploration in the Bering Sea.

Keywords

Oil • Gas • Resources and reserves • Risks • Generation • Migration • Bering Sea

1 Introduction

The presence of an active generation-accumulation system (GAHS) within the Anadyr trough is confirmed by numerous oil and gas shows and fields identified in its land part. Geochemical studies of sedimentary rocks and fluids have shown that deposits of the Upper Cretaceous, Paleogene, and Neogene can be the source of these hydrocarbons. The deposits of the gagarinskaya suit of the Miocene have the highest generation potential, for which relatively increased values of the hydrogen index and organic carbon are noted (Guliev et al., 2018). The results of seismic-geological correlation and the performed paleogeographical reconstructions showed that the area of development of probable oil and gas source strata (OGSS) would spread to the area of the water zone, where an improvement in their generation properties is predicted.

2 Research Method

The methodology comprehensively analyzes geological information about oil and gas source rocks, reservoirs, and seals. It includes four main factors: the presence and properties of oil source strata, the presence, and properties of a pool, the presence of a trap, the ratio of the time of formation of traps, and the process of generation and migration of hydrocarbon accumulation.

3 Results

The results of the performed modeling of hydrocarbon systems showed that, given the present generation properties of potential OGSS, the conditions of their occurrence and the thermal history of the basin, and the peculiarities of its development, the OGSS could provide the traps identified by hydrocarbons (Gordadze et al., 2017; Kerimov &

S. Guryanov (✉) · V. Kerimov · V. Kosyanov
Sergo Ordzhonikidze Russian State University for Geological Prospecting, Moscow, Russia
e-mail: guryanov_1996@inbox.ru

A. Çiner et al. (eds.), *Recent Research on Sedimentology, Stratigraphy, Paleontology, Tectonics, Geochemistry, Volcanology and Petroleum Geology*, Advances in Science, Technology & Innovation,
https://doi.org/10.1007/978-3-031-43222-4_56

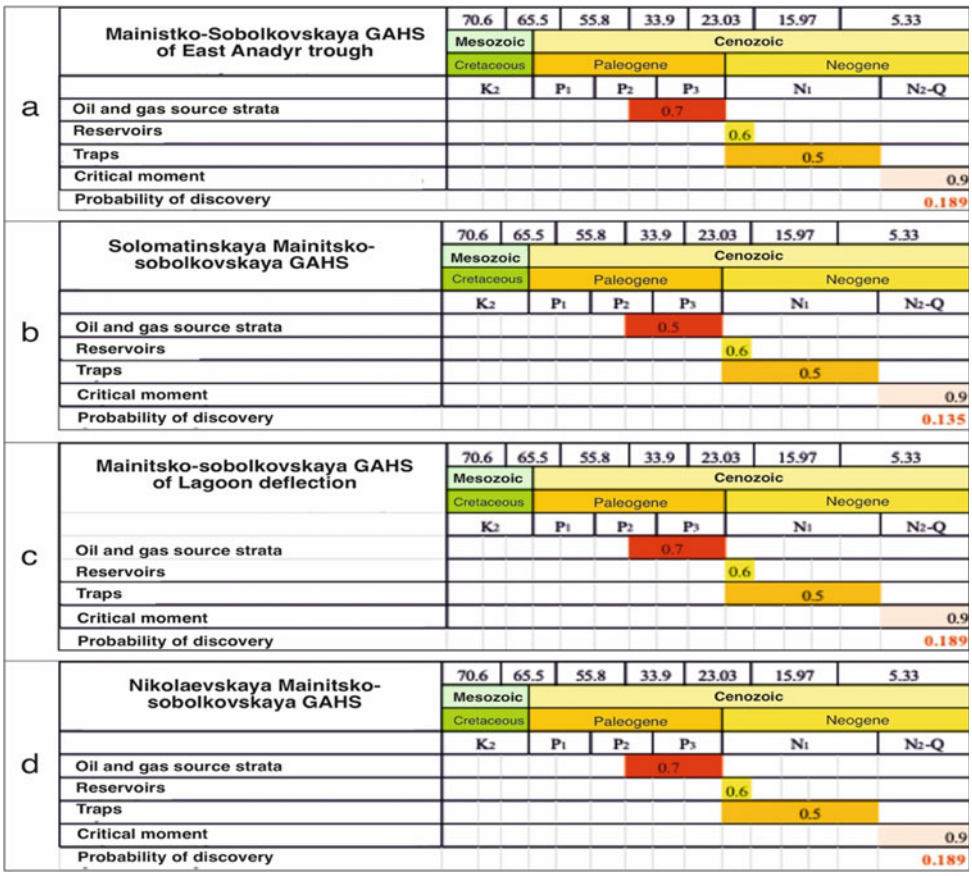

Fig. 1 GAHS maps of the Aptian-Upper Cretaceous complex

Rachinsky, 2016). However, as noted earlier, hydrocarbon generation centers' generation and expulsion potential varies significantly from system to system. Therefore, manito-Sobolkovskie GAHS is characterized by better performance than the Gagarin-Avtakul one. Accordingly, the risks for the factor "Assessment of oil and gas source strata" are assessed from "neutral" to "favorable," taking into account the calculated characteristics of the expulsion potential (Fig. 1). As can be seen from the figures, the highest risks for this factor are characteristic of the GAHS of the Neogene complex (Kerimov et al., 2018a, 2019a; Lapidus et al., 2018; Mustaev et al., 2016).

In the Neogene reservoirs of land deposits, open porosity reaches 30% or more. Therefore, considering those mentioned above, the factor "reservoir assessment" is assessed as "reassuring" − 0.6 for all studied GAHS.

According to the results of seismic studies, it has been established that structural traps are most common in the sedimentary cover of the Anadyr basin—arch-like and tectonically screened (Kerimov et al., 2018b, 2019b; Zaicev et al., 2017). The presence of numerous local erosion and pinch-out zones in combination with structural elements also presupposes the vast development of complex combined traps—structural-stratigraphic and structural-lithological. The areas of structural (anticlinal) traps in Neogene deposits vary from 250 km^2 (Tsentralnaya structure) to 30 km^2 (Vostochno-Vasilievskaya-2, Shakhtyorskaya-2 structures). Closed structural contours of promising objects are located at a level from − 2.4 km (Tsentralnaya structure) to − 1.5 km (Ploskaya structure) from the sea bottom surface. Large areas are typical for pinch-out traps—up to 930 km^2.

4 Conclusions

At the current level of knowledge of the Anadyr trough, the main geological risks are associated with the ability of OGSS to saturate bright objects and the quality of the trap—the presence and quality of the fluid-resistant matter. As a result, the probability of hydrocarbon field discovery in the water zone of the Anadyr trough varies from 0.162 to 0.189 in the lower prospective complex and from 0.135 to 0.162 in the upper one. This corresponds to moderate geological risk.

References

Gordadze, G., Kerimov, V., Gaiduk, A., & Romanyuk, T. (2017). Hydrocarbon biomarkers and diamondoid hydrocarbons from the Katanga saddle's late Precambrian and lower Cambrian rocks (Siberian Platform). *Geochemistry International, 55*, 360–366.

Guliev, S., Mustaev, R., Kerimov, V., & Yudin, M. (2018) Degassing of the earth: Scale and implications. *Gornyi Zhurnal, 11*, 38–42. https://doi.org/10.17580/gzh.2018.11.06

Kerimov, V., & Rachinsky, M. (2016). Geofluid dynamic concept of hydrocarbon accumulation in natural reservoirs. *Doklady Earth Sciences, 471*(1), 1123–1125.

Kerimov, V., Gordadze, G., Mustaev, R., & Bondarev, A. (2018a). Formation conditions of hydrocarbon systems on the Sakhalin shelf of the sea of Okhotsk based on the geochemical studies and modeling. *Oriental Journal of Chemistry, 34*(2), 934–947). https://doi.org/10.13005/ojc/340243

Kerimov, V., Mustaev, R., & Osipov, A. (2018b). Peculiarities of hydrocarbon generation at great depths in the crust. *Doklady Earth Sciences, 483*(1), 1413–1417.

Kerimov, V., Leonov, M., Osipov, A., Mustaev, R., & Hai, V. (2019a). Hydrocarbons in the basement of the South China Sea (Vietnam) shelf and structural-tectonic model of their formation. *Geotectonics, 53*(1), 42–59.

Kerimov, V., Osipov, A., Mustaev, R., Minligalieva, L., & Huseynov, D. (2019b). Conditions of formation and development of the void space at great depths. *Neftyanoe Khozyaystvo—Oil Industry, 4*, 22–27.

Lapidus, A., Kerimov, V., Mustaev, R., Movsumzade, E., & Zakharchenko, M. (2018). Caucasus Maykopian kerogenous shale sequences: Generative potential. *Oil Shale, 35*(2), 113–127.

Mustaev, R., Kerimov, V., Shilov, G., & Dmitrievsky, S. (2016). Modeling of thermobaric conditions formation of the shale hydrocarbon accumulations in low-permeability reservoirs khadum formation Ciscaucasia. In *Geomodel 2016—18th Science and Applied Research Conference on Oil and Gas Geological Exploration and Development*.

Zaicev, V., Kerimov, V., Mustaev, R., & Dmitrievskij, S. (2017). Geomechanical modeling of low permeability shale strata of the Maikop series Ciscaucasia. In *EAGE/SPE Joint Workshop on Shale Science 2017: Prospecting and Development*.

Influence of Trap Magmatism on the Oil and Gas Potential of Sedimentary Deposits

Andrei Shilovskii

Abstract

The depletion of hydrocarbon reserves in the known traditional structural traps leads to an increase in the share of so-called hard-to-recover or substandard resources, which, consequently, leads to an increase in the cost of production. Consequently, there is always a demand for highly profitable oil and gas reserves. Furthermore, the well-known facts of the association of hydrocarbon manifestations and regions with traces of plutonic activity make it necessary to study the possibility of the formation of oil and gas traps under these conditions. It turns out that trap magmatism can be a source of a hydrocarbon formation and, in addition, forms the conditions for the formation of oil and gas traps.

Keywords

Trap magmatism • Oil and gas potential • Sedimentary deposits • Normal sedimentation • Carbon dioxide • Hydrogen • Carbonates

1 Introduction

The issues of prospecting and exploration of hydrocarbon raw materials against the background of, as it is declared, the depletion of known readily available reserves remain the most critical tasks facing oil and gas science. The notorious energy transition, even if partially completed, can be realized only on the basis and at the expense of the resources of the existing hydrocarbon fuel and energy complex. In any case, the fuel and energy complex, primarily the oil and gas industry, will remain the driving force of the economy for many decades.

2 Settings or Methods or Materials and Methods or … Etc.

Analysis of the mechanisms of formation of oil and gas traps consisting in the association of reservoir rocks sealed by rocks–seals. The well-known facts of accompanying magmatic formations with hydrocarbon manifestations (Jamkhindikar & Mukesh Jain, 2013; Ren et al., 2020; Schutter, 2003; Liu et al., 2012; KamNIIKIGS, 1996; Shilovsky, 2013). In total suggest the need to study the possibility of the formation of oil and gas traps due to the influence of plutonic processes.

The first thing that immediately catches the eye is that rock formations of acidic magmatism, due to the high viscosity of the magma, when solidified, form relatively local bodies: dikes, stocks during an intrusive eruption, or cones, domes of a diatreme during effusions. From the point of view of the possibility of creating traps for hydrocarbons, they are hard of interest. Quite different conditions are created during the basic trap magmatism.

Such a grandiose event as trap magmatism at different times affected all tectonic units of our planet. In terms of area, trap magmatism covers platform areas of hundreds and thousands of square kilometers. The scale of this phenomenon can be estimated by the map in Fig. 1. Moreover, the map shows only surface manifestations of trap magmatism. When a chamber of trap magmatism is activated, magmatic matter (mainly basalts), with sufficient eruption power, penetrates the entire sedimentary stratum, involving the enclosing sedimentary rocks; therefore, not only basalts but also various types of diabases are poured on the surface, i.e.,, rocks of trap formations are formed. Due to the low viscosity of the magmatic melt, it spreads over vast territories, filling all the unevenness of the relief. Then, the trap

A. Shilovskii (✉)
Oil and Gas Research Institute of Russian Academy of Science, 119333 Moscow, Russia
e-mail: ashilovsky08@gmail.com

A. Çiner et al. (eds.), *Recent Research on Sedimentology, Stratigraphy, Paleontology, Tectonics, Geochemistry, Volcanology and Petroleum Geology*, Advances in Science, Technology & Innovation,
https://doi.org/10.1007/978-3-031-43222-4_57

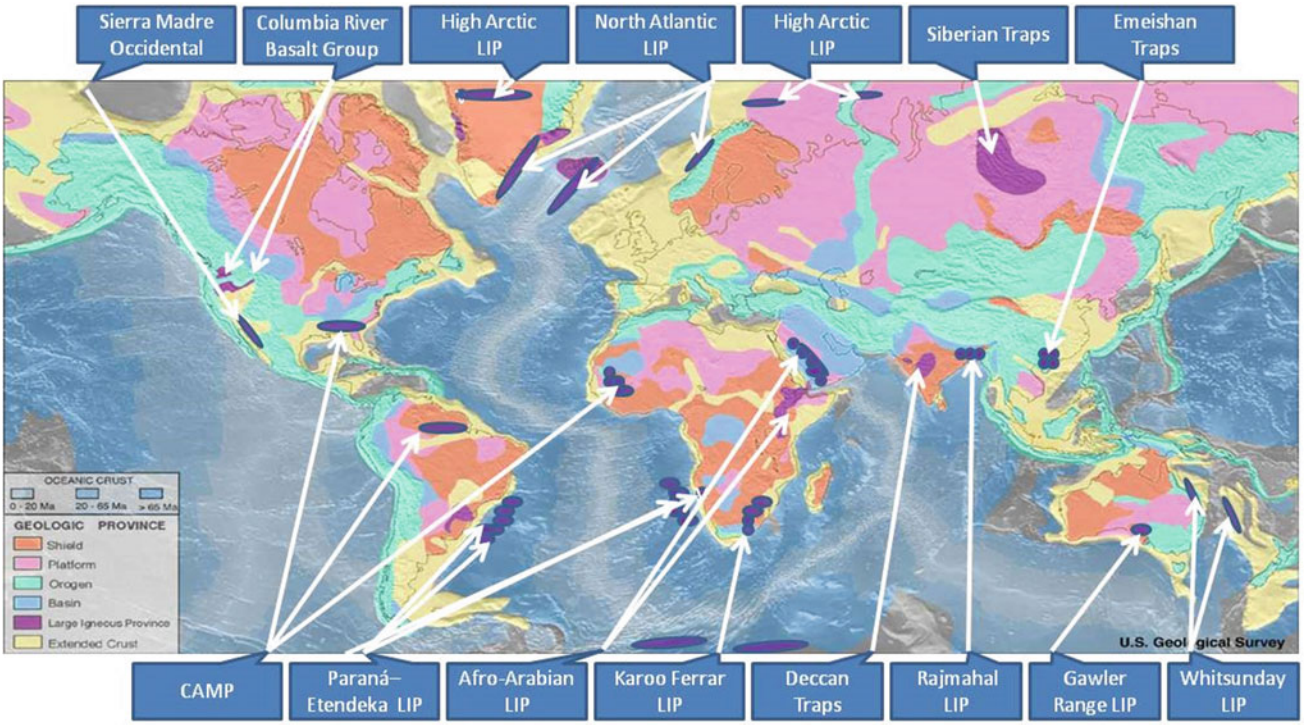

Fig. 1 Only a few of the largest igneous provinces appear (colored dark purple) on this geological map, which depicts crustal geologic provinces as seen in seismic refraction data (https://commons.wikimedia.org/w/index.php?curid=15990676)

fields are covered with new sediments either until the next cycle of magmatic activation, and there are up to several tens of them in a row, or normal sedimentation occurs when trap magmatism decays. That is, the ancient platforms have all the conditions for the presence of buried trap covers.

3 Results

As it rises through the sedimentary strata, the molten magmatic mass, due to the thermal effect, on the one hand, destroys the existing accumulations of hydrocarbons, on the other, increases the oil and gas potential of the enclosing sedimentary deposits by stimulating the catagenesis of dispersed organic matter of plant or animal origin (Jamkhindikar & Mukesh Jain, 2013).

If carbonates represent sedimentary deposits, then under conditions of thermal action, direct transformation of carbonates into hydrocarbons is possible. The process can be schematically represented as follows: under thermal action, the decomposition of carbonates occurs with the release of carbon dioxide, which is converted into methane and heavier hydrocarbons due to the influx of hydrogen formed during the decay of groundwater on the energy-active layer in the pore space (Ryzhenko et al., 2015). For example, in the presence of pyrite:

$$3FeS_2 + 6CaCO_3 + 12H_2O \rightarrow Fe_3O_4 + 6CaSO_4 + 5CH_4 + CO_2 + 2H_2$$

Additionally, in inorganic carbonates, porosity is formed due to thermochemical action in the form of cavities.

The same plutonic process creates conditions for the formation of traps for the hydrocarbons. With a real distribution, molten magmatic matter, accompanied by liquid and gas emanations, forms in the underlying sedimentary rocks the so-called hornfels layer up to 20 m thick, characterized by increased density. The latter is significant from the point of view of creating the oil and gas potential of the underlying sedimentary rocks since a regional seal is created under the crystalline rocks of trap formations (hard but very fragile), that is, in terms of petroleum geology, a regional seal. An example of an industrial oil field within the Deccan trap province can be cited (Jamkhindikar & Mukesh Jain, 2013). In addition, it should be noted that the multistage activation of the trap magmatism process creates conditions for the creation of hydrocarbon traps inside the trap formations due to the intermediate accumulation of sedimentary deposits.

Moreover, the thickness of these intervals reaches several tens of meters (KamNIIKIGS, 1996).

4 Discussion

Trap magmatism plays a vital role on ancient platforms affected by early stages of tectogenesis, which leads to the burial of rocks of trap formations by later sediments at significant depths. In this situation, an additional possibility arises of the formation of deposits of redeposited oils and bitumen in the overlying sediments in the presence of traps (in this situation, it is evident that light fractions will be lost) due to the seepage of hydrocarbons from the subtrap space along cracks formed as a result of tectonic impact (Jamkhindikar & Mukesh Jain, 2013; Liu, 2012).

The practical value of the described mechanism lies in the fact that, for example, a new history of tectonic development has been formulated for the territory of the Moscow sedimentary basin (the Moscow and Mezen syneclises and the Volga-Ural anteclise within the East European Platform). Trap magmatism in this area occurred during the Caledonian phase of tectogenesis, and the rocks of the trap formation are located in the middle of the section in the Lower Devonian sediments. Within the framework of the formulated tectonic structure of a territory with an area of more than 1 million km^2, completely new prospects for the oil and gas potential of the region appear, exceeding, according to the most conservative volume estimates, 20 billion tons of fuel equivalent, even though this territory is still considered unpromising. In addition, the features of the tectonic structure make it possible to substantiate the search criteria for oil and gas traps in the sedimentary strata screened by rocks of trap formations (Shilovsky, 2013).

The analysis of geological and geophysical data and the results of deep drilling made it possible to revise the tectonic structure of the intermediate level of the sedimentary complex of the West Siberian basin with the identification of rocks of trap formations of the Permian–Triassic age, thereby substantiating the direction of strategic development of Russia's largest oil and gas region (Shilovsky, 2016).

5 Conclusions

The above allows us to conclude that trap magmatism plays an active role in increasing the oil and gas potential of sedimentary deposits. This is manifested in the stimulation of the catagenesis of the available organic matter and the direct production of hydrocarbons in the presence of carbonate deposits. In addition, trap magmatism creates conditions for the formation of regional seals.

The buried trap formations create the most favorable conditions for the formation of oil and gas deposits in the sedimentary strata of ancient platforms due to additional screening by overlying sedimentary complexes.

References

Jamkhindikar, A., Jain, M., & Mohanty, S. N. (2013). *Hydrocarbon prospectivity of Deccan trap in Northern Cambay Basin*. https://www.spgindia.org/10_biennial_form/P167.pdf

KamNIIKIGS. (1996). Tyumen superdeep well (interval 0-7502 m). In *Drilling results and research/Scientific drilling in Russia* (Issue 4, p. 374). https://search.rsl.ru/ru/record/01002128724

Liu, J., Wang, P., Zhang, Y., Bian, W., Huang, Y., Tang, H., & Chen, X. (2012). *Volcanic rock-hosted natural hydrocarbon resources: A review*. https://doi.org/10.5772/54587

Ren, K., Zhao, J., Liu, Q., & Zhao, J. (2020). *Hydrocarbons in igneous rock of Brazil: A review*. https://doi.org/10.1016/j.ptlrs.2020.06.001

Ryzhenko, B. N., Sidkina, E. S., & Cherkasova, E. V. (2015). Thermodynamic modeling of water-rock systems to evaluate their generative potential for hydrocarbons. *Geochemistry International, 53*, 825–837. https://doi.org/10.1134/S0016702915090062

Schutter, S. R. (2003). *Occurrences of hydrocarbons in and around igneous rocks* (Vol. 214, pp. 35–68). Geological Society. https://doi.org/10.1144/GSL.SP.2003.214.01.03

Shilovsky, A. P. (2013). Undiscovered hydrocarbon reserves in the depths of the Moscow Sedimentary Basin. *Nedropolzovanie XXI Vek, 3*, 66–69.

Shilovsky, A. P. (2016). West Siberian plate: Analysis of the structure of intermediate stratigraphic stage. *Geology, Geophysics and Development of Oil and Gas Fields, 9*, 25–29.

Williamborg. *Own work—Based on markup of USGS map*. Source: https://commons.wikimedia.org/w/index.php?curid=15990676